INVESTIGATION OF TRANSPORT PROPERTIES OF SITE-SUBSTITUTED SUPERSTRUCTURES OF COMPLEX TRANSITION METAL OXIDES: $(La,Sr)TiO_3/(Ca,Y)VO_3$

A THESIS SUBMITTED TO THE

CENTRAL DEPARTMENT OF PHYSICS

INSTITUTE OF SCIENCE AND TECHNOLOGY

TRIBHUVAN UNIVERSITY

NEPAL

FOR THE AWARD OF

DOCTOR OF PHILOSOPHY

IN PHYSICS

BY

RAJ KUMAR RAI

NOVEMBER 2023

INVESTIGATION OF TRANSPORT PROPERTIES OF THE SITE-SUBSTITUTED SUPERSTRUCTURES OF COMPLEX TRANSITION METAL OXIDES: $(La,Sr)TiO_3/(Ca,Y)VO_3$

A THESIS SUBMITTED TO THE

CENTRAL DEPARTMENT OF PHYSICS

INSTITUTE OF SCIENCE AND TECHNOLOGY

TRIBHUVAN UNIVERSITY

NEPAL

FOR THE AWARD OF

DOCTOR OF PHILOSOPHY

IN PHYSICS

BY

RAJ KUMAR RAI

NOVEMBER 2023

TRIBHUVAN UNIVERSITY

Institute of Science and Technology

DEAN'S OFFICE

Kirtipur, Kathmandu, Nepal

Reference No.:

Institute of Science & Technology
Dean's Office
Kirtipur 2045

EXTERNAL EXAMINERS

The Title of Ph.D. Thesis: "Investigation of Transport Properties of Site-substituted Superstructures of Complex Transition Metal Oxides: (La,Sr) TiO_3/(Ca,Y)VO_3"

Name of Candidate: Raj Kumar Rai

External Examiners:

(1) Prof. Dr. Indra Bahadur Karki
Patan Multiple Campus
Tribhuvan University, NEPAL

(2) Prof. Dr. Rajesh Kumar Shukla
University of Lucknow
Lucknow, INDIA

(3) Prof. Dr. Mohammed Alzuhairi
University of Technology
Baghdad, IRAQ

March 10, 2024

(Dr. Surendra Kumar Gautam)
Asst. Dean

DECLARATION

Thesis entitled "**INVESTIGATION OF TRANSPORT PROPERTIES OF SITE-SUBSTITUTED SUPERSTRUCTURES OF COMPLEX TRANSITION METAL OXIDES: (La,Sr)TiO_3/(Ca,Y)VO_3**" which is being submitted to the Central Department of Physics, Institute of Science and Technology (IOST), Tribhuvan University, Nepal, for the award of the degree of Doctor of Philosophy (Ph.D.), is a research work carried out by me under the supervision of Prof. Dr. Om Prakash Niraula, Central Department of Physics, Tribhuvan University and co-supervised by Assoc. Prof. Dr. Gopi Chandra Kaphle, Central Department of Physics, Tribhuvan University.

This research is original and has not been submitted earlier in part or full in this or any other form to any university or institute, here or elsewhere, for the award of any degree.

.....

Raj Kumar Rai

RECOMMENDATION

This is to recommend that **Mr. Raj Kumar Rai** has carried out research entitled "**INVESTIGATION OF TRANSPORT PROPERTIES OF SITE-SUBSTITUTED SUPERSTRUCTURES OF COMPLEX TRANSITION METAL OXIDES: (La,Sr)TiO_3/(Ca,Y)VO_3**" for the award of Doctor of Philosophy (Ph.D.) in **Physics** under our supervision. To our knowledge, this work has not been submitted for any other degree.

He has fulfilled all the requirements laid down by the Institute of Science and Technology (IOST), Tribhuvan University, Kirtipur for the submission of the thesis for the award of Ph.D. degree.

.....

Dr. Om Prakash Niraula

Supervisor

Professor

Central Department of Physics

Tribhuvan University

Kirtipur, Kathmandu, Nepal

.....

Dr. Gopi Chandra Kaphle

Co-Supervisor

Associate Professor

Central Department of Physics

Tribhuvan University

Kirtipur, Kathmandu, Nepal

November 2023

TRIBHUVAN UNIVERSITY
CENTRAL DEPARTMENT OF PHYSICS
Kirtipur, Kathmandu, Nepal

☎ 4331054
www.tucdp.edu.np

Ref. No.: (F.No .....) CDP .....

Date: .....

LETTER OF APPROVAL

Date: 28/11/2023

On the recommendation of **Prof. Dr. Om Prakash Niraula** and **Associate Prof. Dr. Gopi Chandra Kaphle**, this PhD thesis submitted by **Raj Kumar Rai**, entitled **" INVESTIGATION OF TRANSPORT PROPERTIES OF SITE-SUBSTITUTED SUPERSTRUCTURES OF COMPLEX TRANSITION METAL OXIDES:$(La,Sr)TiO_3/(Ca,Y)VO_3$"** is forwarded by Central Department Research Committee (CDRC) to the Dean, IOST, T.U..

O P Niraula

Dr. Om Prakash Niraula
Professor
Head
Central Department of Physics
Tribhuvan University
Kirtipur, Kathmandu, Nepal

ACKNOWLEDGMENTS

I would like to thank my supervisor Prof. Dr. Om Prakash Niraula and co-supervisor Associate Prof. Dr. Gopi Chandra Kaphle, Central Department of Physics (CDP), Tribhuvan University (TU), Kirtipur, Kathmandu, Nepal, for their valuable supervision in this research work.

I would like to acknowledge Prof. Dr. Binil Aryal (Dean, IOST, TU), Prof. Dr. Ishwar Koirala (Director, Research Directorate, TU). I thankfully acknowledge to the CDRC members: Prof. Dr. Narayan Prasad Adhikari, Prof. Dr. Raju Khanal, Associate Prof. Dr. Balram Ghimire. I gratefully acknowledge Prof. Ragnar Fjelland (University of Bergen, Norway), Prof. Shankar Pd. Khanal (TU, Nepal), Prof. Srijan L. Shrestha (TU , Nepal) and Associate Prof. Chitra Bd. Baniya (TU, Nepal) for the valuable academic courses and fruitful discussion during this time. Furthermore, I would like to thank Prof. Dr. Hari Prasad Lamichhane, Dr. N. P. Pantha, Dr. Madhav Ghimire, Dr. R. P. Koirala, Dr. S. Lamichhane, Dr. H. S. Mallik, Dr. S. P. Gupta, Dr. T. P. Yadav and Dr. S. R. Bhandari for their valuable co-operation for this PhD research work. Similarly, I want to acknowledge Dr. Durga Paudyal, Ames Laboratory, Iowa State University, USA, and more than a dozen of PhD and Master's thesis students of Computational Condensed Matter Physics and Material Sciences group.

I would like to acknowledge various authors, writers, and researchers who contributed invaluable journal articles, books, and papers that are cited in the thesis and served as the conceptual basis for this research work and the framework for thesis manuscript.

I thankfully acknowledge to UGC and NAST for providing partial financial supports, and all of the CDP, PMC and TU personnels for their fruitful interaction and assistance during this PhD project.

Finally, I must acknowledge my friends and family for their continuous support during this research work.

Raj Kumar Rai

November 2023

शोधसार

यस अनुसन्धान कार्यमा जटिल प्रकृतिका ट्रान्जिसन धातुहरुको अक्साईड र तिनीहरुको सुपर संरचनाहरुको संरचनात्मक, रसायनिक र यान्त्रीक स्थायीत्व तथा ईलेक्ट्रोनिक, तापजन्यविद्युतीय र प्रकाश-प्रेरित परिवहन (ट्रान्सपोर्ट) को प्रकृति एवं चालक-अचालकताको अवस्था-संक्रमण (MIT) सम्बन्धित मोडेल प्यारामिटरहरुको विषयमा डेन्सिटी फङ्सनल सिद्धान्त (DFT) र डाईनामिकल मीन फिल्ड सिद्धान्त (DMFT) अन्तर्गतको कन्टिन्युअस टाईम क्वान्टम मोंटे कार्लो (CT-QMC) मध्ये हाईब्रिडाईजेशन विस्तार एल्गोरिदम उपयोग गरी विभिन्न भ्यानेडेट्स: [$(Ca_{1-x}Sr_xVO_3)_n$, $(La_{1-x}Sr_xVO_3)_n$ र $(La_{1-x}Ca_xVO_3)_n$] तथा टाइटानेट्स: [$(Ca_{1-x}Y_xTiO_3)_n$, $(La_{1-x}Sr_xTiO_3)_n$ र $(La_{1-x}Ca_xTiO_3)_n$] पदार्थहरुको विस्तृत अध्ययन तथा अन्वेशण गरिएको छ ।

उर्जा न्यूनिकरण कर्भहरु, कोहेसिभ र फर्मेसन उर्जाहरुको ऋणात्मक मानको आधारमा ति भ्यानेडेट र टाइटानेटहरुको आधारभुत संरचना र सुपर–संरचनाहरुको संरचनात्मक र रसायनिक स्थायीत्व रहेको साथै तिनीहरुलाई प्रयोगशालामा संस्लेषण र निर्माण गरी जीवनोपयोगी प्रयोगमा ल्याउन समेत सकिने निस्कर्ष निकालिएको छ । यसै गरी विभिन्न मेकानिकल प्यारामिटर जस्तै ईलास्टिक कन्सट्यान्ट, ईलास्टिक मोड्युलस, पोइसन तथा पगका अनुपातहरु, काउची दबाब र एनाइसोट्रपिक फ्याक्टरहरुका मानहरुको आधारमा, सम्पूर्ण अध्ययन गरिएका संरचनाहरुले यान्त्रिक स्थायीत्वको प्रत्याभूति गर्दछन् । यि अध्ययनहरुले साइट-प्रतिस्थापित सुपर संरचनाका ईलास्टिक गुणहरु तुलनात्मक रुपले आधारभूत संरचनाहरु भन्दा न्युन देखिएका छन् तथापी तिनीहरुको उपयोग विभिन्न स्मार्ट अनुप्रयोगहरुमा हुन सक्दछन्, जस्तै मोट्रोनिक अनुप्रयोगहरु (न्युरोमोर्फिक कम्प्युटिङ्ग, क्वान्टम कम्प्युटिङ्ग, रजिस्टीभ मेमोरी, कृत्रिम न्यूरोन) तथा उर्जा संकलन अनुप्रयोगहरु (फोटो भोल्टाइक, सौर्य तथा रेडियो आइसोटोपीक तापजन्यविद्युतीय जेनेरेटरहरु, फ्रिजर)को प्रयोजनका लागि सदुपयोग गर्न सकिने निस्कर्ष निकालिएको छ।

यहाँ DFT को अध्ययनको आधारमा, केही आधारभूत संरचनाहरु ($CaVO_3$, $LaVO_3$, $SrVO_3$, YVO_3, $CaTiO_3$, $LaTiO_3$, $SrTiO_3$, $YTiO_3$)का प्राप्त तथ्याङ्कहरु प्रयोगात्मक अध्ययनको तथ्याङ्कहरुसँग भन्दा सैद्धान्तिक अध्ययनसँग हाम्रो निस्कर्षहरु सहमत देखिन्छन् । हाम्रो गणनाले $CaTiO_3$ र $SrTiO_3$ हरुको व्याण्ड ग्याप क्रमशः 2.76 eV र 3.42 eV सहित व्याण्ड अचालकका गुण देखाउछन् । यसरी नै $CaVO_3$, $SrVO_3$ र YVO_3 हरु चाहीं सह-सम्बन्धित चालक गुण देखाउँछन् भने $LaVO_3$, $LaTiO_3$, र $YTiO_3$ चाहीं मोट-अचालकहरु देखिन्छन् । विशेषत: साइट-प्रतिस्थापित सुपर-संरचनाहरु चाहीं सह-सम्बन्धित चालक वा अर्ध-चालक गुण देखाउँछन् ।

यसै गरी हामीले DFT तथ्याङ्कहरुको प्रयोगगरी DMFT सहित म्याक्सिमम इन्ट्रोपी मोडल (MEM) को उपयोग गर्दै मोट ग्याप प्यारामिटरहरु विभिन्न आधारभूत संरचनाहरु र तिनीहरुको साइट-प्रतिस्थापित सुपर-संरचनाहरु मध्ये भ्यानेडेट प्रणाली, $CaVO_3$ (U =5.0 eV, $\beta=6.0(eV)^{-1}$), $LaVO_3$ (U = 4.5 eV, $\beta=8.0(eV)^{-1}$), $SrVO_3$ (U=2.5eV, $\beta=6.0(eV)^{-1}$), $La_{0.50}Sr_{0.50}VO_3$ (U = 4.0 eV, $\beta=10.0(eV)^{-1}$) र $La_{0.40}Ca_{0.60}VO_3$ (U = 5.0 eV, $\beta=10.0(eV)^{-1}$) साथै टाइटानेट प्रणाली, $LaTiO_3$ (U =4.0 eV, $\beta=8.0(eV)^{-1}$), $YTiO_3$ (U = 5.0 eV, $\beta=10.0(eV)^{-1}$), $Ca_{0.33}SrY_{0.67}TiO_3$ (U = 5.0 eV, $\beta=7.0(eV)^{-1}$) र $La_{0.80}Sr_{0.20}TiO_3$ (U = 3.2 eV, $\beta=10.0(eV)^{-1}$)हरुका MIT मोडेल प्यारामिटरहरु कोष्ठमा उल्लेखीत भए बमोजिम गणना गरिएका छन् ।

हाम्रा साइट-प्रतिस्थापित सुपर-संरचना मध्ये $La_{040}Ca_{0.60}VO_3$ र $La_{0.80}Sr_{0.20}TiO_3$ प्रणालीहरुको मोट ग्यापहरु क्रमशः 0.73 eV (U = 5.0 eV, $\beta=10.0(eV)^{-1}$) र 0.74 eV (U = 3.2 eV, $\beta=10.0(eV)^{-1}$) प्राप्त भएका छन् । त्यसरी नै ति दुवै प्रणालीहरुको क्वाजाई पार्टीकल सूचालकता चाहीं एकै मोडेल प्यारामिटरको सेट (U = 3.0 eV, $\beta=6.0(eV)^{-1}$) मा देखिएको छ । अर्कोतर्फ $La_{0.40}Ca_{0.60}VO_3$ प्रणाली संवद्ध एक उच्च तापमानको क्वान्टम क्रिटिकल बिन्दु (QCP) को मोडेल प्यारामिटर (U_C = 2.95 eV, $\beta_C=23.58(eV)^{-1}$) देखिएकोछ ।

यसरी नै बोल्ट्ज ट्रयाप एल्गोरिद्मको उपयोगगरी गणना गरिएको विद्युतीय चालकता, तापजन्य चालकता, सि-वेक गुणाङ्क तथा तापजन्यविद्युतीय पावर फ्याक्टर (TPF) को आधारमा उल्लेखित सुपर-संरचनाहरु तापजन्यविद्युतीय अनुप्रयोगका लागि उपयोग गर्न सकिने प्रबल संभावना देखिएको छ । यस खोजकार्यमा प्रकाश-प्रेरित परिवहन सम्बन्धी अध्ययनको लागि IR - UV (0 – 20.0eV) रेन्जको फोटोन उर्जा प्रयोग गरी डाईलेक्ट्रिक फङ्सन, अपवर्तक सूचकांक, ELOSS फङ्सन, अवशोषण, परावर्तन, समरुल तथा प्रकाशजन्य चालकताहरुको अध्ययनबाट उपरोक्त पदार्थहरु प्रकाश-प्रेरित उपकरण तथा परिवहन कार्यमा उपयोग हुन सक्ने निस्कर्ष प्रस्तुत गरिएको छ ।

ABSTRACT

To unravel the structural, chemical and mechanical stabilities, electronic, thermoelectric, and optically driven transport properties of pristine and site-substituted complex transition metal oxides (titanates and vanadates), we have employed the density functional theory (DFT) and the dynamical mean field theory (DMFT) approach. The continuous time quantum Monte-Carlo (CT-QMC) with hybridization expansion technique is used as impurity solver of DMFT and the maximum entropy model (MEM) is employed for analytic continuation (AC). The study also investigates the metal insulator phase transition (MIT) of the strongly correlated electronic materials by analyzing the variation of spectral density with onsite Coulomb interaction (U) and thermodynamic parameter (β).

Here, the structural, chemical, and mechanical properties of vanadates: $(La_{1-x}Sr_xVO_3)_n$, $(Ca_{1-x}Sr_xVO_3)_n$ and $(La_{1-x}Ca_xVO_3)_n$, and titanates: $(La_{1-x}Ca_xTiO_3)_n$, $(La_{1-x}Sr_xTiO_3)_n$ and $(Ca_{1-x}Y_xTiO_3)_n$ systems studied using the first-principles based calculations. The energy minimization curves, and negative values of cohesive energy (CE) and formation energy (FE) reveal their higher structural and chemical stabilities, indicating that these pristines and the site-substituted vanadates and titanates are chemically stable and viable for laboratory synthesis. The modulus of elasticities, Poisson's and Pugh's ratios, anisotropy factor, and Cauchy pressure of the systems indicate their mechanical stabilities and the results suggest that superstructures are elastically weaker than pristine systems.

The DFT calculation shows the pristine $CaVO_3$, $SrVO_3$, $LaVO_3$, $LaTiO_3$,$YTiO_3$, YVO_3 and all the superstructures are metallic/semiconducting in nature which contradicts the experimental information, whereas resembles with other theoretical calculations. The pristine $SrTiO_3$ and $CaTiO_3$ found to be band insulators with band gaps 3.42 eV and 2.76 eV respectively, which resembles closely to other available information. For the realistic picture of electronic structures, DMFT approach (CT-QMC data) along with MEM are employed and found that MIT parameters for pristines and superstructures of vanadate systems are mentioned in the parentheses, $CaVO_3$ (U = 5.0 eV, β = 6.0 $(eV)^{-1}$), $LaVO_3$ (U = 4.5 eV, β = 8.0 $(eV)^{-1}$), $SrVO_3$ (U = 2.5 eV, β = 6.0 $(eV)^{-1}$), $LaSrV_2O_6$ (U = 4.0 eV, β = 10.0 $(eV)^{-1}$) and $La_{0.4}Ca_{0.6}VO_3$ (U = 5.0 eV, β = 10.0

(eV)$^{-1}$), respectively. Similarly, the DMFT results of pristines and superstructures of titanate systems are also computed (mentioned in the parentheses) as, $LaTiO_3$ (U = 4.0 eV, β = 8.0 (eV)$^{-1}$), $YTiO_3$ (U = 5.0 eV, β = 10.0 (eV)$^{-1}$), $LaSrTi_2O_6$ (U = 4.7 eV, β = 6.0 (eV)$^{-1}$), $La_{0.8}Sr_{0.2}TiO_3$ (U = 3.2 eV, β = 10.0 (eV)$^{-1}$) and $Ca_xY_{1-x}TiO_3$ (U = 5.0 eV, β = 7.0 (eV)$^{-1}$), respectively, and found to be consistent with other results.

The analysis of characteristic sharp quasi-particle peaks reveal that vanadate, $\mathrm{La_{0.40}Sr_{0.60}VO_3}$ and titanate, $\mathrm{La_{0.80}Sr_{0.20}TiO_3}$ superstructures show metallic phases in same set of MIT parameters, (U = 3.0 eV, β = 6.0 (eV)$^{-1}$).

The set of Mott quantum critical point (QCP) for $\mathrm{La_{0.40}Ca_{0.60}VO_3}$ system is observed for an elevated temperatures at (U_C = 2.95 eV, β_C = 23.58 (eV)$^{-1}$). The clear Mott gaps for $\mathrm{La_{0.40}Ca_{0.60}VO_3}$, and $\mathrm{La_{0.80}Sr_{0.20}TiO_3}$ are computed as 0.73 eV (U = 5.0 eV, β =10.0 (eV)$^{-1}$) and 0.74 eV (U = 3.2 eV, β =10.0 (eV)$^{-1}$), respectively.

The BoltzTraP calculations show that $\mathrm{La_{0.40}Ca_{0.60}VO_3}$ and $\mathrm{La_{0.80}Sr_{0.20}TiO_3}$ systems have peak values of electrical conductivities (2.11×10^{20} $(\Omega.m.s)^{-1}$, 3.75×10^{20} $(\Omega.m.s)^{-1}$), and thermal conductivities (1.54×10^{15} $\mathrm{W/(m.K.s)}$ and 2.68×10^{15} $\mathrm{W/(m.K.s)}$), respectively, at room temperature (300 K) for a given chemical potential ($\mu = -0.14eV$). Both have the larger Seebeck coefficient (S), and thermoelectric power factor (TPF) indicating that these superstructures are better candidate for thermoelectric applications. The study of Seebeck coefficient and Hall coefficient reveal that the thermoelectric phase transition occur due to the site-substitutions of the superstructures.

The photo-induced behaviors of materials in IR-to-UV regions, including visible region are investigated using the dielectric function, index of refraction, ELOSS function, absorptivity, reflectivity, optical conductivity and sumrule. The Drude peaks result support the model parameters (U and β) of DMFT calculation for the optically driven MIT in $\mathrm{La_{0.40}Sr_{0.60}VO_3}$ and $\mathrm{La_{0.80}Sr_{0.20}TiO_3}$ superstructure systems.

Finally, the study of the MIT model parameters and diverse phase diagrams help us to fabricate these materials to design Mottronic devices (neuromorphic computing, quantum computing, resistive memory devices and artificial neurons), and energy harvesting devices (photovoltaics, solar and radioisotope thermoelectric generators and freezers).

LIST OF ACRONYMS AND ABBREVIATIONS

AC	:	Analytic Continuation
AIM	:	Anderson Impurity Model
ARPES	:	Angled Resolved Photo-Emission Spectroscopy
BOA	:	Born-Oppenheimer Approximation
BTE	:	Boltzmann Transport Equation
BZ	:	Brillouin Zone
CB	:	Conduction Band
CE	:	Cohesive Energy
CT-QMC	:	Continuous Time Quantum Monte Carlo
CVE	:	Cross Validation Error
DFT	:	Density Functional Theory
DMFT	:	Dynamical Mean Field Theory
DOS	:	Density of States
EM	:	Electromagnetic
eV	:	Electron Volt
FCC	:	Face-Centered Cubic
FE	:	Formation Energy
FiM	:	Ferrimagnetic
FP-LAPW	:	Full-Potential Linearized Augmented Plane Wave
GBR	:	Gutzwiller-Brinkman-Rice
GF	:	Green Function
GGA	:	Generalized Gradient Approximation
HEG	:	Homogeneous Electron Gas
HF	:	Hartree-Fock
HK	:	Hohenberg-Kohn
HRS	:	High Resistance State
KS	:	Kohn-Sham
LAPW	:	Linear Augmented Plane Wave
LDA	:	Local Density Approximation
LIF	:	Leaky Integrate and Fire
LO	:	Local Orbital

LR	:	Logistic Regression
LRS	:	Low Resistance State
MEM	:	Maximum Entropy Model
MIT	:	Metal Insulator Transition
MT	:	Muffin-Tin
ND	:	Normalized Deviation
PBE	:	Perdue, Burke, and Ernzerhof
PDOS	:	Partial Density of States
PM	:	Paramagnetic
QCP	:	Quantum Critical Point
QMC	:	Quantum Monte Carlo
RITEG	:	Radio Isotope Thermoelectric Generator
RRAM	:	Resistive Random Access Memory
RS	:	Resistive Switching
SCF	:	Self Consistent Field
SCS	:	Self Correlated Systems
SD	:	Spectral Density
SF	:	Spectral Function
SOC	:	Spin Orbit Coupling
STEG	:	Solar Thermoelectric Generator
TU	:	Tribhuvan University
TBA	:	Tight Binding Approximation
TDOS	:	Total Density of States
TE	:	Thermoelectric
TFD	:	Thomas-Fermi-Dirac
TMOs	:	Transition Metal Oxides
TPF	:	Thermoelectric Power Factor
VB	:	Valence Band
XC	:	Exchange Correlation
XRD	:	X-ray Diffraction

LIST OF SYMBOLS

α	:	Adjustable Parameter
β	:	Thermodynamic Parameter
$\Delta_\sigma(\mathrm{i}\omega_\nu)$	:	Hybridization Expansion
$\Delta\mathrm{n}$	:	Frequency Index Difference
$\varepsilon_\nu^{\mathrm{bath}}$	:	Energy Level of Bath Electron
$\epsilon(\omega)$	:	Dielectric Function
η_{max}	:	Maximum Strain
Θ_D	:	Debye Frequency
κ	:	Thermal Conductivity
κ_e	:	Electronic Contribution κ
κ_ph	:	Lattice Contribution κ
μ	:	Chemical Potential
$\Sigma^\mathrm{R}(\mathrm{k},\omega)$	:	Retarded Self-energy
$\sum(\omega)$	:	Quasi-particle Self-energy
$\Sigma_\sigma(\mathrm{i}\omega_\nu)$	:	Self-energy of Matsubara Frequency
σ	:	Electron Spin ($\uparrow$ or $\downarrow$)
$\sigma(\omega)$	:	Optical Conductivity
σ/τ	:	Electrical Conductivity per Unit Time
τ	:	Imaginary Time
τ,τ'	:	Imaginary Times
ψ_i	:	Orbital Wavefunction
χ	:	Magnetic Susceptibility
ψ,ψ^*	:	Grassman Variables
ω_ν	:	Matsubara Frequency
$\mathrm{A}(\mathrm{k},\omega)$	:	Spectral Function or Spectral Density
$\hat{\mathrm{a}}^\dagger_{\nu,\sigma}$	:	Creation Operator for Impurity Electrons
κ	:	Thermal Conductivity
$\mathrm{C_{ij}}$	:	Elastic Constant Tensors
$\hat{\mathrm{c}}_{\mathrm{k},\sigma}$	:	Annihilation Operator for Bath Electrons

$\mathrm{G}(\tau)$	:	Green's Function of Imaginary Time
$\mathrm{G}(\omega)$	:	Green's Function of Frequency
$\mathrm{G^R(k,\omega)}$	:	Retarded Green's Function
G_l	:	Legendre Coefficients
$\hat{\mathcal{H}}$	:	Anderson Impurity Hamiltonian
$\mathrm{L}(\omega)$	:	LOSS Function
$\mathrm{k_B}$	:	Boltzmann Constant
$\mathrm{n_{i\sigma}}$	:	Particle Number Operator
R_H	:	Hall Coefficient
S_{eff}	:	Effective Action
$\mathrm{T_s[n(r)]}$	:	Kinetic Energy of Noninteracting Electron Gas
t	:	Hopping Parameter
$\mathrm{t_{ab}}$	:	The Hopping Matrix
$\mathrm{U}^{\mathrm{lm}}_{\sigma\overline{\sigma}}$	:	Coulomb Repulsion Matrix
U	:	Coulomb Interaction
$\mathrm{V}_{ext}(\mathrm{r})$	:	External Potential
V_{KS}	:	Kohn-Sham Potential
$\mathrm{Z_{eff}}(\omega)$	:	Effective Number of Oscillators (Sum Rule)

LIST OF TABLES

Page No.

Table 1: The optimized structural parameters of the pristine ($CaVO_3$, $LaVO_3$) vanadates and their superstructure. 79

Table 2: The optimized structural parameters of the pristine ($SrVO_3$, $LaVO_3$) and superstructure with their cohesive, formation energies. 80

Table 3: The elastic constants C_{ij}, Modulus of elasticities (Y, B, G) for the Vanadates. 82

Table 4: The optimized structural parameters (volumes, densities, velocities, and Debye temperatures), and cohesive and formation energies of the pristine and their site-substituted superstructures. 83

Table 5: The structural parameters of the pristines titanates ($CaTiO_3$, $YTiO_3$) and site-substituted superstructures with cohesive and formation energies of the systems. 85

Table 6: The elastic constants C_{ij}, Modulus of elasticities (Y, B, G) for the Titanates. 86

Table 7: The Mott-gap, MIT model parameter, and quasi-peak parameters for pristine vanadate and their superstructures. 103

Table 8: The Mott-gap, MIT model parameter, and quasi-peak parameters for pristine titanates and their superstructures. 106

Table 9: The electrical (σ/τ) and thermal (κ) conductivities, Seebeck coefficient (S), Hall coefficient (R_H), magnetic susceptibility (χ), molar specific heat capacity (C) and thermoelectric power factor (TPF) of vanadate systems at room temperature (300 K). . . 109

Table 10: The electrical (σ/τ) and thermal (κ) conductivities, Seebeck coefficient (S), magnetic susceptibility (χ), molar specific heat capacity (C), Hall coefficient (R_H) and thermoelectric power factor (TPF) at room temperature (300 K) for titanates systems. . . . 111

Table 11: The real part of static dielectric function ($\omega \sim 0$) Re $\varepsilon(0)$, static refractive index $n(0)$, static real part of optical conductivity $\sigma(0)$, static absorption coefficient $\alpha(0)$, static optical reflectivity R(0), ELOSS function L(0), static optical weight $Z_{eff}(0)$, and plasma frequency (ω_p) from all the examples of ELOSS functions. 116

LIST OF FIGURES

Page No.

Figure 1: The various complex systems evolve through self-organization as the fundamental cause of emergentism 2

Figure 2: Schematic representation of electron addition and removal from a given atomic shell 5

Figure 3: The schematic of rationales for the study of TMOs and its superstructure as quantum materials 10

Figure 4: The schematic representation of interacting ionic cores and electrons in many-body system 20

Figure 5: The ground state density of interacting particles system uniquely related to the external potential 25

Figure 6: The global minimum ground state density is a unique parameter for a many-body system 25

Figure 7: The schematic of pseudo-potential (effective potential) model(red solid lines). The dashed blue lines depict the Coulomb potential(full potential) and the upper corresponding pseudo-wavefunction (red solid line) and full wavefunction (blue dashed lines) near the nucleus. Outside of the cutoff radius (r_c), the pseudopotential and pseudo wavefunctions are compatible with the real system, but they avoid the real-world obstacles such as singularities in potential and wiggles in wavefunctions near nuclei 30

Figure 8: (a) The three mechanisms of metal insulator transition (b) The schematic Mott-Hubbard band splittings 46

Figure 9: The schematics for a local field interaction in a FCC lattice in the limit of $d \to \infty$ or $Z \to \infty$ (infinite dimension) 47

Figure 10: The schematic of self-consistency cycle for DMFT calculation . 50
Figure 11: MC configurations are represented by a sequence of operators on the time interval $0 \leq \tau < \beta$, with full(empty) circles representing annihilation(creation) operators. MC moves involve random insertions or removal of pairs of operators in different channels 51
Figure 12: The graphs for (a) the first five orders of Legendre's polynomials in x (b) the example of calculation using these polynomials for GF of Matsubara frequency 54
Figure 13: F(z) is the AC of f(z) to the larger domain V 56
Figure 14: The flowchart for the general analytical continuation of various methods 60
Figure 15: A schematic representation of the Matsubara frequency points' AC of the GF in the complex plane 61
Figure 16: (a) The graphical representation of posterior probability (b) The logistic regression (LR) curve 64
Figure 17: The various distinct regions for different phases with the variation of model parameters (U and β) at around QCP 70
Figure 18: The structural stability analysis through energy minimization process for (a) $LaVO_3$ and (b) superstructure $La_{0.40}Ca_{0.60}VO_3$. 78
Figure 19: The optimization curve for lattice parameter of (a) $SrVO_3$ unit-cell with the crystal structure (inset) (b) $LaSrV_2O_6$ superstructure system with its crystal structure (inset). 79
Figure 20: The lattice parameter optimization curves and crystal structures (insets) for (a) $CaVO_3$ system (b) $(Ca_{0.50}Sr_{0.50}O_3)_2$ system. 81
Figure 21: The plots of (a) the elastic constants vs. strain of different distorted geometries (b) the corresponding CVE vs. strain for $LaSrV_2O_6$ system. 82
Figure 22: The volume optimization curve with crystal structures (insets) of (a) $LaTiO_3$, and (b) $LaSrTi_2O_6$, systems. 83

Figure 23: The lattice parameter optimization curves for (a) $YTiO_3$ with crystal structure(inset) (b) $Ca_{0.33}Y_{0.67}TiO_3$ system with crystal structure(inset). 84

Figure 24: The plot show (a) the TDOS redistribution with Ca-ions site substitution in $LaVO_3$ supercell (b) the comparative DOS and bandstructures for the spin up channel of the $La_{0.40}Ca_{0.60}VO_3$ system. 87

Figure 25: The PDOS contribution in $La_{0.40}Ca_{0.60}VO_3$ system by (a) La -atoms (b) Ca -atoms (c) V -atoms with U and J. 87

Figure 26: The graphs of (a) the comparative bandstructures (b) the fat bandstructure of the V -d orbitals with Coulomb interaction (c) the fatbandstructure of third atomic V -e_g orbital of $La_{0.40}Ca_{0.60}VO_3$ system. 88

Figure 27: The orbitals contribution of (a) La- 5d (b) La- 4f (c) V-t_{2g} in $La_{0.40}Ca_{0.60}VO_3$ system. 88

Figure 28: The plots of (a) the 2D charge contour map (b) the primitive Brillouin zone (BZ) (inset top left) with the band crossing by Fermi level for 50-175 band levels and Fermi-surface plot at around the Γ point (inset bottom right) of $La_{0.40}Ca_{0.60}VO_3$ system. 89

Figure 29: The plots for (a) the comparative DOS and bandstructures for $CaVO_3$ spin up channel (b) the comparison of the DOS and bandstructure of the $(Ca_{0.50}Sr_{0.50}VO_3)_2$ system for both spin up and down channels. 90

Figure 30: The TDOS plots for spin up/down channels of (a) $CaVO_3$ (b) $SrVO_3$ and (c) $(Ca_{0.50}Sr_{0.50}VO_3)_2$ systems. 90

Figure 31: The plots of (a) La -d and V -d orbitals PDOS contributions for both spin-channels (only V-d orbitals are shown in the inset) (b) the bandstructure together with the DOS (spin-up) (green) and DOS (spin-down) (blue) channels of $LaSrV_2O_6$ system. . 90

Figure 32: The plots for (a) the DOS distributions of spin up and spin down channels for various values of U (b) the Fermi surfaces generated with 35-55 band levels (inset top left) and the band crossing by Fermi level (E_F) along with the 2D and 3D charge density plot of (110) plane (inset lower right) of $LaSrV_2O_6$ system. 91

Figure 33: The band structures plots for (a) $SrTiO_3$ and (b) $LaTiO_3$ showing the band insulator and Mott insulator systems, respectively. The fatbandstrutures of the Ti -atom of $LaTiO_3$ system for (c) the e_g orbitals and (d) t_{2g} orbitals due to splittings of d -orbitals unit cell. 92

Figure 34: The plots show (a) the band shifting caused by SOC in the $LaTiO_3$ system (b) the band gap of $SrTiO_3$ system enhanced by the introduction of mBJ-interaction potential. 92

Figure 35: The bandstructure plots for $La_{0.80}Sr_{0.20}TiO_3$ system (a) the bandstructure for spin down channel (b) the fat-bandstructure for Ti - d orbitals of the system (c) the redistributed bandstructures of the system with U = 2.11 eV, J = 0.25 eV, and SOC. . . 93

Figure 36: The plots for (a) the comparative DOS and bandstructures of both spin-channels of the pristine $YTiO_3$ system (b) the comparative DOS and bandstructures of both spin-channels of the site-substituted $Ca_{1-x}Y_xTiO_3$ system. 93

Figure 37: The plots of (a) the band crossing of Fermi level with 10-40 band levels (i) the primitive BZ (ii) the Fermi surfaces of 10 -40 band levels (iii) the 2D-charge density plot (iv) the 3D - charge density plot for the pristine, $LaTiO_3$ system, (b) the band crossing of Fermi-level plot for 100-189 bands (i) the 2D -contour plot of charge density distribution map in (011) plane (ii) the Fermi surface plot for 100 -189 band levels, (iii) the Fermi surface plot for 100 -189 band levels with tentacles of the site-substituted superstructure, $La_{0.80}Sr_{0.20}TiO_3$. 94

Figure 38: The plots for (a) the GF w.r.t. imaginary time (τ) (b) the corresponding variation of GF w.r.t. frequency (ω) for the different values of β with a constant U = 5.0 eV of $La_{0.40}Ca_{0.60}VO_3$ system (c) the GF of imaginary time (τ) with U = 3.0 eV and β = 6.0 $(eV)^{-1}$ for the site-substituted, $La_{1-x}Ca_xVO_3$ superstructure systems with the various proportion of Ca-ions. 95

Figure 39: The graph of (a) the SD, A(ω) vs. frequency, (ω) with (U = 3.0 eV, β = 10.0 $(eV)^{-1}$) for different proportions of Ca - ions, and (b) the A(ω) vs. (ω) for U = 5.0 eV for a constant β = 10.0 $(eV)^{-1}$ with different stoichiometric combination of $La_{1-x}Ca_xVO_3$ system. 96

Figure 40: The SF of frequency for (U = 3.0 eV and β = 6.0 $(eV)^{-1}$) a quasi-particle peak of $La_{0.40}Ca_{0.60}VO_3$ system. The LR curve (inset upper left) and the curvature (κ) vs. $\log_{10}(\alpha)$ curve (inset upper right) for determining the optimal value of (α) for the material. 96

Figure 41: The plot of (a) the SD of sample frequencies vs. $\log_{10}(\alpha)$ (b) the ND of the Re. and Im. G(ω) vs. frequency with U = 3.0 eV and β = 6.0 $(eV)^{-1}$ and (c) the autocorrelation (AC) of the Re. and Im. G(ω) vs. frequency index difference (Δn). 97

Figure 42: The plot of (a) the differential entropy (S) vs. $\log_{10}(\alpha)$ for extracting optimal information (b) the real(blue) and imaginary (red) parts of the $G^R(\omega)$ vs. frequency (c) the SF, A(ω) vs. frequency (ω) plots for default (hypothetical), and the optimal and minimal values of α (d) the uncertainty in moment orders for the calculations with (U = 3.0 eV, β = 6.0 $(eV)^{-1}$) for $La_{0.40}Ca_{0.60}VO_3$ system. 98

Figure 43: The SF vs. frequency with the variation of U/t versus β/t, for $La_{0.40}Ca_{0.60}VO_3$ system. 98

Figure 44: The graph of MIT using DMFT with MEM self-consistency cycle of calculation. The graph depicts the QCP, C at an elevated temperature in the Uβ -plane and two bifurcation points in the low temperature regime, U_{C_1} and U_{C_2} 99

Figure 45: The graph of (a) GF vs. imaginary time,(τ) for the variation of U with a constant β = 6.0 (eV)$^{-1}$, and the corresponding variation of GF vs. frequency (inset) (b) the SF vs. frequency (ω) with a constant β = 6.0 (eV)$^{-1}$ for the variation of U of $LaSrV_2O_6$ system. 100

Figure 46: The plot of (a) the SD vs. frequency (ω) for a constant U = 4.0 eV for β variation (b) the plot of imaginary part self-energy (Im$\Sigma(i\omega_\nu)$) vs. the Matsubara frequency ($i\omega_\nu$) for the variation of (β) with a constant U = 4.0 eV of the $LaSrV_2O_6$ system. 100

Figure 47: The graph of (a) the SF vs. frequency (ω) for the variation of U values (b) the LR curve for the optimal value of α for U = 4.0 eV and β = 10.0 (eV)$^{-1}$. 101

Figure 48: The graphs of (a) the SF of frequency obtained for optimal and minimal values of α with the default model (dotted line) (b) the differential entropy, S(ω) vs. $\log_{10}(\alpha)$ to observe the optimal value of information (c) the SD for the various sample frequencies vs. of $\log_{10}(\alpha)$ (d) the normalized function of moment orders for the calculations for the minimal value of α (blue) and optimal value of α (red) for $LaSrV_2O_6$ system with (U = 4.0 eV, β = 10.0 (eV)$^{-1}$). 101

Figure 49: The graphs of (a) the ND for the Re. and Im. (ΔG) vs. frequency (ω_ν) with minimal value of α (b) the ND for the Re. and Im. (ΔG) vs. frequency (ω_ν) with the optimal value of α (c) the ND of the real parts of ΔG vs. frequency (ω_ν) with minimal (blue) and optimal (red) values of α (d) the autocorrelation of the real parts of ΔG vs. the difference of the frequency index (Δn) for the minimal (blue) and optimal (red) values of α of the $LaSrV_2O_6$ system. 102

Figure 50: The plots of (a) the GF, G(τ) vs. imaginary time, (τ) and the corresponding plot of the Fourier transform of the GF (inset) with a constant β = 6.0 $(eV)^{-1}$ for various values of U (GBR-phase transition scenario) (b) the SD vs. frequency for demonstrating the MIT with U variation for β = 6.0 $(eV)^{-1}$. At U = 4.5 eV and β = 6.0 $(eV)^{-1}$, the Mott-Hubbard splitting of the $Ca_{0.50}Sr_{0.50}VO_3$ system is achieved. 103

Figure 51: The change of optical conductivity with the varied Coulombian interaction U for a constant, β = 6.0 $(eV)^{-1}$ of the superstructure system. 104

Figure 52: The plots for (a) the GF vs. imaginary time (b) the GF vs. frequency (c) the variation of SD vs. frequency and (d) the imaginary part of $\Sigma(i\omega_\nu)$ vs. Matsubara frequency with the variation of U and a constant β = 6.0 $(eV)^{-1}$ of the pristine, $LaTiO_3$ system. 105

Figure 53: The plots of (a) the GF, G(τ) vs. imaginary time (τ) for the various values of stoichiometric combinations and the corresponding GF, G(ω) vs. frequency (ω) (inset) showing the MIT with the site-substitution of Sr -ion with La -cation for U = 3.0 eV and β = 6.0 $(eV)^{-1}$ of $La_{1-x}Sr_xTiO_3$ systems and (b) The imaginary part of self-energy, (Im Σ (iω_ν)) vs. Matsubara frequency, (iω_ν)) for (U = 3.0 eV and β = 6.0 $(eV)^{-1}$) for the same stoichiometric combinations. 105

Figure 54: The graphs of (a) the SF vs. frequency showing the quasi-particle peak for $La_{0.80}Sr_{0.20}TiO_3$ at U = 3.0 eV and β = 6.0 $(eV)^{-1}$ the LR curve (inset left) and the curvature of the LR curve (inset right) for optimal value of (α) (b) the comparison of optical conductivities vs. frequency indicating the variation of Drude peaks with the various proportion of La^{2+} ions in $La_{1-x}Sr_xTiO_3$ supercells at U = 3.0 eV and β = 6.0 $(eV)^{-1}$ for the optimal value of α. 106

Figure 55: The graphs show (a) the SD, A(ω) vs. frequency (ω) of $YTiO_3$ with LR curve(inset top left) and the curvature of LR curve (inset top right), and (b) the SD, A(ω) vs. frequency (ω) of the superstructure, $Ca_{0.33}Y_{0.67}TiO_3$ with LR curve (inset top left) and the curvature of LR curve (inset top right). 106

Figure 56: The graph of (a) the electrical conductivity (σ/τ) vs. the chemical potential (μ) and the corresponding variation of the same parameter with respect to the absolute scale of temperature (inset) (b) the variation of thermal conductivity (κ) vs. (μ) and the corresponding variation of (κ) with temperature (inset) for the site-substituted superstructures, $La_{1-x}Ca_xVO_3$. 108

Figure 57: The graphs show (a) the Seebeck Coefficient (S) w.r.t. the chemical potential (μ) at room temperature (300 K) and its temperature variation (inset) (b) the variation of the Hall coefficient (R_H) vs. chemical potential (μ) at room temperature (300 K) and its temperature variation for the site-substituted superstructures, $La_{1-x}Ca_xVO_3$. 108

Figure 58: The graphs of various transport parameters (a) electrical conductivity (σ/τ) (b) thermal conductivity (κ) (c) Seebeck coefficient (S) and (d) Hall coefficient (R_H) w.r.t. the absolute temperature scale (T). The variation of the same transport parameters (e) electrical conductivity (σ/τ) (f) thermal conductivity (κ) (g) Seebeck coefficient (S) and (d) Hall coefficient (R_H) w.r.t. chemical potential (μ) for $Ca_{1-x}Sr_xVO_3$ systems. 109

Figure 59: The variation of (a) electrical conductivity (σ/τ) w.r.t. chemical potential (μ) and w.r.t. temperature (inset) (b) thermal conductivity (κ) w.r.t. chemical potential (μ) and temperature (inset) for the site-substituted, $La_{1-x}Sr_xTiO_3$ systems. 110

Figure 60: The variation of (a) the Hall coefficient (R_H) w.r.t. chemical potential (μ) and temperature (inset) (b) Seebeck coefficient (S) with chemical potential (μ) and temperature (inset) of the site-substituted, $La_{1-x}Sr_xTiO_3$ systems. 110

Figure 61: The graphs of various transport parameters w.r.t. the absolute scale of temperature: (a) electrical conductivity (σ/τ) (b) thermal conductivity (κ) (c) Seebeck coefficient (S) and (d) Hall coefficient (R_H) (e) molar specific heat capacity (C) (f) magnetic susceptibility (χ) of the pristine titanates and its site-substituted superstructures, $Ca_{1-x}Y_xTiO_3$ systems. 111

Figure 62: The graphs of (a) the dielectric function (Re ($\varepsilon(\omega)$)) vs. photon energy (b) the ELOSS function, L(ω) vs. photon energy and (c) the Absorptivity, $\alpha(\omega)$ vs. photon energy for the $La_{1-x}Ca_xVO_3$ system. 113

Figure 63: The graphs of (a) the refractive indices, n(ω) vs. photon energy (b) the real part of the optical conductivity Re ($\sigma(\omega)$) vs. photon energy and (c) the optical weight $N_{eff}(\omega)$ versus photon energy for the $La_{1-x}Ca_xVO_3$ systems. 113

Figure 64: The plots of (a) the optical conductivity, $\sigma(\omega)$ vs. (ω) for a constant U and the variation of β of the $La_{1-x}Ca_xVO_3$ system (b) the variation of optical conductivity $\sigma(\omega)$ vs. (ω) with different proportions of Ca-ions substitution for (U = 10.0 eV, β = 15.0 $(eV)^{-1}$) these systems, and (c) the variation of optical conductivity $\sigma(\omega)$ vs. (ω) with various sets of U and β values for $La_{0.40}Ca_{0.60}VO_3$ system. 113

Figure 65: The graphs of (a) the real parts of dielectric function vs. energy (eV) and its imaginary parts (inset) (b) the real part of optical conductivity vs. energy (eV) for the $(La_{1-x}Sr_xVO_3)_n$ systems. 114

Figure 66: The plots of (a) the refractive indices vs. photon energy (b) the absorptivity vs photon energy for the $(La_{1-x}Sr_xVO_3)_n$(n = 2; x = 0, 0.5, 1) system. 115

Figure 67: The plots of (a) the ELOSS function vs. energy (b) the optical weight, $N_{eff}(\omega)$ vs. energy for $(La_{1-x}Sr_xVO_3)_n$ system. 115

Figure 68: The graphs for (a) the optical conductivity $\sigma(\omega)$ vs. frequency (ω) for a constant U = 4.00 eV with β variation (b) the optical conductivity $\sigma(\omega)$ vs. frequency (ω) for a constant β = 10.00 $(eV)^{-1}$ with U variation for $(La_{1-x}Sr_xVO_3)_n$ system. 115

Figure 69: The plots for (a) the dielectric function vs. the photon energy (b) the index of refraction vs. the photon energy (c) the optical conductivity vs. the photon energy (d) the ELOSS function vs. photon energy (e) the reflectivity vs. photon energy, and (f) the optical weights (sumrule) vs. photon energy for the $La_{1-x}Sr_xTiO_3$ systems. 117

Figure 70: The graph of (a) the real and imaginary parts (inset) of the dielectric function w.r.t. photon energy (b) the real part of complex index of refraction and extinction coefficient $\kappa(\omega)$ (inset) w.r.t. photon energy (c) the real part of optical conductivity w.r.t. photon energy (d) the ELOSS function w.r.t. photon energy (e) the absorptivity w.r.t. photon energy, and (f) the variation of optical weights (sumrule) w.r.t. photon energy for the $Ca_{1-x}Y_xTiO_3$ systems. 119

TABLE OF CONTENTS

Letter of Approval i

Declaration ii

Recommendation iii

Letter of Approval iv

Acknowledgements v

Abstract in Nepali vi

Abstract viii

List of Acronyms and Abbreviations x

List of Symbols xii

List of Tables xiv

List of Figures xvi

CHAPTER 1 1

1. INTRODUCTION 1

1.1 Introduction 1

1.1.1 Philosophy of the Present Study 2

1.1.2 Strongly Correlated Electronic System 3

1.2 Rationale of the Study 10

1.3 Objectives 12

1.3.1 General Objective 12

1.3.2 Specific Objectives 12

1.4 Organization of Study 12

CHAPTER 2 **14**

2. LITERATURE REVIEW **14**

CHAPTER 3 **19**

3. MATERIALS AND METHODS **19**

3.1 Theoretical Background 19

3.1.1 The Many-Body Schrödinger Equation 19

3.1.1.1 Born-Oppenheimer Approximation (BOA) 20

3.1.1.2 Hartree Approximation 21

3.1.1.3 Hartree-Fock Approximation 22

3.1.1.4 Thomas-Fermi-Dirac (TFD) Model 23

3.1.1.5 Hohenberg-Kohn Theorems 24

3.1.2 The Density Functional Theory (DFT) 26

3.1.2.1 Kohn-Sham Equations 26

3.1.2.2 Exchange-Correlation Functional 28

3.1.2.3 Solution of KS-Equation 29

3.1.2.4 Pseudo-potentials and Plane Waves 29

3.1.2.5 FP-LAPW Basis and LO Extensions 31

3.1.3 The Local Density Approximation (LDA) 32

3.1.4 GEA, GGA, mBJ and Beyond 33

3.1.5 Electronic Structures 36

3.1.5.1 Electronic Bandstructures 36

3.1.5.2 Density of States 36

3.1.6 Structural and Chemical Stability 37

3.1.6.1 Structural Stability 37

3.1.6.2 Chemical Stability 37

3.1.7 Mechanical Stability and Elastic Properties 38

3.1.8 Transport Properties 41

3.1.9 Optical Properties 43

3.1.10 Metal-Insulator Transition (MIT) 44

3.2 Dynamical Mean Field Theory (DMFT) . . . 46
3.2.1 The Anderson Impurity Model (AIM) . . . 48
3.2.2 The Continuous Time Quantum Monte Carlo (CT-QMC) . . . 49
3.2.3 The Continuous Time Partition Function in Configuration Space . . . 50
3.2.4 Markov Chain Transition . . . 52
3.2.5 CT-QMC with Hybridization Expansion . . . 52
3.2.6 Computing GF from Partition Function . . . 53
3.3 Numerical AC Method . . . 55
3.3.1 Green's Function Methodology . . . 55
3.3.1.1 Analytical Structure of GFs . . . 56
3.3.1.2 Fourier Transform of $G^{>}(\omega)$ and $G^{<}(\omega)$ . . . 58
3.3.1.3 The Analyticity of the Retarded and Advanced GFs . . . 59
3.3.2 AC for Single-site Dynamical Mean-Field Theory . . . 60
3.3.2.1 Flowchart for AC . . . 60
3.3.3 The Maximum Entropy Model (MEM) . . . 62
3.3.3.1 Bayes' Theorem for MEM . . . 63
3.3.3.2 Bayesian Inference Using the Hyper-parameter (α) . . . 66
3.3.3.3 Extracting Information from the GF Input . . . 66
3.3.3.4 The Optimal Value for Hyper-parameter . . . 67
3.4 Optical Conductivity through DMFT . . . 67
3.4.1 Photoinduced Phase Transitions . . . 70
3.5 Computational Details and Experimental Information . . . 72
3.5.1 Computational Softwares for Ab-initio Calculations . . . 72
3.5.1.1 Quantum Espresso Frameworks . . . 72
3.5.1.2 WIEN2k Frameworks . . . 72
3.5.1.3 DMFT Frameworks . . . 72
3.5.2 Computational Details . . . 73
3.5.3 Experimental Information . . . 75

CHAPTER 4 **77**

4. RESULTS AND DISCUSSION **77**

4.1 Structural, Chemical and Mechanical Stability . . . 78

4.1.1 Structural, Chemical and Mechanical Stability of Vanadates . . 78
4.1.1.1 Structural and Chemical Stability of $La_{1-x}Ca_xVO_3$. 78
4.1.1.2 Structural and Chemical Stability of $La_{1-x}Sr_xVO_3$ . . 79
4.1.1.3 Structural and Chemical Stability of $Ca_{1-x}Sr_xVO_3$ . . 80
4.1.1.4 Mechanical and Thermodynamical Stabilities of Vanadates 81
4.1.2 Structural, Chemical, and Mechanical Stability of Titanates . . . 83
4.1.2.1 Structural and Chemical Stability of $La_{1-x}Sr_xTiO_3$ . . 83
4.1.2.2 Structural and Chemical Stability of $Ca_{1-x}Y_xTiO_3$ . . 84
4.1.2.3 Mechanical and Thermodynamical Stabilities of Titanates . 85
4.2 Electronic Structures of Vanadates and Titanates 86
4.2.1 Electronic Structures of Vanadate Systems 86
4.2.1.1 Electronic DOS and Bandstructures of $La_{1-x}Ca_xVO_3$ . . . 86
4.2.1.2 Electronic DOS and Bandstructures of $Ca_{1-x}Sr_xVO_3$ . . . 89
4.2.1.3 Electronic DOS and Bandstructures of $LaSrV_2O_6$ 90
4.2.2 Electronic Structures of Titanate Systems 91
4.2.2.1 Electronic DOS and Bandstructures of $La_xSr_{1-x}TiO_3$ . . . 91
4.2.2.2 Electronic DOS and Bandstructures of $Ca_{1-x}Y_xTiO_3$ . . . 93
4.3 The Electronic Transport Properties of Vanadates and Titanates 95
4.3.1 The Electronic Transport Properties of Vanadate Systems 95
4.3.1.1 Electronic Transport Properties of $La_{1-x}Ca_xVO_3$ 95
4.3.1.2 Electronic Transport Properties of $La_{1-x}Sr_xVO_3$ . . . 99
4.3.1.3 Electronic Transport Properties of $Ca_{1-x}Sr_xVO_3$ . . . 103
4.3.2 The Electronic Transport Properties of Titanates System 104
4.3.2.1 Electronic Transport Properties of $La_{1-x}Sr_xTiO_3$ . . . 104
4.3.2.2 Electronic Transport Properties of $Ca_{1-x}Y_xTiO_3$ . . . 105
4.4 Thermoelectric Properties of Vanadates and Titanates 107
4.4.1 Thermoelectric Transport Properties of Vanadate Systems 107
4.4.1.1 Thermoelectric Transport Properties of $La_{1-x}Ca_xVO_3$ . . 107
4.4.1.2 Thermoelectric Transport Properties of $Ca_{1-x}Sr_xVO_3$ . . . 109
4.4.2 Thermoelectric Transport Properties of Titanate Systems 110
4.4.2.1 Thermoelectric Transport Properties of $La_{1-x}Sr_xTiO_3$ . . 110

4.4.2.2 Thermoelectric Transport Properties of $Ca_{1-x}Y_xTiO_3$ . . . 111
4.5 Optical Properties of the Vanadates and Titanates . . . 112
4.5.1 Optical Properties of the Vanadate Systems . . . 112
4.5.1.1 Optical Properties of $La_{1-x}Ca_xVO_3$ . . . 112
4.5.1.2 Optical Properties of $(La_{1-x}Sr_xVO_3)_n$(n=2) . . . 114
4.5.2 Optical Properties of the Titanate Systems . . . 117
4.5.2.1 Optical Properties of $La_{1-x}Sr_xTiO_3$ . . . 117
4.5.2.2 Optical Properties of $Ca_{1-x}Y_xTiO_3$ . . . 118

CHAPTER 5 **120**

5. CONCLUSIONS AND RECOMMENDATIONS **120**
5.1 Stability of Titanates and Vanadates . . . 120
5.2 Electronic Transport Properties of Titanates and Vanadates . . . 121
5.3 Thermoelectric and Optically Driven Transport Properties . . . 122
5.4 Recommendations for the Future Study . . . 123

CHAPTER 6 **125**

6. SUMMARY **125**

REFERENCES **128**

APPENDICES **154**

CHAPTER 1

INTRODUCTION

1.1 Introduction

In this work, the stability, electronic transport, and thermoelectric and optically induced behaviors of the site-substituted complex transition metal oxides: (La,Sr)TiO_3/(Ca,Y)VO_3, that include band insulators, Mott insulators, semiconductors and correlated metals are examined through theoretical and computational approach. These materials are complex chemical systems with strongly correlated electronic systems due to their couplings of various degrees of freedoms (charge, spin, orbital, and lattice interactions). The site-substituted superstructures of complex transition metal oxides (TMOs) in the various dimensions and morphologies harbors many promising materials of exotic novel behaviors.

To understand these phenomena, we need to probe the scientific philosophy of physical sciences in relation to their communities for the benefit of society as a whole. P.W. Anderson introduced the concept of "More is Different" to explain the complex behaviors (Popper, 1957; Anderson, 1963). The complex physical systems exhibit exotic behaviors beyond their microscopic constituents, and there are no simple rules or principles to examine and predict larger assemblies of matter. Physicists use fundamental laws of nature to describe natural phenomena. The theory of broken symmetry no doubt help to interpret and explain these phenomena (Kuhn, 2012). The scale change impact the understanding of physical phenomena, requiring a different set of fundamental rules and laws. As for example, the general theory of relativity is crucial for cosmological scales, while quantum mechanics is important for atomic and subatomic scales.

1.1.1 Philosophy of the Present Study

The theoretical physicists employed systematic studies to draw logical conclusions, while majority of the experimental physicists sought emergent behavior in complex interactions (Losee, 2001; Kuhn, 2012). Kuhn's normal science paradigm shift (Popper,

Figure 1: The various complex systems evolve through self-organization as the fundamental cause of emergentism (Sayama, 2015).

1957; Feyerabend, 2017) embraces new standards for right and wrong, emphasizing the importance of science and technology for human civilization and global justice. Emergent behavior in physical systems is a complex phenomenon involving various academic disciplines and complex interactions (Conway, 1970; Anderson, 1972; Bar-Yam *et al.*, 1998). Emergentism in philosophy explores larger entities' behaviors through interactions with smaller, simpler entities, based on the belief in emergence phenomena (Fig. 1) (Sayama, 2015). Human knowledge has evolved through observation, experimentation, and trials and errors methods. Philosophers and scientists study various aspects of the world, including the tiniest quarks to the structure of our universe with the help of a suitable model (Popper, 1957; Kuhn, 2012) and a testing environment with reasonable defining parameters are necessary.

Apart from the fundamental knowledge and philosophical insights, TMOs (Byrd *et al.*, 1995) have a diverse variety of technological applications, such as dielectrics, ferroelectrics, magnetic and Mottronics applications. TMO surfaces/interfaces (Dong *et al.*, 2008; Saeed *et al.*, 2014) play critical roles in catalysis, sensing, fuel cells, and photovoltaics. Their conduction qualities range from insulators to semiconductors, metals to superconductors, and they are sometimes found in the same superstructures.

The complexity of TMOs electronic structures presents significant challenges in physics, especially in the Hubbard model. The electron-electron interaction in the 3D shell produces complex correlation phenomena, making early solid state physics difficult to understand. TMO bulk and surface crystal structures are complex, with dislocations, defects, and vacancies. Proper lattice positions and theoretical calculations on defect sites are required to handle and manage these flaws.

Here, we performed the dynamical mean field theory (DMFT) and the maximum entropy model (MEM) to investigate transport properties and other physical properties of pristine and site-substituted complex TMOs.

1.1.2 Strongly Correlated Electronic System

Electronic correlations are a fascinating field in condensed matter physics, involving the interacting electronic systems, which cannot be described by Slater determinants of the Hartree-Fock (HF) method.

The MIT occurs when electron-electron Coulomb repulsion limits delocalization to lower kinetic energy. Correlations are the dependence of an object or event on another, affecting its energy. The techniques to address the correlation effect include upgrading DFT methods to local density approximation (LDA) plus Coulomb interaction (U), DMFT and many more (Silver *et al.*, 1990; Vaugier *et al.*, 2012; Rozenberg, 2019).

Mathematically, correlation is a mathematical quantity describing the variation of correlated objects between any two random variables X and Y (Arfken *et al.*, 2011; Vaugier *et al.*, 2012; Rozenberg, 2019), the expectation value of XY can be expressed as,

$$\mathrm{E[XY]} = \mathrm{E[X]E[Y]} + \mathrm{cov(X, Y)} \tag{1.1}$$

which is not the product of expectation values, where cov(X, Y) $\neq$ 0 "measures" the degree of correlation between X and Y.

$$\mathrm{cov}(\mathrm{X}, \mathrm{Y}) = \mathrm{E}[(\mathrm{X} - \mathrm{E}[\mathrm{X}])(\mathrm{Y} - \mathrm{E}[\mathrm{Y}])] \tag{1.2}$$

In physics, the charge density for an interacting system (Vaugier *et al.*, 2012; Rozenberg, 2019). For the interacting system,

$$\langle \mathrm{n}(\mathbf{r}_\mathrm{i})\mathrm{n}(\mathbf{r}_\mathrm{j})\rangle \neq \langle \mathrm{n}(\mathbf{r}_\mathrm{i})\rangle \langle \mathrm{n}(\mathbf{r}_\mathrm{j})\rangle \tag{1.3}$$

This is because electrons interact via the Coulomb interaction and the Pauli principle.

Electronic correlations are physical effects beyond static mean-field theories, incorporating electron interactions through an effective background potential. These approximations preserve the single-particle approximation, as the Hamiltonian is effectively non-interacting after being determined self-consistently.

Tight-binding approximation (TBA) model (Martin, 2004; Vaugier *et al.*, 2012; Rozenberg, 2019) of atomic chain can be expressed as,

$$\hat{\mathrm{H}}_{\mathrm{TB}} = -\mathrm{t} \sum_{\langle \mathrm{i,j}\rangle,\omega} \hat{\mathrm{c}}^{\dagger}_{\mathrm{i},\sigma} \hat{\mathrm{c}}_{\mathrm{j},\sigma} \tag{1.4}$$

where $\langle i, j\rangle$ denotes a summation exclusively.

The hoping integral derived from the summation of nearest-neighboring sites (Imada *et al.*, 1998; Vaugier *et al.*, 2012) is,

$$\mathrm{t} = \int \langle \phi_\sigma(\mathbf{r} - \mathrm{a})|\hat{\mathrm{H}}|\phi_\alpha(\mathbf{r})\rangle \mathrm{d}\mathrm{r} \tag{1.5}$$

Hamiltonian decreases exponentially with the lattice spacing **a**. A Fourier transformation may be used to solve this Hamiltonian, resulting in the dispersion.

$$\epsilon(\mathbf{k}) = -2\mathrm{t}\cos(\mathbf{k}.\mathbf{a}) \tag{1.6}$$

The system is metallic at half-filling with a single electron per site, crossing the Fermi level at $k = (n+1)\frac{\pi}{2a}$. As lattice spacing increases, band width falls.

The TBA model assumes electrons are closely bonded to individual atoms, with atomic-like orbitals overlapping nearby orbitals. The underlying mechanism of transport events is dictated by the fundamental component of the physical parameter of the materials under consideration. The charge interaction parameter, (U/t), and spin-orbit coupling parameter, (λ/t) are the major parameters for metal-insulator phase transitions (Vale *et al.*, 2018), where t is the electron hopping parameters see (Appendix-I).

As a preliminary observation, the problem of electronic interactions differs greatly between isolated atoms and atoms in solids. The main distinction is the potential of non-local and long-range screening inside solids, which significantly reduces the effective Coulomb repulsion between electrons (Imada *et al.*, 1998; Vaugier *et al.*, 2012). Condensed matter theories encounter basic concerns about how strong the screening is and how to account for it in models. The insertion of the well-known Hubbard parameter U in the single-orbital Hubbard-Kanamori-Gutzwiller model (Hubbard, 1963) were the early attempts for this purpose.

An effective Coulomb interaction (U) parameter, setting at a lower order of magnitude than the bare atomic interactions due to screening. It represents the Coulomb energy cost for inserting and removing electrons at the same atomic site or to the difference in affinity and ionization energy (Fig.2) (Vaugier *et al.*, 2012), as represented by the following equation,

$$\mathrm{U} = \mathrm{E}(\mathrm{d}^{\mathrm{n}+1}) + \mathrm{E}(\mathrm{d}^{\mathrm{n}-1}) - 2\mathrm{E}(\mathrm{d}^{\mathrm{n}}) \tag{1.7}$$

The Hubbard U parameter represents the total energy of a system with n electrons filling the d shells of an atom. It has evolved from a local intra-orbital parameter to a more general on-site, inter-site, and interaction parameter.

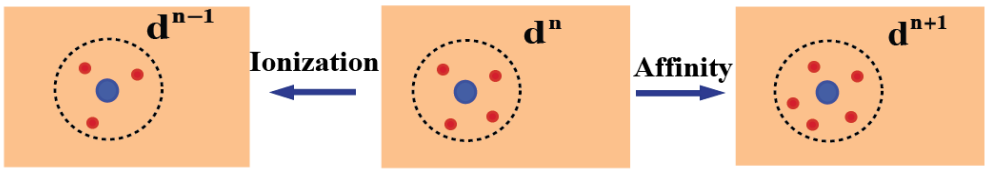

Figure 2: Schematic representation of electron addition and removal from a given atomic shell (Vaugier *et al.*, 2012).

TMOs and related superstructures are being explored for smart materials due to their rich behavior of complex interactions. These interactions are governed by local broken symmetry, electrostatic coupling, charge transfer, strain of various external fields resulting in novel emergent phenomena (Held, 2007).

In recent years, the nanoscale materials' with low-dimensional structure acts as a fascinating field of research in various scientific and technological disciplines. Quantum material interfaces and superstructures engineering have potential applications in everyday life, including smart device applications based on oxide interfaces, organic superstructures, van-der-Waals superstructures, and electrostatically constructed superstructures (Nekrasov *et al.*, 2005; Gibert *et al.*, 2012).

To examine the filling and band control Mott MIT, the ideal cubic phase of $LaVO_3$ is electronically reconstructed to a supercell, $La_{1-x}Ca_xVO_3$ (x = 0, 0.40, 0.60, 1). The study of quantum-matter superstructures and their applications will be a highly rewarding and exciting field of modern science and technology for decades to come (Zubko *et al.*, 2011).

The DFT often fails to represent strongly correlated systems (SCS) and DMFT relies on identifying suitable models for specific materials, with effective dynamical single site lattice models being popular to address the problem (Kotliar & Vollhardt, 2004; Held, 2007). The successful theoretical explanation of strongly correlated materials relies on judicious integration of ab-initio electronic structure and advanced numerical many-body theory, like DMFT (Hirsch & Fye, 1986; Georges *et al.*, 1996).

Furthermore, a comprehensive study of electronic and atomic reconstructions of superstructures of two different TMOs with various site substitution of Ca-atoms in $LaVO_3$ supercell is investigated for the novel properties of correlated system (Metzner & Vollhardt, 1989; Rubtsov *et al.*, 2005; Saeed *et al.*, 2014). The DFT with DMFT can be used to study Mottronics devices, including resistive switches, sensors, memory devices, qbits, magnetic storage and etc. (Paudyal *et al.*, 2006; Palczewski *et al.*, 2008; Kaphle *et al.*, 2015). It is used for theoretical examinations of materials like TMOs, with the Hubbard satellite prediction being a significant success. The CT-QMC is a family of stochastic algorithms that extends the entire partition function of a system as a sequence of Feynman diagrams to solve the AIM at finite temperature. Wick's expansion is used

to convert time ordered group diagrams into determinants, and the resultant series are stochastically summed up using Markov chain Monte Carlo. The quantum impurity problems explain the behavior of a magnetic impurity placed in an electronic bath (host) in general.

The Anderson impurity model (AIM), representing an infinite-dimensional lattice system with an impurity randomly interacting with the surrounding electronic bath, is effective for understanding magnetic impurities in metallic hosts. This approach can be used to solve lattice models like the Hubbard model at half filling (Kotliar & Vollhardt, 2004; Vollhardt, 2012). The filling control method and band control method are used in the MIT in the $La_{1-x}Ca_xVO_3$ system (Maiti *et al.*, 2004). The filling control method involves the substitution of holes or electrons, while the band control method involves site substitution of La -ion with Ca -ion. These experimental methods provide valuable insights into the complex behavior of the system (Blaha *et al.*, 2002; Sevik, 2010).

The transport coefficients are extremely important for predicting and designing novel materials in a variety of domains, including superconductors, transparent conductors, transparent insulators, intermetallic phases, and efficient thermometric materials. Because of the weak orbital overlap, TMOs have narrow conduction band (CB), with localized electrons having low carrier mobilities.

TMOs are potentially recognized as thermoelectric (TE) materials with a scalability for higher temperatures, in addition to the fact that perovskite materials are advantageous for the construction of high efficiency solar cells (Walia *et al.*, 2013; Shi & Jayatissa, 2018). They have higher Seebeck coefficients (S), lower the electronic part of thermal conductivity (κ). For the pristine $CaVO_3$ and $LaVO_3$ and their superstructures, we estimated the Hall coefficient (R_H), molar specific heat capacity (C), magnetic susceptibility (χ), and so on (Chuang *et al.*, 2001; Nekrasov *et al.*, 2005; Sevik, 2010).

In addition to their electronic and thermoelectric properties, the elastic properties of TMOs is another avenue of exploration. Knowledge and understanding of their behavior under severe constraints of high pressure and temperature environments are crucial for new advances and innovations in materials in contemporary technologies of various fields(Reinle-Schmitt *et al.*, 2012).

There are several approaches of DMFT that can be employed, including CT-QMC (Werner *et al.*, 2006; Gull *et al.*, 2007), numerical renormalization group (NRG) (Bulla *et al.*, 2008), exact diagonalization (ED), and others (Imada *et al.*, 1998). The electronic structure of undoped and doped $LaVO_3$ was investigated for Mott-Hubbard splittings (Georges *et al.*, 1996; Kowalski *et al.*, 2019). Mott-insulators with strong repulsive interaction between electrons can be altered by chemical doping, strain, and external field application (Imada *et al.*, 1998; Janod *et al.*, 2015). This electronic phase transition leads to MIT, resistive switching (RS), ferroelectrics, and superconductivity. Researchers are working on smart electronic devices with ultrafast switching rates and low power consumption (Inaba *et al.*, 1995; Nekrasov *et al.*, 2005).

Indeed, the computational physics emerged out from the computers' ability to solve intractable physical problems, making it a speciality and reality (Chatterjee *et al.*, 2019). The MEM, based on Bayesian statistical inferences (Jarrell & Gubernatis, 1996; Bergeron & Tremblay, 2016), is used to reconstruct noisy and oversampled quantum Monte Carlo (QMC) data. This technique can investigate the Mott-Hubbard MIT of TMOs materials (Parragh *et al.*, 2012; Prezioso *et al.*, 2015).

In many-body problems, the electronic Green's function (GF) is typically estimated in terms of imaginary-time or Matsubara frequency using numerical methods such as QMC. The imaginary-time GF, $G(\tau)$ is related to the spectral function (SF), $A(\omega)$ via a Laplace transform, $(i\omega_\nu \rightarrow \omega)$, also known as the analytic continuation. A little change in $G(\tau)$ correlates to a large difference in $A(\omega)$ during its computation, possibly leading to the unphysical situation. That is, the simple inversion of the integral computation is proven to be ill-posed causing a higher numerical noise, resulting in some unphysical situations (Gull & Skilling, 1984; Silver *et al.*, 1990).

The MEM, which is based on the conditional probabilities to obtain the most probable spectrum, is one of the main mathematical tools for solving such problem. Maximum entropy method efficiently solves optimization issue assuming default Gaussian probability distributions (Gubernatis *et al.*, 1991; Jarrell & Gubernatis, 1996; Yoo *et al.*, 2005). Well-designed quantum matter heterostructures are environmentally friendly and commercially viable. Studying structural, electrical, and electrical properties using theoretical models like DMFT, DMRG, and CT-QMC can reveal emergent phenomena like MITs, T_C superconductivity (Calandra & Gunnarsson, 2002) and much more.

Theoretical study on the Hubbard model's electric-field-driven breakdown of a Mott state agrees with an intuitive explanation for the beginning of transition (Stoliar *et al.*, 2017). In all pristine and superstructures of TMOs, the Mott mechanism facilitates the transition from a low resistance state (LRS) to a high resistance state (HRS) and vice versa (Rückamp *et al.*, 2005).

Mott insulators are a class of strongly correlated materials with a variety of emergent new properties that make them suitable for designing artificial neurons for neural networks. This can be accomplished by exploiting the RS that happens in these materials in the presence of an external field (Von Neumann, 1986; Janod *et al.*, 2015; Stoliar *et al.*, 2017). The Mott-FET, which serves as a paradigm for a new category of electronic devices in the Mottronics family, employs the MIT as its fundamental mechanism i.e. a transition from LRS to HRS or vice versa. Intensive research is now being undertaken to control the mechanisms that rely on voltage, strain, pressure, and optical stimulations (Kravtsov *et al.*, 2011; Yao *et al.*, 2020).

One of the fundamental aims of thermoelectric research is to improve the efficiency of various heat-to-electricity conversion technologies. The current goals in this field of study is to create unique and smart material systems with increased conversion efficiency (Hicks & Dresselhaus, 1993; Honda *et al.*, 2002; Bell *et al.*, 2009). The ground breaking work of Hicks and Dresselhaus inspired the concept of decreasing dimensionality to increase the figure of merit for the best values in bulk materials (Hicks & Dresselhaus, 1993; Hirayama *et al.*, 2012).

With the motivation of above mentioned examples and methodologies, we have employed the first-principles based self-consistent calculations for investigating the relevant properties of complex TMOs materials. This work intends to investigate the various properties of various pristines and site-substituted superstructures of titanates ($LaSrTi_2O_6$, $LaCaTi_2O_6$, $La_{1-x}Sr_xTiO_3$ and $Ca_{1-x}Y_xTiO_3$), and vanadates ($Ca_{1-x}Sr_xVO_3$, $LaSrV_2O_6$, $La_{1-x}Sr_xVO_3$ and $La_{1-x}Ca_xVO_3$) systems.

Furthermore, we also extended our work to investigate the influence of cation site-substitutions on MIT of compounds using DFT and DMFT along with MEM. The theoretical insights regarding CT-QMC technique along with the analytic continuation (AC) through MEM for the various behaviors of the materials has also been described.

1.2 Rationale of the Study

There are several models and procedures that used to uncover and modify the physical phenomena of TMOs and their superstructures, including site-substituted heterosuperstructures (Bell *et al.*, 2009). TMOs are complex quantum materials with correlated

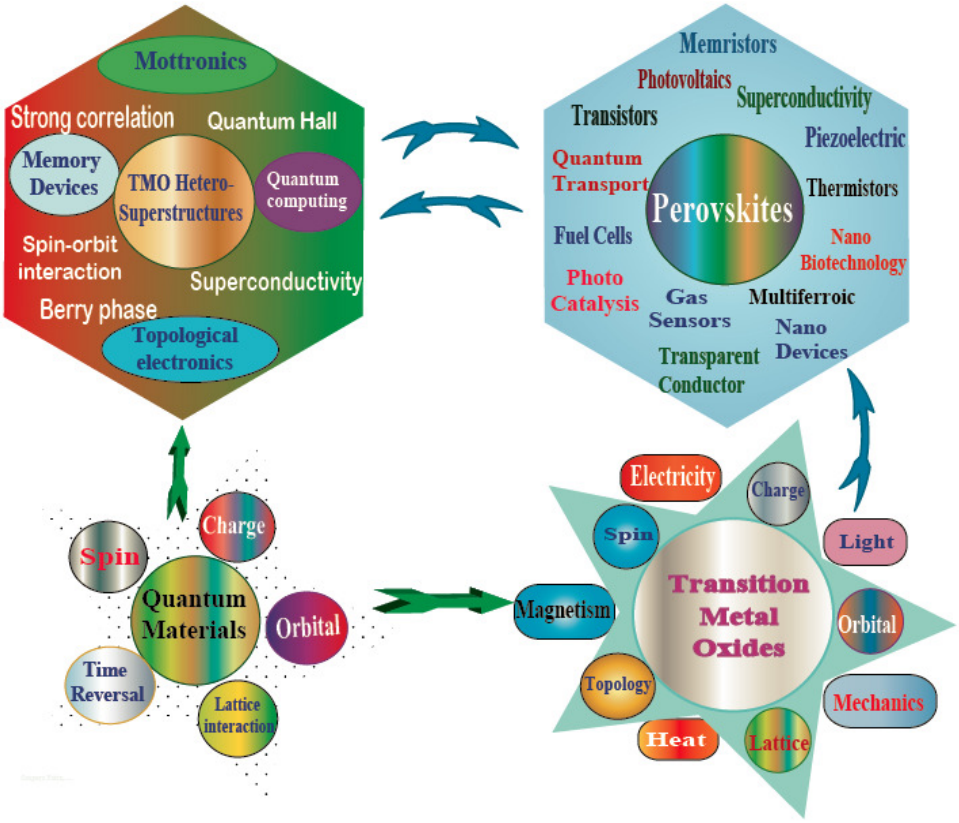

Figure 3: The schematic of rationales for the study of TMOs and its superstructure as quantum materials (Imada *et al.*, 1998; Tokura *et al.*, 2017; Zunger & Malyi, 2021) .

electronic systems, involving charge, spin, orbital, and lattice interactions. These structures exhibit unique novel properties due to competing phase transitions in all dimensions and morphologies (Fig. 3) (Imada *et al.*, 1998; Tokura *et al.*, 2017; Zunger & Malyi, 2021). In order to compute the realistic picture of electronic structure of strongly correlated electronic system and study the Mott-Hubbard MIT, we used self-consistent DMFT calculations (CT-QMC hybridization technique) (Georges *et al.*, 1996; Kowalski *et al.*, 2019). Spectral density (SD) distribution was computed using CT-QMC data through the MEM for statistical inferences (Shao *et al.*, 2017).

The chemical doping, strain, and external field application can change the strong repulsive interaction between electrons in Mott-insulators (Imada *et al.*, 1998; Janod *et al.*, 2015). In fact, ferroelectrics, superconductivity, MIT, and RS are all the outcome of this

electronic phase transition. Researchers are developing smart electronic gadgets with extremely fast switching speeds and little power usage (Nekrasov *et al.*, 2005; Xue *et al.*, 2013; McNally *et al.*, 2019).

These materials have direct applications in modern smart devices, including Mottronics (resistive switches, sensors, actuators etc.); memory devices (qbits; magnetic storage, resistive memory devices, artificial neurons etc.); thermoelectric devices (generators, freezers etc.); and other diverse functional materials (Dong *et al.*, 2008; Pickett *et al.*, 2013; Yao *et al.*, 2020; Zunger & Malyi, 2021).

In this study, we have used the standard DFT and DMFT along with MEM to explore the electronic transport behaviors, and thermoelectric and optically driven transport properties of the pristines and the electronically reconstructed superstructures of vanadate and titanate systems.

Research Gaps

The present study is focused to go more insight into theoretical models and to work on the research gaps obtained from the literatures, viz.

- There is a lack of systematic study of the various properties of pristine and site-substituted superstructures of titanates and vanadates.
- There is a minimal study of the effects on Mott-Hubbard band splittings of cation site-substitutions of various proportions of cations in the superstructures of titanate and vanadate systems.
- There is lack of study of thermoelectric and optically driven transport properties of site-substituted superstructures of titanates and vanadates for predicting and designing efficient energy devices.

The systematic and comparative study of the model parameters for MIT phase transitions and other properties of these complex TMOs are crucially important for tunability for the Mottronics devices, quantum and neuromorphic computing devices, resistive memory devices, machine learning devices and energy harvesting devices.

To explore the above research gaps, we are motivated to work on system's properties like stability, electronic transport, thermoelectric and optical conductivity, and tuning behaviors to gain deeper insights.

1.3 Objectives

The objectives of the present study are organized as follows:

1.3.1 General Objective

Investigation of Transport Properties of Site-substituted Superstructures of Complex TMOs: (La,Sr)TiO_3 /(Ca,Y)VO_3.

1.3.2 Specific Objectives

1. Study of the various stabilities of pristines and site-substituted superstructures of titanates: [$LaSrTi_2O_6$, $LaCaTi_2O_6$, $La_{1-x}Sr_xTiO_3$ and $Ca_{1-x}Y_xTiO_3$], and vanadates: [$Ca_{1-x}Sr_xVO_3$, $LaSrV_2O_6$, $La_{1-x}Sr_xVO_3$ and $La_{1-x}Ca_xVO_3$] systems.
2. Study of the electronic transport, and thermoelectric and optically driven transport properties of pristines and site-substituted superstructures of titanates and vanadates.
3. Study of Mott-Hubbard band splittings of the pristines and their site-substituted superstructures for investigating its tunability of MIT parameters.

1.4 Organization of Study

The thesis entitled "Investigation of Transport Properties of Site-substituted Superstructure of Complex TMOs: (La,Sr)TiO_3/(Ca,Y)VO_3", comprised of the following six chapters:

Chapter-1: The first chapter presents a brief introduction to the scientific philosophy and methods of doing science in connection with the research objectives. Motivation and rationale of study of the SCS in relation to the investigation of MIT, including other physical properties of the TMOs. It also provides the research gaps of the present study.

Chapter-2: This chapter deals with the review of findings of previous work related to present study. This provides the idea of various properties of TMOs, and their superstructures, synthesis process, and their applications. The research questions to be done with motivation have described which ultimately provides the concept to develop and modify the objectives of the present study.

Chapter-3: We present the general theoretical methods, the extended methodology for the ab-initio study of pristine TMOs and their superstructures. The theoretical background (DFT, DMFT, MEM and others) for the investigation of structural, mechanical stability, electronic transport including Mott-Hubbard metal insulator transitions (MIT), and thermoelectric transport and optically influenced transport properties are discussed.

Chapter-4: The overall results of present calculation with physical reasoning are explained within this chapter. This explanation includes the study of the structural, chemical, mechanical stabilities in one section whereas the detail explanation of the electronic transport properties are given in next section before thermoelectric and optically driven transport properties of the strongly correlated pristines and their site substituted superstructures of titanates and vanadates systems respectively.

Chapter-5: The conclusion and recommendations chapter contains the conclusions of main finding of the present work. Further, what can be done in future is recommended as a further research possibilities.

Chapter-6: Summary contains the key points of findings of the present work in brief which describes whole idea of our research work.

Finally, we have included the references, appendices, publications, and participations in the last portion of the thesis.

CHAPTER 2

LITERATURE REVIEW

The TMOs are strongly correlated electronic systems with strong electron-electron interactions comparable to or greater than kinetic energy. These class of quantum materials unequivocally harbors a large number of novel smart behaviors, which are extremely useful for the current and future technological needs. In this study, we examine the structural, chemical, mechanical, electronic transport and other physical properties of the complex TMOs, which is mainly focused on the investigation of Mott-Hubbard MIT of these materials. The metallic phase of the Hubbard model ($d \rightarrow \infty$) is used to investigate quasi peaks and Hubbard bands in these systems, using generic properties on the single-impurity Anderson model and self-consistency condition. We are actually motivated to do this research work based upon the following chronologically ordered literature reviews as follows.

Thermal issues are a significant limiting factor in complementary metal oxide semiconductor (CMOS) scaling, causing over half of electrical failures. Thus, studying thermal management and logic flow concurrently is crucially important for system-level approaches (Bar-Cohen, 1987).

The concept of maximum entropy using the Bayesian statistical inferences were introduced by Jarrell *et al.* (1996), for the analytical continuation of QMC data to analyze the strongly correlated system (Jarrell & Gubernatis, 1996). The effect on metal insulator transition (MIT) of materials through filling control, band control, dimensionality, vacancy effects, etc. were investigated theoretically and experimentally on various TMOs (Titanates/Vanadates/Ruthanates/Manganates/Nickelates/Cuprates) (Imada *et al.*, 1998).

Sachdev, in 1999, investigated the competing ground states in low dimensions and nonzero temperature dynamic features around QCP using a simple model for correlated

systems in a two-dimensional square lattice electron gas (Sachdev, 1999). Inoue *et al.* (2002), used a detailed de Haas-van Alphen effect of the perovskites for testing the electronic structure calculations in a 3d TMOs through experimental and Fermi surface study of the cubic perovskite structures (Inoue *et al.*, 2002).

Sekiyama *et al.* (2004), studied Sr_{1-x} Ca_xVO_3 systems using the bulk photoemission spectra and the LDA + DMFT with non-perturbative technique (Sekiyama *et al.*, 2004). Piskunov *et al.* (2004) studied the electronic structures using HF and DFT with B3PW, B3LYP correlations for the titanates of (Ba,Sr,Pb) and compared the band gaps (Piskunov *et al.*, 2004). Ohtomo *et al.*, in the same year, studied polar discontinuities at hetero-interfaces in crystalline materials, which cause local atomic and electronic structures, impacting electron mobility in $LaAlO_3$/$SrTiO_3$ systems (Ohtomo & Hwang, 2004; Nazir *et al.*, 2015). By the same year, Maiti *et al.* investigated the electronic and transport properties of La_{1-x} Ca_xVO_3, for x= 0.4 and 0.5, studied using the experimental method (polycrystalline samples were prepared from stoichiometric amounts of predried La_2O_3,$CaCO_3$, and V_2O_5 and characterized by EDAX, XRD, XPS etc.) (Maiti *et al.*, 2004).

Ferrero *et al.* (2005), studied the Mott MIT in infinite dimensions using Gutzwiller variational wave function and dynamical mean-field theory, which was compatible with various scenarios, including narrow-gap semiconductors and semimetals (Ferrero *et al.*, 2005). In the same year, Rückamp *et al.*, investigated the competition between orbital fluctuations (for dominant exchange coupling) and crystal field effect (CFE) splitting (for dominant coupling to the lattice) at low energies (Rückamp *et al.*, 2005).

Held (2007), investigated the realistic picture of electronic structures of SCSs using LDA + DMFT (IPT, NCA etc.) and experimental (PES, XAS etc.) for the various titanates/vanadates/ruthanates systems (Held, 2007). In the same year, Haule studied the electronic structures of SCS through computational method (DMFT within full-potential method (Haule, 2007). Dong *et al.* (2008) studied the metal-insulator physics of early TMOs (ABO_3 type with rare earth using the DFT + U and DFT + DMFT approaches, with an emphasis on p-d covalency. This led to the metal-insulator phase diagrams for materials.

All deep-space probe power sources use thermoelectric (TE) generators like radioisotope thermoelectric generator (RITEG) and solar thermoelectric generator (STEG) to convert heat generated by nuclear fissile materials and solar radiation to electricity. Many low-power devices, such as hearing aids and wrist watches, use micro-thermoelectric generators (Ryu *et al.*, 2010; Kanatzidis, 2010; LeBlanc, 2014).

The theoretical analysis of Matsubara GFs of quantum impurity models, based on Legendre orthogonal polynomials, revealed that their direct representation is more compact, enabling the development of a systematic technique for filtering out Monte-Carlo noise in physical quantities (Boehnke *et al.*, 2011). Hirayama *et al.* (2012), studied the band structure of $LaAlO_3$/$SrTiO_3$ interfaces with strongly entangled bands. For transition metal-oxide heterostructures, the effective Hamiltonian parameters are computed using a multi-scale ab-initio approach for correlated electrons and a constrained random phase approximation (Hirayama *et al.*, 2012; Gandolfi *et al.*, 2017; Santana *et al.*, 2020). In the same year, Vaugier *et al.* investigated the materials with strong electronic Coulomb interactions to compute the local effective Coulomb interaction matrix, and Hund's exchange J in TMOs (Vaugier *et al.*, 2012). For mapping the electronic reconstruction at the interface in $LaVO_3$/$SrVO_3$ heterostructures, the Pulsed Laser Deposition, HAADF-STEM, STEM-EELS etc. were employed (Tan *et al.*, 2013).

Mahmood *et al.* (2014), investigated the high thermopower at ambient temperature in n-type $AgNbO_3$ compared to $AgTaO_3$ utilizing FP-LAPW + LO approach employed by the BoltzTraP code in the DFT framework (Mahmood *et al.*, 2014). The resistive switching (RS) in a narrow gap Mott insulators ($V_{1-x}Cr_x)_2O_3$, $Ni(S,Se)_2$, AM_4Q_8) and correlated systems are studied experimentally for designing and testing artificial neuron (Von Neumann, 1981; Janod *et al.*, 2015; Fournier *et al.*, 2020).

Benedict *et al.* (2016), examined the essential TE parameters of $LaCoO_3$ (Benedict *et al.*, 2016), the influence of the exposure of electron beam on various characteristics were investigated. Transparent conductive oxides (TCOs) of perovskite type are promising candidates for photovoltaic applications (Zhang *et al.*, 2016; Jellite *et al.*, 2018). ABO_3 perovskite oxide with material modification via doping will enhance the conductivity. By mixing and doping materials, the ideal TCO with improved transparency and electrical resistivity (crucial optoelectrical characteristics) were obtained (Zitko *et al.*, 2013; Riza

et al., 2016). Tunability of electron-electron interaction could be useful tool in simulating quantum devices. Complex oxide hetero-structuring method are used to store qubits or perform gate operation in quantum computing systems (Zhong & Hansmann, 2017; Ohshima *et al.*, 2017). Topologically protected qubits or hybrid systems (e.g., N-V centers) with quantum wires for superconducting qubits are feasible.

It is demonstrated that strongly correlated metallic perovskites are a novel family of materials with high potential for RS applications due to their inherent MIT features, which enhance a robust volumetric RS effect. The artificial neuron can be achieved by taking use of the RS that happens in the correlated materials in an electric field (Pruschke & Bulla, 2005; Feng & Lam, 2011; Stoliar *et al.*, 2017). Eisenlohr *et al.* (2019), studied the Mott quantum criticality in the Hubbard model (Vale *et al.*, 2018; Eisenlohr *et al.*, 2019) using the DMFT, power-law spectra, and scaling (analytically and numerically).

Madsen *et al.* (2018), described that the BoltzTraP algorithm interpolates band structures, calculates semi-classical transport coefficients, explores thermoelectric transport properties using linearized Boltzmann transport equation (BTE) (Madsen *et al.*, 2018). The thermoelectric phenomena is a method for converting waste thermal energy into useful electricity without the need of hazardous chemicals such as CFCs or other components for cooling the environment (Adewale *et al.*, 2018; Wang *et al.*, 2019).

Nanowires can effectively satisfy the criteria for high performance thermoelectric devices (Dominguez-Adame *et al.*, 2019). Experimentally grown set of 6 nm thick samples of high-quality, surfaces namely $LaNiO_3$ on $LaAlO_3$ (LNO/LAO), $NdNiO_3$ on $LaAlO_3$ (NNO/LAO) and $NdNiO_3$ on $NdGaO_3$ (NNO/NGO) using CSD method and characterized with C-AFM, STM, TEM, PPMS (Gonzalez-Rosillo *et al.*, 2020). The upconversion (UC) emissions and their ambient dependencies of $SrTiO_3$ polycrystals co-doped in Er^{3+} and Yb^{3+} at different substitution sites were investigated using the experimental synthesis and characterizations with XRD, PLE (Shin *et al.*, 2021).

Ronchi *et al.* (2021), reported that the MIT are the basic mechanism for Mottronics to regulate MIT via voltage, strain, heat, and light stimulations (Ronchi *et al.*, 2021). Resistive Random Access Memory (RRAM) are promising candidates for universal memory in future devices due to their excellent scalability, endurance, retention, and switching speeds, surpassing current technologies like Flash and Dynamic RAM.

Beck *et al.* (2023), have investigated the thickness dependence of electronic reconstruction within the $LaVO_3/SrVO_3$ layers. The layer dependent spectral weight at Fermi level as well as the layer dependent t_{2g} occupations as a function of Coulombian interaction, U parameter (Beck & Ederer, 2023).

Based upon the above literature review, we are motivated to focus our study on the structural, chemical, mechanical stabilities, and thermoelectric and optically induced transport properties of pristines and site-substituted titanates: $CaTiO_3$, $LaTiO_3$, $SrTiO_3$, $YTiO_3$, $LaSrTi_2O_6$, $LaCaTi_2O_6$, $Ca_{0.33}Y_{0.67}TiO_3$ and $La_{0.80}Sr_{0.20}TiO_3$ systems, and the vanadates: $CaVO_3$, $LaVO_3$, $SrVO_3$, YVO_3, $(La_{1-x}Sr_xVO_3)_n$, $(Ca_{1-x}Sr_xVO_3)_n$ and $(La_{1-x}Ca_xVO_3)_n$, systems, which are useful for the tuning behaviors TMOs materials for all smart devices of current and future technological needs.

CHAPTER 3

MATERIALS AND METHODS

3.1 Theoretical Background

To comprehend the microscopic behaviors of a material, one must address the atomistic level of investigation, where the individual identity of electrons is ignored. The basic methodologies for studying their desirable properties varies depending on their atomic or molecular organizations. We have used the standard DFT for the stability, electronic transport properties, and optical properties, whereas the DMFT along with the DFT data for studying the metal-insulator phase transition using MEM. We also perform a complementary calculation using the MEM for the realistic representation of DMFT data. The quantum mechanical method of the many body SWE represents the electronic structure (properties) of a material made of numerous interacting nuclei and electrons (Martin, 2020).

3.1.1 The Many-Body Schrödinger Equation

The Hamiltonian for the Schrödinger wave equation for a many-body system with electrons and nuclei (Born & Oppenheimer, 1927) is,

$$\hat{\mathrm{H}} = -\frac{\hbar^2}{2\mathrm{m_e}}\sum_{\mathrm{i}=1}\nabla_{\mathrm{i}}^2 + \frac{1}{2}\sum_{\mathrm{i}\neq\mathrm{j}}\frac{\mathrm{e}^2}{|\mathbf{r}_\mathrm{i}-\mathbf{r}_\mathrm{j}|} - \frac{1}{2}\sum_{\mathrm{i,I}}\frac{\mathrm{Z_I e}^2}{|\mathbf{r}_\mathrm{i}-\mathbf{R}_\mathrm{I}|} - \sum_{\mathrm{I}}\frac{\hbar^2\nabla_{\mathrm{I}}^2}{2\mathrm{M_I}} + \frac{1}{2}\sum_{\mathrm{I}\neq\mathrm{J}}\frac{\mathrm{Z_I Z_J e}^2}{|\mathbf{R}_\mathrm{I}-\mathbf{R}_\mathrm{J}|} \tag{3.1}$$

where the indices I, J sum over all nuclei, whereas i, j sum over the electrons with m_e and M_I representing the masses of electron and nucleus, respectively (Fig. 4).

In short, the equation (3.1) can be expressed as,

$$\hat{\mathrm{H}} = \hat{\mathrm{T}}_\mathrm{e} + \hat{\mathrm{V}}_\mathrm{ee} + \hat{\mathrm{V}}_\mathrm{Ne} + \hat{\mathrm{T}}_\mathrm{N} + \hat{\mathrm{V}}_\mathrm{NN}. \tag{3.2}$$

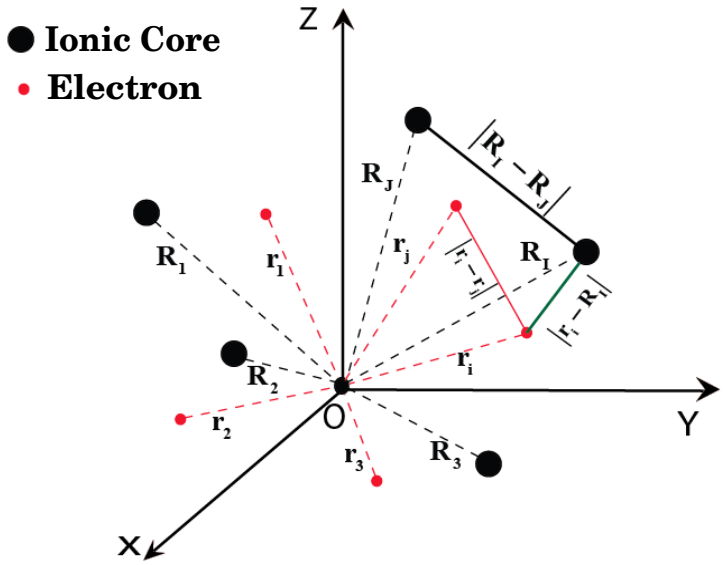

Figure 4: The schematic representation of interacting ionic cores and electrons in many-body system (Martin, 2020).

where,

$$\hat{\mathrm{T}}_{\mathrm{e}} = -\frac{\hbar^2}{2\mathrm{m_e}} \sum_{\mathrm{i}=1} \nabla_{\mathrm{i}}^2 \quad : \quad \text{K. E.of electrons}$$

$$\hat{\mathrm{V}}_{\mathrm{ee}} = \frac{1}{2} \sum_{\mathrm{i}\neq\mathrm{j}} \frac{\mathrm{e}^2}{|\mathbf{r}_\mathrm{i} - \mathbf{r}_\mathrm{j}|} \quad : \quad \text{Electron and electron Coulomb repulsion energy}$$

$$\hat{\mathrm{V}}_{\mathrm{Ne}} = -\frac{1}{2} \sum_{\mathrm{i,I}} \frac{\mathrm{Z_I e}^2}{|\mathbf{r}_\mathrm{i} - \mathbf{R}_\mathrm{I}|} \quad : \quad \text{Electron and nuclei Coulomb attraction energy}$$

$$\hat{\mathrm{T}}_{\mathrm{N}} = -\sum_{\mathrm{I}} \frac{\hbar^2 \nabla_{\mathrm{I}}^2}{2\mathrm{M_I}} \quad : \quad \text{K. E of nuclei}$$

$$\hat{\mathrm{V}}_{\mathrm{NN}} = \frac{1}{2} \sum_{\mathrm{I}\neq\mathrm{J}} \frac{\mathrm{Z_I Z_J e}^2}{|\mathbf{R}_\mathrm{I} - \mathbf{R}_\mathrm{J}|} \quad : \quad \text{N-N Coulomb repulsion energy}$$

If $\psi(\mathbf{R}_\mathrm{I}, \mathbf{r}_\mathrm{I})$ is the complete w.f. of the system, so that the Schrödinger equation becomes,

$$\hat{\mathrm{H}}\psi(\mathbf{R}_\mathrm{I}, \mathbf{r}_\mathrm{I}) = \mathrm{E}\psi(\mathbf{R}_\mathrm{I}, \mathbf{r}_\mathrm{I}) \tag{3.3}$$

The Schrödinger equation is exact but unachievable due to a high computational cost. Born and Oppenheimer proposed the Born-Oppenheimer approximation (BOA) in 1927 to overcome such problems and separate nuclear and electronic motion, providing essential information for solving the Schrödinger equation (Ashcroft & Mermin, 1976; Martin, 2020).

3.1.1.1 Born-Oppenheimer Approximation (BOA)

In BOA the nuclei are assumed to be at rest, compared to electron motion calculated using the Schrödinger equation. An external potential is generated by nuclei, separating

the wavefunction into nuclear and electronic components (Born & Oppenheimer, 1927) as,

$$\psi(\mathbf{R}_\mathrm{I}, \mathbf{r}_\mathrm{I}) = \chi(\mathbf{R}_\mathrm{I}).\phi(\mathbf{R}_\mathrm{I}, \mathbf{r}_\mathrm{I}) \tag{3.4}$$

where $\chi(\mathbf{R}_\mathrm{I})$ represents nuclei and $\phi(\mathbf{R}_\mathrm{I}, \mathbf{r}_\mathrm{I})$ represents electronic parts of the wavefunction. The electronic portion of the Hamiltonian comprises of interacting electrons under the influence of a static external (nuclear) potential as given by,

$$\hat{\mathrm{H}}_\mathrm{e} = -\frac{\hbar^2}{2\mathrm{m}_\mathrm{e}} \sum_{\mathrm{i}=1}^{\mathrm{N}} \nabla_\mathrm{i}^2 - \frac{1}{2} \sum_{\mathrm{i,I}} \frac{\mathrm{Z_I e}^2}{|\mathbf{r}_\mathrm{i} - \mathbf{R}_\mathrm{I}|} + \frac{1}{2} \sum_{\mathrm{i} \neq \mathrm{j}} \frac{\mathrm{e}^2}{|\mathbf{r}_\mathrm{i} - \mathbf{r}_\mathrm{j}|}. \tag{3.5}$$

Hence, the Schrödinger equations for the interacting nuclear part of Hamiltonians can be written as,

$$\left[-\sum_\mathrm{I} \frac{\hbar^2 \nabla_\mathrm{I}^2}{2\mathrm{M_I}} + \hat{\mathrm{V}}(\mathbf{R}_\mathrm{I}) \right] \chi(\mathbf{R}_\mathrm{I}) = \mathrm{E}' \chi(\mathbf{R}_\mathrm{I}) \tag{3.6}$$

The energy eigenvalues of a system with interaction potential, $\mathrm{V}(\mathbf{R}_I)$, are parametrically dependent on nuclear positions. It can be obtained by solving equations (3.3), which can be used to solve nuclear motion. The energy of the system can be approximated using these solutions (3.6). There are various approaches for using independent particle approximation, viz. (a) the wave-function method and (b) density-functional theory method. We discuss Hartree (Hartree *et al.*, 1939; Perdew *et al.*, 1996) and Hartree-Fock (Fock, 1930; Eschrig, 1996) approximations within the wave-function approach.

3.1.1.2 Hartree Approximation

D. R. Hartree (Hartree *et al.*, 1939) was the first to create independent electron approximation, in which electrons are uncorrelated except for the Pauli-exclusion principle. Each electron moves under the effective potential of average Coulombian interactions, and the overall w.f. of electrons is the product of N one-electron w.f., Thus, the many-body wave function may be expressed as,

$$\psi_\mathrm{H}(\mathbf{r_1}, \mathbf{r_2}, \cdots, \mathbf{r_n}) = \phi_1(\mathbf{r}_1)\phi_2(\mathbf{r}_2), \cdots, \phi_\mathrm{n}(\mathbf{r}_\mathrm{n}) \tag{3.7}$$

The total energy can be computed as,

$$\hat{\mathrm{H}}\psi_{\mathrm{H}}(\mathbf{r_1}, \mathbf{r_2}, \cdots, \mathbf{r_n}) = \mathrm{E}\psi_{\mathrm{H}}(\mathbf{r_1}, \mathbf{r_2}, \cdots, \mathbf{r_n}) \tag{3.8}$$

The self-consistent variational approach is used to find the solutions. Although the Hartree's principle helps in reducing the complexity of the interacting many electron system, it ignores antisymmetric electronic wave-functions and does not account for exchange and correlation energy.

3.1.1.3 Hartree-Fock Approximation

Hartree-Fock (HF) theory introduces anti-symmetric electronic wave function for the inclusion of spin degree of freedom (Fock, 1930; Hartree *et al.*, 1939; Löwdin, 1955), where the wave functions are expressed in terms of single Slater (Slater, 1951; Becke, 1993) determinant of N different orbitals with spin indices, σ_i as,

$$\psi_{\mathrm{HF}} = \frac{1}{\sqrt{\mathrm{N}!}} \begin{vmatrix} \phi_1(\mathbf{r}_1, \sigma_1) & \phi_1(\mathbf{r}_2, \sigma_2) & \cdots & \phi_1(\mathbf{r}_n, \sigma_n) \\ \phi_2(\mathbf{r}_1, \sigma_1) & \phi_2(\mathbf{r}_2, \sigma_2) & \cdots & \phi_2(\mathbf{r}_n, \sigma_n) \\ \vdots & \vdots & & \vdots \\ \phi_n(\mathbf{r}_1, \sigma_1) & \phi_n(\mathbf{r}_2, \sigma_2) & \cdots & \phi_n(\mathbf{r}_n, \sigma_n) \end{vmatrix} \tag{3.9}$$

Hence the Hamiltonian equation in the form of $\phi_i(\mathbf{r})$ becomes (in Hartree units),

$$\begin{aligned} \left(-\tfrac{\nabla^2}{2} + \hat{\mathrm{V}}_{\mathrm{ext}}\right)\phi_{\mathrm{i}}(\mathbf{r}) + \int \mathrm{d}^3\mathrm{r}' \tfrac{1}{(|\mathbf{r}-\mathbf{r}'|)} \textstyle\sum_{\mathrm{j}\neq\mathrm{i}} \phi_{\mathrm{j}}^*(\mathbf{r}')\phi_{\mathrm{j}}(\mathbf{r}')\phi_{\mathrm{i}}(\mathbf{r}) \\ - \textstyle\sum_{\mathrm{j}\neq\mathrm{i}} \phi_{\mathrm{j}}^*(\mathbf{r}')\phi_{\mathrm{i}}(\mathbf{r}')\phi_{\mathrm{j}}(\mathbf{r})\delta_{\mathrm{s_i s_j}} = \varepsilon_{\mathrm{i}}\phi_{\mathrm{i}}(\mathbf{r}). \end{aligned} \tag{3.10}$$

This Hamiltonian includes exchange potential, which is defined by,

$$\hat{\mathrm{V}}_{\mathrm{X}} = -\sum_{\mathrm{j}\neq\mathrm{i}} \frac{1}{|\mathbf{r}-\mathbf{r}'|}\phi_{\mathrm{j}}^*(\mathbf{r}')\phi_{\mathrm{i}}(\mathbf{r}')\phi_{\mathrm{j}}(\mathbf{r}) \tag{3.11}$$

The Hartree-Fock approximation (Fock, 1930; Hartree *et al.*, 1939; Löwdin, 1955), which incorporates Hartree and exchange terms in screening potential is,

$$\left[-\frac{\nabla^2}{2} + \hat{\mathrm{V}}_{\mathrm{ext}} + \hat{\mathrm{V}}_{\mathrm{sc}}\right] \phi_{\mathrm{i}}(\mathbf{r}) = \varepsilon_{\mathrm{i}}\phi_{\mathrm{i}}(\mathbf{r}) \tag{3.12}$$

with

$$\hat{\mathrm{V}}_{\mathrm{sc}} = \hat{\mathrm{V}}_{\mathrm{H}} + \hat{\mathrm{V}}_{\mathrm{X}}$$

The 1^{st} and 2^{nd} terms on l.h.s. of equation (3.12) consists of electron kinetic energy and electron-ion interaction energy, respectively, and 3^{rd} term represent the electrostatic interactions between electrons, including self-interaction.

The equation excludes the self-interaction term, following the Pauli-exclusion principle. The electron correlation, crucial in systems, is not included, which can be taken as E^0_{exact} - E^0_{HF}. Hartree and Hartree-Fock approximations are useful but require to handle a large number of variables (3N degrees of freedom) and need of a high computational cost. DFT, based on the Thomas-Fermi model, is an alternative approach for solving many-electron wave-functions with a single electronic density variable, extracting all information from electronic wave-functions.

3.1.1.4 Thomas-Fermi-Dirac (TFD) Model

Thomas and Fermi used electron density to solve interacting particle systems (Thomas, 1927; Fermi, 1928; Dirac, 1930), allowing the total energy as the functional of electron density with external potential $\mathrm{V}_{ext}(\mathbf{r})$ as,

$$\begin{aligned}\mathrm{E}_{\mathrm{TF}}[\mathrm{n}(\mathbf{r})] = \mathrm{C}_1 \int (\mathrm{n}(\mathbf{r}))^{5/3} \mathrm{d}^3\mathrm{r} + \int \mathrm{V}_{\mathrm{ext}}(\mathbf{r})(\mathrm{n}(\mathbf{r}))^{5/3}\mathrm{d}^3\mathrm{r} \\ + \tfrac{1}{2}\int\int \tfrac{\mathrm{n}(\mathbf{r})\mathrm{n}(\mathbf{r}')}{|\mathbf{r}_{\mathrm{i}} - \mathbf{r}_{\mathrm{j}}|}\mathrm{d}^3\mathrm{r}\mathrm{d}^3\mathrm{r}'\end{aligned} \tag{3.13}$$

The 1^{st} term on r.h.s. of equation (3.13) relates the KE of non-interacting electrons in HEG (in atomic units, $m_e = e = \hbar = \frac{4\pi}{\epsilon_0}$ =1) with $\mathrm{C}_1 = \frac{3}{10}(3\pi^2)^{2/3}$. The 2^{nd} term represents Coulomb interaction between nuclei and electrons, and the last term, called Hartree energy, which represents electrostatic Coulomb repulsion energy between electrons.

The kinetic energy of HEG can be derived using KE density information by summing up all the free - electron energy states, $\epsilon_k = \frac{k^2}{2}$ up to the Fermi wave vector, $k_F = [3\pi^2 n(\mathbf{r})]^{1/3}$ as,

$$T_0[n(\mathbf{r})] = \frac{2}{(2\pi)^3}\int 4\pi k^2 dk = C_1(n(\mathbf{r}))^{5/3} \tag{3.14}$$

The interchange and correlation of electrons were ignored in the Thomas-Fermi model (Thomas, 1927; Fermi, 1928; Dirac, 1930). Later that year, Dirac expanded the local exchange term with $C_2 = -\frac{3}{4}(\frac{3}{\pi})^{1/3}$ and hence the TFD equation expressed as,

$$\begin{aligned} E_{TFD}[n(\mathbf{r})] &= C_1\int (n(\mathbf{r}))^{5/3}d^3r + \int V_{ext}(\mathbf{r})(n(\mathbf{r}))^{5/3}d^3r \\ &+ \frac{1}{2}\int\int \frac{n(\mathbf{r})n(\mathbf{r}')}{|\mathbf{r}_i - \mathbf{r}_j|}d^3r d^3r' + C_2\int (n(\mathbf{r}))^{4/3}d^3r \end{aligned} \tag{3.15}$$

Minimizing energy functional (3.15) for all possible $n(\mathbf{r}')$ with $\int n(\mathbf{r}')dr' = N$ can obtain ground state energy and density.

Although the Fermi-Dirac model is credited for developing the notion of density-functional theory, it lacks information on shell structures of atoms and molecular binding energy. In this context, It fails to describe electrons in solids.

3.1.1.5 Hohenberg-Kohn Theorems

The Hohenberg-Kohn (HK) theorems (Hohenberg & Kohn, 1964) are fundamental building blocks of modern DFT, establishing density as the basic variable in interacting particles subjected to external potentials. There are two HK theorems described here under,

Theorem I : *The non-degenerate ground state electron density determines the external potential,* $V_{ext}(r)$ *uniquely (one-to-one correspondence between ground state density and external potential) of interacting particles, except for a constant.*

There is a unique one-to-one correspondence of external potential $V_{ext}(\mathbf{r})$ with ground state density (Fig. 5).

Theorem II: *The total energy functional* $E^{HK}[n(r), V_{ext}(r)]$ *reaches its minimum value (global minimum) with the ground state electron density* $n_0(r)$*, corresponding to a*

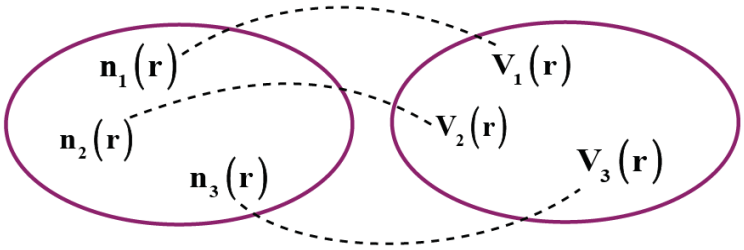

Figure 5: The ground state density of interacting particles system uniquely related to the external potential (Hohenberg & Kohn, 1964).

constant external potential, $\mathrm{V_{ext}(r)}$*, such that,*

$$\mathrm{E^{HK}[n(r), V_{ext}(r)] \geq E^{HK}[n_0(r), V_{ext}(r)]} \tag{3.16}$$

for each of the trial electron density n(r).

That is to say there is only one global minimum ground state density, $\mathrm{n_0(r)}$ for the given system (Fig. 6). Furthermore, the known GS particle density $\mathrm{n_0(\mathbf{r})}$ allows to calculate the various properties of the system.

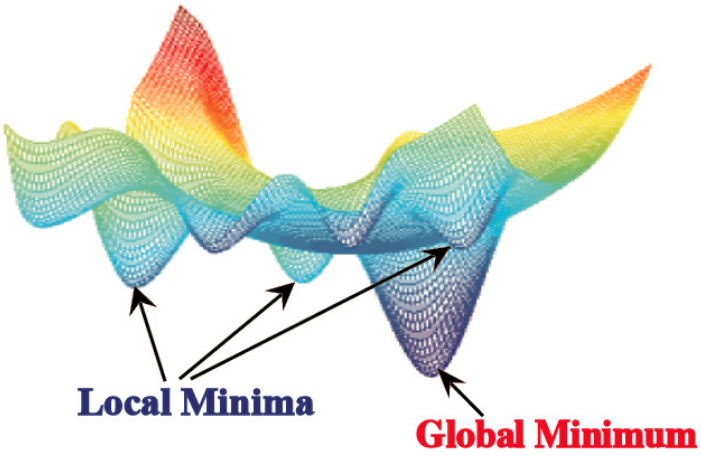

Figure 6: The global minimum ground state density is a unique parameter for a many-body system (Hohenberg & Kohn, 1964).

The HK energy functional (excluding nuclear interaction energy) can be expressed as,

$$\mathrm{E^{HK}[n(\mathbf{r}), V_{ext}(\mathbf{r})] = T[n(\mathbf{r})] + E_{int}[n(\mathbf{r})] + \int V_{ext}(\mathbf{r})n(\mathbf{r})d^3r} \tag{3.17}$$

The first and second terms on r.h.s represent KE and Coulomb potential energy of interacting electrons, which are unaffected by external potential and represented by a

functional of density, F[n(r)],

$$\mathrm{F}[\mathrm{n}(\mathbf{r})] = \mathrm{T}[\mathrm{n}(\mathbf{r})] + \mathrm{E}_{\mathrm{int}}[\mathrm{n}(\mathbf{r})]. \tag{3.18}$$

The third term in equation (3.17) reveals unique electron-nuclei interactions, which is a linear functional of electron density and F[n(**r**)], it becomes,

$$\mathrm{E}^{(\mathrm{HK})}[\mathrm{n}(\mathbf{r}); \mathrm{V}_{\mathrm{ext}}(\mathbf{r})] = \mathrm{F}[\mathrm{n}(\mathbf{r})] + \int \mathrm{V}_{\mathrm{ext}}(\mathbf{r})\mathrm{n}(\mathbf{r})\mathrm{d}^3\mathrm{r} \tag{3.19}$$

Again, the second HK theorem asserts that the energy functionals minimizing density is the exact GS density, thereby enabling the minimization of the energy functional (3.19) with the electron density variations.

All of the GS properties of the system may then be determined in principle using this information. However, the exact energy functional is unknown in reality. The functional of the electron-electron interaction term $\mathrm{E}_{int}(n(\mathbf{r}))$ is also unknown. The KS model (Kohn & Sham, 1965) solves, actually the algorithm difficulty.

3.1.2 The Density Functional Theory (DFT)

The DFT represents many-body particles system by assuming ground state density $\mathrm{n}_0(\mathbf{r})$ as a single variable (Kohn & Sham, 1965). This electron density functional explains electronic properties of solids, molecules, and finite systems, encapsulating information from many-body wavefunctions and reducing degree of freedom.

A single DFT-based Schrödinger equation, solves N-electron systems with 3N degrees of freedom. Thomas and Fermi introduced the concept in 1927 (Thomas, 1927; Slater, 1930), followed by Dirac's correction with exchange and correlation terms in 1930. The TFD approximation gained practical use with the HK theorems and KS formulation.

3.1.2.1 Kohn-Sham Equations

The Kohn-Sham (KS) equation (Kohn & Sham, 1965), based on HK theorems, studies the system's electronic structure using auxiliary particle approximation and exchange-correlation functional. However, exchange-correlation functional is unknown, requiring approximations for energy density functional. The accuracy for the calculations is

purely dependent on the approximations used in exchange-correlation functionals, such as LDA and GGA for calculations in analyzing various condensed matter systems. These approximations are accurate for most of the systems, including semiconductors, metals, insulators, and molecular systems with covalent or ionic bondings. KS equations published in 1965 led to accurate analysis of the properties of condensed matter system.

Furthermore, the hybrid systems (Becke, 1993; Casida & Chong, 1995; Adamo & Barone, 1999), and van der Waals effects (Klimeš & Michaelides, 2012) have been added to standard DFTs to compensate for shortcomings. Electrons move under the potential $\mathrm{V}_{KS}(\mathbf{r})$, rather than the original system's potential. The Hamiltonian for an auxiliary independent particle system can be expressed as follows,

$$\hat{\mathrm{H}}_{\mathrm{KS}} = -\frac{1}{2}\nabla_{\mathrm{i}}^2 + \hat{\mathrm{V}}_{\mathrm{KS}}(\mathbf{r}). \tag{3.20}$$

For N-independent electrons, we may have N Schrödinger equations,

$$\left[-\frac{1}{2}\nabla_{\mathrm{i}}^2 + \hat{\mathrm{V}}_{\mathrm{KS}}(\mathbf{r})\right]\ \psi_{\mathrm{i}}(\mathbf{r}) = \epsilon_{\mathrm{i}}\psi_{\mathrm{i}}(\mathbf{r}) \tag{3.21}$$

We may obtain the GS energy densities or energies by solving these equations iteratively until we reach a self-consistent condition see (Appendix-II).

Each electron will occupy the orbitals with the lowest eigenvalue ϵ_i. The density of the auxiliary system is,

$$\mathrm{n}(\mathbf{r}) = \sum_{\mathrm{i}=1}^{\mathrm{N}} |\psi_{\mathrm{i}}(\mathbf{r})|^2 \tag{3.22}$$

With the density of the orbitals, the GS energy functional for a many-body interacting system using the KS model (Kohn & Sham, 1965) is expressed as,

$$\mathrm{E}[\mathrm{n}(\mathbf{r})] = \mathrm{T}_{\mathrm{s}}[\mathrm{n}(\mathbf{r})] + \mathrm{E}_{\mathrm{H}}[\mathrm{n}(\mathbf{r})] + \mathrm{E}_{\mathrm{XC}}[\mathrm{n}(\mathbf{r})] + \int \mathrm{V}_{\mathrm{ext}}(\mathbf{r})\mathrm{n}(\mathbf{r})\mathrm{d}^3\mathrm{r} \tag{3.23}$$

The first term (3.23) on the right is (independent-particle) kinetic energy ,

$$\mathrm{T}_{\mathrm{s}}[\mathrm{n}(\mathbf{r})] = \sum_{\mathrm{i}}^{\mathrm{N}} \int \psi^*(\mathbf{r}) \bigtriangledown^2 \psi(\mathbf{r}) \tag{3.24}$$

The second term is referred to as classical electrostatic energy (Hartree energy), and the third term is referred to as exchange correlation (XC) energy. A self-consistent solution requires an approximation since the XC energy (Laird *et al.*, 1996; Tao, 2005) is unknown. This term comprises (a) the difference between the precise KE and the non-interacting KE assumed in the KS method (b) all remaining many body interactions between electrons that are not included in the Hartree term, such as exchange and correlation energies.

The last term denotes the external field, if any, as well as the potential due to nuclei. The GS of the energy functional can be found by minimizing the equation w.r.t. electron density while keeping the number of electrons conserved. This approach may be used to compute the equivalent KS one-particle potential (Kohn & Sham, 1965) as,

$$\hat{\mathrm{V}}_{\mathrm{KS}}(\mathbf{r}) = \hat{\mathrm{V}}_{\mathrm{ext}}(\mathbf{r}) + \hat{\mathrm{V}}_{\mathrm{H}}(\mathbf{r}) + \hat{\mathrm{V}}_{\mathrm{XC}}(\mathbf{r}) \tag{3.25}$$

$$= \hat{\mathrm{V}}_{\mathrm{ext}}(\mathbf{r}) + \frac{\partial \mathrm{E}_{\mathrm{H}}[\mathrm{n}(\mathbf{r})]}{\partial \mathrm{n}(\mathbf{r})} + \frac{\partial \mathrm{E}_{\mathrm{XC}}[\mathrm{n}(\mathbf{r})]}{\partial \mathrm{n}(\mathbf{r})} \tag{3.26}$$

where $\hat{\mathrm{V}}_{\mathrm{XC}} = \frac{\partial \mathrm{E}_{\mathrm{XC}}[\mathrm{n}(\mathbf{r})]}{\partial \mathrm{n}(\mathbf{r})}$ is the functional derivative of XC energy, and is called XC potential. Similarly $\hat{\mathrm{V}}_{\mathrm{H}} = \frac{\partial \mathrm{E}_{\mathrm{H}}[\mathrm{n}(\mathbf{r})]}{\partial \mathrm{n}(\mathbf{r})}$ is the Hartree potential. The equations (3.21) together with (3.22) and (3.25) are called KS equations, and can be solved self-consistently.

Furthermore, the Kohn-Sham energy functional after diagonalization is given by,

$$\mathrm{E}_{\mathrm{KS}}[\mathrm{n}(\mathbf{r})] = \sum_{\mathrm{i}} \epsilon_{\mathrm{i}} - \frac{1}{2} \int \int \frac{\mathrm{n}(\mathbf{r})\mathrm{n}(\mathbf{r}')}{|\mathbf{r} - \mathbf{r}'|} \mathrm{d}^3\mathrm{r}\mathrm{d}^3\mathrm{r}' + \int \epsilon_{\mathrm{XC}}[\mathrm{n}(\mathbf{r})]\mathrm{n}(\mathbf{r}')\mathrm{d}^3\mathrm{r}' - \int \frac{\delta \mathrm{E}_{\mathrm{XC}}}{\delta \mathrm{n}(\mathbf{r})} \mathrm{n}(\mathbf{r}')\mathrm{d}^3\mathrm{r}' \tag{3.27}$$

where, the 1^{st} term in right hand side is the sum of energy of each orbitals, 2^{nd} term is the Hartree potential, the 3^{rd} term is the XC energy functional, and 4^{th} term is the XC chemical potential.

3.1.2.2 Exchange-Correlation Functional

The KS method calculates particle kinetic energy, Hartree energy, and exchange correlation energy for a system of interacting particles. It uses the self-consistent approach and the KS potential for charge density calculation. The XC term requires approximations like LDA and GGA (Perdew *et al.*, 1996). Additional interactions can be considered based on relevance in the calculations.

3.1.2.3 Solution of KS-Equation

The KS approach is an iterative method that starts with selecting an initial electron density based on atoms' electron densities. The KS potential is determined using this density, which is then used to solve KS equations and determine new electron density. The system is considered conversed if the difference is less than the set thresholds (criteria), and necessary properties are extracted. If the difference is greater than the threshold, the previous iteration's density is mixed with the new ones, and the procedure is repeated until convergence criteria are achieved. In this study, we have used pseudo-potential based quantum espresso frameworks and full-potential based WIEN2k frameworks for the ab-initio calculations, which are described briefly as follows:

3.1.2.4 Pseudo-potentials and Plane Waves

The solution of the SWE for a periodic system satisfy the fundamental property of Bloch's theorem (Bloch, 1929)) and may be written as,

$$\psi_{\mathrm{k}}(\mathbf{r}) = \mathrm{u_k(r)e^{i\mathbf{k}.\mathbf{r}}} \tag{3.28}$$

where, $u_k(\mathbf{r})$ is the periodic potential that is compatible with the period of the unit cell. In this scenario, the Schrödinger equation may be solved individually for each value of k. The functions $e^{i\mathbf{k}.\mathbf{r}}$ are known as plane waves, and k's are the reciprocal vectors.

These plane waves are orthonormal and independent of positions and energy, making them suitable for exact variational calculations based on a discrete numerical grid. However, an infinite sum of plane waves is not practical for real-world computations. In real-world computations, the wave function should be described by plane waves within a specific energy cut-off, E_{cut}. Caution should be used when defining E_{cut} to ensure smooth wave function and proper convergence of parameters like total energy. Choosing E_{cut} is a trade-off between accuracy and computational resource cost.

In all electron DFT computations, wave functions are used for solving numerous basis functions, including core and valence electron wave functions. Core electron wave functions have a significant Fourier component, while valence wave functions are smooth on the exterior but have wiggles near the nucleus Fig.7 (Mizutani, 2001). Nodal structures of valence electron wave functions are useful for orthogonality but require larger plane

wave cut-off and plane waves. A pseudopotential is a virtual potential that freezes core electrons with nuclei, eliminating the need for separate wave functions. This reduces wave functions, basis sets, and matrices size, eliminating Coulomb singularity at the origin and reducing the number of wave functions needed for a coherent model.

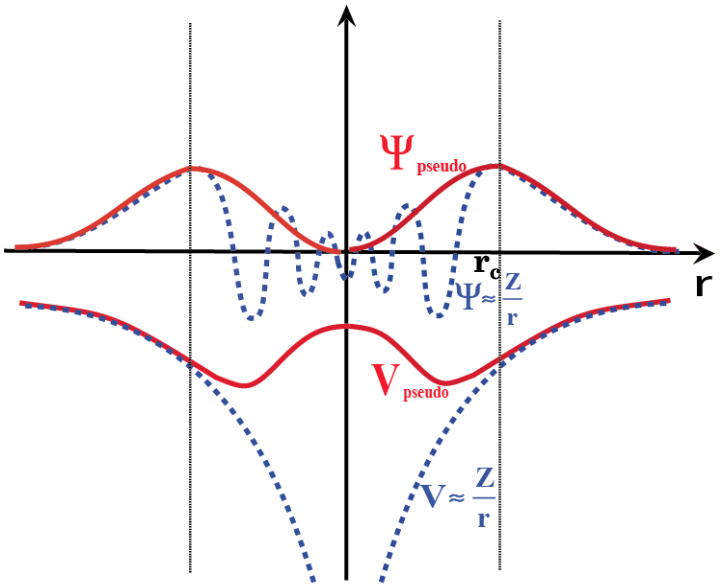

Figure 7: The schematic of pseudo-potential (effective potential) model (red solid lines). The dashed blue lines depict the Coulomb potential(full potential) and the upper corresponding pseudo- wavefunction (red solid line) and full wavefunction (blue dashed lines) near the nucleus. Outside the cutoff radius (r_c), the pseudopotential and pseudo wavefunctions are compatible with the real system or full potential approach (Mizutani, 2001).

As previously mentioned, pseudopotentials replace the strong electrostatic potential of nuclei and core electrons. This provides the same wave function outside the core as the true wave function to accustom the real properties.

The electrons in the inner and outer areas of the cutoff radius are referred to as core and valence electrons, respectively. Because the core electrons are frozen to the nucleus, potentials with small (r_c) are referred to as hard pseudopotentials, while those with larger (r_c) are referred to as soft pseudopotentials. Regardless of whether any of the pseudopotentials are correct, a good pseudopotential should be soft and transferable (Martin, 2020). A soft pseudopotential contains fewer valence electrons and needs fewer plane waves due to the larger (r_c). A pseudopotential must perform consistently over a wide range of chemical conditions in order to be transferable, and softer pseudopotentials may have limitations in this regard.

A norm-conserving pseudopotential conserves electronic charge, ensuring accurate description of scattering features. However, they have high computational cost. Ultrasoft pseudopotentials reduce this cost by having separate cutoffs for charge density and kinetic energy. Selecting the right pseudopotential is a complex task with careful consideration to maintain desirable properties at reasonable costs.

All electron method like Gaussian functions (Pietro & Hehre, 1983), projector augmented-wave (Blöchl *et al.*, 1994), and linearized muffin-tin orbitals (Jarlborg & Arbman, 1977; Faleev *et al.*, 2005) treat core and valence electrons equally. The FP-LAPW method (Blaha *et al.*, 2020) provides an exact basis for all-electron computations, enabling investigations of electronic structures in various materials and chemical compositions.

3.1.2.5 FP-LAPW Basis and LO Extensions

The FP-LAPW approach divides space into muffin-tin (MT) spheres and the interstitial region (IR), treating core states as localized in a spherically symmetric atomic potential. The augmented plane wave basis functions for valence electrons are piecewise defined, and the LAPW basis sets energy-dependent radial functions with energy-independent functions evaluated at predefined energy parameters E_l, linearly superposed to match plane waves at MT sphere edges. In this basis there are two radial functions for angular momentum quantum numbers l: the solution $\mathrm{u_l}(\mathbf{r}, \mathrm{E_l})$ and its energy derivative, $\dot{\mathrm{u}}_\mathrm{l}(\mathbf{r}, \mathrm{E_l}) = \partial \mathrm{u_l}(\mathbf{r}, \mathrm{E})/\partial \mathrm{E}|_{\mathrm{E=E_l}}$.

The radial functions, $\mathrm{u_l}(\mathbf{r}, \mathrm{E})$ can be represented linearly in $\mathrm{E} - \mathrm{E_l}$ using the LAPW basis set, providing an accurate all-electron description for various materials (Krasovskii *et al.*, 1993). The linearization error is determined by energy parameters E_l and MT radii R_{MT}, which cannot be chosen using a variational method. Ideally, E_l and R_{MT} should not affect the final results within a reasonable error. Implementing LO for the expansion of the basis can solve this issue.

The spherical effective potential near atomic nuclei is used to compute core states from the relativistic radial Dirac equation. Core states decrease towards the MT sphere boundary, ensuring they are orthogonal to the radial functions needed for the LAPW

basis for valence electrons (Singh, 1991; Betzinger *et al.*, 2011).

$$\phi_{\mathrm{kG}}(\mathbf{r}) = \begin{cases} \frac{1}{\sqrt{\Omega}} e^{i(\mathbf{k}+\mathbf{G})r} & \text{for } r \in \mathrm{IR} \\ \sum\limits_{\mathrm{L}} \mathrm{R}^{\mathrm{kG}}_{\mathrm{L}\alpha}(\mathbf{r}_\alpha, \mathrm{E}_{\mathrm{l}\alpha}) \mathrm{Y}_{\mathrm{L}}(\mathbf{r}_\alpha) & \text{for } r \in \mathrm{MT}_\alpha \end{cases} \tag{3.29}$$

The equation is based on the unit-cell volume, Ω, reciprocal lattice vectors, $\mathbf{G}$, angular momentum and magnetic quantum number ($L = (l, m)$), position vector ($\mathbf{r}_\alpha$) relative to the MT sphere center (R^α) of atom(α) and its spherical harmonics ($\mathrm{Y}_L(\mathbf{r}_\alpha)$). The cutoff parameter G_{max} restricts the number of basis functions and implies the cutoff parameter $l_{max\alpha}$ with $l \leq l_{max\alpha}$ via the rule of thumb, $l_{max\alpha} = \mathrm{G}_{max}\mathrm{R}_{MT\alpha}$ (Sjfistedt *et al.*, 2000).

3.1.3 The Local Density Approximation (LDA)

The major problem of DFT is to choose a suitable exchange and correlation functionals is the major challenge of DFT calculation. The LDA is being the most commonly used approximation (Perdew *et al.*, 1998; Cohen *et al.*, 2007), which is the foundation for all approximate exchange-correlation functionals and presupposes homogeneous probability density in the system under investigation. Its core concept is a uniform electron gas and the premise that E_{xc} may be expressed as follows,

$$\mathrm{E}^{\mathrm{LDA}}_{\mathrm{XC}}[\mathrm{n}(\mathbf{r})] = \int \mathrm{n}(\mathbf{r}) \epsilon_{\mathrm{XC}}[\mathrm{n}(\mathbf{r})] \mathrm{d}^3\mathrm{r} \tag{3.30}$$

Here, $\epsilon_{XC}[n(\mathbf{r})]$ denotes the XC energy per particle of a UEG with density $n(\mathbf{r})$. We may calculate the XC potential by taking the functional derivative of $\mathrm{E}^{\mathrm{LDA}}_{\mathrm{XC}}[\mathrm{n}(\mathbf{r})]$ as,

$$\mathrm{v}^{\mathrm{LDA}}_{\mathrm{XC}}[\mathrm{n}(\mathbf{r})] = \frac{\delta \mathrm{E}^{\mathrm{LDA}}_{\mathrm{XC}}[\mathrm{n}(\mathbf{r})]}{\delta \mathrm{n}(\mathbf{r})} = \epsilon_{\mathrm{XC}}[\mathrm{n}(\mathbf{r})] + \mathrm{n}(\mathbf{r}) \frac{\partial \epsilon_{\mathrm{XC}}[\mathrm{n}(\mathbf{r})]}{\partial \mathrm{n}(\mathbf{r})} \tag{3.31}$$

The XC energy per particle, $\epsilon_{XC}[n(\mathbf{r})]$ can be further divide into exchange part and correlation part as,

$$\epsilon_{\mathrm{XC}}[\mathrm{n}(\mathbf{r})] = \epsilon_{\mathrm{X}}[\mathrm{n}(\mathbf{r})] + \epsilon_{\mathrm{C}}[\mathrm{n}(\mathbf{r})] \tag{3.32}$$

Now, equation (3.30) can be written as,

$$\mathrm{E_{XC}^{LDA}[n(\mathbf{r})]} = \int \mathrm{n(\mathbf{r})}\left[\epsilon_{\mathrm{X}}[\mathrm{n(\mathbf{r})}] + \epsilon_{\mathrm{c}}[\mathrm{n(\mathbf{r})}]\right]\mathrm{d^3r} = \mathrm{E_X[n(\mathbf{r})]} + \mathrm{E_C[n(\mathbf{r})]} \tag{3.33}$$

For a spin polarized system,

$$\begin{aligned}\mathrm{E_{XC}^{LSDA}[n_\uparrow(\mathbf{r}), n_\downarrow(\mathbf{r})]} &= \int \mathrm{n(\mathbf{r})}\epsilon_{\mathrm{XC}}[\mathrm{n_\uparrow(\mathbf{r}), n_\downarrow(\mathbf{r})}]\mathrm{d^3r} \\ &= \int \mathrm{n(\mathbf{r})}\left[\epsilon_{\mathrm{X}}[\mathrm{n_\uparrow(\mathbf{r}), n_\downarrow(\mathbf{r})}] + \epsilon_{\mathrm{C}}[\mathrm{n_\uparrow(\mathbf{r}), n_\downarrow(\mathbf{r})}]\right]\mathrm{d^3r}\end{aligned} \tag{3.34}$$

The exchange term, $\epsilon_X[n(\mathbf{r})]$ was derived originally by Bloch and Dirac in atomic units as,

$$\epsilon_X[n(\mathbf{r})] = -\frac{0.458}{r_s} \tag{3.35}$$

where, r_s is the radius of a sphere for an electron, which can be computed by, $(4\pi/3)r_s^3 = n(\mathbf{r})^{-1}$. The correlated part was first estimated by E. P. Wigner, which can be computed as,

$$\epsilon_C[n(\mathbf{r})] = -\frac{0.44}{r_s + 7.8} \tag{3.36}$$

The LDA accuracy is satisfactory in condensed matter systems but less in atomic and molecular physics.

3.1.4 GEA, GGA, mBJ and Beyond

The LDA employs density information at point r, considering the spatially inhomogeneous density $n(\mathbf{r})$. It includes rate of variation in the functional using semilocal functionals like gradient-expansion approximations (GEA) and GGA. GEA systematically computes gradient-corrections of the type $|\nabla n(\mathbf{r})|$, $|\nabla n(\mathbf{r})|^2$, $\nabla^2 n(\mathbf{r})$, etc. (Perdew *et al.*, 1998; Kurth *et al.*, 1999; Casida, 2009), such as the lowest-order gradient correction to the Thomas-Fermi approximation as,

$$\mathrm{T_s[n(\mathbf{r})]} \approx \mathrm{T_s^W[n(\mathbf{r})]} = \mathrm{T_s^{LDA}[n(\mathbf{r})]} + \frac{\hbar^2}{8\mathrm{m}}\int \mathrm{d^3r}\,\frac{|\nabla \mathrm{n(\mathbf{r})}|^2}{\mathrm{n(\mathbf{r})}} \tag{3.37}$$

where, the 2^{nd} term on the r.h.s is called the Weizsäcker term.

Similarly, in the exchange term,

$$\mathrm{E_X[n(\mathbf{r})] \approx E_X^{GEA}[n(\mathbf{r})] = E_X^{LDA}[n(\mathbf{r})] - \frac{10q^2}{432\pi(3\pi^2)^{1/3}} \int d^3r \frac{|\nabla n(\mathbf{r})|^2}{(n(\mathbf{r}))^{4/3}}} \quad (3.38)$$

The 2^{nd} term on the right hand side is the lowest-order gradient correction to $\mathrm{E_X^{LDA}[n(\mathbf{r})]}$, which do not improve the approximation but worsen it. Higher-order(e.g. $\propto |\nabla n(\mathbf{r})|^\alpha$ or $\propto |\nabla n(\mathbf{r})|^\beta$ with $\alpha, \beta > 2$) corrections are complex to compute. In the 1980s, GGA was discovered, which incorporates density gradient corrections in exchange-correlation functional E_{XC}[n(r)], addressing the limitation of power-series-like systematic gradient expansions.

The exchange correlation energy (Perdew *et al.*, 1998; Cohen *et al.*, 2007), E_{XC}[n(**r**)] in GGA is;

$$\mathrm{E_{XC}^{GGA}\,[n(\mathbf{r})] = \int f[n(\mathbf{r}), \nabla n(\mathbf{r})] d^3r} \quad (3.39)$$

The symbol f is some functional of $n(\mathbf{r})$ and it's gradient $\nabla n(\mathbf{r})$.

The XC energy $\mathrm{E_{XC}^{GGA}}$[n(**r**)] of the GGA approach consists of exchange and correlation parts, similar to LDA. There are various methods employed to obtain exchange correlation functionals, with popular and reliable GGAs being Perdew-Burke-Ernzerhof (PBE) (Perdew *et al.*, 1998) and BLYP (Lee *et al.*, 1988; Finley, 2004). Additionally, the other GGA-type functionals are also being used, and the new ones are being developed.

Beyond GGA, the modified Becke-Johnson (mBJ) potential, meta-GGA and hyper-GGA are also employed for the popular approximations of $\epsilon_{XC}[(n_\uparrow, n_\downarrow); \mathbf{r}]$, for the accuracy and realistic calculations, which are the function of parameters at point r, and different other parameter selections as depicted by the different rungs of a "Jacob's ladder" (Perdew *et al.*, 1998; Kurth *et al.*, 1999; Casida, 2009) of approximation see (Appendix-III). As the accuracy tend to rise up the ladder, so as the efficiency falls down the ladder.

The modified Beck-Johnson (mBJ) potential as given by,

$$\mathrm{v_{x,\sigma}^{BJ}(\mathbf{r}) = v_{x,\sigma}^{BR}(\mathbf{r}) + \frac{1}{\pi}\sqrt{\frac{5}{6}}\sqrt{\frac{t_\sigma(\mathbf{r})}{n_\sigma(\mathbf{r})}}} \quad (3.40)$$

where, $n_\sigma(\mathbf{r}) = \Sigma_{i=1}^{N_\sigma}|\psi_{i,\sigma}(\mathbf{r})|^2$ is the electron density and

$$\mathrm{t}_\sigma = \frac{1}{2}\Sigma_{\mathrm{i}=1}^{\mathrm{N}_\sigma}\nabla\psi_{\mathrm{i},\sigma}^{*}.\nabla\psi_{\mathrm{i},\sigma} \tag{3.41}$$

is kinetic energy density, and

$$\mathrm{v}_{\mathrm{x},\sigma}^{\mathrm{BR}}(\mathbf{r}) = -\frac{1}{\mathrm{b}_\sigma(\mathbf{r})}\left(1 - \mathrm{e}^{-\mathrm{x}_\sigma(\mathbf{r})} - \frac{1}{2}\mathrm{x}_\sigma(\mathbf{r})\mathrm{e}^{-\mathrm{x}_\sigma(\mathbf{r})}\right) \tag{3.42}$$

is the Becke-Roussel potential.

To be noted here, the Coulomb potential is modeled using exchange hole, where $\mathrm{x}_\sigma(\mathbf{r})$ involves terms like, n_σ, ∇n_σ, $\nabla^2 n_\sigma$ and t_σ. With,

$$\mathrm{b}_\sigma(\mathbf{r}) = \left[\mathrm{x}_\sigma^3\mathrm{e}^{-\mathrm{x}_\sigma}/8\pi\mathrm{n}_\sigma\right]^{1/2} \tag{3.43}$$

This is the new scheme of potential to enhance the band gap of the materials. The TB-mBJ potential consists of a modified version of BJ potential for exchange (which reproduces the exact KS potential of atoms) and LDA for correlation (Becke & Johnson, 2006; Koller *et al.*, 2011; Blaha *et al.*, 2020). With the exchange part depend on the kinetic energy density t_σ, the TB-mBJ potential is,

$$\mathrm{v}_{\mathrm{x},\sigma}^{\mathrm{TB-mBJ}}(\mathbf{r}) = \mathrm{cv}_{\mathrm{x},\sigma}^{\mathrm{BR}}(\mathbf{r}) + (3\mathrm{c} - 2)\frac{1}{\pi}\sqrt{\frac{5}{6}}\sqrt{\frac{\mathrm{t}_\sigma(\mathbf{r})}{\mathrm{n}_\sigma(\mathbf{r})}} \tag{3.44}$$

where, c = $\alpha + \beta\mathrm{g}^{\mathrm{p}}$ with,

$$\mathrm{g} = \frac{1}{\mathrm{V}_{\mathrm{cell}}}\int_{\mathrm{cell}}\frac{|\nabla\mathrm{n}(\mathbf{r}')|}{\mathrm{n}(\mathbf{r}')}\mathrm{d}^3\mathrm{r}' \tag{3.45}$$

where, V_{cell}, the unit cell volume, and α and β are two free parameters, whose values, α = -0.012 and β = 1.023 bohr$^{1/2}$ were determined by minimizing the mean absolute error of the band gap of the crystalline materials.

3.1.5 Electronic Structures

3.1.5.1 Electronic Bandstructures

In general, the bandstructure gives the detailed picture of allowed energy levels for electrons in a crystal as function of wave vector (k) (Kittel, 1996; Ashcroft & Mermin, 1976). In condensed matter physics, the bandstructures are approximated through tight-binding approach (1.4) or plane-wave approach (DFT) method, and so on. In tight-binding approach, the dispersion relation is obtained by diagonalizing the Hamiltonian contributed from each atom or ion in the crystal as,

$$\varepsilon_{\mathrm{k}} = \varepsilon_0 - 2\mathrm{t}\sum_{\mathrm{i}} \cos(\mathbf{k}.\mathbf{a}_{\mathrm{i}}) \tag{3.46}$$

where, ε_0 is the energy of atomic orbital in itself, $\mathrm{t} = \int \langle \phi_\sigma(\mathbf{r} - \mathbf{a}_{\mathrm{i}})|\mathrm{H}|\phi_\alpha(\mathbf{r})\rangle \mathrm{dr}$ is associated with the interaction energy (hopping parameters) of the electrons, and $\mathbf{a}_i$ is the lattice spacings.

In DFT approach, the bandstructure calculations are computed using the KS equation, called the dispersion relation.

3.1.5.2 Density of States

The DOS provides the information of the number of electronic states per unit energy range at each energy level in a material. It can be obtained from the bandstructure by integrating over all k-space within a given energy range(Kittel, 1996; Ashcroft & Mermin, 1976; Martin, 2020). The DOS available in the energy given energy range ε to $\varepsilon + d\varepsilon$ is,

$$\mathrm{D}(\varepsilon_{\mathrm{n}}(\mathbf{k})) = \sum_{\mathrm{n}} \frac{2}{8\pi^3} \int_{\mathrm{n}} \delta(\varepsilon - \varepsilon_{\mathrm{n}}(\mathbf{k}))\mathrm{dk} \tag{3.47}$$

where, $\mathrm{D}(\varepsilon_{\mathrm{n}}(\mathbf{k}))$ is the DOS at energy level $(\varepsilon_n(\mathbf{k}))$, the factor 2 comes from the spin up and down cases, and the integral is over a primitive unitcell. The Dirac delta function ensure the counting of the states at specific energy levels only.

To compute the spin polarization, we have,

$$\mathrm{P(T)} = \frac{\mathrm{D_{\downarrow}}(0) - \mathrm{D_{\uparrow}}(0)}{\mathrm{D_{\downarrow}}(0) + \mathrm{D_{\uparrow}}(0)} \tag{3.48}$$

where, $\mathrm{D_{\downarrow}}(0)$ and $\mathrm{D_{\uparrow}}(0)$ are the DOS of spin-down and spin-up channels at the Fermi level E_F.

3.1.6 Structural and Chemical Stability

3.1.6.1 Structural Stability

The energy minimization technique is used to investigate the structural stability of prototype cubic ABO_3 type cubic perovskites with (A = Ca, La, Sr, Y and B = Ti, V) metal ions. The optimized lattice parameters within the permissible error bars are obtained through energy minimization curves. These pristine systems are then promoted to their superstructures for the studying the effect of site-substitutions on A and B sites (Maiti & Sarma, 2000; Sage *et al.*, 2008).

3.1.6.2 Chemical Stability

We have computed the cohesive energy (CE) and formation energy (FE) of all of the titanates and vanadates to study their chemical stabilities. The ground state total energy and CE per atom (Boudali *et al.*, 2009; Murugeswari *et al.*, 2020) can be calculated using a set of optimal parameters. The CE, $\mathrm{E}_{cohesive}$ for a compound $\mathrm{A}_x\mathrm{B}_y\mathrm{C}_z$ (ABC) can be calculated as,

$$\mathrm{E_{cohesive}} = \frac{\mathrm{E^{ABC}_{total}} - \left(\mathrm{xE^{A}_{atom}} + \mathrm{yE^{B}_{atom}} + \mathrm{zE^{C}_{atom}}\right)}{\mathrm{x + y + z}} \tag{3.49}$$

where E^A_{atom}, E^B_{atom} and E^C_{atom} are the isolated spin-polarized atomic energies and x, y, and z are stoichiometric weights.

Similarly, the FE, $\mathrm{E}_{formation}$, is the measure of the relative stability of the given system. For $\mathrm{A}_x\mathrm{B}_y\mathrm{C}_z$ (ABC) compound, the FE per atom can be computed as follows,

$$\mathrm{E_{formation}} = \frac{\mathrm{E^{ABC}_{total}} - \left(\mathrm{xE^{A}_{bulk}} + \mathrm{yE^{B}_{bulk}} + \mathrm{zE^{C}_{bulk}}\right)}{\mathrm{x + y + z}} \tag{3.50}$$

where E^{A}_{bulk}, E^{B}_{bulk}, and E^{C}_{bulk} are the estimated energies of the bulk(solid) form the constituent atoms of the unitcell, and x, y, and z are the stoichiometric weights. The structural and chemical stability (Bouhemadou & Khenata, 2007) are examined through the negative values of cohesive and formation energies for these compounds.

3.1.7 Mechanical Stability and Elastic Properties

The mechanical and thermodynamical stabilities can be examined through the elastic information. The elastic constants are used for calculating solid mechanical properties, structural stability, anisotropy, and bondings. Using structural and experimental data, this study calculates ground state parameters, including lattice parameters (at T = 0 K and P = 0 GPa). For computational analysis, many equation of states (EOS) techniques can be applied.

The bulk modulus B and its pressure derivative (B') are calculated by fitting total energy to the Birch EOS (Birch, 1938; Barron & Klein, 1965; Rose *et al.*, 1984). Pressure-volume data for different pressures are fitted to the Birch-Murnaghan (Murnaghan, 1944) and Vinet equations of state EOS, providing the necessary information for understanding the mechanical behavior of the material as given by,

$$\begin{cases} \mathrm{E}\left(\mathrm{V}\right) = \mathrm{E}_0 + \frac{9\mathrm{B}_0\mathrm{V}_0}{16}\left[\left\{\left(\mathrm{V}_0/\mathrm{V}\right)^{2/3} - 1\right\}^3 \mathrm{B}_0' + \left\{\left(\mathrm{V}_0/\mathrm{V}\right)^{2/3} - 1\right\}^2 \left\{6 - 4\left(\mathrm{V}_0/\mathrm{V}\right)^{2/3}\right\}\right], \\ \mathrm{P}\left(\mathrm{V}\right) = \frac{3}{2}\mathrm{B}_0\left\{\left(\mathrm{V}_0/\mathrm{V}\right)^{7/3} - \left(\mathrm{V}_0/\mathrm{V}\right)^{5/3}\right\}\left[1 + \frac{3}{4}\left(\mathrm{B}_0' - 4\right)\left\{\left(\mathrm{V}_0/\mathrm{V}\right)^{2/3} - 1\right\}\right], \\ \mathrm{P}\left(\mathrm{V}\right) = 3\mathrm{B}\left(\frac{\mathrm{V}_0}{\mathrm{V}}\right)^{-2/3}\left\{1 - \left(\frac{\mathrm{V}_0}{\mathrm{V}}\right)^{-2/3}\right\}\exp\left[-\frac{2}{3}\left(\mathrm{B}_0' - 1\right)\left\{\left(\frac{\mathrm{V}_0}{\mathrm{V}}\right)^{1/3} - 1\right\}\right], \end{cases} \tag{3.51}$$

where E_0 is the equilibrium energy, V_0 is the unit-cell volume at zero pressure. When a crystal is deformed using a strain η_{i}, the stress comes into action to restore the equilibrium configuration, called Hooke's law (Birch, 1938) as,

$$\sigma_{\mathrm{i}} = \sum_{\mathrm{ij}} \mathrm{C}_{\mathrm{ij}}\eta_{\mathrm{j}} \tag{3.52}$$

where C_{ij} denotes the elastic constant tensor. We may calculate the total energy of a

system for limited and small stresses using the following relationship as,

$$E(\eta) = E_0 + V_0 \sum_i \sigma_i^0 \eta_i + \frac{V_0}{2!} \sum_{ij} \eta_i C_{ij} \eta_j + ... \tag{3.53}$$

where E_0 and V_0 are the energy and volume of the crystal in equilibrium. The elastic constants may be calculated by using various orders of the strain η and fitting the energy with a polynomial function.

The nonzero components of the elastic constants tensor for a cubic system are $C_{12} = C_{13} = C_{23}$, $C_{11} = C_{22} = C_{33}$, and $C_{44} = C_{55} = C_{66}$ (Nye, 1985; Corso, 2016)

For a tetragonal system, the non-zero elastic constant components, C_{11}, C_{33}, C_{12},C_{13}, C_{44} and C_{66} are determined by solving the equations for energy with the corresponding strains.

For the cubic system, the reduced three independent elastic constants are C_{11}, C_{12}, and C_{44} and the mechanical stability criterion for a cubic crystal are given by (Bouhemadou & Khenata, 2007; Parvin & Naqib, 2017),

$$C_{11} + 2C_{12} > 0, C_{44} > 0, C_{11} - C_{12} > 0, C_{12} < B < C_{11} \tag{3.54}$$

Similarly, the criteria of mechanical stability for the tetragonal system are,

$$\begin{cases} C_{11} > 0, C_{33} > 0, C_{44} > 0, C_{66} > 0, \\ 2(C_{11} + C_{12}) + C_{12} + 4C_{13} > 0 \\ C_{11} - C_{12} > 0, C_{11} + C_{33} - 2C_{13} > 0, \end{cases} \tag{3.55}$$

The Zener anisotropy factor (A) for a cubic system contains essential information on structural stability and may be computed as follows,

$$A = \frac{2C_{44}}{C_{11} - C_{12}} \tag{3.56}$$

For a totally isotropic material, the anisotropy factor is one. The Cauchy pressure, CP = $C_{12} - C_{44}$, is connected with the kind of chemical bondings, which offers stiffness and flexibility information. Within the elastic limit, the values of elasticities are computed as

follows,

$$\begin{cases} \mathrm{Y} = 9\mathrm{BG}/(3\mathrm{B}+\mathrm{G}), \\ \mathrm{G} = (\mathrm{G_V}+\mathrm{G_R})/2, \\ \mathrm{B} = \frac{1}{3}\left(\mathrm{C_{11}}+2\mathrm{C_{12}}\right), \end{cases} \tag{3.57}$$

where,

$\mathrm{G_V} = \frac{1}{5}\left(\mathrm{C_{11}}-\mathrm{C_{12}}+3\mathrm{C_{15}}\right)$, and $\mathrm{G_R} = [5\left(\mathrm{C_{11}}-\mathrm{C_{12}}\right)\mathrm{C_{44}}]/[3(\mathrm{C_{11}}-\mathrm{C_{12}})+4\mathrm{C_{44}}]$ are the shear modulus in Voigt notation and Reuss notation, respectively. The materials with higher values of Y (Needs *et al.*, 1986) have a stiffer and more covalent nature. The Poisson's ratio,

$$\nu = \frac{3}{2}\frac{3\mathrm{B}-2\mathrm{G}}{3\mathrm{B}+\mathrm{G}} \tag{3.58}$$

It examines the ductility, whose values for various compounds, respectively, are around 0.1, 0.25, and 0.33 (Cinthia *et al.*, 2015).

Similarly, using the Voigt - Reuss - Hill (VRH) average schemes, the Bulk modulus (B_H), Shear modulus (G_H), Young's modulus (Y_H), and Poisson's ratio (ν) of the tetragonal system are computed as,

$$\begin{cases} \mathrm{Y_H} = 9\mathrm{B_H}\mathrm{G_H}/(3\mathrm{B_H}+\mathrm{G_H}), \\ \mathrm{G_H} = (\mathrm{G_V}+\mathrm{G_R})/2, \\ \mathrm{B_H} = (\mathrm{B_V}+\mathrm{B_R})/2, \\ \nu = (3\mathrm{B_H}-\mathrm{Y_H})/6\mathrm{B_H} \end{cases} \tag{3.59}$$

Furthermore, the thermodynamical parameter, called the Debye temperature (Θ_D) is computed as,

$$\Theta_\mathrm{D} = \frac{\hbar}{\mathrm{k_B}}\left(\frac{6\pi^2}{\mathrm{V_{cell}}}\right)^{1/3}\langle \mathrm{v} \rangle \tag{3.60}$$

With,

$$\begin{cases} \langle \mathrm{v} \rangle = \left[\frac{1}{3} \left(2\mathrm{v_l}^{-3} + \mathrm{v_t}^{-3} \right) \right]^{-1/3}, \\ \mathrm{v_l} = \left[\frac{3\mathrm{B}+4\mathrm{G}}{3\rho} \right]^{1/2}, \\ \mathrm{v_t} = \left(\frac{\mathrm{G}}{\rho} \right)^{1/2}, \end{cases} \tag{3.61}$$

where, v_l, v_t and $\langle \mathbf{v} \rangle$ are the longitudinal, transverse, and average velocity velocities of sound in isotropic media, while $\hbar$, k_B, V_{cell} and ρ represent known constants (Anderson, 1963; Golesorkhtabar & Draxl, 2013).

The accuracy of elastic-constant calculations for stress and strain measurement requires proper handling of a function that can only be calculated for a small number of strain values. Precision is achieved using DFT data and the leave-one-out cross-validation (LOO-CV) approach to control parameters and estimate errors in energy and stress. The technique creates a training data set from the samples except one (so called testing data set), and selecting the best model dataset using polynomial fitting and cross validated with this testing data set.

We chose the optimal elastic calculation model with the lowest cross validation error (CVE) computed as,

$$\delta_{\mathrm{CV}}^{(\mathrm{n})} = \sqrt{\frac{1}{\mathrm{N}} \sum_{\mathrm{i}=1}^{\mathrm{N}} \left[\mathrm{E_i} - \mathrm{p}^{(\mathrm{n})}(\eta_\mathrm{i}) \right]^2} \tag{3.62}$$

where $\mathrm{p}^{(\mathrm{n})}(\eta_\mathrm{i})$ is the polynomial function at η_i of strain, excluding the value of pair $(\eta_\mathrm{i}, \mathrm{E_i})$, such that $\mathrm{E}(\eta_\mathrm{i}) = \sum_{\mathrm{i}=1}^{6} \mathrm{A_i} \eta^\mathrm{i}$ (Anderson, 1963; Golesorkhtabar & Draxl, 2013).

For cross validation of the DFT data, we used polynomial fitting, which is the generalization of error estimation use to avoid either over-fitting or under-fitting w.r.t. real information about the elastic properties of the materials.

3.1.8 Transport Properties

The BoltzTraP algorithm is efficient for calculating quasi-particle energies using Kohn-Sham eigenvalues (Kohn & Sham, 1965) and can be trivially parallelized. It can also calculate derivatives for the BTE directly from intra-band momentum matrix elements

(Ohtani *et al.*, 1970; Adewale *et al.*, 2018). However, when quasi-particle energies cannot be calculated using a fixed multiplicative KS potential, using momentum matrix elements or alternative interpolation methods may be advantageous (Pizzi *et al.*, 2014; Berland & Persson, 2018). BoltzTraP codes introduce both eigenvalues and momentum matrix elements, ensuring accurate reproduction of value and derivative at calculated points. This approach is suitable for beyond-KS approaches and can handle temperature-dependent transport distribution functions due to electron-phonon coupling (Ashcroft & Mermin, 1976; Kittel, 1996; Sevik, 2010). BoltzTraP is mainly used for evaluating transport coefficients but can also be useful for interpolating periodic functions.

The BTE is a mathematical model that considers the distribution function, $\mathrm{f}_{\mu}(\mathrm{T},\mu)$ in steady state due to external fields and scattering phenomena for electrons or holes. It is used to compute the transport properties of TMOs for optimized systems using the BoltzTraP algorithm, which implements the linearized BTE (Ziman, 1972; Sevik, 2010) as given by,

$$\begin{aligned}\frac{\partial \mathrm{f}_{\mu}(\mathrm{T},\mu)}{\partial \mathrm{t}} &= -\mathrm{v}_{\alpha}(\mathrm{i},\mathbf{k})\frac{\partial \mathrm{f}_{\mu}(\mathrm{T},\mu)}{\partial \mathrm{r}}|_{\mathrm{diffusion}} \\ &- \frac{\mathrm{e}}{\mathrm{h}}(\mathrm{E}-\frac{1}{\mathrm{c}}\mathrm{v}_{\alpha}(\mathrm{i},\mathbf{k})\times \mathrm{H})\frac{\partial \mathrm{f}_{\mu}(\mathrm{T},\mu)}{\partial \mathrm{k}_{\alpha}}|_{\mathrm{field}} + \frac{\partial \mathrm{f}_{\mu}(\mathrm{T},\mu)}{\partial \mathrm{t}}|_{\mathrm{scattering}}\end{aligned} \tag{3.63}$$

with $\mathrm{f}_{\mu}(\mathrm{T},\mu) = \frac{1}{\exp\left[\frac{\mu-\mathrm{E_F}}{\mathrm{k_B T}}\right]+1}$ represents the Fermi-Dirac distribution, and $\mathrm{v}_{\alpha}(\mathrm{i},\mathbf{k}) = \frac{1}{\hbar}\frac{\partial \varepsilon_{\mathrm{i},\mathbf{k}}}{\partial \mathrm{k}_{\alpha}}$ denotes the carriers' group velocity.

The thermoelectric parameters, such as Seebeck coefficient ($\mathrm{S}_{\alpha\beta}$), and TPF etc. are computed as follows,

$$\begin{cases} \mathrm{S}_{\alpha\beta}(\mathrm{T},\mu) = \frac{8\pi^2\mathrm{k_B^2}}{3\mathrm{eh}^2}\mathrm{m}^*\mathrm{T}\left(\frac{\pi}{3\mathrm{n}}\right)^{2/3}, \\ \mathrm{TPF} = \sigma_{\alpha\beta}(\mathrm{T},\mu)\mathrm{S}^2_{\alpha\beta}. \end{cases} \tag{3.64}$$

where, $\mathrm{e}, \mathrm{h}, \mathrm{k_B}$ and m^* are the electronic charge, Plank constant, Boltzmann constant and carrier effective mass, respectively, and $\sigma_{\alpha\beta}(\mathrm{T},\mu)$, $\kappa_{\alpha\beta}(\mathrm{T},\mu)$, $\mathrm{S}_{\alpha\beta}(\mathrm{T},\mu)$ are the electrical conductivity, thermal conductivity, and Seebeck coefficient tensors, respectively.

with,
$\sigma_{\alpha\beta}(\mathrm{T},\mu) = \frac{1}{\Omega}\int \langle\sigma_{\alpha\beta}(\varepsilon)\rangle\left[-\frac{\partial \mathrm{f}_{\mu}(\mathrm{T},\mu)}{\partial\varepsilon}\right]\mathrm{d}\varepsilon$, is the electrical conductivity tensor,

$\kappa_{\alpha\beta}(\mathrm{T},\mu) = \frac{1}{\Omega \mathrm{e}^2 \mathrm{T}} \int \langle \sigma_{\alpha\beta}(\varepsilon) \rangle (\varepsilon - \mu) \left[-\frac{\partial \mathrm{f}_\mu(\mathrm{T},\mu)}{\partial \varepsilon} \right] \mathrm{d}\varepsilon$, is the thermal conductivity tensor, $\mathrm{S}_{\alpha\beta}(\mathrm{T},\mu) = \frac{1}{\Omega \mathrm{T} \sigma_{\gamma\alpha}(\mathrm{T},\mu)} \int \langle \sigma_{\alpha\beta}(\varepsilon) \rangle (\varepsilon - \mu)^2 \left[-\frac{\partial \mathrm{f}_\mu(\mathrm{T},\mu)}{\partial \varepsilon} \right] \mathrm{d}\varepsilon$, is the thermoelectric Seebeck coefficients,

$\langle \sigma_{\alpha\beta}(\varepsilon) \rangle = \frac{\mathrm{e}^2}{\mathrm{N}} \Sigma_{\mathrm{i},\mathbf{k}} \tau_{\mathrm{i,k}} \mathrm{v}_\alpha(\mathrm{i},\mathbf{k}) \mathrm{v}_\beta(\mathrm{i},\mathbf{k}) \delta(\varepsilon - \varepsilon_{\mathrm{i},\mathbf{k}})$, is the kernel of transport coefficients required for computing the thermoelectric parameters (Saeed *et al.*, 2014), which can be done by the Fourier interpolation of the band structures. Where, α and β are the tensor indices, Ω is the volume of unit cell and μ is the chemical potential. We calculated the various TE parameters for the $CaVO_3$ and $LaVO_3$ superstructures (Dehkordi *et al.*, 2015; Adewale *et al.*, 2018). Acoustic phonons are the largest contributors to overall thermal conductivity, $\kappa_{\alpha\beta}$, in bulk semiconducting and insulating TMOs. However, electronic thermal conductivity is crucial for highly doped and non-stoichiometric TMOs. The κ_{ph} (phonon contribution) and κ_e (electronic contribution) are defined by the kinetic theory of electron gas as,

$$\kappa_{ph} = \frac{1}{3} v_s C_v l_{ph} \tag{3.65}$$

and,

$$\kappa_e = \frac{1}{3} c_v v \Lambda = L \sigma_{\alpha\beta} T \tag{3.66}$$

where v_s is the sound velocity, C_v is the constant volume heat capacity, l_{ph} is the phonon mean free path, c_v is the electronic specific heat per volume, and v is the electron velocity that can be taken to equal the Fermi velocity, v_F, the electron mean free path, Λ and the Lorenz number (L = 2.45×10^{-8} $\mathrm{V^2K^2}$).

3.1.9 Optical Properties

For optically driven behaviors of materials (Ambrosch-Draxl & Sofo, 2006), optical properties such as the dielectric function, optical conductivity and electron loss function (ELOSS) etc. are computed as,

$$\begin{cases} \varepsilon_{ij}(\omega) = \mathrm{Re}[\varepsilon_{ij}(\omega)] + \mathrm{Im}[\varepsilon_{ij}(\omega)], \\ \mathrm{Im}[\varepsilon_{ij}(\omega)] = \left(\frac{16\pi^2}{\Omega\omega^2}\right) \sum_{i,j} \langle \psi_k^c | \hat{p}_i | \psi_k^v \rangle \langle \psi_k^c | \hat{p}_j | \psi_k^v \rangle \times \delta\left(E_{c,\mathbf{k}} - E_{v,\mathbf{k}} - \omega\right), \\ \mathrm{Re}[\varepsilon_{ij}(\omega)] = \delta_{ij} + \frac{2}{\pi} p \int_0^\infty \frac{\omega' \mathrm{Im}[\varepsilon_{ij}(\omega')]}{\omega'^2 - \omega^2} d\omega', \\ \mathrm{Re}[\sigma_{ij}(\omega)] = \frac{\omega}{4\pi} \mathrm{Im}[\varepsilon_{ij}(\omega)] \\ L_{ii}(\omega) = -\mathrm{Im}\left\{\frac{1}{\varepsilon_{ii}(\omega)}\right\}. \end{cases} \tag{3.67}$$

And, the index of refraction, extinction coefficient, reflectivity, absorptivity, sum rules etc. (Tohyama *et al.*, 2005; Nakano *et al.*, 2007) are computed as follows,

$$\begin{cases} n_{ii}(\omega) = \sqrt{\frac{|\varepsilon_{ii}(\omega)| + \mathrm{Re}[\varepsilon_{ii}(\omega)]}{2}}, \\ k_{ii}(\omega) = \sqrt{\frac{|\varepsilon_{ii}(\omega)| - \mathrm{Re}[\varepsilon_{ii}(\omega)]}{2}}, \\ \alpha_{ii}(\omega) = \frac{(n_{ii}-1)^2 + k_{ii}^2}{(n_{ii}+1)^2 + k_{ii}^2}, \\ A_{ii}(\omega) = \frac{2\omega k_{ii}(\omega)}{c}, \\ N_{\mathrm{eff}}(\omega) = \int_0^\omega \sigma(\omega')\omega' d\omega'. \end{cases} \tag{3.68}$$

3.1.10 Metal-Insulator Transition (MIT)

The electron transport determines the electrical conductivity of a material. As a matter of fact, the electron transport is affected by three distinct effects, viz.

1. the potential of the ions
2. the Coulomb interaction
3. external (electrical or magnetic) fields

The study uses a complex formalism to determine transport parameters in interacting many-particle systems out of thermal equilibrium. The focus is on conducting properties near to thermal equilibrium, where external fields cause slight perturbations. The first step is to categorize insulators using Ohm's law as,

$$\mathbf{j}_\alpha(\mathbf{k}, \omega) = \sum_\beta \sigma_{\alpha\beta}(\mathbf{k}, \omega) \mathbf{E}_\beta(\mathbf{k}, \omega) \tag{3.69}$$

The conductivity tensor $\sigma_{\alpha\beta}(\mathbf{k},\omega)$ can be derived from the current-current correlation function (3.69), using the fluctuation-dissipation theorem. This property can be expressed as a correlation function in thermal equilibrium. However, the calculation of the conductivity tensor requires evaluating a two-electron correlation function, and single-electron properties alone cannot explain electron transport in the solid state.

At zero temperature, an insulator's static electrical conductivity disappears.

$$\sigma^{\mathrm{DC}}_{\alpha\beta}(\mathrm{T}=0) = \lim_{\mathrm{T}\to 0}\lim_{\omega\to 0}\lim_{|\mathbf{k}|\to 0}\mathrm{Re}\{\sigma_{\alpha\beta}(\mathbf{k},\omega)\} = 0 \tag{3.70}$$

Definition of a Drude metal with finite metallic conductivity is,

$$\mathrm{Re}[\sigma_{\alpha\beta}(\mathrm{T}=0,\omega\to 0)] = (\mathrm{D_C})_{\alpha\beta}\frac{\tau}{\pi(1+\omega^2\tau^2)} \tag{3.71}$$

where, $(\mathrm{D_C})_{\alpha\beta}$ is Drude weight and τ is scattering time for uncorrelated electron collisions. The Drude theory, we have,

$$(\mathrm{D_C})_{\alpha\beta} = \frac{\pi \mathrm{ne}^2}{\mathrm{m}^*}\delta_{\alpha\beta}$$

with e represents the electronic charge and n/m* represents the ratio of charge carrier concentration to effective mass. If electron scattering is absent, translational invariance is restored, resulting in ideal metallic behavior,

$$\mathrm{Re}[\sigma_{\alpha\beta}(\mathrm{T}=0,\omega\to 0,\tau^{-1}\to 0)] = (\mathrm{D_C})_{\alpha\beta}\delta(\omega) \tag{3.72}$$

The MIT is a fundamentally least understood problem in condensed matter physics, involving materials like silicon and germanium as insulators and metals like silver and gold. These materials' highly stable physical properties make them challenging to manipulate or modify for modern technology or explore novel phenomena.

Mott Insulator

The Mott insulating behavior of materials involve strong Coulombian repulsion preventing particles' flow in the system. In general, the ground states have one particle on each site, suppressing large repulsion between particles. Band insulators, including

semiconductors, are states produced by quantum interference effects. Electronic states with charge gaps, such as Mott and Bloch-Wilson insulators Fig. 8(a) (Mott, 1949; Gull *et al.*, 2011), occur in crystalline systems at isolated occupation numbers. Mott state are insulating states, in fact arise due to various reasons, and can be characterized by spontaneous broken symmetry, quasi-particle behavior, low energy neutral particle excitations, topological order and charge fractionalization. The Mott criteria for metal insulator transition is,

$$a_0 n_c^{1/3} \sim 0.25 \tag{3.73}$$

where, $a_0 = 0.53$ Å is the Bohr radius of H-atom and n_c is the critical carrier concentration for MIT to occur.

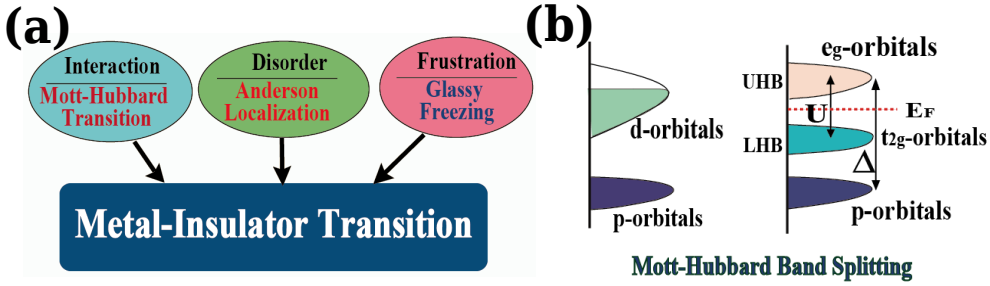

Figure 8: (a) The three mechanisms of metal insulator transition (Gull *et al.*, 2011) (b) The schematic Mott-Hubbard band splittings (Mott, 1949; Vollhardt, 2012).

The Mott transition is crucial for modeling strongly correlated electrons, addressing the competition between kinetic energy and correlation energy (Mott, 1949; Deng *et al.*, 2013). The Mott-Hubbard MIT is important for understanding condensed matter physics, which is the consequence of splitting of CB into two bands, UHB and LHB as shown in Fig. 8(b) (Mott, 1949; Gull *et al.*, 2011). Proper accounts of itinerant electron systems are necessary for obtaining a complete electronic picture of strongly correlated materials. One of the best possible solution is to use the DMFT framework for such materials.

3.2 Dynamical Mean Field Theory (DMFT)

The Hartree-Fock mean-field approximations are insufficient for electronic systems like the Hubbard model with strong electronic interactions. DMFT preserves system dynamics in large coordination numbers ($1/Z \to 0$), unlike Weiss molecular-field theory for the Ising model.

DMFT is diagrammatically controlled and has no additional approximation or physical parameter constraints, making it an excellent starting point for further improvements.

The interacting system is represented by a single site Hubbard Hamiltonian (Hubbard, 1963) as,

$$\hat{\mathrm{H}} = -\mathrm{t}\sum_{\mathrm{ij},\sigma} \hat{\mathrm{c}}^{\dagger}_{\mathrm{i}\sigma}\hat{\mathrm{c}}_{\mathrm{j}\sigma} + \mathrm{U}\sum_{\mathrm{i}} \hat{\mathrm{n}}_{\mathrm{i}\uparrow}\hat{\mathrm{n}}_{\mathrm{i}\downarrow}, \tag{3.74}$$

The first term on rhs of (3.74) is the non-local part,

$$\hat{\mathrm{H}}_{\mathrm{non-local}} = -\mathrm{t}\sum_{\mathrm{ij},\sigma} \left(\hat{\mathrm{c}}^{\dagger}_{\mathrm{i}\sigma}\hat{\mathrm{c}}_{\mathrm{j}\sigma} + \hat{\mathrm{c}}^{\dagger}_{\mathrm{j}\sigma}\hat{\mathrm{c}}_{\mathrm{i}\sigma}\right) \tag{3.75}$$

And the second term on the rhs of (3.74) is the local part on site interaction at i is,

$$\hat{\mathrm{H}}_{\mathrm{local}} = \mathrm{U}\sum_{\mathrm{i}} \hat{\mathrm{c}}^{\dagger}_{\mathrm{i}\uparrow}\hat{\mathrm{c}}_{\mathrm{i}\uparrow}\hat{\mathrm{c}}^{\dagger}_{\mathrm{i}\downarrow}\hat{\mathrm{c}}_{\mathrm{i}\downarrow} \tag{3.76}$$

The Hubbard and AIM are used to analyze the fermionic situation at site i as in Fig. 9 (Vollhardt, 2012), capturing interactions on real crystal lattice site i. The impurity Hamiltonian is the cornerstone of DMFT, and various solutions, including CT-QMC method, can be implemented reliably (Morosan *et al.*, 2012).

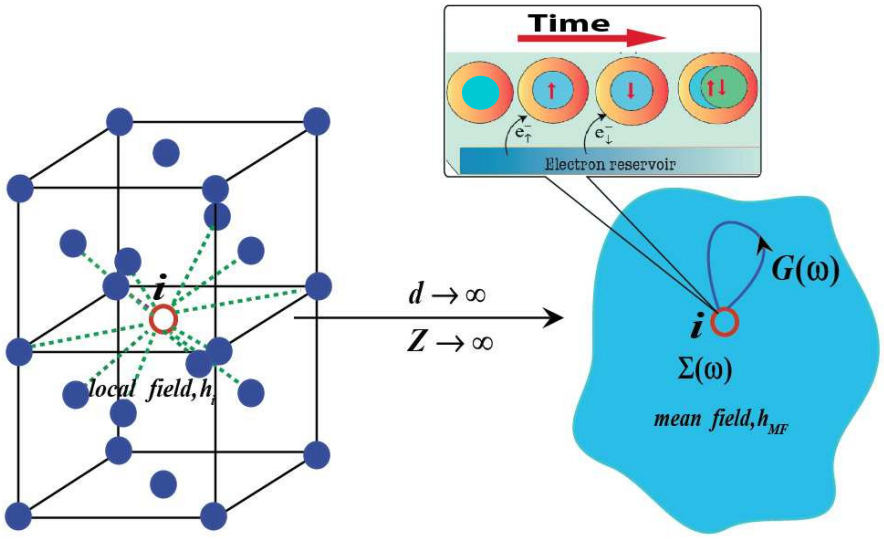

Figure 9: The schematics for a local field interaction in a face-centered cubic (FCC) lattice in the limit of $d \to \infty$ or $Z \to \infty$ (infinite dimension) (Vollhardt, 2012; Morosan *et al.*, 2012).

3.2.1 The Anderson Impurity Model (AIM)

The AIM represents a many-body system Hamiltonian (Anderson, 1967; Georges *et al.*, 1996; Held *et al.*, 2006) as,

$$\hat{\mathcal{H}} = \sum_{\sigma=\uparrow,\downarrow} \epsilon_0(\mathbf{k})\ \hat{\mathrm{c}}^{\dagger}_{\sigma}\hat{\mathrm{a}}_{\sigma} + \mathrm{U}\mathrm{n}_{\mathrm{a}\uparrow}\mathrm{n}_{\mathrm{a}\downarrow} + \sum_{\mathrm{k},\sigma}[\mathrm{V}_{\mathrm{k},\sigma}(\mathbf{k})\hat{\mathrm{c}}^{\dagger}_{\mathrm{k},\sigma}\hat{\mathrm{a}}_{\sigma} + \mathrm{h.c.}] + \sum_{\mathrm{k},\sigma} \epsilon_{\mathrm{k},\sigma}(\mathbf{k})\hat{\mathrm{c}}^{\dagger}_{\mathrm{k},\sigma}\hat{\mathrm{c}}_{\mathrm{k},\sigma} \tag{3.77}$$

where $\epsilon_0(\mathbf{k})$ is the impurity's energy level, $\hat{a}^{\dagger}_{\sigma}$ (corr. $\hat{a}_{\sigma}$) is the creation (corr. annihilation) operators on the impurity with spin σ. The energy spectrum of the bath is represented by $\epsilon_{k,\sigma}(\mathbf{k})$. And, $\hat{c}^{\dagger}_{k,\sigma}$ (corr. $\hat{c}_{k,\sigma}$) is the creation (corr. annihilation) operators in the bath with spin σ and momentum k, and $\mathrm{V}_{\mathrm{k},\sigma}(\mathbf{k})$ is the hybridization parameter (Arita *et al.*, 2012). The impurity and its fermionic bath have the following partition function (PF):

$$Z \quad = \quad \mathrm{Tr}[exp(-\beta\hat{\mathcal{H}})] \tag{3.78}$$

The PF is the path integral over Grassman variables and it is a successful method for evaluating systems using numerical techniques with imaginary time formalism (Fujimori *et al.*, 1992). It is expressed as a function of $\hat{a}^{\dagger}_{\sigma}$ and $\hat{a}_{\sigma}$, can be expressed as,

$$\mathrm{Z} = \int \mathcal{D}\left[\hat{\mathrm{a}}^{\dagger}_{\sigma}, \hat{\mathrm{a}}_{\sigma}\right] \exp(-\mathrm{S}_{\mathrm{eff}}) \tag{3.79}$$

where, $\mathrm{S}_{\mathrm{eff}}$, represents the effective action of the Hubbard model Hamiltonian, which can be solved by mapping onto a single-site AIM Hamiltonian (3.77).

$$\mathrm{S}_{\mathrm{eff}} = -\sum_{\sigma}\int_0^{\beta} \mathrm{d}\tau\mathrm{d}\tau'\hat{\mathrm{a}}^{\dagger}_{\sigma}(\tau)\mathcal{G}^{-1}_{0\sigma}(\tau-\tau')\hat{\mathrm{a}}_{\sigma}(\tau') + \int_0^{\beta}\mathrm{d}\tau\mathrm{U}\hat{\mathrm{n}}_{\mathrm{a}\uparrow}(\tau)\hat{\mathrm{n}}_{\mathrm{a}\downarrow}(\tau) \tag{3.80}$$

The non-interacting (U = 0) GF,

$$\mathcal{G}^{-1}_{0\sigma}(\mathrm{i}\omega_{\nu}) = \mathrm{i}\omega_{\nu} - \varepsilon_0 - \Delta_{\sigma}(\mathrm{i}\omega_{\nu}) \tag{3.81}$$

The hybridization part of interaction is,

$$\Delta_{\sigma}(\mathrm{i}\omega_{\nu}) = \sum_{\mathrm{k}} \frac{|\mathrm{V}_{\mathrm{k}\sigma}(\mathbf{k})|^2}{\mathrm{i}\omega_{\nu} - \varepsilon_{\mathrm{k}\sigma}(\mathbf{k})} \tag{3.82}$$

it describes the transition between the electronic bath and the orbitals (Kotliar & Vollhardt, 2004; Gull *et al.*, 2011).

3.2.2 The Continuous Time Quantum Monte Carlo (CT-QMC)

The MC method, which is a kernel of the CT-QMC, generates pseudo random numbers to simulate natural random processes like electronic fluctuation in lattice sites (Georges *et al.*, 1996; Held *et al.*, 2006). The theoretical explanations for estimating the Mott-Hubbard MIT phase transition in solid systems are discussed. The Mott-Hubbard MIT arises due to quasi-particle electron behavior. The DMFT self-consistent cycle Fig. 10 (Kotliar & Vollhardt, 2004; Gull *et al.*, 2011) of calculation addresses the Mott transition problem in strongly correlated electronic systems (Hubbard, 1963).

The CT-QMC algorithm is a stochastic process used to solve the AIM at finite temperature, consisting of a Hamiltonian with some limited number of states and hybridization processes, enabling particle exchange with the fermionic bath (Dirks *et al.*, 2010). These algorithms are crucial in the DMFT for approximating fermions' properties on infinite-dimensional lattice sites (Werner *et al.*, 2006). MC Integration is essential for converting the integral of a function to a discrete sum as,

$$\int_{a}^{b} f(x)dx = \frac{b-a}{N}\sum_{i=1}^{N} f\left(a + i\frac{b-a}{N}\right) + O\left(\frac{1}{N}\right) \tag{3.83}$$

The Monte Carlo approach incorporates sampling, errors, Markov chains, and Metropolis-Hastings algorithm to get the results (Bauer *et al.*, 2011). The Monte Carlo technique is a method for computing the sums of probability distributions functions p(x) for sampling functions f(x) in a given configuration space (Bauer *et al.*, 2011).

$$\sum_{x} p(x)f(x),$$

where, p(x) > 0, and,

$$\sum_{x} p(x) = 1 \tag{3.84}$$

The variable, $x = (\tau, \sigma, ...)$ represents the set of variables under study.

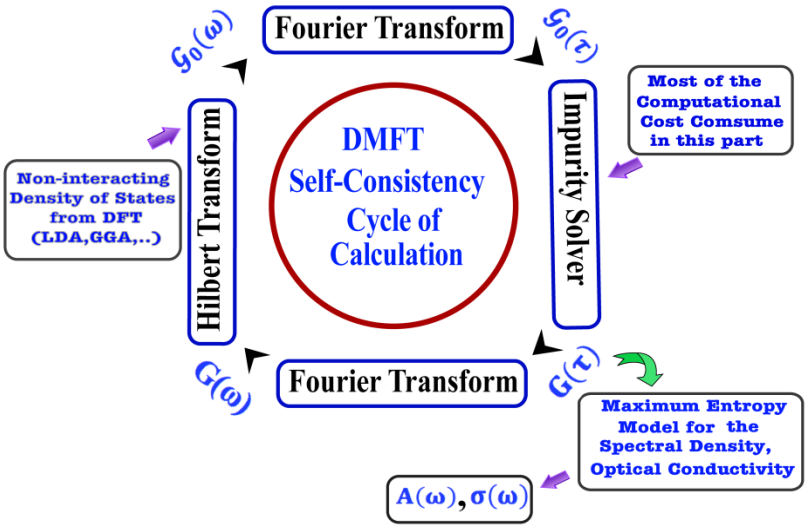

Figure 10: The schematic of self-consistency cycle for DMFT calculation (Georges *et al.*, 1996; Held *et al.*, 2006).

3.2.3 The Continuous Time Partition Function in Configuration Space

Monte-Carlo sampling partition function with infinite series on imaginary time parameters is given by,

$$\mathrm{Z} = \sum_{\mathrm{n}=0}^{\infty} \iiint_{0}^{\beta} \mathrm{d}\tau_1, \cdots, \mathrm{d}\tau_{\mathrm{n}} \mathrm{p}(\tau_1, \tau_2, \cdots, \tau_{\mathrm{n}}) \tag{3.85}$$

represented by the sum of expansion orders over n slices of imaginary time steps $\tau_1, \cdots, \tau_n$. This function is integrated over probability densities $\mathrm{p}(\tau_1, \cdots, \tau_n)$ from τ = 0 to β, imaginary time intervals (Loh Jr *et al.*, 1990).

The partition function of a single parameter is calculated in first order using the integrand uniquely described by a set of imaginary time $\{\tau_1\}$ as given by,

$$\mathrm{Z}_1 = \int_{0}^{\beta} \mathrm{d}\tau_1 \mathrm{p}(\tau_1) \tag{3.86}$$

The Monte Carlo technique (Reinle-Schmitt *et al.*, 2012) is used to sample Eq. (3.85) up to first order uniformly distributed random numbers of imaginary time τ_1 in the interval [0, β]. This allows for a better understanding of the integral's lowest orders and its contribution to the partition function as,

$$\mathrm{Z}_1 = \lim_{\mathrm{N}\to\infty} \frac{1}{\mathrm{N}} \sum_{0}^{\beta} \mathrm{p}(\tau_{\mathrm{j}}) \tag{3.87}$$

The second order calculation generates uniformly distributed value pairs in the interval [0, β] using imaginary time (τ_1, τ_2). The integral is truncated using Metropolis' algorithm (Gull *et al.*, 2011) to accept or reject transitions. The number of MC samples may have MC error, which scales as $\frac{1}{\sqrt{N}}$ with the samples (Nekrasov *et al.*, 2005).

$$\mathrm{Z_1} = \lim_{\mathrm{N}\to\infty} \frac{1}{\mathrm{N}} \sum_{0}^{\beta} \mathrm{p}(\tau_\mathrm{j}, \tau_2) \tag{3.88}$$

For the potential ordering s, let us define all of the configuration spaces as,

C ={ {..} , $\{\tau_1\}, \{\tau_1, \tau_2\}, ..., \{\tau_1, ..., \tau_\mathrm{n}\}$ },

The PF is a set of continuous imaginary time variables τ_j, each adding value to the partition function. To prevent sign problems, the expansion coefficients above are assumed to be positive (Yoo *et al.*, 2005; Gull *et al.*, 2011), as otherwise, the function is time-ordered. i.e. $\tau_1, \tau_2, \cdots, \tau_\mathrm{n}$.

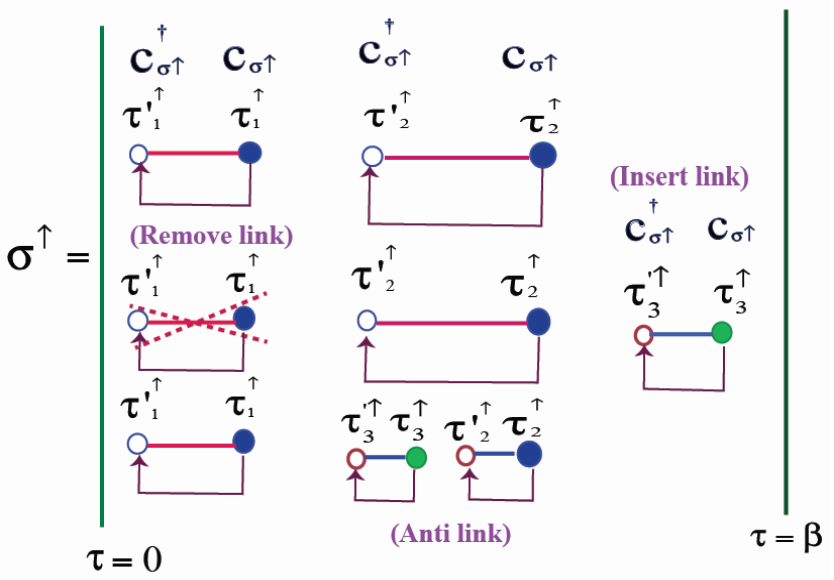

Figure 11: MC configurations are represented by a sequence of operators on the time interval $0 \leq \tau < \beta$, with full(empty) circles representing annihilation(creation) operators. MC moves involve random insertions or removal of pairs of operators in different channels (Ferrero *et al.*, 2005; Haule, 2007).

The diagrammatic MC codes are implemented by raising the order for updating the transition $\mathrm{x_n} \to \mathrm{x_{n+1}}$, adding a link (additional vertex, τ_j), or lowering the order, removal of a link (removal of a vertex, τ_i), or local changes on the same site ($\tau_j \to \tau_j'$), like a spinflip or the change over a τ as in Fig. 11 (Ferrero *et al.*, 2005; Haule, 2007).

3.2.4 Markov Chain Transition

To perform updates using the Metropolis algorithm refer to (Appendix-IV), the probability must meet the detailed balance condition. For a given configuration $x = (\tau_1), ..., (\tau_n)$, inserting a time vertex (τ_{n+1}) to obtain $y = (\tau_1), ..., (\tau_n), (\tau_{n+1})$ ensures the condition. The transition probability density $\mathrm{W_{x,y}}$ of transitioning from state x to state y is crucial.

The CT-QMC hybridization algorithm is used to determine the partition function for different configurations (x $\rightarrow$ y) with weight, $\omega(C)$ with which, the GF of imaginary time or frequency can be calculated.

3.2.5 CT-QMC with Hybridization Expansion

We must focus on the simplest AIM which can be generalized as a multi-orbital approach. To calculate an expansion near the atomic limit, we use the hybridization approach (Georges *et al.*, 1996; Kotliar & Vollhardt, 2004; Held *et al.*, 2006). The effective action is the sum of local terms and hybridization to the bath.

$$\begin{aligned} \mathrm{S_{eff}} &= \mathrm{S_{loc}} + \textstyle\sum_\sigma \int_0^\beta \mathrm{d}\tau \mathrm{d}\tau' \hat{\mathrm{c}}^\dagger_\sigma(\tau) \Delta_\sigma(\tau - \tau') \hat{\mathrm{d}}_\sigma(\tau') \\ &= \mathrm{S_{loc}} + \textstyle\sum_\sigma \mathrm{S^\sigma_{hyb}} \end{aligned} \tag{3.89}$$

From (3.79), we get,

$$\begin{aligned} \mathrm{Z} &= \int \mathcal{D}\left[\hat{a}^\dagger_\sigma, \hat{a}_\sigma\right] \exp(-S_{loc} + \sum_\sigma S^\sigma_{hyb}) \\ &= \int \mathcal{D}\left[\hat{a}^\dagger_\sigma, \hat{a}_\sigma\right] \exp(-S_{loc}) \left[\prod_\sigma \frac{(-1)^n_\sigma}{n_{\sigma!}} \left(S^\sigma_{hyb}\right)^n\right] \end{aligned} \tag{3.90}$$

From the path integral QMC using SSE, we may write,

$$\mathrm{Z} = \textstyle\sum_{\mathrm{n}\uparrow,\mathrm{n}\downarrow=0}^\infty \left\langle \mathrm{Tr} \prod_\sigma \frac{(-1)^{\mathrm{n}}_\sigma}{\mathrm{n}_{\sigma!}} \left(\mathrm{S^\sigma_{hyb}}\right)^{\mathrm{n}} \right\rangle_{\mathrm{loc}} \tag{3.91}$$

$$\begin{aligned} \mathrm{Z} &= \textstyle\sum_{\mathrm{n}\uparrow,\mathrm{n}\downarrow=0}^\infty \int_0^\beta \mathrm{d}\tau^\sigma_1 ... \mathrm{d}\tau'^\sigma_{\mathrm{n}\uparrow} \int_0^\beta \mathrm{d}\tau^{\sigma'}_1 ... \mathrm{d}\tau'^{\sigma'}_{\mathrm{n}\downarrow} \\ &\times \prod_\sigma \frac{(-1)^{\mathrm{n}}_\sigma}{\mathrm{n}_{\sigma!}} \prod_{\mathrm{i}=1}^{\mathrm{n}_\sigma} \Delta_\sigma \left(\tau^\sigma_{\mathrm{i}} - \tau'^\sigma_{\mathrm{i}}\right) \end{aligned}$$

$$\times \mathrm{Tr}\left[\mathrm{e}^{-\beta\hat{\mathcal{H}}_{\mathrm{loc}}}\mathrm{Tr}\prod_{\mathrm{i}=1}^{\mathrm{n}\uparrow}\hat{\mathrm{c}}_{\uparrow}^{\dagger}\left(\tau_{\mathrm{i}}^{\sigma}\right)\hat{\mathrm{c}}_{\uparrow}\left(\tau_{\mathrm{i}}^{'\sigma}\right)\prod_{\mathrm{i}=1}^{\mathrm{n}\sigma'}\hat{\mathrm{c}}_{\downarrow}^{\dagger}\left(\tau_{\mathrm{i}}^{\sigma'}\right)\hat{\mathrm{c}}_{\downarrow}^{\dagger}\left(\tau_{\mathrm{i}}^{'\sigma'}\right)\right] \tag{3.92}$$

Which is the sum of continuous variables and product of hybridization functions with trace involving spin up and spin down operators.

$$\therefore \mathrm{Z} = \int_{\mathrm{C}} \omega(\mathrm{C}) \approx \Sigma_{\mathrm{C}}^{\mathrm{MC}}\mathrm{sign}(\omega\mathrm{C}) \tag{3.93}$$

where $\omega(C)$ is the weights of configurations C in the limit $\mathrm{N} \to \infty$ gives the probability,

$$\mathrm{p}(\mathrm{C}) = \frac{1}{\mathrm{Z}}\omega(\mathrm{C}) \tag{3.94}$$

$$\therefore \langle \mathrm{f} \rangle = \frac{1}{\mathrm{Z}}\int_{\mathrm{C}} \omega(\mathrm{C})\mathrm{f}(\mathrm{C}) \sim \frac{1}{\mathrm{Z}}\Sigma_{\mathrm{C}}^{\mathrm{MC}}\mathrm{f}(\mathrm{C})\mathrm{sign}(\omega(\mathrm{C})) \tag{3.95}$$

The $\omega(C)$ is computed as,

$$\begin{aligned}\omega(\mathrm{C}) = \mathrm{Tr} \times \mathrm{e}^{-\beta\hat{\mathcal{H}}_{\mathrm{loc}}}\mathrm{Tr}\prod_{\mathrm{i}=1}^{\mathrm{n}\uparrow}\hat{\mathrm{a}}_{\uparrow}^{\dagger}\left(\tau_{\mathrm{i}}^{\sigma}\right)\hat{\mathrm{a}}_{\uparrow}\left(\tau_{\mathrm{i}}^{'\sigma}\right) \\ \times \prod_{i=1}^{n\downarrow}\hat{a}_{\downarrow}^{\dagger}\left(\tau_{i}^{\sigma'}\right)\hat{a}_{\downarrow}\left(\tau_{i}^{'\sigma'}\right) \\ \times \prod_{\sigma}\frac{(-1)_{\sigma}^{\mathrm{n}}}{\mathrm{n}_{\sigma!}}\prod_{\mathrm{i}=1}^{\mathrm{n}_{\sigma}}\Delta_{\sigma}\left(\tau_{\mathrm{i}}^{\sigma} - \tau_{\mathrm{i}}^{\sigma}\right)\end{aligned} \tag{3.96}$$

Unfortunately, this calculations face alternating signs problems, requiring evaluation of PF using imaginary time step diagram and sum of possible permutations of the electronic fluctuations.

3.2.6 Computing GF from Partition Function

The impurity GF represents the logarithmic derivative of Z w.r.t. hybridization $\Delta(\tau)$ as given by,

$$\mathrm{G}_{\sigma}(\tau) = -\frac{1}{\beta}\frac{\delta\mathrm{log}\mathrm{Z}}{\delta\Delta_{\sigma}(-\tau)}\left[\because \mathrm{G}(\tau) = -\frac{\delta\mathrm{log}\mathrm{Z}}{\delta\Delta(\tau)}\right] \tag{3.97}$$

$$G_{\uparrow}(\tau) = -\frac{1}{Z\beta}\int_{C}\frac{\delta \det\Delta_{\uparrow C}}{\delta\Delta_{\uparrow}(-\tau)} \times (-1)^{n\uparrow+n\downarrow}\det\Delta_{\downarrow C}\mathrm{Tr}C \tag{3.98}$$

Configurations contribute for a discrete set of imaginary times,

$$G_{\sigma}(\tau) \sim -\tfrac{1}{Z\beta}\sum_{C}^{MC}\sum_{k,l}\delta(\tau_{k}^{\sigma} - \tau_{l}^{'\sigma} + \tau) \times \left[\Delta_{\sigma C}^{-1}\right]_{k,l} \times \mathrm{sign}\left(\omega(C)\right) \tag{3.99}$$

The study, in reality helps estimate contributions and reduces the high frequency noise in Matsubara frequencies. It investigates the single-particle imaginary time GF, G(τ) on the interval [0, β] (Boehnke *et al.*, 2011; Iazzi & Troyer, 2015) to compute its Legendre representation. Expanding GF in terms of Legendre polynomials $P_l(x)$ Fig. 12(a) (Boehnke *et al.*, 2011), the authors derive the imaginary time GF over an interval [-1, 1] as,

$$G(\tau) = \sum_{l\geq 0}\frac{\sqrt{2l+1}}{\beta}P_l[x(\tau)]G_l \tag{3.100}$$

where, $x(\tau) = \frac{2\tau}{\beta} - 1$, and G_l is the Legendre coefficients defined as,

$$G_l = \sqrt{2l+1}\int_0^{\beta} d\tau G(\tau)P_l[x(\tau)] \tag{3.101}$$

The Legendre coefficients are crucial for accurate representation of observables and

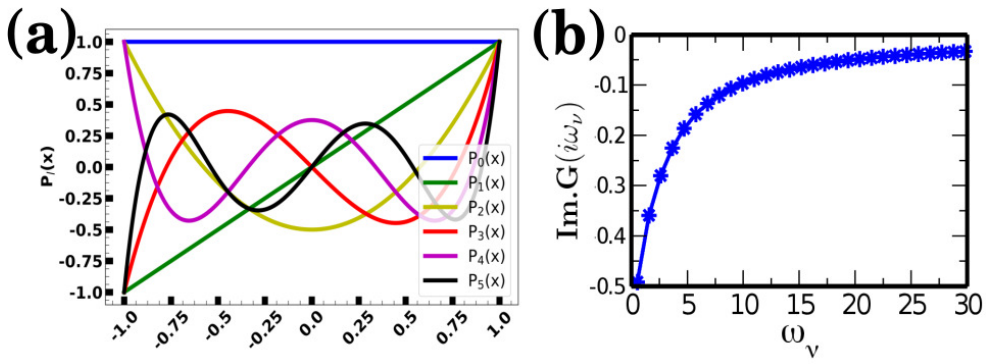

Figure 12: The graphs for (a) the first five orders of Legendre's polynomials in x (b) the example of calculation using these polynomials for GF of Matsubara frequency (Boehnke *et al.*, 2011; Iazzi & Troyer, 2015).

inferring them is difficult by looking at the coefficients themselves. A recent approach is using the Kernel polynomial method with an intermediate representation (IR) basis

(Boehnke *et al.*, 2011). Truncating Legendre coefficients within the acceptable error bars reduce Matsubara frequency noise. This method is shown in Fig. 12 (b), showing the imaginary part of GF of Matsubara frequency.

3.3 Numerical AC Method

3.3.1 Green's Function Methodology

The electronic GF for a single particle is crucial in solving the model of strong correlation. Its properties are summarized, used to improve the Padé approximation method. The finite temperature Matsubara approach with time-independent Hamiltonian can be written as the single-electron GF as,

$$\mathrm{G}(\tau) = -\langle \mathrm{T}[\hat{\mathrm{c}}(\tau)\hat{\mathrm{c}}^{\dagger}(0)]\rangle \tag{3.102}$$

where τ denotes imaginary time, T denotes time ordering operator, and $\hat{c}(\tau)(\hat{c}^{\dagger}(\tau))$ denote annihilation(creation) operators. We employ a single orbital model system, which may be expanded for multi-orbital systems, to avoid the need for to many subscripts. The predicted value of (3.102) represents the thermal average. $G(\tau)$ is the GF defined on the interval $\tau \in [-\beta, \beta]$, where β is the thermodynamical temperature. Because $G(\tau)$ is (anti)periodic with the imaginary axis, so the Matsubara GF with period β as well. In other words, it may be expressed as a Fourier series (Held *et al.*, 2006; Haule, 2007; Gull *et al.*, 2011) as,

$$\mathcal{G}(\tau) = \frac{1}{\beta}\sum_{n=-\infty}^{\infty} e^{-i\omega_\nu \tau}\mathcal{G}_\nu \tag{3.103}$$

where the Fourier coefficients is,

$$\mathcal{G}_\nu = \int_0^\beta \mathrm{d}\tau e^{i\omega_\nu \tau}\mathcal{G}(\tau) \tag{3.104}$$

wit, the Matsubara frequencies,

$$\omega_\nu = \frac{(2\nu+1)\pi}{\beta}(\text{fermions}),$$

And, (3.105)

$$\omega_\nu = \frac{2\nu\pi}{\beta}(\text{bosons})$$

There exists a complete set of G_ν-values for a unique SD $\rho(\omega)$, which is associated via the Hilbert transform as,

$$G(z) = \int_{-\infty}^{\infty} d\omega \frac{1}{z-\omega}\rho(\omega) \tag{3.106}$$

Where, $z = \omega + i\omega_\nu$ is the complex frequency.

3.3.1.1 Analytical Structure of GFs

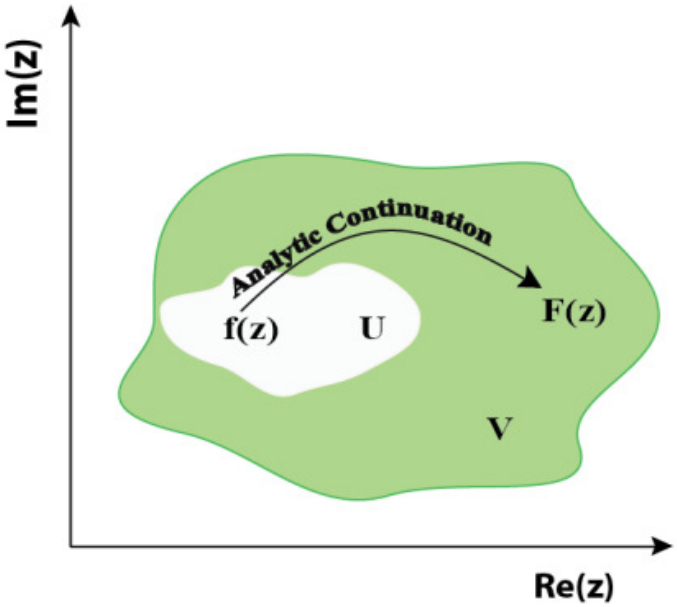

Figure 13: F(z) is the AC of f(z) to the larger domain V (Shao & Sandvik, 2023).

A complex function, f(z), is said to be analytic on an open set D if it can be represented by a convergent power series in the neighborhood of any point Fig. 13 (Shao & Sandvik,

2023), $z_0 \epsilon D$,

$$f(z) = \sum_{\nu=0}^{\infty} a_\nu (z - z_0)^\nu \tag{3.107}$$

For the system under consideration, the CT-QMC with hybridization expansion approach generates GFs data (Werner *et al.*, 2006; Pickett *et al.*, 2013; Shao & Sandvik, 2023). The PF in relation to the impurity model is given by,

$$Z = \int \mathcal{D}\hat{c}^\dagger \mathcal{D}\hat{c} \exp(-S_{\text{eff}}). \tag{3.108}$$

Here, the effective action S_{eff} takes the form,

$$S_{\text{eff}} = S_{\text{loc}} + \sum_{ab} \int_0^\beta d\tau d\tau' \Delta_{ab}(\tau' - \tau) \hat{c}_a^\dagger(\tau') \hat{c}_b(\tau) \tag{3.109}$$

where, the hybridization function, Δ_{ab} takes the indices a and b for spin and the corresponding site of the electrons, respectively. If S_{loc} is the local component of action that comprises solely the interactions' instantaneous terms, the Hamiltonian associated with it is,

$$\hat{\mathcal{H}}_{\text{loc}} = -\sum_{ab} t_{ab} \hat{c}_a^\dagger \hat{c}_b + \sum_{abcd} V_{abcd} \hat{c}_a^\dagger \hat{c}_b^\dagger \hat{c}_c \hat{c}_d. \tag{3.110}$$

The field theory may be used to create a transformed single-particle basis, and the creation and annihilation operators of any single-particle basis, $\psi_k(x)$ described as,

$$\hat{c}_a^\dagger = \int dx \psi_k(x) \psi^\dagger(x) \tag{3.111}$$

$$\hat{c}_a = \int dx \psi_k^*(x) \psi(x) \tag{3.112}$$

With these operators, the GFs of the single-particle basis are expressed as,

$$\begin{aligned} G_{k,k'}^{>}(t, t') &= -i \left\langle \hat{c}_k(t) \hat{c}_{k'}^\dagger(t') \right\rangle \\ G_{k,k'}^{<}(t, t') &= \pm i \left\langle \hat{c}_{k'}^\dagger(t') \hat{c}_k(t) \right\rangle \end{aligned} \tag{3.113}$$

3.3.1.2 Fourier Transform of $G^{>}(\omega)$ and $G^{<}(\omega)$

The greater GF is limited over the real time axis and the Fourier transforms of greater and lesser GFs (Werner *et al.*, 2006; Pickett *et al.*, 2013; Shao & Sandvik, 2023) are written as,

$$\begin{aligned} G^{>}(\omega) &= \int_{-\infty}^{\infty} dt e^{i\omega t} G^{>}(t) \\ G^{<}(\omega) &= \int_{-\infty}^{\infty} dt e^{i\omega t} G^{<}(t) \end{aligned} \tag{3.114}$$

Also, the greater and lesser GFs in the time domain are related to the frequency domain as given by,

$$G^{>}(\omega) = \mp e^{\beta\omega} G^{<}(\omega) \tag{3.115}$$

These GFs are related to the Fourier transform of the SF as,

$$A(\omega) = i\left[G^{>}(\omega) - G^{<}(\omega)\right] \tag{3.116}$$

We define it using the weight function,

$$\begin{aligned} G^{>}(\omega) &= -iA(\omega)f(\omega) \\ G^{<}(\omega) &= iA(\omega)f(-\omega) \end{aligned} \tag{3.117}$$

Where, the weight function,

$$f(\omega) = \pm\frac{1}{1 \pm e^{-\beta\omega}} = \pm n(\omega) \tag{3.118}$$

which is related to particle statistics. The Fermi-Dirac distribution is given by the +ve sign, while the Bose-Einstein distribution is given by the -ve sign. The retarded GF is defined as follows to evaluate the GF in the limit of $\eta \to 0$,

$$\lim_{\eta \to 0^{+}} G(\omega + i\eta) = G^{R}(\omega) \tag{3.119}$$

and,

$$\lim_{\eta \to 0^+} \frac{1}{\omega + \mathrm{i}\eta - \mathrm{i}\omega_\nu} = \frac{1}{\omega - \mathrm{i}\omega_\nu} \tag{3.120}$$

since $\omega - i\omega_\nu = 0$ for every real ω_ν. When the integral is evaluated using the Matsubara frequencies, the real component of the GF, $\mathrm{G}(\omega)$, is removed, and we have,

$$\mathrm{G}(\mathrm{i}\omega_\nu) = \frac{1}{2\pi} \int_{-\infty}^{\infty} \mathrm{d}\omega \frac{\mathrm{Im}\left[\mathrm{G}^{\mathrm{R}}(\omega)\right]}{\omega - \mathrm{i}\omega_\nu} \tag{3.121}$$

3.3.1.3 The Analyticity of the Retarded and Advanced GFs

To obtain the Fourier transform of the retarded GF, substitute (Werner *et al.*, 2006; Pickett *et al.*, 2013; Shao & Sandvik, 2023) ω with $\omega + i\eta$ as,

$$\mathrm{G}^{\mathrm{R}}(\omega) = \int \frac{\mathrm{d}\omega}{2\pi} \frac{\mathrm{A}(\omega')}{\omega + \mathrm{i}\eta - \omega'} \tag{3.122}$$

Similarly, the SF is related to the Fourier transform of the advanced GF,

$$\mathrm{G}^{\mathrm{A}}(\omega) = \int \frac{\mathrm{d}\omega}{2\pi} \frac{\mathrm{A}(\omega')}{\omega - \mathrm{i}\eta - \omega'} \tag{3.123}$$

It is analytic in the lower and upper half-planes separately because of the jump $\mathrm{G}^{\mathrm{R}}(\omega) - \mathrm{G}^{\mathrm{A}}(\omega)$ across the real axis. To determine this difference, we have,

$$\mathrm{G}^{\mathrm{R}}(\omega) - \mathrm{G}^{\mathrm{A}}(\omega) = \int \frac{\mathrm{d}\omega}{2\pi} \frac{\mathrm{A}(\omega')}{\omega + \mathrm{i}\eta - \omega'} - \int \frac{\mathrm{d}\omega}{2\pi} \frac{\mathrm{A}(\omega')}{\omega - \mathrm{i}\eta - \omega'} \tag{3.124}$$

applying the identity,

$$\frac{1}{\omega \pm \mathrm{i}\eta} = \mathcal{P}\frac{1}{\omega} \mp \pi \mathrm{i}\delta(\omega) \tag{3.125}$$

where $\mathcal{P}$ denotes the principal value. The SF is computed as the jump over the real axis,

$$\mathrm{G}^{\mathrm{R}}(\omega) - \mathrm{G}^{\mathrm{A}}(\omega) = -\mathrm{i}\mathrm{A}(\omega) \tag{3.126}$$

Or,

$$\mathrm{A}(\omega) = \mathrm{i}\left[\mathrm{G}^{\mathrm{R}}(\omega) - \mathrm{G}^{\mathrm{A}}(\omega)\right] \tag{3.127}$$

3.3.2 AC for Single-site Dynamical Mean-Field Theory

Finally, the AC of the DMFT data using the impurity solver (Georges *et al.*, 1996; Backes *et al.*, 2017) for the Hubbard model is shown in the flowchart Fig. 14. The covariance matrices are constructed with a limited relative error using the GFs of the DMFT computation. The topic was thoroughly investigated using DMFT for low temperature and high precision (Backes *et al.*, 2017). The peak around the Fermi level is observed to be fairly sharp at low temperature. This is obviously a critical issue since the retarded functions of these GF and correlation function values on the real axis, which can determine a system's dynamical properties.

3.3.2.1 Flowchart for AC

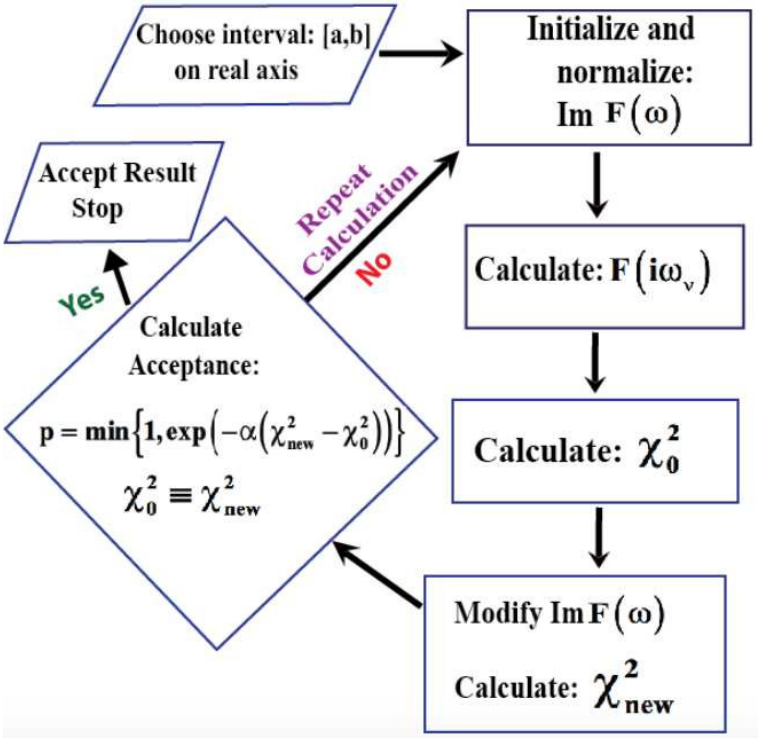

Figure 14: The flowchart for the general analytical continuation of various methods (Backes *et al.*, 2017).

In general, the flowchart Fig. 14 (Backes *et al.*, 2017) depicts the real implementation of AC. For this, we consider the initial input data $\mathrm{F}_{measure}\ (i\omega_\nu)$ on N Matsubara points

$(i\omega_\nu)$ (such as GF, $G_{in}(i\omega_\nu)$). The real frequency axis is to be discretized, and the new function values are updated using a process similar to Metropolis-MC algorithm. Multiple iterations are performed simultaneously for different values of the adjustable hyper-parameter α in order to generate the final SF (Vollhardt, 2012; Morosan *et al.*, 2012).

These techniques based on GF formalism are not directly related to real energies, but it is more easier to work with complex energies for computing real energies using AC, as illustrated in Fig. 15 (Shao & Sandvik, 2023).

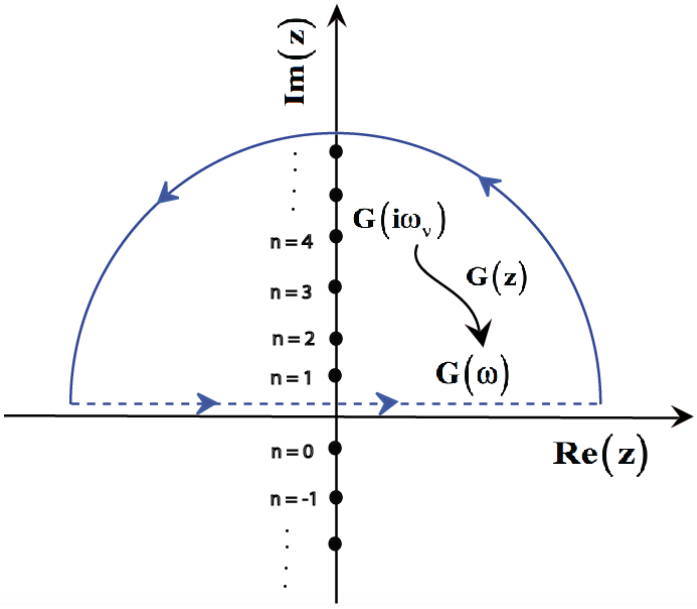

Figure 15: A schematic representation of the Matsubara frequency points' AC of the GF in the complex plane (Shao & Sandvik, 2023).

If a function is known with infinite discrete points on the imaginary axis with infinite precision (Sandvik & Kurkijärvi, 1991), even if there exists a unique continuation, which is irrelevant for normal computations. As a result, the issue is referred as ill-posed one, especially when previous knowledge about the function of the real axis is unavailable. Padé approximation is an AC method used in condensed matter physics to solve Eliashberg equations by parameterizing numerical functions using polynomial ratios (Vidberg & Serene, 1977; Beach *et al.*, 2000).

GFs and self-energies properties, step-by-step improvements, accuracy tests, stability with Matsubara noise, and numerical routine precision are discussed (Shao *et al.*, 2017). Modern machine learning techniques effectively solve AC (Gunnarsson *et al.*, 2010) of

physics related problems, with hybrid approaches integrating ML methodology with physics intuitions is being the best solution thesedays (Yao *et al.*, 2022).

3.3.3 The Maximum Entropy Model (MEM)

Analytically, the GF of Matsubara frequency, $\mathrm{G}(\mathrm{i}\omega_\nu)$, is transformed to the GF of real frequency, $\mathrm{G}(\omega)$. It should be noted that calculating GF for a given SF is simple, however obtaining the SF by simply inverting the integral equation is an ill-posed issue.

$$\mathrm{G}(\mathrm{i}\omega_\nu) = \int \mathrm{d}\omega \frac{\mathrm{A}(\omega)}{\mathrm{i}\omega_\nu - \omega} \tag{3.128}$$

$$= \int \mathrm{d}\omega \mathrm{K}(\mathrm{i}\omega_\nu, \omega)\mathrm{A}(\omega) \tag{3.129}$$

where the kernel $\mathrm{K}(i\omega_\nu, \omega)$ has several forms depending on the problems.

The least squares approach is the most basic and easy means of solving any linear equations as,

$$\chi^2[\mathrm{A}] = \sum_{\mathrm{i}\omega_\nu}^{\mathrm{N_{freq}}} |\mathrm{G} - \mathbf{K}\mathrm{A}|^2 \tag{3.130}$$

The main question with this method is how to cope with the inherent noises. The maximum entropy technique (Silver *et al.*, 1990) is the method to regularize the least-square fit approach. One can define entropy as,

$$\mathrm{S}\,[\mathrm{A}] = -\int \mathrm{d}\omega\, \mathrm{A}(\omega) \ln \frac{\mathrm{A}(\omega)}{\mathrm{D}(\omega)} \tag{3.131}$$

relative to a default model $\mathrm{D}(\omega)$. The default model can encode any information about the spectrum that is known beforehand. If $\mathrm{D}(\omega)$ is non-negative and has the same norm $\mathcal{N}$ as the spectrum $\mathrm{A}(\omega)$, the entropy S will be non-positive and maximum for $\mathrm{D}(\omega)$. It should be noticed that we are not minimizing χ, but rather the following quantity,

$$\mathrm{Q}[\mathrm{A}] = \chi^2[\mathrm{A}] - \alpha \mathrm{S}[\mathrm{A}] \tag{3.132}$$

In this case, α is a hyper-parameter. This optimization problem may be solved numerically with fixed α to minimize spectrum $\mathrm{A}_\alpha(\omega)$. The default model $\mathrm{D}(\omega)$ spectrum is

obtained in the range $\alpha \to \infty$. In the limit $\alpha \to 0$, on the other hand, the least-square fit is properly applied. The easiest way for parameter elimination is to use the spectrum, where $\chi^2 \sim 1$, to avoid overfitting the data while maintaining the differences between model and data within the permissible error bar. We could employ more complex ways by reinterpreting MEM using Bayesian statistical rules (Gull *et al.*, 2011).

3.3.3.1 Bayes' Theorem for MEM

The Bayesian principles of conditional probability may be employed to reformulate the MEM with the various associated parameters in the AC problem. Taking P[A] as the **prior probability** for $\mathrm{A}(\omega)$. The quantity $\mathrm{P}[\mathrm{A}|\bar{\mathrm{G}}]$ is known as the **posterior probability** for $\mathrm{A}(\omega)$ given the data $\bar{\mathrm{G}}(\omega)$ and $\mathrm{P}[\bar{\mathrm{G}}|\mathrm{A}]$ (**likelihood function**). The Bayes' theorem (Bayes, 1958) asserts the following with these probabilities, as depicted in Fig.16(a) (Jarrell & Gubernatis, 1996; Bergeron & Tremblay, 2016)

$$\mathrm{P}[\mathrm{A}|\bar{\mathrm{G}}] = \frac{\mathrm{P}[\bar{\mathrm{G}}|\mathrm{A}]\mathrm{P}[\mathrm{A}]}{\mathrm{P}[\bar{\mathrm{G}}]} \tag{3.133}$$

The probability $\mathrm{P}[\bar{\mathrm{G}}]$ is known as the **evidence** and is used to normalize the posterior probability $\mathrm{P}[\mathrm{A}|\bar{\mathrm{G}}]$,

$$\mathrm{P}[\bar{\mathrm{G}}] = \int \mathcal{D}\mathrm{A}\, \mathrm{P}[\bar{\mathrm{G}}|\mathrm{A}]\, \mathrm{P}[\mathrm{A}] \tag{3.134}$$

One can identifies,

$$\mathrm{P}[\bar{\mathrm{G}}|\mathrm{A}] = \frac{1}{\mathrm{Z}_1} \exp(-\chi^2[\mathrm{A}]) \tag{3.135}$$

and

$$\mathrm{P}[\mathrm{A}] = \frac{1}{\mathrm{Z}_2} \exp(\alpha \mathrm{S}[\mathrm{A}]). \tag{3.136}$$

where,

$$\mathrm{Z}_1 = \int \mathcal{D}\bar{\mathrm{G}}\, \mathrm{e}^{-\chi^2[\mathrm{A}]} \tag{3.137}$$

and

$$\mathrm{Z}_2 = \int \mathcal{D}\mathrm{A}\, \mathrm{e}^{\alpha \mathrm{S}[\mathrm{A}]} \tag{3.138}$$

are used to normalize the probabilities. The posterior probability can be written as,

$$\mathrm{P}[\mathrm{A}|\bar{\mathrm{G}}] = \frac{\mathrm{e}^{-\mathrm{Q}[\mathrm{A}]}}{\mathrm{Z}_1 \mathrm{Z}_2 \mathrm{P}[\bar{\mathrm{G}}]}. \tag{3.139}$$

with

$$\mathrm{P}[\bar{\mathrm{G}}] = \frac{\int \mathcal{D}\mathrm{A}\, \mathrm{e}^{-\mathrm{Q}[\mathrm{A}]}}{\mathrm{Z}_1 \mathrm{Z}_2} \tag{3.140}$$

As a result, minimizing Q means maximizing the posterior probability $\mathrm{P}[\mathrm{A}|\bar{\mathrm{G}}] \sim \mathrm{e}^{-\mathrm{Q}}$. Given the input data $\bar{\mathrm{G}}$, the MEM finds the **most probable** spectrum of A is obtained by maximizing $\mathrm{P}[\bar{\mathrm{G}}|\mathrm{A}]\mathrm{P}(\mathrm{A})$. For example, if the data are generated using a stochastic approach, the probability is derived using the **central limit theorem**. We have, for an element of G,

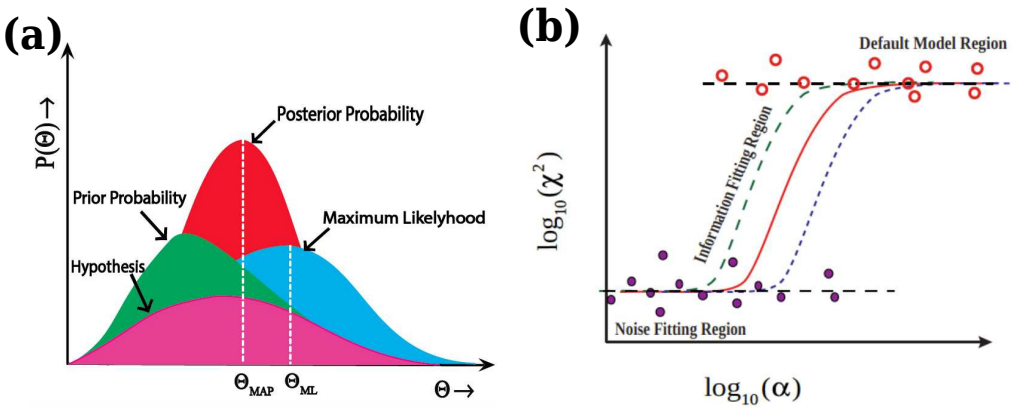

Figure 16: (a) The graphical representation of posterior probability (red) (b) The logistic regression (LR) curve (Jarrell & Gubernatis, 1996; Bergeron & Tremblay, 2016) .

$$\mathrm{P}[\mathrm{G_i}|\bar{\mathrm{G}}_\mathrm{i}] \propto \mathrm{e}^{-\frac{(\mathrm{G_i}-\bar{\mathrm{G}}_\mathrm{i})^2}{2\sigma_\mathrm{i}^2}} \tag{3.141}$$

where $\bar{\mathrm{G}}_\mathrm{i}$ is the statistical averaged value of $\mathrm{G_i}$ and σ_i^2 is the variance. For all the elements of G, we thus have,

$$\mathrm{P}[\mathrm{G}|\bar{\mathrm{G}}] \propto \mathrm{e}^{-\frac{\chi^2[\mathrm{A}]}{2}} \tag{3.142}$$

where,

$$\chi^2[\mathrm{A}] = \sum_{\mathrm{i}} \frac{(\mathrm{G_i} - \bar{\mathrm{G}}_\mathrm{i})^2}{\sigma_\mathrm{i}^2} \tag{3.143}$$

The goodness of fit is determined by the covariance matrix, $\mathbf{C}$, with diagonal elements. If the covariance is not diagonal, one must instead use,

$$\chi^2[\mathrm{A}] = \left(\mathrm{G} - \bar{\mathrm{G}}\right)^{\mathrm{T}} \mathbf{C}^{-1} \left(\mathrm{G} - \bar{\mathrm{G}}\right) \tag{3.144}$$

Here, in matrix form, where $\mathbf{C}$ is the covariance matrix. Given a spectrum A, $\bar{\mathrm{G}} = \mathbf{K}\mathrm{A}$, where $\mathbf{K}$ is the kernel matrix, and so

$$\mathrm{P}[\bar{\mathrm{G}}|\mathrm{A}] \propto \mathrm{e}^{-\frac{\chi^2[\mathrm{A}]}{2}} \tag{3.145}$$

with

$$\chi^2[\mathrm{A}] = (\mathrm{G} - \mathbf{K}\mathrm{A})^{\mathrm{T}} \mathbf{C}^{-1} (\mathrm{G} - \mathbf{K}\mathrm{A}) \tag{3.146}$$

It should be noted that the basic assumptions of using (3.135) as the probability are listed as,

1. $\bar{\mathrm{G}} = \mathbf{K}\mathrm{A}$ is the good approximation to the exact GF.
2. The elements of $\Delta\mathrm{G_U} = \mathrm{U}^\dagger(\mathrm{G} - \bar{\mathrm{G}}) = \mathrm{U}^\dagger(\mathrm{G} - \mathbf{K}\mathrm{A})$, with U are the uncorrelated random variables, including the eigenvectors of the covariance matrix $\mathbf{C}$.

From (3.139), the posterior probability can be expressed as,

$$\mathrm{P}[\mathrm{A}|\bar{\mathrm{G}}] \propto \mathrm{e}^{\alpha\mathrm{S} - \frac{\chi^2}{2}} \tag{3.147}$$

To get the spectrum A, this amount must be maximized, and hence it is named as **MEM** approach.

3.3.3.2 Bayesian Inference Using the Hyper-parameter (α)

There are more advanced formulations problem to eliminate the free parameter, α (Bergeron & Tremblay, 2016; Goulko *et al.*, 2017) (3.133) may be rewritten as,

$$\mathrm{P}[\mathrm{A},\alpha|\bar{\mathrm{G}}] = \frac{\mathrm{P}[\bar{\mathrm{G}}|\mathrm{A},\alpha]\mathrm{P}[\mathrm{A},\alpha]}{\mathrm{P}[\bar{\mathrm{G}}]} \tag{3.148}$$

When the Bayes' theorem is used to factorize $\mathrm{P}[\mathrm{A},\alpha]$ and integrate over A, the relationship becomes,

$$\begin{aligned}\mathrm{P}[\alpha|\bar{\mathrm{G}}] =& \mathrm{P}[\alpha]\int \mathcal{D}\mathrm{A}\,\frac{\mathrm{P}[\bar{\mathrm{G}}|\mathrm{A},\alpha]\;\mathrm{P}[\mathrm{A}|\alpha]}{\mathrm{P}[\bar{\mathrm{G}}]} \\ =& \frac{\mathrm{P}[\alpha]}{\mathrm{Z}_1\mathrm{Z}_2\mathrm{P}[\bar{\mathrm{G}}]}\int \mathcal{D}\mathrm{A}\,\mathrm{e}^{-\mathrm{Q}[\mathrm{A}]}\end{aligned} \tag{3.149}$$

In this case, the probability $\mathrm{P}[\alpha|\bar{\mathrm{G}}]$ is calculated around the maximum. On a similar logical basis, $\mathrm{P}[\bar{\mathrm{G}}|\mathrm{A},\alpha] \sim \exp(-\chi^2[\mathrm{A}])$ and $\mathrm{P}[\mathrm{A}|\alpha] \sim \exp(\alpha \mathrm{S}[\mathrm{A}])$ may be identified.

The evidence

$$\mathrm{P}[\bar{\mathrm{G}}] = \int \mathrm{d}\alpha \frac{\mathrm{P}[\alpha]\int \mathcal{D}\mathrm{A}\,\mathrm{e}^{-\mathrm{Q}[\mathrm{A}]}}{\mathrm{Z}_1\mathrm{Z}_2} \tag{3.150}$$

is a normalization constant that is independent on α. Except for $\mathrm{P}[\alpha]$, the prior probability of α, all of the parameters in this equation are known. However, the choice of $\mathrm{P}[\alpha]$ has minimal effect on the resulting spectra.

A numerical treatment of the equations (3.139) and (3.150) is conceivable if the probabilities involved are of the Gaussian type.

3.3.3.3 Extracting Information from the GF Input

For the preprocessing step of calculation, we may extract two types of information: (a) moments and (b) a low frequency peak with its breadth and weight. When accessible, the initial step in the calculation is to extract that information.

The required spectrum is obtained as a function of α within the relevant range, which we must minimize, $\mathrm{Q} = \frac{\chi^2}{2} - \alpha\mathrm{S}$, where χ^2 is given by (3.130) and S, by (3.131). This is a function that is bounded from below and has a distinct minimum, $\nabla Q = 0$. Because

entropy is a non-linear component of the equation, it cannot be solved accurately. We may solve the issue iteratively using the linearized version.

3.3.3.4 The Optimal Value for Hyper-parameter

To identify the ideal value of α, we must compute the curvature of $\log_{10}(\chi^2)$ vs. γ $\log_{10}\alpha$, where $\gamma \leq 1$ is an adjustable parameter. It is utilized to raise the magnitude of the peak in the LR curve Fig. 16(b) (Bergeron & Tremblay, 2016) corresponding to the crossover zone. The value of $\gamma \sim 0.2$ was discovered to be a reasonable balance for clearly identifying the proper peak in the curve while not affecting the value of α too much.

When we plot the graph of the function $\chi^2(\alpha)$ in log-log scale, we get the schematic curve given in Fig.16(b) (Bergeron & Tremblay, 2016), which shows three distinct regimes as,

a. For large α values, χ^2 does not vary considerably, and so the SF deviates only little from its default model, referred to as the default-model.

b. Under a certain value of α, while αS still a substantial term, χ^2 is not insignificant and hence acts as a restriction. In that range, α governs how well that constraint is fitted, which is referred to as the information-fitting regime.

c. Under some α values, the lowering parameter has minimal effect on χ^2. In reality, it is the zone where the variation in G is also fitted, which is known as the noise-fitting regime.

The function $\Delta \mathrm{G}(\mathrm{i}\omega_\nu) = \mathrm{G}_{\mathrm{in}}(\mathrm{i}\omega_\nu) - \mathrm{K}(\mathrm{i}\omega_\nu)\mathrm{A}$ can be used to determine the correspondence between the small slope region at low α. It is important to note that the value of α above which, the slope starts decreasing rapidly, and the function contains mainly noise. At the point of the drop, $\mathrm{G}_{\mathrm{out}}(\mathrm{i}\omega_\nu) = \mathrm{K}(\mathrm{i}\omega_\nu)\mathrm{A}$ is a good fit of the input data $\mathrm{G}_{\mathrm{in}}(\mathrm{i}\omega_\mathrm{n})$.

3.4 Optical Conductivity through DMFT

This work investigates electronic transport properties, such as optical conductivity $\sigma_\alpha(\omega)$, using current-current correlation function.

$$\hat{\Lambda}_\alpha(\tau) = \langle \hat{\mathbf{j}}_\alpha(\tau)\hat{\mathbf{j}}_\alpha(0)\rangle \tag{3.151}$$

Here, $\mathbf{j}_\alpha$ is a current operator along the α-direction which can be defined as

$$\hat{\mathbf{j}}_\alpha = -\mathrm{i}\sum_{\mathbf{i},\sigma} \mathbf{t}(\hat{\mathbf{c}}^\dagger_{\mathbf{i},\sigma}\hat{\mathbf{c}}_{\mathbf{i}+\delta_\alpha,\sigma} - \hat{\mathbf{c}}^\dagger_{\mathbf{i}+\delta_\alpha,\sigma}\hat{\mathbf{c}}_{\mathbf{i},\sigma}), \tag{3.152}$$

The current operator is also written as $\hat{\mathbf{j}}_\alpha(\tau) = \exp(\mathrm{H}\tau)\,\hat{\mathbf{j}}\,\exp(-\mathrm{H}\tau)$. It is sufficient to consider only the α component of $\Lambda_\alpha(\tau)$ for the clusters under consideration.

Indeed, the optical conductivity $\sigma_\alpha(\omega)$ is related to the current-current correlation function by,

$$\Lambda_\alpha(\tau) = \int \frac{d\omega}{\pi}\frac{\omega e^{-\tau\omega}}{1-e^{-\beta\omega}}\sigma_\alpha(\omega) \tag{3.153}$$

We use CT-QMC with the AC of the current correlator in imaginary time (Gunnarsson *et al.*, 2010; Blümer & Gorelik, 2011) to extract the optical conductivity. Further information is provided in (Sakai *et al.*, 2004), which includes data from larger cluster simulations suggesting minor finite size effects.

Here, the equivalence of the two directions given by $(\alpha = x, y)$ does not hold in the specified clusters and boundary conditions, as we have previously shown in the (Imada, 2005; Nakano *et al.*, 2007). The optical conductivity is given by,

$$\sigma(\omega) = 2\pi \mathrm{D_w}\delta(\omega) + \sigma^{\mathrm{reg}}(\omega). \tag{3.154}$$

The second term in the r.h.s. is the regular component of the optical conductivity, often known as the incoherent part, which is obtained by the average of the these components,

$$\sigma^{\mathrm{reg}}(\omega) = [\sigma^{\mathrm{reg}}_{\mathrm{x}}(\omega) + \sigma^{\mathrm{reg}}_{\mathrm{y}}(\omega)]/2; \tag{3.155}$$

each of $\sigma^{\mathrm{reg}}_\alpha(\omega)$ given by,

$$\sigma^{\mathrm{reg}}_\alpha(\omega) = \frac{\pi}{\mathrm{N_s}}\sum_{\ell\neq 0}\frac{|\langle\ell|\mathbf{j}_\alpha|0\rangle|^2}{\mathrm{E}_\ell - \mathrm{E}_0}\delta(\omega - \mathrm{E}_\ell + \mathrm{E}_0), \tag{3.156}$$

is calculated by the continued-fraction expansion method.

Where $\mathbf{j}_\alpha$ is the current vector along the α-direction, and $|l\rangle$ denotes an eigenstate with

the energy eigenvalue E_l. It is worth noting that the ground state is defined by $l = 0$. The Drude weight $\mathrm{D_w}$ (Nakano *et al.*, 2007) may be obtained by combining $\sigma(\omega)$ with the sum rule.

$$\int_0^\infty \sigma(\omega)\mathrm{d}\omega = \pi\mathrm{K}, \tag{3.157}$$

where -4K denotes the kinetic energy per site, i.e. $-4\mathrm{K} = \langle \mathcal{H}_{\mathrm{hop}} \rangle / \mathrm{N_s}$. When U = 0, the incoherent component is missing, resulting in $\mathrm{D_w}$ = K. It is well known that the incoherent component emerges when U > 0. When U is large enough, the reactions toward the upper-Hubbard band may be clearly identified in $\sigma(\omega)$. In such a scenario, a frequency slightly below the upper-Hubbard band may be determined to be ω_c; we can compute definite integrals.

$$\mathrm{N_{eff}} = \frac{1}{\pi}\int_0^{\omega_c} \sigma(\omega)\mathrm{d}\omega, \tag{3.158}$$

which is the effective carrier density.

DMFT calculates temperature-dependent dc resistivity using zero-frequency optical conductivity as $\rho = 1/\sigma(\omega = 0)$ and gives it in units of $\rho_{\mathrm{Mott}} = \hbar a/e^2$. The frequency-dependent optical conductivity can be calculated as,

$$\begin{aligned}\sigma(\omega) =& 2\pi\frac{\mathrm{e}^2}{\hbar \mathrm{a}}\int_{-\infty}^{\infty}\mathrm{d}\omega' \, \frac{\mathrm{n_F}(\omega') - \mathrm{n_F}(\omega'+\omega)}{\omega} \\ & \times \int_{-\infty}^{\infty}\mathrm{d}\epsilon \; \rho(\epsilon)\left(\mathrm{v}(\epsilon)\right)^2 \mathrm{A}(\epsilon,\omega')\mathrm{A}(\epsilon,\omega'+\omega)\end{aligned} \tag{3.159}$$

using $n_f(w)$ as the Fermi function and $\mathrm{v}(\epsilon) = \sqrt{\mathrm{W}^2 - \epsilon^2}/\sqrt{3}$ as the velocity, in this case for the Bethe lattice in $z \to \infty$ (Georges *et al.*, 1996; Merino & McKenzie, 2000). The SF, often known as

$$\mathrm{A}(\epsilon,\omega) = -\mathrm{Im}\left(\mathrm{G}(\epsilon,\omega)\right)/\pi \tag{3.160}$$

which can be calculated from the Green's function,

$$\mathrm{G}(\epsilon,\omega) = \left[(\mathrm{G}_0^{-1}(\epsilon,\omega) - \Sigma(\omega)\right]^{-1} \tag{3.161}$$

The non-interacting GF, $G_0(\epsilon, w) = 1/(w - \epsilon + \mu)$ is affected by the one-particle energy ϵ, which is utilized as a quantum number in place of momentum. The current vertex adjustments are missing in DMFT (Georges *et al.*, 1996), implying that the single-particle spectrum and conductivity are directly connected. For three peaks structures in SF (Hubbard bands and quasi-peaks), the local SF, $A(\omega)$, can be plotted for many values of the interaction parameters in DMFT (Georges & Kotliar, 1992).

3.4.1 Photoinduced Phase Transitions

The photoinduced phase transitions uses optical methods to elicit a collective response in a particular material, resulting in a new macroscopic ordered phase (Sachdev, 1999; Choi *et al.*, 2012). The resulting alteration can be investigated using x-rays, direct current transport and other electronic or structural probes.

QMC Results for MIT

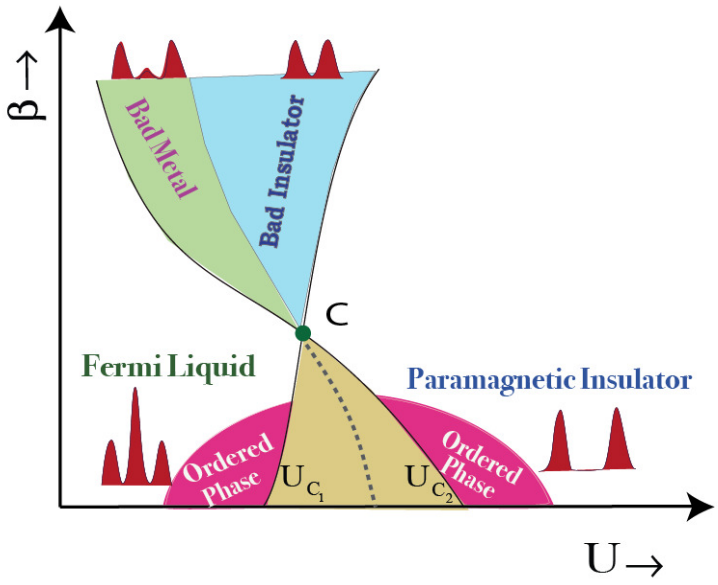

Figure 17: The various distinct regions for different phases with the variation of model parameters (U and β) at around QCP (Si *et al.*, 2001; Kotliar *et al.*, 2006; Vollhardt, 2012).

The QCP is the point at which matter becomes unstable for a new forms of order. The fluctuations between order and disorder that arise at this moment cause substantial changes in the material's finite temperature electronic behaviors (Millis, 1993; Moeller *et al.*, 1995; Isakov *et al.*, 2012; Rai *et al.*, 2023). External fields and other chemical environments are suitable for tuning a material in the neighborhood of QCP to be explored.

Ballistic electron motion stops at a QCP, creating an unconventional conductor where electrons couple into the electron fluid's current carrying motion. The theoretical and practical investigation of the bandwidth control Mott MIT reveals quantum criticality of electrical resistivity at higher temperatures, despite the low-temperature phase transition being first order (Millis, 1993; Sachdev, 1999; Hameed *et al.*, 2022).

The interaction-driven MIT is an example of strong correlation effects, but poorly understood. The DMFT framework has made significant theoretical progress, approximating electronic self-energy locally in space and becoming exact in infinite dimensions. Numerical analysis reveals that changing the chemical potential doesn't alter the first-order transition, resulting in finite T_C(T) and quantum criticality. Two-dimensional experimental systems show minimal momentum dependencies and local correlations effect, contradicting full space-time quantum criticality.

The metal remains stable and depends on Coulomb interaction until its energy reaches the insulating solution at U_{C_2}(T) (Fig. 17) (Vollhardt, 2012; Kotliar *et al.*, 2006). When the insulator becomes unstable at U_{C_1}(T), solutions differ energetically. The Hubbard model near MIT provides insight into quasiparticle behavior, with the energy of the metallic phase expected to be lower than the insulator and no crossing occurring in relevant properties. At T = 0, the metal approaches the insulator continuously, with both energy and its derivative fluctuating smoothly at U_{C_2}(T).

At a critical temperature (T_C), a paramagnetic (PM) metallic and insulating phase coexist in the regime $\mathrm{U_{C_1}(T)} < \mathrm{U} < \mathrm{U_{C_2}(T)}$. As U increases, the metallic phase disappears at $\mathrm{U_{C_2}(T)}$, and when U drops to $\mathrm{U_{C_1}(T)}$, the insulating phase terminates. A first-order MIT line exists between phases $\mathrm{U_{C_1}(T)}$ and $\mathrm{U_{C_2}(T)}$ with identical free energies. At critical temperature, both phases equal U_C, and a second-order transition occurs. When U increases over $\mathrm{T_C}$, the system changes from metallic to insulating phase through crossover.

3.5 Computational Details and Experimental Information

3.5.1 Computational Softwares for Ab-initio Calculations

3.5.1.1 Quantum Espresso Frameworks

Quantum ESPRESSO, an acronym for Quantum-opEn-Source Package for Research in Electronic Structure, Simulation, and Optimization, is a multi-purpose package for electronic structure calculations, simulation, and optimization. It contains codes for first-principles calculations in condensed matter systems (Trimarchi *et al.*, 2008). The package is based on DFT and plane wave/pseudo-potential descriptions of the electronic ground state, making it ideal for structural optimizations, linear response calculations, and high-temperature molecular dynamics. Examples of applications are briefly discussed in the text (Kohn & Sham, 1965; Perdew *et al.*, 1998).

3.5.1.2 WIEN2k Frameworks

The WIEN 2k package in Fortran performs quantum mechanical calculations on periodic solids using Augmented Plane Wave methods. The LAPW method is highly accurate for computing the electronic structure of crystals (Blaha *et al.*, 2002). Electronic and other related calculations are performed within DFT using the LAPW plus local orbital (LO) method (Schwarz *et al.*, 2010). The exchange correlation functional for self-consistent calculations is GGA (Blaha *et al.*, 2002; Schwarz *et al.*, 2010).

3.5.1.3 DMFT Frameworks

The ALPS (Algorithms and Libraries for Physics Simulations) program provides computational physics libraries and applications for simulation of lattice models and SCSs. These libraries are reusable components for developing condensed matter physics simulation codes, aiming to create proven computational algorithms. The ALPS core libraries offer physical insights into various subfields of condensed matter, including nonequilibrium dynamics, CT-QMC (Kotliar & Vollhardt, 2004; Bauer *et al.*, 2011; Gull *et al.*, 2011), LDA + DMFT materials simulations, quantum and classical spin systems, correlated boson and fermion models, and cuprate superconductivity (Caffarel & Krauth, 1994; Betzinger *et al.*, 2011; Gonze *et al.*, 2016).

The projector augmented-wave method offers an alternative to standard norm-conserving

pseudopotentials, allowing for geometry optimizations and ab initio molecular dynamics as treated in ABINIT frameworks. It can treat materials like insulators, metals, and magnetically ordered systems like Mott-Hubbard insulators, enabling the calculation of forces and stresses (Trimarchi *et al.*, 2008; Gonze *et al.*, 2016).

3.5.2 Computational Details

In this study, we have employed the standard DFT based plane wave self-consistent field (PWscf) with ultrasoft pseudopotential approach to study the structural and chemical stability with energy minimization techniques. The FP-LAPW is utilized to study the stability, electronic structure, electronic charge density distribution, thermoelectric and optically driven transport properties of pristine TMOs and their superstructures (Kohn & Sham, 1965; Mizutani, 2001; Sholl & Steckel, 2022). The KS equations are solved using self-consistent calculations of total energy within the GGA framework (Perdew *et al.*, 1998; Blaha *et al.*, 2002). Conventional DFT approaches are used to compare and increase computational accuracy (Kaphle *et al.*, 2015; Rai *et al.*, 2023).In addition to the standard DFT, we employed the self-consistent DMFT calculations with a CT-QMC hybridization technique to compute the realistic electronic structure of TMOs and investigate the Mott-Hubbard MIT (Antonov *et al.*, 2001; Rohringer *et al.*, 2018; Jana *et al.*, 2020; Rai *et al.*, 2021). SD distribution is derived using the MEM for statistical inferences (Shao & Sandvik, 2023).

The site-substitution of the extended pristine cubic perovskite, $SrTiO_3$ is used to reconstruct the transition metal oxide superstructure system, La_{1-x} Sr_xTiO_3. Through DFT + DMFT (Held *et al.*, 2008; Shin *et al.*, 2021; Rai *et al.*, 2023), the MIT phase transition is explored for the strongly correlated parameter (U, and β). For the pristine TMOs unit cell of an ideal cubic crystal system with Pm-3m (Hermann Mauguin) space-group, we chose a Monk-horst pack of 7 $\times$ 7 $\times$ 7 k-mesh grid for pristine sample. The 19 $\times$ 19 $\times$ 3 k-mesh grid for superstructure is used for self-consistent computations with energy and charge convergence criteria of 10^{-5} eV and 10^{-3}e, respectively (Sevik, 2010). Thermal conductivity, electrical conductivity, Seebeck coefficients, and TPF of optimized $La_{1-x}Ca_xVO_3$ superstructures are computed using the BoltzTraP codes.

The structural optimization of vanadate systems involves determining K-points, RK_{max},

and G_{max}. The optimized R_{MT} values of La-, Ca-, V-, and O- are obtained for both pristine and site-substituted superstructures (Kohn & Sham, 1965; Perdew *et al.*, 1996). This investigate MIT's through band and filling controlled approaches, we employ CT-QMC as an impurity solvers with hybridization expansion technique for $La_{1-x}Ca_{1-x}VO_3$, $La_{1-x}Sr_xVO_3$, $Ca_{1-x}Sr_xVO_3$, $Ca_{1-x}Y_xTiO_3$ and $La_{1-x}Sr_xTiO_3$ superstructure systems (Löhneysen *et al.*, 2007; Rai *et al.*, 2023). To estimate the critical value of MIT for each of the superstructure, DFT + DMFT calculations are done for various Coulombian interactions, U and the thermodynamical parameters β. DFT and DMFT are used to evaluate the optical conductivities of the materials, with the MIT phase transition expected based on Drude peaks analysis that vary depending on the spectral weight ratio and mass enhancement factor. The DMFT calculation uses parameters like chemical potential (μ), Matsubara frequency (ω_ν), imaginary time bins, thermalization sweeps, maximum sweeps in a single iteration (10000), and MC steps between measurements (5000).

$$m^*/m \simeq SW_{Drude+MIR}/SW_{Drude} \simeq K_{band}/K_{exp} \tag{3.162}$$

The mass enhancement in Mott insulators is evaluated by reducing kinetic energy of quasiparticles due to dynamical correlations. The overall kinetic energy remains constant, but intraband transitions contribute to conduction electrons' kinetic energy, which is transferred from the Drude peak into mid-infrared (MIR) or higher energy.

The DFT and other computational software packages are intended to perform a wide range of calculations, including ground-state energy, structural optimizations, response characteristics, spin polarization, molecular dynamics, electrostatic dipole, magnetic structures, and many more (Capelle, 2006; Cohen *et al.*, 2007; Martin, 2020; Sholl & Steckel, 2022).

The validity and accuracy of self-consistent calculations are crucially important for various properties of the materials under investigation and are determined by several factors, viz.

a. The accuracy of calculations is influenced by the choice of basis set (plane-wave cutoff), pseudopotentials, full-potentials and so on.

b. The choice of exchange-correlation functional (LDA, GGA, hybrid functionals etc.) affects the accuracy of calculations. The accuracy of functionals can vary depending on the system being studied.

c. Convergence criteria for self-consistency iterations, k-point mesh density, and energy cutoff for plane wave basis set and charge density convergence.

d. Proper handling of symmetry operations and accurate input geometries are important for validity of calculations. The incorrect input geometries, such as overlapping atomic orbitals or unrealistic bond lengths, can cause numerical instability or convergence problems.

e. The size of the system, the number of atoms, and the complexity of the electronic structure can influence the accuracy of calculations. Larger systems might require more careful convergence and higher computational resources.

3.5.3 Experimental Information

Experimental works have studied the Mott-Hubbard MITs in vanadates and titanates systems for various values of U and β. Ca doped $La_{1-x}Ca_xVO_3$ system was synthesized and characterized to study the resistivity and magnetic susceptibility for Mott and band insulators (Antonides *et al.*, 1977; Sawatzky & Allen, 1984; Makino *et al.*, 1997; Maiti *et al.*, 2004). Bulk-sensitive high-resolution PES and XAS were used to study the spectra of $CaVO_3$ and $SrVO_3$ (Inoue *et al.*, 1998; Mossanek *et al.*, 2008).

All heterostructures grown on $SrTiO_3$ substrates were found to be metallic upon measuring transport and Hall measurements up to 5T of magnetic field (Cohen *et al.*, 2007). MIT behavior in $La_{1-x}Sr_xVO_3$ samples was investigated using optical spectra (Inaba *et al.*, 1995; Inoue *et al.*, 1998). For $La_{1-x}Ca_xVO_3$, Maiti (Maiti & Sarma, 2000) found an antiferromagnetic (AFM) to PM transition near x = 0.2. Single crystals of superstructures, $Ca_{1-x}Sr_xVO_3$, were studied for optical conductivity, photometrics, and optical reflectivity measurements. The spectra of $SrVO_3$ and $CaVO_3$ were also investigated using the bulk-sensitive high-resolution PES and XAS.

Kowalski et al. investigated d-orbital splitting and local Coulomb interactions using the CT-QMC hybridization technique, explaining Mott insulating behavior (Kowalski *et al.*,

2019; Caputo *et al.*, 2022). In addition, they employed angle resolved photoemission spectroscopy (ARPES) to investigate Hubbard band splitting (Sekiyama & Suga, 2004).

These experimental findings actually motivate us for the theoretical research into the stability, electronic transport, thermoelectric, and optical properties of these strongly correlated materials, which have applications in Mottronics, neuromorphic computations, resistive memory devices, and thermoelectric and energy devices.

CHAPTER 4

RESULTS AND DISCUSSION

We describe the principal findings of the study using numerous standard analyses and discussions in this chapter. It includes the investigation of structural, chemical and mechanical stabilities, and related properties, electronic structures along with the MITs, thermoelectric transport properties, and optically induced behaviours of pristine transition metal oxides and their site-substituted derivatives.

The CE and FE estimations are utilized to determine the system's structural and chemical stability. Mechanical and chemical bonding information are obtained through the elastic constants for the modulus of elasticities, Poisson's ratio, Cauchy pressure, Pugh's ratio, and anisotropy factors.

The preliminary investigation of density of states (DOS) and bandstructures are used to conjecture the electronic structures with various techniques of ab-initio calculations, but these calculations are insufficient to address the realistic picture of electronic structure of SCSs (e.g. perovskites, double perovskites) systems. For the impurity solver of Anderson's impurity Hamiltonian, we employed the DFT + DMFT approximation using the CT-QMC hybridization expansion technique. Furthermore, the QMC data are used to determine the real frequency data using MEM, which is extremely important for studying the MIT behaviours of the systems. We have investigated their optically induced behaviors using DFT and DFT + DMFT approximations, and hence revealed the potential candidates for field driven devices (Kamerbeek *et al.*, 2015; Paul & Birol, 2019) of TMOs.

4.1 Structural, Chemical and Mechanical Stability

4.1.1 Structural, Chemical and Mechanical Stability of Vanadates

4.1.1.1 Structural and Chemical Stability of $La_{1-x}Ca_xVO_3$

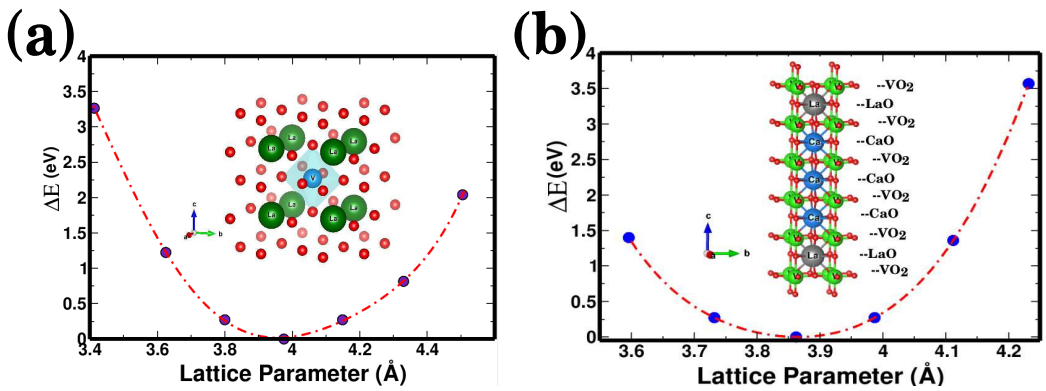

Figure 18: The structural stability analysis through energy minimization process for (a) $LaVO_3$ and (b) superstructure $La_{0.40}Ca_{0.60}VO_3$.

The $CaVO_3$ and $LaVO_3$ crystal structures are a prototype $SrFeO_3$ face-centered cubic (FCC) type perovskites structure having space group Pm-3m (221). The ideal cubic unitcell of $LaVO_3$ (Fig. 18(a)) has La -atom at the origin (0.0, 0.0, 0.0) a, V-atom at the body center (0.5, 0.5, 0.5) a, and the O-atoms at the three face centers: (0.5, 0.5, 0.5) a, (0.0, 0.5, 0.5) a, and (0.5, 0.0, 0.5) a. Where, the lattice constant, a = 3.94 Å (Frenkel & Ladd, 1984; Piskunov *et al.*, 2004; Basov *et al.*, 2011).

Furthermore, the ideal cubic unitcell of $LaVO_3$ is electronically promoted to a supercell, $La_{1-x}Ca_xVO_3$ of $1 \times 1 \times 3$ dimension for studying their structural, mechanical stability, electronic transport, and optically driven transport properties. One of the superstructure, $La_{0.40}Ca_{0.60}VO_3$, is found to be converged with space group P4/mm (99) in a tetragonal primitive supercell. The optimized structural parameters are presented in Table. 1 for pristine and superstructure systems.

The results are consistent with the existing data for ($CaVO_3$, $LaVO_3$), and its superstructure $La_{0.40}Ca_{0.60}VO_3$ system (Inoue *et al.*, 1998; Sclauzero *et al.*, 2016). The slight change in the pristine parameters is discovered to be the result of structural change during the electronic reconstruction of the superstructure, and it agrees with the previous results (Fig.18(b)).

Table 1: The optimized structural parameters*, cohesive and formation energies in electron volt (eV) of the pristine ($CaVO_3$, $LaVO_3$) vanadates and their superstructure.

Physical Parameters	$CaVO_3$	$LaVO_3$	$La_{0.40}Ca_{0.60}VO_3$
Lattice Parameter (Å)	3.71 3.80★, 3.83#	3.94 3.92★, 3.95#	a = b = 3.86, c = 19.48
Space-Group	Pm-3m (221)	Pm-3m (221)	P4/mm (99)
K-points	800	800	750
RK_{max}	7.0	7.5	7.5
G_{max}	14.0	16.0	15.0
Cohesive Energy (eV/atom)	-7.53	-7.56	-7.20
Formation Energy (eV/atom)	-3.01 -2.90★, -2.89#	-3.18 -3.25★, -3.09#	-2.99

* The optimized lattice parameters are consistent with the available data. The variation of lattice parameter ($\pm\Delta a$) with their corresponding energy differences (ΔE) about their optimized values are shown in Appendix -V (a),(b).

★ (Long *et al.*, 2013; Kirklin *et al.*, 2015), # (Wold & Ward, 1954; Ali & Yashima, 2005; Balachandran *et al.*, 2017)

The calculated CE and FE for $CaVO_3$, $LaVO_3$, $SrVO_3$, $LaSrV_2O_6$ and $La_{0.40}Ca_{0.60}VO_3$ systems are found to be negative (Table. 1, 2).

Thus, the formation energies of pristine and superstructure systems are negative, indicating energetically favorable for synthesis and better chemical and thermodynamical stability. Higher negative values indicate structural and chemical stability (Santana *et al.*, 2017).

4.1.1.2 Structural and Chemical Stability of $La_{1-x}Sr_xVO_3$

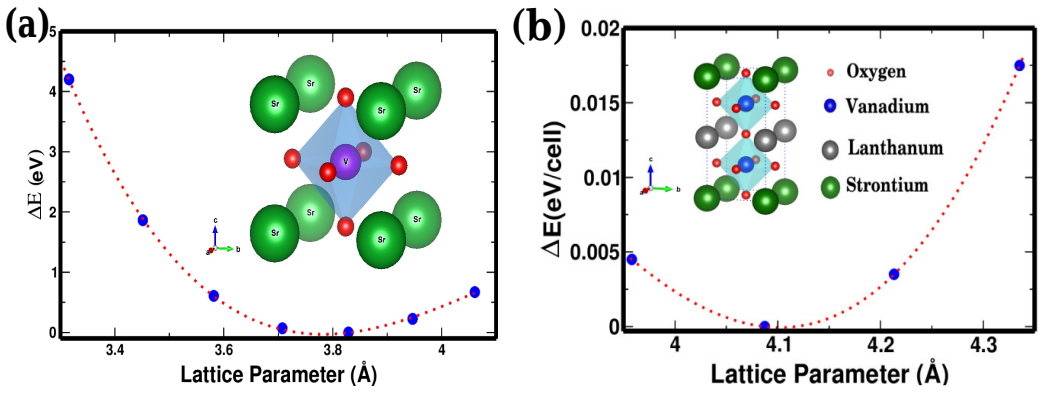

Figure 19: The optimization curve for lattice parameter of (a) $SrVO_3$ unitcell with the crystal structure (inset) (b) $LaSrV_2O_6$ superstructure system with its crystal structure (inset).

Table 2: The optimized structural parameters† of the pristine ($SrVO_3$, $LaVO_3$) and superstructure with their cohesive, formation energies.

Physical Parameters	$SrVO_3$	$LaVO_3$	$LaSrV_2O_6$
Lattice Parameters (Å)	a = 3.86 3.86★, 3.90⊗	a = 3.94 3.92★, 3.95⊗	a = b = 3.96, c = 7.92
Opt. Volume ($Å^3$)	57.51	61.20	124.20
Cohesive Energy (eV/atom)	-6.96	-7.56	-7.79
Formation Energy (eV/atom)	-2.97 -2.90★, -2.87⊗	-3.18 -3.25★, -3.09⊗	-3.60

† The optimized lattice parameters are consistent with the available data. The variation of lattice parameter ($\pm\Delta a$) with their corresponding energy differences (ΔE) about their optimized values are shown in Appendix -V (c).

★ (Long *et al.*, 2013; Kirklin *et al.*, 2015), ⊗ (Wold & Ward, 1954; Balachandran *et al.*, 2017; Lan *et al.*, 2003)

The energy minimization technique is used to investigate the structural stability of prototype cubic $SrVO_3$ and $LaVO_3$ systems (Fig. 19(a)) whose optimized lattice parameters are found to be 3.86 Å and 3.94 Å, respectively (Maiti & Sarma, 2000; Mossanek *et al.*, 2008; Sage *et al.*, 2008; Wang *et al.*, 2011). The optimized lattice parameters (Table. 2) of superstructure, $LaSrV_2O_6$ with the space-group P4/mmm (123) (Fig. 19(b)) are consistent values with the previous results (Wang *et al.*, 2011; Sage *et al.*, 2008). The computed values of cohesive and formation energies are presented, which reflect the chemical stability of these vanadate compounds.

4.1.1.3 Structural and Chemical Stability of $Ca_{1-x}Sr_xVO_3$

The optimized lattice parameters for pristine $SrVO_3$ and $CaVO_3$ are found to match the experimental results. The superstructures, $Ca_{1-x}Sr_xVO_3$ reconstructed using the frameworks $1 \times 1 \times 2$ of pristine unitcell of $SrVO_3$, and then site-substituted with Ca-atoms in the supercell. These stabilized superstructures with space-group P4/mmm were examined using an energy minimization approach. The energy difference vs. volume optimization curves for $CaVO_3$ and $(Ca_{0.50}Sr_{0.50}VO_3)_2$ systems, together with their model crystal structures (in insets), are shown in (Fig. 20(a),(b)).

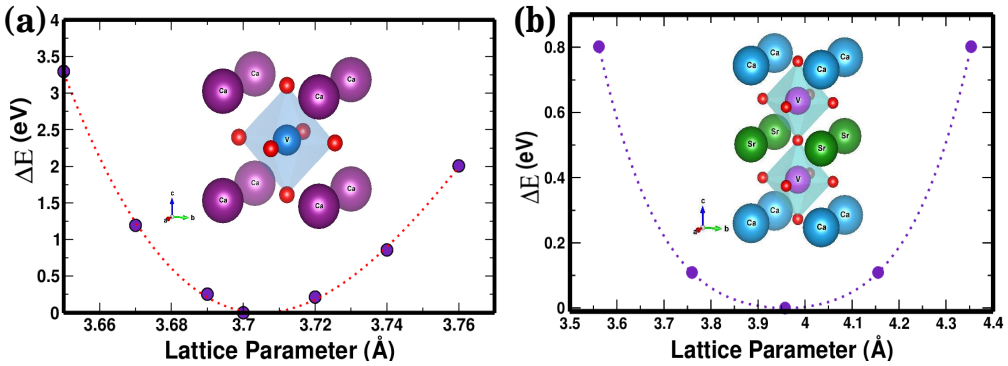

Figure 20: The lattice parameter optimization curves and crystal structures (insets) for (a) $CaVO_3$ system (b) $(Ca_{0.50}Sr_{0.50}O_3)_2$ system.

4.1.1.4 Mechanical and Thermodynamical Stabilities of Vanadates

The mechanical and thermodynamical stability parameters of optimized structures of vanadates are listed in Table. 3, which are consistent with existing available information (Ambrosch-Draxl & Sofo, 2006; Boudali *et al.*, 2009). Positive Cauchy pressure values for $CaVO_3$, $LaVO_3$, $SrCaV_2O_6$, $LaSrV_2O_6$, and $LaCaV_2O_6$ indicate ductile metallic nature, while negative values for $SrVO_3$ imply covalent bonding (Cinthia *et al.*, 2015). Furthermore, the values obtained from equations (3.54 - 3.61) satisfy the criterion for the mechanical stability.

The calculated elastic parameters show that the superstructure has weaker elastic behavior than pristine systems (Kim, 2018; Bouhemadou & Khenata, 2007). The elastic wave information is also used to compute the system's Debye temperature (Θ_D), which is the cutoff frequency or Debye frequency (ω_D) of vibrating chains of masses characterizing the motion of ions in a crystal.

The elastic tensor along with the other mechanical information of the materials can be calculated using the polynomial fitting of energy vs. strain. The accuracy and validity of prediction of these calculation were investigated using the CVE method (one of the methods of selecting the best model using the optimal hyperparameter).

The CVE approach optimizes the fitting procedures on statistical data using a portion of the training data set and a complementary subset (testing data set), which ensure that the model captures the trend while ignoring the noise. We have used the leave-one-out (LOO) type of CVE method to select the best model (Fig.21(a)). The best model is predicted to be deformation-5 (Geometry-5) out of 6 different distorted samples of the

Table 3: The elastic constants C_{ij}, Modulus of elasticities (Y, B, G) for the Vanadates.

Physical Parameters	$SrVO_3$	$CaVO_3$	$LaVO_3$	$SrCaV_2O_6$	$LaSrV_2O_6$	$LaCaV_2O_6$
C_{11} (GPa)	519.90	446.30	576.20	183.30	256.50	209.00
C_{12} (GPa)	141.00	140.50	200.90	107.40	90.50	122.00
C_{13} (GPa)				99.50	94.30	123.20
C_{22} (GPa)						149.60
C_{23} (GPa)						114.90
C_{33} (GPa)				157.60	148.10	152.70
C_{44} (GPa)	155.30	111.00	124.00	78.10	66.10	63.50
C_{55} (GPa)						63.50
C_{66} (GPa)				77.50	64.20	64.30
Y (GPa)	418.69	325.99	388.97	158.21	131.46	129.75
B (GPa)	267.27	242.42	325.99	126.34	113.21	136.84
G (GPa)	168.97	127.75	149.48	61.26	50.31	48.34
CP (GPa)	-14.30	29.50	76.90	29.30	21.90	58.50
ν	0.24	0.28	0.30	0.29	0.31	0.34
PR	1.58	1.89	2.18	2.06	2.25	2.83
AF(%)	0.47	1.23	2.05	7.04	8.74	13.01

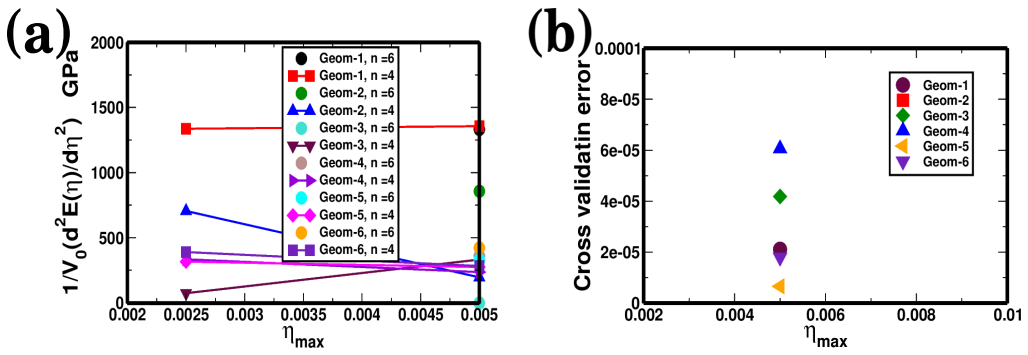

Figure 21: The plots of (a) the elastic constants vs. strain of different distorted geometries (b) the corresponding CVE vs. strain for $LaSrV_2O_6$ system.

$LaSrV_2O_6$ system, according to (Fig. 21(b)).

Furthermore, we have examined the dynamical stability of the pristine vanadates through the calculation of phonon properties (shown in Appendix -VI (a), (b) and (c)). These prototype pristine unitcell of TMOs were used for the electronic reconstruction of site-substituted superstructures.

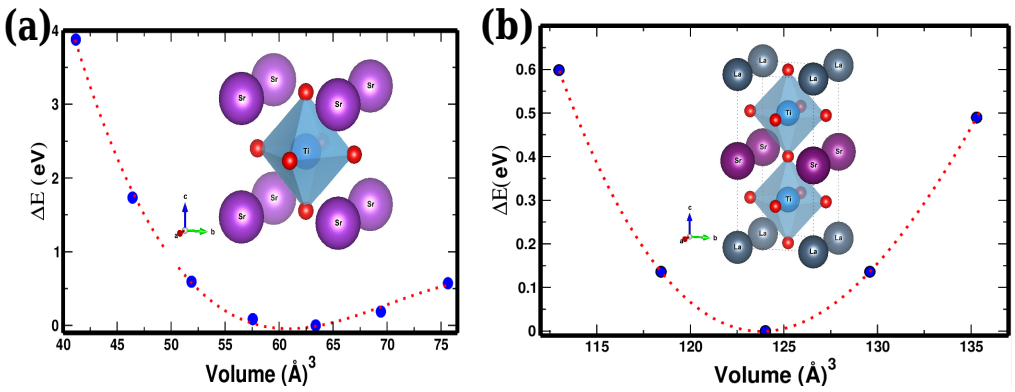

Figure 22: The volume optimization curve with crystal structures (insets) of (a) $LaTiO_3$, and (b) $LaSrTi_2O_6$, systems.

Table 4: The optimized structural parameters‡ (volumes, densities, Debye temperatures), cohesive and formation energies of the pristine and their site-substituted superstructures.

Physical Parameters	$SrTiO_3$	$LaTiO_3$	$LaSrTi_2O_6$	$LaCaTi_2O_6$
Lattice	a = 3.94	a = 3.92	a = b = 3.96	a = b = 3.85
Parameters(Å)	3.92★, 3.91#	3.93★, 3.96#	c = 7.92	c = 7.91
Opt. Volume ($Å^3$)	58.09	50.65	123.47	124.12
ρ(g/cm^3)	6.30	7.29	5.57	4.97
ν_t (m/s)	2983.51	4467.21	3707.23	3373.41
ν_l (m/s)	6288.25	6965.06	6084.34	5326.89
ν_m (m/s)	3356.55	5906.76	4094.82	3710.74
Θ_D (K)	397.07	567.00	454.34	403.22
Cohesive Energy (eV/atom)	-7.74	-7.65	-7.71	-7.68
Formation Energy (eV/atom)	-2.72 -3.35★, -3.45#	-2.97 -3.47★, -3.59#	-3.07	-3.05

‡ The optimized lattice parameters are consistent with the available data. The variation of lattice parameter ($\pm\Delta a$) with their corresponding energy differences (ΔE) about their optimized values are shown in Appendix -VII (a), (b).

★ (Long *et al.*, 2013; Kirklin *et al.*, 2015), # (Balachandran *et al.*, 2017; Jauch & Palmer, 1999; Kestigian & Ward, 1954)

4.1.2 Structural, Chemical, and Mechanical Stability of Titanates

4.1.2.1 Structural and Chemical Stability of $La_{1-x}Sr_xTiO_3$

The optimum lattice parameters for the given TMOs systems are determined using first-principles based energy minimization procedures. The cubic phase of $SrTiO_3$ with space group Pm-3m (221) is a band insulator. In the unitcell, the Wyckoff co-ordinates of Sr atom is at (0.0, 0.0, 0.0) a, Ti atom is at body center (0.5, 0.5, 0.5) a, and the three O atoms sitting at the face centers (0.5, 0.5, 0.5) a, (0.0, 0.5, 0.5) a, and (0.5, 0.5, 0.5) a

positions, with the lattice parameter, a = 3.94 Å.

Similarly, the prototype cubic unit cell of $LaTiO_3$ contains La-atom at the origin, Ti-atom at the body center, and three O-atoms at the three face centers positions; whose optimized lattice parameter is a = 3.92 Å. For $SrTiO_3$ the convergence parameters, K-points = 500, RK_{max} = 7.0, and G_{max} = 17 are chosen with R_{MT}-values of 2.40 for Sr-atom, 1.78 for Ti-atom, and 1.61 for O-atom. These convergence parameters are also obtained for $LaTiO_3$ system. The volume optimization curves with crystal structures (insets) of $LaTiO_3$, and its superstructure, $LaSrTi_2O_6$ are shown in (Fig. 22(a),(b)).

The cubic unitcell of optimized $SrTiO_3$ is electronically promoted to a supercell of dimension $1 \times 1 \times 3$, in order to investigate the effect of the site-substituted $SrTiO_3$ supercell by La -ions. We have studied the effect on their structural, mechanical, electronic structure, transport and optically induced properties of $La_{1-x}Sr_xTiO_3$ superstructures systems (Rai *et al.*, 2020). For a typical superstructure, $LaSrTi_2O_6$ system of space group P4/mmm (123), the optimized lattice parameters are listed in Table. 4. R_{MT} values for La, Sr, Ti and O atoms are found to be 2.50, 2.45, 1.71, and 1.55, respectively.

4.1.2.2 Structural and Chemical Stability of $Ca_{1-x}Y_xTiO_3$

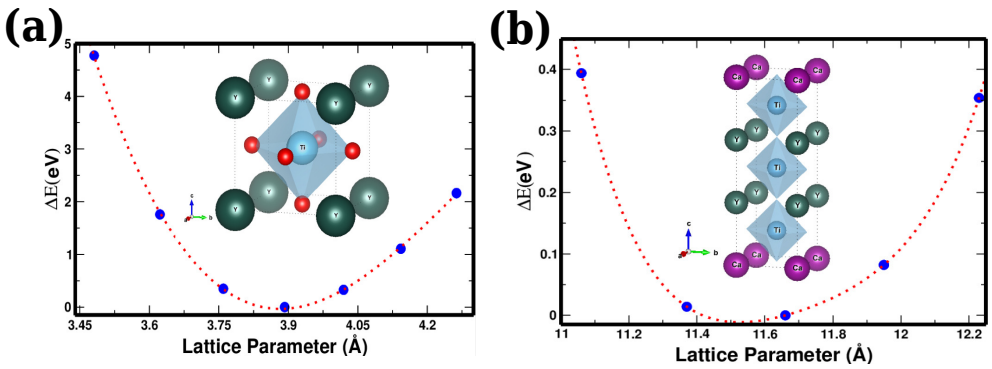

Figure 23: The lattice parameter optimization curves for (a) $YTiO_3$ with crystal structure(inset) (b) $Ca_{0.33}Y_{0.67}TiO_3$ system with crystal structure(inset).

The structural and chemical stabilities of the pristine $CaTiO_3$, $YTiO_3$ and their superstructure, $Ca_{1-x}Y_xTiO_3$ are examined through the energy minimization curve (Fig. 23(a),(b)) using variational principle. The cohesive and formation energies are used to study their chemical stability and the results are tabulated in Table. 5.

Table 5: The structural parameters* of the pristines titanates ($CaTiO_3$, $YTiO_3$) and site-substituted superstructure with cohesive and formation energies of the systems.

Physical Parameters	$CaTiO_3$	$YTiO_3$	$Ca_{0.33}Y_{0.67}TiO_3$
Lattice Parameter (Å)	3.88 3.86♦, 3.89⊕	3.89 3.87♦, 3.89⊕	a = b = 3.87, c = 11.67
Space-group	Pm-3m (221)	Pm-3m (221)	P4/mmm (123)
Opt. Volume $(Å)^3$	58.78	58.94	176.34
Cohesive Energy (eV/atom)	-7.15	-6.90	-7.00
Formation Energy (eV/atom)	-3.34 -3.38♦, -3.36⊕	-3.20 -3.26♦, -3.48⊕	-3.27

* The optimized lattice parameters are consistent with the available data. The variation of lattice parameter ($\pm\Delta a$) with their corresponding energy differences (ΔE) about their optimized values are shown in Appendix -VII (c),(d).

♦ (Long *et al.*, 2013; Kirklin *et al.*, 2015; Kestigian & Ward, 1954; Zubkov *et al.*, 1984), ⊕(Balachandran *et al.*, 2017; Ali & Yashima, 2005)

4.1.2.3 Mechanical and Thermodynamical Stabilities of Titanates

Furthermore, we have also investigated the mechanical stabilities of pristine titanates and the site-substituted superstructures using the various elastic parameters as listed in Table. 6.

Finally, the study of structural, chemical and mechanical stabilities of vanadates and titanates revealed the following concluding remarks:

The study examines the structural, mechanical, and thermodynamical stability of pristine TMOs and their superstructures, ($La_{1-x}Ca_xVO_3$, $La_{1-x}Sr_xVO_3$, $Ca_{1-x}Sr_xVO_3$, $Ca_{1-x}Y_xTiO_3$, $La_{1-x}Ca_xTiO_3$ and $La_{1-x}Sr_xTiO_3$) using ab-initio schemes from standard computational softwares. Equilibrium properties, including cohesive and formation energies per atom, modulus of elasticities, and related parameters are used to understand structural, thermodynamic and chemical stabilities. The positive values of Cauchy pressure indicate metallic nature with ductile properties and negative values indicate covalent chemical bonding with brittleness of the materials.

Table 6: The elastic constants C_{ij}, Modulus of elasticities (Y, B, G) for the Titanates.

Physical Parameters	$CaTiO_3$	$LaTiO_3$	$SrTiO_3$	$YTiO_3$	$LaSrTi_2O_6$	$Ca_{0.33}Y_{0.67}TiO_3$
C_{11} (GPa)	369.50	597.20	397.70	273.50	324.70	330.20
C_{12} (GPa)	72.40	161.50	127.90	138.50	167.90	131.10
C_{13} (GPa)					167.90	118.80
C_{22} (GPa)					230.80	149.60
C_{23} (GPa)					117.90	114.90
C_{33} (GPa)					230.30	290.30
C_{44} (GPa)	91.10	99.60	133.90	37.20	91.20	53.40
C_{55} (GPa)					88.60	63.50
C_{66} (GPa)					92.50	55.80
Y (GPa)	280.12	380.05	334.29	135.75	202.34	189.84
B (GPa)	171.41	306.71	217.83	183.48	188.13	187.58
G (GPa)	114.09	146.91	134.34	49.30	76.60	71.30
CP (GPa)	-18.70	61.90	-6.00	101.30	76.70	316.10
ν	0.23	0.29	0.30	0.38	0.32	0.33
PR	1.50	1.89	2.25	3.72	2.13	2.63
AF	2.85	7.18	2.48	4.22	3.99	4.08

4.2 Electronic Structures of Vanadates and Titanates

4.2.1 Electronic Structures of Vanadate Systems

4.2.1.1 Electronic DOS and Bandstructures of $La_{1-x}Ca_xVO_3$

The contribution of V -d and La -f orbitals at around the Fermi level for the DOS and bandstructures of $La_{0.40}Ca_{0.60}VO_3$ system are clearly observed. The redistribution of DOS with the various proportion of Ca^{2+} ions site substitution is shown (Fig. 24(a)), in which the asymmetry in spin up/down channels are observed in systems with 40% and 60% Ca^{2+} ions replacement. The comparative DOS and bandstructures are depicted for the spin up channel (Fig. 24(b)) for $La_{0.40}Ca_{0.60}VO_3$ system.

The redistributed DOS shifts towards the valence band (VB) as the value changes for onsite interaction, U and Hund's coupling, J see (Appendix -VIII) and (Appendix -IX), respectively. The GGA + U technique is used to calculate the partial density of states (PDOS) of two La-atoms, three Ca-atoms, five V-atoms, and fifteen O-atoms in a $La_{0.40}Ca_{0.60}VO_3$ system unitcell. The PDOS peaks are observed at about 4.5 and 7.0 eV due to La - and Ca -atomic contributions, respectively (Fig. 25(a),(b)). However, for 3^{rd} V -atoms, the PDOS peak is greatly pushed towards the VB, as seen in (Fig. 25(c)).

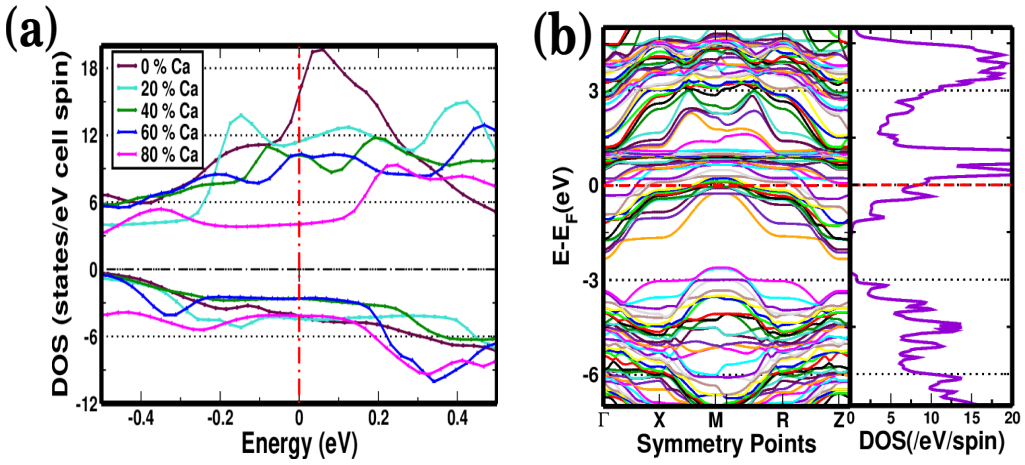

Figure 24: The plot show (a) the TDOS redistribution with Ca-ions site substitution in $LaVO_3$ supercell (b) the comparative DOS and bandstructures for the spin up channel of the $La_{0.40}Ca_{0.60}VO_3$ system.

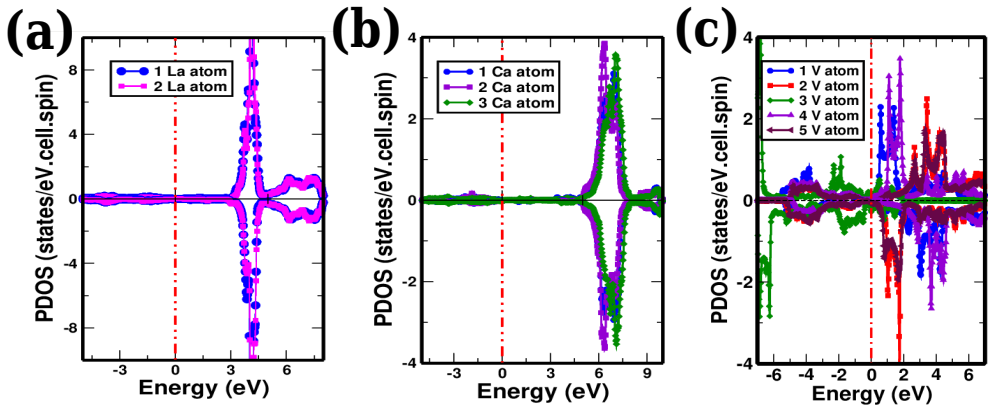

Figure 25: The PDOS contribution in $La_{0.40}Ca_{0.60}VO_3$ system by (a) La -atoms (b) Ca -atoms (c) V -atoms with U and J.

The quantity of Ca^{2+} ion site-substitution affects the net magnetic moment (MM) in the $LaVO_3$ supercell. These dopings result in a ferrimagnetic (FiM) phase transition due to the contribution of La -5d orbitals to the magnetic moment of the superstructures.

The comparative bandstructures plot for spin up and spin down channels is shown in (Fig. 26(a)) for a typical site-substituted superstructure, $La_{0.40}Ca_{0.60}VO_3$. The hybridization of the V -t_{2g} and La -4f orbitals considerably stabilizes the energy of the t_{2g} orbitals (Fig. 26(b)). The V -e_g orbital is pushed towards the Fermi-level substantially, with correlation parameter, U = 4.11 eV and exchange coupling, J = 0.50 eV, indicates the material's quasi metallic behavior (Fig. 26(c)). The spin-orbit couplings (SOC) in the superstructure did not significantly alter the electronic structure of the $La_{0.40}Ca_{0.60}VO_3$ system. Using the traditional DFT revealed metallic (Fermi liquid phase) of these systems (Ohtomo & Hwang, 2004; Salehi, 2011). The conduction bands are formed by La -4f orbitals, and at the Γ -point, the La -5d orbitals hybridize with the La -4f orbitals

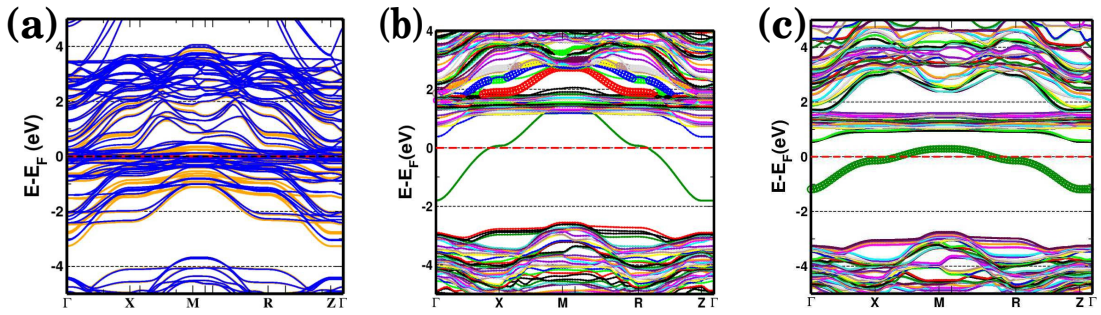

Figure 26: The graphs of (a) the comparative bandstructures (b) the fat bandstructure of the V -d orbitals with Coulomb interaction (c) the fatbandstructure of third atomic V -e_g orbital of $La_{0.40}Ca_{0.60}VO_3$ system.

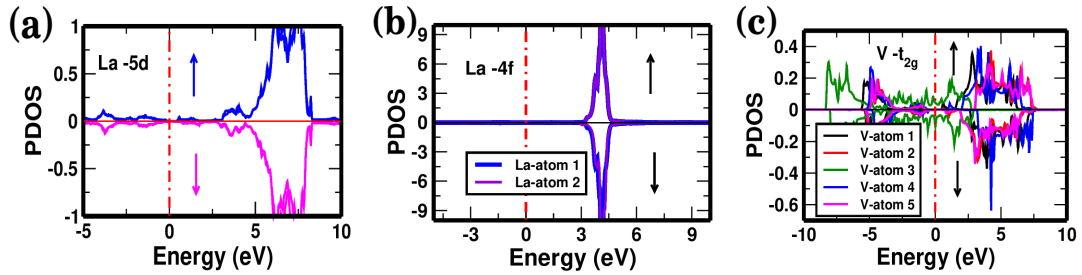

Figure 27: The orbitals contribution of (a) La- 5d (b) La- 4f (c) V-t_{2g} in $La_{0.40}Ca_{0.60}VO_3$ system.

(Fig. 27(a),(b)). (Fig. 27(c)) shows the contribution of V -3d orbitals.

Crystal field effect (CFE) see (Appendix -X) and p -d hybridization are crucial for the electronic structure and related physical properties of transition metal oxides, including magnetic properties. These oxides have an octahedron environment with transition metal ions and 3 -oxygen atoms, which can split degenerate bands into two energy levels. Orbital wavefunctions in t_{2g} -states point between neighboring O^{2-} ions, while e_g -state wavefunctions point to adjacent O^{2-} ions and exhibit higher orbital overlap. These states are distinguished by p -d hybridization, with t_{2g} -orbitals bonding with O -2p orbitals, and e_g -orbitals bonding with O -2p orbitals. The t_{2g} -orbitals form π -bonding with the O -2p orbitals, whereas the e_g -orbitals form σ -bonding with those orbitals. As a result, the degenerate O -2p states are no longer present.

The energy scale of CFE is generally, comparable to Hund's coupling energy (J_H). According to Hund's rule, electrons tend to align in the same spin direction while filling the empty states to form a high spin state. Instead, electrons prefer to remain in a low spin state, and hence the electronic and magnetic properties of the materials differ from those in a high spin state.

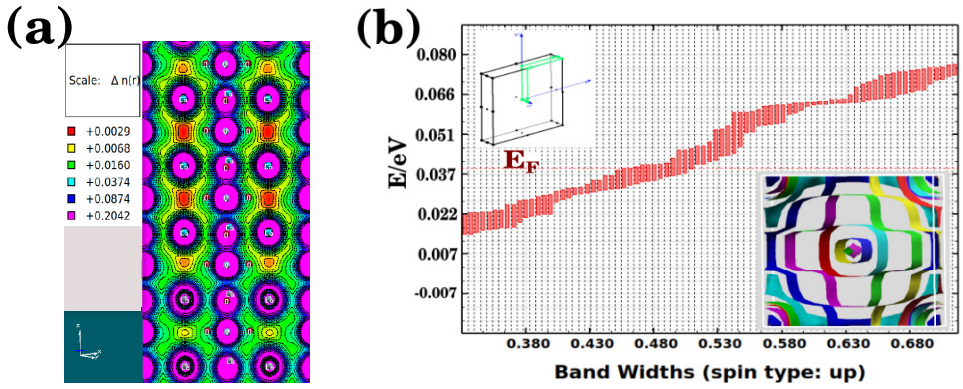

Figure 28: The plots of (a) the 2D charge contour map (b) the primitive Brillouin zone (BZ) (inset top left) with the band crossing by Fermi level for 50 -175 band levels and Fermi-surface plot at around the Γ point (inset bottom right) of $La_{0.40}Ca_{0.60}VO_3$ system.

The study of charge density maps and Fermi surfaces of $La_{1-x}Ca_xVO_3$ also dictates about the electronic structures of the system. The 2D electronic charge contour map indicates the probability of electrons being present at specific time and location (Capelle, 2006). The charge density contour map for $La_{0.40}Ca_{0.60}VO_3$ in the (111) plane (Fig. 28(a)) shows electron density distribution primarily around ionic cores (Li *et al.*, 2018). The Fermi-surface, a constant energy surface defined by Fermi momentum k_F, is composed of multiple electron and hole orbits (Fig. 28(b)) and generated for 50 -175 band levels, centered around Γ points representing different electron and hole pockets. A metallic system's Fermi surface is positioned outside the first Brillouin zone (BZ). It is to be noted that the external field can change the shape of the Fermi surface.

4.2.1.2 Electronic DOS and Bandstructures of $Ca_{1-x}Sr_xVO_3$

The DOS and bandstructures plots of the $CaVO_3$ and $SrVO_3$ systems agree well with other theoretical and experimental data. Both of these compounds are correlated metal complexes. The combined DOS and bandstructures plot for the pristine and their superstructure, $(Ca_{0.50}Sr_{0.50}VO_3)_2$ are presented in (Fig. 29(a),(b)) supporting that the superstructure is correlated metal according to the conventional DFT calculation.

The asymmetric nature of DOS for spin up/down channels of $CaVO_3$ and $(Ca_{0.50}Sr_{0.50}VO_3)_2$ superstructure show that the system are in FiM orderings with a magnetic moment of 1.47 μ_B/unitcell of the superstructure (Fig. 30).

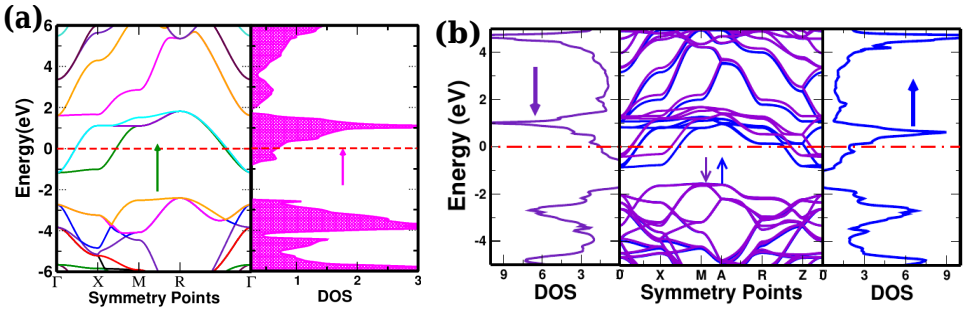

Figure 29: The plots for (a) the comparative DOS and bandstructures for $CaVO_3$ spin up channel (b) the comparison of the DOS and bandstructure of the $(Ca_{0.50}Sr_{0.50}VO_3)_2$ system for both spin up and down channels.

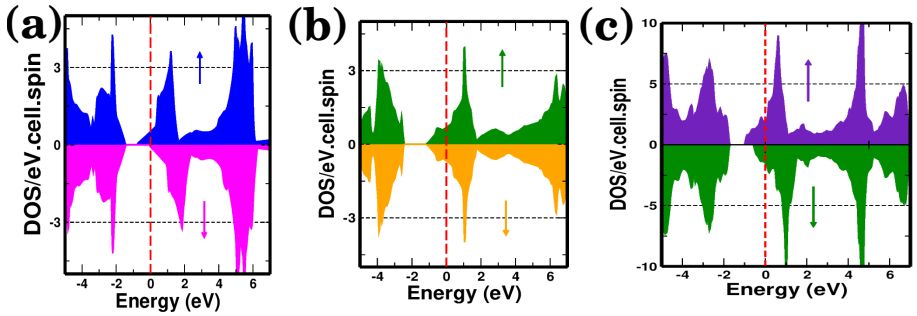

Figure 30: The TDOS plots for spin up/down channels of (a) $CaVO_3$ (b) $SrVO_3$ and (c) $(Ca_{0.50}Sr_{0.50}VO_3)_2$ systems.

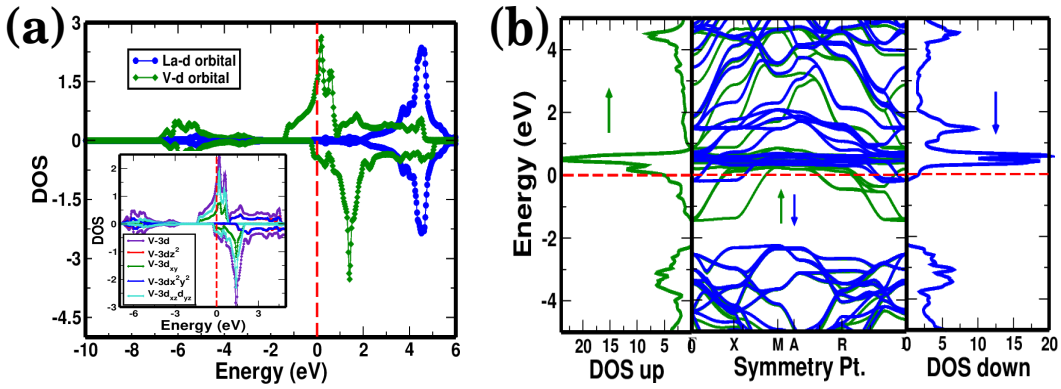

Figure 31: The plots of (a) La -d and V -d orbitals PDOS contributions for both spin-channels (only V-d orbitals are shown in the inset) (b) the bandstructure together with the DOS (spin-up) (green) and DOS (spin-down) (blue) channels of $LaSrV_2O_6$ system.

4.2.1.3 Electronic DOS and Bandstructures of $LaSrV_2O_6$

The comparative DOS and bandstructures (Fig. 31(a),(b)) suggest that the $LaSrV_2O_6$ system is a correlated metal. Due to the asymmetric distribution of total PDOS (Fig. 31(a)) provided by La - and V -atoms, the superstructure exhibit the FiM (2.23 μ_B/unitcell) ordering. Ferri-magnetism is caused by the contribution of e_g (d_{z^2}, $d_{x^2y^2}$) and t_{2g} (d_{xy},d_{yz}, d_{xz}) orbitals of Vanadium transition metals, whereas Lanthanum shows PM behavior (Dong *et al.*, 2008; Kaphle *et al.*, 2012; Lide *et al.*, 2020) in the $LaSrV_2O_6$ system.

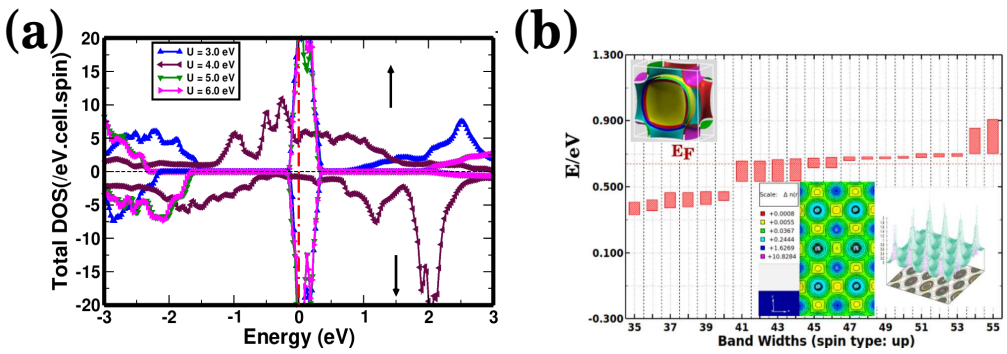

Figure 32: The plots for (a) the DOS distributions of spin up and spin down channels for various values of U (b) the Fermi surfaces generated with 35-55 band levels (inset top left) and the band crossing by Fermi level (E_F) along with the 2D and 3D charge density plot of (110) plane (inset lower right) of $LaSrV_2O_6$ system.

This metallic feature remains unaltered with the introduction of the effective Coulomb interaction (Fig. 32(a)), showing that DFT was unable to solve the electronic structures of these systems. As a result, we employed the DMFT to examine the realistic picture of electronic structures, as well as the MIT behaviors and tunability of such materials.

The Fermi-surface that characterize the gapless electronic excitations actually constitute the fundamental idea of metallic phase (Mizutani, 2001; Kawamura, 2019; Martin, 2020). The Fermi surface of $LaSrV_2O_6$ (Fig. 32(b)) as well as the 2D and 3D charge density maps support the systems are metallic.

4.2.2 Electronic Structures of Titanate Systems

4.2.2.1 Electronic DOS and Bandstructures of $La_xSr_{1-x}TiO_3$

To investigate the electronic structure, transport behaviors, and other features of $SrTiO_3$ and $LaTiO_3$ systems, optimized pristine structures were derived self-consistently. The ground state for the given system was computed using the energy minimization technique. Fig. 33(a) depicts the predicted energy band structure for the cubic phase of the $SrTiO_3$ system.

The cubic phase prototype $LaTiO_3$ has bandstructures around the Fermi-level primarily due to the e_g and t_{2g} orbitals of transition metals (Ti -atoms) (Fig. 33(b),(c),(d)). The crystal field and electrostatic interactions between Ti -cation and non -bonding O -2p orbitals cause splitting of d -orbitals (Sclauzero *et al.*, 2016). The bandstructure is redistributed by increasing the effective value of Coulomb interaction U and the introduction of SOC as well (Fig. 34(a)).

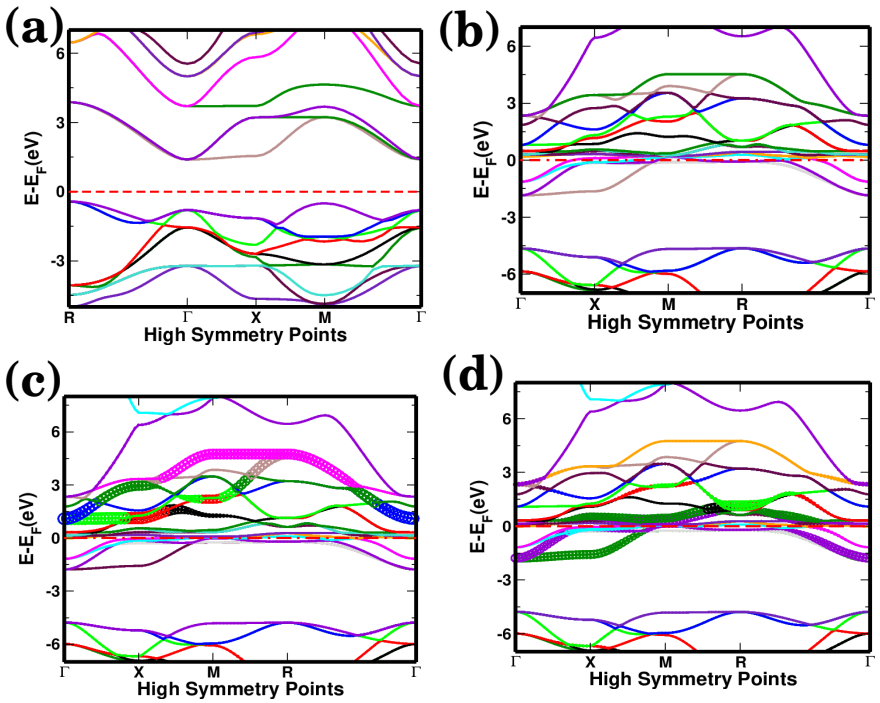

Figure 33: The band structures plots for (a) $SrTiO_3$ and (b) $LaTiO_3$ showing the band insulator and Mott insulator systems, respectively. The fatbandstrutures of the Ti -atom of $LaTiO_3$ system for (c) the e_g orbitals and (d) t_{2g} orbitals due to splittings of d -orbitals unit cell.

The oxygen 2p orbital generates three doubly degenerate VBs separated by a direct gap of 2.20 eV (at the Γ point) from the transition-metal d -orbitals derived (Ti -conduction band). The band gap is upgraded to 3.42 eV using the modified Beck-Johnson (mBJ) potential (Fig. 34(b)). It is found that the modified Beck-Johnson interaction potential in conjunction with a GGA computation enhanced the band gap (Georges *et al.*, 1996; Gebhard *et al.*, 1997) for the band insulator, $SrTiO_3$ system.

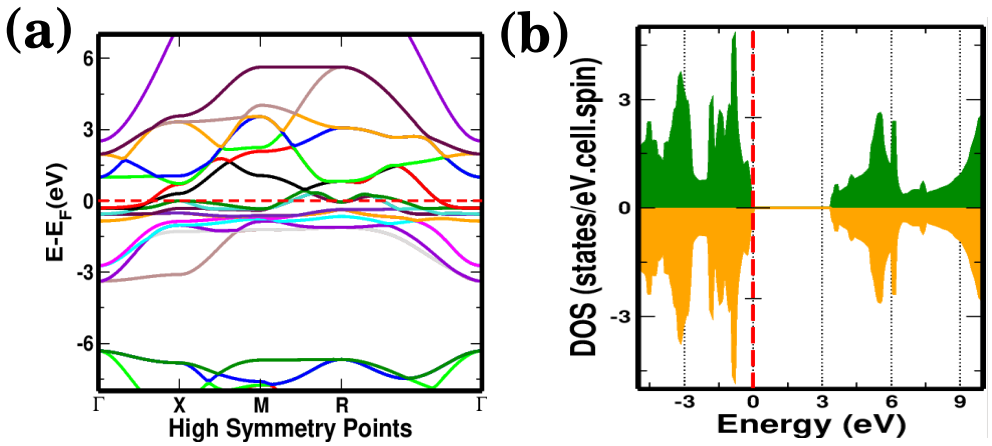

Figure 34: The plots show (a) the band shifting caused by SOC in the $LaTiO_3$ system (b) the band gap of $SrTiO_3$ system enhanced by the introduction of mBJ-interaction potential.

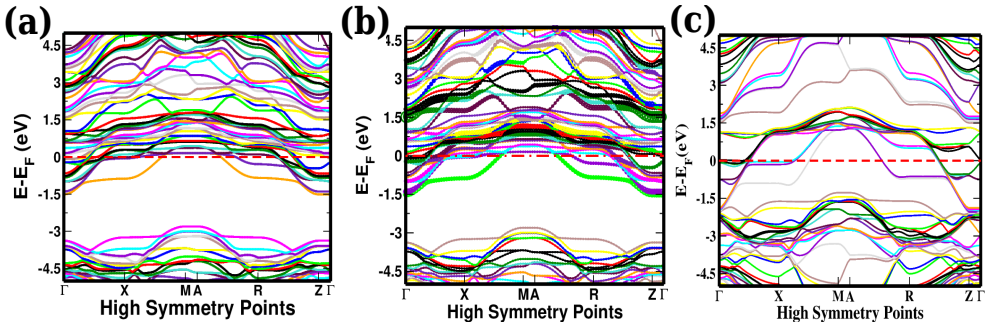

Figure 35: The bandstructure plots for $La_{0.80}Sr_{0.20}TiO_3$ system (a) the bandstructure for spin down channel (b) the fat-bandstructure for Ti - d orbitals of the system (c) the redistributed bandstructures of the system with U = 2.11 eV, J = 0.25 eV, and SOC.

Furthermore, the electronic bandstructure of a superstructure, $La_{0.80}Sr_{0.20}TiO_3$ shows a correlated metal system in which the Coulombian interaction (U), exchange interaction (J), and SOC are important factors for its electronic structures (Fig. 35(a),(b),(c)).

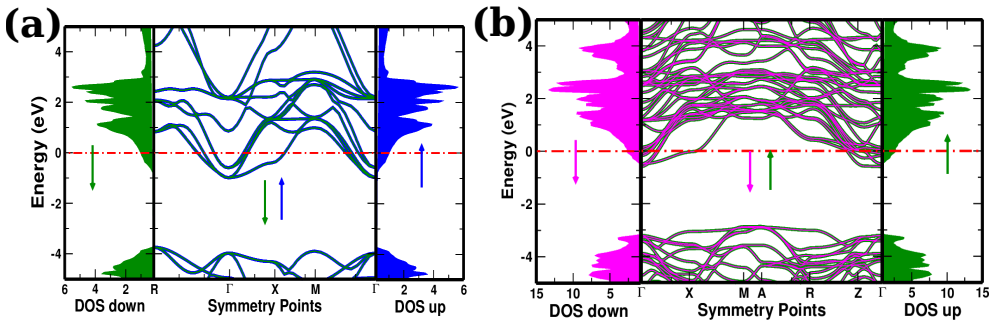

Figure 36: The plots for (a) the comparative DOS and bandstructures of both spin-channels of the pristine $YTiO_3$ system (b) the comparative DOS and bandstructures of both spin-channels of the site-substituted $Ca_{1-x}Y_xTiO_3$ system.

4.2.2.2 Electronic DOS and Bandstructures of $Ca_{1-x}Y_xTiO_3$

The DOS and bandstructures of both spin channels of pristine $YTiO_3$ (Fig. 36(a)) and its site-substituted superstructures are symmetric distributions and the redistribution of DOS and bandstructures on the supercell is vivid due to the contribution of Ca^{++} ions on Y-sites (Fig. 36(b)).

The charge density map along with the Fermi surface plot of $La_xSr_{1-x}TiO_3$ actually provides the crucial information about chemical bonding and nature of the materials. The overlap (hybridization) of Ti -3d orbitals and O -2p orbitals led to strong covalent bonds between Ti - and O -atoms, which is consistent with experimental work on perovskites compounds. The 2D contour map $LaTiO_3$ shows chemical bonding occurs primarily between adjacent atoms in $(\bar{1}10)$, while the 3D charge density map confirms electron

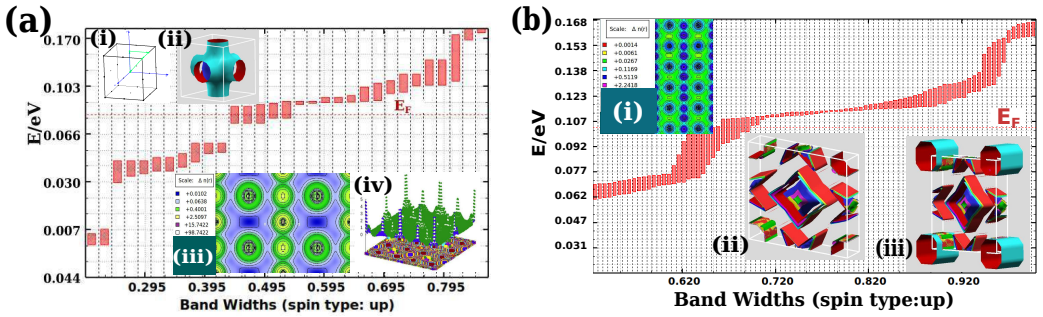

Figure 37: The plots of (a) the band crossing of Fermi level with 10-40 band levels (i) the primitive BZ (ii) the Fermi surfaces of 10 -40 band levels (iii) the 2D-charge density plot (iv) the 3D -charge density plot for the pristine, $LaTiO_3$ system, (b) the band crossing of Fermi-level plot for 100-189 bands (i) the 2D -contour plot of charge density distribution map in (011) plane (ii) the Fermi surface plot for 100 -189 band levels, (iii) the Fermi surface plot for 100 -189 band levels with tentacles of the site-substituted superstructure, $La_{0.80}Sr_{0.20}TiO_3$.

density localization near ionic cores (Fig. 37(a)(iii),(iv)). The high peak of 3D charge density plots corresponds to Ti-atoms, which are symmetric about the atomic cores. The Fermi surface of these titanates systems are studied, which corroborate the findings of the DOS and band structures. For 20-40 band levels of $LaTiO_3$ systems, the Fermi surfaces produced by numerous electron and hole orbits around the various atomic lattice sites (Inoue *et al.*, 2002) are shown in (Fig. 37(a)(ii)). Charge density contour plot of the $La_{0.80}Sr_{0.20}TiO_3$ superstructures system with a Fermisurface plot of 100-189 band levels are shown (Fig. 37(b))

The study of electronic structures of vanadates and titanates lead us to the following concluding remarks:

The investigation of titanate electronic structures reveals that the band gap of $CaTiO_3$ and $SrTiO_3$ at the Γ point in the BZ are underestimated owing to GGA with PBE exchange correlation functionals. The band gap for these band insulators were enhanced to 2.76 eV and 3.42 eV, respectively by using a modified Beck-Johnson (mBJ) interaction potential. The metal-insulator phase transition of the site-substituted superstructures, $La_{1-x}Sr_xTiO_3$, $La_{1-x}Ca_xTiO_3$ and $Ca_{1-x}Y_xTiO_3$ (titanates), $Ca_{1-x}Sr_xVO_3$, $La_{1-x}Sr_xVO_3$, and $La_{1-x}Ca_xVO_3$ (vanadates) investigated using both standard DFT and DMFT. We used the 2D and 3D charge density maps, as well as the Fermi-surfaces, to investigate the electronic structures and related properties of these complex TMOs. To investigate the MIT behavior of SCS, we used GGA + DMFT approximation with MEM complimentary calculation. The DOS and bandstructures with GGA, GGA + U, GGA +

U + J, GGA + SOC substantially alter their structures but the realistic electronic transport behaviors of these SCSs remain unsolved. Thus, we have employed DMFT with MEM calculation for the investigation of MIT behavior of these systems in the subsequent section of results and discussion.

4.3 The Electronic Transport Properties of Vanadates and Titanates

4.3.1 The Electronic Transport Properties of Vanadate Systems

4.3.1.1 Electronic Transport Properties of $La_{1-x}Ca_xVO_3$

As since, the typical DFT calculations fail to predict the electronic transport behaviors of highly correlated systems, and hence the CT-QMC hybridization expansion was used to solve the problem. In this work, we used GF of the imaginary time or frequency (Georges *et al.*, 1996; Pollet *et al.*, 2007; Pavarini *et al.*, 2014) as QMC data, and then MEM is employed to construct the real frequency spectrum function A(ω). The graph depicts the GF, G(τ) vs. imaginary time (τ) and it's Fourier transform for various values of (β) (Fig. 38(a),(b)).

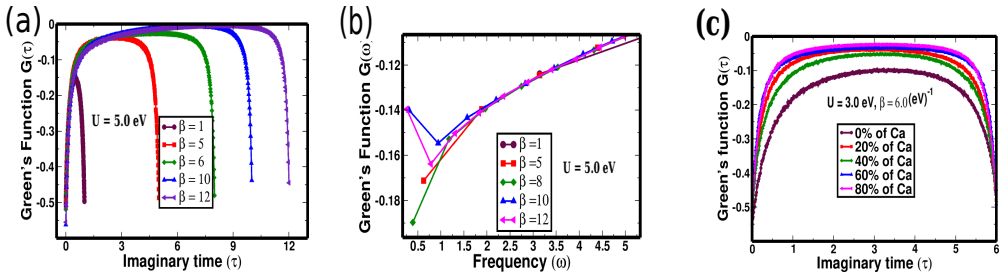

Figure 38: The plots for (a) the GF w.r.t. imaginary time (τ) (b) the corresponding variation of GF w.r.t. frequency (ω) for the different values of β with a constant U = 5.0 eV of $La_{0.40}Ca_{0.60}VO_3$ system (c) the GF of imaginary time (τ) with U = 3.0 eV and β = 6.0 $(eV)^{-1}$ for the site-substituted, $La_{1-x}Ca_xVO_3$ superstructure systems with the various proportion of Ca-ions.

A strongly correlated electronic system's MIT is completely tunable using the model parameters (U and β). The plot of GF data for the superstructures $La_{1-x}Ca_xVO_3$ for the variation of stoichiometric combination (Fig. 38(c)) and its corresponding variation of SD, $A(\omega)$ w.r.t. frequency, is presented using the MEM data analysis algorithm (Fig. 39(a)). The graph of A(ω) vs. frequency using DMFT with MEM is analogous to the graph of DOS vs. energy of conventional DFT. Table. 7 shows the Mott-Hubbard MIT with a typical set of U and β values for the pristine and their superstructures. The quasi-particles peak features of t_{2g} are observed at lower U near Fermi level and have a

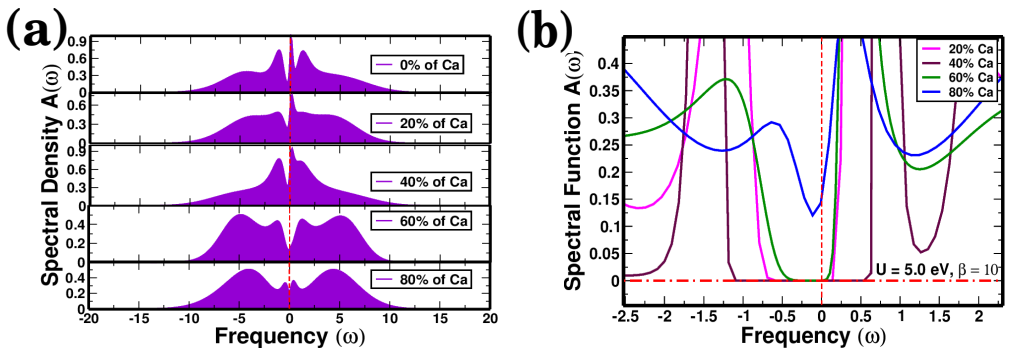

Figure 39: The graph of (a) the SD, A(ω) vs. frequency, (ω) with (U = 3.0 eV, β = 10.0 (eV)$^{-1}$) for different proportions of Ca -ions, and (b) the A(ω) vs. (ω) for U = 5.0 eV for a constant β = 10.0 (eV)$^{-1}$ with different stoichiometric combination of $La_{1-x}Ca_xVO_3$ system.

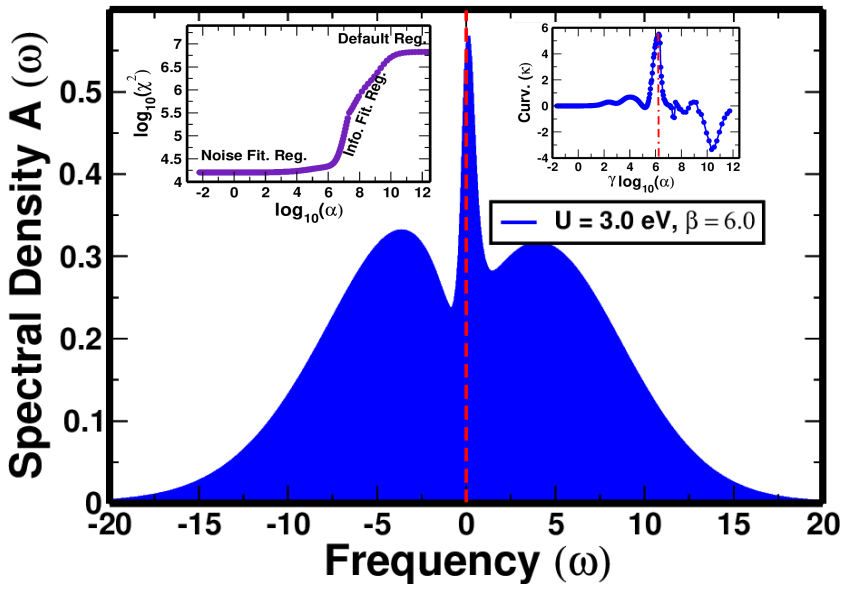

Figure 40: The SF of frequency for (U = 3.0 eV and β = 6.0 (eV)$^{-1}$) a quasi-particle peak of $La_{0.40}Ca_{0.60}VO_3$ system. The LR curve (inset upper left) and the curvature (κ) vs. $\log_{10}(\alpha)$ curve (inset upper right) for determining the optimal value of (α) for the material.

narrower Hubbard band at negative energies, consistent with ARPES (Sekiyama & Suga, 2004). The SF w.r.t. frequency for various proportions of site-substituted Ca-atoms in $LaVO_3$ supercells is significantly different for various U values and a constant value of β = 10.0 (eV)$^{-1}$. The apparent Mott gaps (Fig. 39(b)) for the samples with 40% and 60% Ca^{2+} ions doping levels are 1.64 eV and 0.74 eV, respectively.

Table. 7 shows the results of DMFT findings for Mott gaps of pristines and superstructures, which are consistent with previously published data for ($CaVO_3$, $LaVO_3$) (Blümer, 2007; Mossanek *et al.*, 2008; Basov *et al.*, 2011), and its superstructure, $La_{0.40}Ca_{0.60}VO_3$ system (Sclauzero *et al.*, 2016). The data obtained for SF, A(ω) of a quasi-particle peak, including its height, width, and overall spectral weight, is verified and cross validated

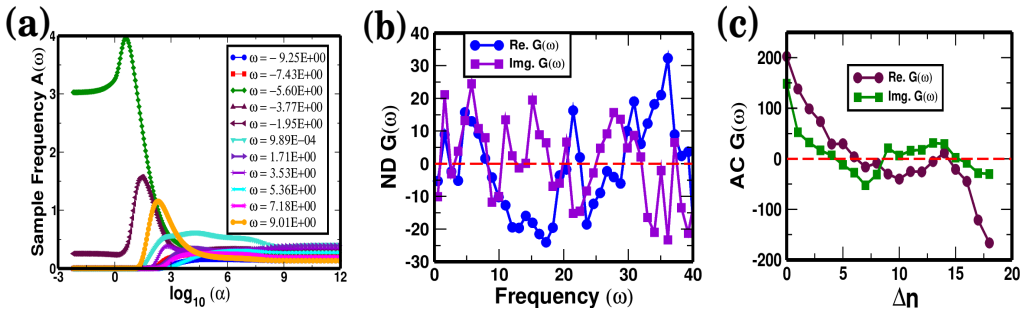

Figure 41: The plot of (a) the SD of sample frequencies vs. $\log_{10}(\alpha)$ (b) the ND of the Re. and Im. G(ω) vs. frequency with U = 3.0 eV and β = 6.0 $(\text{eV})^{-1}$ and (c) the autocorrelation (AC) of the Re. and Im. G(ω) vs. frequency index difference (Δn).

using LR curve obtained by using MEM. The optimal value of the hyperparameter, α, is determined by the maximum value of the peak of the curvature (κ) vs. $\gamma\log_{10}(\alpha)$ curve(inset), as shown in (Fig. 40). The sample frequencies vs. $\log_{10}(\alpha)$ curves, as shown in (Fig. 41(a)), may also be used to speculate the best values of α. In Fig. 41(b) and Fig. 41(c), the normalized deviation (ND) of the real and imaginary parts of the ΔG, and its autocorrelation are illustrated to assess the permissible standard error.

The system's realistic information requires the optimal relative entropy of information (S) (Fig. 42(a)). The retarded GF, $\text{G}^R(\omega)$, is associated with the self-energy of frequency and hence the real frequency SF. The real part of retarded GF, (Re $\text{G}^R(\omega)$) indicates an excitation energy shift, whereas the imaginary part (Im $\text{G}^R(\omega)$) give widening of the original Delta-function-like excitation (Fig. 42(b)). The Fig. 42(c) depicts the effect of changing the hyperparameter (α) on the SF. Fig. 42(d) depicts the errors in the various computations with the different moment orders with minimal and optimum (α).

Electron localization and delocalization can be accomplished by altering the hopping parameter, t. Here, $\text{U}/\text{t} \ll 1$ is the delocalization limit implies that a metallic phase. And $\text{U}/\text{t} \gg 1$ is the localization limit meaning the insulating phase of the system (Georges & Kotliar, 1992; Kotliar *et al.*, 2006). Metal-insulator phase transitions for the correlated system may be easily modeled by plotting U/t vs. β/t. The SF, A(ω) of the material changes rapidly for a small change in the model parameters (U/t and β/t) (Fig. 43 (a),(b)).

We have studied the QCP of an elevated temperature for the correlated system ($\text{La}_{0.40}\text{Ca}_{0.60}\text{VO}_3$) using the MEM results of MIT. The Mott-Hubbard MIT involving U and β, helps us to determine the QCP for observing Mott-Hubbard phase transitions by adjusting these

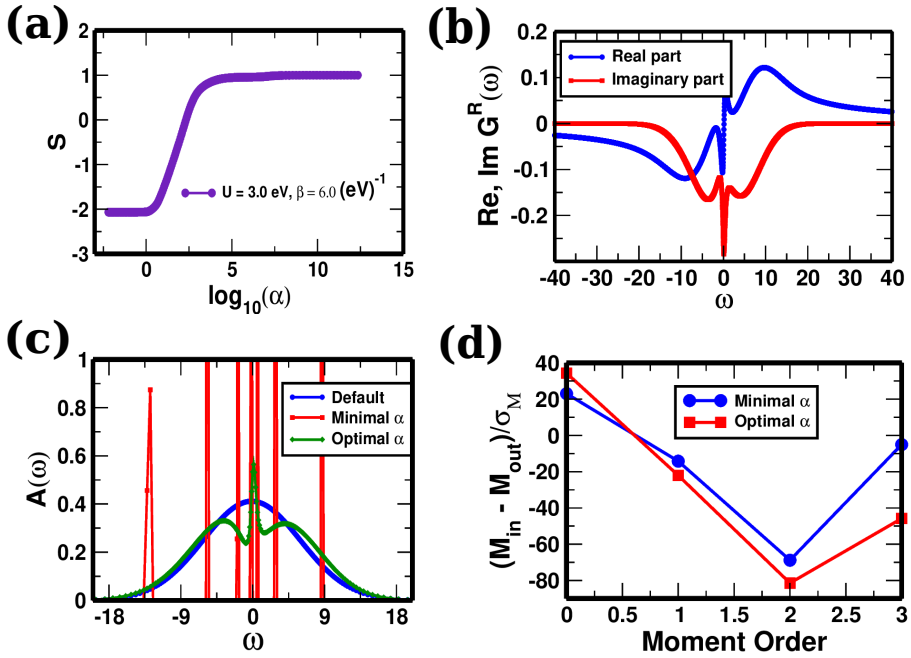

Figure 42: The plot of (a) the differential entropy (S) vs. $\log_{10}(\alpha)$ for extracting optimal information (b) the real(blue) and imaginary (red) parts of the $G^R(\omega)$ vs. frequency (c) the SF, $A(\omega)$ vs. frequency (ω) plots for default (hypothetical), and the optimal and minimal values of α (d) the uncertainty in moment orders for the calculations with (U = 3.0 eV, β = 6.0 $(\text{eV})^{-1}$) for $La_{0.40}Ca_{0.60}VO_3$ system.

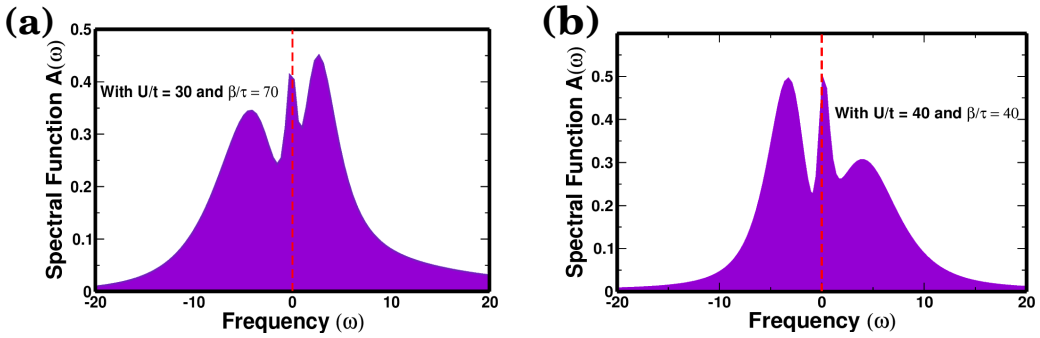

Figure 43: The SF vs. frequency with the variation of U/t versus β/t, for $La_{0.40}Ca_{0.60}VO_3$ system.

correlation parameters. In general, a new class of phase transition occurs around absolute zero. The QMC is unable to directly compute the free energy, it has trouble in locating and describing phase transitions inside DMFT. In large dimensions (d $\rightarrow \infty$), the fully-frustrated Bethe lattice, meaning the homogeneous phase Hubbard model with semi-elliptic DOS is the default model for calculation. One of the first questions addressed following the establishment of DMFT was how to numerically actualize the contradicting scenarios of Hubbard (Hubbard, 1963) and Brinkman and Rice (Brinkman & Rice, 1970) for the MIT. The Mott metal-insulator phase transition in $La_{0.40}Ca_{0.60}VO_3$ is characterized by Coulombian interaction, U variation, and thermodynamical parameter (β). The graph shows QCP at U_C = 2.96 eV and β_C = 23.65 $(\text{eV})^{-1}$ as depicted in

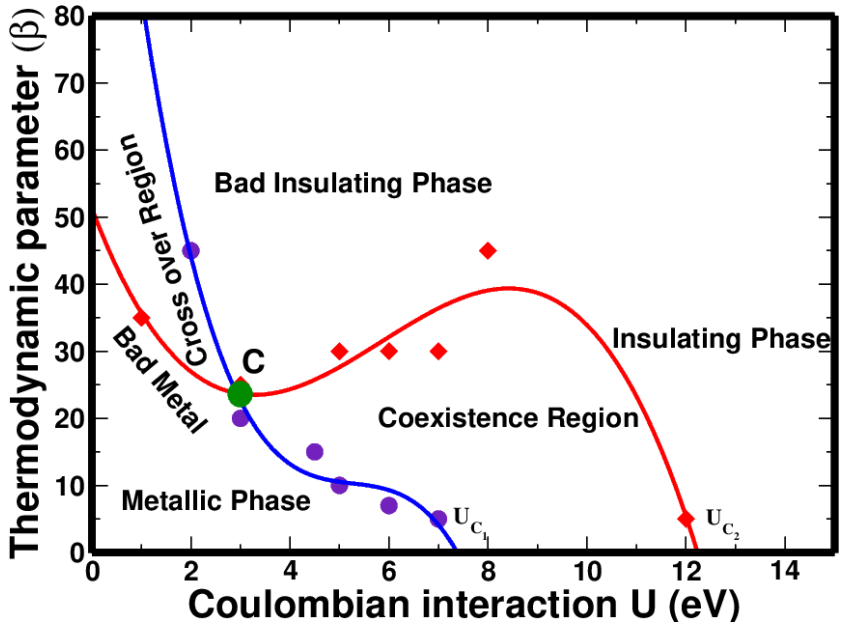

Figure 44: The graph of MIT using DMFT with MEM self-consistency cycle of calculation. The graph depicts the QCP, C at an elevated temperature in the Uβ -plane and two bifurcation points in the low temperature regime, $\mathrm{U_{C_1}}$ and $\mathrm{U_{C_2}}$.

Fig. 44 (Kotliar *et al.*, 2006; Gull *et al.*, 2008). Two essential Coulombian parameters are observed: $\mathrm{U_{C_1}(T)}$ = 7.40 eV, where insulating nature disappears, and $\mathrm{U_{C_2}(T)}$ = 12.30 eV, where metallic nature disappears.

The crossover region in the Uβ-plane is the area between two widom lines and above the critical point, C. It consists of four unique regions due to correlation hysteresis: the Fermi liquid (metallic) region on the left side of the $\mathrm{U_{C_1}(T)}$ widom line and the PM insulating regions on the right side of the $\mathrm{U_{C_2}(T)}$ widom line. This region separates the Uβ-plane into two parts: the bad metallic region with high resistivity and the bad insulating region with decreasing resistivity whenever the temperature is raised. A smooth transition from a metallic phase to an insulating phase is occurs quickly at the crossover region. The metallic phase is thermodynamically stable for $\mathrm{U} \leq \mathrm{U_C}$ but remains a well-defined metastable solution of the DMFT equations for $\mathrm{U_{C_1}} \leq \mathrm{U} \leq \mathrm{U_{C_2}}$ (co-existence region).

4.3.1.2 Electronic Transport Properties of $\mathbf{La_{1-x}Sr_xVO_3}$

The DFT and DMFT in conjunction with MEM, were employed to determine the real electronic structure of the pristine TMOs and their superstructures (Haule, 2007; Beck & Ederer, 2023). In order to find the MIT model parameters, we employ the DMFT to run a series of computations. The calculations show that the insulating phase started at U =

4.0 eV with β = 6.0 $(eV)^{-1}$ (Fig. 45(a)) and the clear insulating phase is obtained at (U = 6.0 eV and β = 6.0 $(eV)^{-1}$), as illustrated in (Fig. 45(b)).

Similarly, using U = 4.0 eV as a starting point, the weak metallic phase is observed at β = 6.0 $(eV)^{-1}$, but a clear insulating phase is obtained at β = 10.0 $(eV)^{-1}$ (Fig. 46(a)). For various values β of with a constant U = 4.0 eV, the same patterns are seen in the imaginary part of the self-energy vs. Matsubara frequency plot (Fig. 46(b)) (Georges & Kotliar, 1992; Sekiyama & Suga, 2004; Held *et al.*, 2008).

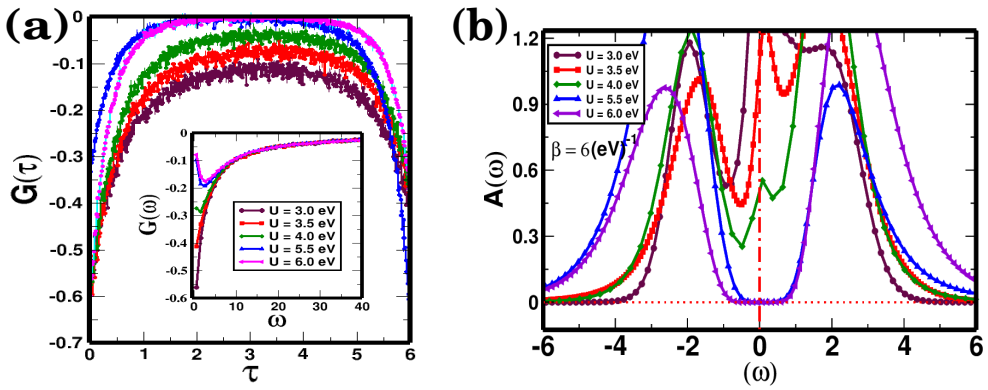

Figure 45: The graph of (a) GF vs. imaginary time,(τ) for the variation of U with a constant β = 6.0 $(eV)^{-1}$, and the corresponding variation of GF vs. frequency (inset) (b) the SF vs. frequency (ω) with a constant β = 6.0 $(eV)^{-1}$ for the variation of U of $LaSrV_2O_6$ system.

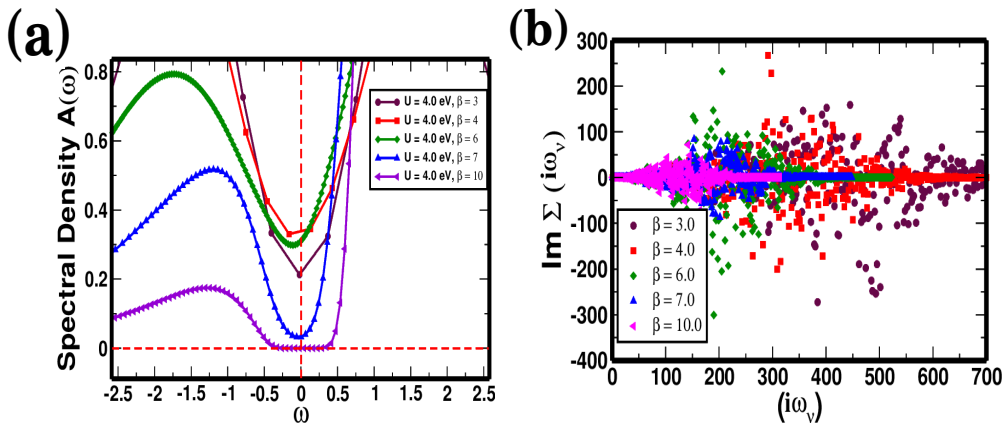

Figure 46: The plot of (a) the SD vs. frequency (ω) for a constant U = 4.0 eV for β variation (b) the plot of imaginary part self-energy (Im$\Sigma(i\omega_\nu)$) vs. the Matsubara frequency ($i\omega_\nu$) for the variation of (β) with a constant U = 4.0 eV of the $LaSrV_2O_6$ system.

The SD graphs (Fig. 47 (a)) show the consistent outcome of decreasing the quasi-particle peak (metallic phase) to the clear Mott-Hubbard band splitting, called Gutzwiller-Brinkman-Rice (GBR) phase transition scenario insulating phase for the various U values (Mott insulating at U = 4.0 eV and β = 10.0 $(eV)^{-1}$)).

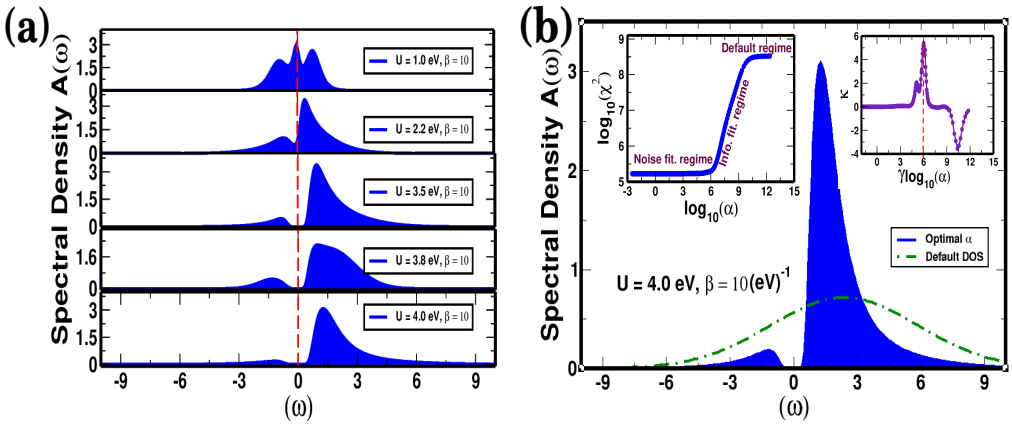

Figure 47: The graph of (a) the SF vs. frequency (ω) for the variation of U values (b) the LR curve for the optimal value of α for U = 4.0 eV and β = 10.0 $(\text{eV})^{-1}$.

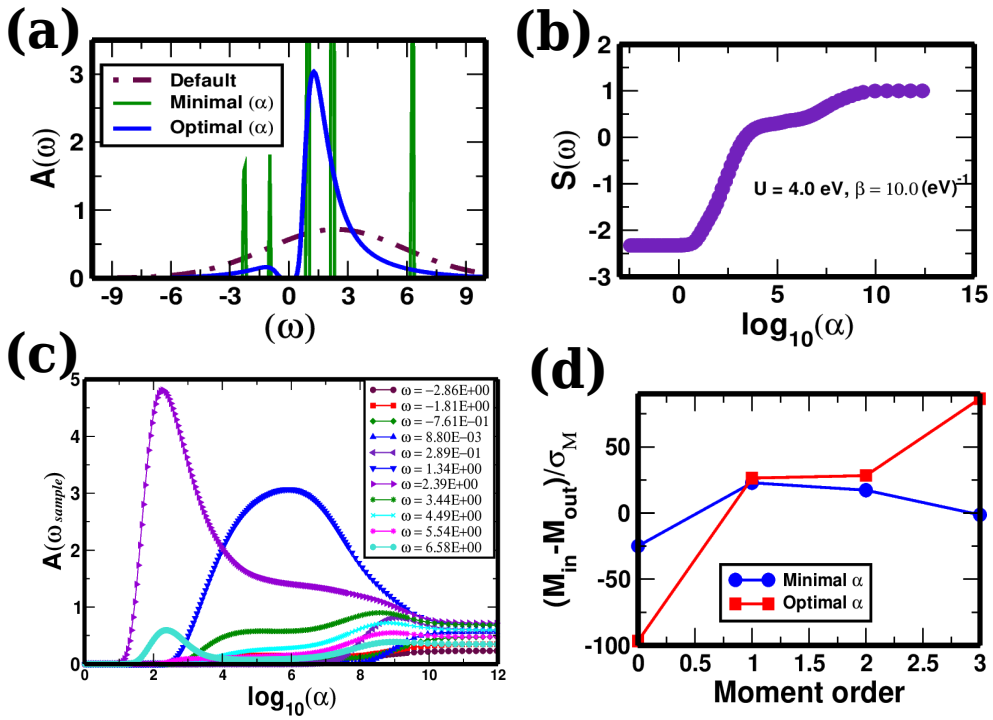

Figure 48: The graphs of (a) the SF of frequency obtained for optimal and minimal values of α with the default model (dotted line) (b) the differential entropy, S(ω) vs. $\log_{10}(\alpha)$ to observe the optimal value of information (c) the SD for the various sample frequencies vs. of $\log_{10}(\alpha)$ (d) the normalized function of moment orders for the calculations for the minimal value of α (blue) and optimal value of α (red) for $LaSrV_2O_6$ system with (U = 4.0 eV, β = 10.0 $(\text{eV})^{-1}$).

We perform a LR analysis on the Mott-insulating phase (Fig. 47 (b)) calculation using the MaxEnt model for the validity and accuracy of the calculated data. The LR curve (inset upper left corner) displays the fitting of curve of data with optimal α, which is chosen by the maximum value of curvature (κ) of the LR curve (inset upper right corner) (Bergeron & Tremblay, 2016).

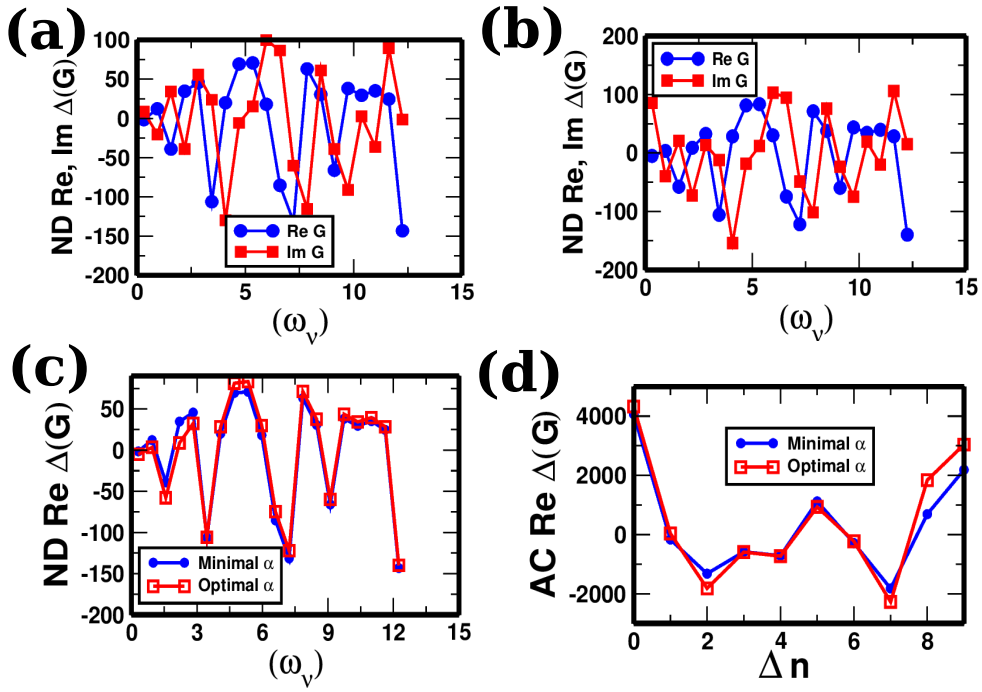

Figure 49: The graphs of (a) the ND for the Re. and Im. (ΔG) vs. frequency (ω_ν) with minimal value of α (b) the ND for the Re. and Im. (ΔG) vs. frequency (ω_ν) with the optimal value of α (c) the ND of the real parts of ΔG vs. frequency (ω_ν) with minimal (blue) and optimal (red) values of α (d) the autocorrelation of the real parts of ΔG vs. the difference of the frequency index (Δn) for the minimal (blue) and optimal (red) values of α of the $LaSrV_2O_6$ system.

Figure 48(a) compares the SD, A(ω) vs. frequency, (ω) for minimal, ideal values of α with the default model (dotted curve). The graph for S(ω) vs. α to determine the optimum information (Fig. 48(b)). The sample frequencies vs. $\log_{10}(\alpha)$ graph (Fig.48(c)) is also used to identify the optimal value of α (d) The normalized function of moment orders vs. moment of order (Fig.48(d)) for the minimal(blue) and optimal (red) value of α of $LaSrV_2O_6$ system with (U = 4.0 eV, β = 10.0 $(eV)^{-1}$) (Table. 7).

Furthermore, the Mott gap prediction error is estimated using ND of uncertainty in GF vs. Matsubara frequency with (a) the minimal value of α (b) the optimal value of α (Fig.49(a),(b)) (Jarrell & Gubernatis, 1996; Bergeron & Tremblay, 2016) and (c) the ND of real part of (ΔG) vs. Matsubara frequency, and (d) the autocorrelation of real part of (ΔG) vs. index of frequency difference as shown in Fig. 49(a),(b).

The ND for the real part of ΔG vs. the frequency (ω_ν) for the minimal and optimal value of (α) as well as the autocorrelation of the real part of ΔG vs. the difference of the frequency index (Δn) for the minimal and optimal value of (α) (Fig. 49(c),(d)) for the $LaSrV_2O_6$ system with U = 4.0 eV and β = 10.0 $(eV)^{-1}$.

Table 7: The Mott-gap, MIT model parameter, and quasi-peak parameters for pristine vanadate and their superstructures.

Compounds	Mott-gap	Mott-gap Parameters		Quasi-peak Parameters	
	(eV)	U (eV)	$\beta\ (eV)^{-1}$	U (eV)	$\beta\ (eV)^{-1}$
$SrVO_3$	0.90	2.50	6.00	2.00	10.00
$CaVO_3$	0.04	5.00	6.00	3.40	6.00
$LaVO_3$	0.93	4.50	8.00	2.00	6.00
$(La_{0.50}Sr_{0.50}VO_3)_2$	0.74	4.00	10.00	1.00	10.00
$(Ca_{0.50}Sr_{0.50}VO_3)_2$	0.44	5.50	6.00	3.00	6.00
$La_{0.40}Ca_{0.60}VO_3$	0.73	5.00	10.00	3.00	6.00

4.3.1.3 Electronic Transport Properties of $Ca_{1-x}Sr_xVO_3$

The Mott-Hubbard MIT phenomena of a SCS are investigated using the numerical simulation using the input of standard DFT data. The GF, G(τ) vs. imaginary time (τ)

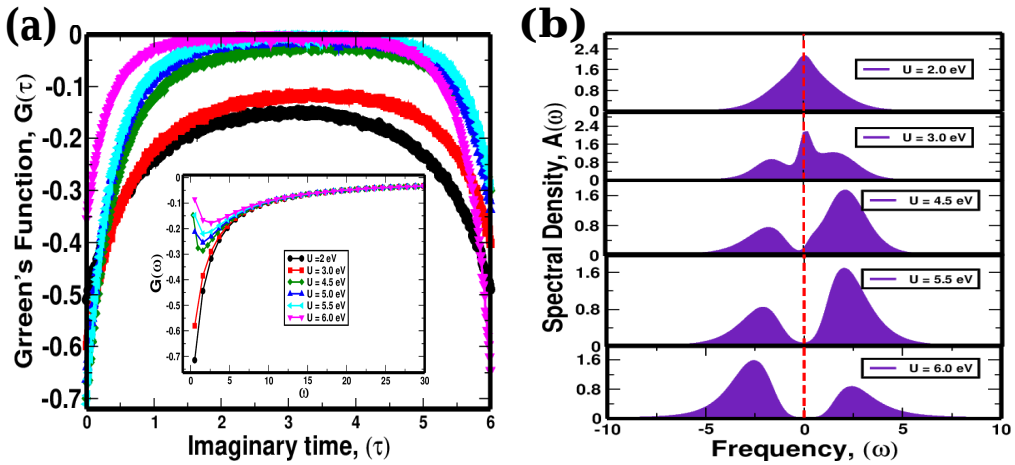

Figure 50: The plots of (a) the GF, G(τ) vs. imaginary time, (τ) and the corresponding plot of the Fourier transform of the GF (inset) with a constant β = 6.0 $(eV)^{-1}$ for various values of U (GBR-phase transition scenario) (b) the SD vs. frequency for demonstrating the MIT with U variation for β = 6.0 $(eV)^{-1}$. At U = 4.5 eV and β = 6.0 $(eV)^{-1}$, the Mott-Hubbard splitting of the $Ca_{0.50}Sr_{0.50}VO_3$ system is achieved.

for the $Ca_{1-x}Sr_xVO_3$ system for the different values of U with a constant β = 6.0 $(eV)^{-1}$ is shown in Fig. 50(a) and its Fourier transform G(ω) vs. frequency (ω) (inset). The corresponding SF, A(ω) vs. frequency (ω) is depicted in (Fig. 50(b)), obtained using the MEM algorithm (Tan *et al.*, 2013; Bergeron & Tremblay, 2016).

The validity of the data for the SF, A(ω) produced from the MEM is examined through LR analysis, as stated elsewhere. The optical conductivities for the respective spectrum functions are presented in Fig. 51, confirming that the MIT occurs for acceptable values of U and β parameters for $Ca_{0.50}Sr_{0.50}VO_3$ system.

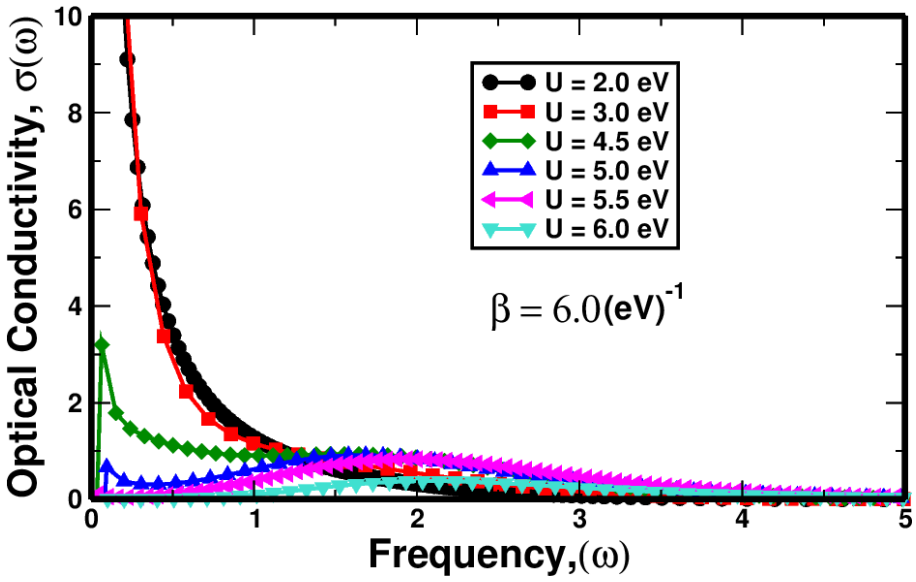

Figure 51: The change of optical conductivity with the varied Coulombian interaction U for a constant, β = 6.0 $(eV)^{-1}$ of the superstructure system.

4.3.2 The Electronic Transport Properties of Titanates System

4.3.2.1 Electronic Transport Properties of $La_{1-x}Sr_xTiO_3$

Figure 52(a) depicts the typical variation of the GF of imaginary time, (τ), with the variation of (U) for a constant β = 6.0 $(eV)^{-1}$. The corresponding variation in GF of (ω) (Fig. 52(b)) displaying the MIT for U = 4.0 eV and higher for a constant, β = 6.0 $(eV)^{-1}$. The variation of SD, A(ω), obtained from DMFT data using the MEM, as shown in (Fig. 52(c), and (d)) the variation of self-energy with several values of U and a constant β = 6.0 $(eV)^{-1}$ (Fig. 52(d)) for pristine, $LaTiO_3$ system. The fluctuation of U has no substantial effect on the self-energy.

Furthermore, for the same set of model parameters U = 3.0 eV, β = 6.0 $(eV)^{-1}$, the variation of GFs of imaginary time (τ) with various proportions of site-substitutions of La -ions is plotted as shown in (Fig. 53(a)) and the corresponding GFs of frequency(ω) (inset). In (Fig. 53(b)) depicts the variation of imaginary part of self-energy vs. Matsubara frequency for U = 3.0 eV, β = 6.0 $(eV)^{-1}$ of $La_{0.80}Sr_{0.20}TiO_3$ system. The SF, A(ω) for a quasi-particle peak representing metallic phase is shown in (Fig. 54(a)). The realistic information of calculated data, such as central peak, height, width, and overall weight is obtained through the LR's curve (inset left) and the maximum value of curvature of LR curve (inset right). In (Fig. 54(b)), the variation of optical conductivity vs. frequency depicts the shifting and diminishing Drude peaks with the proportion of La -atoms in $La_{0.80}Sr_{0.20}TiO_3$

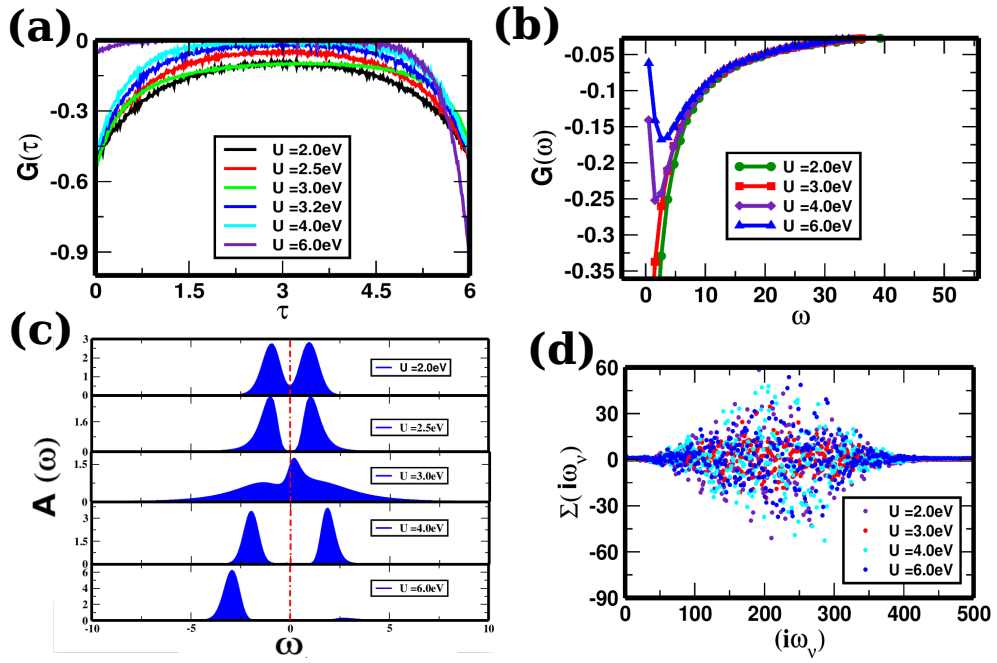

Figure 52: The plots for (a) the GF vs. imaginary time (b) the GF vs. frequency (c) the variation of SD vs. frequency and (d) the imaginary part of $\Sigma(i\omega_\nu)$ vs. Matsubara frequency with the variation of U and a constant β = 6.0 $(\text{eV})^{-1}$ of the pristine, $LaTiO_3$ system.

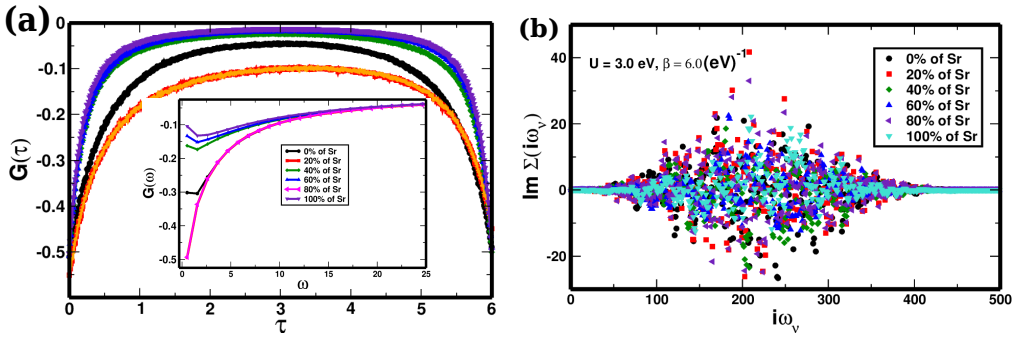

Figure 53: The plots of (a) the GF, G(τ) vs. imaginary time (τ) for the various values of stoichiometric combinations and the corresponding GF, G(ω) vs. frequency (ω) (inset) showing the MIT with the site-substitution of Sr -ion with La -cation for U = 3.0 eV and β = 6.0 $(\text{eV})^{-1}$ of $La_{1-x}Sr_xTiO_3$ systems and (b) The imaginary part of self-energy, (Im Σ (iω_ν)) vs. Matsubara frequency, (iω_ν)) for (U = 3.0 eV and β = 6.0 $(\text{eV})^{-1}$) for the same stoichiometric combinations.

superstructures for the same U = 3.0 eV and β = 6.0 $(\text{eV})^{-1}$. The Model MIT parameters and the related Mott gaps for titanates are listed in Table. 8.

4.3.2.2 Electronic Transport Properties of $Ca_{1-x}Y_xTiO_3$

The DMFT with MEM results are depicted in (Fig. 55(a),(b)) for the $YTiO_3$ and its superstructures, $Ca_{0.33}Y_{0.67}TiO_3$ system showing the band splittings with (U = 5.0 eV and β = 10.0 $(\text{eV})^{-1}$) and (U = 5.0 eV and β = 7.0 $(\text{eV})^{-1}$), respectively. The corresponding Mott-gaps for these systems are tabulated in Table. 8. The optimal value

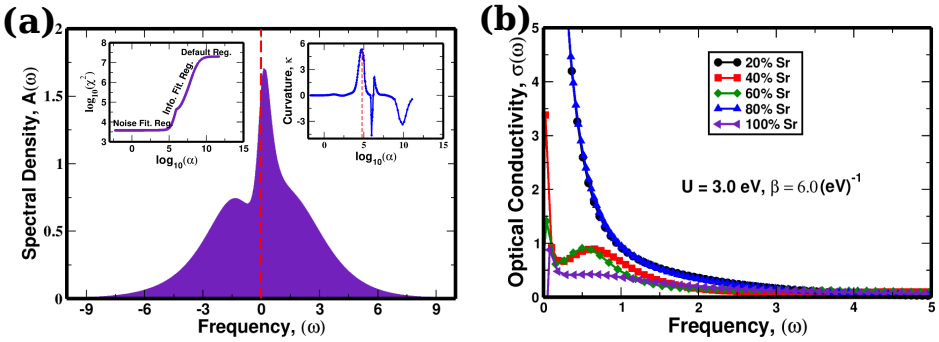

Figure 54: The graphs of (a) the SF vs. frequency showing the quasi-particle peak for $La_{0.80}Sr_{0.20}TiO_3$ at U = 3.0 eV and β = 6.0 $(eV)^{-1}$ the LR curve (inset left) and the curvature of the LR curve (inset right) for optimal value of (α) (b) the comparison of optical conductivities vs. frequency indicating the variation of Drude peaks with the various proportion of La^{2+} ions in $La_{1-x}Sr_xTiO_3$ supercells at U = 3.0 eV and β = 6.0 $(eV)^{-1}$ for the optimal value of α.

Table 8: The Mott-gap, MIT model parameter, and quasi-peak parameters for pristine titanates and their superstructures.

Compounds	Mott-gap	Mott-gap Parameters		Quasi-peak Parameters	
	(eV)	U (eV)	$\beta\ (eV)^{-1}$	U (eV)	$\beta\ (eV)^{-1}$
$YTiO_3$	0.63	5.00	10.00	3.00	6.00
$LaTiO_3$	0.93	4.00	8.00	3.00	6.00
$LaSrTi_2O_6$	0.35	4.70	6.00	2.20	6.00
$La_{0.80}Sr_{0.20}TiO_3$	0.74	3.20	10.00	3.00	6.00
$Ca_{0.33}Y_{0.67}TiO_3$	0.41	5.00	7.00	1.50	6.00

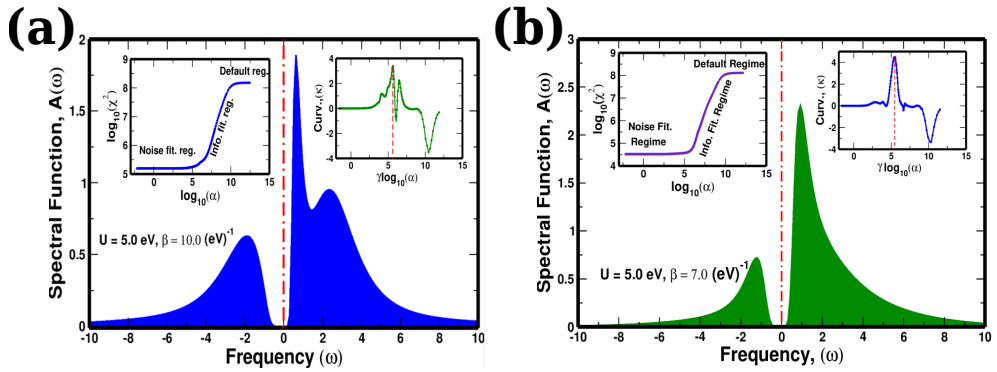

Figure 55: The graphs show (a) the SD, A(ω) vs. frequency (ω) of $YTiO_3$ with LR curve(inset top left) and the curvature of LR curve (inset top right), and (b) the SD, A(ω) vs. frequency (ω) of the superstructure, $Ca_{0.33}Y_{0.67}TiO_3$ with LR curve (inset top left) and the curvature of LR curve (inset top right).

of hyperparameter (α) is determined using the LR curve (inset left) and the curvature of LR curve (inset right) of (Fig. 55(a),(b)).

In brief, the concluding remarks from the study of electronic transport properties (MIT behaviors) of vanadates and titanates are as follows:

The effect of various cationic site-substitutions on Mott-Hubbard MIT for various SCSs, such as $La_{1-x}Ca_xVO_3$, $La_{1-x}Sr_xVO_3$, $Ca_{1-x}Sr_xVO_3$, and $La_{1-x}Sr_xTiO_3$ systems are

investigated through GGA + DMFT along with the MEM as the complementary calculation. The CT-QMC with hybridization expansion is employed as the quantum impurity solvers (DMFT equation solvers) for generating GF data of imaginary time and frequency, which are used for investigating the metal-insulator phase transition using MEM. The investigation of Mott gaps are crucially important for various technological and engineering purposes, whereas the MIT modal parameters for quasi-particle peak are vitally important for quantum information technology. The MIT behaviors are used to design Mottronics devices like as neuromorphic computers, resistive memory devices, Leaky-Integrate-Fire (LIF) artificial neurons for neural networks, and so on (Messerschmitt *et al.*, 2014; Jaiswal *et al.*, 2017). The coexistence regime between the metallic and insulating phases is computed along with the elevated QCP for $La_{0.40}Ca_{0.60}VO_3$ system. The QCP has also been computed at an elevated temperature for U_C = 2.95 eV and β_C = 23.58 $(eV)^{-1}$.

4.4 Thermoelectric Properties of Vanadates and Titanates

4.4.1 Thermoelectric Transport Properties of Vanadate Systems

4.4.1.1 Thermoelectric Transport Properties of $La_{1-x}Ca_xVO_3$

In the BoltzTraP approach, the linearized BTE is solved to calculate the different thermoelectric transport parameters for pristine and Ca-ions substituted $LaVO_3$ supercells. Electrical conductivity (σ/τ) varies with altering chemical potential (Fig. 56(a)), and thermal conductivity (κ) follows a similar trend (Fig. 56(b)). The variation of these parameters w.r. to the absolute temperature scale is depicted in the corresponding insets (Saeed *et al.*, 2014).

Similarly, for various doping levels of the $La_{1-x}Ca_xVO_3$ system, the variation of the Seebeck coefficient (S) and the Hall coefficient (R_H) is illustrated in (Fig. 57(a),(b)), and the same parameters w.r.t. temperature are shown in the corresponding insets. The various thermoelectric parameters of the superstructure vary dramatically, indicating that it might be a possible candidate for thermoelectric applications (Sofo & Mahan, 1994; Wang *et al.*, 2019).

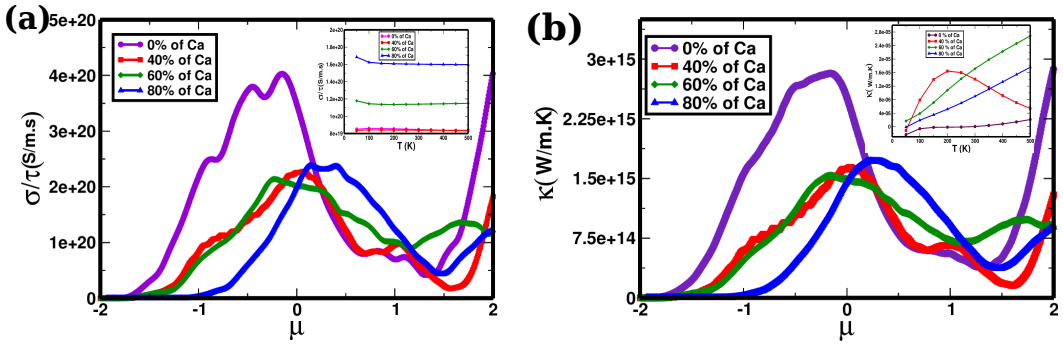

Figure 56: The graph of (a) the electrical conductivity (σ/τ) vs. the chemical potential (μ) and the corresponding variation of the same parameter with respect to the absolute scale of temperature (inset) (b) the variation of thermal conductivity (κ) vs. (μ) and the corresponding variation of (κ) with temperature (inset) for the site-substituted superstructures, $La_{1-x}Ca_xVO_3$.

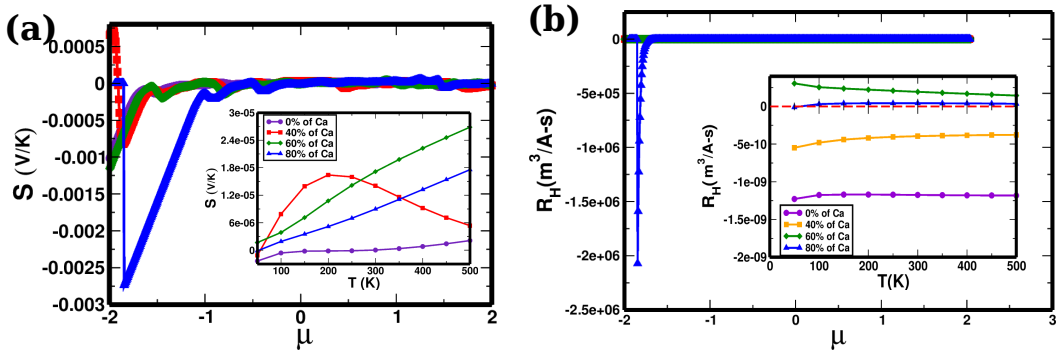

Figure 57: The graphs show (a) the Seebeck Coefficient (S) w.r.t. the chemical potential (μ) at room temperature (300 K) and its temperature variation (inset) (b) the variation of the Hall coefficient (R_H) vs. chemical potential (μ) at room temperature (300 K) and its temperature variation for the site-substituted superstructures, $La_{1-x}Ca_xVO_3$.

The Seebeck coefficient (S), which changes near the chemical potential $\mu \sim -2.0eV$, indicates a change in carrier concentration with varying amounts of Ca^{2+} ions substitution in a supercell (Fig. 57(a)). This change is associated with temperature and is unique to the 40% Ca-doped system (inset Fig. 57(a)). The Hall coefficient (R_H) of the material is expressed as, $n = \frac{1}{eR_H}$ (Ohtani *et al.*, 1970). The metallic phase has a lower Hall coefficient than the non-metallic phase and a negative (Ohtani *et al.*, 1970), showing that the number of carriers rapidly rises as it varies from the non-metallic to the metallic phase. According to the notion of weakly correlated systems, R_H is temperature independent, as illustrated in (Fig. 57(b)).

The observed Hall coefficient in the compound, substantially positive R_H for the sample higher than 60% of Ca-ions (Takagi *et al.*, 1989; Maeno *et al.*, 1994). In Table 9, the estimated thermoelectric parameters for pristine and superstructure vanadate systems at room temperature are tabulated.

Table 9: The electrical (σ/τ) and thermal (κ) conductivities, Seebeck coefficient (S), Hall coefficient (R_H), magnetic susceptibility (χ), molar specific heat capacity (C) and thermoelectric power factor (TPF) of vanadate systems at room temperature (300 K).

Physical Parameters	$CaVO_3$	$LaVO_3$	$LaSrV_2O_6$	$La_{0.40}Ca_{0.60}VO_3$
σ/τ (1/(Ωm.s))	4.55×10^{20}	4.40×10^{20}	2.87×10^{20}	2.00×10^{20}
κ (W/m.K.s)	2.75×10^{15}	3.90×10^{15}	1.94×10^{15}	1.50×10^{15}
R_H (m^3/C)	-2.07×10^{-10}	-2.15×10^{-10}	-1.05×10^{-10}	-1.73×10^{-10}
S (V/K)	-1.66×10^{-6}	-2.49×10^{-6}	-64.00×10^{-6}	7.34×10^{-6}
χ (m^3/mol)	6.00×10^{-10}	5.84×10^{-10}	39.40×10^{-10}	82.30×10^{-10}
C (J/mol.K)	0.88	1.24	7.55	12.31
TPF	0.92×10^{9}	2.00×10^{9}	0.50×10^{9}	10.20×10^{9}

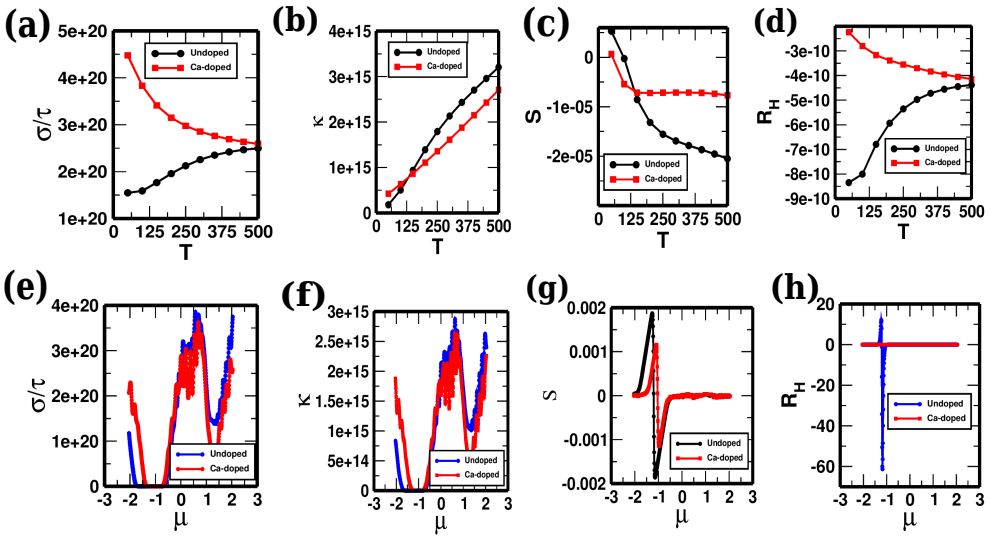

Figure 58: The graphs of various transport parameters (a) electrical conductivity (σ/τ) (b) thermal conductivity (κ) (c) Seebeck coefficient (S) and (d) Hall coefficient (R_H) w.r.t. the absolute temperature scale (T). The variation of the same transport parameters (e) electrical conductivity (σ/τ) (f) thermal conductivity (κ) (g) Seebeck coefficient (S) and (d) Hall coefficient (R_H) w.r.t. chemical potential (μ) for $Ca_{1-x}Sr_xVO_3$ systems.

4.4.1.2 Thermoelectric Transport Properties of $Ca_{1-x}Sr_xVO_3$

The thermoelectric transport properties of $Ca_{1-x}Sr_xVO_3$ superstructures are determined using a semiclassical linearized variant of BTE through BoltzTraP frameworks. The graph compares (a) electrical conductivity (b) thermal conductivity (c) Seebeck coefficient, and (d) Hall coefficient with absolute temperature scales for undoped and Ca-doped systems (Fig. 58(a)→(d)). The corresponding variations are presented w.r.t. chemical potential at room temperature (Fig. 58 (e)→(h)) to study the tunabilities of thermoelectric behaviors of these systems.

4.4.2 Thermoelectric Transport Properties of Titanate Systems

4.4.2.1 Thermoelectric Transport Properties of $La_{1-x}Sr_xTiO_3$

First principles based computations have become more precise and easy as computational power has improved. The material transport properties are determined by the electronic bandstructure. The BoltzTraP algorithm employ the linearized BTE to determine transport coefficients for a various of materials, such as the site-substituted $La_{1-x}Sr_xTiO_3$ systems (Sevik, 2010; Wang *et al.*, 2019). The nature of variation of electrical and the

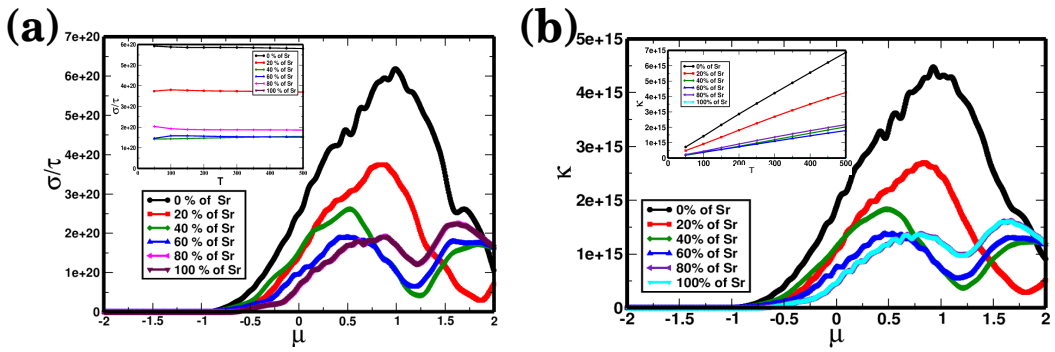

Figure 59: The variation of (a) electrical conductivity (σ/τ) w.r.t. chemical potential (μ) and w.r.t. temperature (inset) (b) thermal conductivity (κ) w.r.t. chemical potential (μ) and temperature (inset) for the site-substituted, $La_{1-x}Sr_xTiO_3$ systems.

electronic thermal conductivities for $La_{1-x}Sr_xTiO_3$ systems are similar with the chemical potential, (μ) as expected for the given materials depicted in (Fig. 59(a), (b)) and the variation of the same parameters w.r.t. temperature for various proportion of Sr-ions are shown in insets.

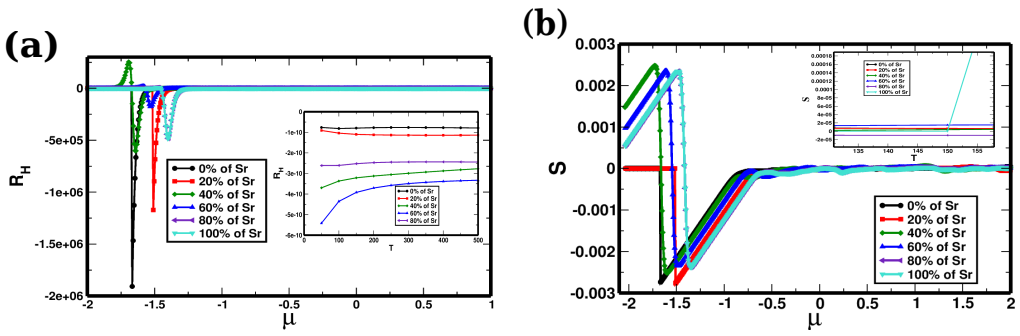

Figure 60: The variation of (a) the Hall coefficient (R_H) w.r.t. chemical potential (μ) and temperature (inset) (b) Seebeck coefficient (S) with chemical potential (μ) and temperature (inset) of the site-substituted, $La_{1-x}Sr_xTiO_3$ systems.

The ultimate goal of studying the transport properties of site-substituted superstructures, $La_xSr_{1-x}TiO_3$ is to investigate prospective thermoelectric materials by understanding

Table 10: The electrical (σ/τ) and thermal (κ) conductivities, Seebeck coefficient (S), magnetic susceptibility (χ), molar specific heat capacity (C), Hall coefficient (R_H) and thermoelectric power factor (TPF) at room temperature (300 K) for titanates systems.

Physical Parameters	$SrTiO_3$	$LaTiO_3$	$LaSrTi_2O_6$	$La_{0.80}Sr_{0.20}TiO_3$
σ/τ (1/(Ωm.s))	1.04×10^{20}	4.66×10^{20}	1.18×10^{20}	0.68×10^{20}
κ (W/m.K.s)	7.89×10^{14}	73.20×10^{14}	8.25×10^{14}	4.76×10^{14}
S (V/K)	-35.8×10^{-6}	-7.22×10^{6}	3.90×10^{-6}	-2.12×10^{-6}
χ (m^3/mol)	9.09×10^{-10}	7.36×10^{-10}	16.50×10^{-10}	21.30×10^{-10}
C (J/mol.K)	1.58	1.11	4.40	3.59
R_H (m^3/C)	-6.66×10^{-10}	-2.70×10^{-10}	-8.06×10^{-10}	-18.00×10^{-10}
TPF	1.35×10^{11}	2.96×10^{11}	0.02×10^{11}	0.003×10^{11}

the key parameters affecting the thermoelectric efficiency. The variation of the Hall coefficient (R_H) and Seebeck coefficient (S) w.r.t. chemical potential (μ) and temperature (inset) are depicted in (Fig. 60(a),(b)). The greater the TPF value, the better the potential materials for thermoelectric applications (Dominguez-Adame *et al.*, 2019). Some of the thermoelectric transport parameters for the titanates systems at room temperature (300 K) are tabulated in Table. 10.

4.4.2.2 Thermoelectric Transport Properties of $Ca_{1-x}Y_xTiO_3$

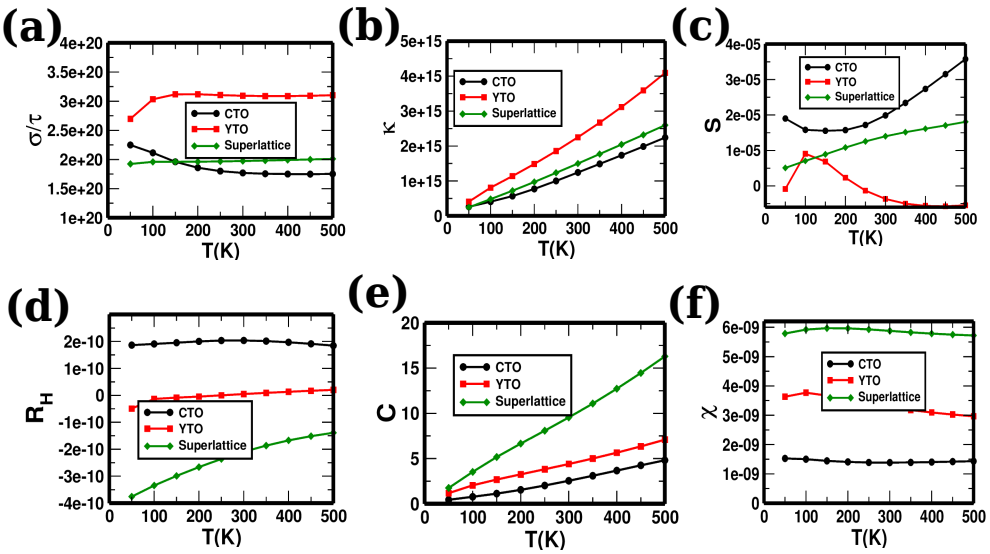

Figure 61: The graphs of various transport parameters w.r.t. the absolute scale of temperature: (a) electrical conductivity (σ/τ) (b) thermal conductivity (κ) (c) Seebeck coefficient (S) and (d) Hall coefficient (R_H) (e) molar specific heat capacity (C) (f) magnetic susceptibility (χ) of the pristine titanates and its site-substituted superstructures, $Ca_{1-x}Y_xTiO_3$ systems.

Furthermore, the effect of reconstruction of superstructures from the pristine titanates, in case of thermoelectric properties are depicted in (Fig. 61(a) $\rightarrow$ (f)) as compared with the pristines constituents. The pristine $CaTiO_3$ (CTO), $YTiO_3$ (YTO) and their

superstructure, $Ca_{0.33}Y_{0.67}TiO_3$ compared for predicting the potential tunability of TE properties of the materials.

From the Study of Thermoelectric Transport Properties of Vanadates and Titanates, we have the following concluding remarks:

The goal of thermoelectric research is to improve the efficiency of heat-to-electricity conversion using various methods. One of the current priorities in this dynamic area is the search for novel and efficient material systems with excellent heat-to-electricity conversion capabilities. There various routes of designing efficient and stable thermoelectric materials, such as site-substituted materials with various proportion of stoichiometric combinations. The thermal conductivity of a system varies with temperature, whereas its electrical conductivity almost remains constant. The Seebeck and Hall coefficients are compared for superstructures with various Sr -ions site-substitutions. For the system with the various concentration of Sr-ions, the thermoelectric phase transition with chemical potential is determined to be at around $\mu \sim$ -1.40 eV. Both of the systems $La_{1-x}Sr_xTiO_3$ and $La_{1-x}Ca_xVO_3$ could be the promising candidate for thermoelectric applications. In brief, it can be inferred that the tunabilities for better and efficient TE devices (STEG, RITEG, Freezer and so on) are possible with the site-substitution of cations and re-construction of hetero-structuring these TMOs materials.

4.5 Optical Properties of the Vanadates and Titanates

4.5.1 Optical Properties of the Vanadate Systems

4.5.1.1 Optical Properties of $La_{1-x}Ca_xVO_3$

The optical response of the materials is used to examine the optically induced behavior of materials. The variation of the real component of the dielectric function, ELOSS function, reflectivity, and absorptivity w.r.t. photon energy (eV) for various Ca^{+2} ions in the superstructure are shown in (Fig. 62(a),(b),(c)). These findings reveal that a 60% Ca-doped vanadate has a distinct response and is active in the infrared and visible regions, indicating that it is a viable option for photo-induced applications.

The real part of refractive index and optical conductivity vs. photon energy (eV) curves show variations for different doping levels (Fig. 63(a),(b)). These curves show larger

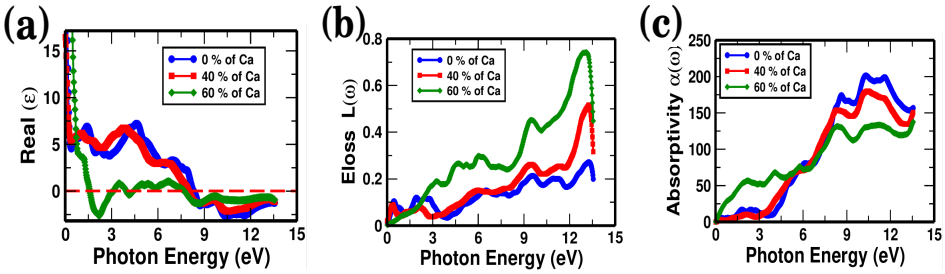

Figure 62: The graphs of (a) the dielectric function (Re $(\varepsilon(\omega))$ vs. photon energy (b) the ELOSS function, L(ω) vs. photon energy and (c) the Absorptivity, $\alpha(\omega)$ vs. photon energy for the $La_{1-x}Ca_xVO_3$ system.

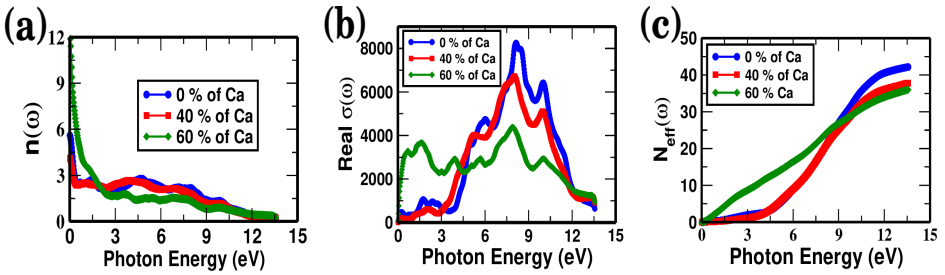

Figure 63: The graphs of (a) the refractive indices, n(ω) vs. photon energy (b) the real part of the optical conductivity Re $(\sigma(\omega))$ vs. photon energy and (c) the optical weight $N_{eff}(\omega)$ versus photon energy for the $La_{1-x}Ca_xVO_3$ systems.

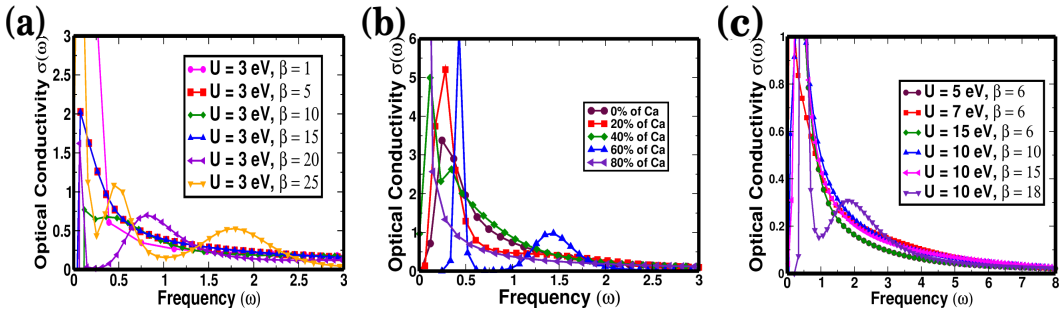

Figure 64: The plots of (a) the optical conductivity, $\sigma(\omega)$ vs. (ω) for a constant U and the variation of β of the $La_{1-x}Ca_xVO_3$ system (b) the variation of optical conductivity $\sigma(\omega)$ vs. (ω) with different proportions of Ca-ions substitution for (U = 10.0 eV, β = 15.0 $(eV)^{-1}$) these systems, and (c) the variation of optical conductivity $\sigma(\omega)$ vs. (ω) with various sets of U and β values for $La_{0.40}Ca_{0.60}VO_3$ system.

optical conductivity for IR and visible EM spectrum with the superstructure of 60% Ca^{2+} substituted sample (Fig. 63(b)). However, other superstructures show maxima values at around 8-9 eV (UV radiation) with an optical gap at the start. The f-sum rules of transition measure the optical weight (the effective number of oscillators or electrons) during the electromagnetic interactions (Fig. 63(c)), which are compatible with optical conductivity at all frequencies. The MEM approach of AC is used to estimate optical conductivity from CT-QMC data across various values of U and β ranges. The material exhibits insulating behavior below $\beta \approx 15.0(eV)^{-1}$ with U = 3.0 eV (Fig. 64(a)). Additional peaks beyond the Drude peak indicate different kinds of transition (Blümer, 2007), with larger conductivity associated with a narrowing peak at $\omega = 0$.

At low frequency regime the quasiparticle conductivity is accounted for the Drude peak in the spectrum. Its breadth indicates the charge carriers' dispersion rate, while its total weight represents their effective mass. By comparing the weight to the value in the DFT, the mass augmentation induced by dynamical correlations is computed.

In practice, the correlations effect diminishes the Drude weight and causes its value to vanish in a Mott insulator (Blümer, 2007). Our calculations reproduce conventional DMFT results without disorder (Tohyama *et al.*, 2005; Nakano *et al.*, 2007), revealing optical conductivity with a Drude peak at low frequencies. The frequency dependence of optical conductivity changes qualitatively by the introduction of disorder. The Hubbard-Anderson model's optical conductivity is strongly impacted on varying stoichiometric compositions of La/Ca ratios (Fig. 64(b)). The redistribution of optical conductivities are estimated for various U and β values (Fig. 64(c)), show that lower U and β values lead to closer Drude peaks and diminished Drude peaks at higher values of U and β.

4.5.1.2 Optical Properties of $(La_{1-x}Sr_xVO_3)_n$(n=2)

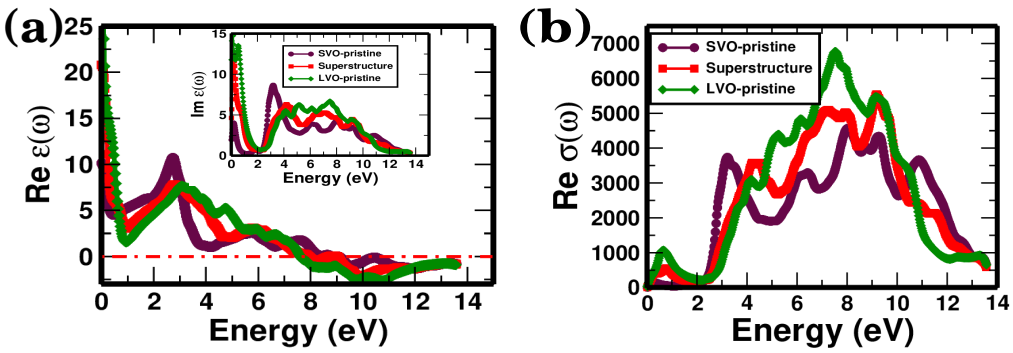

Figure 65: The graphs of (a) the real parts of dielectric function vs. energy (eV) and its imaginary parts (inset) (b) the real part of optical conductivity vs. energy (eV) for the $(La_{1-x}Sr_xVO_3)_n$ systems.

The study explores the relationship between the real and imaginary parts of the dielectric function $\varepsilon(\omega)$ and optical conductivity for pristines $SrVO_3$, $LaVO_3$, and $LaSrV_2O_6$ superstructure (Fig. 65(a). It shows a decreasing dispersiveness with photon energy, becoming negative at around 7.5 eV of UV region (Wooten, 1973; Scafetta *et al.*, 2014). The imaginary part of the dielectric function is related to optical conductivity, $\sigma(\omega)$ and other optical parameters.

The typical peak values of the optical conductivity for pristine SVO, LVO, and $LaSrV_2O_6$ are found to be 4605.26 $(\Omega cm)^{-1}$, 6736.84 $(\Omega cm)^{-1}$, and 5447.37 $(\Omega cm)^{-1}$, respectively, which lies around (7-10) eV of photon energy of UV regions (Fig. 65(b)). The real part of complex refractive indices for all the superstructures show similar variation with

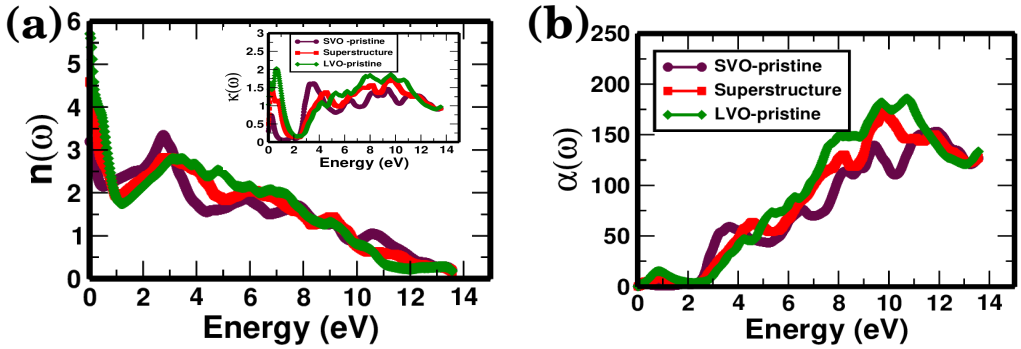

Figure 66: The plots of (a) the refractive indices vs. photon energy (b) the absorptivity vs photon energy for the $(La_{1-x}Sr_xVO_3)_n$(n = 2; x = 0, 0.5, 1) system.

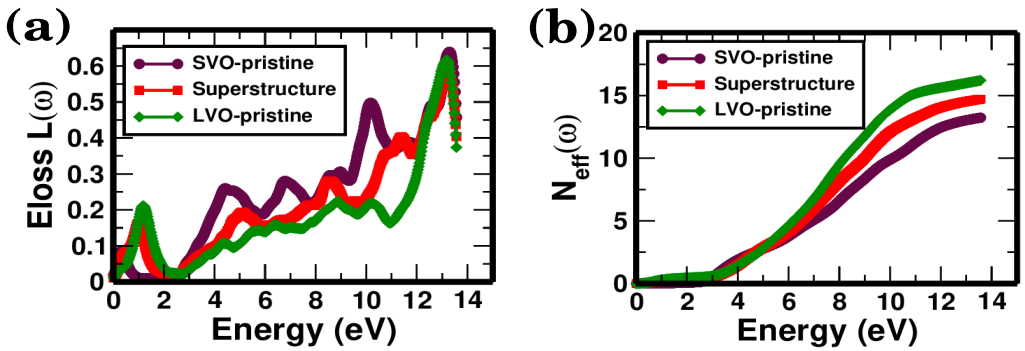

Figure 67: The plots of (a) the ELOSS function vs. energy (b) the optical weight, $N_{eff}(\omega)$ vs. energy for $(La_{1-x}Sr_xVO_3)_n$ system.

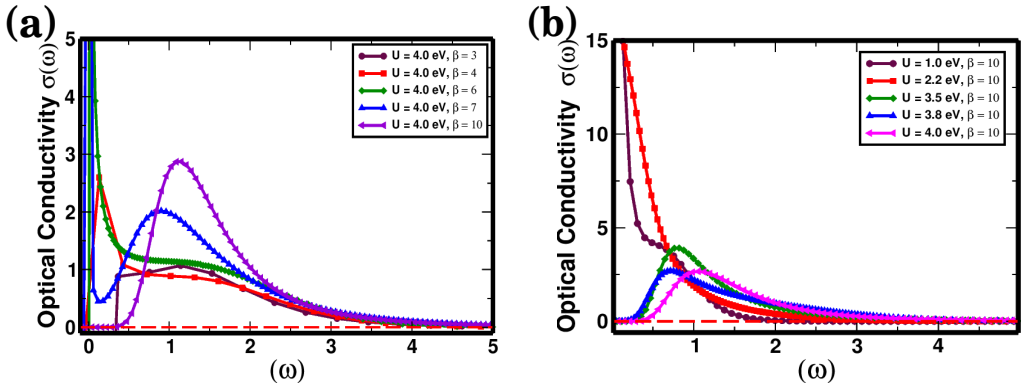

Figure 68: The graphs for (a) the optical conductivity $\sigma(\omega)$ vs. frequency (ω) for a constant U = 4.00 eV with β variation (b) the optical conductivity $\sigma(\omega)$ vs. frequency (ω) for a constant β = 10.00 $(eV)^{-1}$ with U variation for $(La_{1-x}Sr_xVO_3)_n$ system.

higher values in the infrared region (Fig. 66(a)) and secondary peaks at around 3.00 eV photon energy. Materials' absorptivity during EM interaction is measured (Fig. 66(b)), and the interband optical transition occurs through photon absorption, which occurs when photon energy equals the optical gap's energy.

The electron energy loss spectroscopy is a useful optical parameter for analyzing electromagnetic interaction with materials. Its peak values are close to 0.60 in arb. units

(Fig. 67(a)) for all superstructures. Energy losses in materials are mainly generated by simple electronic and collective excitations(called plasmon excitation), evaluating the likelihood of volume loss of energy in the solid (McAlister & Stern, 1963). The photon energy (eV) associated with the highest peak of ELOSS function corresponds to plasma resonance associated with plasma frequency (ω_p).

The f-sum rules for transitions measure optical weight, which contribute to the effective number of oscillators during absorption or emission of EM radiation (Fig. 67(b)). These rules are consistent with optical conductivity at any frequency. Some of the static values ($\omega \sim 0$) of optical parameters are tabulated in Table. 11.

Table 11: The real part of static dielectric function ($\omega \sim 0$) Re $\varepsilon(0)$, static refractive index $n(0)$, static real part of optical conductivity $\sigma(0)$, static absorption coefficient $\alpha(0)$, static optical reflectivity R(0), ELOSS function L(0), static optical weight $Z_{eff}(0)$, and plasma frequency (ω_p) from all the examples of ELOSS functions.

Optical Parameters	$SrVO_3$	$LaVO_3$	$LaSrV_2O_6$	$La_{0.40}Ca_{0.60}VO_3$
Re.$\varepsilon(0)$	230.25	-1401.15	20.85	140.07
n(0)	15.25	67.43	4.58	12.06
Re.$\sigma(0)$ $(1/\Omega.cm)$	0.07	19064	0.02	0.04
$\alpha(0)$ $(10^4/cm)$	0.08	0.05	0.15	0.22
L(0) (arb. units)	0.00	0.00	0.01	0.00
$Z_{eff}(0)$	0.00	0.11	0.01	0.04
ω_p(eV/$\hbar$)	8.31	12.94	13.20	13.12

The CT-QMC along with MEM approach is used to compute the optical properties of superstructures (Bergeron & Tremblay, 2016), estimating optical conductivity using the MaxEnt model and SF with optimal α value.

The variation of these model parameters broadens or suppresses the metallic Drude peak at zero frequency ($\omega \sim 0$) (Fig. 68(a)) (Blümer, 2007; Kim, 2018). The Mott-Hubbard band splittings are supported by Drude peaks for different combinations of model parameters (U and β).

The Drude peaks at around $\omega \sim 0$ vanish with larger U (Fig. 68(b)), indicating a phase change from metallic to insulating due to carrier localization of the systems.

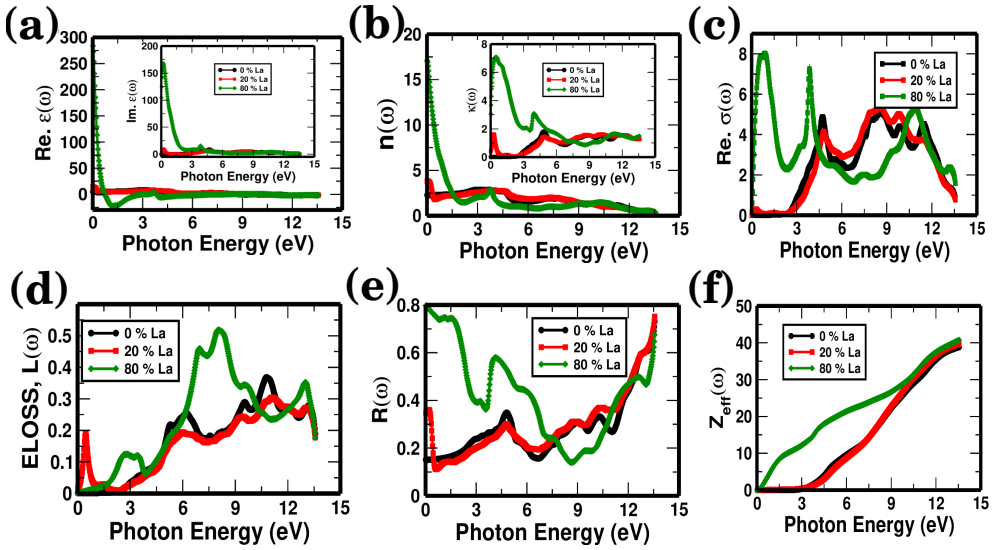

Figure 69: The plots for (a) the dielectric function vs. the photon energy (b) the index of refraction vs. the photon energy (c) the optical conductivity vs. the photon energy (d) the ELOSS function vs. photon energy (e) the reflectivity vs. photon energy, and (f) the optical weights (sumrule) vs. photon energy for the $La_{1-x}Sr_xTiO_3$ systems.

4.5.2 Optical Properties of the Titanate Systems

4.5.2.1 Optical Properties of $La_{1-x}Sr_xTiO_3$

The dispersive behavior of a material is associated with the real part, $\mathrm{Re}\ \varepsilon_{ij}(\omega)$, whereas the absorptive behavior is associated with the imaginary part, $\mathrm{Im}\ \varepsilon_{ij}(\omega)$, as shown in Fig. 69(a). The static dielectric function is defined as the value of $\mathrm{Re}.\varepsilon_{ij}(\omega)$ at zero frequency and is represented by $\varepsilon_{ij}(0)$, and its value varies for various site-substituted supercells, $La_{1-x}Sr_xTiO_3$. The refraction index of a material is described by the expression $n_{ii}(\omega)$, which is determined for $La_{0.80}Sr_{0.20}TiO_3$ and depicted in Fig. 69(b). The zero frequency index of refraction is represented by the static number $n_{ii}(0) \sim 17.00$. In the visible area of the electromagnetic spectrum, $n_{ii}(\omega)$ drops beyond this value.

Beyond this point, the real part of dielectric function, $\mathrm{Re}\ \varepsilon_{ij}(\omega)$ changes and reaches a maximum of 282.65 for $La_{0.80}Sr_{0.20}TiO_3$, suggesting that the static dielectric function is significantly higher than other superstructures. At $\sim$ 0.71 eV energy, the $\mathrm{Re}\ \varepsilon_{ij}(\omega)$ curve goes to the negative side, corresponding to the point of high optical conductivity and high reflectivity of the $La_{0.80}Sr_{0.20}TiO_3$ system. As a result, the $La_{0.80}Sr_{0.20}TiO_3$ system loses its dielectric property and exhibits metallic nature in the energy range of 0.71 eV to 3.10 eV (Fig. 69(c),(e)). In the visible range, the optically active system among the three superstructures is $La_{0.80}Sr_{0.20}TiO_3$. The imaginary part of the dielectric function, $\mathrm{Re}\ \varepsilon_{ij}(\omega)$, represents absorptive behaviors of the materials.

The real part of optical conductivity, $\mathrm{Re}\ \sigma_{\mathrm{ij}}(\omega)$, exhibits extremely small values in the IR and visible areas for superstructures with 0% and 20% La -ions. After then, the conductivity rises due to the shift from O -2p to V -3d orbitals, resulting in several peaks in the ultraviolet area for these superstructures.

The static reflectivity, $\mathrm{R_{ij}}(0)$ has a maximum value of $\sim$80% occurs at around zero frequency and the minima of reflectivity $\sim$13% occurs at around 8.8 eV photon energy for $\mathrm{La_{0.80}Sr_{0.20}TiO_3}$ system.

Energy loss (ELOSS) function, $\mathrm{L_{ij}}(\omega)$ is associated with the resonance of plasmon frequency of incident radiations. For the samples with 0% and 20% site-substituted systems the plasmon resonance occur at around $\approx$ 11.00 eV are plotted in (Fig. 69(d)). But, the ELOSS function varies with energy uniquely for $\mathrm{La_{0.80}Sr_{0.20}TiO_3}$ system having four major peaks at around 2.90 eV, 6.93 eV, 8.15 eV and 13.00 eV of photon energies, respectively.

In the VB, the effective number of oscillators (electrons) per unit cell, $\mathrm{N}_{eff}(\omega)$ can be estimated from the sum rule as shown in (Fig. 69(f)). These are the electrons which take part in inter- and intra -band transitions. For the superstructures of 0% and 20% La -ions substitution, there is no significant number of oscillator in the IR and visible regions, but it increases gradually and almost linearly in the UV region. In case of $\mathrm{La_{0.80}Sr_{0.20}TiO_3}$ system, the value of $\mathrm{N}_{eff}(\omega)$ is significant in the vision region as well, indicating that this superstructure is viable for optically induced device applications.

4.5.2.2 Optical Properties of $\mathbf{Ca_{1-x}Y_xTiO_3}$

In this case also, it is clearly observed that the optical parameters are substantially altered due to site -substitution of Ca -ions by Y -ions as shown in (Fig. 70(a) $\rightarrow$ (f)) in $\mathrm{Ca_{1-x}Y_xTiO_3}$ system.

Finally, the study of optical properties of vanadates and titanates revealed the following concluding remarks:

The frequency -dependent optical conductivity, $\sigma(\omega)$ and optical weight (sum -rule) are consistent with the results of MIT, as expected by DMFT and the MEM. The optical properties calculations show that site substituted compositions undergo electronic MIT

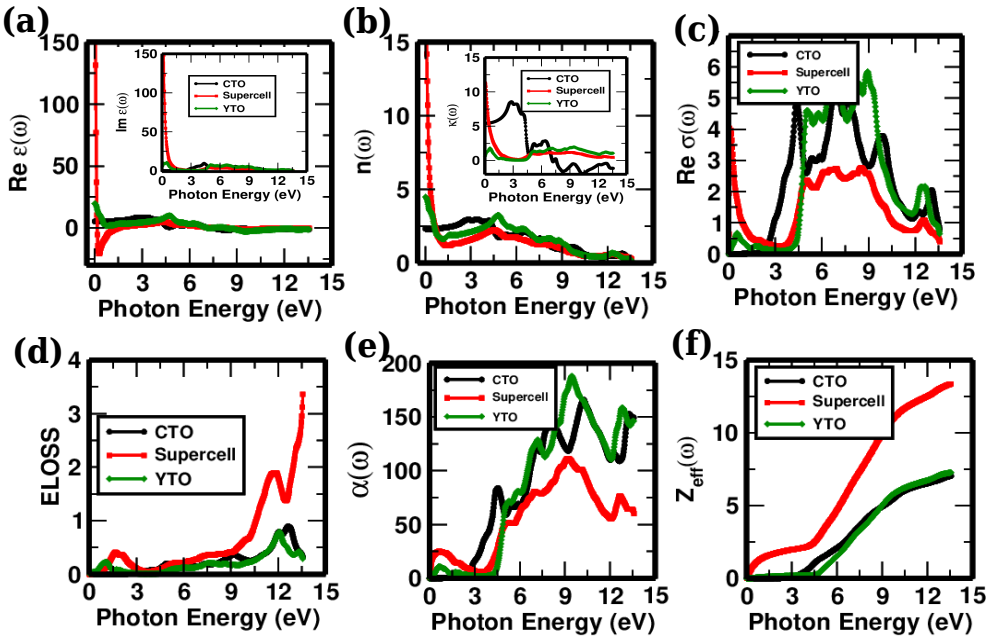

Figure 70: The graph of (a) the real and imaginary parts (inset) of the dielectric function w.r.t. photon energy (b) the real part of complex index of refraction and extinction coefficient $\kappa(\omega)$ (inset) w.r.t. photon energy (c) the real part of optical conductivity w.r.t. photon energy (d) the ELOSS function w.r.t. photon energy (e) the absorptivity w.r.t. photon energy, and (f) the variation of optical weights (sumrule) w.r.t. photon energy for the $Ca_{1-x}Y_xTiO_3$ systems.

based on U and β interaction. The optically induced conductivity are clearly observed for some of the stoichiometric compositions indicating that (a) The field driven memristors are potential candidates for neuromorphic computing due to the feasibility of their ultrahigh -density 3D integration and their ultralow energy consumption. (b) Mott insulators are the class of strongly correlated materials with emergent properties useful for designing the artificial neural networks, and (c) Resistive Switching (RS) of Mott Insulators are highly applicable for designing RRAM devices, an emerging type of non-volatile memories, based on the external perturbation (electrical, thermal,chemical, optical) driven RS of an active material.

CHAPTER 5

CONCLUSIONS AND RECOMMENDATIONS

The overall conclusions drawn from the present study of the pristine titanates and vanadates systems, and their site-substituted superstructures are presented briefly as follows,

5.1 Stability of Titanates and Vanadates

The structural stability of the pristine and its superstructures are investigated using the energy minimization approach whereas the chemical and mechanical stabilities are examined through cohesive and formation energies calculation, and elastic parameters. The energy vs. lattice parameter (or volume) curves provide the information of structural stability. The optimized lattice parameters for the pristine titanates are mentioned in the parentheses, $LaTiO_3$ (a = 3.92 Å), $CaTiO_3$ (a = 3.88 Å), $YTiO_3$ (a = 3.89 Å) and $SrTiO_3$ (a = 3.94 Å), and the optimized lattice parameters for pristine vanadates are, $LaVO_3$ (a = 3.94 Å), $CaVO_3$ (a = 3.71 Å), $SrVO_3$ (a = 3.86 Å) and YVO_3 (a = 3.85 Å), respectively, which are followed by the optimized lattice parameters (mentioned in the parentheses) for their typical superstructures, $[(La_{1-x}Sr_xVO_3)_n$ (a = b = 3.96 Å, c = 7.92 Å)] , $[(Ca_{1-x}Sr_xVO_3)_n$ (a = b = 3.95 Å, c = 7.91 Å)], $[(La_{1-x}Ca_xVO_3)_n$ (a = b = 3.95 Å, c = 19.48 Å)], $[(LaCaTi_2O_6)_n$ (a = b = 3.85 Å, c = 7.91 Å)], $[(Ca_{1-x}Y_xTiO_3)_n$ (a = b = 3.88 Å, c = 11.67 Å)], $[(LaSrTi_2O_6)_n$ (a = b = 3.96 Å, c = 7.92 Å)], and $[(La_{1-x}Sr_xTiO_3)_n$ (a = b = 3.85 Å, c = 19.44 Å)] systems, respectively.

The formation energies are found to be, -3.01 eV/atom, -3.18 eV/atom, -2.97 eV/atom, -0.59 eV/atom eV/atom, -3.60 eV/atom, and -2.99 eV/atom for $CaVO_3$, $LaVO_3$, $SrVO_3$, YVO_3, $LaSrV_2O_6$, and $La_{0.40}Ca_{0.60}VO_3$ systems, respectively and cohesive energies for $CaVO_3$, $LaVO_3$, $SrVO_3$, YVO_3, $LaSrV_2O_6$, and $La_{0.40}Ca_{0.60}VO_3$ systems are found to

be -7.53 eV/atom, -7.56 eV/atom, -6.96 eV/atom, -3.53 eV/atom, -7.79 eV/atom, and -7.20 eV/atom, respectively. Similarly, the formation energies for the titanates, $CaTiO_3$, $LaTiO_3$, $SrTiO_3$, $YTiO_3$, $LaSrTi_2O_6$, ,$LaCaTi_2O_6$, $Ca_{0.33}Y_{0.67}TiO_3$ and $La_{0.80}Sr_{0.20}TiO_3$ are calculated to be, 3.34 eV/atom, -2.97 eV/atom, -2.72 eV/atom, 3/20 eV/atom, -3.07 eV/atom, -3.05 eV/atom, -3.27 eV/atom and -2.66 eV/atom, respectively and the cohesive energies for $CaTiO_3$, $LaTiO_3$, $SrTiO_3$, $YTiO_3$, $LaSrTi_2O_6$, $LaCaTi_2O_6$, $Ca_{0.33}Y_{0.67}TiO_3$ and $La_{0.80}Sr_{0.20}TiO_3$ are calculated to be, -7.15 eV/atom, -7.65 eV/atom, -7.74 eV/atom, -6.90 eV/atom, -7.71 eV/atom, -7.68 eV/atom, 7.00 eV/atom and -2.83 eV/atom, respectively. The negative values of cohesive and formation energies signify the chemical stabilities of the systems. The findings are consistent with the available theoretical and experimental data.

Mechanical stability criteria based on elastic parameters reveal that all these materials are mechanically stable. In short, all the pristine titanates and vanadate systems under study and their super structures show structural, chemical and mechanical stabilities. Hence, they are viable to experimental synthesis for the present and future device applications.

5.2 Electronic Transport Properties of Titanates and Vanadates

The electronic related properties are discussed firstly using DFT approach with PBE exchange correlation functionals under GGA and mBJ frameworks. The data whatever obtained from DFT are used for DMFT (CTQMC-Technique) along with MEM model.

All the pristine systems except $SrTiO_3$ and $CaTiO_3$ are metallic in nature which contradict with the available experimental results, while they supports other theoretical calculations. Experimentally $CaVO_3$, $SrVO_3$ are found to be correlated metals, whereas $LaVO_3$, $LaTiO_3$, $YTiO_3$ and YVO_3 are Mott insulators. The systems $SrTiO_3$ and $CaTiO_3$ show band insulating properties with band gap 3.42 eV and 2.76 eV under the GGA and mBJ approaches. Most of the site-substituted superstructures are observed to be the correlated metals or semiconductors in nature.

For the realistic picture, we implemented DMFT approach for these correlated systems. From the calculation the MIT parameters for band splittings of pristines and superstructures of titanate systems are mentioned in the parentheses as, $LaTiO_3$ (U = 4.0 eV, β = 8.0 $(eV)^{-1}$), $YTiO_3$ (U = 5.0 eV, β = 10.0 $(eV)^{-1}$), $LaSrTi_2O_6$ (U = 4.7 eV, β = 6.0 $(eV)^{-1}$),

$La_{0.8}Sr_{0.2}TiO_3$ (U = 3.2 eV, β = 10.0 $(eV)^{-1}$) and $Ca_{0.33}Y_{0.67}TiO_3$ (U = 5.0 eV, β = 7.0 $(eV)^{-1}$), respectively. Similarly, the MIT parameters of pristines and superstructures of vanadate systems are mentioned in the parentheses as, $CaVO_3$ (U = 5.0, eV, β = 6.0 $(eV)^{-1}$), $LaVO_3$ (U = 4.5 eV, β = 8.0 $(eV)^{-1}$), $SrVO_3$ (U = 2.5 eV, β = 6.0 $(eV)^{-1}$), $LaSrV_2O_6$ (U = 4.0 eV, β = 10.0 $(eV)^{-1}$) and $La_{0.4}Ca_{0.6}VO_3$ (U = 5.0 eV, β = 10.0 $(eV)^{-1}$) respectively.

The quasi-particle spike around the Fermi level of the $\mathrm{La_{0.80}Sr_{0.20}TiO_3}$ and $\mathrm{La_{0.40}Ca_{0.40}VO_3}$ systems are observed with the same set of model parameters, U = 3.0 eV and β = 6.0 $(eV)^{-1}$. We calculated the coexistence region of metallic and insulating phases, as well as the materials' QCP. The Mott QCP at an elevated temperature are found to be U_C = 2.95 eV and β_C = 23.58 $(eV)^{-1}$ for $\mathrm{La_{0.40}Ca_{0.40}VO_3}$ superstructure system.

5.3 Thermoelectric and Optically Driven Transport Properties

The electrical and thermal conductivities vary in a similar fashion w.r.t. the chemical potential for different systems at a constant temperature. The thermal conductivity changes linearly w.r.t. temperature, while the electrical conductivity is observed to be less temperature dependent for a given system. The peak value of Seebeck coefficient and the thermoelectric phase transition occurring at around, $\mu \sim$ -1.40 eV for $La_{0.80}Sr_{0.20}TiO_3$ systems, indicating that, the system is promising candidates for thermoelectric applications. Furthermore, the peak values of the electrical and thermal conductivities at room temperature of $\mathrm{La_{0.40}Ca_{0.60}VO_3}$ specimen are calculated to be, 2.11$\times$ 10^{20} $(\Omega\ \mathrm{m\ s})^{-1}$ and 1.54$\times$ 10^{15} $\mathrm{W/(m.K.s)}$, respectively, for a chemical potential μ = - 0.14 eV.

The calculations of dielectric function and related optical parameters w.r.t. photon energy (eV) in the IR-to-UV (0 -20.0 eV) region help to understand the photo -induced behaviors of materials. It is to be noted here that the thermoelectrically active materials: $\mathrm{La_{0.40}Ca_{0.60}VO_3}$ and $\mathrm{La_{0.80}Sr_{0.20}TiO_3}$ are also interestingly active optically in the visible range of EM spectrum.

The values of static dielectric function ($\epsilon_{\mathrm{ij}}(0)$) depend upon the concentration of site-substituted elements on the supercell, $\mathrm{La_{1-x}Sr_xTiO_3}$. The value of $\mathrm{Re}\ \epsilon_{\mathrm{ij}}(\omega)$ varies and reaches a maximum of 282.65 for $\mathrm{La_{0.80}Sr_{0.20}TiO_3}$, suggesting that the static dielectric function is significantly greater than the other superstructures. At $\sim$ 0.71 eV photon

energy, the $\mathrm{Re}\ \epsilon_{ij}(\omega)$ curve shifts to the negative side, corresponding to the point of high optical conductivity and high reflectivity of the $La_{0.80}Sr_{0.20}TiO_3$ system. It loses its dielectric property at this point and exhibits metallic nature in the energy range of 0.71 eV to 3.10 eV. It is to be noted here that the optically active systems among the superstructures are found to be, $La_{0.40}Ca_{0.60}VO_3$ and $La_{0.80}Sr_{0.20}TiO_3$ for the visible spectral ranges. The frequency-dependent optical conductivity $\sigma(\omega)$ and spectral weight are consistent with the MIT as expected by the results of DMFT and the MEM.

The optical properties of site-substituted superstructures are anisotropic in nature which is important for controlling Mott-mechanism for the materials. The tuning of Mott-resistive mechanism through photo induced applications is also a highly sought applications for resistive switching, neuromorphic computing, resistive memory devices and artificial neuron.

5.4 Recommendations for the Future Study

The following recommendation have been proposed for the further enhancement and implementation of the present study.

a. These materials harbor plethora of exotic novel properties, so one can design and study various morphological structures (0 D, 1 D, 2 D, 3 D etc.) for smart device applications.

b. Resistive switching (reversible switching) of Mott insulators are useful for designing resistive random access memories (RRAM) devices, an emerging type of non-volatile memories that can outperform the existing technology (Flash memory, Dynamic RAM), could be driven by the external perturbation (electrical, thermal, chemical, optical, and mechanical etc.)

c. We recommend to work on the electronic device miniaturization through heterostructuring and nanostructuring of the systems for various smart devices, such as the quantum and neuromorphic computing, artificial neuron, and other machine learning devices from a mesoscopic scale to nanoscopic scale to improve their efficiencies.

There are many researchers exploring the promising category of materials and new physical phenomena using hetero-structuring, nano-structuring, and band control and filling control methods for building quantum dots, quantum wires, quantum wells, and various smart materials of the present and future technological needs.

CHAPTER 6

SUMMARY

In this study, we used various theoretical models to investigate the structural, chemical and mechanical stabilities, and electronic, thermoelectric and optically driven transport properties of various site-substituted superstructures of complex transition metal oxides: ((La,Sr)TiO_3/(Ca,Y)VO_3). The DFT, DMFT and MEM are employed for electronic transport properties. Using the non-interacting parameter (electron density), the DFT estimates the ground state characteristics of a many-body interacting system. The data obtained from DFT calculation are then used for the electronic, and thermoelectric and optically driven transport properties.

The optimized energy vs. lattice parameter(or volume) shows the structural stability of a system. The optimized lattice parameters for the pristine titanates are mentioned in the parentheses, $LaTiO_3$ (a = 3.92 Å), $CaTiO_3$ (a = 3.88 Å), $YTiO_3$ (a = 3.89 Å) and $SrTiO_3$ (a= 3.94 Å), and the optimized lattice parameters for the pristine vanadates are, $LaVO_3$ (a = 3.94 Å), $CaVO_3$ (a = 3.71 Å), $SrVO_3$ (a = 3.86 Å) and YVO_3 (a = 3.85 Å), respectively followed by the optimized lattice parameters (mentioned in the parentheses) of their typical superstructures are, $[(La_{1-x}Sr_xVO_3)_n$ (a = b = 3.96 Å, c = 7.92 Å)] , $[(Ca_{1-x}Sr_xVO_3)_n$ (a = b = 3.95 Å, c = 7.91 Å)], $[(La_{1-x}Ca_xVO_3)_n$ (a = b = 3.95 Å, c = 19.48 Å)], $[(LaCaTi_2O_6)_n$ (a = b = 3.85 Å, c = 7.91 Å)], $[(Ca_{1-x}Y_xTiO_3)_n$(a = b = 3.88 Å, c = 11.67 Å)], $[(LaSrTi_2O_6)_n$ (a = b = 3.96 Å, c = 7.92 Å)], and $[(La_{1-x}Sr_xTiO_3)_n$ (a = b = 3.85 Å, c = 19.44 Å)] systems.

The negative values of formation energies of the vanadates are found to be, -3.01 eV/atom, -3.18 eV/atom, -2.97 eV/atom, -0.56 eV/atom, -3.60 eV/atom, and -2.99 eV/atom for $CaVO_3$, $LaVO_3$, $SrVO_3$, YVO_3, $LaSrV_2O_6$, and $La_{0.40}Ca_{0.60}VO_3$ systems, respectively and the cohesive energies for $CaVO_3$, $LaVO_3$, $SrVO_3$, YVO_3, $LaSrV_2O_6$, and $La_{0.40}Ca_{0.60}VO_3$ systems are found to be, -7.53 eV/atom, -7.56 eV/atom, -6.96 eV/atom, -3.53 eV/atom, -7.79 eV/atom, and -7.20 eV/atom, respectively.

Similarly, the formation energies for the titanates: $CaTiO_3$, $LaTiO_3$, $SrTiO_3$, $YTiO_3$, $LaSrTi_2O_6$, ,$LaCaTi_2O_6$, $Ca_{0.33}Y_{0.67}TiO_3$ and $La_{0.80}Sr_{0.20}TiO_3$ systems, are calculated as, 3.34 eV/atom,

-2.97 eV/atom, -2.72 eV/atom, 3/20 eV/atom, -3.07 eV/atom, -3.05 eV/atom, -3.27 eV/atom and -2.66 eV/atom, respectively and the cohesive energies for $CaTiO_3$, $LaTiO_3$, $SrTiO_3$, $YTiO_3$, $LaSrTi_2O_6$, $LaCaTi_2O_6$, $Ca_{0.33}Y_{0.67}TiO_3$ and $La_{0.80}Sr_{0.20}TiO_3$ systems are calculated as, -7.15 eV/atom, -7.65 eV/atom, -7.74 eV/atom, -6.90 eV/atom, -7.71 eV/atom, -7.68 eV/atom, 7.00 eV/atom and -2.83 eV/atom, respectively. The higher negative values of the cohesive and formation energies signify the stronger the system's structural and chemical stability and viability for experimental synthesis. From the elastic calculation, the positive Cauchy pressure values imply that the systems are metallic with ductile properties, whereas negative values indicate that the systems are covalently bonded.

The data obtained from DFT is taken as input data for CT-QMC with hybridization expansion solving the DMFT equation, which gives the GF data of imaginary time and frequency, which is then used for investigating the metal-insulator phase transition (MIT) through MEM. From the study, the MIT parameters for Mott-Hubbard band splittings of pristines and superstructures of vanadate systems are mentioned in the parentheses, $CaVO_3$ (U = 5.0 eV, β = 6.0 $(eV)^{-1}$), $LaVO_3$ (U = 4.5 eV, β = 8.0 $(eV)^{-1}$), $SrVO_3$ (U = 2.5 eV, β = 6.0 $(eV)^{-1}$), $LaSrV_2O_6$ (U = 4.0 eV, β = 10.0 $(eV)^{-1}$) and $La_{0.4}Ca_{0.6}VO_3$ (U = 5.0 eV, β = 10.0 $(eV)^{-1}$), respectively. Similarly, the DMFT results of MIT parameters of pristines and superstructures of titanate systems are mentioned in the parentheses, $LaTiO_3$ (U = 4.0 eV, β = 8.0 $(eV)^{-1}$), $YTiO_3$ (U = 5.0 eV, β = 10.0 $(eV)^{-1}$), $LaSrTi_2O_6$ (U = 4.7 eV, β = 6.0 $(eV)^{-1}$), $La_{0.8}Sr_{0.2}TiO_3$ (U = 3.2 eV, β = 10.0 $(eV)^{-1}$) and $Ca_{0.33}Y_{0.67}TiO_3$ (U = 5.0 eV, β = 7.0 $(eV)^{-1}$), respectively.

The MEM is used to compute the Mott gap and quasi-peak model parameters via analytic continuation of CT-QMC data. The study of Mott gaps are critical for a variety of technological and engineering purposes, whereas the MIT model parameters for quasi-particle peaks are critical for quantum information technology. The MIT parameters are crucially important for designing Mottronic devices like neuromorphic computing, quantum computing, resistive memory devices, LIF artificial neurons for neural networks, and so on.

Furthermore, we calculated the coexistence region of metallic and insulating phases as well as the QCP at an elevated temperature for the $La_{0.40}Ca_{0.60}VO_3$ system. The Mott QCP is attained at U_C = 2.95 eV and β_C = 23.58 $(eV)^{-1}$.

The thermal conductivity of a system varies dramatically with temperature, although the electrical conductivity remains constant with temperature. The Seebeck coefficient (S) and Hall coefficient (R_H) for superstructures with different proportions of Sr or Ca-ions

are compared. Thus, the $La_{1-x}Sr_xTiO_3$ and $La_{1-x}Ca_xVO_3$ systems with 20%, 60%, and 80% site-substituted compounds are promising candidates for higher temperature thermoelectric applications. The study show that these titanates and vanadates systems suggests that tunabilities for improved and more efficient TE devices are conceivable by site-substitution of cations and re-construction of superstructuring these systems.

The optical properties calculations reveal that site substituted combinations of materials undergo electronic MIT due to U and β interactions, which is consistent with previous calculations. From the calculation of the frequency dependence of optical conductivity $\sigma(\omega)$ and optical spectral weight confirm the MIT predicted by DMFT and MEM.

In short, these materials are crucially important for developing next-generation quantum technologies, aiming for a safe and sustainable development of our society. The potential applications include dissipationless electronics, energy harvesting devices, secure communications, quantum computing, neuromorphic computing, resistive memory, and all kinds of machine learning devices.

REFERENCES

Adamo, C. and Barone, V. (1999). Toward Reliable Density Functional Methods without Adjustable Parameters: The PBE0 model. *The Journal of Chemical Physics*, **110**(13): 6158-6170. https://doi.org/10.1063/1.478522

Adewale, A. A., Chik, A., Zaki, R. M., Pa, F. C., Keat, Y. C., *et al.* (2018). Thermoelectric Transport Properties of $SrTiO_3$ Doped with Pm. *Solid State Phenomena*, **280**: 3-8. https://doi.org/10.4028/www.scientific.net/SSP.280.3

Ali, R. and Yashima, M. (2005). Space Group and Crystal Structure of the Perovskite $CaTiO_3$ from 296 to 1720 K. *Journal of Solid State Chemistry*, **178**(9): 2867-2872. https://doi.org/10.1016/j.jssc.2005.06.027

Ambrosch-Draxl, C. and Sofo, J. O. (2006). Linear Optical Properties of Solids within the Full-potential Linearized Augmented Planewave Method. *Computer Physics Communications*, **175**(1): 1-14. https://doi.org/10.1016/j.cpc.2006.03.005

Anderson, O. L. (1963). A Simplified Method for Calculating the Debye Temperature from Elastic Constants. *Journal of Physics and Chemistry of Solids*, **24**(7): 909-917. https://doi.org/10.1016/0022-3697(63)90067-2

Anderson, P. W. (1961). Localized Magnetic States in Metals. *Physical Review*, **124**(1): 41-53. https://doi.org/10.1103/PhysRev.124.41

Anderson, P. W. (1967). Ground State of a Magnetic Impurity in a Metal. *Physical Review*, **164**(2): 352-359. https://doi.org/10.1103/PhysRev.164.352

Anderson, P. W. (1972). More is Different: Broken Symmetry and the Nature of the Hierarchical Structure of Science. *Science*, **177**(4047): 393-396. https://doi.org/10.1126/science.177.4047.393

Antonides, E., Janse, E., and Sawatzky, G. (1977). LMM Auger Spectra of Cu, Zn, Ga, and Ge I. Transition Probabilities, Term Splittings, and Effective Coulomb Interaction. *Physical Review B*, **15**(4): 1669-1679. https://doi.org/10.1103/PhysRevB.15.1669

Antonov, V. N., Harmon, B. N., Antropov, V. P., Perlov, A. Y. and Yaresko, A. N., (2001). Electronic Structure and Magneto-optical Kerr Effect of Fe_3O_4 and Mg^{2+} or Al^{3+} -substituted Fe_3O_4. *Physical Review B*, **64**(13): 134410 (1-12). https://doi.org/10.1103/PhysRevB.64.134410

Arbuznikov, A. V., Kaupp, M., and Bahmann, H. (2006). From Local Hybrid Functionals to "Localized Local Hybrid" Potentials: Formalism and Thermochemical Tests. *The Journal of Chemical Physics*, **124**(20): 204102 (1-15). https://doi.org/10.1063/1.2196883

Arfken, G. B., Weber, H. J., and Harris, F. E. (2011). *Mathematical methods for physicists: a comprehensive guide*, Academic Press, USA.

Arita, R., Kuneš, J., Kozhevnikov, A., Eguiluz, A., and Imada, M. (2012). Ab-initio Studies on the Interplay between Spin-orbit Interaction and Coulomb Correlation in Sr_2IrO_4 and Ba_2IrO_4. *Physical Review Letters*, **108**(8): 086403 (1-5). https://doi.org/10.1103/PhysRevLett.108.086403

Ashcroft, N. W. (1966). Electron-ion Pseudopotentials in Metals. *Physics Letters*, **23**(1): 48-50. https://doi.org/10.1016/0031-9163(66)90251-4

Ashcroft, N. W., & Mermin, N. D. (1976). *Solid state physics.* Saunders College Publishing, USA.

Backes, D., Huang, D., Mansell, R., Lanius, M., Kampmeier, J., *et al.* (2017). Disentangling Surface and Bulk Transport in Topological-insulator P-N Junctions. *Physical Review B*, **96**(12): 125125 (1-10). https://doi.org/10.1103/PhysRevB.96.125125

Balachandran, J., Lin, L., Anchell, J. S., Bridges, C. A., and Ganesh, P. (2017). Defect Genome of Cubic Perovskites for Fuel Cell Applications. *The Journal of Physical Chemistry C*, **121**(48): 26637-26647. https://doi.org/10.1021/acs.jpcc.7b08716

Bar-Cohen, A. (1987). Thermal Management of Air-and Liquid-cooled Multichip Modules. *IEEE Transactions on components, hybrids, and manufacturing technology*, **10**(2): 159-175. https://doi.org/10.1109/TCHMT.1987.1134734

Bar-Yam, Y., McKay, S. R., and Christian, W. (1998). Dynamics of Complex Systems (Studies in Nonlinearity). *Computers in Physics*, **12**(4): 335-336. https://doi.org/10.1063/1.4822633

Barron, T. and Klein, M. (1965). Second-order Elastic Constants of a Solid under Stress. *Proceedings of the Physical Society*, **85**(3): 523-532. doi:10.1088/0370-1328/85/3/313

Basov, D. N., Averitt, R. D., Van Der Marel, D., Dressel, M., and Haule, K. (2011). Electrodynamics of Correlated Electron Materials. *Reviews of Modern Physics*, **83**(2): 471-541. https://doi.org/10.1103/RevModPhys.83.471

Bauer, B., Carr, L. D., Evertz, H. G., Feiguin, A., Freire, J., *et al.* (2011). The Alps Project Release 2.0: Open Source Software for Strongly Correlated Systems. *Journal of Statistical Mechanics: Theory and Experiment*, **2011**(5): P05001 (1-15). doi:10.1088/1742-5468/2011/05/P05001

Bayes, T. (1958) An Essay towards Solving a Problem in the Doctrine of Chances. *Biometrika*, **45**(3): 296-315. https://doi.org/10.1093/biomet/45.3-4.296

Beach, K., Gooding, R., and Marsiglio, F. (2000). Reliable Padé Analytical Continuation Method Based on a High-accuracy Symbolic Computation Algorithm. *Physical Review B*, **61**(8): 5147-5157. https://doi.org/10.1103/PhysRevB.61.5147

Beck, S., and Ederer, C. (2023). Interfacial Doping in $LaVO_3/SrVO_3$ Multilayers from DFT+ DMFT. *Physical Review Materials*, **7**(5): 055003 (1-8). https://doi.org/10.1103/PhysRevMaterials.7.055003

Becke, A. D. (1993). A New Mixing of Hartree-Fock and Local Density Functional Theories. *The Journal of Chemical Physics*, **98**(2): 1372-1377. https://doi.org/10.1063/1.464304

Becke, A. D. and Johnson, E. R. (2005). A Density-functional Model of the Dispersion Interaction. *The Journal of Chemical Physics*, **123**(15): 154101 (1-9). https://doi.org/10.1063/1.2065267

Becke, A. D. and Johnson, E. R. (2006). A Simple Effective Potential for Exchange. *The Journal of Chemical Physics*, **124** : 221101 (1-4). https://doi.org/10.1063/1.2213970

Bell, C., Harashima, S., Kozuka, Y., Kim, M., Kim, B. G., *et al.* (2009). Dominant Mobility Modulation by the Electric Field Effect at the $LaAlO_3/SrTiO_3$ Interface. *Physical Review Letters*, **103**(22): 226802 (1-4). https://doi.org/10.1103/PhysRevLett.103.226802

Benedict, C. J., Rao, A., Sanjeev, G., Okram, G., and Babu, P. (2016). A Systematic Study on the Effect of Electron Beam Irradiation on Structural, Electrical, Thermoelectric Power and Magnetic Property of $LaCoO_3$. *Journal of Magnetism and Magnetic Materials*, **397**: 145-151. https://doi.org/10.1016/j.jmmm.2015.08.111

Bergeron, D. and Tremblay, A. M. (2016). Algorithms for Optimized Maximum Entropy and Diagnostic Tools for Analytic Continuation. *Physical Review E*, **94**(2): 023303 (1-25). https://doi.org/10.1103/PhysRevE.94.023303

Berland, K. and Persson, C. (2018). Thermoelectric Transport of GaAs, InP, and PbTe: Hybrid Functional with $\mathbf{k}.\tilde{\mathbf{p}}$ Interpolation versus Scissor-corrected Generalized Gradient Approximation. *Journal of Applied Physics*, **123**(20): 205703 (1-17). https://doi.org/10.1063/1.5030395

Betzinger, M., Friedrich, C., Blügel, S., and Görling, A. (2011). Local Exact Exchange Potentials within the All-electron FP-LAPW Method and a Comparison with Pseudopotential Results. *Physical Review B*, **83**(4): 045105 (1-11). https://doi.org/10.1103/PhysRevB.83.045105

Birch, F. (1938). The Effect of Pressure upon the Elastic Parameters of Isotropic Solids, According to Murnaghan's Theory of Finite Strain. *Journal of Applied Physics*, **9**(4): 279-288. https://doi.org/10.1063/1.1710417

Blaha, P., Schwarz, K., Madsen, G., Kvasnicka, D., and Luitz, J. (2002). *WIEN2k, an augmented plane wave plus local orbital package for the electronic structure of solids.* TU Wien Academic Press, Vienna, Austria. https://doi.org/10.1107/S1574870720003171

Blaha, P., Schwarz, K., Tran, F., Laskowski, R., Madsen, G. K., *et al.* (2020). WIEN2k: An APW + LO Program for Calculating the Properties of Solids. *The Journal of Chemical Physics*, **152**(7): 074101 (1-30). https://doi.org/10.1063/1.5143061

Bloch, F. (1929). Über die Quantenmechanik der Elektronen in Kristallgittern. *Zeitschrift für Physik*, **52**(7): 555-600. https://doi.org/10.1007/BF01339455

Blöchl, P. E., Jepsen, O., and Andersen, O. K. (1994). Improved Tetrahedron Method for Brillouin-zone Integrations. *Physical Review B*, **49**(23): 16223-16233. https://doi.org/10.1103/PhysRevB.49.16223

Blümer, N. (2007). Efficiency of Quantum Monte Carlo Impurity Solvers for the Dynamical Mean-field Theory. *Physical Review B*, **76**(20): 205120 (1-5). https://doi.org/10.1103/PhysRevB.76.205120

Blümer, N. and Gorelik, E. V. (2011). Quantum Monte Carlo Simulations of Antiferromagnetism in Ultracold Fermions on Optical Lattices within Real-space Dynamical Mean-field Theory. *Computer Physics Communications*, **182**(1): 115-118. https://doi.org/10.1016/j.cpc.2010.07.011

Boehnke, L., Hafermann, H., Ferrero, M., Lechermann, F., and Parcollet, O. (2011). Orthogonal Polynomial Representation of Imaginary-time Green's Functions. *Physical Review B*, **84**(7): 075145 (1-14). https://doi.org/10.1103/PhysRevB.84.075145

Born, M. and Oppenheimer, W. (1927). Zur Quantentheorie der Molekeln *Annalen der Physik*, **389**(20): 457-484. https://doi.org/10.1002/andp.19273892002

Boudali, A., Amrani, B., Abada, A., and Amara, K. (2009). First-principles Study of Structural, Elastic, Electronic, and Thermal Properties of $LaAlO_3$ Perovskite. *Computational Materials Science*, **45**(4): 1068-1072. https://doi.org/10.1016/j.commatsci.2009.01.011

Bouhemadou, A. and Khenata, R. (2007). Ab-initio Study of the Structural, Elastic, Electronic and Optical Properties of the Antiperovskite $SbNMg_3$. *Computational Materials Science*, **39**(4): 803-807. https://doi.org/10.1016/j.commatsci.2006.10.003

Brinkman, W. F. and Rice, T. M. (1970). Application of Gutzwiller's Variational Method to the Metal-insulator Transition. *Physical Review B*, **2**(10): 4302-4304. https://doi.org/10.1103/PhysRevB.2.4302

Bulla, R., Costi, T. A., and Pruschke, T. (2008). Numerical Renormalization Group Method for Quantum Impurity Systems. *Reviews of Modern Physics*, **80**(2): 395-450. https://doi.org/10.1103/RevModPhys.80.395

Byrd, R., Lu, P., and Nocedal, J. (1995). On the Limited Memory BFGS Method for Large Scale Minimization. *SIAM Journal on Scientific and Statistical Computing*, **16**(5): 1190-1208.

Caffarel, M. and Krauth, W. (1994). Exact Diagonalization Approach to Correlated Fermions in Infinite Dimensions: Mott Transition and Superconductivity. *Physical Review Letters*, **72**(10): 1545-1548. https://doi.org/10.1103/PhysRevLett.72.1545

Calandra, M. and Gunnarsson, O. (2002). Electrical Resistivity at Large Temperatures: Saturation and Lack Thereof. *Physical Review B*, **66**(20): 205105 (1-20). https://doi.org/10.1103/PhysRevB.66.205105

Capelle, K. (2006). A Bird's-eye View of Density Functional Theory. *Brazilian Journal of Physics*, **36**(4A): 1318-1343.

Caputo, M., Jandke, J., Cappelli, E., Chaluvadi, S. K., Guedes, E. B., *et al.* (2022). Metal to insulator transition at the surface of V_2O_3 thin films: An in-situ view. *Applied Surface Science*, **574**: 151608 (1-8). https://doi.org/10.1016/j.apsusc.2021.151608

Casida, M. E. and Chong, D. (1995). *Recent advances in density functional methods.* World Scientific, Singapore.

Casida, M. E., (2009). Time-dependent Density Functional Theory for Molecules and Molecular Solids. *Journal of Molecular Structure: THEOCHEM*, **914**(1): 3-18. https://doi.org/10.1016/j.theochem.2009.08.018

Chatterjee, B., Skolimowski, J., Makuch, K., and Byczuk, K. (2019). Real-space Dynamical Mean-field Theory of Friedel Oscillations in Strongly Correlated Electron Systems. *Physical Review B*, **100**(11): 115118 (1-15). https://doi.org/10.1103/PhysRevB.100.115118

Choi, W., Cho, M. Y., Konar, A., Lee, J. H., Cha, G. B., *et al.* (2012). High-detectivity Multilayer MoS_2 Phototransistors with Spectral Response from Ultraviolet to Infrared. *Advanced Materials* , **24**(43): 5832-5836. https://doi.org/10.1002/adma.201201909

Chuang, Y. D., Gromko, A., Dessau, D., Kimura, T., and Tokura, Y. (2001). Fermi Surface Nesting and Nanoscale Fluctuating Charge/Orbital Ordering in Colossal Magnetoresistive Oxides. *Science*, **292**(5521): 1509-1513. https://doi.org/10.1126/science.1059255

Cinthia, A. J., Priyanga, G. S., Rajeswarapalanichamy, R., and Iyakutti, K. (2015). Structural, Electronic and Mechanical Properties of Alkaline Earth Metal Oxides MO (M= Be, Mg, Ca, Sr, Ba). *Journal of Physics and Chemistry of Solids*, **79**: 23-42. https://doi.org/10.1016/j.jpcs.2014.10.021

Cohen, A. J., Mori-Sánchez, P., and Yang, W. (2007). Development of Exchange-correlation Functionals with Minimal Many-electron Self-interaction Error. *The Journal of Chemical Physics*, **126**(19): 191109 (1-6). https://doi.org/10.1063/1.2741248

Conway, J. (1970). The Game of Life. *Scientific American*, **223**(4): 120-123.

Dal Corso, A. (2016). Elastic Constants of Beryllium: a First-principles Investigation. *Journal of Physics: Condensed Matter*, **28**(7): 075401 (1-7). doi:10.1088/0953-8984/28/7/075401

Dehkordi, A. M., Zebarjadi, M., He, J., and Tritt, T. M. (2015). Thermoelectric Power Factor: Enhancement Mechanisms and Strategies for Higher Performance Thermoelectric Materials. *Materials Science and Engineering: R: Reports*, **97**: 1-22. https://doi.org/10.1016/j.mser.2015.08.001

Deng, X., Mravlje, J., Ferrero, M., Kotliar, G., and Georges, A. (2013). How Bad Metals Turn Good: Spectroscopic Signatures of Resilient Quasiparticles. *Physical Review Letters*, **110**(8): 086401 (1-5). https://doi.org/10.1103/PhysRevLett.110.086401

Dirac, P. A. (1930). Note on Exchange Phenomena in the Thomas Atom. *In Mathematical Proceedings of the Cambridge Philosophical Society*, **26**(3): 376-385. https://doi.org/10.1017/S0305004100016108

Dirks, A., Werner, P., Jarrell, M., and Pruschke, T. (2010). Continuous-time Quantum Monte Carlo and Maximum Entropy Approach to an Imaginary-time Formulation of Strongly Correlated Steady-state Transport. *Physical Review E*, **82**(2): 026701 (1-17). https://doi.org/10.1103/PhysRevE.82.026701

Dominguez-Adame, F., Martin-Gonzalez, M., Sanchez, D., and Cantarero, A. (2019). Nanowires: A Route to Efficient Thermoelectric Devices. *Physica E: Low-dimensional Systems and Nanostructures*, **113**: 213-225. https://doi.org/10.1016/j.physe.2019.03.021

Dong, S., Yu, R., Yunoki, S., Alvarez, G., Liu, J. M., *et al.* (2008). Magnetism, Conductivity, and Orbital Order in $(LaMnO_3)_{2n}/(SrMnO_3)_n$ Superlattices. *Physical Review B*, **78**(20): 201102 (1-4). https://doi.org/10.1103/PhysRevB.78.201102

Eisenlohr, H., Lee, S. S. B., and Vojta, M. (2019). Mott Quantum Criticality in the One-band Hubbard Model: Dynamical Mean-field Theory, Power-law Spectra, and Scaling. *Physical Review B*, **100**(15): 155152 (1-11). https://doi.org/10.1103/PhysRevB.100.155152

Eschrig, H. (1996). *The Fundamentals of Density Functional Theory*, **32** Springer, Germany https://doi.org/10.1002/(SICI)1096-987X(19990115)20:1%3C23::AID-JCC5%3E3.0.CO;2-N

Faleev, S. V., Léonard, F., Stewart, D. A., and van Schilfgaarde, M. (2005). Ab-initio Tight-binding LMTO method for Nonequilibrium Electron Transport in Nanosystems. *Physical Review B*, **71**(19): 195422 (1-18). https://doi.org/10.1103/PhysRevB.71.195422

Feng, Z. and Lam, J. (2011). Stability and Dissipativity Analysis of Distributed Delay Cellular Neural Networks. *IEEE Transactions on Neural Networks*, **22**(6): 976-981. https://doi.org/10.1109/TNN.2011.2128341

Fermi, E. (1928). A Statistical Method for Determining some Properties of the Atom and its Application to the Theory of the Periodic System of Elements. *Magazine for Physics*, **48**: 73–79.

Ferrero, M., Becca, F., Fabrizio, M., and Capone, M. (2005). Dynamical Behavior across the Mott Transition of two Bands with Different Bandwidths. *Physical Review B*, **72**(20): 205126 (1-11). https://doi.org/10.1103/PhysRevB.72.205126

Feyerabend, P. (2017). *Science in a free society.* Verso Books, NY, USA.

Finley, J. P. (2004). Using the Local Density Approximation and the LYP, BLYP and B3LYP Functionals within Reference-state One-particle Density-matrix Theory. *Molecular Physics*, **102**(7): 627-639. https://doi.org/10.1080/00268970410001687452

Fock, V. (1930). Approximation Method for Solving the Quantum Mechanical Many-body Problem. *Magazine for Physics*, **61** : 126-148. http://dx.doi.org/10.1007/BF01340294

Fournier, R., Wang, L., Yazyev, O. V., and Wu, Q. (2020). Artificial Neural Network Approach to the Analytic Continuation Problem. *Physical Review Letters*, **124**(5): 056401 (1-6). https://doi.org/10.1103/PhysRevLett.124.056401

Frenkel, D. and Ladd, A. J. (1984). New Monte Carlo Method to Compute the Free Energy of Arbitrary Solids. Application to the FCC and HCP Phases of Hard Spheres. *The Journal of Chemical Physics*, **81**(7): 3188-3193. https://doi.org/10.1063/1.448024

Fujimori, A., Hase, I., Nakamura, M., Namatame, H., Fujishima, Y., *et al.* (1992). Doping-induced Changes in the Electronic Structure of $La_xSr_{1-x}TiO_3$: Limitation of the One-electron Rigid-band Model and the Hubbard model. *Physical Review B*, **46**(15): 9841-9844. https://doi.org/10.1103/PhysRevB.46.9841

Gandolfi, M., Celardo, G. L., Borgonovi, F., Ferrini, G., Avella, A., *et al.* (2017). Emergent Ultrafast Phenomena in Correlated Oxides and Heterostructures. *Physica Scripta*, **92**(3): 034004 (1-22). doi:10.1088/1402-4896/aa54cc

Gebhard, F., Bott, K., Scheidler, M., Thomas, P., and Koch, S. W. (1997). Optical Absorption of Non-interacting Tight-binding Electrons in a Peierls-distorted Chain at Half Band-filling. *Philosophical Magazine B*, **75**(1): 1-12. https://doi.org/10.1080/13642819708205700

Georges, A. and Kotliar, G. (1992). Hubbard Model in Infinite Dimensions. *Physical Review B*, **45**(12): 6479-6483. https://doi.org/10.1103/PhysRevB.45.6479

Georges, A., Kotliar, G., Krauth, W., and Rozenberg, M. J. (1996). Dynamical Mean-field Theory of Strongly Correlated Fermion Systems and the Limit of Infinite Dimensions. *Reviews of Modern Physics*, **68**(1): 13-125. https://doi.org/10.1103/RevModPhys.68.13

Gibert, M., Zubko, P., Scherwitzl, R., Iniguez, J., and Triscone, J. M. (2012). Exchange Bias in $LaNiO_3$-$LaMnO_3$ Superlattices. *Nature Materials*, **11**(3): 195-198. https://doi.org/10.1038/nmat3224

Golesorkhtabar, R., Pavone, P., Spitaler, J., Puschnig, P., and Draxl, C. (2013). Elastic: A Tool for Calculating Second-order Elastic Constants from First Principles. *Computer Physics Communications*, **184**(8): 1861-1873. https://doi.org/10.1016/j.cpc.2013.03.010

Gonzalez-Rosillo, J. C., Catalano, S., Maggio-Aprile, I., Gibert, M., Obradors, X., *et al.* (2020). Nanoscale Correlations between Metal-insulator Transition and Resistive Switching Effect in Metallic Perovskite Oxides. *Small*, **16**(23): 2001307 (1-10). https://doi.org/10.1002/smll.202001307

Gonze, X., Jollet, F., Araujo, F. A., Adams, D., Amadon, B., *et al.* (2016). Recent Developments in the Abinit Software Package. *Computer Physics Communications*, **205**: 106-131. https://doi.org/10.1016/j.cpc.2016.04.003

Goulko, O., Mishchenko, A. S., Pollet, L., Prokof'ev, N., and Svistunov, B. (2017). Numerical Analytic Continuation: Answers to Well-posed Questions. *Physical Review B*, **95**(1): 014102 (1-11). https://doi.org/10.1103/PhysRevB.95.014102

Gubernatis, J., Jarrell, M., Silver, R., and Sivia, D. (1991). Quantum Monte Carlo Simulations and Maximum Entropy: Dynamics from Imaginary-time Data. *Physical Review B*, **44**(12): 6011-6029. https://doi.org/10.1103/PhysRevB.44.6011

Gull, E., Millis, A. J., Lichtenstein, A. I., Rubtsov, A. N., Troyer, M., *et al.* (2011). Continuous-time Monte Carlo Methods for Quantum Impurity Models. *Reviews of Modern Physics*, **83**(2): 349-404. https://doi.org/10.1103/RevModPhys.83.349

Gull, E., Werner, P., Millis, A., and Troyer, M. (2007). Performance Analysis of Continuous-time Solvers for Quantum Impurity Models. *Physical Review B*, **76**(23): 235123 (1-9). https://doi.org/10.1103/PhysRevB.76.235123

Gull, E., Werner, P., Parcollet, O., and Troyer, M. (2008). Continuous-time Auxiliary-field Monte Carlo for Quantum Impurity Models. *Europhysics Letters*, **82**(5): 57003 (1-6). doi:10.1209/0295-5075/82/57003

Gull, S. F. and Skilling, J., (1984) Maximum Entropy Method in Image Processing. *IEE proceedings F (communications, radar and signal processing)*, **131**(6): 646-659. https://doi.org/10.1049/ip-f-1.1984.0099

Gunnarsson, O., Haverkort, M., and Sangiovanni, G. (2010). Analytical Continuation of Imaginary Axis Data for Optical Conductivity. *Physical Review B*, **82**(16): 165125 (1-8). https://doi.org/10.1103/PhysRevB.82.165125

Hameed, S., Pelc, D., Anderson, Z. W., Klein, A., Spieker, R. J., *et al.* (2022). Enhanced Superconductivity and Ferroelectric Quantum Criticality in Plastically Deformed Strontium Titanate. *Nature Materials*, **21**(1): 54-61. https://doi.org/10.1038/s41563-021-01102-3

Hartree, D. R., Hartree, W., and Swirles, B. (1939). Self-consistent Field, Including Exchange and Superposition of Configurations, with some Results for Oxygen. *Philosophical Transactions of the Royal Society of London. Series A, Mathematical and Physical Sciences*, **238**(790): 229-247. https://doi.org/10.1098/rsta.1939.0008

Haule, K. (2007). Quantum Monte Carlo Impurity Solver for Cluster Dynamical Mean-field Theory and Electronic Structure Calculations with Adjustable Cluster Base. *Physical Review B*, **75**(15): 155113 (1-12). https://doi.org/10.1103/PhysRevB.75.155113

Held, K. (2007). Electronic Structure Calculations using Dynamical Mean Field Theory. *Advances in Physics*, **56**(6): 829-926. doi:10.1088/0953-8984/20/6/064202

Held, K., Andersen, O., Feldbacher, M., Yamasaki, A., and Yang, Y. (2008). Bandstructure Meets Many-body Theory: the LDA + DMFT Method. *Journal of Physics: Condensed Matter*, **20**(6): 064202 (1-7). doi:10.1088/0953-8984/20/6/064202

Held, K., Nekrasov, I., Keller, G., Eyert, V., Blümer, N., *et al.* (2006). Realistic Investigations of Correlated Electron Systems with LDA+ DMFT. *Physica Status Solidi (b)*, **243**(11): 2599-2631. https://doi.org/10.1002/pssb.200642053

Hicks, L. D., and Dresselhaus, M. S. (1993). Thermoelectric Figure of Merit of a One-dimensional Conductor. *Physical Review B*, **47**(24): 16631-16634. https://doi.org/10.1103/PhysRevB.47.16631

Hirayama, M., Miyake, T., and Imada, M. (2012). Ab-initio Low-energy Model of Transition-metal-oxide Heterostructure $LaAlO_3/SrTiO_3$. *Journal of the Physical Society of Japan*, **81**(8): 084708 (1-11). https://doi.org/10.1143/JPSJ.81.084708

Hirsch, J. E. and Fye, R. M. (1986). Monte Carlo Method for Magnetic Impurities in Metals. *Physical Review Letters*, **56**(23): 2521-2524. https://doi.org/10.1103/PhysRevLett.56.2521

Hohenberg, P. and Kohn, W. (1964). Inhomogeneous Electron Gas. *Physical Review*, **136**(3B): B864-B871. https://doi.org/10.1103/PhysRev.136.B864

Honda, H., Takamastu, H., and Wei, J. (2002). Enhanced Boiling of FC-72 on Silicon Chips with Micro-pin-fins and Submicron-scale Roughness. *Journal Heat Transfer*, **124**(2): 383-390. https://doi.org/10.1115/1.1447937

Hubbard, J. (1963). Electron Correlations in Narrow Energy Bands. *Proceedings of the Royal Society of London. Series A. Mathematical and Physical Sciences*, **276**(1365): 238-257. https://doi.org/10.1098/rspa.1963.0204

Iazzi, M. and Troyer, M. (2015). Efficient Continuous-time Quantum Monte Carlo Algorithm for Fermionic Lattice Models. *Physical Review B*, **91**(24): 241118 (1-5). https://doi.org/10.1103/PhysRevB.91.241118

Imada, M. (2005). Universality Classes of Metal-insulator Transitions in Strongly Correlated Electron Systems and Mechanism of High-temperature Superconductivity. *Physical Review B*, **72**(7): 075113 (1-18). https://doi.org/10.1103/PhysRevB.72.075113

Imada, M., Fujimori, A., and Tokura, Y. (1998). Metal-insulator Transitions. *Reviews of Modern Physics*, **70**(4): 1039-1263. 10, 1039-1263. https://doi.org/10.1103/RevModPhys.70.1039

Inaba, F., Arima, T., Ishikawa, T., Katsufuji, T., and Tokura, Y. (1995). Change of Electronic Properties on the Doping-induced Insulator-metal Transition in $La_{1-x}Sr_xVO_3$. *Physical Review B*, **52**(4): R2221-R2224. https://doi.org/10.1103/PhysRevB.52.R2221

Inoue, I., Goto, O., Makino, H., Hussey, N., and Ishikawa, M. (1998). Bandwidth Control in a Perovskite-type $3d^1$ -correlated Metal $Ca_{1-x}Sr_xVO_3$ Evolution of the Electronic Properties and Effective Mass. *Physical Review B*, **58**(8): 4372-4383. https://doi.org/10.1103/PhysRevB.58.4372

Inoue, I. H., Bergemann, C., Hase, I., and Julian, S. R. (2002). Fermi Surface of 3 d^1 Perovskite $CaVO_3$ near the Mott Transition. *Physical Review Letters*, **88**(23): 236403 (1-4). https://doi.org/10.1103/PhysRevLett.88.236403

Isakov, S. V., Melko, R. G., and Hastings, M. B. (2012). Universal Signatures of Fractionalized Quantum Critical Points. *Science*, **335** : 193-195. https://doi.org/10.1126/science.1212207

Jaiswal, A., Roy, S., Srinivasan, G., and Roy, K. (2017). Proposal for a Leaky-integrate-fire Spiking Neuron Based on Magnetoelectric Switching of Ferromagnets. *IEEE Transactions on Electron Devices*, **64**(4): 1818-1824. https://doi.org/10.1109/TED.2017.2671353

Jana, A., Raghunathan, R., Rawat, R., Choudhary, R., and Phase, D. (2020). Enhanced Charge-transfer Character in the Monoclinic Phase of Mott Insulator $LaVO_3$ Thin Films. *Physical Review B*, **102**(23): 235108 (1-11). https://doi.org/10.1103/PhysRevB.102.235108

Janod, E., Tranchant, J., Corraze, B., Querré, M., Stoliar, P. R., *et al.* (2015). Resistive Switching in Mott Insulators and Correlated Systems. *Advanced Functional Materials*, **25**(40): 6287-6305. https://doi.org/10.1002/adfm.201500823

Jaramillo, J., Scuseria, G. E., and Ernzerhof, M. (2003). Local Hybrid Functionals. *The Journal of Chemical Physics*, **118**(3): 1068-1073. https://doi.org/10.1063/1.1528936

Jarlborg, T., and Arbman, G. (1977). The Electronic Structure of some A15 Compounds by Semi-self-consistent Band Calculations. *Journal of Physics F: Metal Physics*, **7**(9): 1635-1649. doi:10.1088/0305-4608/7/9/009

Jarrell, M., and Gubernatis, J. E. (1996). Bayesian Inference and the Analytic Continuation of Imaginary-time Quantum Monte Carlo Data. *Physics Reports*, **269**(3): 133-195. https://doi.org/10.1016/0370-1573(95)00074-7

Jauch, W., and Palmer, A. (1999). Anomalous Zero-point Motion in $SrTiO_3$: Results from γ-ray Diffraction. *Physical Review B*, **60**(5): 2961-2963. https://doi.org/10.1103/PhysRevB.60.2961

Jellite, M., Rehspringer, J. L., Fazio, M., Muller, D., Schmerber, G., *et al.* (2018). Investigation of $LaVO_3$ Based Compounds as a Photovoltaic Absorber. *Solar Energy*, **162**: (1-7). https://doi.org/10.1016/j.solener.2017.12.061

Johnson, E. R. and Becke, A. D. (2005). A Post Hartree-Fock Model of Intermolecular Interactions. *The Journal of Chemical Physics*, **123**: 024101 (1-7). https://doi.org/10.1063/1.1949201

Kamerbeek, A. M., Högl, P., Fabian, J., and Banerjee, T. (2015). Electric Field Control of Spin Lifetimes in Nb-$SrTiO_3$ by Spin-orbit Fields. *Physical Review Letters*, **115**(13): 136601 (1-5). https://doi.org/10.1103/PhysRevLett.115.136601

Kanatzidis, M. G. (2010). Nanostructured Thermoelectrics: the New Paradigm? *Chemistry of Materials*, **22**(3): 648-659. https://doi.org/10.1021/cm902195j

Kaphle, G. C., Ganguly, S., Banerjee, R., Banerjee, R., Khanal, R., *et al.* (2012). A Study of Magnetism in Disordered Pt-Mn, Pd-Mn and Ni-Mn Alloys: an Augmented Space

Recursion Approach. *Journal of Physics: Condensed Matter*, **24**(29): 295501 (1-12). doi:10.1088/0953-8984/24/29/295501

Kaphle, G. C., Adhikari, N., and Mookerjee, A. (2015). Study of Spin Glass Behavior in Disordered Pt_xMn_{1-x} alloys: an Augmented Space Recursion Approach. *Advanced Science Letters*, **21**(9): 2681-2687. https://doi.org/10.1166/asl.2015.6341

Kaupp, M., Bahmann, H., and Arbuznikov, A. V. (2007). Local Hybrid Functionals: An Assessment for Thermochemical Kinetics. *The Journal of Chemical Physics*, **127**(19): 194102 (1-12). https://doi.org/10.1063/1.2795700

Kawamura, M. (2019). Fermisurfer: Fermi-surface Viewer Providing Multiple Representation schemes. *Computer Physics Communications*, **239**:197-203. https://doi.org/10.1016/j.cpc.2019.01.017

Kestigian, M. and Ward, R. (1954). The Preparation of Lanthanum Titanium Oxide, $LaTiO_3$. *Journal of the American Chemical Society*, **76**(23): 6027-6027. https://doi.org/10.1021/ja01652a044

Kim, M. (2018). Signatures of Spin-orbital States of t_{2g} System in Optical Conductivity: RVO_3(R = Y and La). *Physical Review B*, **97**(15): 155141 (1-9). https://doi.org/10.1103/PhysRevB.97.155141

Kirklin, S., Saal, J. E., Meredig, B., Thompson, A., Doak, J. W., *et al.* (2015) The Open Quantum Materials Database (OQMD): Assessing the Accuracy of DFT Formation Energies. *npj Computational Materials*, **1**(1): 1-15. https://doi.org/10.1038/npjcompumats.2015.10

Kittel, C. (1996). *Introduction to solid state physics.* John Wiley and sons, inc., USA.

Klimeš, J. and Michaelides, A. (2012). Perspective: Advances and Challenges in Treating van der Waals Dispersion Forces in Density Functional Theory. *The Journal of Chemical Physics*, **137**(12): 120901 (1-12). https://doi.org/10.1063/1.4754130

Kohn, W. and Sham, L. J. (1965). Self-consistent Equations Including Exchange and Correlation Effects. *Physical Review*, **140**(4A): A1133-A1138. https://doi.org/10.1103/PhysRev.140.A1133

Koller, D., Tran, F., and Blaha, P. (2011). Merits and Limits of the Modified Becke-Johnson Exchange Potential. *Physical Review B*, **83**(19): 195134 (1-10). https://doi.org/10.1103/PhysRevB.83.195134

Kotliar, G., Savrasov, S. Y., Haule, K., Oudovenko, V. S., Parcollet, O., *et al.* (2006). Electronic Structure Calculations with Dynamical Mean-field Theory. *Reviews of Modern Physics*, **78**(3): 865-951. https://doi.org/10.1103/RevModPhys.78.865

Kotliar, G. and Vollhardt, D. (2004). Strongly Correlated Materials: Insights from Dynamical Mean-field Theory. *Physics Today*, **57**(3): 53-60. https://doi.org/10.1063/1.1712502

Kowalski, A., Hausoel, A., Wallerberger, M., Gunacker, P., and Sangiovanni, G. (2019). State and Superstate Sampling in Hybridization-expansion Continuous-time Quantum Monte Carlo. *Physical Review B*, **99**(15): 155112 (1-14). https://doi.org/10.1103/PhysRevB.99.155112

Krasovskii, E., Nemoshkalenko, V., and Antonov, V. (1993). On the Accuracy of the Wave-functions Calculated by LAPW Method. *Zeitschrift für Physik B Condensed Matter*, **91**: 463-466. https://doi.org/10.1007/BF01316824

Kravtsov, K., Fok, M. P., Rosenbluth, D., and Prucnal, P. R. (2011). Ultrafast All-optical Implementation of a Leaky Integrate and Fire Neuron. *Optics express*, **19**(3): 2133-2147. https://doi.org/10.1364/OE.19.002133

Kuhn, T. S. (2012). *The structure of scientific revolutions*. University of Chicago Press, USA.

Kurth, S., Perdew, J. P., and Blaha, P. (1999). Molecular and Solid-state Tests of Density Functional Approximations: LSD, GGAs, and meta-GGAs. *International Journal of Quantum Chemistry*, **75**(4): 889-909. https://doi.org/10.1002/(SICI)1097-461X(1999)75:4/5%3C889::AID-QUA54%3E3.0.CO;2-8

Laird, B. B., Ross, R. B., and Ziegler, T. (1996). Chemical Applications of Density Functional Theory. *American Chemical Society*, **629**, Washington, DC, USA.

Lan, Y. C., Chen, X. L., and He, M. (2003). Structure, Magnetic Susceptibility and Resistivity Properties of $SrVO_3$. *Journal of Alloys and Compounds*, **354**(1): 95-98. https://doi.org/10.1016/S0925-8388(02)01349-X

LeBlanc, S. (2014). Thermoelectric Generators: Linking Material Properties and Systems Engineering for Waste Heat Recovery Applications. *Sustainable Materials and Technologies*, **1**: 26-35. https://doi.org/10.1016/j.susmat.2014.11.002

Lee, C., Yang, W., and Parr, R. G. (1988). Development of the Colle-Salvetti Correlation-energy Formula into a Functional of the Electron Density. *Physical Review B*, **37**(2): 785-789. https://doi.org/10.1103/PhysRevB.37.785

Li, C., Ravichandran, N. K., Lindsay, L., and Broido, D. (2018). Fermi Surface Nesting and Phonon Frequency Gap Drive Anomalous Thermal Transport. *Physical Review Letters*, **121**(17): 175901 (1-6). https://doi.org/10.1103/PhysRevLett.121.175901

Lide, D. R., Kehiaian, H. V. (2020). *CRC handbook of thermophysical and thermochemical data.* CRC Press, FL, USA.

Loh Jr, E., Gubernatis, J., Scalettar, R., White, S., Scalapino, D., *et al.* (1990). Sign Problem in the Numerical Simulation of Many-electron Systems. *Physical Review B*, **41**(13): 9301-9307. https://doi.org/10.1103/PhysRevB.41.9301

Löhneysen, H. V., Rosch, A., Vojta, M., and Wölfle, P. (2007). Fermi-liquid Instabilities at Magnetic Quantum Phase Transitions. *Reviews of Modern Physics*, **79**(3): 1015-1075. https://doi.org/10.1103/RevModPhys.79.1015

Long, J., Yang, L., and Wei, X. (2013). Lattice, Elastic Properties and Debye Temperatures of $ATiO_3$ (A= Ba, Ca, Pb, Sr) from First-principles. *Journal of Alloys and Compounds*, **549**: 336-340. https://doi.org/10.1016/j.jallcom.2012.08.120

Losee, J. (2001). *A historical introduction to the philosophy of science.* OUP Oxford, UK.

Löwdin, P. O. (1955). Quantum Theory of Many-particle Systems. ii. Study of the Ordinary Hartree-Fock Approximation. *Physical Review*, **97**(6): 1490-1508. https://doi.org/10.1103/PhysRev.97.1474

Madsen, G. K., Carrete, J., and Verstraete, M. J. (2018). BoltzTraP2, a Program for Interpolating Band Structures and Calculating Semi-classical Transport Coefficients. *Computer Physics Communications*, **231**: 140-145. https://doi.org/10.1016/j.cpc.2018.05.010

Maeno, Y., Hashimoto, H., Yoshida, K., Nishizaki, S., Fujita, T., *et al.* (1994). Superconductivity in a Layered Perovskite without Copper. *Nature*, **372**(6506): 532-534. https://doi.org/10.1038/372532a0

Mahmood, A., Ramay, S. M., Rafique, H. M., Al-Zaghayer, Y., and Khan, S. U. D. (2014). First-principles Study of Electronic, Optical and Thermoelectric Properties in Cubic Perovskite Materials $AgMO_3$ (M = V, Nb, Ta). *Modern Physics Letters B*, **28**(10): 1450077 (1-12). https://doi.org/10.1142/S0217984914500778

Maiti, K., Kumar, A., Sarma, D., Weschke, E., and Kaindl, G. (2004). Surface and Bulk Electronic Structure of $La_{1-x}Ca_xVO_3$. *Physical Review B*, **70**(19): 195112 (1-7). https://doi.org/10.1103/PhysRevB.70.195112

Maiti, K. and Sarma, D. (2000). Spectroscopic Investigations of the Electronic Structure and Metal-insulator Transitions in a Mott-Hubbard System $La_{1-x}Ca_xVO_3$. *Physical Review B*, **61**(4): 2525-2534. https://doi.org/10.1103/PhysRevB.61.2525

Makino, H., Inoue, I., Rozenberg, M., Iga, F., Aiura, Y., *et al.* (1997). Optical Spectra of the Correlated Metallic System $Ca_{1-x}Sr_xVO_3$. *Physica B: Condensed Matter*, **237**: 56-58. https://doi.org/10.1016/S0921-4526(97)00047-1

Martin, R. (2004). *Electronic structure–basic theory and practical methods*. Cambridge University Press, NY, USA.

Martin, R. M. (2020). *Electronic structure: basic theory and practical methods*. Cambridge University Press, USA.

McAlister, A. J. and Stern, E. (1963). Plasma Resonance Absorption in Thin Metal Films. *Physical Review*, **132**(4): 1599-1602. https://doi.org/10.1103/PhysRev.132.1599

McNally, D. E., Lu, X., Pelliciari, J., Beck, S., Dantz, M., *et al.* (2019). Electronic Localization in $CaVO_3$ Films via Bandwidth Control. *npj Quantum Materials*, **4**(1): 1-7. https://doi.org/10.1038/s41535-019-0146-3

Merino, J. and McKenzie, R. H. (2000). Transport Properties of Strongly Correlated Metals: A Dynamical Mean Field Approach. *Physical Review B*, **61**(12): 7996-8008. https://doi.org/10.1103/PhysRevB.61.7996

Messerschmitt, F., Kubicek, M., Schweiger, S., and Rupp, J. L. (2014). Memristor Kinetics and Diffusion Characteristics for Mixed Anionic-electronic $SrTiO_{3-\delta}$ Bits: the Memristor-based Cottrell Analysis Connecting Material to Device Performance. *Advanced Functional Materials*, **24**(47): 7448-7460. https://doi.org/10.1002/adfm.201402286

Metzner, W. and Vollhardt, D. (1989). Correlated Lattice Fermions in d = ∞ Dimensions. *Physical Review Letters*, **62**(3): 324-327. https://doi.org/10.1103/PhysRevLett.62.324

Millis, A. (1993). Effect of a Nonzero Temperature on Quantum Critical Points in Itinerant Fermion Systems. *Physical Review B*, **48**(10): 7183-7196. https://doi.org/10.1103/PhysRevB.48.7183

Mizutani, U. (2001). *Introduction to the electron theory of metals*. Cambridge University Press, NY, USA.

Moeller, G., Si, Q., Kotliar, G., Rozenberg, M., and Fisher, D. S. (1995). Critical Behavior Near the Mott Transition in the Hubbard Model. *Physical Review Letters*, **74**(11): 2082-2085. https://doi.org/10.1103/PhysRevLett.74.2082

Mori-Sánchez, P., Cohen, A. J., and Yang, W. (2006). Many-electron Self-interaction Error in Approximate Density Functionals. *The Journal of Chemical Physics*, **125**(20): 201102 (1-4). https://doi.org/10.1063/1.2403848

Morosan, E., Natelson, D., Nevidomskyy, A. H., and Si, Q. (2012). Strongly Correlated Materials. *Advanced Materials*, **24**(36): 4896-4923. https://doi.org/10.1002/adma.201202018

Mossanek, R., Abbate, M., Fonseca, P., Fujimori, A., Eisaki, H., *et al.* (2009). Optical Conductivity and X-ray Absorption Spectra of the Mott-Hubbard Compound RVO_3 (R= Sr, Ca, La, and Y). *Physical Review B*, **80**(19): 195107 (1-6). https://doi.org/10.1103/PhysRevB.80.195107

Mossanek, R., Abbate, M., Yoshida, T., Fujimori, A., Yoshida, Y., *et al.* (2008). Evolution of the Spectral Weight in the Mott-Hubbard Series $SrVO_3$ -$CaVO_3$ -$LaVO_3$ -YVO_3 . *Physical Review B*, **78**(7): 075103 (1-7). https://doi.org/10.1103/PhysRevB.78.075103

Mott, N. F. (1949). The Basis of the Electron Theory of Metals, with Special Reference to the Transition Metals. *Proceedings of the Physical Society. Section A*, **62**(7): 416-422. doi:10.1088/0370-1298/62/7/303

Murnaghan, F. D. (1944). The Compressibility of Media Under Extreme Pressures. *Proceedings of the National Academy of Sciences*, **30**(9): 244-247. https://doi.org/10.1073/pnas.30.9.244

Murugeswari, R., Manikandan, M., Rajeswarapalanichamy, R., and Milton Franklin Benial, A. (2020). Structural, Elastic, Magnetic and Electronic Properties of Ti-based Heusler Alloys. *International Journal of Modern Physics B*, **34**(07): 2050055 (1-18). https://doi.org/10.1142/S0217979220500551

Nakano, H., Takahashi, Y., and Imada, M. (2007). Drude Weight of the Two-dimensional Hubbard Model Re-examination of Finite-size Effect in Exact Diagonalization Study. *Journal of the Physical Society of Japan*, **76**(3): 034705 (1-9). https://doi.org/10.1143/JPSJ.76.034705

Nazir, S., Cheng, J., Behtash, M., Luo, J., and Yang, K. (2015). Interface Energetics and Charge Carrier Density Amplification by Sn-doping in $LaAlO_3$/$SrTiO_3$ Heterostructure. *ACS Applied Materials Interfaces*, **7**(26):14294-14302. https://doi.org/10.1021/acsami.5b02770

Needs, R. J., Martin, R. M., and Nielsen, O. (1986). Total Energy Calculations of the Structural Properties of the Group-V Element Arsenic. *Physical Review B*, **33**(6): 3778-3784. https://doi.org/10.1103/PhysRevB.33.3778

Nekrasov, I. A., Keller, G., Kondakov, D., Kozhevnikov, A., Pruschke, T., *et al.* (2005). Comparative Study of Correlation Effects in $CaVO_3$ and $SrVO_3$. *Physical Review B*, **72**(15): 155106 (1-6). https://doi.org/10.1103/PhysRevB.72.155106

Nye, J. F. (1985). *Physical properties of crystals: their representation by tensors and matrices*. Oxford University Press, UK.

Ohshima, R., Ando, Y., Matsuzaki, K., Susaki, T., Weiler, M., *et al.* (2017). Strong Evidence for d-electron Spin Transport at Room Temperature at a $LaAlO_3/SrTiO_3$ Interface. *Nature Materials*, **16**(6): 609-614. https://doi.org/10.1038/nmat4857

Ohtani, T., Kosuge, K., and Kachi, S. (1970). Hall Effect of NiAs -type $Ni_{1-x}S$. *Journal of the Physical Society of Japan*, **28**(6): 1588-1588. https://doi.org/10.1143/JPSJ.28.1588

Ohtani, T., Kosuge, K., and Kachi, S. (1970). Thermoelectric Power of $Ni_{1-x}S$. *Journal of the Physical Society of Japan*, **29**(2): 521-521. https://doi.org/10.1143/JPSJ.29.521

Ohtomo, A. and Hwang, H. (2004). A High-mobility Electron Gas at the $LaAlO_3/SrTiO_3$ Heterointerface. *Nature*, **427**(6973): 423-426. https://doi.org/10.1038/nature02308

Ohtomo, A., Muller, D., Grazul, J., and Hwang, H. Y. (2002). Artificial Charge-modulation in Atomic-scale Perovskite Titanate Superlattices. *Nature*, **419**(6905): 378-380. https://doi.org/10.1038/nature00977

Palczewski, A. D., Kondo, T., Khasanov, R., Kolesnikov, N. N., Timonina, A. V., *et al.* (2008). Origins of Large Critical Temperature Variations in Single-layer Cuprates. *Physical Review B*, **78**(5): 054523 (1-5). https://doi.org/10.1103/PhysRevB.78.054523

Parragh, N., Toschi, A., Held, K., and Sangiovanni, G. (2012). Conserved Quantities of SU(2)-invariant Interactions for Correlated Fermions and the Advantages for Quantum Monte Carlo Simulations. *Physical Review B*, **86**(15): 155158 (1-4). https://doi.org/10.1103/PhysRevB.86.155158

Parvin, F. and Naqib, S. (2017). Elastic, Thermodynamic, Electronic, and Optical Properties of Recently Discovered Superconducting Transition Metal Boride NbRuB: An Ab-initio Investigation. *Chinese Physics B*, **26**(10): 106201 (1-9). doi:10.1088/1674-1056/26/10/106201

Paudyal, D., Pecharsky, V. K., Gschneidner Jr, K. A., and Harmon, B. N. (2006). Electron Correlation Effects on the Magnetostructural Transition and Magnetocaloric Effect in $Gd_5Si_2Ge_2$. *Physical Review B*, **73**(14): 144406 (1-12). https://doi.org/10.1103/PhysRevB.73.144406

Paul, A. and Birol, T. (2019). Applications of DFT + DMFT in Materials Science. *Annual Review of Materials Research*, **49**: 31-52. https://doi.org/10.1146/annurev-matsci-070218-121825

Pavarini, E. (2021). Solving the Strong-correlation Problem in Materials. *La Rivista del Nuovo Cimento* , **44**: 597-640. https://doi.org/10.1007/s40766-021-00025-8

Perdew, J., Burke, K., and Ernzerhof, M. (1998). Perdew, Burke, and Ernzerhof Reply. *Physical Review Letters*, **80**(4): 891-891. https://doi.org/10.1103/PhysRevLett.80.891

Perdew, J. P., Burke, K., and Ernzerhof, M. (1996). Generalized Gradient Approximation Made Simple. *Physical Review Letters*, **77**(18): 3865-3868. https://doi.org/10.1103/PhysRevLett.77.3865

Perdew, J. P. and Levy, M. (1985). Extrema of the Density Functional for the Energy: Excited States from the Ground-state Theory. *Physical Review B*, **31**(10): 6264-6272. https://doi.org/10.1103/PhysRevB.31.6264

Pickett, M. D., Medeiros-Ribeiro, G., and Williams, R. S. (2013). A Scalable Neuristor Built with Mott Memristors. *Nature Materials*, **12**(2): 114-117. https://doi.org/10.1038/nmat3510

Pietro, W. J. and Hehre, W. J. (1983). Molecular Orbital Theory of the Properties of Inorganic and Organometallic Compounds. 3. STO-3G Basis Sets for First and Second-row Transition Metals. *Journal of Computational Chemistry*, **4**(2): 241-251. https://doi.org/10.1002/jcc.540040215

Piskunov, S., Heifets, E., Eglitis, R. I., and Borstel, G. (2004). Bulk Properties and Electronic Structure of $SrTiO_3$, $BaTiO_3$, $PbTiO_3$ Perovskites: an Ab-initio HF/DFT Study. *Computational Materials Science*, **29**(2): 165-178. https://doi.org/10.1016/j.commatsci.2003.08.036

Pizzi, G., Volja, D., Kozinsky, B., Fornari, M., and Marzari, N. (2014). Boltzwann: A Code for the Evaluation of Thermoelectric and Electronic Transport Properties with a Maximally-localized Wannier Functions Basis. *Computer Physics Communications*, **185**(1): 422-429. https://doi.org/10.1016/j.cpc.2013.09.015

Pollet, L., Van Houcke, K., and Rombouts, S. M. (2007). Engineering Local Optimality in Quantum Monte Carlo Algorithms. *Journal of Computational Physics*, **225**(2): 2249-2266. https://doi.org/10.1016/j.jcp.2007.03.013

Popper, K. (1957). Philosophy of Science. *British Philosophy in the Mid-Century(British Journal for the Philosophy of Science)*, **10**(38): 159-160

Prezioso, M., Merrikh-Bayat, F., Hoskins, B., Adam, G. C., Likharev, K. K., *et al.* (2015). Training and Operation of an Integrated Neuromorphic Network Based on Metal-oxide Memristors. *Nature*, **521**(7550): 61-64. https://doi.org/10.1038/nature14441

Pruschke, T. and Bulla, R. (2005). Hund's Coupling and the Metal-insulator Transition in the Two-band Hubbard Model. *The European Physical Journal B-Condensed Matter and Complex Systems*, **44**(2): 217-224. https://doi.org/10.1140/epjb/e2005-00117-4

Rai, R. K, Ray, R. B., Kaphle, G. C, and Niraula, O. P. (2020). Electronic Structure and Transport Properties of Superlattices: $La_{1-x}Sr_xTiO_3$ (x = 0, 0.20, 0.80, 1). *Journal of Nepal Physical Society*, **6**(2): 134-148. http://doi.org/10.3126/jnphyssoc.v6i2.34869

Rai, R. K, Ray, R. B., Kaphle, G. C, and Niraula, O. P. (2021). Electronic and Transport properties of Sr-site Substituted: $Ca_{1-x}Sr_xVO_3$ (x = 0, 0.33, 0.67, 1). *Journal of Nepal Physical Society*, **7**(1): 6-17. http://doi.org/10.3126/jnphyssoc.v7i1.36968

Rai, R. K, Ray, R. B., Kaphle, G. C, and Niraula, O. P. (2021). A Continuous Time Quantum Monte Carlo as an Impurity Solver for Strongly Correlated System. *Journal of Nepal Physical Society*, **7**(3): 14-26. https://doi.org/10.3126/jnphyssoc.v7i3.42185

Rai, R. K., Kaphle, G. C., Ray, R. B., and Niraula, O. P. (2023). Unraveling the Structural and Mechanical Stability, Electronic, and Optical Properties of $(La_xSr_{1-x}VO_3)_n$ (n = 1, 2; x = 0, 0.5, 1). *Solid State Communications*, **368**(1): 115173 (1-11). https://doi.org/10.1016/j.ssc.2023.115173

Rai, R. K., Ray, R. B., and Niraula, O. P. (2023). Stability, Electronic, Optical and Thermoelectric Properties of Site-substituted $LaVO_3$. *Materials Today Communications*, **35**: 105510 (1-14). https://doi.org/10.1016/j.mtcomm.2023.105510

Reinle-Schmitt, M., Cancellieri, C., Li, D., Fontaine, D., Medarde, M., *et al.* (2012). Tunable Conductivity Threshold at Polar Oxide Interfaces. *Nature Communications*, **3**(1): 1-6. https://doi.org/10.1038/ncomms1936

Rey, M. J., Dehaudt, P., Joubert, J. C., Lambert-Andron, B., Cyrot, M., *et al.* (1990). Preparation and Structure of the Compounds $SrVO_3$ and Sr_2VO_4. *Journal of Solid State Chemistry*, **86**(1): 101-108. https://doi.org/10.1016/0022-4596(90)90119-I

Riza, M. A., Ibrahim, M. A., Ahamefula, U. C., Mat Teridi , M. A., Ahmad Ludin, N., *et al.* (2016). Prospects and Challenges of Perovskite Type Transparent Conductive Oxides in Photovoltaic Applications. Part I - Material Developments. *Solar Energy*, **137**: 371-378. https://doi.org/10.1016/j.solener.2016.08.042

Rohringer, G., Hafermann, H., Toschi, A., Katanin, A., Antipov, A., *et al.* (2018). Diagrammatic Routes to Nonlocal Correlations Beyond Dynamical Mean Field Theory. *Reviews of Modern Physics*, **90**(2): 025003 (1-53). https://doi.org/10.1103/RevModPhys.90.025003

Ronchi, A., Franceschini, P., Homm, P., Gandolfi, M., Ferrini, G., *et al.* (2021). Light-assisted Resistance Collapse in a V_2O_3 Based Mott-Insulator Device. *Physical Review Applied*, **15**(4): 044023 (1-9). https://doi.org/10.1103/PhysRevApplied.15.044023

Rose, J. H., Smith, J. R., Guinea, F., and Ferrante, J. (1984). Universal Features of the Equation of State of Metals. *Physical Review B*, **29**(6): 2963-2969. https://doi.org/10.1103/PhysRevB.29.2963

Rozenberg, M. (2019). *Dynamical mean field theory and the Mott transition.* Lecture Notes of the Autumn School, 2019, Jülich, Germany.

Rubtsov, A. N., Savkin, V. V., and Lichtenstein, A. I. (2005). Continuous-time Quantum Monte Carlo Method for Fermions. *Physical Review B*, **72**(3): 035122 (1-9). https://doi.org/10.1103/PhysRevB.72.035122

Rückamp, R., Benckiser, E., Haverkort, M., Roth, H., Lorenz, T., *et al.* (2005). Optical Study of Orbital Excitations in Transition Metal Oxides. *New Journal of Physics*, **7**(1): 144 (1-35). doi:10.1088/1367-2630/7/1/144

Ryu, H. J., Aksamija, Z., Paskiewicz, D., Scott, S., Lagally, M., *et al.* (2010). Quantitative Determination of Contributions to the Thermoelectric Power Factor in Si Nanostructures. *Physical Review Letters*, **105**(25): 256601 (1-4). https://doi.org/10.1103/PhysRevLett.105.256601

Sachdev, S. (1999). Universal Relaxational Dynamics Near Two-dimensional Quantum Critical Points. *Physical Review B*, **59**(21): 14054-14073. https://doi.org/10.1103/PhysRevB.59.14054

Sachdev, S., (1999). Quantum Phase Transitions. *Physics World*, **12**(4): 33-38. doi:10.1088/2058-7058/12/4/23

Saeed, Y., Singh, N., and Schwingenschlögl, U. (2014). Enhanced Thermoelectric Figure of Merit in Strained Tl -doped Be_2Se_3. *Applied Physics Letters*, **105**(3): 031915 (1-4). https://doi.org/10.1063/1.4890858

Sage, M., Blake, G., and Palstra, T. (2008). Insulator to Metal Transition in (R, Ca)VO_3(R = Pr, Sm and Y). *Physical Review B*, **77**(15): 155121 (1-8). https://doi.org/10.1103/PhysRevB.77.155121

Sakai, S., Arita, R., and Aoki, H. (2004). Numerical Algorithm for the Double-orbital Hubbard Model: Hund-coupled Pairing Symmetry in the Doped Case. *Physical Review B*, **70**(17): 172504 (1-4). https://doi.org/10.1103/PhysRevB.70.172504

Salehi, H. (2011). First-principles Studies on the Electronic Structure and Bandstructure of Paraelectric $SrTiO_3$ by Different Approximations. *Journal of Modern Physics*, **2**(9): 934-943. http://dx.doi.org/10.4236/jmp.2011.29111

Sandvik, A. W. and Kurkijärvi, J. (1991). Quantum Monte Carlo Simulation Method for Spin Systems. *Physical Review B*, **43**(7): 5950-5961. https://doi.org/10.1103/PhysRevB.43.5950

Santana, J. A., Krogel, J. T., Kent, P. R., and Reboredo, F. A. (2017). Diffusion Quantum Monte Carlo Calculations of $SrFeO_3$ and $LaFeO_3$. *The Journal of Chemical Physics*, **147**(3): 034701 (1-9). https://doi.org/10.1063/1.4994083

Santana, J. A., Krogel, J. T., Okamoto, S., and Reboredo, F. A. (2020). Electron Confinement and Magnetism of $(LaTiO_3)_1/(SrTiO_3)_5$ Heterostructure: A Diffusion Quantum Monte Carlo Study. *Journal of Chemical Theory and Computation*, **16**(1): 643-650. https://doi.org/10.1021/acs.jctc.9b00678

Sawatzky, G. and Allen, J. (1984). Magnitude and Origin of the Band Gap in NiO. *Physical Review Retters*, **53**(24): 2339-2342. https://doi.org/10.1103/PhysRevLett.53.2339

Sayama, H. (2015). *Introduction to the modeling and analysis of complex systems*. Open SUNY Textbooks, USA.

Sayama, H., Pestov, I., Schmidt, J., Bush, B.J., Wong, C., *et al.* (2013). Modeling Complex Systems with Adaptive Networks. *Computers and Mathematics with Applications*, **65**(10): 1645-1664. https://doi.org/10.1016/j.camwa.2012.12.005

Scafetta, M. D., Cordi, A. M., Rondinelli, J. M., and May, S. J. (2014). Band Structure and Optical Transitions in $LaFeO_3$: Theory and Experiment. *Journal of Physics: Condensed Matter*, **26**(50): 505502 (1-7). doi:10.1088/0953-8984/26/50/505502

Schwarz, K., Blaha, P., and Trickey, S. (2010). Electronic Structure of Solids with Wien2k. *Molecular Physics*, **108**(21): 3147-3166. https://doi.org/10.1080/00268976.2010.506451

Sclauzero, G., Dymkowski, K., and Ederer, C. (2016). Tuning the Metal-insulator Transition in d^1 and d^2 Perovskites by Epitaxial Strain: A First-principles Based Study. *Physical Review B*, **94**(24): 245109 (1-11). https://doi.org/10.1103/PhysRevB.94.245109

Sekiyama, A., Fujiwara, H., Imada, S., Suga, S., Eisaki, H., *et al.* (2004). Mutual Experimental and Theoretical Validation of Bulk Photoemission Spectra of $Sr_{1-x}Ca_xVO_3$. *Physical Review Letters*, **93**(15): 156402 (1-4). https://doi.org/10.1016/j.elspec.2004.02.004

Sekiyama, A. and Suga, S. (2004). High-energy Bulk-sensitive Angle Resolved Photoemission Study of Strongly Correlated Systems. *Journal of Electron Spectroscopy and Related Phenomena*, **137**: 681-685. https://doi.org/10.1016/j.elspec.2004.02.004

Sevik, C. and Cagin, T. (2010). Ab-initio Study of Thermoelectric Transport Properties of Pure and Doped Quaternary Compounds. *Physical Review B*, **82**(4): 045202 (1-7). https://doi.org/10.1103/PhysRevB.82.045202

Shao, H., Qin, Y. Q., Capponi, S., Chesi, S., Meng, Z. Y., *et al.* (2017). Nearly Deconfined Spinon Excitations in the Square-lattice Spin-1/2 Heisenberg Antiferromagnet. *Physical Review X*, **7**(4): 041072 (1-26). https://doi.org/10.1103/PhysRevX.7.041072

Shao, H., and Sandvik, A. W. (2023). Progress on Stochastic Analytic Continuation of Quantum Monte Carlo Data. *Physics Reports*, **1003**: 1-88. https://doi.org/10.1016/j.physrep.2022.11.002

Shi, Z., and Jayatissa, A. H. (2018). Perovskites-based Solar Cells: a Review of Recent Progress, Materials and Processing Methods. *Materials*, **11**(5): 729 (1-34). https://doi.org/10.3390/ma11050729

Shin, B. S., Lim, H., Jang, S., Lee, D. J., and Lee, Y. S. (2021). Substitution-site and Ambient Annealing Dependences of Upconversion Emission of $SrTiO_3$. *Current Applied Physics*, **22**: 55-60. https://doi.org/10.1016/j.cap.2020.12.007

Sholl, D. S. and Steckel, J. A. (2022). *Density functional theory: A practical introduction*. John Wiley and Sons, NJ, USA.

Si, Q., Rabello, S., Ingersent, K., and Smith, J. L. (2001). Locally Critical Quantum Phase Transitions in Strongly Correlated Metals. *Nature*, **413**(6858): 804-808. https://doi.org/10.1038/35101507

Silver, R. N., Sivia, D. S., and Gubernatis, J. E. (1990). Maximum-entropy Method for Analytic Continuation of Quantum Monte Carlo Data. *Physical Review B*, **41**(4): 2380-2389. https://doi.org/10.1103/PhysRevB.41.2380

Singh, D. (1991). Ground-state Properties of Lanthanum: Treatment of Extended-core States. *Physical Review B*, **43**(8): 6388-6392. https://doi.org/10.1103/PhysRevB.43.6388

Sjfistedt, E., NordstrOm, L., and Singh, D. (2000). An Alternative Way of Linearizing the Augmented Plane-wave Method. *Solid State Communication*, **114**: 15-20. https://doi.org/10.1016/S0038-1098(99)00577-3

Slater, J. C. (1930). Atomic Shielding Constants. *Physical Review*, **36**(1): 57-64. https://doi.org/10.1103/PhysRev.36.57

Slater, J. C. (1951). A Simplification of the Hartree-Fock Method. *Physical Review*, **81**(3): 385-390. https://doi.org/10.1103/PhysRev.81.385

Sofo, J. O. and Mahan, G. (1994). Thermoelectric Figure of Merit of Superlattices. *Applied Physics Letters*, **65**(21): 2690-2692. https://doi.org/10.1063/1.112607

Staroverov, V. N., Scuseria, G. E., Tao, J., and Perdew, J. P. (2004). Tests of a Ladder of Density Functionals for Bulk Solids and Surfaces. *Physical Review B*, **69**(7): 075102 (1-11). https://doi.org/10.1103/PhysRevB.69.075102

Stoliar, P., Tranchant, J., Corraze, B., Janod, E., Besland, M. P., *et al.* (2017). A Leaky Integrate and Fire Neuron Analog Realized with a Mott Insulator. *Advanced Functional Materials*, **27**(11): 1604740 (1-7). https://doi.org/10.1002/adfm.201604740

Takagi, H., Ido, T., Ishibashi, S., Uota, M., Uchida, S., *et al.* (1989). Superconductor to Nonsuperconductor Transition in $(La_{1-x}Sr_x)_2CuO_4$ as Investigated by Transport and Magnetic Measurements. *Physical Review B*, **40**(4): 2254-2261. https://doi.org/10.1103/PhysRevB.40.2254

Tan, H., Egoavil, R., Béché, A., Martinez, G. T., Van Aert, S., *et al.* (2013). Mapping Electronic Reconstruction at the Metal-insulator Interface in $LaVO_3/SrVO_3$ Heterostructures. *Physical Review B*, **88**(15): 155123 (1-6). https://doi.org/10.1103/PhysRevB.88.155123

Tao, J. (2005). Explicit Inclusion of Paramagnetic Current Density in the Exchange-correlation Functionals of Current-density Functional Theory. *Physical Review B*, **71**(20): 205107 (1-5). https://doi.org/10.1103/PhysRevB.71.205107

Tao, J., Perdew, J. P., Staroverov, V. N., and Scuseria, G. E. (2003). Climbing the Density Functional Ladder: Nonempirical meta-Generalized Gradient Approximation Designed for Molecules and Solids. *Physical Review Letters*, **91**(14): 146401 (1-4). https://doi.org/10.1103/PhysRevLett.91.146401

Thomas, L. H. (1927). The Calculation of Atomic Fields. In *Mathematical Proceedings of the Cambridge Philosophical Society*, **23**(5): 542-548 https://doi.org/10.1017/S0305004100011683

Tohyama, T., Inoue, Y., Tsutsui, K., and Maekawa, S. (2005). Exact Diagonalization Study of Optical Conductivity in the Two-dimensional Hubbard Model. *Physical Review B*, **72**(4): 045113 (1-5). https://doi.org/10.1103/PhysRevB.72.045113

Tokura, Y., Kawasaki, M., and Nagaosa, N. (2017). Emergent Functions of Quantum Materials. *Nature Physics*, **13**(11): 1056-1068. https://doi.org/10.1038/nphys4274

Trimarchi, G., Leonov, I., Binggeli, N., Korotin, D., and Anisimov, V. (2008). LDA + DMFT Implemented with the Pseudopotential Plane-wave Approach. *Journal of Physics: Condensed Matter*, **20**(13): 135227 (1-7). doi:10.1088/0953-8984/20/13/135227

Vale, J. G., Calder, S., Donnerer, C., Pincini, D., Shi, Y. G., *et al.* (2018). Crossover from Itinerant to Localized Magnetic Excitations through the Metal-insulator Transition in $NaOsO_3$ *Physical Review B*, **97**(18): 184429 (1-17). https://doi.org/10.1103/PhysRevB.97.184429

Vaugier, L., Jiang, H., and Biermann, S. (2012). Hubbard U and Hund Exchange J in Transition Metal Oxides: Screening versus Localization Trends from Constrained Random Phase Approximation. *Physical Review B*, **86**(16): 165105 (1-21). https://doi.org/10.1103/PhysRevB.86.165105

Vidberg, H. and Serene, J. (1977). Solving the Eliashberg Equations by means of N-point Padé Approximants. *Journal of Low Temperature Physics*, **29**(3): 179-192. https://doi.org/10.1007/BF00655090

Vollhardt, D. (2012). Dynamical Mean Field Theory for Correlated Electrons. *Annalen der Physik*, **524**(1): 1-19. https://doi.org/10.1002/andp.201100250

Von Neumann, J. (1986). *Papers of John Von Neumann on computers and computer theory.* OSTI, USA.

Von Neumann, J., (1981). The Principles of Large-scale Computing Machines. *Annals of the History of Computing*, **3**(3): 263-273. https://doi.org/10.1109/MAHC.1981.10025

Vosk, R., Huse, D. A., and Altman, E. (2015). Theory of the Many-body Localization Transition in One-dimensional Systems. *Physical Review X*, **5**(3): 031032 (1-14). https://doi.org/10.1103/PhysRevX.5.031032

Walia, S., Balendhran, S., Nili, H., Zhuiykov, S., Rosengarten, G., *et al.* (2013). Transition Metal Oxides-thermoelectric Properties. *Progress in Materials Science*, **58**(8): 1443-1489 https://doi.org/10.1016/j.pmatsci.2013.06.003

Wang, P., Li, Y., and Lu, Y. (2011). Enhanced Piezoelectric Properties of $(Ba_{0.85}Ca_{0.15})(Ti_{0.9}Zr0.1)O_3$ Lead-free Ceramics by Optimizing Calcination and Sintering Temperature. *Journal of the European Ceramic Society*, **31**(11): 2005-2012. https://doi.org/10.1016/j.jeurceramsoc.2011.04.023

Wang, R., Mujahid, M., Duan, Y., Wang, Z. K., Xue, J., *et al.* (2019). A Review of Perovskites Solar Cell Stability. *Advanced Functional Materials*, **29**(47): 1808843 (1-25). https://doi.org/10.1002/adfm.201808843

Werner, P., Comanac, A., De'Medici, L., Troyer, M., and Millis, A. J. (2006). Continuous-time Solver for Quantum Impurity Models. *Physical Review Letters*, **97**(7): 076405 (1-4). https://doi.org/10.1103/PhysRevLett.97.076405

White, S. R. (1992). Density Matrix Formulation for Quantum Renormalization Groups. *Physical Review Letters*, **69**(19): 2863-2866. https://doi.org/10.1103/PhysRevLett.69.2863

Wold, A. and Ward, R. (1954). Perowskite-type Oxides of Cobalt, Chromium and Vanadium with some Rare Earth Elements. *Journal of the American Chemical Society*, **76** (4): 1029-1030. https://doi.org/10.1021/ja01633a031

Wooten, F. (1973). Optical Properties of Solids. *American Journal of Physics*, **41**(7): 939-940. https://doi.org/10.1119/1.1691372

Xue, Z. Y., Shao, L. B., Hu, Y., Zhu, S. L., and Wang, Z. D. (2013). Tunable Interfaces for Realizing Universal Quantum Computation with Topological Qubits. *Physical Review A*, **88**(2): 024303 (1-4). https://doi.org/10.1103/PhysRevA.88.024303

Yao, J., Wang, C., Yao, Z., and Zhai, H. (2022). Noise Enhanced Neural Networks for Analytic Continuation. *Machine Learning: Science and Technology*, **3**(2): 025010 (1-8). doi:10.1088/2632-2153/ac6f44

Yao, P., Wu, H., Gao, B., Tang, J., Zhang, Q., *et al.* (2020). Fully Hardware-implemented Memristor Convolutional Neural Network. *Nature*, **577**(7792): 641-646. https://doi.org/10.1038/s41586-020-1942-4

Yoo, J., Chandrasekharan, S., Kaul, R. K., Ullmo, D., and Baranger, H. U. (2005). On the Sign Problem in the Hirsch-Fye Algorithm for Impurity Problems. *Journal of Physics A: Mathematical and General*, **38** (48): 10307-10310. doi:10.1088/0305-4470/38/48/004

Zhang, L., Zhou, Y., Guo, L., Zhao, W., Barnes, A., *et al.* (2016). Correlated Metals as Transparent Conductors. *Nature Materials*, **15**(2): 204-210. https://doi.org/10.1038/nmat4493

Zhong, Z. and Hansmann, P. (2017). Band Alignment and Charge Transfer in Complex Oxide Interfaces. *Physical Review X*, **7**(1): 011023 (1-13). https://doi.org/10.1103/PhysRevX.7.011023

Ziman, J. M. (1972). *Principles of the Theory of Solids.* Cambridge University Press, UK.

Zitko, R., Hansen, D., Perepelitsky, E., Mravlje, J., Georges, A., *et al.* (2013). Extremely Correlated Fermi Liquid Theory Meets Dynamical Mean Field theory: Analytical Insights into the Doping-driven Mott Transition. *Physical Review B*, **88**(23): 235132 (1-18). https://doi.org/10.1103/PhysRevB.88.235132

Zubko, P., Gariglio, S., Gabay, M., Ghosez, P., and Triscone, J. M. (2011). Interface Physics in Complex Oxide Heterostructures. *Annual Review of Condensed Matter Physics*, **2**(1): 141-165. https://doi.org/10.1146/annurev-conmatphys-062910-140445

Zubkov, V. G., Berger, I. F., Artamonova, A. M., and Bazuev, G. V. (1984). Crystal Structure Refinement of Solid Solutions in the $LaTiO_3$-YTO_3 System. *Kristallografiya*, **29**(3): 494-497.

Zunger, A. and Malyi, O. I. (2021). Understanding Doping of Quantum Materials. *Chemical Reviews*, **121**(5): 3031-3060. https://doi.org/10.1021/acs.chemrev.0c00608

APPENDIX

Appendix -I: The Generic Phase Transitions in TMOs Materials

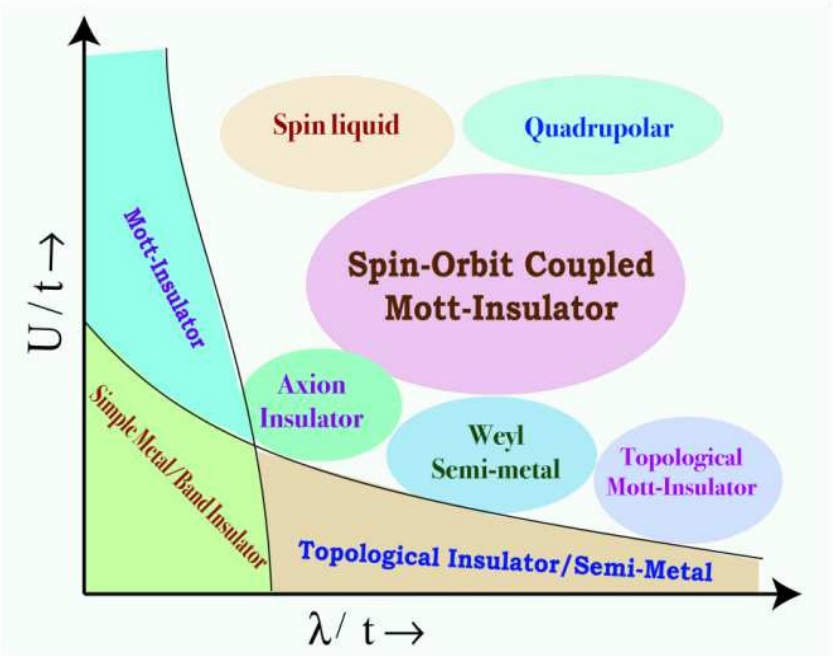

Figure 71: The underlying mechanism of transport phenomena are dictated by the fundamental component of the physical circumstances of the materials such as the Coulomb interaction parameter, (U/t), and spin-orbit coupling parameter, (λ/t) are the major component for metal-insulator phase transitions, where t is the electron hopping parameters (Vale *et al.*, 2018).

Appendix -II: The Kohn-Sham Self-Consistent Field Approximation Method

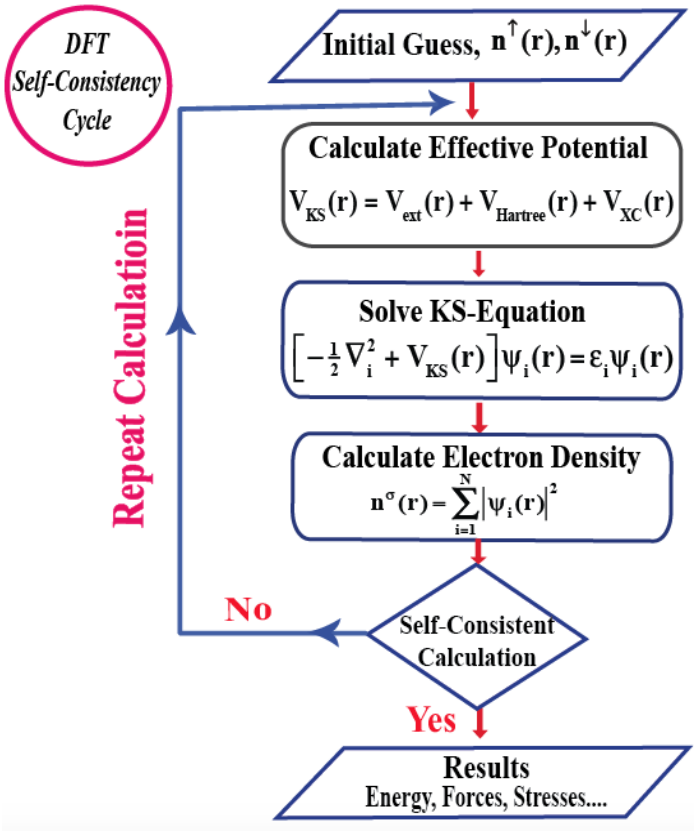

Figure 72: The schematic representation of the self-consistent field iterative calculation for the solution of Kohn–Sham equations. For the case of spin-polarized system there are two such loops that must be implemented simultaneously, to consider both of the spin density of states (Kohn & Sham, 1965).

Appendix -III: The Jacob's Ladder Interpretation of Efficiency of SCF Calculations

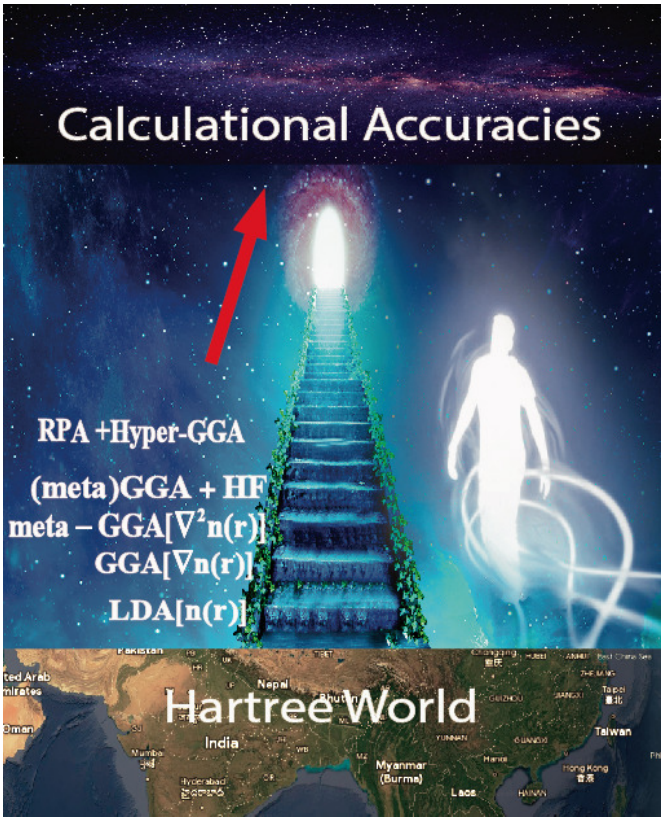

Figure 73: The Jacob's ladder for the required calculational efficiency and accuracy of the first-principle based calcuations (Perdew *et al.*, 1996; Jaramillo *et al.*, 2003; Becke & Johnson, 2005).

The first three rungs of the local spin density approximation (LSDA) involve semilocal components ($n_\uparrow(r)$ and $n_\downarrow(r)$) from infinitesimal neighborhood density or orbitals, with non-empirical constructions, and are accurate only for homogeneous or slowly changing electron gas (Kohn & Sham, 1965; Vosk *et al.*, 2015).

The second rung in the GGA involves adding the gradients $\nabla^2 n_\uparrow(r)$ and $\nabla^2 n_\downarrow(r)$ as in the PBE (Kohn & Sham, 1965; Perdew *et al.*, 1998), and PBEsol (Perdew & Levy, 1985) nonempirical constructions.

The third rung is meta-GGA,includes positive orbital kinetic energy densities(tive orbital kinetic energy densities $\tau_\uparrow(r)$ and $\tau_\downarrow(r)$), as in the Tao-Perdew-Staroverov-Scuseria (TPSS) nonempirical construction (Tao *et al.*, 2003; Staroverov *et al.*, 2004).

The fourth rung (see Fig. 73) of hyper-GGA (Perdew *et al.*, 1996; Jaramillo *et al.*, 2003; Becke & Johnson, 2005; Mori-Sánchez *et al.*, 2006; Arbuznikov *et al.*, 2006; Cohen

et al., 2007; Kaupp *et al.*, 2007), introduces a nonlocal parameter, the exact-exchange energy per electron, which is non-unique and gauge-dependent, unlike total energies.

Appendix -IV: Monte-Carlo Method with Metropolis-Hasting Algorithm

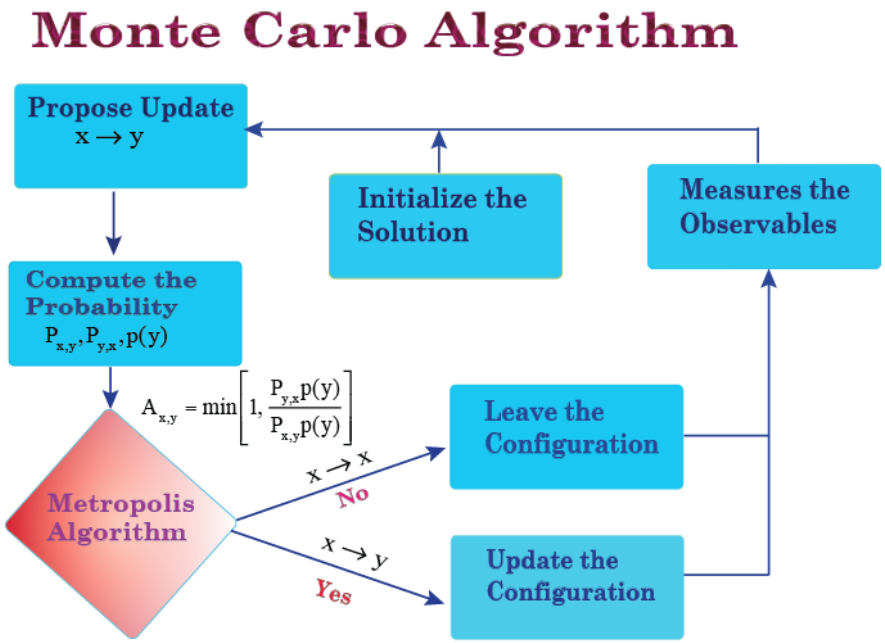

Figure 74: The schematic representation of Markov chain Monte-Carlo method with Metropolis Hasting selection criteria (Werner *et al.*, 2006; Gull *et al.*, 2011).

For sampling the configurations C that contribute to the value of the partition function Z, we employ the Markov chain Monte Carlo approach. Assuming that x_0 is the beginning configuration (or zeroth order configuration), we must proceed with a random walk in phase space from a current configuration, x to a new one, $y(x_j)$ as,

$$x_0 \rightarrow x_1 \rightarrow x_2 \rightarrow \ldots \rightarrow x_{n+1}\ldots. \tag{6.1}$$

To sum up probabilities, the Markov chain must reach a stationary distribution, be thermalized, and have clearly correlated successive points. Autocorrelation effects must be considered when computing Monte Carlo statistical errors. To create a Markov chain of diagrams, two moves can be used: insertion of a link (anti-link) and removal of a link. These moves ensure the system is thermalized and the autocorrelation effects are considered for computing the Monte Carlo statistical errors (Werner *et al.*, 2006).

Starting with an arbitrary Markov chain distribution, the process will converge expo-

nentially to a stationary distribution p(x) if the following two requirements are met: (i) Ergodicity: each configuration x is accessible in a limited number of Markov steps from any other configuration y. That is to say,

$\forall \mathrm{xy} \exists \mathrm{n} : (\mathrm{W}^{\mathrm{n}})_{\mathrm{xy}} \neq 0$

(ii) Detailed balance: The probability W_{xy} of moving from configuration x to configuration y with probability density p(x) meets the detailed balance requirement.

$$\int_{\mathrm{c}} \mathrm{W}_{\mathrm{xy}} \mathrm{p}(\mathrm{x}) = \mathrm{p}(\mathrm{y}) \tag{6.2}$$

To perform updates using the Metropolis algorithm in Markov chain Monte Carlo as shown in (Fig. 74) (Gull *et al.*, 2011), the probability must meet the detailed balance condition. For a given configuration $x = (\tau_1), ..., (\tau_n)$, inserting a time vertex (τ_{n+1}) to obtain $y = (\tau_1), ..., (\tau_n), (\tau_{n+1})$ ensures the condition. The transition probability density $\mathrm{W}_{\mathrm{x,y}}$ of transitioning from state x to state y is crucial.

$$\mathrm{W}_{\mathrm{x,y}} = \mathrm{W}_{\mathrm{prop}}(\mathrm{x} \to \mathrm{y}) \mathrm{A}_{\mathrm{acc}}(\mathrm{x} \to \mathrm{y}) \tag{6.3}$$

Where, $\mathrm{W}_{\mathrm{prop}}(\mathrm{x} \to \mathrm{y})$ is the proposal (proposed) probability density and $\mathrm{A}_{\mathrm{acc}}(\mathrm{x} \to \mathrm{y})$ is the acceptance probability density of going from x to y respectively.

Similarly, the transition probability $\mathrm{W}_{\mathrm{y,x}}$ of transitioning from state y to state x is,

$$\mathrm{W}_{\mathrm{y,x}} = \mathrm{W}_{\mathrm{prop}}(\mathrm{y} \to \mathrm{x}) \mathrm{A}_{\mathrm{acc}}(\mathrm{y} \to \mathrm{x}) \tag{6.4}$$

Furthermore, the probability density of inserting a time vertex (τ_{n+1}) is provided by the likelihood of selecting the imaginary time location τ_{n+1},

$$\mathrm{W}_{\mathrm{prop}}(\mathrm{x} \to \mathrm{y}) = \frac{\mathrm{d}\tau}{\beta} \tag{6.5}$$

The proposed probability density of removing a time vertex, on the other hand, is just the chance of picking that particular vertex among the n+1 available vertices,

$$\mathrm{W}_{\mathrm{prop}}(\mathrm{y} \to \mathrm{x}) = \frac{1}{\mathrm{n}+1} \tag{6.6}$$

Now, selecting the acceptance probabilities $\mathrm{A_{acc}(x \to y)}$ and $\mathrm{A_{acc}(y \to x)}$, we have,

$$\begin{aligned}\frac{\mathrm{W_{x,y}}}{\mathrm{W_{y,x}}} &= \frac{\mathrm{d}\tau}{\beta}\frac{\mathrm{n}+1}{1}\frac{\mathrm{A_{acc}(x \to y)}}{\mathrm{A_{acc}(y \to x)}} \\ &= \frac{\mathrm{p(y)}}{\mathrm{p(x)}}\frac{\mathrm{A_{acc}(x \to y)}}{\mathrm{A_{acc}(y \to x)}} = \frac{\mathrm{p(y)}}{\mathrm{p(x)}}\frac{1/(\mathrm{n}+1)}{\mathrm{d}\tau/\beta}\end{aligned} \tag{6.7}$$

Applying Metropolis' algorithm to fulfill the detailed balance principle we obtain the acceptance ratio as,

$$\begin{aligned}\mathrm{A_{acc}} &= \min\left[1, \tfrac{\mathrm{p(y)W_{prop}(y \to x)}}{\mathrm{p(x)W_{prop}(x \to y)}}\right] \\ &= \min\left[1, \tfrac{1}{\mathrm{n}+1}\tfrac{\beta}{\mathrm{d}\tau}\tfrac{\mathrm{p(y)}}{\mathrm{p(x)}}\right]\end{aligned} \tag{6.8}$$

Because the ratio of configuration probability densities p(y)/p(x) is infinitesimally small, the transition rate from configuration x to configuration y remains finite (White, 1992; Ferrero *et al.*, 2005).

Appendix -V: The Variation of Energy (ΔE) with the Variation of Lattice Parameter (Δa) for Pristine and Superstructure of Vanadates.

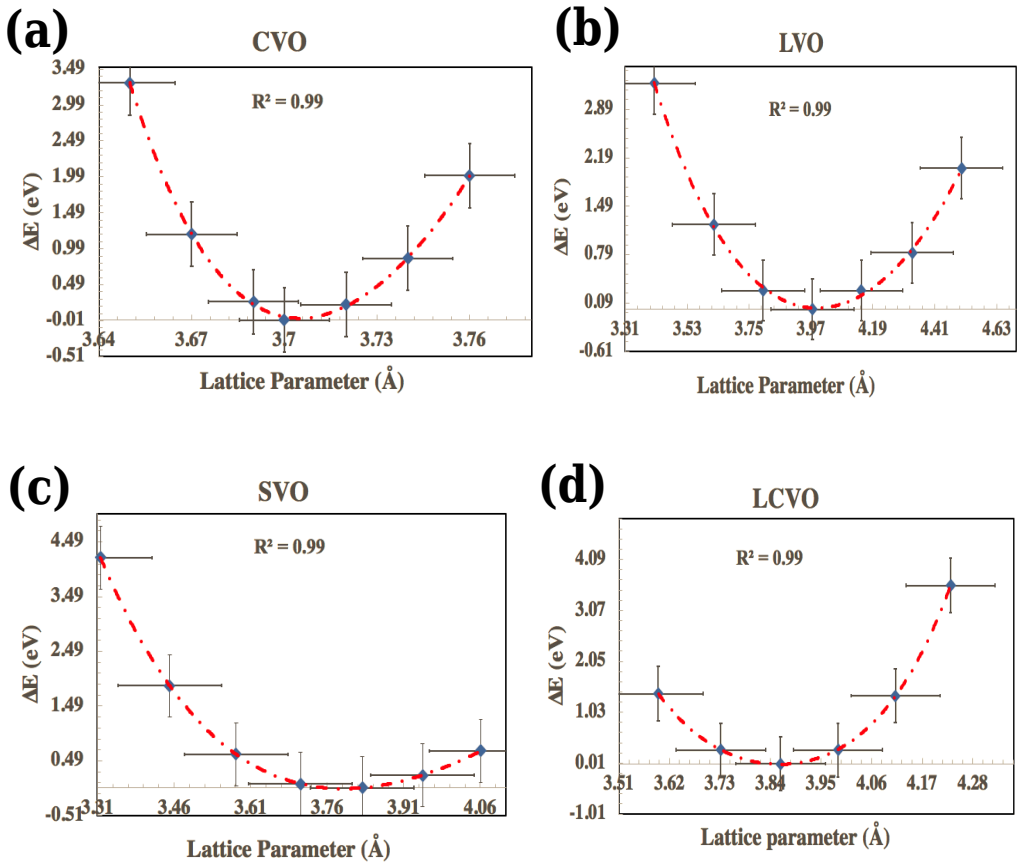

Figure 75: The energy difference vs. lattice parameters calculated at around their optimized values for (a) pristine $CaVO_3$ (CVO) (b) pristine $LaVO_3$ (LVO) (c) pristine $SrVO_3$ (SVO), and (d) superstructure $La_{0.40}Ca_{0.60}VO_3$ (LCVO) systems. All of the lattice parameters are computed within the computional error bars of convergence criteria. The coefficient of determination ($R^2 \simeq 1$) indicates the correctness of polynomial curve fittings.

Appendix -VI: The Comparative Phonon DOS and Bandstructure of Pristine Vanadates Showing the Acoustical and Optical Modes of Vibration in these systems.

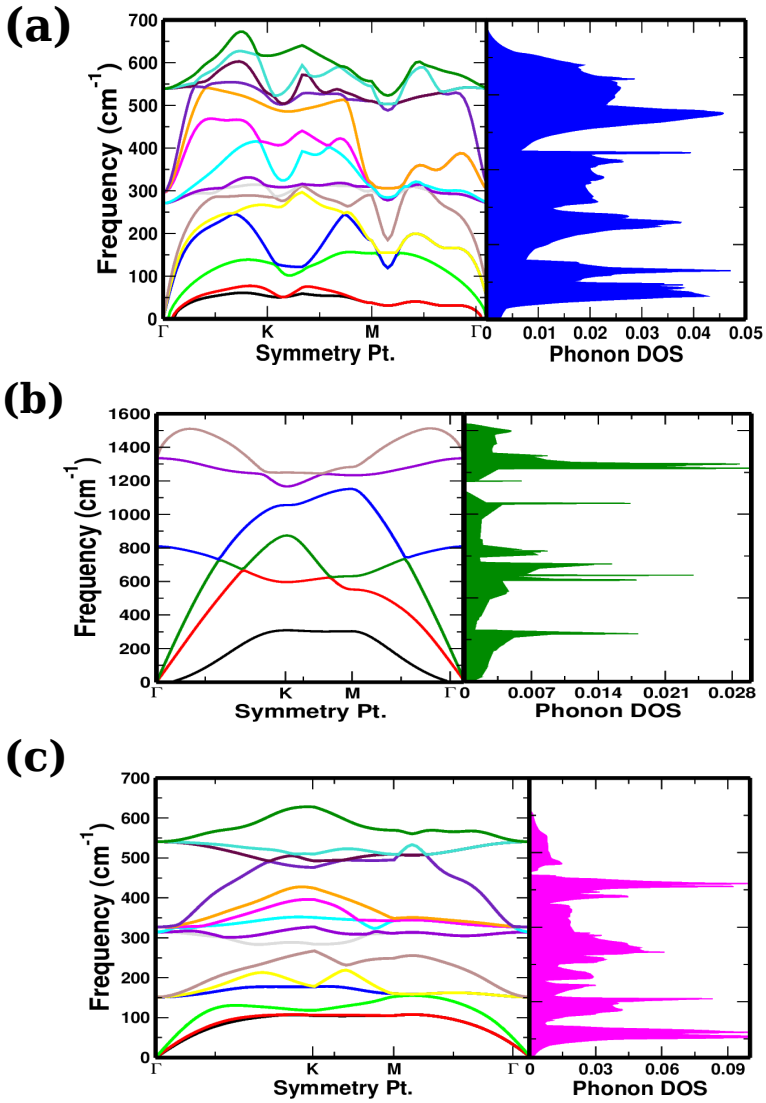

Figure 76: The phonon DOS and bandstructures for (a) pristine $CaVO_3$ (CVO) (b) pristine $LaVO_3$ (LVO) and (c) pristine $SrVO_3$ (SVO) systems.

Appendix -VII: The Variation of Energy (ΔE) with the Variation of Lattice Parameter (Δa) for Pristine Titanates.

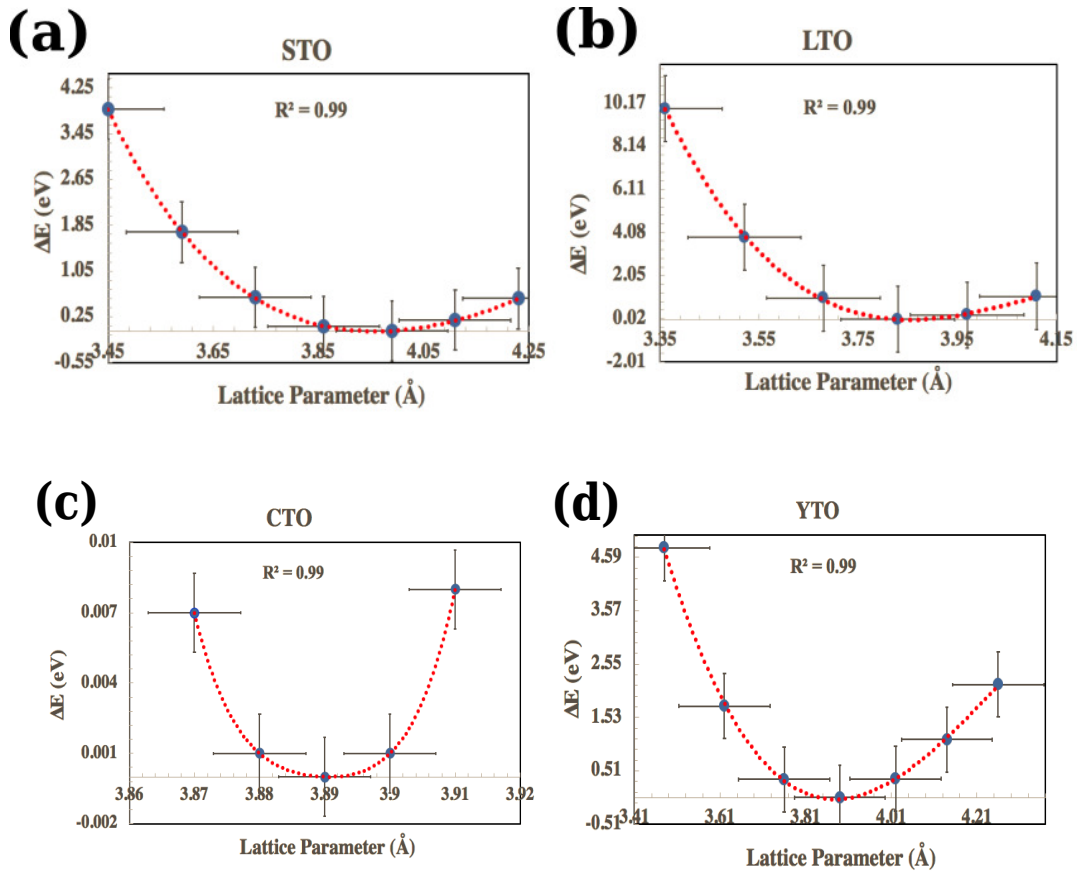

Figure 77: The energy difference vs. lattice parameters calculated at around their optimized values for (a) pristine $SrTiO_3$ (STO) (b) pristine $LaTiO_3$ (LTO) (c) pristine $CaTiO_3$ (CTO), and (d) pristine $YTiO_3$ (YTO) systems. All of the lattice parameters are computed within the computational error bars of convergence criteria. The coefficient of determination ($R^2 \simeq 1$) indicates the correctness of polynomial curve fittings.

Appendix -VIII: Parameterization of $U_{mm'm''m'''}$ by Spherical Symmetry

The parameterization of rotationally invariant two-body interaction tensor $U_{mm'm''m'''}$ in terms of invariant radial integrals F_k and proves the sum rule of isotropic and anisotropic integrals.

Based on the assumptions of two body on-site interaction tensor (Martin, 2004; Vaugier *et al.*, 2012), we have,

$$\begin{aligned} \mathrm{U_{mm'm''m'''}} = \sum_{k=0}^{\infty} \frac{4\pi}{2k+1} F_k \sum_{q=-k}^{k} \int d\Omega_1 \, Y^*_{lm}(r_1) Y_{kq}(r_1) Y_{lm''}(r_1) \\ \times \int d\Omega_2 \, Y^*_{lm'}(r_2) Y^*_{kq}(r_2) Y_{lm'''}(r_2) \end{aligned} \tag{6.9}$$

with the radial integrals F_k. The radial and angular integrals are separated using $\mathrm{d^3r} = \mathrm{r^2 dr d\Omega}$ in spherical coordinates. We may next use $Y_{lm}(r) = (-1)^m Y_{l,-m}(r)$ and its relation to the Wigner $3j$-symbols

$$\begin{aligned} \int \mathrm{d\Omega} \, \mathrm{Y_{l_1 m_1}}(r) Y_{l_2 m_2}(r) Y_{l_3 m_3}(r) = \sqrt{\frac{(2l_1+1)(2l_2+1)(2l_3+1)}{4\pi}} \\ \times \begin{pmatrix} l_1 & l_2 & l_3 \\ 0 & 0 & 0 \end{pmatrix} \begin{pmatrix} l_1 & l_2 & l_3 \\ m_1 & m_2 & m_3 \end{pmatrix} \end{aligned} \tag{6.10}$$

to obtain the interaction matrix elements

$$\begin{aligned} \mathrm{U_{mm'm''m'''}} = (2l+1)^2 \sum_{k=0}^{\infty} F_k \begin{pmatrix} l & k & l \\ 0 & 0 & 0 \end{pmatrix}^2 \sum_{q=-k}^{k} (-1)^{m+m'+q} \\ \times \begin{pmatrix} l & k & l \\ -m & q & m'' \end{pmatrix} \begin{pmatrix} l & k & l \\ -m' & -q & m''' \end{pmatrix} \end{aligned} \tag{6.11}$$

The Wigner $3j$-symbols selection rules limit the summation of k to even numbers from 0 to $2l$, rewriting it as $2k$ with the new variable k summing from 0 to l.

$$\mathrm{U_{mm'm''m'''}} = (2l+1)^2 \sum_{k=0}^{l} F_{2k} \begin{pmatrix} l & 2k & l \\ 0 & 0 & 0 \end{pmatrix}^2 \sum_{q=-2k}^{2k} (-1)^{m+m'+q} \times \begin{pmatrix} l & 2k & l \\ -m & q & m'' \end{pmatrix} \begin{pmatrix} l & 2k & l \\ -m' & -q & m''' \end{pmatrix} \tag{6.12}$$

The interaction tensor $\mathrm{U}_{mm'm''m'''}$ is parameterized by the radial integrals as the linear coefficients of the universal Wigner $3j$-symbols.

Appendix -IX: Expressing U and J in Terms of F_{2k}

From the definition of Hubbard U, we have

$$\mathrm{U} = \sum_{\mathrm{k=0}}^{\mathrm{l}} \mathrm{F_{2k}} \begin{pmatrix} l & 2k & l \\ 0 & 0 & 0 \end{pmatrix}^2 \sum_{\mathrm{mm'}} (-1)^{\mathrm{m+m'}} \begin{pmatrix} l & 2k & l \\ -m & 0 & m \end{pmatrix} \begin{pmatrix} l & 2k & l \\ -m' & 0 & m' \end{pmatrix} \tag{6.13}$$

The selection rule of Wigner $3j$-symbols (Martin, 2004; Vaugier *et al.*, 2012) was used to select the $q = 0$ term, followed by applying the sum rule.

$$\sum_{\mathrm{m}} (-1)^{\mathrm{l+m}} \begin{pmatrix} l & k & l \\ -m & 0 & m \end{pmatrix} = \sqrt{2\mathrm{l}+1}\, \delta_{\mathrm{k0}}. \tag{6.14}$$

Only the $k = 0$ term survives and we obtain

$$\mathrm{U} = (2\mathrm{l}+1)\, \mathrm{F}_0 \begin{pmatrix} l & 0 & l \\ 0 & 0 & 0 \end{pmatrix}^2 = \mathrm{F}_0. \tag{6.15}$$

Next we calculate the sum

$$\sum_{\mathrm{m}} \mathrm{J_{mm'}} = (2l+1)^2 \sum_{k=0}^{l} F_{2k} \begin{pmatrix} l & 2k & l \\ 0 & 0 & 0 \end{pmatrix}^2 \sum_{qm} \begin{pmatrix} l & 2k & l \\ -m & q & m' \end{pmatrix} \begin{pmatrix} l & 2k & l \\ -m' & -q & m \end{pmatrix} \tag{6.16}$$

The selection rule requires $q = m - m'$, which may not be within $q \in [-2k, 2k]$; canceling the sign $(-1)^{m+m'+q}$ in (6.12), we show the last two symbols are equal. We have,

$$\begin{pmatrix} \mathrm{j}_1 & j_2 & j_3 \\ m_1 & m_2 & m_3 \end{pmatrix} = (-1)^{j_1+j_2+j_3} \begin{pmatrix} j_1 & j_2 & j_3 \\ -m_1 & -m_2 & -m_3 \end{pmatrix} = \begin{pmatrix} j_3 & j_2 & j_1 \\ -m_3 & -m_2 & -m_1 \end{pmatrix} \tag{6.17}$$

which then leads to

$$\sum_{\mathrm{m}} \mathrm{J}_{\mathrm{mm}'} = (2\mathrm{l}+1)^2 \sum_{\mathrm{k}=0}^{\mathrm{l}} \mathrm{F}_{2\mathrm{k}} \begin{pmatrix} l & 2k & l \\ 0 & 0 & 0 \end{pmatrix}^2 \sum_{\mathrm{qm}} \begin{pmatrix} l & 2k & l \\ -m & q & m' \end{pmatrix}^2 . \tag{6.18}$$

We now use the orthonormality relation of Wigner $3j$-symbols

$$(2\mathrm{l}+1) \sum_{\mathrm{m_1 m_2}} \begin{pmatrix} j_1 & j_2 & l \\ m_1 & m_2 & m \end{pmatrix} \begin{pmatrix} j_1 & j_2 & l' \\ m_1 & m_2 & m' \end{pmatrix} = \delta_{\mathrm{ll}'} \delta_{\mathrm{mm}'}, \tag{6.19}$$

to further reduce (6.18) into

$$\sum_{\mathrm{m}} \mathrm{J}_{\mathrm{mm}'} = (2\mathrm{l}+1) \sum_{\mathrm{k}=0}^{\mathrm{l}} \mathrm{F}_{2\mathrm{k}} \begin{pmatrix} l & 2k & l \\ 0 & 0 & 0 \end{pmatrix}^2 . \tag{6.20}$$

The result is based on rotational symmetry and Hund's coupling J with U, as per equations (6.15) and (6.20), we have,

$$\mathrm{J} = \frac{1}{2\mathrm{l}} \left(\sum_{\mathrm{m}} \mathrm{J}_{\mathrm{mm}'} - \mathrm{F}_0 \right) = \frac{2\mathrm{l}+1}{2\mathrm{l}} \sum_{\mathrm{k}=1}^{\mathrm{l}} \mathrm{F}_{2\mathrm{k}} \begin{pmatrix} l & 2k & l \\ 0 & 0 & 0 \end{pmatrix}^2 \tag{6.21}$$

The Hubbard U and Hund's coupling J are the isotropic and anisotropic parts of the interaction, respectively, represented by equations (6.15) and (6.21).

Appendix -X: Crystal Field Effect

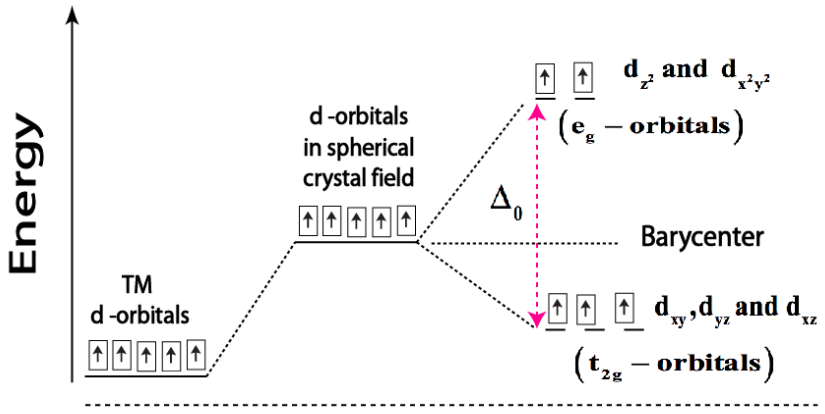

Figure 78: A level diagram of the d -orbitals that shows t_{2g} and e_g groups with different energies due to the CFE splitting (Jarlborg & Arbman, 1977; Vaugier *et al.*, 2012).

Crystals are formed when atoms interact with the electrostatic field generated by surrounding ions. When an isolated metal ion is placed in a crystal, its orbitals interact with potential from neighboring atoms (ligands) in the crystal lattice. The d or f orbitals of the ion have the same energy and are degenerate. However, when placed in the crystal, the orbitals interact with the potential from neighboring atoms (ligands) in the crystal lattice. For example, d_{z^2}, d_{xz}, d_{yz}, d_{xy} and $d_{x^2-y^2}$ orbitals have various interactions with ligands oriented along x, y, and z. The d -orbitals along ligand axes experience more repulsion, making it less energetically favorable to place an electron in one of the d_{z^2} or $d_{x^2-y^2}$ orbitals as shown in (Fig. 78). This process is known as crystal field splitting (CFE). The study focused on the CFE for the $3d^{2,3}$ electron of Ti or V, describing the interaction between the f-electron and surrounding ligands using the effective potential (V_{CFE}) in the atomic Hamiltonian.

$$\mathrm{H} = \underbrace{\sum_{i=1}^{Z} \frac{p_i^2}{2m}}_{\mathrm{H_0}} + \underbrace{\sum_{i<j}^{Z} \frac{e^2}{|r_i - r_j|} - \sum_{i=1}^{Z} \frac{Ze^2}{r_i}}_{\mathrm{V_1}} + \underbrace{\sum_{i=1}^{Z} g(r_i) l_i \cdot s_i}_{\mathrm{V_2}} + \mathrm{e} \sum_{\mathrm{i}} \mathrm{V_{CFE}(r_i)} \quad (6.22)$$

where V_1 represents self-consistent potential corrections and V_2 represents spin-orbit coupling. The potential at the point r of the charge q_j situated at the point R_j is described by V_{CFE}. It is more convenient to write it using the unit point charge potential's spherical

harmonics (Jarlborg & Arbman, 1977) as,

$$\mathrm{V_{CFE}(r)} = \sum_{\mathrm{j=1}}^{\mathrm{N}} \frac{\mathrm{q_j}}{|\mathrm{R_j - r}|} = \sum_{\mathrm{l=0}}^{\infty} \frac{\mathrm{q_j r^l}}{\mathrm{R_j^{l+1}}} \sum_{\mathrm{m=-l}}^{\mathrm{l}} \frac{4\pi}{2\mathrm{l}+1} \mathrm{Y^{\star}_{lm}}(\theta_{\mathrm{r}}\phi_{\mathrm{r}}) \mathrm{Y_{lm}}(\theta_{\mathrm{R_j}}\phi_{\mathrm{R_j}}). \tag{6.23}$$

It is also feasible to rewrite (6.22) using tesseral harmonics, which are defined in terms of spherical harmonics:$\mathrm{Z_{l0}} = \mathrm{Y_l^0}$, $\mathrm{Z^c_{lm}} = (\mathrm{Y_l^{-m}} + \mathrm{Y_l^m})/\sqrt{2}$, $\mathrm{Z^s_{lm}} = \mathrm{i}(\mathrm{Y_l^{-m}} + \mathrm{Y_l^m})/\sqrt{2}$, and also by incorporating a coefficient $\gamma_{l\alpha}$ associated to the charge distribution, $\rho(\mathrm{r}) = \sum \mathrm{q_j}\delta(\mathrm{R_j - r})$

$$\mathrm{V_{CFE}}(\mathrm{r},\theta,\phi) = \sum_{\mathrm{l=0}}^{\infty} \mathrm{r^l} \sum_{\alpha} \underbrace{\left(\frac{4\pi}{2l+1} \int \frac{\rho(r)}{r^{l+1}} Z_{l\alpha}(\theta,\phi)\mathrm{d}^3 r \right)}_{\gamma_{\mathrm{l}\alpha}} \mathrm{Z_{l\alpha}}(\theta,\phi). \tag{6.24}$$

Rare-earth ions have a small crystal-field splitting due to the small perturbation (6.23) compared to spin-orbit coupling (SOC). This results in insignificant intermixing of different J values, allowing for neglecting off-diagonal elements in the Hamiltonian and determination of matrix elements of potential functions representations. This method, described to use Stevens operator equivalents to write the CFE Hamiltonian are obtained by replacing x, y, and z by different combinations of $\mathrm{J_x}, \mathrm{J_y}, \mathrm{J_z}$ (Vaugier *et al.*, 2012).

PUBLICATIONS

International Journals

1. **Rai, R. K., Kaphle, G. C., Ray, R. B., and Niraula, O. P. (2023).**

   Unraveling the structural and mechanical stability, electronic, and optical properties of $(La_xSr_{1-x}VO_3)_n$ (n =1, 2; x = 0, 0.5, 1). *Solid State Communications* **368** (1):115173 (1-11).

   DOI:https://doi.org/10.1016/j.ssc.2023.115173

2. **Rai, R. K., Ray, R. B., and Niraula, O. P. (2023).**

   Stability, electronic, optical and thermoelectric properties of site-substituted $LaVO_3$. *Materials Today Communications* **35**: 105510 (1-14).

   DOI:https://doi.org/10.1016/j.mtcomm.2023.105510

3. **Rai, R. K., Kaphle, G. C., Ray, R. B., and Niraula, O. P. (2023).**

   Exploring the Electronic Transport, Magnetic, and Optical Properties of Strongly Correlated Systems: A Numerical Analytical Continuation Approach. *International Journal of Modern Physics B*. **Online** (2023).(Published on September 21, 2023)

   DOI:https://doi.org/10.1142/S0217979224503417

National Journals

1. **Rai, R. K., Kaphle, G. C., Ray, R. B., and Niraula, O. P. (2020).**

   Electronic Structure and Transport Properties of Superlattices: $La_{(1-x)}Sr_xTiO_3$ (x =0, 0.20, 0.80, 1). *Journal of Nepal Physical Society* **6** (2): 134-148.

   DOI:http://doi.org/10.3126/jnphyssoc.v6i2.3486

2. **Rai, R. K., Kaphle, G. C., Ray, R. B., and Niraula, O. P. (2021).**

   Electronic and Transport Properties of Sr-site Substituted: $Ca_{(1-x)}Sr_xVO_3$. *Journal of Nepal Physical Society* **7** (1): 6-17.

   DOI:http://doi.org/10.3126/jnphyssoc.v7i1.36968

3. **Rai, R. K., Kaphle, G. C., Ray, R. B., and Niraula, O. P. (2021).**

   A Continuous Time Quantum Monte Carlo as an Impurity Solver for Strongly Correlated System.*Journal of Nepal Physical Society* **7** (3): 14-26.

   DOI:http://doi.org/10.3126/jnphyssoc.v7i3.42185

PRESENTATIONS/PARTICIPATIONS

I have presented/participated in several National and International Conferences, Seminars, Workshops and Schools conducted by various organizations, viz.

Oral Presentations

I. **Rai, R. K., Kaphle, G. C., Ray, R. B., and Niraula, O. P. (2022).**
"Numerical Analytic Continuation to Probe the Electronic Structure of Strongly Correlated System: Maximum Entropy Model"
"ANPA-Conference 2022" [15-17, July, 2022].
Organized by:Association of Nepali Physicists in America (ANPA)

II. **Rai, R. K., Kaphle, G. C., Ray, R. B., and Niraula, O. P. (2021).**
"Electronic Structure, Thermoelectric and Optical Properties of Os-based Double Perovskites"
"International Conference on Material Science and Characterization Technology (ICMSCT-2021) [26-28, September, 2021].
Organized by: Department of Physics, St. Xavier's College, Maitighar, Kathmandu, Nepal

III. **Rai, R. K., Kaphle, G. C., Ray, R. B., and Niraula, O. P. (2021).**
"Electronic Structure, Thermoelectric and Optical Properties of $\mathrm{La_xSr_{1-x}VO_3}$ $(0 \leq x \leq 1)$"
"ANPA conference 2021" [16-18, July, 2021].
Organized by: Association of Nepali Physicist of America (ANPA)

IV. **Rai, R. K., Kaphle, G. C., Ray, R. B., and Niraula, O. P. (2020).**
"A Continuous Time Quantum Monte Carlo (CT-QMC) as an Impurity Solver Method for Strongly Correlated System"
"37th AGM, Nepal Physical Society" [23, 24, October, 2020].
Organized by: Nepal Physical Society, Kathmandu, Nepal

V. **Rai, R. K., Kaphle, G. C., Ray, R. B., and Niraula, O. P. (2020).**
"First-Principles Study of Electronic Structures And Transport Properties of Heterostructure of (La, Ca)VO_3"
"ANPA Conference-2020" [17-19, July, 2020].
Organized by: Association of Nepali Physicist of America (ANPA)

VI. **Rai, R. K., Kaphle, G. C., Ray, R. B., and Niraula, O. P. (2019).**
"First-Principle Study of Filling Control Effect on Electronic Structures and Transport Properties of Heterostructures of $LaTiO_3$/$SrTiO_3$"
"36th AGM, Nepal Physical Society" [8-9, November, 2019].
Organized by: Nepal Physical Society, Kathmandu, Nepal

VII. **Rai, R. K., Kaphle, G. C., Ray, R. B., and Niraula, O. P. (2019).**
"Ab-initio Study of the Doping Effect on Electronic Structure and Transport Properties of Heterostructures of $LaTiO_3$/$SrTiO_3$"
"International Seminar on Correlative Advancement on Analytical and Applied Physics (CAAAP-2019)"[21-22, October, 2019].
Organized by: Department of Physics of St. Joseph's College, Northpoint, Darjeeling, India

VIII. **Rai, R. K., Kaphle, G. C., Ray, R. B., and Niraula, O. P. (2019).**
"First-Principle Study of Electronic Structure and Transport Properties of $SrVO_3$/$LaVO_3$"
"National Symposium on Research, Development and Innovation in Physics (NSRDIP-2019)" [3-4, September, 2019].
Organized by: St. Xavier's College, Maitighar, Kathmandu, Nepal

IX. **Rai, R. K., Kaphle, G. C., Ray, R. B., and Niraula, O. P. (2019).**
"Electronic structure and Transport properties of Complex Transition Metal Oxides: $LaTiO_3$/$CaVO_3$"
"International Conference on Nanoscience and High Energy Physics (ICNHEP-2019)"[4-6, February, 2019].
Organized by: Central Department of Physics, Tribhuvan University(T.U.), Nepal

★ *Besides the above mentioned presentations, I have presented* **9** *biannual reports and* **5** *oral presentations on Thursday's weekly seminars conducted by CDP along with many more participations on seminars, and webinars conducted by NPS, CDP and others during my PhD works.*

Participations/Posters

I. **Rai, R. K. (8-12, June, 2023),"Summer School of Material Science and Computatinal Physics (SSMSCP-2023)"**.
Organized by: IEEE, EDS Nepal Chapter.

II. **Rai, R. K. (15-19, September, 2021),"Refresher Course on Material Science (RCMS-2021)"**.
Organized by: Central Department of Physics, T.U., Kirtipur, Nepal.

III. **Rai, R. K. (4-6, October, 2021), "International Workshop on Computational Materials Engineering (CME-2021)"**.
Organized by: Central Department of Physics, T.U., Kirtipur, Nepal.

IV. **Rai, R. K. (From 4 th July, 2020 – 31 st January, 2021)"NPS School of Computing-2020"**.
Organized by: Nepal Physical Society Ghantaghar, Kathmandu, Nepal.

V. **Rai, R. K. (22-24, January, 2021), "Three Days Workshop on Data Analysis: Python and Origin-2020"**.
Organized by: Department of Physics, St. Xavier's College, Maitighar, Nepal

VI. **Rai, R. K. (9-10, July, 2020), "First International e-Conference on Recent Advances in Physics Material Science-2020 (IC-RAPMS-2020)"**.
Organized by: Kurseong College, Darjeeling, West Bengal, India-734203.
► **Rai, R. K., Kaphle, G. C., Ray, R. B., and Niraula, O. P. (2019).**
Poster presentation entitled "Electronic structure and Transport properties of Complex Transition Metal Oxides: $LaTiO_3/CaVO_3$", CDP (February, 2019).

► **Rai, R. K., Kaphle, G. C., Ray, R. B., and Niraula, O. P. (2019).**
Poster presentation entitled "Electronic structure of complex transition metal oxides: $LaTiO_3/SrTiO_3$" on One day seminar, RECAST (2019).

Solid State Communications 368 (2023) 115173

Contents lists available at ScienceDirect

Solid State Communications

journal homepage: www.elsevier.com/locate/ssc

Full length article

Unraveling the structural and mechanical stability, electronic, and optical properties of $(La_xSr_{1-x}VO_3)_n$ (n =1, 2; x = 0, 0.5, 1)

Raj Kumar Rai [a,b], Gopi Chandra Kaphle [a,*], Ram Babu Ray [a,c], Om Prakash Niraula [a]

[a] Central Department of Physics, Tribhuvan University, Kathmandu, Nepal
[b] Patan Multiple Campus, Tribhuvan University, Patandhoka, Lalitpur, Nepal
[c] Amrit Science Campus, Tribhuvan University, Lainchaur, Kathmandu, Nepal

ARTICLE INFO

Communicated by Luis Brey

Keywords:
DFT
DMFT
Elastic constant
MIT
Spectral function

ABSTRACT

We have investigated the structural, chemical, and mechanical stabilities, electronic structures, and optical characteristics of $(La_xSr_{1-x}VO_3)_n$ (where, n =1,2; x = 0, 0.5, 1) systems using the ab-initio calculations. The negative values obtained from formation and cohesive energy calculations, modulus of elasticities, Poisson's and Pugh's ratios, anisotropy factor, and Cauchy pressure indicate that these materials have excellent structural and mechanical stability, which can be synthesized experimentally. Furthermore, the Mott-Hubbard metal-insulator transition (MIT) is investigated using the maximum entropy model (MEM) from the data obtained from dynamical mean field theory (DMFT). From the calculation, MIT are observed for pristine $LaVO_3$ and $SrVO_3$ at U = 4.5 eV with β = 8.0 $(eV)^{-1}$ and U = 2.5 eV with β = 6.0 $(eV)^{-1}$, and the MIT parameters for $LaSrV_2O_6$ system are observed at U = 4.0 eV with β = 10.0 $(eV)^{-1}$ respectively. The photo-induced behaviors of these materials have also been investigated using the dielectric function, index of refraction, Eloss function, absorptivity, and optical conductivity in the IR-to-UV regions, including the visible spectrum.

1. Introduction

The transition metal oxides (TMOs) and their superstructures are of great interest, as since their versatile applications in the fields of Mottronics [1,2], resistive memory devices [3], artificial neuron for neuromorphic computing [4], high T_C superconductors [5], photo-voltaic application [6], shielding effects [7,8]. The properties of pristine TMOs can be tuned in the desirable applications through filling control and band control methods at the interfaces [9–11]. To explore the tuning properties of material with high T_C on or above the ambient temperature, one must have the thorough understanding of their structural and electronic related properties [12,13].

Ohtomo and Hwang (2004) reported a high-mobility of electron gas at the interfaces of $SrTiO_3$ and $LaAlO_3$ [14] even though both of them are band insulators [15]. The conductivity around the interfaces also depends upon the terminations used in the heterostructures. Quantum oscillations were also reported for this kind of interfaces [16] which is another signature of high-mobility quantum transport. A sharp insulator-to-metal transition was reported for $LaAlO_3/SrTiO_3$ films grown by pulsed laser deposition with subsequent annealing at the room temperature [14]. The structural phase transitions of ABO_3 type perovskites depend upon the Goldschmidt tolerance factor [16,17]. In the present calculations, we have used a prototype cubic phase of the perovskites and their superstructures. Actually the phase transitions in perovskites and their superstructures depends upon the various parameters, viz. electric field [18], stress or strain [19], cation substitution [20], isotope substitution [21], defects and defect centers [22], terraces (layers) [15] and so on. Here, we focus our attention towards cations substitutions.

Moreover, to get the real information about the mechanical stability and chemical bondings of the materials, elastic parameters have to be calculated. The study of elastic behaviors of the transition metal oxides (TMOs) is the another faucet of investigation along with their electronic, thermodynamic properties [23,24].

For the strongly correlated system, the dynamical mean field theory is highly successful approximation, which is the solution of the quantum impurity problems. In the quantum impurity model an atom or molecule is embedded in the electronic bath, which is created by a set of orbitals interacting with spin exchange and hybridization [25]. To solve the quantum impurity model, we need to evaluate the Green's function of imaginary time (τ), $G(\tau) = -\langle T_\tau \psi(\tau)\psi^\dagger(0)\rangle$, where T_τ is the time ordering operator and $\psi^\dagger(0)$ is the creation operator at initial moment [26]. There are various techniques used for solving the quantum impurity model including the continuous time quantum

* Corresponding author.
E-mail address: gopi.kaphle@cdp.tu.edu.np (G.C. Kaphle).

https://doi.org/10.1016/j.ssc.2023.115173
Received 16 January 2023; Received in revised form 1 April 2023; Accepted 10 April 2023
Available online 18 April 2023

Monte Carlo (CT-QMC) method [1,27–29]. Here we have used the CT-QMC with hybridization expansion technique to obtain the Green's function of imaginary time or frequency [2].

Kowalski et al. (2019) employed the CT-QMC hybridization method for studying the splitting of conduction band consisting of d-orbitals with the local Coulomb interactions, which explains the Mott insulating behavior [30,31]. Experimentally, the Hubbard bands splitting was observed by the angle resolved photoemission spectroscopy (ARPES) [32]. The real frequency spectral function have been calculated from the Green's function data obtained by CT-QMC using Maximum Entropy Model (MEM) algorithm for analytic continuation [33,34].

The Mossanek et al. (2010) investigated the Mott-Hubbard band splittings in $LaVO_3$ by substituting the divalent Ca^{2+} ions at the place of trivalent La^{3+} ions [35]. The Mott-Hubbard phase transition phenomenon in VO_2 thin film has been employed for a memristor, volume resistive switching, machine learning devices [36] for designing actuators [37].

The metal–insulator transition (MIT) phenomenon has been studied for both fundamental physics and potential applications in Mottronics and resistive random access memory (RRAM) devices, artificial neurons [3,4]. The Mott-insulators in which the insulating phase actually comes from the strong Coulombian interaction between d or f electronic states, which are controlled by chemical doping, pressure, applying external fields. The novel electronic phase transition of strongly correlated system, leading to the various phases like superconductivity, MIT, resistive switching (RS) and dielectric breakdown has been attracting attention for designing smart low power electronic devices with ultrafast switching action [38,39]. Tunable Electron-Electron Interactions is reported [40] for perovskite heterostructures. The electron–electron interaction is attractive for a lower chemical potential, characterized by Hubbard, $U > 0$ (with d_{xy} populated), and the pairing is local Bose–Einstein condensate (BEC) like interaction. When the chemical potential is raised by using the external influences, the interaction becomes repulsive characterized by $U < 0$ (with d_{yz}/d_{xz} populated) and the pairing is non-local Bardeen-Cooper-Schrieffer (BCS) like interaction. A tunable electron–electron interaction is a useful tools, which could potentially be used for quantum devices and its simulation [41].

The complex oxide heterostructures can be used for storing qubits or performing gate operations for a quantum computing devices [42]. Topologically-protected qubits (e.g., Majorana fermions) are possible systems with flying qubits along quantum channels, or it is possible to construct hybrid systems storage qubits (e.g., N-V centers), which are coupled by quantum wires for creating a superconducting qubit.

Here, we unravel the structural, mechanical, electronic, and optical properties of newly designed superstructure, $(La_xSr_{1-x}VO_3)_n$ (where, $n = 1, 2; x = 0, 0.5, 1$) systems using the conventional DFT and CT-QMC technique with hybridization expansion, and analytic continuation through Maximum Entropy model. The possible applications of these materials for Mottronics, photovoltaics, memristors and artificial neural networks for neuromorphic computations. The optical behaviors of these materials have also been studied to get the comprehensive information for the optoelectronic applications.

2. Theoretical backgrounds and computational details

2.1. Theoretical basis

The structural, chemical and mechanical stabilities, electronic structure and optical properties of strongly correlated electronic systems ($LaVO_3$ and $SrVO_3$, and their superstructures) have been investigated using Kohn–Sham equation through the full potential linearized augmented plane wave (FP-LAPW) method with local orbitals approach [43–45].

$$\left[\frac{-1}{2m}\nabla^2 + v_{eff}(r, n_e(r))\right]\psi_i(r) = \varepsilon_i\psi_i(r) \tag{1}$$

Where,

$$v_{eff}(r) = V_{ion}(r) + \int d^3(r)V_{ee}(r)n_e(r) + V_{xc}(r) \tag{2}$$

and $V_{xc(r)} = \frac{\delta E_{xc}(n_e(r))}{\delta n_e(r)}$ is the exchange correlation interaction with the probability density $n_{e(r)} = \sum_{i=1}^{N}\psi_i(r)^2$. Once the self-consistent calculation converged with the known $n_e(r) \sim n_0(r)$ the GGA calculates the exchange correlation energy as,

$$E_{xc}^{GGA-PBE}[n_e(r)] = \int d^3rF_{xc}(n_e(r), \nabla n_e(r)) \tag{3}$$

and the ground state properties will be analyzed by the help of density of states per unit energy range and the electronic bandstructure calculations such that, $D_n(\varepsilon) = \frac{2}{8\pi^2}\int \delta[E_F - \varepsilon_n(k)]d\varepsilon$.

2.1.1. Structural and chemical stability

The structural stability of the system in the ground state is estimated through the energy minimization process. And the chemical stability of the compounds are predicted by estimating the cohesive energy and formation energy [46,47], that is the measure of the strength of forces which binds the atoms together in the materials. $E_{cohesive}$ for a compound $X_kY_mZ_n$ (XYZ), one can calculate it as,

$$E_{cohesive}^{XYZ} = \frac{E_{total}^{XYZ} - \left(kE_{atom}^{X} + mE_{atom}^{Y} + nE_{atom}^{Z}\right)}{k + m + n} \tag{4}$$

where E_{atom}^{X}, E_{atom}^{Y} and E_{atom}^{Z} are the energies of the isolated atoms with k, m, and n are the stoichiometric weights.

And, the formation energy, $E_{formation}$ of the XYZ compound is,

$$E_{formation}^{XYZ} = \frac{E_{total}^{XYZ} - \left(kE_{solid}^{X} + nE_{solid}^{Y} + nE_{solid}^{Z}\right)}{k + m + n} \tag{5}$$

where E_{solid}^{X}, E_{solid}^{Y} and E_{solid}^{Z} are the calculated energies of the bulk form per formula unit with k, m and n are the stoichiometric weights.

2.1.2. Mechanical stability

The mechanical stability includes the calculation of elastic constants, modulus of elasticities, Poisson's and Pugh's ratios, Cauchy pressure, anisotropy factor and Debye temperature of the systems using calculated elastic constant parameters through Birch–Murnaghan equation of state [48,49] (6) as given by,

$$E(V) = E_0 + \frac{9B_0V_0}{16}\left[\left(V_0/V\right)^{2/3} - 1\right]^3 B_0' + \frac{9B_0V_0}{16}\left\{\left[\left(V_0/V\right)^{2/3} - 1\right]^2\left[6 - 4\left(V_0/V\right)^{2/3}\right]\right\} \tag{6}$$

where E_0 is the energy of equilibrium, V_0 is the zero pressure volume of unit-cell. When a crystal is deformed with a given strain η_i stress tends to bring it back to the equilibrium configuration, which is described by the generalized Hooke's law [50,51] as,

$$\sigma_i = \sum_{ij} C_{ij}\eta_j \tag{7}$$

where C_{ij} is the elastic constant tensor.

From this relationship, we compute the total energy for finite and small strains of a system as,

$$E(\eta) = E_0 + V_0\sum_i \sigma_i^0\eta_i + \frac{V_0}{2!}\sum_{ij}\eta_i C_{ij}\eta_j + \cdots. \tag{8}$$

Where, E_0 and V_0 are clearly the energy and volume of the equilibrium structure respectively. By choosing the various form of the strain η and using the polynomial fitting of the energy with a quadratic function, we can calculate the elastic constants.

For a cubic system the nonzero components of the elastic constants tensor are independent on the Laue class and are $C_{12} = C_{13} = C_{23}$, $C_{11} = C_{22} = C_{33}$, and $C_{44} = C_{55} = C_{66}$[52,53].

Similarly, for computing the non-zero components of the elastic constants of a tetragonal system, we have to solve the equations for

energy with the corresponding strain, to obtain the elastic constants, $C_{11}, C_{33}, C_{12}, C_{13}, C_{44}$ and C_{66}. Out of these elastic constants C_{ij}, the reduced three independent elastic constants for the cubic symmetry are C_{11}, C_{12} and C_{44}. The mechanical stability conditions for a cubic crystal are, [54]

$$C_{11} + 2C_{12} > 0, C_{11} - C_{12} > 0, C_{44} > 0, C_{12} < B < C_{11} \tag{9}$$

Similarly, the mechanical stability criteria for tetragonal system are,

$$\begin{cases} C_{11} > 0, C_{33} > 0, C_{44} > 0, C_{66} > 0, \\ C_{11} - C_{12} > 0, C_{11} + C_{33} - 2C_{13} > 0, \\ 2(C_{11} + C_{12}) + C_{12} + 4C_{13} > 0 \end{cases} \tag{10}$$

For a cubic system, Zener anisotropy factor, A has important information about structural stability is calculated as,

$$A = \frac{2C_{44}}{C_{11} - C_{12}} \tag{11}$$

The anisotropy factor is one for a full isotropic material. The stiffness and flexibility are estimated via Cauchy pressure, $CP = C_{12} - C_{44}$, which is associated with the nature of chemical bondings. The value of Young's modulus (Y), bulk modulus (B) and shear modulus (G) within elastic zone are obtained as,

$$\begin{cases} Y = 9BG/(3B + G), \\ B = \frac{1}{3}\left(C_{11} + 2C_{12}\right), \\ G = (G_V + G_R)/2, \end{cases} \tag{12}$$

Where, $G_V = \frac{1}{5}\left(C_{11} - C_{12} + 3C_{15}\right)$, is the shear modulus in Voigt notation and

$G_R = [5\left(C_{11} - C_{12}\right)C_{44}]/[3(C_{11} - C_{12}) + 4C_{44}]$, is the shear modulus in Reuss notation. The higher value of Y indicates the stiffer and more covalent type of materials [49]. The Poisson's ratio,

$$\nu = \frac{3}{2}\frac{3B - 2G}{3B + G} \tag{13}$$

indicates the ductility of the materials. Its value for the covalent, ionic and soft compound are approximately equal to 0.1, 0.25, and 0.33 respectively [55]. Similarly, the Bulk modulus (B_H), Shear modulus (G_H), Young's modulus (Y_H) and Poisson's ratio (ν) for the tetragonal system are estimated by using the Voigt–Reuss–Hill (VRH) average schemes as follows,

$$\begin{cases} B_H = (B_V + B_R)/2, \\ G_H = (G_V + G_R)/2, \\ Y_H = 9B_H G_H/(3B_H + G_H), \\ \nu = (3B_H - Y_H)/6B_H. \end{cases} \tag{14}$$

Furthermore, the Debye temperature (Θ_D) is computed using

$$\Theta_D = \frac{\hbar}{k_B}\left(\frac{6\pi^2}{V_{cell}}\right)^{1/3}\langle v\rangle \tag{15}$$

With,

$$\begin{cases} \langle v\rangle = \left[\frac{1}{3}\left(2v_l^{-3} + v_t^{-3}\right)\right]^{-1/3}, \\ v_l = \left[\frac{3B+4G}{3\rho}\right]^{1/2}, \\ v_t = \left(\frac{G}{\rho}\right)^{1/2}, \end{cases} \tag{16}$$

Where, v_l, v_t, $\langle v\rangle$, $\hbar$, k_B, N_A, V_{cell} and ρ represent the isotropic longitudinal sound velocity, transverse sound velocity, average sound wave velocity, reduced Planck's constant, Boltzmann constant, Avogadro's number, volume of unitcell and density of the materials [56].

The numerical accuracy of elastic-constant calculations for the material of a system employing the numerical differentiation required for stress and strain measurement are to be addressed properly. In fact, we are dealing with a function (energy or stress) that can only be computed for a limited range of strain values. The calculated DFT data

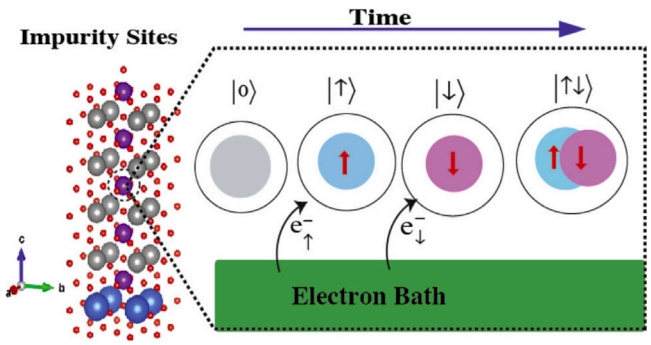

Fig. 1. (Color online) The Schematic representation of probable electronic fluctuations in DMFT with single-site impurity model [25].

are acquired to a certain degree of precision. To keep all of these factors under control and estimate the numerical errors in energy and stresses, we used leave-one-out cross-validation (LOO-CV) method which is one of the exhaustive cross validation approach. In this approach each training data set is created by taking all samples except one,called the testing data set (the sample left out). Now we select the best model dataset from the polynomial fitting of multiple training dataset samples with the help of testing data set. In the case of elastic calculations, we choose the best model having lowest cross validation error obtained from,

$$\delta_{CV}^{(n)} = \sqrt{\frac{1}{N}\sum_{i=1}^{N}\left[E_i - p^{(n)}(\eta_i)\right]^2} \tag{17}$$

where, $p^{(n)}(\eta_i)$ is the value of the polynomial function of order n to N-1 at η_i, excluding the value of pair (η_i, E_i) such that $E(\eta_i) = \sum_{i=1}^{6} A_i \eta^i$. Here, we used the polynomial fitting upto the sixth order (n = 6) for cross validation of data obtained from DFT calculation. It is the generalization of error estimation that is used to verify the performance of the estimator for either over-fitting or under fitting of the realistic information regarding the elastic parameters of the given materials.

2.1.3. Optical properties through DFT

The analysis of optical properties is performed by the calculation of dielectric tensor ($\epsilon_{ij}(\omega)$), optical conductivity($\sigma(\omega)$), electron loss tensor (ELOSS)($L_{ii}(\omega)$), reflectivity($R(\omega)$), absorptivity($\alpha(\omega)$), and the effective numbers of oscillators (sum rules)($Z_{eff}(\omega)$) [38,39] using the following expressions:

$$\begin{cases} \epsilon_{ij}(\omega) = real[\epsilon_{ij}(\omega)] + Img.[\epsilon_{ij}(\omega)], \\ L_{ii}(\omega) = -Img.\left\{\frac{1}{\epsilon_{ii}(\omega)}\right\}, \\ \text{real}[\sigma_{ij}(\omega)] = \frac{\omega}{4\pi} Img.[\epsilon_{ij}(\omega)]. \\ R_{ii}(\omega) = \frac{(n_{ii}-1)^2 + k_{ii}^2}{(n_{ii}+1)^2 + k_{ii}^2} \\ \alpha_{ij}(\omega) = \frac{2\omega k_{ij}(\omega)}{c} \\ Z_{eff} = \sum_f f_{fi} = \frac{2\mu}{\hbar^2}\sum_f \left(E_f^0 - E_i^0\right)|x_{ii}|^2 \end{cases} \tag{18}$$

Where, E_f^0, E_i^0, and $|x_{ii}|^2$ are the energy of final state, initial state, and the square modulus of transition matrix, respectively.

2.1.4. Dynamical mean field theory and maximum entropy model

The strongly correlated systems are studied through the DMFT calculation for investigating Mott-Hubbard transition using the modified

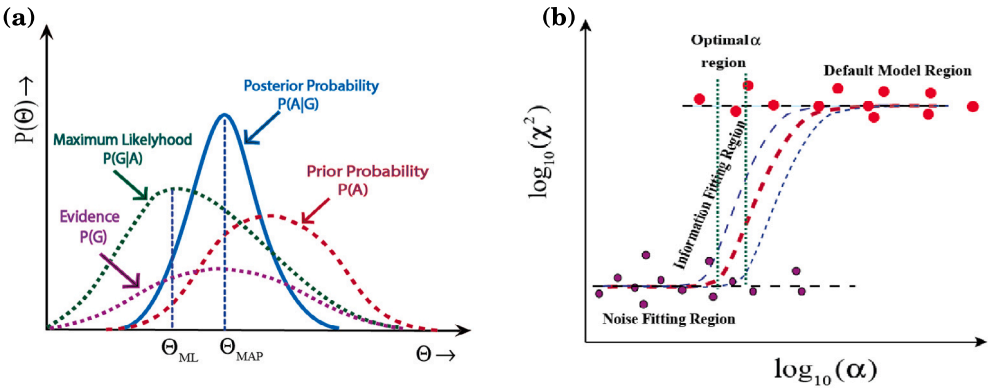

Fig. 2. (Color online) (a) The Baye's theorem for the conditional probability (b) The logistic regression curve for finding the optimal value of α [34].

form of a single site Hubbard Hamiltonian ($\hat{H} = \sum_{ij\sigma}\left[t_{ij}\ \hat{c}^{\dagger}_{i\sigma}\hat{c}_{j\sigma} + c.c.\right] + U\sum_i n_{i,\uparrow}n_{i,\downarrow}$), called Anderson impurity model Hamiltonian as given by,

$$\hat{H}_{AIM} = \sum_{\sigma=\uparrow,\downarrow}\epsilon_0(k)\ \hat{c}^{\dagger}_{\sigma}\hat{c}_{\sigma} + Un_{c\uparrow}n_{c\downarrow} + \sum_{k,\sigma}[V_{k,\sigma}(k)\hat{d}^{\dagger}_{k,\sigma}\hat{c}_{\sigma} + h.c.] + \sum_{k,\sigma}\epsilon_{k,\sigma}(k)\hat{d}^{\dagger}_{k,\sigma}\hat{d}_{k,\sigma} \quad (19)$$

where t_{ij} is tight-binding hopping amplitude between the lattice sites i and j, with $\hat{c}^{\dagger}_{i\sigma}\ (\hat{c}_{j\sigma})$ is the creation (annihilation) operators, $n_i = \hat{c}^{\dagger}_{i\sigma}\hat{c}_{j\sigma}$ represents the occupation number on a local site,i and $\hat{d}^{\dagger}_{k,\sigma}$ represents the localized interacting electrons with electronic bath as shown in Fig. 1 via $V_{k,\sigma}(k)$, which is the amplitude of hybridization [57].

Though, there are various impurity solvers to solve the Anderson impurity model Hamiltonian (19) such as NRG, ED, IPT, NCA, CT-QMC [58–60], we have employed the CT-QMC with hybridization expansion method [25,60]. This technique solves the Dyson equation [1,61] for the interacting Green's function of frequency $G(\omega)$ and self energy, $\Sigma(\omega)$ as,

$$\mathcal{G}_0^{-1}(\omega) = \Sigma(\omega) + G_{ii}^{-1}(\omega). \quad (20)$$

In this study, we use the analytic continuation to obtain the spectral function, $A(\omega) = -\frac{1}{\pi}Im\left[G^R(\omega)\right]$, from the Green's function data using the Maximum Entropy model [33,34]. It is the real frequency data for investigating the band splitting [1,62] phenomena, which is comparable to the ARPES experimental results [32,60].

In fact, the data from the DMFT calculation ($G(\tau)$, $G(\omega)$) and self-energy ($\Sigma(\omega)$) are incomplete, noisy or oversampled, which may lead to an unphysical results. To avoid this discrepancy, we have employed OmegaMaxEnt algorithm, which is essentially, works on the idea of the Maximum Entropy model (MEM) for finding the most probable spectrum [33,38]. The MEM is based on the Bayesian statistical theorem as given by,

$$P(A|G) = \frac{P(G|A)P(A)}{P(G)}. \quad (21)$$

Where, P(A|G), P(G|A), and P(A) are the *posterior*, *likelihood* and *prior probability* for A, respectively. For the present case, P(G) is a constant that can be ignored since the data are fixed. The most probable A, given the data G is true, is thus obtained by maximizing P(G|A)P(A). The required posterior probability is approximated with the other probabilities as in Fig. 2(a), which is computed as,

$$P(A|G) \propto e^{\alpha S - \frac{\chi^2}{2}}. \quad (22)$$

Where, α is hyperparameter, $S = -\int \frac{d\omega}{2\pi}A(\omega)\ln\frac{A(\omega)}{D(\omega)}$ (differential entropy), and $\chi^2 = \sum_i \frac{(G_i - \bar{G}_i)^2}{\sigma_i^2}$ (goodness of fit) respectively [33,34].

The maximum likelihood (P(G|A)) of the required information is computed by choosing the optimal value of α lies in the lower portion of information fitting region of the logistic regression curve (Fig. 2(b)) [63–66].

Finally, the frequency-dependent optical conductivity computed as,

$$\sigma(\omega) = 2\pi\frac{e^2}{\hbar a}\int_{-\infty}^{\infty}d\omega'\ \frac{n_F(\omega') - n_F(\omega'+\omega)}{\omega} \times \int_{-\infty}^{\infty}dk\ \rho(k)\,(v(k))^2\,A(k,\omega')A(k,\omega'+\omega) \quad (23)$$

with $n_F(\omega)$ as the Fermi distribution, $v(k) = \sqrt{W^2 - k^2}/\sqrt{3}$ is the velocity [25,59,67,68], and $\rho(k) = \frac{2\sqrt{W^2-k^2}}{\pi W^2}$ is the semi-circular density of states (DOS) for the Bethe lattice with the semi-bandwidth W = 2t (where, t is the hopping integral).

2.2. Computational details and experimental information

We have used the generalized gradient approximation (GGA) with the exchange energy correlation functional implemented by Perdew, Burke and Ernzerhof [69,70]. In the part of the density functional theory, we used the full-potential linearized augmented plane wave (FP-LAPW) code with local orbital approximation for this investigation.

For the case of pristine $LaVO_3$ and $SrVO_3$, we perform fully ionic optimization. In case of superstructures, $(La_xSr_{1-x}VO_3)_n$ (n =1, 2; x = 0, 0.5, 1), we perform standard energy minimization technique through self-consistent calculation criteria without affecting the position of ions by varying the lattice parameters. Actually, the superstructure is reconstructed by promoting the optimized cubic phase of $SrVO_3$ within the frameworks of 1×1×2 dimension, and La -ions are substituted on Sr-sites for studying the various properties of the superstructures, $La_xSr_{1-x}VO_3$ (Fig. 3(a), 3(b)). For the ground state calculation of systems, we have used the k-mesh grid (Monkhorst–Pack) of 11×11×5 (without the shift of k-mesh mode) using the linearized augmented plane wave (LAPW) basis set with local orbitals defined by the cutoff $R_{MT}K_{MAX}$ =7.0, G_{MAX} = 12.0. Inside the atomic spheres, the potential and charge densities are expanded in crystal harmonics up to L = 16. The self-consistent calculation of the entire system are carried out with the convergence criteria of 10^{-5} eV for energy and 10^{-3} e for charge, and 0.01 eV/Å for the force convergence [71–73]. Furthermore, the structural, chemical, and mechanical stability of the pristine and their superstructures of the TMOs are examined through the calculation of cohesive and formation energies, and their elastic parameters.

The single crystal elastic constants, C_{ij} are used for calculating various criteria of mechanical stability, such as various elastic moduli under different types of stresses. The anisotropy factor gives the uneven responses of stresses with respect to the directions of applied forces and the Cauchy pressure calculation is used for determining nature of chemical bonding [23].

For solving DMFT equation, we have employed the CT-QMC with hybridization technique for the impurity solver, through which, we

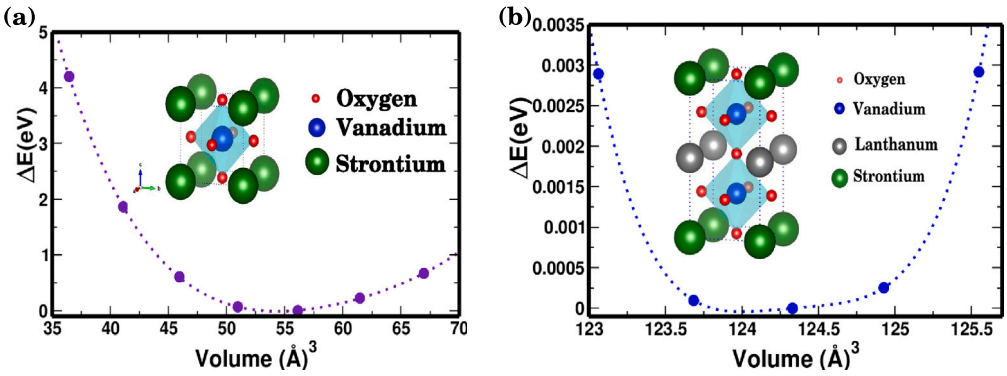

Fig. 3. (Color online) (a) The volume optimization curve of unitcell $SrVO_3$, and (b) $LaSrV_2O_6$ systems with their respective crystal structures (crystal structures are in insets).

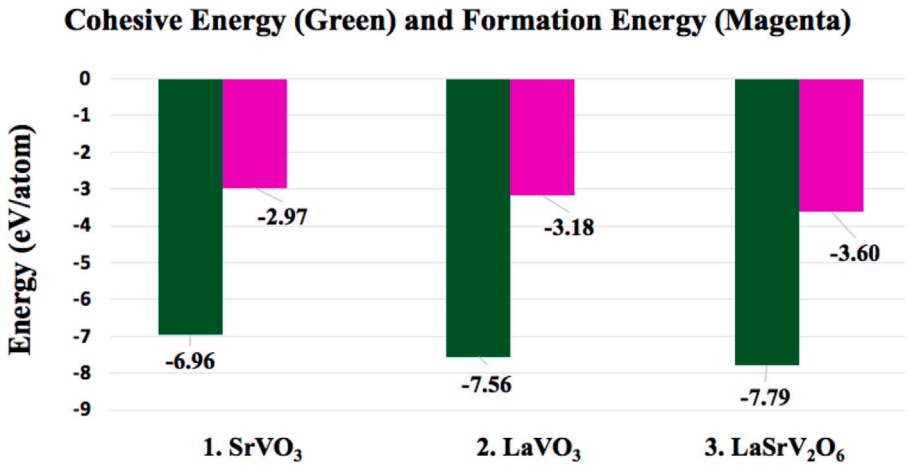

Fig. 4. (Color online) The Cohesive and Formation energies of the pristine ($LaVO_3$ and $SrVO_3$) and the superlattice $LaSrV_2O_6$.

have computed the Green's functions, G(τ) or G(ω) and self-energy $\Sigma(\omega)$, of the system under investigation. Further the data from the DMFT is used for obtaining the spectral function or spectral density, A(ω) using the Maximum entropy model to evaluate the electronic phase transition of the materials.

Taking the base of experimental samples reported by Inaba et al. [74], and K. Maiti et al. [75], we were motivated to study the MIT behavior of $(La_xSr_{1x}VO_3)_n$ (n =1, 2; x = 0, 0.5, 1) theoretically through DFT and DMFT self-consistent calculations.

3. Results and discussion

3.1. Structural, chemical, and mechanical stabilities

The structural stability of the compounds are obtained through energy minimization process. The calculation show that the volume optimized lattice parameters of the most stable structure of ideal cubic $SrVO_3$ (Fig. 3(a)) is 3.86 Å and $LaVO_3$ is 3.94 Å (not shown here) respectively, which are consistent with experimental results [35,76–79]. Similarly, the optimized superstructures $LaSrV_2O_6$(a = b = 3.96 Å and c = 7.92 Å) is found to have similar values with same space-group p4/mmm (123) (Fig. 3(b)). The negative values of cohesive and formation energies depicted in Fig. 4 reveals the chemical stability of the systems and could be realized through experimental synthesis.

The calculated formation energies −2.97 eV/atom, −3.18 eV/atom and −3.60 eV/atom for $SrVO_3$, $LaVO_3$ and $LaSrV_2O_6$ systems, respectively, are all negative implying that the systems are energetically favorable for synthesis and stable structures in terms of thermodynamical and its chemical stabilities. The cohesive energies are computed as −6.96 eV/atom, −7.56 eV/atom and −7.79 eV/atom for $SrVO_3$, $LaVO_3$ and $LaSrV_2O_6$ systems, respectively. The greater the negative values of the cohesive and formation energies, the higher the structural and chemical stability of the systems.

The Mechanical stability parameters(elastic constants, modulus of elasticities, Poisson's and Pugh's ratios, Cauchy pressure, Anisotropy factor, Debye temperature) of optimized structures [23,54] for both the pristine and superstructures are listed in Table 1, which are consistent with the available information [23,39,48,56,80]. Furthermore, the values obtained from Eqs. (9)–(13) are satisfied the mechanical stability criteria of the systems. The positive values of Cauchy pressure (C_{12} - C_{44}) for $LaVO_3$, and $LaSrV_2O_6$ show the metallic nature with ductile property, whereas, the negative value for $SrVO_3$ shows covalent bonding [55].

The elastic moduli and other elastic parameters calculation reveal that the superstructure is weaker specimen than pristine systems in terms of elastic behavior [80,81]. The Debye temperature (Θ_D) of the systems are also calculated by using the elastic waves information, which is related with the cutoff frequency (Debye frequency, ω_D) of harmonic chains of masses, describing the motion of ions in a crystal.

We employed polynomial fitting of energy vs. strain calculation to obtain the elastic tensor and its related physical information of the materials. Its accuracy and validity in estimating uncertainties are further evaluated using cross-validation error (CVE) method, which is a statistical technique for selecting the best model for the data set with the best hyperparameter (adjustable parameter) for the estimator (algorithm). In this method, the subset of the dataset is used for training, and the model's performance is evaluated using a complementary subset of the dataset that was not used for training. It ensures that the model is appropriately capturing trend from data without taking into account noise from the data. In general, the CVE approach enables

Table 1
The mechanical stability and elastic information of the pristine $LaVO_3$, $SrVO_3$ and its superlattice $LaSrV_2O_6$ system.

S.N.	Physical parameters		$LaVO_3$	$SrVO_3$	$LaSrV_2O_6$
1.	Elastic Constant (GPa)	C_{11}	576.2	519.9	256.5
		C_{12}	200.9	141.0	90.5
		C_{13}	–	–	106.6
		C_{33}	–	–	235.6
		C_{44}	124.0	155.3	68.6
		C_{66}	–	–	70.6
2.	Poisson's Ratio	ν	0.30	0.24	0.30
3.	Young's Modulus	Y	335.99	267.27	150.68
4.	Shear Modulus	G	149.48	168.97	70.72
5.	Bulk Modulus	B	388.97	418.69	184.55
6.	Cauchy Pressure (GPa)	C.P. = C_{12} -C_{44}	76.9	−14.3	21.9
7.	Pugh's Ratio,	P.R. = $\frac{B_v}{G_v}$	2.25	1.58	2.13
8.	Volume in Equilibrium (Å^3)	V_0	50.65	58.09	123.47
9.	Anisotropy	A_v	2.48	0.47	0.34
10.	Debye Temperature (K)	Θ_D	465.85	395.76	232.58

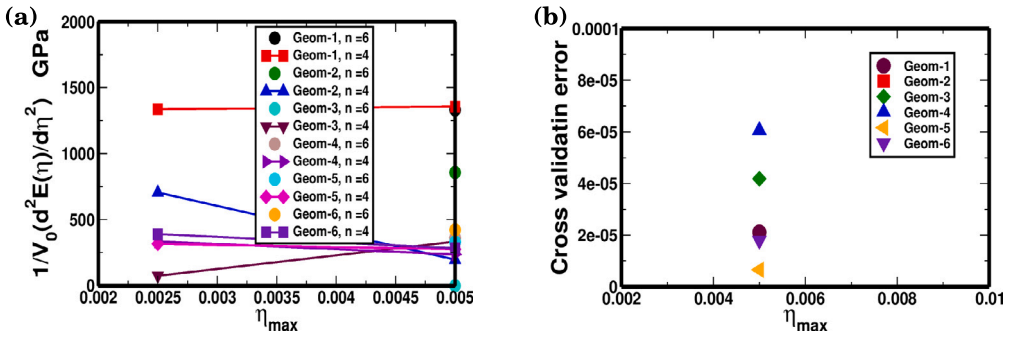

Fig. 5. (Color online) (a) The elastic constants obtained through polynomial fitting of superlattice $LaSrV_2O_6$ (b) The CVE corresponding to the calculation of elastic constants of superlattice $LaSrV_2O_6$.

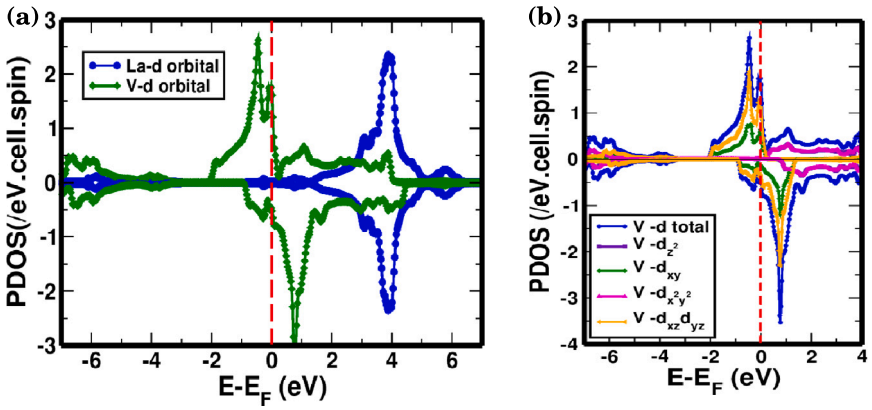

Fig. 6. (Color online) (a) The PDOS for both spin-channels of La- and V- d orbitals only (b) The PDOS of various V -d orbitals (e_g and t_{2g}) orbitals around the Fermi level for both spin channels of $LaSrV_2O_6$ system.

optimization of the fitting operation on a sample of statistical data. In this investigation, the leave-one-out (LOO) cross-validation error approach was used to determine the optimum model, as shown in Fig. 5(a). Higher order fitting produces good results for elastic constants with a considerable number of strain points. From Fig. 5(b), it is predicted that the best models are deformation-5 or 6(Geometry-5 or 6) out of 6 distorted samples of the $LaSrV_2O_6$ system.

3.2. Density of states, bandstructures and fermi surfaces of the system

The DOS and bandstructure plots reveal that superstructure is correlated metal. The asymmetric nature of total PDOS (Fig. 6(a)) contributed by La-, V- atoms signify that the superlattice is ferri-magnetic materials(2.43 μ_B). From the calculations, it is found that ferri-magnetism comes from the contribution of $e_g(d_{z^2}, d_{x^2y^2})$ and $t_{2g}(d_{xy}, d_{yz}, d_{xz})$ orbitals of Vanadium transition metals, whereas Lanthanum acts as a paramagnet [82] in $LaSrV_2O_6$. The combined DOS and bandstructures is depicted in Fig. 7(b) which indicate that the superlattice system is metallic in nature. This metallic nature remains unaltered even after the application of effective Hubbard-Coulomb interaction Fig. 8(a) indicating that DFT could not resolve the issue of the correlated electronic structures (see Fig. S_1 for more DOS redistribution). Hence, we employed DMFT for further investigation regarding the metal–insulator transition and tuning properties of such materials.

The Fermi level, the highest energy level occupied by the electron at absolute zero temperature of a system. A set of points in momentum space(Fermi-surface) at zero Kelvin(K), describes the gapless

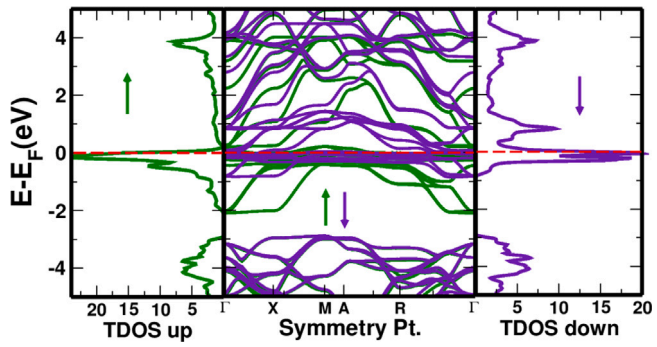

Fig. 7. (Color online) The bandstructure along with total DOS spin-up channel(green) and total DOS spin-down channel (indigo) of $LaSrV_2O_6$ system..

electronic excitations, and depicts the nature of dynamics of electrons, which is the central concept of metallic phase [83–85]. The Fermi surface plot along with the charge density distribution of the system actually provides the insightful information of the electronic structures of the systems. The 2D and 3D charge density plot of $LaSrV_2O_6$ (Fig. 8(b)) show the localization of charge density around the ionic cores and covalent chemical bondings between the neighboring atoms. The Fermi surface plots for 35–55 band levels around the Fermi level demonstrated that the system is basically metallic in nature (Fig. 8(c)).

3.3. The results of DMFT+MaxEnt model

The DFT and DMFT along with the MEM have been used for the realistic calculation of electronic structure of the pristine TMOs and its superstructures [58]. From the DMFT, we perform a set of calculations to find out the MIT model parameters. The calculations(Fig. 9(a)) show that the insulating phase started from U = 4.0 eV with β = 6.0 $(eV)^{-1}$. Here, the clear insulating phase is observed at U = 6.0 eV, which is clearly seen in Fig. 9(b). Similarly,by taking base of U = 4.0 eV, the metallic phase weakens at β = 6.0 $(eV)^{-1}$ however, a distinct insulating phase is seen with β = 10.0 $(eV)^{-1}$ (Fig. 10(a)). Same kind of features at β = 10.0 $(eV)^{-1}$ is observed in imaginary part of self-energy vs. Matsubara frequency plot, while plotting for various values of β with a constant U = 4.0 eV(Fig. 10(b)). We have also computed the MIT model parameters(U and β) for pristine $LaVO_3$ and $SrVO_3$, which are consistent with previously calculated results(Table 2 [28,29,32,34,59,71]). The spectral density plots (Fig. 11(a)) are demonstrated for diminishing quasi-particle peak (metallic phase) to the Mott-Hubbard insulating phase for various U values, follows the consistent result(Mott insulating at U = 4.0 eV and β = 10.0 $(eV)^{-1}$)).

To check the validity and accuracy of the calculations, we perform logistic regression analysis through MaxEnt model for quasi-particle(follow Fig. S_2), bad metal, and Mott-insulating phase (Fig. 11(b)). The logistic regression curve (inset upper left corner) shows the goodness of fit of the data with optimal α, which is taken from the maximum value of curvature of the logistic regression curve (inset upper right corner) [33]. The optimal value of α is also speculated using the sample frequencies vs. $\log_{10}(\alpha)$ graph (Fig. 12(a)). Furthermore, the error in the prediction of Mott gap(band splitting) is estimated through the normalized deviation (ND) of real and Imaginary parts of Green's function (ΔG) vs. Matsubara frequency, and the autocorrelation (AC) of the real and Imaginary parts of (ΔG) vs. the difference in index of refraction for the optimal value of α as shown in Fig. 12(b),(c) representing real data within the exceptable error bar with the experiments [33,34](For other error estimations follow Fig. S_3)

Table 2
The DMFT results of electronic structures of the pristine $SrVO_3$, $LaVO_3$ (see Fig. S_4) and its superlattice.

S.N.	Physical parameters	$SrVO_3$ (per unitcell)	$LaVO_3$ (per unitcell)	$LaSrV_2O_6$ (per supercell)
1.	MIT U Parameters (eV)	2.5	4.5	4.0
2.	MIT β Parameters $(eV)^{-1}$	6.0	8.0	10.0
3.	Mott Gap (eV)	0.89	0.93	0.74

3.4. Optical Properties of $(La_{1-x}Sr_xVO_3)_n$

Here, we observed the real and Imaginary parts (inset) of dielectric function and optical conductivity for pristine $SrVO_3$(SVO-pristine), $LaVO_3$(LVO-pristine) and $LaSrV_2O_6$, superstructures (Fig. 13(a)) indicating that the variation of dispersiveness decrease with the energy of photon and becomes negative at around ~ 7.5 eV of UV region for all of the systems [8,11]. The imaginary parts of dielectric function, which is associated with optical conductivity, Eloss function and other optical parameters significantly suppressed at near visible range. The photo-induced optical conductivity is estimated by plotting the real part of the optical conductivity $\sigma(\omega)$ vs. photon energy. The peak values of the real part of optical conductivity for pristine SVO, LVO and $LaSrV_2O_6$ superlattices are found to be 4605.26 $(\Omega\ cm)^{-1}$, 6736.84 $(\Omega\ cm)^{-1}$ and 5447.37 $(\Omega\ cm)^{-1}$ respectively, that lies at around (7–10)eV of photon energy of UV regions (Fig. 13(b)).

The real part of complex refractive indices are found to be similar variation showing higher values in the IR region with secondary peaks at around 3.0 eV photon energy(Fig. 14(a)). The absorptivity $\alpha(\omega)$ characterizes the part of energy of photon absorbed by the materials during EM interaction (Fig. 14(b)). Photon absorption is at the origin of the interband optical transition, which will not take place unless the photon energy is equivalent to the energy of the optical gap.

The electron energy loss spectroscopy(EELS) function or Eloss function, $L(\omega)$ is a useful optical parameter for investigating various aspects of the electromagnetic interaction with the materials. The highest peak values of the loss function for all of the superlattices are nearly 0.60 in arb.units(Fig. 15(a)). The energy losses are mainly due to a simple electronic excitation and a collective excitation (plasmon excitation) in the materials, which measures the probability of diffusion of volume losses of energy in the solid. The highest peaks around ~13 eV photon energy corresponds to the plasma resonance associated with the plasma frequency, ω_p [7].

In Fig. 15(b) shows the f-sum rules of transition, which measures the total optical weight, contributing to the effective number of oscillators or electrons during the absorption or emission of electromagnetic radiation. The sum rules is consistent with the optical conductivity to arbitrary frequencies.

The optical properties of these superstructures are computed through CT-QMC+MEM algorithm as well. In all cases, the optical conductivity are calculated from the spectral function with the optimal value of α using MaxEnt model [33]. We show the real part of optical conductivity of Anderson model at half-filling for different combinations of U and β parameters for $(La_{1-x}Sr_xVO_3)_n$ systems. It is found that the metallic Drude peak at zero frequency($\omega \sim 0$) is broadened or suppressed by raising these parameters (Fig. 16(a)) [80,86]. The Drude peaks of various parameters for different combinations of MIT parameters (U and β) supports the Mott-Hubbard band splittings consistent with the previous calculations. In Fig. 16(b), the curves with various values of U for a constant β = 10.0 $(eV)^{-1}$ demonstrate that the Drude peaks at around $\omega \sim 0$ vanished for higher U indicating the transitions from metallic phase to insulating due to localization of carriers of the systems.

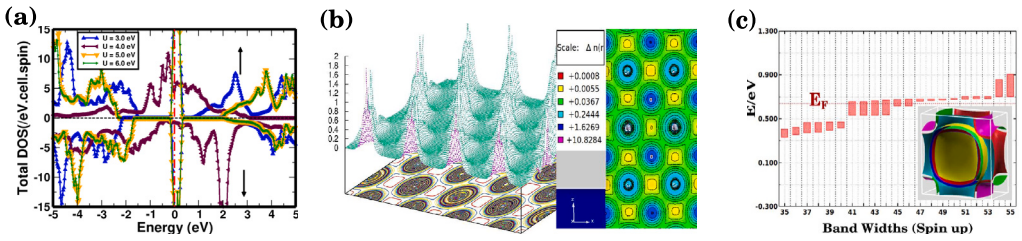

Fig. 8. (Color online) (a) The asymmetric TDOS distributions with various values of U (b) The 2D charge contour map in (110) plane (right) and 3D charge density plot (left), and (c) Fermi surface plot for 35–55 band levels(inset bottom right) showing the Fermi level (E_F).

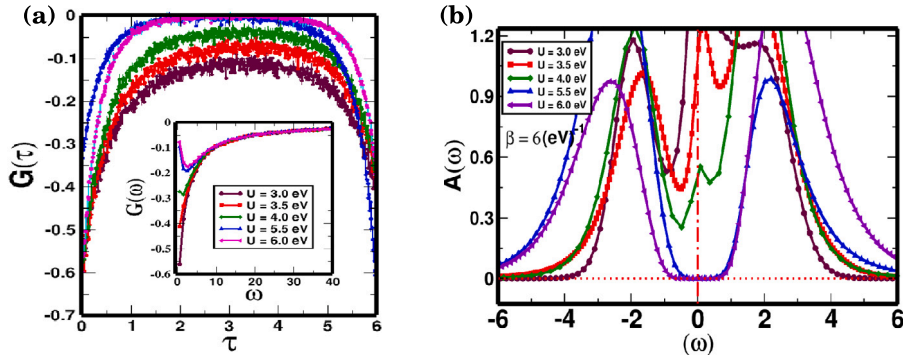

Fig. 9. (Color online) (a) The Green's function vs. imaginary time for various U with a constant $\beta = 6.0\ (eV)^{-1}$ and the corresponding variation of Green's function vs. frequency(inset) (b) The variation of spectral function vs. frequency with different values of U for a constant $\beta = 6.0\ (eV)^{-1}$ on $LaSrV_2O_6$ system.

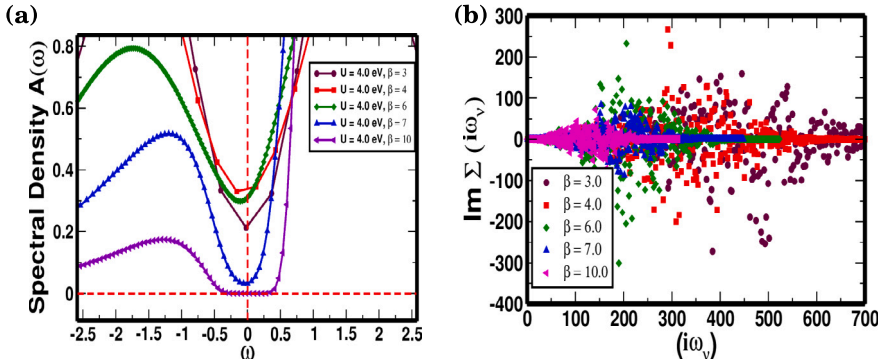

Fig. 10. (Color online) (a) The spectral density variation with (β) for a constant U = 4.0 eV (b) The imaginary part self-energy vs. Matsubara frequency (ω_ν) for various values of (β) with a constant U = 4.0 eV of $LaSrV_2O_6$ system.

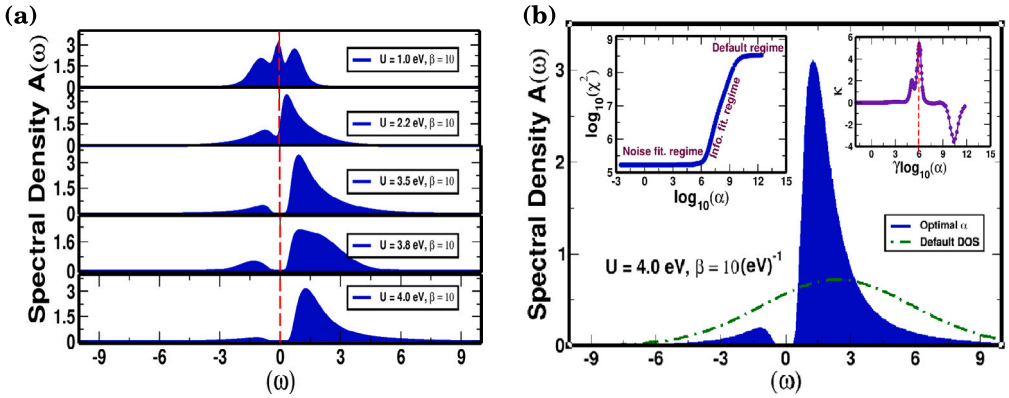

Fig. 11. (Color online) (a) The variation of spectral function A(ω) vs. frequency (ω) for various values of U with a constant β= 10.0 $(eV)^{-1}$ (b) The band splitting of $LaSrV_2O_6$ for U = 4.0 eV and β= 10.0 $(eV)^{-1}$ with the logistic regression (LR) curve with the optimal value of α in the (inset left), which is obtained from the maximal value of the curvature of the LR curve (inset right).

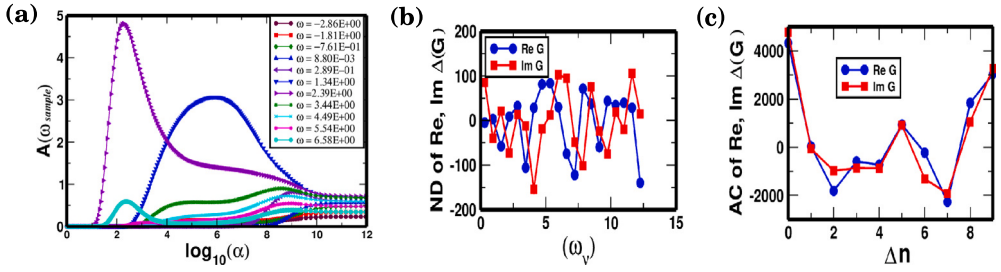

Fig. 12. (Color online) (a) The spectral density distribution of various sample frequencies with variation of α, (b) The normalized deviation of real and Imaginary part of ΔG vs. the frequency (ω_v) with optimal value of (α) and, (c) The autocorrelation of real and Imaginary part of ΔG for optimal value of α, for $LaSrV_2O_6$ system with U = 4.0 eV and β= 10.0 $(eV)^{-1}$.

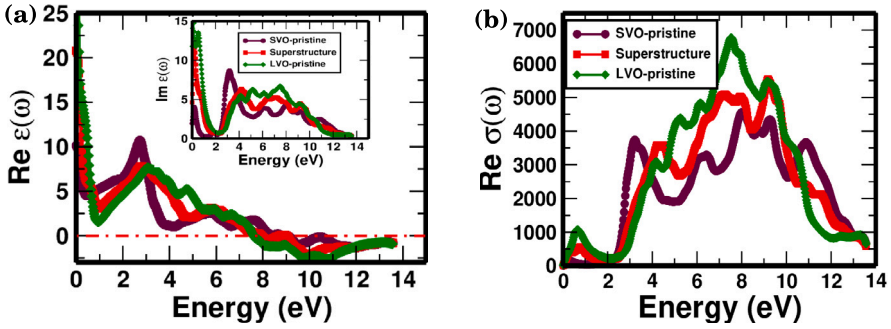

Fig. 13. (Color online) (a) The real part and imaginary part (inset) of dielectric function vs. the photon energy (b) The real part of optical conductivity vs. photon energy for $(La_{1-x}Sr_xVO_3)_n$ (n = 2; x = 0, 0.5, 1) system.

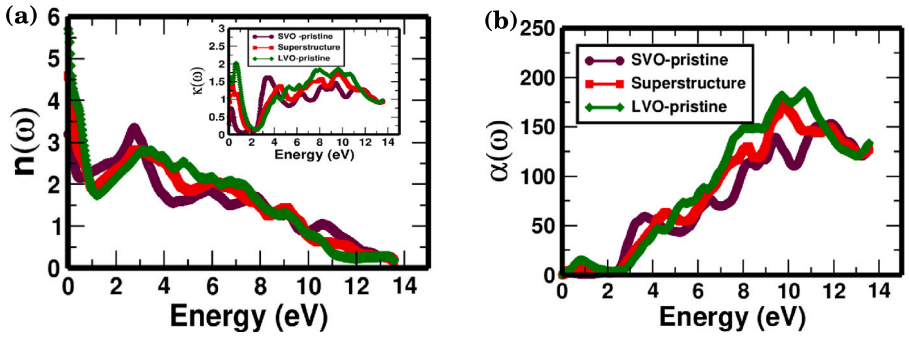

Fig. 14. (Color online) (a) The comparative plot of refractive indices vs. photon energy(eV) (b) The absorptivity vs. photon energy (eV) for $(La_{1-x}Sr_xVO_3)_n$(n = 2; x = 0, 0.5, 1) system.

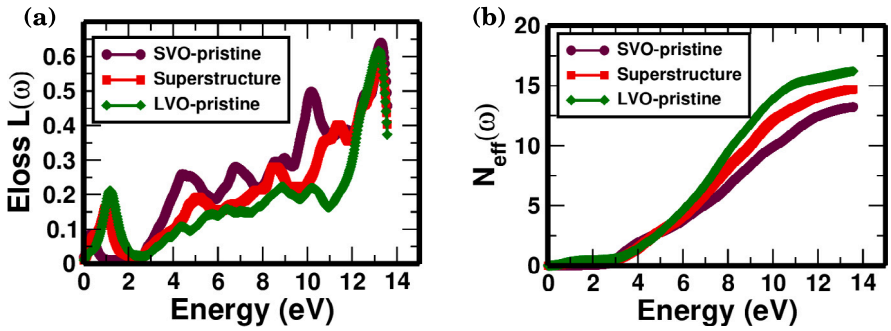

Fig. 15. (Color online) (a) The comparative plot of energy Eloss function vs. photon energy(eV) (b) The optical weight $N_{eff}(\omega)$ vs. photon energy (eV) for $(La_{1-x}Sr_xVO_3)_n$ (n = 2; x = 0, 0.5, 1) system.

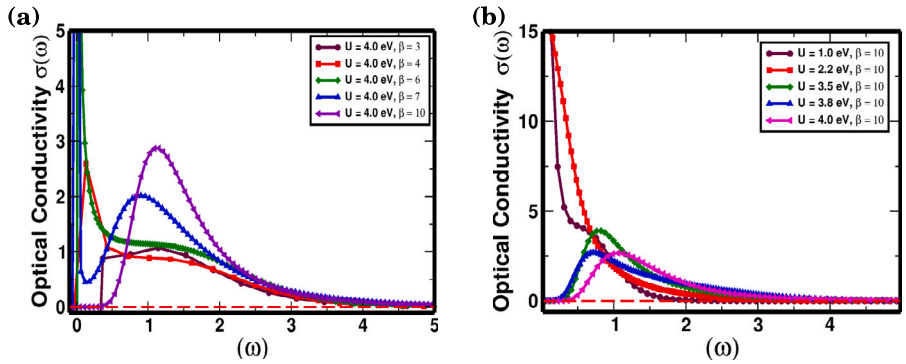

Fig. 16. (Color online) (a) The comparative plot of the variation of optical conductivity $\sigma(\omega)$ vs. frequency (ω) with a constant U = 4.0 eV (variable β) (b) The variation of optical conductivity $\sigma(\omega)$ vs. frequency (ω) with a constant $\beta = 10.0$ $(eV)^{-1}$ (variable U), for $(La_{1-x}Sr_xVO_3)_n$ (n = 2; x = 0.5) system.

4. Conclusions

The formation energies of $LaVO_3$, $SrVO_3$, and $LaSrV_2O_6$ systems are estimated as, −3.18 eV, −2.97 eV and −3.60 eV respectively, and the respective cohesive energies are estimated as, −6.96 eV, −7.56 eV and −7.79 eV, indicating that these systems are structurally and chemically stable. The elastic calculations reveal that these systems are also mechanically stable. The lattice parameters for $LaVO_3$, $SrVO_3$, and $LaSrV_2O_6$ are (3.94 Å), (3.86 Å), and (a = b = 3.96 Å and c = 7.92 Å) respectively, which are fairly agree with available experimental data within the acceptable error bar. From the calculation, MIT model parameters for pristine $LaVO_3$ and $SrVO_3$ are at U = 4.5 eV with β = 8.0 $(eV)^{-1}$ and U = 2.5 eV with β = 6.0 $(eV)^{-1}$, respectively, whereas, a typical set of MIT parameters for $LaSrV_2O_6$ system are U = 4.0 eV with $\beta = 10.0$ $(eV)^{-1}$. As expected, the modulus of elasticities, Poisson's and Pugh's ratios, Cauchy pressure, Anisotropy factor show excellent mechanical stability of these materials. Dielectric function, refractive indexes, Eloss function, reflectivity, absorptivity, and optical conductivity calculations within the range of IR-region through UV region reveal that these materials are good candidate for photo induced applications as well. The redistributed Drude peaks for various values of U and β parameters, show the metal–insulator phase transition of the materials which could be useful for designing Mottronics devices, artificial neurons for neuromorphic computing, machine learning and the other resistive memory devices.

CRediT authorship contribution statement

Raj Kumar Rai: Study design, Methodology, Calculations, Visualization, Manuscript writing, Analysis and interpretation. **Gopi Chandra Kaphle:** Study design, Methods, Visualization, Review of manuscript writing, Analysis and interpretation, Discussion, Managing software. **Ram Babu Ray:** Manuscript writing, Calculations, Discussion and interpretation of data. **Om Prakash Niraula:** Study design, Managing software, Review of manuscript, Discussion.

Declaration of competing interest

The authors declare that they have no known competing financial interests or personal relationships that could have appeared to influence the work reported in this paper.

Data availability

Data will be made available on request.

Acknowledgments

The authors gratefully acknowledge the partial financial supports from the UGC, Nepal and NAST, Nepal. We acknowledge KU for offering HPC facility. We would also like to acknowledge NPA of CDP, T.U. and D. Paudyal, Ames Laboratory, USA for their assistant with computational resources and meaningful discussion and suggestions. The authors acknowledge ABINIT and ALPS codes libraries in parts for DMFT calculations.

References

[1] M. Imada, A. Fujimori, Y. Tokura, Rev. Modern Phys. 70 (1998) 1039.
[2] T. Zou, J. Peng, M. Gottschalk, P. Zhang, Z. Mao, et al., J. Phys.: Condens. Matter 31 (2019) 195602.
[3] M.D. Pickett, G. Medeiros-Ribeiro, R.S. Williams, Nature Mater. 12 (2013) 114.
[4] A. Jaiswal, S. Roy, G. Srinivasan, K. Roy, Trans. Electron Devices 64 (2017) 1818.
[5] J. Biscaras, N. Bergea, A. Kushwaha, T. Wolf, A. Rastogi, et al., Nature Commun. 1 (2010) 1.
[6] C. Wang, H. Zhang, K. Deepak, C. Chen, A. Fouchet, et al., Phys. Rev. Mater. 3 (2019) 115001.
[7] A.J. McAlister, E. Stern, Phys. Rev. 132 (1963) 1599.
[8] F. Wooten, Am. J. Phys. 41 (1973) 939.
[9] M. Veit, M. Chan, B. Ramshaw, R. Arras, R. Pentcheva, et al., Phys. Rev. B 99 (2019) 115126.
[10] S. Beck, C. Ederer, Phys. Rev. Mater. 4 (2020) 125002.
[11] M.D. Scafetta, A.M. Cordi, J.M. Rondinelli, J. Phys.: Condens. Matter 26 (2014) 505502.
[12] I.A. Nekrasov, G. Keller, D. Kondakov, A. Kozhevnikov, T. Pruschke, et al., Phys. Rev. B 72 (2005) 155106.
[13] E. Morosan, D. Natelson, A.H. Nevidomskyy, Q. Si, Adv. Mater. 24 (2012) 4896.
[14] A. Ohtomo, H. Hwang, Nature 427 (2004) 423.
[15] P. Brinks, W. Siemons, J. Kleibeuker, G. Koster, G. Rijnders, et al., Appl. Phys. Lett. 98 (2011) 242904.
[16] E. Maniv, M.B. Shalom, A. Ron, M. Mograbi, A. Palevski, et al., Nature Commun. 6 (2015) 1.
[17] J.C. Gonzalez-Rosillo, R. Ortega-Hernandez, J. Jareño-Cerulla, E. Miranda, J. Suñe, X, et al., J. Electroceramics 39 (2017) 185.
[18] J. Hemberger, P. Lunkenheimer, R. Viana, R. Böhmer, A. Loidl, Phys. Rev. B 52 (1995) 13159.
[19] W. Burke, R. Pressley, Solid State Commun. 9 (1971) 191.
[20] J. Bednorz, K. Müller, Phys. Rev. Lett. 52 (1984) 2289.
[21] R. Wang, M. Itoh, Phys. Rev. B 64 (2001) 174104.
[22] Y.S. Kim, J. Kim, S. Moon, W. Choi, G. Chang, et al., Appl. Phys. Lett. 94 (2009) 202906.
[23] A. Boudali, B. Amrani, A. Abada, K. Amara, et al., Comput. Mater. Sci. 45 (2009) 1068.
[24] B. Amrani, H. Achour, S. Louhibi, A. Tebboune, N. Sekkal, Solid State Commun. 148 (2008) 59.
[25] E. Gull, P. Werner, A. Millis, M. Troyer, Phys. Rev. B 76 (2007) 235123.
[26] P. Werner, A. Comanac, L. De'Medici, M. Troyer, A.J. Millis, Phys. Rev. Lett. 97 (2006) 076405.
[27] M. Imada, Phys. Rev. B 72 (2005) 075113.
[28] G. Kotliar, S.Y. Savrasovm, K. Haule, V.S. Oudovenko, O. Parcollet, et al., Rev. Modern Phys. 78 (2006) 865.
[29] K. Held, O. Andersen, M. Feldbacher, A. Yamasaki, Y. Yang, J. Phys.: Condens. Matter 20 (2008) 064202.

[30] A. Kowalski, A. Hausoel, M. Wallerberger, P. Gunacker, G. Sangiovanni, Phys. Rev. B 99 (2019) 155112.
[31] M. Caputo, J. Jandke, E. Cappelli, S.K. Chaluvadi, E.B. Guedes, et al., App. Surf. Sci. 574 (2022) 151608.
[32] A. Sekiyama, S. Suga, J. Electron Spectrosc. Relat. Phenom. 137 (2004) 681.
[33] D. Bergeron, A.M. Tremblay, Phys. Rev. E 94 (2016) 023303.
[34] M. Jarrell, J.E. Gubernatis, Phys. Rep. 269 (1996) 133.
[35] R. Mossanek, M. Abbate, T. Yoshida, A. Fujimori, Y. Yoshida, et al., J. Phys.: Condens. Matter 22 (2010) 095601.
[36] H. Driscoll, B. Kim, B. Chae, Y. Kim, N. Lee, et al., Science 325 (2009) 1518.
[37] K. Liu, C. Cheng, Z. Cheng, K. Wang, R. Ramesh, et al., Nano Lett. 12 (2012) 6302.
[38] K. Kravtsov, M.P. Fok, D. Rosenbluth, P.R. Prucnal, Opt. Express 19 (2011) 2133.
[39] C. Ambrosch-Draxl, J.O. Sofo, Comput. Phys. Comm. 175 (2006) 1.
[40] G. Cheng, M. Tomczyk, A.B. Tacla, H. Lee, S. Lu, et al., Phys. Rev. X 6 (2016) 041042.
[41] A. Kamerbeek, A.P. Högl, J. Fabian, T. Banerjee, Phys. Rev. Lett. 115 (2015) 136601.
[42] R. Ohshima, Y. Ando, K. Matsuzaki, T. Susaki, M. Weiler, et al., Nature Mater. 16 (2017) 609.
[43] W. Kohn, L.J. Sham, Phys. Rev. 140 (1965) A1133.
[44] G.C. Kaphle, S. Ganguly, R. Banerjee, R. Khanal, C.M. Adhikari, et al., J. Phys.: Condens. Matter 24 (2012) 295501.
[45] J.P. Perdew, K. Burke, M. Ernzerhof, Phys. Rev. Lett. 77 (1996) 3865.
[46] J. Feng, B. Xiao, J. Chen, Y. Du, J. Yu, R. Zhou, Mater. Des. 32 (2011) 3231.
[47] R. Murugeswari, M. Manikandan, R. Rajeswarapalanichamy, A. Milton Franklin Benial, Internat. J. Modern Phys. B 34 (2020) 2050055.
[48] F. Birch, J. Appl. Phys. 9 (1938) 279.
[49] R.J. Needs, R.M. Martin, O. Nielsen, Phys. Rev. B 33 (1986) 3778.
[50] F. Birch, J. Geophys. Res. Solid Earth 91 (1986) 4949.
[51] D.S. Sholl, J.A. Steckel, Density Functional Theory: A Practical Introduction, John Wiley & Sons, USA, 2011.
[52] J.F. Nye, Physical Properties of Crystals: Their Representation By Tensors and Matrices, Oxford University Press, U.K., 1985.
[53] A. Dal Corso, J. Phys.: Condens. Matter 28 (2016) 075401.
[54] F. Parvin, S.H. Naqib, Chin. Phys. B 26 (2017) 106201.
[55] A.J. Cinthia, G.S. Priyanga, R. Rajeswarapalanichamy, K. Iyakutti, J. Phys. Chem. Solids 79 (2015) 23.
[56] O.L. Anderson, J. Phys. Chem. Solids 24 (1963) 909.
[57] W. Metzner, D. Vollhardt, Phys. Rev. Lett. 62 (1989) 324.
[58] K. Haule, Phys. Rev. B 75 (2007) 155113.
[59] A. Georges, G. Kotliar, Phys. Rev. B 45 (1992) 6479.
[60] K. Held, I. Nekrasov, G. Keller, V. Eyert, N. Blümer, et al., Phys. Status Solidi (b) 243 (2006) 2599.
[61] A.N. Rubtsov, V.V. Savkin, A.I. Lichtenstein, Phys. Rev. B 72 (2005) 035122.
[62] N.F. Mott, A.M. Stoneham, J. Phys. C: Solid State Phys. 10 (1977) 3391.
[63] J. Schött, I.L. Locht, E. Lundin, O. Grånäs, O. Eriksson, et al., Phys. Rev. B 93 (2016) 075104.
[64] H. Yoon, J.H. Sim, M.J. Han, Phys. Rev. B 98 (2018) 245101.
[65] R. Fournier, L. Wang, O.V. Yazyev, Q. Wu, Phys. Rev. Lett. 124 (2020) 056401.
[66] H. Shao, A.W. Sandvik, Progress on stochastic analytic continuation of quantum Monte Carlo data, 2022, Phys. Rep. 1003 (2023) 1.
[67] K. Held, Adv. Phys. 56 (2007) 829.
[68] A. Georges, G. Kotliar, W. Krauth, M.J. Rozenberg, Rev. Modern Phys. 68 (1996) 13.
[69] K. Schwarz, P. Blaha, S. Trickey, Mol. Phys. 108 (2010) 3147.
[70] Q. Si, S. Rabello, K. Ingersent, J.L. Smith, Nature 413 (2001) 804.
[71] E. Gull, P. Werner, O. Parcollet, M. Troyer, Europhys. Lett. 82 (2008) 57003.
[72] H.J. Monkhorst, J.D. Pack, Phys. Rev. B 13 (1996) 5188.
[73] T.H. Fischer, J. Almlof, J. Phys. Chem. 96 (1992) 9768.
[74] F. Inaba, T. Arima, T. Ishikawa, T. Katsufuji, Y. Tokura, Phys. Rev. B 52 (4) (1995) R2221.
[75] K. Maiti, A. Kumar, D. Sarma, E. Weschke, G. Kaindl, Phys. Rev. B 70 (2004) 195112.
[76] K. Maiti, M. Unnikrishnan, I. Inoue, D. Sarma, Thin Solid Films 486 (2005) 162.
[77] M.M. Rahaman, K.M. Hossain, M.H.K. Rubel, A.A. Islam, S. Kojima, et al., ACS Omega 7 (2019) 20914.
[78] L. Wang, Y. Li, A. Bera, C. Ma, F. Jin, et al., Phys. Rev. A 3 (2015) 064015.
[79] M. Sage, G. Blake, G.T. Palstra, Phys. Rev. B 77 (2008) 155121.
[80] M. Kim, Phys. Rev. B 97 (2018) 155141.
[81] A. Bouhemadou, R. Khenata, Comput. Mater. Sci. 39 (2007) 803.
[82] D.R. Lide, CRC Handbook of Chemistry and Physics, Vol. 89, 2005, p. 3.
[83] R.M. Martin, Electronic Structure: Basic Theory and Practical Methods, Cambridge University Press, U.K., 2020.
[84] U. Mizutani, Introduction To the Electron Theory of Metals, Cambridge University Press, U.K., 2001.
[85] M. Kawamura, Comput. Phys. Comm. 239 (2019) 197.
[86] N. Blümer, Phys. Rev. B 76 (2007) 205120.

Materials Today Communications 35 (2023) 105510

Contents lists available at ScienceDirect

Materials Today Communications

journal homepage: www.elsevier.com/locate/mtcomm

Stability, electronic, optical and thermoelectric properties of site-substituted $LaVO_3$

Raj Kumar Rai [a,b,*], Ram Babu Ray [a,c], Om Prakash Niraula [a]

[a] Central Department of Physics, Tribhuvan University, Kirtipur, Kathmandu, Nepal
[b] Patan Multiple Campus,Tribhuvan University, Patandhoka, Lalitpur, Nepal
[c] Amrit Science Campus, Tribhuvan University, Lainchaur, Kathmandu, Nepal

ARTICLE INFO

Keywords:
DFT
DMFT
Figure of merit
MIT
Spectral function

ABSTRACT

To unravel the structural and chemical stability, electronic, transport, and optical properties of pristine and site substituted lanthanum vanadate, $LaVO_3$, we employed the density functional theory (DFT) and the dynamical mean field theory (DMFT). The generalized gradient approximation (GGA) and the DMFT with continuous time quantum Monte Carlo (CT-QMC) approach is used for the impurity solver. The variation of the spectral density are studied with different values of the onsite Coulomb interaction (U) and exchange interaction (J), as well as the thermodynamic parameter (β), to investigate the metal insulator transition (MIT) for these materials, which are useful for designing Mottronics, neuromorphic computing devices. The predicted values of U and β for the Mott–Hubbard MIT in $La_{0.40}Ca_{0.60}VO_3$ are consistent with current experimental data. The studied sample's a characteristic sharp quasi-particle peak is found to be at U = 5 eV and β = 6 $(eV)^{-1}$. The Mott quantum critical point (QCP) is also computed for an elevated temperatures and it is found at U = 2.95 eV and β = 23.58 $(eV)^{-1}$. With U = 5.0 eV, β = 10.0 $(eV)^{-1}$, the clear Mott gaps for $La_{0.40}Ca_{0.60}VO_3$ and $La_{0.60}Ca_{0.40}VO_3$ are estimated as 0.74 eV and 1.64 eV, respectively. The electrical and thermal conductivities are calculated at room temperature using the BoltzTraP code, and they are found to be 2.11 $(\Omega\ m\ s)^{-1}$ and 1.51 W/(m K s), respectively, for a given chemical potential μ = −0.14 eV of the system. The figure of merit (ZT) is estimated to be 1.78 at μ = −1.44 eV. Larger values of the Seebeck coefficient (S), ZT, and thermoelectric power factor (TPF) indicate that $La_{0.40}Ca_{0.60}VO_3$ system is a good candidate of thermoelectric material. The calculated frequency dependent optical conductivity (Drude weight) on the dependency of U and β for the metal insulator transition supports the other calculations.

1. Introduction

A wide variety of novel smart materials, such as transition metal oxides (TMOs), are being sought in different fields of scientific study and innovation [1]. The behaviors of TMOs resulting from complicated interactions between their different degrees of freedom, including charge, spin, valley, and lattice interaction, which may be tuned via filling control and band control methods. These interactions are tailored at the interfaces of various oxides by the effects of local symmetry breaking, charge transfer, electrostatic coupling, strain, and frustration, resulting the novel emergent states [2].

The TMOs are formed as a simple cubic perovskite ABO_3 (Pm-3m) type structure, where the A (alkaline earth or rare earth) and B (transition metal) cations are arranged on a simple cubic lattice, and the O anions lie on the face centers nearest to the cations Fig. 1(a) [3]. The pristine $LaVO_3$($CaVO_3$) is considered to be a cubic phase perovskites for a prototype sample, with V-atom sitting at the body center, La (Ca)-atom sitting at the origin of the unit cell, and O-atoms sitting at the face center positions [4]. For substituting Ca-atoms on the La-atomic sites, the unit cell of the $LaVO_3$ Fig. 1(a) was promoted to a supercell of $1 \times 1 \times 3$ dimension in the z-direction Fig. 1(b).

The $LaVO_3$ thin film shows second-order multiple magnetic phase transitions from paramagnetic (PM) to ferromagnetic (FM) to antiferromagnetic (AFM), as well as a first-order structural phase transition with C-type spin and G-type orbital orderings [5]. Coulomb, hopping, thermodynamic, and spin–orbit coupling factors were used to investigate the mechanism of transport properties on site substituted $LaVO_3$. After doping with a particular electron or hole rich materials or reconstructing the cell interface, the electrical and optical behaviors of $LaVO_3$ demonstrated its use on solar cells and as a transparent conducting material [6].

* Corresponding author at: Central Department of Physics, Tribhuvan University, Kirtipur, Kathmandu, Nepal.
E-mail addresses: rairajk@gmail.com, raj.rai@pmc.edu.np (R.K. Rai), ram.ray@ac.tu.edu.np (R.B. Ray), om.niraula@cdp.tu.edu.np (O.P. Niraula).

https://doi.org/10.1016/j.mtcomm.2023.105510
Received 27 October 2022; Received in revised form 14 January 2023; Accepted 27 January 2023
Available online 2 February 2023

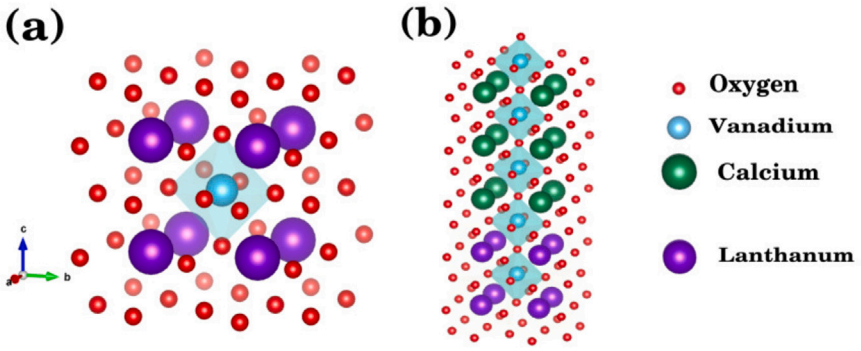

Fig. 1. (Color online) The crystal structures of (a) pristine ideal cubic phase $LaVO_3$, and (b) tetragonal primitive superstructure, $La_{0.40}Ca_{0.60}VO_3$.

It was also experimentally verified that the epitaxial films of $LaVO_3$ and $LaTiO_3$ on $SrTiO_3$ substrate, which acts as a Mott insulator in bulk state [7], observed metallicity due to the strain-induced electronic structure modifications and electronic reconstruction at the interface [8].

The sufficient concentration of Ni doping on V site of Mott-Hubbard insulator $LaVO_3$ shift the hybridized band of Ni 3d-O 2p towards higher energy, leading to the disappearance of the Mott–Hubbard gap [9]. The metallic characteristic found on doping of different concentrations of Ca on superstructure $Ca_xLa_{1-x}VO_3$ was evaluated through dynamical mean field theory (DMFT) [10]. Theoretically, it was observed that $La_{1-x}Sr_xTiO_3$ [11] system are strongly correlated metals, which violates the Landau's Fermi liquid hypothesis at paramagnetic (PM) states [12]. Similarly, in the superstructure, $LaAlO_3/SrTiO_3$, the La -4f orbital contribution is estimated to be near the Fermi level. However, in the real material, the La-4f bands were expected to be of higher energy, and, as a consequence, did not strongly screen the interactions between the electrons in the V t_{2g} bands [13]. The hybridization between the La -4f and Ti t_{2g} orbitals also slightly stabilizes the energy of the t_{2g} orbitals. These layer dependent potential localizes carriers at the interface. As a matter of fact, it is experimentally observed that there was a transition into 2D superconducting state, namely the Berezinskii-Kosterlitz-Thouless (BKT) transition at the interface of the $LaAlO_3/SrTiO_3$[14].

There are four different mechanisms of structural and electronic symmetry breaking that can exercise their ability to lower the total energy, which may lead to the specific mechanism of MIT in oxide perovskites [15].

A tunable electronic and optical properties have also shown in Sr doped $LaFeO_3$ on La site of $La_{1-x}Sr_xFeO_3$ and Mn doped $LaFeO_3$ on Fe site $LaMn_{1-x}Fe_xO_3$ thin film [16]. For A-site doped of $SrTiO_3$ with the rare-earth elements such as Pr, Dy and La were found to have enhanced figure of merit, ZT with the reduced thermal conductivity [17]. The effects of doping, compositing, and nanostructuring were discussed for the enhanced ZT factor of TE TMOs at cryogenic, ambient and elevated temperatures. TMOs with high Seebeck coefficients and tunable electrical properties applicable for temperature, gas and bio sensors with high sensitivities in which very small heat generations or alteration of electrical and thermal properties used in many lab-on-a-chip applications [18].

The DFT analysis of the interband contribution to the optical response function shows that $LaGaO_3$ of cubic phase was reported to be good absorber of ultraviolet with reasonable reflectivity used in photonic, optical, and optoelectronic devices in the high frequency range for transparent coating, shielding and lens applications [19]. The insulating, metallic and superconducting behaviors are analyzed with the help of Drude weight (D_w) and superconducting weight (D_s) [20]. The frequency dependence of the optical conductivity $\sigma(\omega)$ (Drude weight) and the optical spectral weight (f-sumrule) are also consistent with the result of metal–insulator transition as predicted by DMFT and further complemented by the maximum entropy model [21].

There are various types of insulating phases depending upon the periodic potential of ions (Bloch-Wilson type), static lattice deformation (Peierls type), impurities or imperfections (Anderson type), and on site interactions (Mott type) [22]. Specifically, the Mott insulator is caused by the strong correlation effects of heavy fermions. In this material, near the transition point, the metallic state shows fluctuations and orderings in the spin, charge, and orbital degrees of freedom as well as the lattice interaction. The Metal–insulator transition was accompanied by a large resistivity change [23], which was indeed induced in most of the pristine and superlattices of transition metal oxides, such as Ca-doped $LaVO_3$, by the external field, carrier concentration, and lattice distortion [24]. The Mott–Hubbard metal–insulator transition behavior have been shown in a series of $3d^3$ perovskites $SrVO_3$ -$CaVO_3$ -$LaVO_3$ - YVO_3 with electron–electron correlations. This MIT is mainly due to bandwidth control, Filling control and dimensionality control [25]. The tuning of MIT can also be achieved via controlling the bandwidth and local site environment through thickness selection, which actually controls the V 3d -O 2p hybridization (overlappings) [26].

The calculation showed that the charge transfer transitions dominated by crystal field splitting and exchange interactions within V 3d band of these perovskites through Core-level and valence-band optical spectra [27].

The local density approximation (LDA) with dynamical mean-field theory (DMFT) and exact quantum Monte Carlo simulations (QMC) was employed to investigate the Mott-Hubbard MIT for low concentration of Cr on $(V_xCr_{1-x})_2O_3$ compounds [28].

In most of the cases electronic structure of strongly correlated system was studied through DMFT at which MIT was analyzed by employing the continuous time quantum Monte Carlo (CT-QMC) technique as well as the Maximum entropy model. The spectral function obtained through theoretical approach as described above is consistent with the angle resolved photoemission spectroscopy (ARPES) [29]. These study reveal that theoretical calculation of U and β clearly explain the MIT behaviors which was closely agreed with the experimental observations for the TMOs [30].

We chose a particular compound $La_{0.40}Ca_{0.60}VO_3$ over the other superstructures because of its high figure of merit and thermoelectric power factor, which has more or less constant electrical conductivity with temperature (K). Such characteristics are good indicators of thermoelectric candidates. Additionally, this compound has better optical conductivity in the visible range than the other superstructures. As a result, these features motivated us to delve more into this specific compound. The present study intends to investigate the stability, electronic, optical, and transport properties, as well as the influence on MIT, of compounds $La_{1-x}Ca_xVO_3$(x = 0, 0.20, 0.40, 0.60, 0.80) due to the site-substitution of Ca^{2+} ions on superstructure systems using DFT+DMFT and analytic continuation (Maximum Entropy model). The paper also includes potential uses for these materials in Mottronics, photovoltaics, , neuromorphic devices, and thermoelectric devices. The superstructure with 60% Ca^{2+} ions doped specimen with its unique variation of

optical and thermoelectric behaviors is then investigated further to get the comprehensive information for the electronic, thermoelectric, and optoelectronic behaviors and applications.

2. Theoretical background, computational details and experimental information

2.1. Theoretical background

The density functional theory based on the full potential linearized augmented plane-wave (FP-LAPW) with the generalized gradient approximation (GGA) is used for studying electronic structure, thermoelectric and optical properties of the materials. The exchange correlation functional proposed by Perdew, Burke and Ernzerhof (PBE) used for the calculation is expressed as,

$$E_{xc}^{GGA-PBE}[n_e(r)] = \int d^3r F_{xc}(n_e(r), \nabla n_e(r)) \tag{1}$$

where, $\nabla n_e(r)$ is the inhomogeneous gradient of density of carriers. The density of states (DOS) is calculated through,

$$D_n(\varepsilon) = \frac{2}{8\pi^2} \int \delta[E_F - \varepsilon_n(k)] d\varepsilon \tag{2}$$

with the allowed wavevector in the nth band energy range, $\varepsilon \le \varepsilon_n(k) \le \varepsilon + d\varepsilon$ is just the volume of a k-space primitive cell. The thermoelectric parameters, such as Seebeck coefficient ($S_{\alpha\beta}$), figure of merit (ZT) and thermoelectric power factor (TPF) respectively, are calculated as,

$$\begin{cases} S_{\alpha\beta}(T,\mu) = \frac{8\pi^2 k_B^2}{3eh^2} m^* T \left(\frac{\pi}{3n}\right)^{2/3}, \\ ZT = \frac{S_{\alpha\beta}^2 \sigma_{\alpha\beta}(T,\mu) T}{\kappa_{\alpha\beta}} = \frac{S_{\alpha\beta}^2 \sigma_{\alpha\beta}(T,\mu) T}{(\kappa_e + \kappa_L)}, \\ TPF = \sigma_{\alpha\beta}(T,\mu) S_{\alpha\beta}^2. \end{cases} \tag{3}$$

Where, e, k_B, h, m^*, $\sigma_{\alpha\beta}(T,\mu)$, $\kappa_{\alpha\beta}(T,\mu)$, $S_{\alpha\beta}(T,\mu)$ are electronic charge, Boltzmann constant, Planck constant, and carrier effective mass, electrical conductivity tensor, thermal conductivity tensor, and Seebeck coefficient respectively.

For the optical properties, the dielectric function, electron loss function (ELOSS), optical conductivity and so on are computed, as the followings,

$$\begin{cases} \epsilon_{ij}(\omega) = Re.[\epsilon_{ij}(\omega)] + Img.[\epsilon_{ij}(\omega)], \\ L_{ii}(\omega) = -Img.\left\{\frac{1}{\epsilon_{ii}(\omega)}\right\}, \\ Re.[\sigma_{ij}(\omega)] = \frac{\omega}{4\pi} Img.[\epsilon_{ij}(\omega)]. \end{cases} \tag{4}$$

Moreover, the effective number of carriers $N_{eff}(\omega_c)$ participating in the optical transitions is calculated by f-sumrule equation as,

$$\int_0^{\omega_c} \sigma(\omega')\omega' d\omega' = N_{eff}(\omega_c) \tag{5}$$

Where, ω_c is the cut-off energy frequency.

Similarly, the optical conductivity of the system and its MIT behaviors is computed through DMFT [31] using CT-QMC [32] along with Maximum entropy model. The optical conductivity, in terms of the Kubo formalism [33] is expressed as,

$$\sigma(\omega) = \frac{2\pi e^2}{\hbar} \int d\omega' [f(\omega') - f(\omega + \omega')]/\omega \times \int d\epsilon \Phi(\epsilon) A_k(\omega') A_k(\omega' + \omega) \tag{6}$$

Where $f(\omega)$, $A_k(\omega')$ and $\Phi(\epsilon)$ are Fermi function, spectral function and transport function respectively [34]. Furthermore, MIT behavior of strongly correlated system is analyzed through Hubbard Model with CT-QMC hybridization technique as the impurity solver [35]. During this process the interacting Green function and self energy have been calculated self-consistently using the Fourier transformed Dyson equation of impurity model as,

$$\mathcal{G}_0^{-1}(\omega) = G^{-1}(\omega) + \Sigma(\omega) \tag{7}$$

Where, $\mathcal{G}_0$ and $G(\omega)$ are the non-interacting and interacting Green's function of Anderson's impurity model respectively. A step-wise self-consistent DMFT calculation is carried out for obtaining Green's function data [36]. Using the Monte Carlo sampling of partition functions [37] for multiple imaginary time steps, $\tau_{1\uparrow}^{\sigma} > \cdots . > \tau_{n\uparrow}^{\sigma}$ and summing over all the permutation of $\{\tau_i^{\sigma}\}$ various imaginary time steps, we will have to compute the weight. The impurity Green's function could also be regarded as the logarithmic derivative of Z with respect to the hybridization, $\Delta(\tau)$ as given by,

$$G_\sigma(\tau) = -\frac{1}{\beta}\frac{\delta \log Z}{\delta \Delta_\sigma(-\tau)} \left[\because G(\tau) = -\frac{\delta \log Z}{\delta \Delta(\tau)}\right] \tag{8}$$

Where

$$Z = \int \mathcal{D}[\psi]\mathcal{D}[\psi^*] e^{\mathcal{S}_{eff}} \tag{9}$$

is the partition function with $\mathcal{S}_{eff}$ as the effective action.

Each configuration gives for a discrete data set of imaginary times, which is accounted as the Green's function data,

$$G_\sigma(\tau) \sim -\frac{1}{Z\beta} \sum_{C}^{MC} \sum_{k,l} \delta(\tau_k^\sigma - \tau_l'^\sigma + \tau) \times \left[\Delta_{\sigma C}^{-1}\right]_{k,l} \times \text{sign}(\omega(C)) \tag{10}$$

This calculation involves with a high frequency noise in Matsubara frequencies which can be reduced by truncating the Legendre coefficients G_l which are zero within their error bars. The single-particle imaginary time Green's function $G(\tau)$ defined on the interval $[0, \beta]$[38] are computed with the Legendre polynomials $P_l(x)$, defined over an interval $[-1, 1]$(11).

$$G(\tau) = \sum_{l \ge 0} \frac{\sqrt{2l+1}}{\beta} P_l[x(\tau)] G_l \tag{11}$$

Where, G_l is the Legendre coefficients that decays very quickly, which may be defined as,

$$G_l = \sqrt{2l+1} \int_0^\beta d\tau G(\tau) P_l[x(\tau)] \tag{12}$$

Where, $x(\tau) = \frac{2\tau}{\beta} - 1$, maps out the interval $[0, \beta]$ to $[-1,1]$.

The Green's function of frequency, $G(\omega)$ (or the corresponding spectral function $A(\omega)$) be extracted from imaginary-time data $G(\tau)$ or the Fourier transformed Matsubara-frequency data $G(i\omega_\nu)$ using the analytic continuation. As a matter of fact, the spectral function, which can be computed with the imaginary part of Green function at a given momentum is a Dirac delta function [1]as,

$$A(\omega, \mathbf{k}) = -\frac{1}{\pi} Im[G(k,\omega)] = \delta(\omega - \varepsilon_k) \tag{13}$$

The CT-QMC data so obtained from DMFT is further reconstructed through Maximum entropy model based on the Bayesian statistical theorem [39].

$$P[A(\omega)|G(\omega)] = \frac{P[G(\omega)|A(\omega)]\, P[A(\omega)]}{P[G(\omega)]} \tag{14}$$

Where, $P[A(\omega)|G(\omega)]$ and $P[G(\omega)|A(\omega)]$, are the posterior probability and maximum likelihood of $A(\omega)$ for given data $G(\omega)$, and $P[A(\omega)]$ and $P[G(\omega)]$ are the prior or marginal probabilities [40], such that

$$P[G(\omega)|A(\omega)] \propto e^{-\frac{\chi^2}{2}} \tag{15}$$

and,

$$P[A(\omega)|G(\omega)] \propto e^{\alpha S - \frac{\chi^2}{2}} \tag{16}$$

Where, α, S and χ^2 are the adjustable parameter, the differential entropy and chi-square test respectively.

To obtain more realistic information of the bimodal data distribution, we use logistic regression approach for optimal value of α, which is obtained through sigmoid curve(graph between $\log_{10}(\chi^2)$ vs.

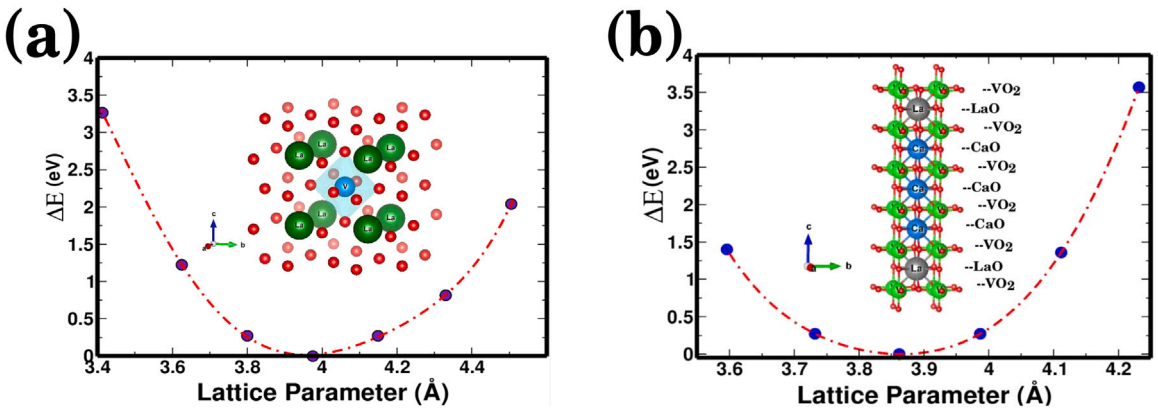

Fig. 2. (Color online) The optimization curve plotted between (a) Energy vs. lattice parameter of $LaVO_3$ system, and (b)The lattice parameter optimization curve of superstructure $La_{0.40}Ca_{0.60}VO_3$ considered to be the interacting ionic layers.

$\log_{10}(\alpha)$). The optimal value of α is obtained for the minimum value of $Q = \chi^2 - \alpha S$ ($\Delta Q = 0$) such that,

$$\chi^2 = (G - KA)^T C^{-1} (G - KA) \tag{17}$$

where, A is the vector obtained after discretizing ω, KA is an approximation to Green's function with kernel K and C is the covariance matrix of Green's function. The differential entropy [41] is defined as,

$$S = -\int \frac{d\omega}{2\pi} A(\omega) \ln \frac{A(\omega)}{D(\omega)} \tag{18}$$

is the relative entropy (Kullback–Leibler divergence)

The Mott-Hubbard transition provides the transport properties of the system, which is obtained by plotting the various sets of U and β in U β-plane. This plane contains four different distinct regimes:(a) Metallic (Fermi-liquid) regime (b) Co-existence regime (c) Insulating regime, and (d) Cross-over regime [42]. The MIT is obtained in the neighborhood of quantum critical point (QCP), where all regimes co-exist, at (U_C, T_C) in Uβ -plane. Actually, MIT is obtained at U_{C_1} along the widomline while going from metallic to insulating phase, whereas this widomline shifted to U_{C_2} while moving from insulating to metallic phase. The regime between U_{C_1} and U_{C_2}, so called metal-insulating co-existence regime. We observe that there are four distinct regions to be realized during the quantum phase transitions [43].

The exact phase transition line, $U_c(T)$ is calculated uniquely as,

$$U_c(T) = U^* + \int_{T^*}^{T} dT' f(T', U_c(T')); T < T^* \tag{19}$$

Where, $f(T, U) = \frac{\Delta E(T,U)}{\Delta D(T,U)}$ with $D \equiv \langle n \uparrow n \downarrow \rangle$ is the double occupancy, E is the Helmholtz Energy [44].

2.2. Computational details and experimental information

The FP-LAPW method with local orbitals approach was used to solve the Kohn–Sham equations within the local spin-density approximation for computing the electronic, transport and optical properties of the materials being studied [45]. The GGA, GGA+U, GGA+U+J, and GGA+SOC schemes have been employed for the ground state calculations. In particular, the GGA+DMFT is used for investigating the MIT of the strongly correlated systems [46].

The energy and charge convergence criteria for self-consistent calculation of the entire system are 10^{-5} eV and 10^{-3} e with force convergence 0.05 eV/Å. The results are consistent with the available information for ($CaVO_3$, $LaVO_3$) [47–49], and its superlattice $La_{0.40}Ca_{0.60}VO_3$ system. The band controlled method of MIT is theoretically studied using the CT-QMC as impurity solvers with hybridization expansion for $La_{1-x}Ca_xVO_3$ systems [50]. The DFT+DMFT calculations are performed for various sets of coulombian interaction, U and the thermodynamical parameter, β in order to identify the critical value of MIT for each of the superstructures. The DMFT calculation have been employed using the parameters, such as chemical potential (μ) = 0.0, number of Matsubara frequency (ω_v) = 500, number of imaginary time bins = 500, number of thermalization sweeps = 500, maximum number of sweeps in a single iteration = 10 000, and the number of Monte Carlo steps between measurements = 5000.

The BoltzTraP codes were employed with 1500 k-points mesh for computing the thermal conductivity, electrical conductivity, Seebeck coefficients and figure of merit (ZT), thermoelectric power factor (TPF) using the optimized $La_{1-x}Ca_xVO_3$ superlattices [51,52]. The algorithm is based on a smooth Fourier expression for periodic functions, which implements the band and k -dependent quasi-particle energies along with the intra-band optical transition matrix elements and scattering rates as input [53]. The optical properties of the materials is analyzed using DFT as well as DMFT at which MIT phase transition is predicted on the basis of Drude peaks which depends on the spectral weight ratio associated with mass enhancement factor as,

$$m^*/m \simeq SW_{Drude+MIR}/SW_{Drude} \simeq K_{band}/K_{exp} \tag{20}$$

It is also possible to assess the mass enhancement due to dynamical correlations as the reduction of the kinetic energy of the quasiparticles [54] due to correlations, K_{exp}/K_{band}, which is indeed vanished in a Mott insulating case. The overall kinetic energy does not vanish due to correlation but the spectral weight of intraband transitions always adds up to the conduction electrons kinetic energy and hence it is rather transferred from the Drude peak into mid-infrared (MIR) or higher energy features [55].

Experimentally, Ca doped $La_{1-x}Ca_xVO_3$ for x = 0.2, 0.3, 0.4 and 0.5 were synthesized to study the temperature dependent resistivity and susceptibility for the Mott and band insulators [56].

The spectra of $CaVO_3$ and $SrVO_3$ are also studied with bulk-sensitive high-resolution PES and XAS $(V_{1-x}Ti_x)_2O_3$ for the experimental realization of Mott transitions in V_2O_3 doped with Cr or Ti [47]. The perovskite-type TMOs, $LaTiO_3$ and $CaVO_3$ are studied for the effect of stoichiometric composition on MIT phase transition. The Mott-Hubbard insulating gap for different values of U for vanadates and titanates system were also studied from the various experimental works [25]. Thus, the more theoretical study is required to understand the impact onto the electronic, optical and transport properties of such strongly correlated materials in relation to the various applications in Mottronics and neuromorphic computing devices, and thermoelectric and energy devices.

3. Results and discussion

3.1. Geometric optimization and structural stability

The ideal crystal structures of pristine $CaVO_3$ and $LaVO_3$ are considered as a prototype cubic perovskite, $SrFeO_3$ structure with the

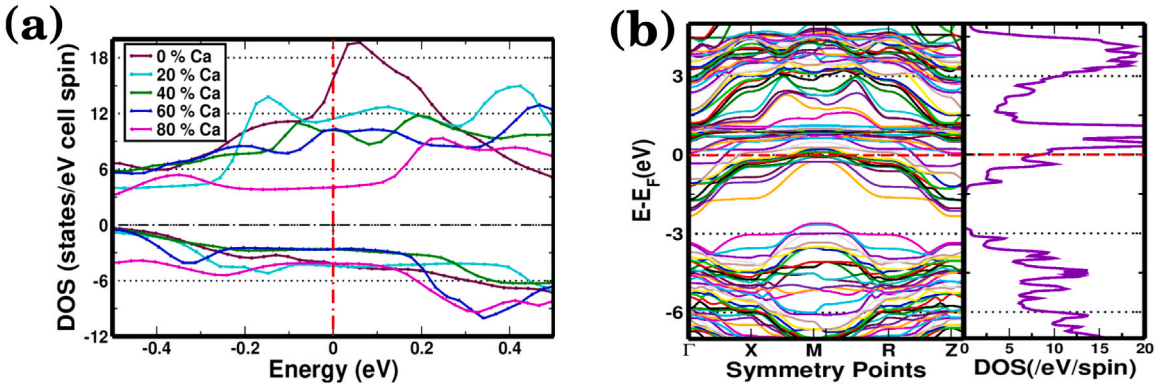

Fig. 3. (Color online) (a) The redistribution of total DOS with the site-substitution of Ca-atom in $LaVO_3$ supercell in $La_{1-x}Ca_xVO_3$ system (b) The comparative DOS and band structures of $La_{0.40}Ca_{0.60}VO_3$.

Table 1
The optimized structural parameters of the pristine $CaVO_3$, $LaVO_3$ and its superlattice: $La_{0.40}Ca_{0.60}VO_3$. The cohesive energy and formation energy for these vanadate systems, and their optimized volumes and densities.

Physical info.	$CaVO_3$	$LaVO_3$	$La_{0.40}Ca_{0.60}VO_3$	Other works
Lattice Parameters (Å)	a =3.86	a =3.94	a=b=3.95 c =19.48	[47,58] [48,49]
Space-group	Pm-3 m (221)	Pm-3 m (221)	P4/mm (99)	
Cohesive Energy (eV)	−7.53	−7.56	−7.20	[61,62]
Formation Energy (eV)	−3.01	−3.18	−2.99	
Opt. Volume Energy (Å^3)	57.51	61.20	303.94	
Density ρ (g/cm^3)	6.30	7.29	9.67	

space group pm-3m(221). The cubic unit cell with Wyckoff coordinate of V at the origin (0.0, 0.0, 0.0)a, the La/Ca-atoms are sitting at the body center (0.5, 0.5, 0.5)a and the three O-atoms at the three face centers (0.5, 0.5, 0.0)a, (0.0, 0.5, 0.5)a, and (0.5, 0.0, 0.5)a; the lattice constant is a = 3.86 Å [57]. The structural optimization curve for $LaVO_3$ is shown in Fig. 2(a) Furthermore, the ideal unitcell of the $LaVO_3$ is then promoted to a supercell of $1 \times 1 \times 3$ dimension for the investigation of electronic, transport and optical properties. The geometrical structure of superlattice is found to be converged in tetragonal primitive supercell with space group p4/mm (99). The convergence structure parameters of $La_{0.40}Ca_{0.60}VO_3$ superlattice sample are tabulated in Table 1. The slight change in the pristine parameters are found due to structural change while forming the superstructure, which are comparable with the previously calculated data [58,59]. The lattice parameter optimization curve for the pristine $LaVO_3$ and superstructures, $La_{0.40}Ca_{0.60}VO_3$ are shown in (Fig. 2(a),(b)).

The Monkhorst–Pack of 1000 k-points mesh grid is used for self-consistent calculation of these tetragonal primitive superstructures with p4/mm space group (99) comparable to the previously calculated data [60] The doping induced insulator–metal transition in $La_{1-x}Ca_xVO_3$ is studied using the ab-initio GGA+DMFT scheme. The calculated equilibrium properties: cohesive energies, formation energies, volume per atom, bulk modulus and its pressure derivative can be used to understand the thermodynamic stability as well as chemical stability of the systems.

3.1.1. Cohesive energy:

Using a set of optimized lattice constants and with each ion relaxation, the ground state total energy calculation was performed, and the cohesive energy per atom [61,62] $E_{cohesive}$ for a compound $A_xB_yC_z$ (ABC), one can calculate it as,

$$E_{\text{cohesive}} = \frac{\left(xE^{A}_{\text{atom}} + yE^{B}_{\text{atom}} + zE^{C}_{\text{atom}}\right) - E^{ABC}_{\text{total}}}{x + y + z} \tag{21}$$

where E^{A}_{atom}, E^{B}_{atom} and E^{C}_{atom} are the energies of the isolated non-spherical spin-polarized atoms with x, y, and z are the stoichiometric weights.

3.1.2. Formation energy:

Beside the cohesive energy, another measure of relative stability of the given system is the formation energy $E_{formation}$. The formation energy per atom of a compound $A_xB_yC_z$ (ABC) can be calculated as,

$$E_{\text{formation}} = \frac{E^{ABC}_{\text{total}} - \left(xE^{A}_{\text{bulk}} + yE^{B}_{\text{bulk}} + zE^{C}_{\text{bulk}}\right)}{x + y + z} \tag{22}$$

where E^{A}_{bulk}, E^{B}_{bulk}, and E^{C}_{bulk} are the calculated energies of the bulk form the respective constituent elements of the unit cell with x, *y* and z are the stoichiometric weights.

The calculated values of the cohesive energies and formation energies are given in Table 1[63], reveal that the systems under investigation are stable and viable for experimental synthesis. The calculation of the formation energies for the pristine and superstructure are obtained as, −3.01 eV/atom, −3.18 eV/atom and −2.99 eV/atom for $CaVO_3$, $LaVO_3$ and $La_{0.40}Ca_{0.60}VO_3$ systems, respectively, which are all negative imply that the systems are energetically favorable for synthesis and stable structure for thermodynamical and its chemical stabilities. The cohesive energy is a measure of the strength of the forces that bind atoms together in the solid state and is useful for studying the phase stability. The computed cohesive energies are −7.53 eV/atom, 7.56 eV/atom and −7.20 eV/atom for $CaVO_3$, $LaVO_3$ and $La_{0.40}Ca_{0.60}VO_3$ systems, respectively. The higher the negative values of cohesive and formation energies signify the better structural and chemical stability of the systems.

3.2. Electronic structure

3.2.1. Density of states and band structures

The density of states (DOS) and band structure graphs demonstrate the contribution of V d-orbitals and La f-orbitals near the Fermi level. The redistribution of DOS structures for the variation of site substitution of Ca^{2+} ions in the $La_{1-x}Ca_xVO_3$ system Fig. 3(a). The asymmetry of DOS distribution of spin up/down channels was clearly observed in systems with 40% and 60% replacement of Ca^{2+} ions (both are not shown here). The comparative DOS and band structures are shown in Fig. 3(b). With the increasing U values, the peaks of the DOS distribution shift towards the valence band. The partial density of states (PDOS) of 2 La-atoms, 3 Ca-atoms, and 5 V-atoms for a unit

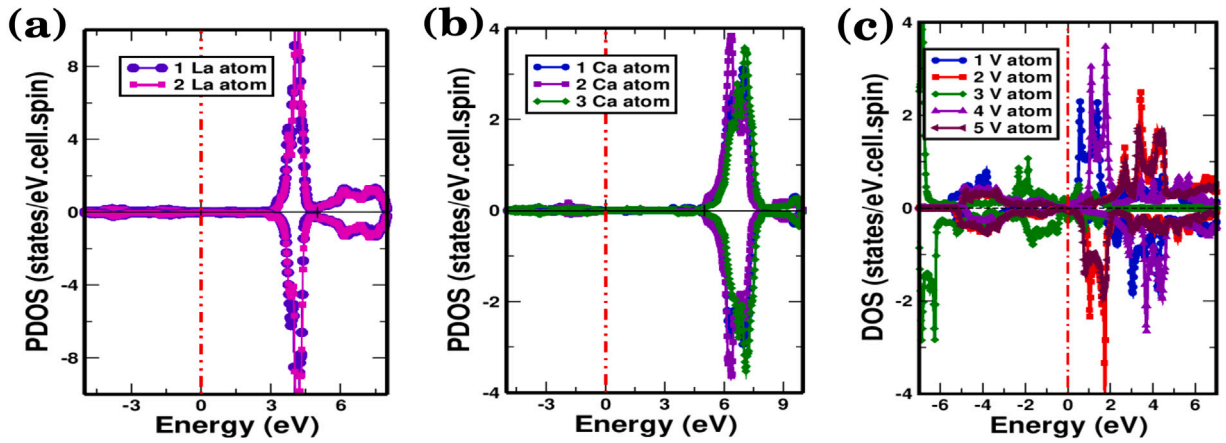

Fig. 4. (Color online) The total PDOS contribution of (a) La-atoms (b) Ca-atoms (c) V-atoms in $La_{0.40}Ca_{0.60}VO_3$ with U =3.11 eV and J =0.

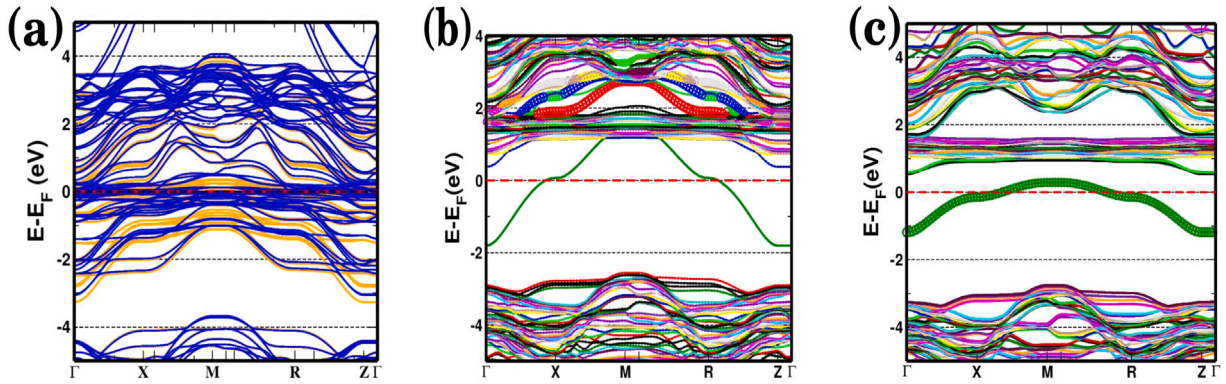

Fig. 5. (Color online) (a) The band structure up (blue) and down (orange) spin channel of $La_{0.40}Ca_{0.60}VO_3$ (b) The fat band structure of V d orbital $La_{0.40}Ca_{0.60}VO_3$ with U and J (c) The third atomic V-e_g orbital (thick green) fatbands is pushed sizably towards the Fermi level with, U = 4.11 eV and J = 0.50 eV of $La_{0.40}Ca_{0.60}VO_3$ system. (For interpretation of the references to color in this figure legend, the reader is referred to the web version of this article.)

cell of $La_{0.40}Ca_{0.60}VO_3$ are calculated using the GGA+U method. DOS peaks are found at around 4.5 eV and 7.0 eV for La- and Ca-atomic contributions, respectively (Fig. 4(a), (b)). However, in the case of the 3^{rd} V-atoms, the DOS peak is primarily pushed towards the valence band, as seen in Fig. 4(c). The asymmetry of the DOS distribution indicates that the presence of net magnetic moment (MM), which varies with the amount of site substitution of Ca^{2+} ions in the $LaVO_3$ supercell. It is found that there is a ferrimagnetic phase transition occurs due to these dopings. This demonstrates that the MM for the superstructures is mostly contributed by separate La-5d orbitals. The hybridization of the La -4f and V-t_{2g} orbitals, as seen in fat band structures Fig. 5(b), slightly stabilizes the energy of the t_{2g} orbitals. The V-e_g orbital is significantly pushed towards the Fermi-level in Fig. 5(c), with U = 4.11 eV and J =0.50 eV indicating the quasi behavior of the materials. There was no substantial change in the electronic structure with SOC in the superstructure, $La_{0.40}Ca_{0.60}VO_3$ system. The insertion of varied values of U and J, on the other hand, clearly shows the redistribution of DOS, including the shifting of the band structure of the $La_{0.40}Ca_{0.60}VO_3$ system (Fig. 5(a),(b),(c)). These systems were found to be in metallic phase (Fermi liquid phase) through standard DFT [13]. The lower narrow conduction bands are derived from the 4f orbitals of La sites, and the La-5d orbitals are hybridized with the La-4f orbitals at the Γ-point (Fig. 6(a), (b)).

To be noted here, the crystal field splitting (CFS) and p-d hybridizations play crucial role for the electronic structure, magnetic properties and other physical behaviors of transition metal oxides. The transition metal ion in TMOs is surrounded by six oxygen atoms, providing an octahedron environment that may split the degenerate bands into two energy levels (three t_{2g}-states and two e_g-states). The orbital wavefunctions in t_{2g}-states point between nearby O^{2-} ions. The wavefunctions in e_g-states point toward nearby O^{2-} ions and exhibit greater orbital overlap than t_{2g}. These states are further divided by p-d hybridization between V-d-orbitals and O-2p orbitals as in (Fig. 7(a), (b)). The t_{2g}-orbitals form π-bonding, and the e_g-orbitals create σ-bonding with O-2p orbitals. As a result, O-2p states become non-degenerate as well. The typical energy scale of crystal field splitting is of several electron volts (eV), which is equivalent to Hund's coupling energy (J_H). When filling out the empty states, electrons prefer to align in the same spin direction to generate a high spin state, according to Hund's rule. This may not be the case if the crystal field splitting is comparable enough to CFS. Instead, the electrons will prefer to align in a low spin state, and the material will have different electrical and magnetic properties and other than in the high spin state. The electronic charge density map shows the likelihood of electrons being present at a given time and place [45]. The 2D charge density distribution map for $La_{0.40}Ca_{0.60}VO_3$ in the (111) plane, as shown in Fig. 8(a), demonstrates that the electron density distribution is primarily confined towards the nuclear centers, as predicted for different ionic cores [64]. The Fermi-surface is the constant energy surfaces at various lattice sites as defined by Fermi momentum, k_F constituted by multiple electron and hole orbits are presented for the $La_{0.40}Ca_{0.60}VO_3$ systems as shown in Fig. 8(b), which is the Fermi surfaces generated with 50–175 band levels.

The Fermi surfaces are centered around the Γ points with various electrons and hole pockets. The Fermi surface of a metallic system is located outside the first Brillouin zone. The shape of the Fermi surface is susceptible for being altered by an external field.

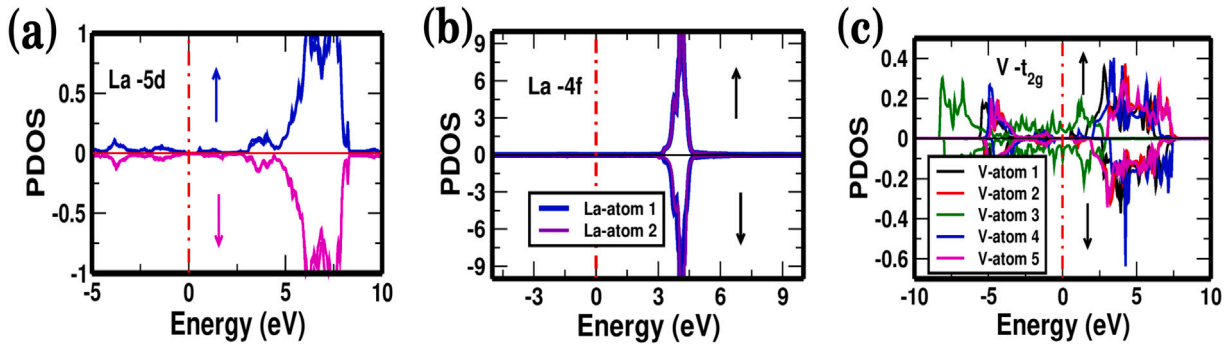

Fig. 6. (Color online) The total PDOS contribution of (a) La-5d orbitals (b) La-4f orbitals (c) V-t_{2g} orbitals in $La_{0.40}Ca_{0.60}VO_3$ system.

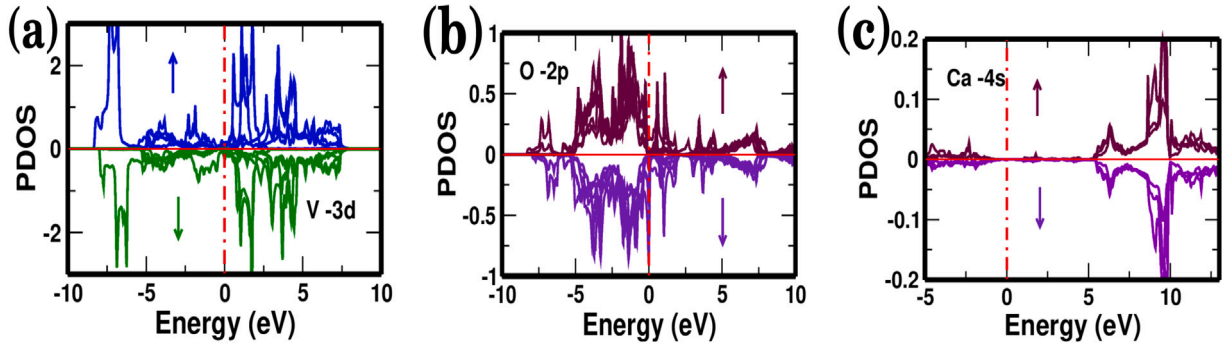

Fig. 7. (Color online) The PDOS contribution of (a) V-3d orbitals (b) O-2p orbitals (c) Ca-4s orbitals in $La_{0.40}Ca_{0.60}VO_3$ system.

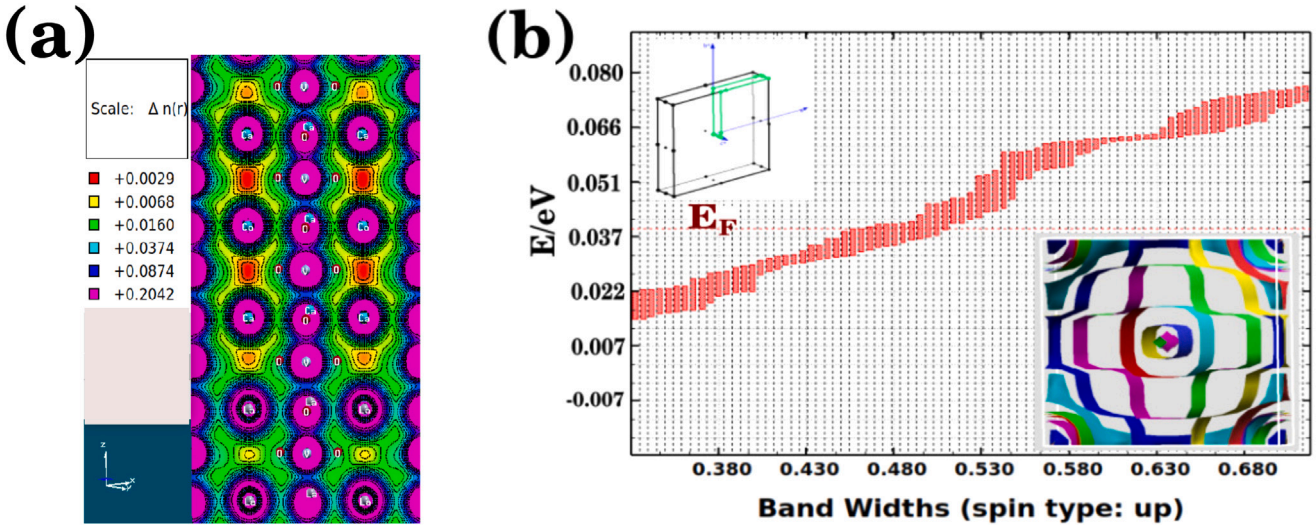

Fig. 8. (Color online) (a) The 2D charge density map of $La_{0.40}Ca_{0.60}VO_3$ system (b) The Fermi level band crossing for 50–175 band levels and the Fermi-surface plots around Γ point (inset bottom right) with a primitive Brillouin zone (inset top left) of $La_{0.40}Ca_{0.60}VO_3$ system.

3.2.2. *Electronic structure by GGA+DMFT*

In the case of strongly correlated system, the DFT fails to address accurate prediction of their electronic structures and hence the dynamical mean field theory (DMFT) using CT-QMC hybridization technique has been employed for the same purpose. It provides the Green's function data as a function of imaginary time and frequency [65,66]. These data are used for obtaining the spectral function of real frequency using Maximum entropy model. The variation of Green's function of imaginary time G(τ), vs. the imaginary time (τ) for various values of β and the corresponding Fourier transform G(ω) as in Fig. 9(a), (b). The metal–insulator transition of strongly correlated electronic system are perfectly tunable by adjusting the Coulombian parameter (U) by keeping the same thermodynamic parameter (β). The Green's function data for the superstructures $La_{1-x}Ca_xVO_3$ system with various stoichiometric combinations are shown in Fig. 9(c) and the corresponding variation of spectral density, A(ω) with the frequency (ω) is shown in Fig. 10(a), which is obtained by using the maximum entropy model of data analysis algorithm. The plot of the spectral function A(ω) vs. frequency (ω) is actually analogous to the density of states (DOS) vs. energy of the conventional DFT. The Mott–Hubbard transition with a typical set of U and β parameters for the pristine and the superstructure are tabulated in Table 2. It was found that the expected features of a t_{2g} quasi-particles peak at lower value of U around the Fermi level and a lower Hubbard band at negative energies of the same t_{2g} nature,

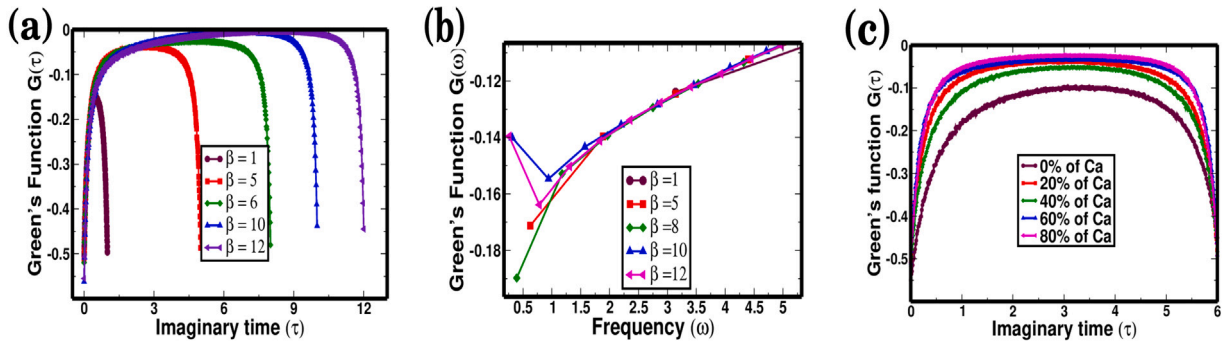

Fig. 9. (Color online) (a) The Green's function vs. imaginary time for the variation of β with a constant U = 5eV (b) The corresponding variation of Green's function vs. frequency (ω) of $La_{0.40}Ca_{0.60}VO_3$ system, and (c) The Green's function vs. imaginary time (τ) with U = 3 eV and $\beta = 6\,(eV)^{-1}$ for various level of Ca-ions dopings in $La_{1-x}Ca_xVO_3$ systems.

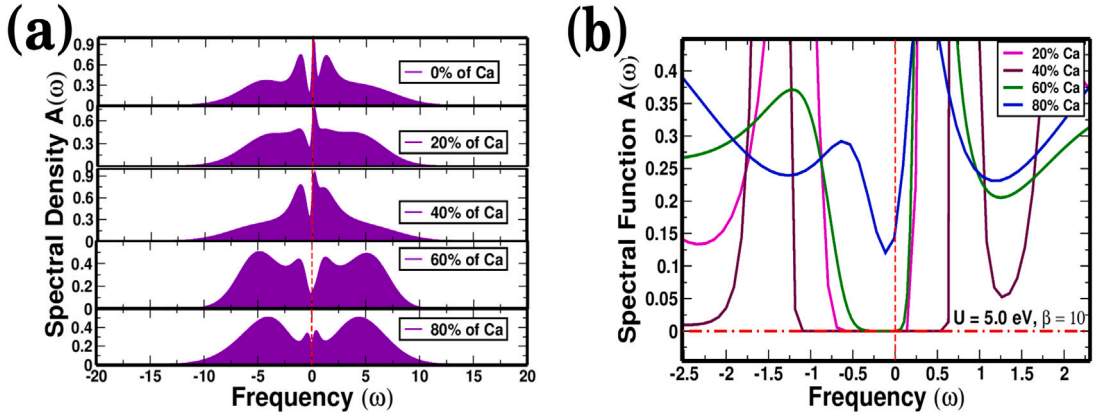

Fig. 10. (Color online) (a) The Spectral density vs. frequency (ω) with U = 3 eV and $\beta = 10\,(eV)^{-1}$ of $La_{1-x}Ca_xVO_3$ supercell for various proportion of Ca-atoms, and (b) The spectral function vs. frequency for U = 5.0 eV with a constant $\beta = 10.0\,(eV)^{-1}$ for $La_{1-x}Ca_xVO_3$ system.

Table 2
The DMFT results (Mott gaps) of electronic structures of the pristine $CaVO_3$, $LaVO_3$ and its superlattice: $La_{0.40}Ca_{0.60}VO_3$ system.

S.N.	Physical parameters	$CaVO_3$	$LaVO_3$	$La_{0.40}Ca_{0.60}VO_3$	Other works
1.	MIT U Parameters (eV)	5.0	4.5	5.0	[47,68]
2.	MIT β Parameters $(eV)^{-1}$	6.0	8.0	10.0	
3.	Mott Gap (eV)	0.04	0.93	0.74	[48,49]

which is in agreement with the angle-resolved photoemission spectra(ARPES) [67]. The variation of spectral function with the frequency for different proportion of substituted Ca-atoms in $LaVO_3$ supercell for U = 5eV with a constant value of $\beta = 10\,(eV)^{-1}$ are observed to be significantly different as in Fig. 10(b). It shows that the clear Mott gaps for 40% and 60% Ca^{2+} ions doped specimens are found to be 1.64 eV and 0.74 eV respectively.

The DMFT results with Mott gaps of pristine and its superstructure are tabulated as in Table 2 and consistent with the available information for ($CaVO_3$, $LaVO_3$) [47,68–70], and its superlattice $La_{0.40}Ca_{0.60}VO_3$ system [48,49]

The validity and accuracy of the calculated data obtained for spectral function (Fig. 11), such as its height and width of the central peak, and the overall spectral weight is necessary to be implemented using logistic regression (LR) curve as shown in Fig. 11 (inset upper left) using the maximum entropy model. The optimized value of adjustable parameter, α has to be implemented to include the real information of the material concerned. The optimal value of α can be found by using the maximal value of curvature of LR curve on plotting $\log_{10}(\chi^2)$ vs. $\log_{10}(\alpha)$ as in Fig. 11 (inset upper right). There have been observed three distinct regions, such as noise fitting region, information fitting region and default model region in a LR curve. The location of the optimal α can be determined by choosing the peak value of curvature (κ) vs. $\gamma\log_{10}(\alpha)$ curve as in Fig. 11 (inset upper right). The sample frequencies vs. $\log_{10}(\alpha)$ curves can also be used for predicting the optimal values of α as shown in Fig. 12(a). For the statistical inferences such as the normalized deviation of real and imaginary parts of the uncertainty in Green's function of frequency ΔG and its auto correlation are estimated within the permissible standard error bar as in Fig. 12(b) and Fig. 12(c) respectively.

The localization or delocalization of electrons can be realized by adjusting appropriate values of hopping parameter, t of a system. For the metallic phase of the system requires delocalization limit, $U/t \ll 1$. And for the insulating phase of the system requires a localization limit, $U/t \gg 1$[24,35]. On plotting graph between U/t versus β/t, the metal–insulator phase transitions can easily be realized for the correlated system(not shown here). The spectral function of the material particle is changes abruptly for a very small change in the ratio of these model parameters (U/t and β/t)(Figures are not shown here).

3.2.3. *Quantum Critical Point (QCP) for the correlated system*

The Mott metal–insulator phase transition for the strongly correlated system with the variation of Coulombian interaction (U) versus the thermodynamic parameter (β) is shown in Fig. 13. The figure shows that QCP is located at $U_C = 23.65$ eV and $\beta_C = 2.96\,(eV)^{-1}$. It has been observed two critical values of Coulombian parameters, $U_{C_1}(T) = 7.40$ eV at which insulating behavior disappears and $U_{C_2}(T) = 12.30$ eV at which metallic behavior disappears.

The region in between these two widom lines and above the critical point is called crossover region. Four different distinct regions have been observed in Uβ-plane due to correlation hysteresis. The paramagnetic insulating regions on the right side of $U_{C_2}(T)$ widom line and

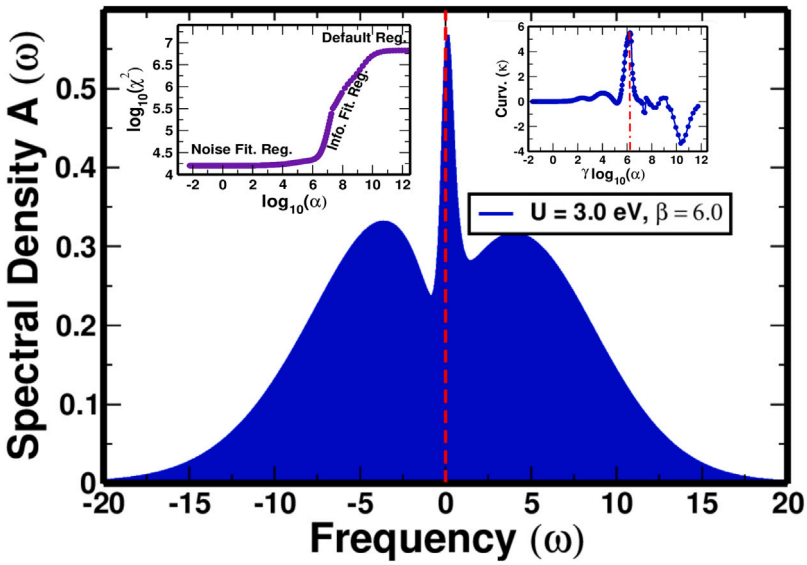

Fig. 11. (Color online) (a) The spectral density with quasi-particle peak vs. frequency of $La_{0.40}Ca_{0.60}VO_3$ system with U = 3.0 eV and $\beta = 6\,(eV)^{-1}$. The corresponding logistic regression curve (inset upper left) and the curvature of $\log_{10}(\chi^2)$ vs. $\log_{10}(\alpha)$ (inset upper right) to find the optimal values of α for the real representation of data.

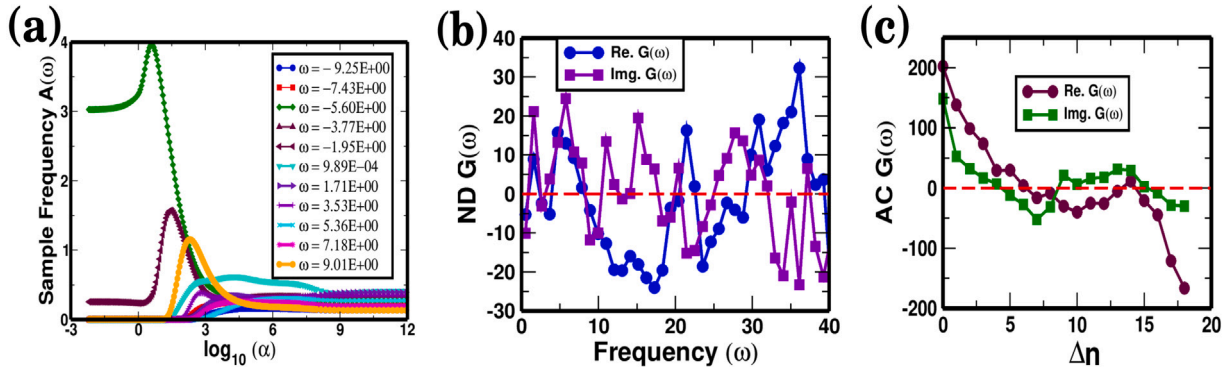

Fig. 12. (Color online) (a) The spectral function A(ω) of sample frequencies vs. $\log_{10}(\alpha)$ for its optimal value (b) The normalized deviation (ND) of Real and Imaginary part of Green's function vs. α with U =3.0 eV and $\beta = 6\,(eV)^{-1}$ for $La_{0.40}Ca_{0.60}VO_3$ system, and (c) The auto-correlation (AC) of Real and Imaginary part of Green's function vs. Frequency index difference(Δn).

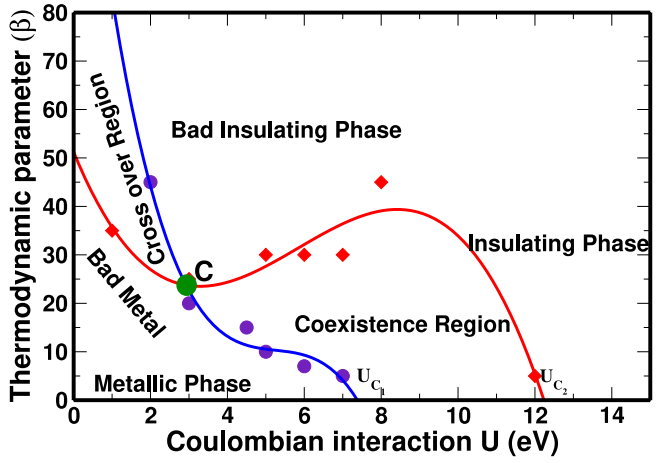

Fig. 13. (Color online) The Metal-Insulator phase transition is used for finding the elevated temperature quantum critical point, C in the U-β plane. At low temperature regime, there are two bifurcation points, U_{C_1} and U_{C_2}.

the Fermi liquid (metallic) regions on the left side of the $U_{C_1}(T)$ widom line. The crossover region divides Uβ-plane into bad metallic region for which the material exhibit anomalously large resistivity and on the other hand a bad insulating region for which the resistivity decreases on increasing temperature. On increasing Coulombian interaction U, a smooth transition from a metal towards an insulator is observed, the change is most rapid within the crossover region. The metallic phase is thermodynamically stable for $U \leq U_C$, but remains a well-defined metastable solution of the DMFT equations for $U_{C_1} \leq U \leq U_{C_2}$ (co-existence region).

3.3. *Transport properties of* $La_{1-x}Ca_xVO_3$

We used the BoltzTraP algorithm to solve the linearized Boltzmann transport equation (BTE) and compute the transport behaviors of systems with the DFT based frameworks using a 1500 k-point mesh for Brillouin zone integration. Using optimized systems and appropriate convergence criteria, we have computed Seebeck coefficients (S), Hall coefficients(R_H), electrical conductivity (σ/τ), thermal conductivity (κ), thermoelectric figure of merit (ZT), thermoelectric power factor (TPF) and so on.

The sharp variation of Seebeck coefficient (S) at around chemical potential, $\mu \sim -2$ eV dynamically as shown in Fig. 14 (a), reflecting the changing carrier concentration with the various amounts of Ca^{2+}

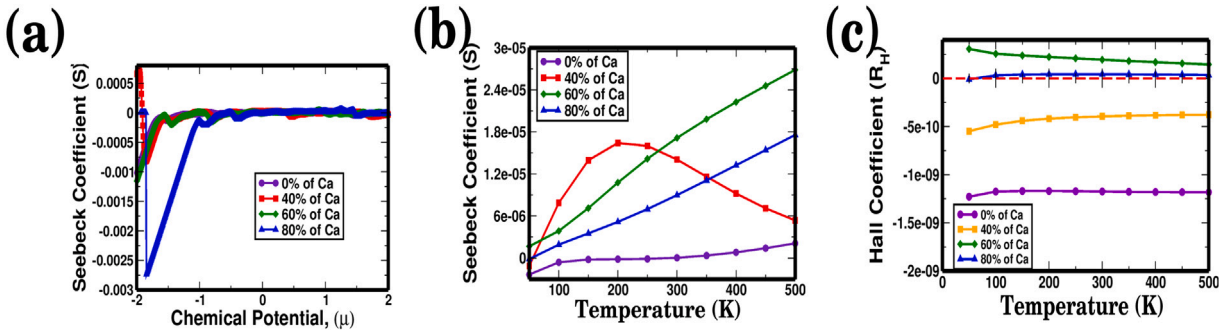

Fig. 14. (Color online) (a) The variation of Seebeck Coefficient (S) at room temperature with respect to the chemical potential μ, (b) The variation of Seebeck coefficient with temperature (T) for a constant chemical potential (μ), and (c) The variation of Hall coefficient (R_H) vs. temperature (T) for a constant chemical potential (μ) for $La_{1-x}Ca_xVO_3$ superlattice system.

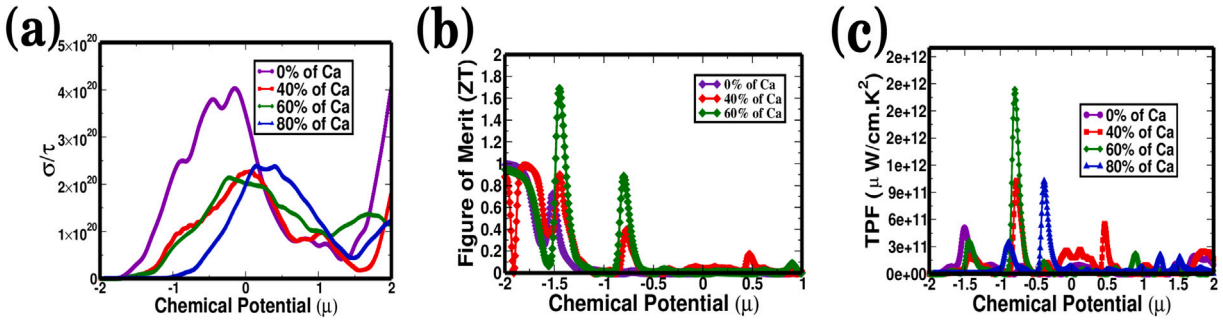

Fig. 15. (Color online) (a) The variation of electrical conductivity (σ/τ) at room temperature with respect to the chemical potential μ at room temperature (b) The Figure of merit (ZT) at room temperature with chemical potential (μ), and (c) The comparison of TPF vs. chemical potential (μ) for $La_{1-x}Ca_xVO_3$ superlattice system.

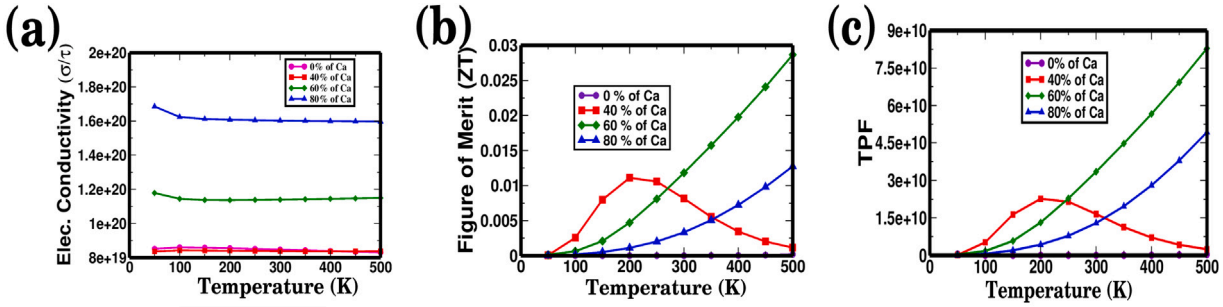

Fig. 16. (Color online) (a) The variation of electrical conductivity (σ/τ) with respect to temperature, (b) The Figure of merit (ZT) with temperature, and (c) The comparison of TPF vs. temperature at a constant chemical potential ($\mu = 0.82$ eV) for $La_{1-x}Ca_xVO_3$ superlattice system.

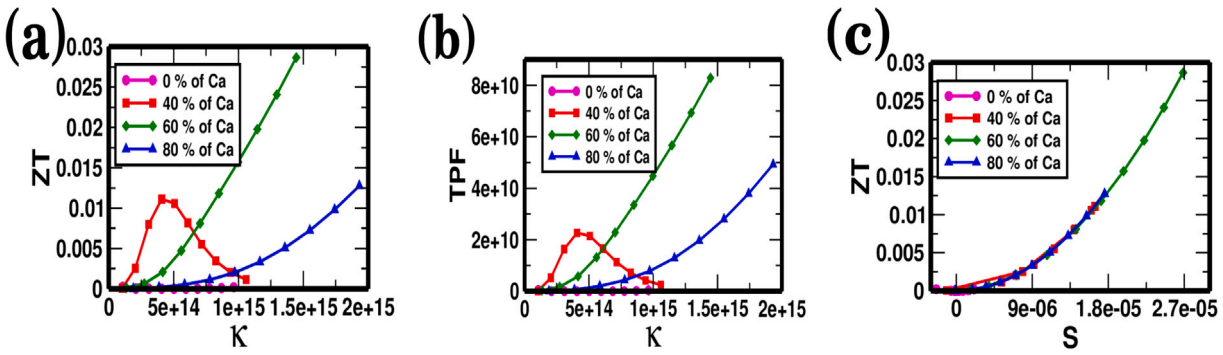

Fig. 17. (Color online) (a) The Figure of merit vs. the thermal conductivity (κ) for various samples at room temperature. (b) The corresponding variation of TPF vs. thermal conductivity (κ), and (c) The Figure of merit vs. Seebeck coefficient (S) at room temperature.

ion substitution in the superlattice. The Seebeck coefficient is roughly proportional to temperature in general, indicating that the materials are metallic, but the fluctuation is unique for the 40% Ca-doped system illustrated in Fig. 14 (b). The classical Hall coefficient (R_H) is

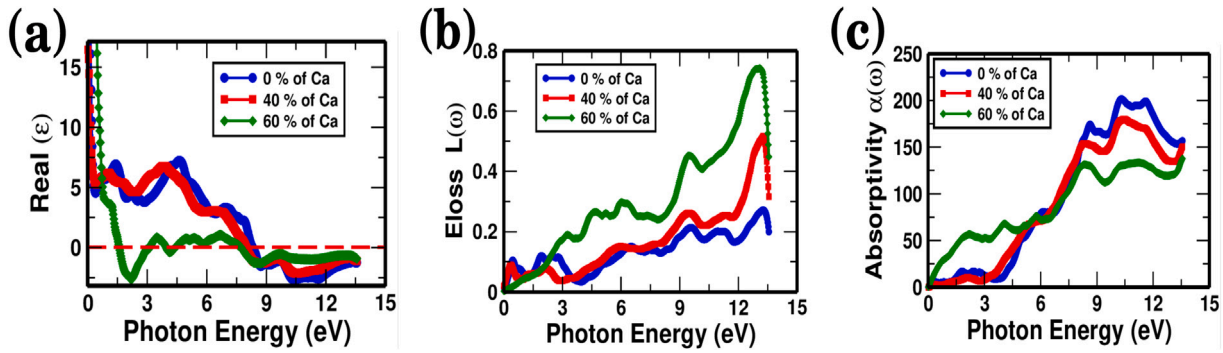

Fig. 18. (Color online) (a) The real part of dielectric function vs. the photon energy (b) The comparison of Eloss function vs. photon energy, and (c) The comparison of absorbance vs. photon energy for $La_{1-x}Ca_xVO_3$ system.

Table 3
The electrical conductivity σ/τ $\left(\frac{1}{\Omega m\ s}\right)$, thermal conductivity κ(W/m K s), Hall coefficient R_H (m^3/C), Seebeck coefficient S (V/K), magnetic susceptibility χ (m^3/mol), specific heat capacity C (J/mol K), figure of merit(ZT), and thermoelectric power factor (TPF) at room temperature.

Physical parameters	$CaVO_3$	$LaVO_3$	$La_{0.40}Ca_{0.60}VO_3$	Other works
σ/τ	4.55×10^{20}	4.40×10^{20}	2.00×10^{20}	[71,72]
κ	2.75×10^{15}	3.90×10^{15}	1.50×10^{15}	
R_H	-2.07×10^{-10}	-2.15×10^{-10}	-1.73×10^{-10}	[73,74]
S	-1.66×10^{-6}	-2.49×10^{-6}	-11.47×10^{-6}	
χ	6.00×10^{-10}	5.84×10^{-10}	8.23×10^{-9}	
C	0.888	1.24	12.31	
ZT	0.003	0.007	0.012	
TPF	9.16×10^{8}	4.24×10^{10}	1.02×10^{10}	

related to the material's carrier density, $n = \frac{1}{eR_H}$ [71,72]. The Hall coefficient in the metallic phase is less than in the non-metallic phase and negative [75], indicating that the number of carriers increases dramatically while material changes from the non-metallic phase to the metallic phase [75]. As seen in Fig. 14(c), R_H is temperature independent according to the theory of weakly correlated systems. At low temperatures, however, the reported Hall coefficient in the compound is hole-like, with a substantial positive value of R_H [73,74]. The different signs of the Hall coefficient and Seebeck coefficient, as well as the temperature dependence of the latter, indicate two types of carriers: n-type and p-type. The electrical conductivity (σ/τ) and thermal conductivity (κ) change with Ca-doping levels. The variation of electrical conductivity with the change in chemical potential is illustrated in Fig. 15(a), and a similar pattern is followed by thermal conductivity (κ) (not shown here). The value of the figure of merit (ZT) is 1.88 at about chemical potential $\mu = -1.5$ eV, as shown in Fig. 15(b) for the $La_{0.40}Ca_{0.60}VO_3$, showing that this superlattice is a promising candidate for a thermoelectric material [76].

The computed values of various thermoelectric calculations for the pristine and the superstructure vanadate systems are tabulated as in Table 3 at room temperature. Similarly, the Seebeck coefficient and the thermoelectric power factor (TPF) (Fig. 15(c)) support the same conclusion as the curve for ZT vs. chemical potential. Fig. 16(a), (b) and (c) illustrate the variation of electrical conductivity, Figure of merit (ZT), Seebeck coefficient (S), and thermoelectric power factor (TPF) with absolute temperature scale with a constant $\mu = 0.82$ eV for $La_{1-x}Ca_xVO_3$ systems.

We have also examined the variation of ZT and TPF with thermal conductivity (κ) as in (Fig. 17(a),(b)) and its variation with Seebeck coefficient (S) as in (Fig. 17(c)). These superlattices exhibit a better Seebeck coefficient (S), low thermal conductivity (κ), and a better Figure of merit (ZT) and thermoelectric power factor(TPF), indicating that the sample with 60% of Ca, is a good candidate for thermoelectric applications [77].

3.4. Optical properties of $La_{1-x}Ca_xVO_3$

The optically induced behaviors of materials are studied by knowing the optical response of the materials. The variation of real part of dielectric function, energy loss, absorptivity with respect to photon energy for various concentration of Ca^{2+} ions in the supercell are plotted as in (Fig. 18(a),(b),(c)). From these graphs 60% Ca-doped specimen shows the unique response and found to be active within the IR and visible regions, indicating that this material is useful for photo-induced applications.

The variation of real part of refractive index vs. photon energy for various doping levels of superstructures is shown in Fig. 19(a). The real part of optical conductivity vs. photon energy curves Fig. 19(b), indicating that the optical conductivity, fairly larger for infrared and visible electromagnetic radiation for 60% Ca^{2+} substituted system, but other two superstructures show the maxima values at around 8–9 eV (UV radiation) with a optical gap at the start. In Fig. 19(c) shows the f-sum rules of transition, which measures the total optical weight, contributing to the effective number of oscillators or electrons during the absorption or emission of electromagnetic radiation. The sum rules is consistent with the optical conductivity to arbitrary frequencies. The optical conductivity from the result of CT-QMC data with MaxEnt analytic continuation over a wide range of U and β are computed. The optical conductivity at half-filling, demonstrates insulating behavior below roughly $\beta \approx 15\,(\text{eV})^{-1}$ with U = 3eV Fig. 20(a). The Drude peak at around zero frequency indicates the metallic phase and the appearance of other peaks other than Drude peak indicate other transition [78] the increase in conductivity is primarily associated with narrowing of the $\omega = 0$ peak.

Indeed, the quasiparticle contribution to the conductivity is accounted as the Drude peak in the spectrum at low frequency. Its width accounts for the scattering rate of the charge carriers, whereas its total weight accounts for their effective mass. The mass enhancement due to dynamical correlations can be assessed by comparing the weight with the value obtained in DFT. In fact, the correlations effect reduce the Drude weight, and in a Mott insulator its value vanishes [79].

Without disorder our calculations reproduce conventional DMFT results [20,34] where optical conductivity is characterized by the usual Drude peak at low frequencies and wide maximum at about $\omega \sim$ U, which corresponds to optical transitions to upper Hubbard band. The peak of the Drude peak diminishes and disappears as the value of U increases at Mott transition. Introduction of disorder leads to qualitative change of the frequency dependence of optical conductivity. The optical conductivity of Hubbard–Anderson model at half-filling for different stoichiometric composition of La/Ca ratios are significantly affected as in Fig. 20(b). The redistribution of the optical conductivities are estimated for various set of values of U and β as in Fig. 20(c). It is seen that the lower the values of U and β the Drude peaks are observed at very close to $\omega \approx 0$ otherwise it is shifted and diminished for the higher values.

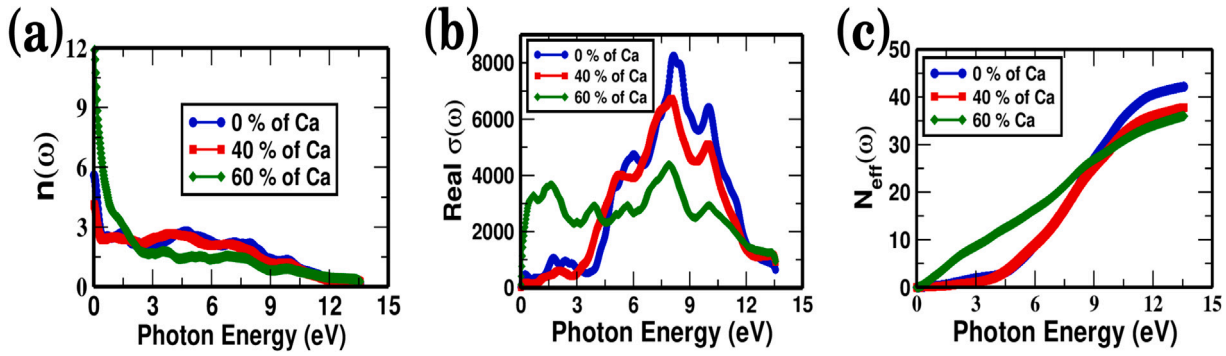

Fig. 19. (Color online) (a) The comparison of refractive indices vs. photon energy (b) The comparison of the real part of conductivity $\sigma(\omega)$ vs. photon energy, and (c) The comparison of optical weight $N_{eff}(\omega)$ vs. photon energy (eV)for $La_{1-x}Ca_xVO_3$ system.

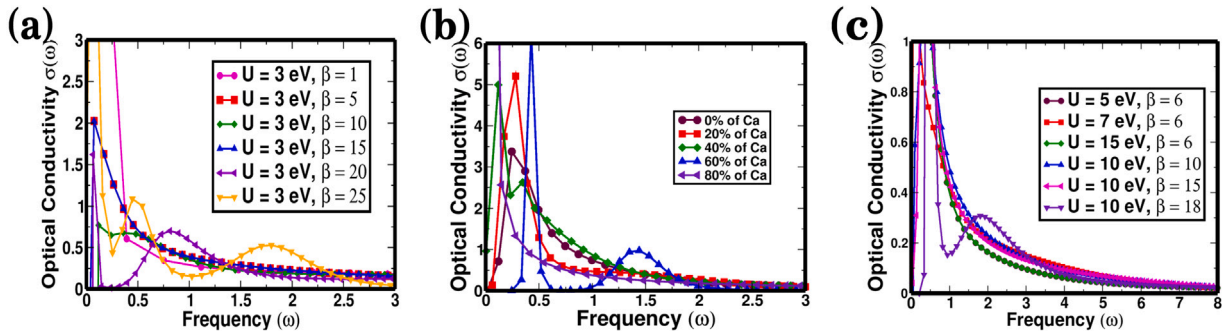

Fig. 20. (Color online) (a) The comparison of the variation of optical conductivity $\sigma(\omega)$ vs. frequency (ω) with a constant U for $La_{0.40}Ca_{0.60}VO_3$ system (b) The variation of optical conductivity $\sigma(\omega)$ vs. frequency (ω) with various proportion of Ca-atom substitutions for U = 10eV and $\beta = 15\,(eV)^{-1}$ of $La_{1-x}Ca_xVO_3$ systems, and (c) The comparison of the variation of optical conductivity $\sigma(\omega)$ vs. frequency (ω) with different set of U and β values on the for $La_{0.40}Ca_{0.60}VO_3$ system.

4. Conclusions

The cohesive and formation energy calculations reveal that the pristine and their superstructure are structurally and chemically stable and viable for synthesis in laboratory. The electronic structure, thermoelectric transport, and optical behaviors of the site substituted vanadate systems are investigated using DFT+DMFT along with the maximum entropy model. The typical MIT for $La_{0.40}Ca_{0.60}VO_3$ and $La_{0.60}Ca_{0.40}VO_3$ systems occur at (U = 5 eV and β = 10 $(eV)^{-1}$) and (U = 5 eV and β = 7 $(eV)^{-1}$), respectively.

At U = 2.95 eV and β = 23.58 $(eV)^{-1}$, the Mott quantum critical point (QCP) at an elevated temperature is attained for the $La_{0.40}Ca_{0.60}VO_3$ system. The specimen of 60% Ca-doped system is found to be optically active uniquely in the visible spectrum of electromagnetic radiation. The electrical and thermal conductivities are estimated to be 2.11 $(\Omega\ m\ s)^{-1}$ and 1.51 W/(m K s), respectively, assuming a chemical potential of μ = - 0.14 eV using the BoltzTraP codes.

The calculated figure of merit (ZT) is ~ 1.78 at μ = −1.44 eV, and the thermoelectric power factor (TPF) is ~ 2×10^{12} $\mu W/(cmK^2)$ of the $La_{0.40}Ca_{0.60}VO_3$ system is comparatively higher than those of other compositions, indicating the potential thermoelectric candidate. The frequency dependence of optical conductivity $\sigma(\omega)$ (Drude weight) and optical spectral weight (f-sumrule) is consistent with the metal–insulator transition estimated by DMFT and the maximum entropy model. Finally, the studied samples are suitable candidate for optically induced Mottronics devices, resistive memory devices, neuromorphic devices and thermoelectric devices.

CRediT authorship contribution statement

Raj Kumar Rai: Concept, Methodology, Calculations, Visualization, Writing, Analysis. **Ram Babu Ray:** Manuscript writing, Calculations, Visualization, Discussion. **Om Prakash Niraula:** Concept, Managing, Software, Review of manuscript.

Declaration of competing interest

The authors declare the following financial interests/personal relationships which may be considered as potential competing interests: Raj Kumar Rai reports travel plus partial financial support were provided by National Academy of Science and Technology (NAST), University Grants Commission (UGC) of Nepal.

Data availability

Data will be made available on request.

Acknowledgments

The authors acknowledge NPA of CDP, T.U., GCK of CDP, T.U., Durga Paudyal of Ames Laboratory, USA, and HPC facility, KU for supporting and providing valuable discussion and computational resources. RKR thankfully acknowledges to UGC of Nepal and NAST of Nepal for a partial financial financial support for this research work. The authors gratefully acknowledge the ABINIT and ALPS codes library in parts for DMFT calculations.

Ethics statement

In this work, there is no issues of ethical values.

References

[1] K. Held, Electronic structure calculations using dynamical mean field theory, Adv. Phys. 56 (6) (2007) 829.

[2] M. Imada, A. Fujimori, Y. Tokura, Metal–Insulator transitions, Rev. Mod. Phys. 70 (4) (1998) 1039.

[3] P. Zubko, S. Gariglio, M. Gabay, P. Ghosez, J.M. Triscone, Interface physics in complex oxide heterostructures, Annu. Rev. Condens. Matter Phys. 2 (1) (2011) 141.

[4] S. Piskunov, E. Heifets, R. Eglitis, G. Borstel, Bulk properties and electronic structure of $SrTiO_3$, $BaTiO_3$, $PbTiO_3$ Perovskites: An ab initio HF/DFT study, Comput. Mater. Sci. 29 (2) (2004) 165.

[5] D. Lovinger, M. Brahlek, P. Kissin, D. Kennes, A. Millis, R. Engel-Herbert, R. Averitt, Influence of spin and orbital fluctuations on Mott-Hubbard exciton dynamics in $LaVO_3$ thin films, Phys. Rev. B 102 (11) (2020) 115143.

[6] J.G. Vale, S. Calder, C. Donnerer, D. Pincini, Y. Shi, Y. Tsujimoto, K. Yamaura, M.M. Sala, J. Van Den Brink, A.D. Christianson, et al., Evolution of the magnetic excitations in $NaOsO_3$ through its metal–insulator transition, Phys. Rev. Lett. 120 (22) (2018) 227203.

[7] K. Held, I. Nekrasov, G. Keller, V. Eyert, N. Blümer, A. McMahan, R. Scalettar, T. Pruschke, V. Anisimov, D. Vollhardt, Realistic investigations of correlated electron systems with LDA+ DMFT, Physica Status Solidi (B) 243 (11) (2006) 2599.

[8] A. Savoia, D. Paparo, P. Perna, Z. Ristic, M. Salluzzo, F.M. Granozio, U.S. Di Uccio, C. Richter, S. Thiel, J. Mannhart, et al., Polar catastrophe and electronic reconstructions at the $LaAlO_3/SrTiO_3$ interface: Evidence from optical second harmonic generation, Phys. Rev. B 80 (7) (2009) 075110.

[9] A. Jana, R. Raghunathan, R. Rawat, R. Choudhary, D. Phase, Enhanced charge-transfer character in the monoclinic phase of Mott insulator $LaVO_3$ thin films, Phys. Rev. B 102 (23) (2020) 235108.

[10] S. LeBlanc, Thermoelectric generators: Linking material properties and systems engineering for waste heat recovery applications, Sustainable Mater. Technol. 1 (2014) 26.

[11] B. Keimer, D. Casa, A. Ivanov, J. Lynn, M. v. Zimmermann, J. Hill, D. Gibbs, Y. Taguchi, Y. Tokura, Spin dynamics and orbital state in $LTtiO_3$, Phys. Rev. Lett. 85 (18) (2000) 3946.

[12] L. Craco, M. Laad, S. Leoni, E. Müller-Hartmann, Insulator–metal transition in the doped $3d^1$ transition metal oxide $LaTiO_3$, Phys. Rev. B 70 (19) (2004) 195116.

[13] A. Ohtomo, H. Hwang, A high-mobility electron gas at the $LaAlO_3/SrTiO_3$ heterointerface, Nature 427 (6973) (2004) 423.

[14] M. Hirayama, T. Miyake, M. Imada, Ab initio low-energy model of transition-metal-oxide heterostructure $LaAlO_3/SrTiO_3$, J. Phys. Soc. Japan 81 (8) (2012) 084708.

[15] J. Varignon, M. Bibes, A. Zunger, Origin of band gaps in 3D perovskite oxides, Nature Commun. 10 (1) (2019) 1.

[16] M.D. Scafetta, Optical Properties and Electronic Structure of Non-d^0 Perovskite Oxide Epitaxial Films and Heterostructures, Drexel University, USA, 2015.

[17] A.A. Adewale, A. Chik, R.M. Zaki, F. Che Pa, Y.C. Keat, N. Jamil, Thermoelectric transport properties of $SrTiO_3$ doped with Pm, solid state phenomena, Trans. Tech. Publ. 280 (2018) 3.

[18] S. Walia, S. Balendhran, H. Nili, S. Zhuiykov, G. Rosengarten, Q.H. Wang, M. Bhaskaran, S. Sriram, M.S. Strano, K. Kalantar-zadeh, Transition metal oxides–thermoelectric properties, Prog. Mater. Sci. 58 (8) (2013) 1443.

[19] C.J. Benedict, A. Rao, G. Sanjeev, G. Okram, P. Babu, A systematic study on the effect of electron beam irradiation on structural, electrical, thermo-electric power and magnetic property of $LaCoO_3$, J. Magn. Magn. Mater. 397 (2016) 145.

[20] H. Nakano, Y. Takahashi, M. Imada, Drude weight of the two-dimensional Hubbard model-reexamination of finite-size effect in exact diagonalization study-, J. Phys. Soc. Japan 76 (3) (2007) 034705.

[21] J. Skilling, S. Sibisi, Fundamentals of maxent in data analysis, in: Maximum Entropy in Action, Oxford, Clarendon, UK, 1991.

[22] N.F. Mott, The basis of the electron theory of metals, with special reference to the transition metals, Proc. Phys. Soc. Sect. A 62 (7) (1949) 416.

[23] P.W. Anderson, Localized magnetic states in metals, Phys. Rev. 124 (1) (1961) 41.

[24] A. Georges, G. Kotliar, Hubbard model in infinite dimensions, Phys. Rev. B 45 (12) (1992) 6479.

[25] I. Inoue, C. Bergemann, I. Hase, S. Julian, Fermi surface of $3d^1$ perovskite $CaVO_3$ near the Mott transition, Phys. Rev. Lett. 88 (23) (2002) 236403.

[26] D.E. McNally, X. Lu, J. Pelliciari, S. Beck, M. Dantz, M. Naamneh, T. Shang, M. Medarde, C.W. Schneider, V.N. Strocov, et al., Electronic localization in $CaVO_3$ films via bandwidth control, NPJ Quant. Mater. 4 (1) (2019) 1.

[27] R. Mossanek, M. Abbate, P. Fonseca, A. Fujimori, H. Eisaki, S. Uchida, Y. Tokura, Optical conductivity and X-ray absorption spectra of the Mott-Hubbard compounds RVO_3 (R=Sr, Ca, La, and Y), Phys. Rev. B 80 (19) (2009) 195107.

[28] E. Janod, J. Tranchant, B. Corraze, M. Querre, P. Stoliar, M. Rozenberg, T. Cren, D. Roditchev, V.T. Phuoc, M.P. Besland, et al., Resistive switching in Mott insulators and correlated systems, Adv. Functional Mater. 25 (40) (2015) 6287.

[29] A. Sekiyama, H. Fujiwara, S. Imada, S. Suga, H. Eisaki, S. Uchida, K. Takegahara, H. Harima, Y. Saitoh, I. Nekrasov, et al., Mutual experimental and theoretical validation of bulk photoemission spectra of $Sr_{1-x}Ca_xVO_3$, Phys. Rev. Lett. 93 (15) (2004) 156402.

[30] E. Gull, A.J. Millis, A.I. Lichtenstein, A.N. Rubtsov, M. Troyer, P. Werner, Continuous-time Monte Carlo methods for quantum impurity models, Rev. Modern Phys. 83 (2) (2011) 349.

[31] K. Haule, C.-H. Yee, K. Kim, Dynamical mean-field theory within the full-potential methods: Electronic structure of $CeIrIn_5$, $CeCoIn_5$, and $CeRhIn_5$, Phys. Rev. B 81 (19) (2010) 195107.

[32] E. Gull, P. Werner, O. Parcollet, M. Troyer, Continuous-time auxiliary-field Monte Carlo for quantum impurity models, EPL (Europhys. Lett.) 82 (5) (2008) 57003.

[33] R. Resta, Drude weight and superconducting weight, J. Phys.: Condens. Matter 30 (41) (2018) 414001.

[34] T. Tohyama, Y. Inoue, K. Tsutsui, S. Maekawa, Exact diagonalization study of optical conductivity in the two-dimensional Hubbard model, Phys. Rev. B 72 (4) (2005) 045113.

[35] G. Kotliar, S.Y. Savrasov, K. Haule, V.S. Oudovenko, O. Parcollet, C. Marianetti, Electronic structure calculations with dynamical mean-field theory, Rev. Modern Phys. 78 (3) (2006) 865.

[36] A. Georges, G. Kotliar, W. Krauth, M. J., Dynamical mean-field theory of strongly correlated fermion systems and the limit of infinite dimensions, Rev. Modern Phys. 68 (1) 13.

[37] A.N. Rubtsov, V.V. Savkin, A.I. Lichtenstein, Continuous-time quantum Monte Carlo method for fermions, Phys. Rev. B 72 (3) (2005) 035122.

[38] L. Boehnke, H. Hafermann, M. Ferrero, F. Lechermann, O. Parcollet, Orthogonal polynomial representation of imaginary-time Green's functions, Phys. Rev. B 84 (7) (2011) 075145.

[39] M. Jarrell, J.E. Gubernatis, Bayesian inference and the analytic continuation of imaginary-time quantum Monte Carlo data, Phys. Rep. 269 (3) (1996) 133.

[40] D. Bergeron, A.-M. Tremblay, Algorithms for optimized maximum entropy and diagnostic tools for analytic continuation, Phys. Rev. E 94 (2) (2016) 023303.

[41] K. Ghanem, E. Koch, Average spectrum method for analytic continuation: Efficient blocked-mode sampling and dependence on the discretization grid, Phys. Rev. B 101 (8) (2020) 085111.

[42] T. Senthil, A. Vishwanath, L. Balents, S. Sachdev, M.P. Fisher, Deconfined quantum critical points, Sci. 303 (5663) (2004) 1490.

[43] G. Kotliar, D. Vollhardt, Strongly correlated materials: Insights from dynamical mean-field theory, Phys. Today 57 (3) (2004) 53.

[44] F. Gebhard, K. Bott, M. Scheidler, P. Thomas, S.W. Koch, Optical absorption of non-interacting tight-binding electrons in a Peierls-distorted chain at half band-filling, Philos. Magazine B 75 (1) (1997) 1.

[45] K. Capelle, A bird's-eye view of density-functional theory, Brazilian J. Phys. 36 (4A) (2006) 1318.

[46] R.M. Martin, Electronic Structure: Basic Theory and Practical Methods, Cambridge University Press, UK, 2020.

[47] R. Mossanek, M. Abbate, T. Yoshida, A. Fujimori, Y. Yoshida, N. Shirakawa, H. Eisaki, S. Kohno, F. Vicentin, Evolution of the spectral weight in the Mott-Hubbard series $SrVO_3$-$CaVO_3$-$LaVO_3$-YVO_3, Phys. Rev. B 78 (7) (2008) 075103.

[48] L. Wang, Y. Li, A. Bera, C. Ma, F. Jin, K. Yuan, W. Yin, A. David, W. Chen, W. Wu, et al., Device performance of the Mott insulator $LaVO_3$ as a photovoltaic material, Phys. Rev. A 3 (6) (2015) 064015.

[49] G. Sclauzero, K. Dymkowski, C. Ederer, Tuning the metal–insulator transition in d^1 and d^2 perovskites by epitaxial strain: A first-principles-based study, Phys. Rev. B 94 (24) (2016) 245109.

[50] H.v. Löhneysen, A. Rosch, M. Vojta, P. Wölfle, Fermi-liquid instabilities at magnetic quantum phase transitions, Rev. Modern Phys. 79 (3) (2007) 1015.

[51] J.P. Perdew, K. Burke, M. Ernzerhof, Generalized gradient approximation made simple, Phys. Rev. Lett. 77 (18) (1996) 3865.

[52] W. Kohn, L.J. Sham, Self-consistent equations including exchange and correlation effects, Phys. Rev. 140 (4A) (1965) A1133.

[53] J. Deisz, D. Hess, J. Serene, Incipient antiferromagnetism and low-energy excitations in the half-filled two-dimensional Hubbard model, Phys. Rev. Lett. 76 (8) (1996) 1312.

[54] M. Qazilbash, J. Hamlin, R. Baumbach, L. Zhang, D.J. Singh, M. Maple, D. Basov, Electronic correlations in the iron pnictides, Nat. Phys. 5 (9) (2009) 647.

[55] A.J. Millis, P.B. Littlewood, B.I. Shraiman, Double exchange alone does not explain the resistivity of $La_{1-x}Sr_x$ MnO_3, Phys. Rev. Lett. 74 (25) (1995) 5144.

[56] K. Maiti, D. Sarma, Spectroscopic investigations of the electronic structure and metal–insulator transitions in a Mott-Hubbard system $La_{1-x}Ca_x$ VO_3, Phys. Rev. B 61 (4) (2000) 2525.

[57] D. Paudyal, V.K. Pecharsky, K.A. Gschneidner Jr., B.N. Harmon, Electron correlation effects on the magnetostructural transition and magnetocaloric effect in $Gd_5Si_2Ge_2$, Phys. Rev. B 73 (14) (2006) 144406.

[58] I. Inoue, O. Goto, H. Makino, N. Hussey, M. Ishikawa, Bandwidth control in a perovskite-type $3d^1$-correlated metal $Ca_{1-x}Sr_xVO_3$ evolution of the electronic properties and effective mass, Phys. Rev. B 58 (8) (1998) 4372.

[59] D. Bauernfeind, M. Zingl, R. Triebl, M. Aichhorn, H.G. Evertz, Fork tensor product states: Efficient multi-orbital real-time DMFT solver, Phys. Rev. X 7 (3) (2017) 031013.

[60] A. Avella, A.M. Oleś, P. Horsch, Fingerprints of spin–orbital polarons and of their disorder in the photoemission spectra of doped Mott insulators with orbital degeneracy, Phys. Rev. B 97 (15) (2018) 155104.

[61] R. Murugeswari, M. Manikandan, R. Rajeswarapalanichamy, A. Milton Franklin Benial, Structural, elastic, magnetic and electronic properties of Ti-based Heusler alloys, Int. J. Mod. Phys. B 34 (07) (2020) 2050055.

[62] J. Feng, B. Xiao, J. Chen, Y. Du, J. Yu, R. Zhou, Stability, thermal and mechanical properties of Pt_xAl_y compounds, Mater. Des. 32 (6) (2011) 3231.
[63] J.A. Santana, J.T. Krogel, P.R. Kent, F.A. Reboredo, Diffusion quantum Monte Carlo calculations of $SrFeO_3$ and $LaFeO_3$, J. Chem. Phys. 147 (3) (2017) 034701.
[64] M. Veit, M. Chan, B. Ramshaw, R. Arras, R. Pentcheva, Y. Suzuki, Three-dimensional character of the fermi surface in ultrathin $LaTiO_3/SrTiO_3$ heterostructures, Phys. Rev. B 99 (11) (2019) 115126.
[65] A. Georges, G. Kotliar, W. Krauth, M.J. Rozenberg, Dynamical mean-field theory of strongly correlated fermion systems and the limit of infinite dimensions, Rev. Modern Phys. 68 (1) (1996) 13.
[66] E. Pavarini, D. Vollhardt, E. Koch, A. Lichtenstein, Dmft: From Infinite Dimensions to Real Materials, Tech. rep., Theoretische Nanoelektronik, 2018.
[67] X. Shi, J. Yang, J.R. Salvador, M. Chi, J.Y. Cho, H. Wang, S. Bai, J. Yang, W. Zhang, L. Chen, Multiple-filled skutterudites: high thermoelectric figure of merit through separately optimizing electrical and thermal transports, J. Ame. Chem. Soc. 133 (20) (2011) 7837.
[68] H. Eisenlohr, S.-S.B. Lee, M. Vojta, Mott quantum criticality in the one-band Hubbard model: Dynamical mean-field theory, power-law spectra, and scaling, Phys. Rev. B 100 (15) (2019) 155152.
[69] D.N. Basov, R.D. Averitt, D. Van Der Marel, M. Dressel, K. Haule, Electrodynamics of correlated electron materials, Rev. Modern Phys. 83 (2) (2011) 471.
[70] N. Blumer, Efficiency of quantum Monte Carlo impurity solvers for the dynamical mean-field theory, Phys. Rev. B 76 (20) (2007) 205120.
[71] T. Ohtani, K. Kosuge, S. Kachi, Hall effect of NiAs-type $Ni_{1-x}S$, J. Phys. Soc. Japan 28 (6) (1970) 1588.
[72] T. Ohtani, K. Kosuge, S. Kachi, Thermoelectric power of $Ni_{1-x}S$, J. Phys. Soc. Jpn. 29 (2) (1970) 521.
[73] H. Takagi, T. Ido, S. Ishibashi, M. Uota, S. Uchida, Y. Tokura, Superconductor-to-nonsuperconductor transition in $(La_{1-x}Sr_x)_2CuO_4$ as investigated by transport and magnetic measurements, Phys. Rev. B 40 (4) (1989) 2254.
[74] Y. Maeno, H. Hashimoto, K. Yoshida, S. Nishizaki, T. Fujita, J. Bednorz, F. Lichtenberg, Superconductivity in a layered perovskite without copper, Nature 372 (6506) (1994) 532.
[75] E. Barthelemy, O. Gorochov, H. McKinzie, The electrical and magnetic properties of the transition in nickel sulfide, Mater. Res. Bull. 8 (12) (1973) 1401.
[76] Y. Saeed, N. Singh, U. Schwingenschlogl, Thickness and strain effects on the thermoelectric transport in nanostructured Bi_2Se_3, Appl. Phys. Lett. 104 (3) (2014) 033105.
[77] R. Wang, M. Mujahid, Y. Duan, Z.-K. Wang, J. Xue, Y. Yang, A review of perovskites solar cell stability, Adv. Funct. Mater. 29 (47) (2019) 1808843.
[78] N. Blümer, E. Gorelik, Quantum Monte Carlo simulations of antiferromagnetism in ultracold fermions on optical lattices within real-space dynamical mean-field theory, Comput. Phys. Comm. 182 (1) (2011) 115.
[79] M. Nakajima, S. Ishida, T. Tanaka, K. Kihou, Y. Tomioka, T. Saito, C.H. Lee, H. Fukazawa, Y. Kohori, T. Kakeshita, et al., Strong electronic correlations in iron pnictides: Comparison of optical spectra for $BaFe_2As_2$-related compounds, J. Phys. Soc. Japan 83 (10) (2014) 104703.

International Journal of Modern Physics B | Online Ready

Exploring the electronic transport, magnetic, and optical properties of strongly correlated systems: A numerical analytical continuation approach

R. K. Rai, G. C. Kaphle, R. B. Ray, and O. P. Niraula

https://doi.org/10.1142/S0217979224503417 | **Cited by:** 0 **(Source: Crossref)**

< Previous Next >

Abstract

The electronic, magnetic and optical properties of the double perovskites Ca_2NiOsO_6 and Fe-doped derivative were calculated using the full potential linearized augmented plane wave technique through the GGA + U with PBE exchange correlation functionals. The calculations show that both of the systems are half-metallic with Fe-doped system as a ferromagnet, whereas the undoped system shows the ferrimagnetic ordering. Additionally, the study is extended for calculating the Mott parameters through dynamical mean field theory (DMFT) with the maximum entropy model (MEM). It is found that the MIT model parameters (U, β) for Ca_2NiOsO_6 and $Ca_2Fe_{0.50}Ni_{0.50}OsO_6$ systems are (5.7 eV, 6.0 $(eV)^{-1}$) and (6.0 eV, 6.0 $(eV)^{-1}$), respectively. Furthermore, the calculations agree with optical Drude peak analysis. The optical conductivity, reflectivity, absorptivity, ELOSS function, dielectric function refractive index and sum-rule are also explored in relation to the photoinduced behaviors of the materials.

Keywords: Analytic continuation ▪ DMFT ▪ GGA ▪ maximum entropy model ▪ strongly correlated system

PACS: 31.10.+z, 31.15E–, 71.15.Nc, 71.23–k, 72.90.+y, 78.20.Bh

History
Received 26 February 2023
Revised 5 June 2023
Accepted 11 June 2023
Published: 21 September 2023

Electronic Structure and Transport Properties of Superlattices: $La_{(1-X)}Sr_xTiO_3$ (X =0, 0.20, 0.80, 1)

R. K. Rai, G. C. Kaphle, R. B. Ray, O. P. Niraula

Journal of Nepal Physical Society

Volume 6, Issue 2, December 2020

ISSN: 2392-473X (Print), 2738-9537 (Online)

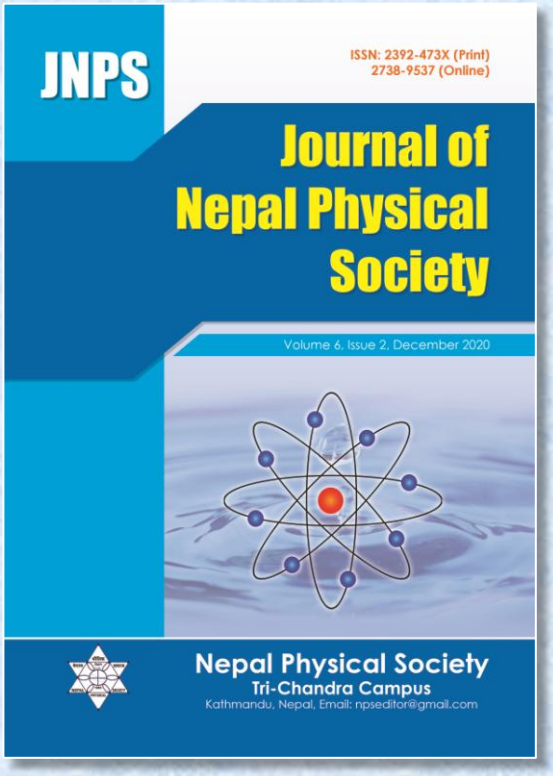

JNPS, **6** (2), 134-148 (2020)

DOI: http://doi.org/10.3126/jnphyssoc.v6i2.34869

Published by:

Nepal Physical Society

P.O. Box: 2934

Tri-Chandra Campus

Kathmandu, Nepal

Email: npseditor@gmail.com

JNPS ***6*** *(2): 134-148 (2020)*
ISSN: 2392-473X (Print), 2738-9537 (Online)

Research Article *© Nepal Physical Society*
DOI: http://doi.org/10.3126/jnphyssoc.v6i2.34869

Electronic Structure and Transport Properties of Superlattices: $La_{(1-X)}Sr_xTiO_3$ (X =0, 0.20, 0.80, 1)

R. K. Rai[1, 2], G. C. Kaphle[1, *], R. B. Ray[1, 3], O. P. Niraula[1]
[1]Central Department of Physics, Kirtipur Campus, Tribhuvan University, Nepal
[2]Patan Multiple Campus, Lalitpur, Tribhuvan University, Nepal
[3]Amrit Campus, Tribhuvan University, Kathmandu, Nepal
[*]Corresponding Email: gck223@gmail.com

Received: *21 October, 2020;* ***Revised:*** *24 November, 2020;* ***Accepted:*** *28 December, 2020*

Abstract

The conventional density functional theory (DFT) and dynamical mean field theory (DMFT) is used to study the structural, electronic and the Mott-Hubbard metal-insulator phase transition of the pristine and superstructures, $La_{(1-x)}Sr_xTiO_3$ (x = 0, 0.20, 0.80, 1). The electrical and thermal conductivities, Seebeck coefficient, Figure of merit are calculated using the BoltzTraP codes. The present study reveals that the direct band gap of 2.20 eV and indirect band gap ~2.0 eV at the Γ point in the Brillouin zone of $SrTiO_3$ is upgraded to 3.423eV by using modified Beck-Johnson (mBJ) interaction potential. The metal-insulator transition (MIT) of $LaTiO_3$ and the superlattice $La_{(1-x)}Sr_xTiO_3$ have been investigated by using conventional density functional theory (DFT) and dynamical mean field theory (DMFT). The Mott-Hubbard metal-insulator transitions for pristine $LaTiO_3$ for a Coulombian parameter, U = 2.5 eV and the thermodynamic parameter $\beta = 6\ (eV)^{-1}$ are consistent with the experimental results. A typical set of these correlation parameters for MIT $La_{0.20}Sr_{0.80}TiO_3$ and $La_{0.80}Sr_{0.20}TiO_3$ systems are found to be U = 3.5 eV and $\beta = 10(eV)^{-1}$ and U = 3.2 eV and $\beta = 10\ (eV)^{-1}$ respectively. The characteristic sharp quasi-particle peak for a sample of $La_{0.80}Sr_{0.20}TiO_3$ superlattice systems is obtained correlation parameter U = 3.0 eV and $\beta = 6(eV)^{-1}$. A thermoelectric phase transition is observed for Seebeck Coefficient at temperature 300 K at near chemical potential, μ= 1eV of $SrTiO_3$. The corresponding figure of merit (ZT) with chemical potential (μ) appears to be unity at near μ= 1eV.

Keywords: DFT, DMFT, MIT, Superlattice, TMOs.

1. INTRODUCTION

The complex transition metal oxides (TMOs) are the promising smart materials for the scientific and technological innovations as well as theoretical investigation of material world. The TMOs are complex strongly correlated materials with various degrees of freedom (dof), such as charge, spin, orbital, valley and lattice interactions. The heterostructures and nanostructures of such compounds have exotic and novel properties highly useful for Mottronics applications [1, 2].

In general, these materials are found in a simple cubic perovskite ABO_3 type structures, where the A and B cations are arranged on a simple cubic lattice, and the O anions lie on the face centers nearest to the cations (B = transition metals) as shown in Fig. 1.

The cations (A = earlier transition metals or rare earths) are at the centers of the oxygen, O octahedral, while the A cations lie at the larger 12-fold coordinated sites [3-6]. The bonding between La and TiO_2 is mainly ionic, and the TiO_2 entity is bound covalently in the $LaTiO_3$ system.

The density functional theory (DFT) along with the dynamical mean field theory (DMFT) is employed for figuring out the realistic electronic structure of strongly correlated system. The spectral density of distribution (spectral function) is obtained using the maximum entropy model for the La-atom substituted on Sr-site $La_{(1-x)}Sr_xTiO_3$ supercell have

been studied using various impurity solvers including quantum Monte Carlo (QMC) [7].

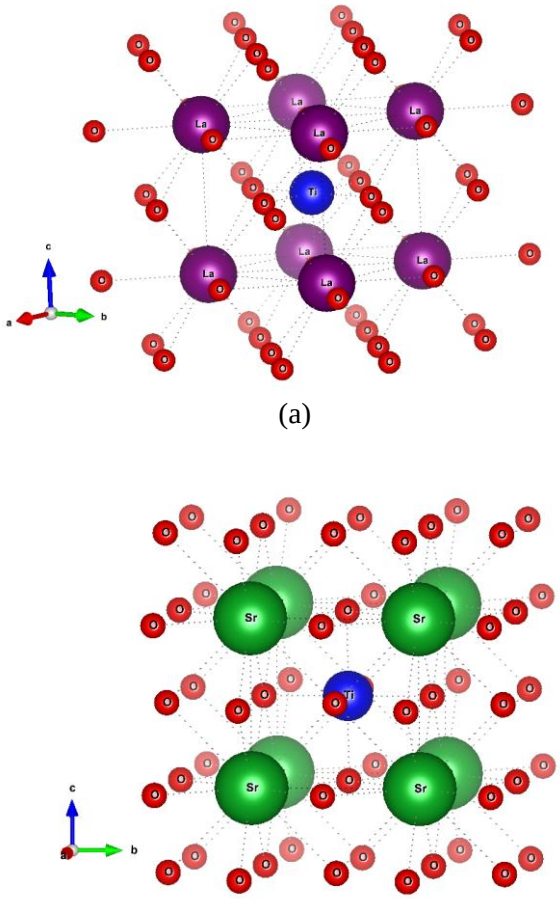

(a)

(b)

Fig. 1: (color online) The crystal structures of cubic phase of pristine (a) $LaTiO_3$ and (b) $SrTiO_3$ systems.

The strong electron correlation and other anomalous electronic properties in the metallic phase transition (MIT) are of great interest. The Mott transition in $La_{(1-x)}Sr_xTiO_3$ system is studied experimentally employing filling control method, through the appropriate doping of the holes or electrons to the system and band control method through the site substitution of Sr-ion with La-ion to the system [4,8-10].

The transition metal oxides have narrow conduction bands due to weak orbital overlap, which leads to localized electrons with low carrier mobilities. Transition metal oxides have recently been considered as thermoelectric (TE) materials that can operate at high temperature and they have their transport properties with high Seebeck coefficients (S) and low thermal conductivity (*K*). We have computed the thermal conductivity *K*, electrical conductivity (σ/τ), Seebeck coefficients (S), and Figure of merit (ZT) etc. for the $SrTiO_3$ and $LaTiO_3$ [11, 12].

The Mottness (the resistive switching) behaviours of TMOs are highly applicable for designing novel devices, including sensing, signal conversion, non-volatile memory, artificial neurons and so on. Those oxides devices have far more better over the conventional semiconductor devices in terms of efficiency, durability, additional functionality and future downsizing to the nanoscale structures [13, 14].

2. METHODOLOGY AND COMPUTATIONAL DETAILS

2.1 Theoretical Backgrounds:

The electronic structure and transport properties of Mott-insulator $LaTiO_3$ and band-insulator $SrTiO_3$ and their superlattices systems have been investigated by using density functional theory (DFT) based quantum mechanical approach [15-17].

The optimized cubic phase of $SrTiO_3$ and $LaTiO_3$ are taken for the GGA, GGA+U+J, SOC and DOS calculations by solving self consistent Kohn-Sham equation for the many-body system as given by,

$$\left[-\frac{\hbar^2}{2m}\nabla^2 + v_{eff}(r)\right]\psi_i = \varepsilon_i\psi_i \qquad (1)$$

Where the effective Kohn-Sham potential is expressed as,

$$v_{eff}(r) = v(r) + \int \frac{\left[n_e(r')\right]}{|r-r'|}dr' + v_{xc}(r) \qquad (2)$$

And, $v_{xc}(r) = \frac{\delta E\left[n_e(r)\right]}{\delta n_e(r)}$ is the exchange correlation potential with the probability density as,

$$n_e(r) = \sum_{i=1}^{N}\left|\psi_i(r)\right|^2$$

The electronic structure and other properties of these materials are also examined by using statistical method, such as the density of states (DOS) per unit energy range as given by

$$D_n(\varepsilon) = \frac{2}{8\pi^2}\int \delta\left(E_F - \varepsilon_n(k)\right)d\varepsilon \qquad (3)$$

with the allowed wavevector in the n^{th} band energy range, $\varepsilon \leq \varepsilon_n(k) \leq \varepsilon + d\varepsilon$ is just the volume of a k-space primitive cell, divided by the volume per allowed wave vector,

$$\Delta k = {}^{2\pi^3}/_{V}.$$

The transport coefficients of the TMOs are investigated for the optimized systems by using BoltzTraP code, a patching software of WIEN2k framework, which implements the linearized Boltzmann Transport Equation (BTE) [18] as given by,

$$\frac{\partial f_\mu(T,\mu)}{\partial t} = -v_\alpha(i,k).\frac{\partial f_\mu(T,\mu)}{\partial r} - \frac{e}{\hbar}\left(E - \frac{1}{c}v_\alpha(i,k) \times H\right).\frac{\partial f_\mu(T,\mu)}{\partial k_\alpha} + \frac{\partial f_\mu(T,\mu)}{\partial t}\Big|_{scattering} \quad (4)$$

with $f_\mu(T,\mu) = \frac{1}{\exp^{[\mu - E_F]}/_{k_B T} + 1}$ is the Fermi-Dirac distribution for electron and

$v_\alpha(i,k) = \frac{1}{\hbar}\frac{\partial \varepsilon_{i,k}}{\partial k_\alpha}$ is the group velocity of the carriers.

From the first-principle, the Seebeck coefficient (S) and figure of merit (ZT) are calculated as,

$$ZT = \frac{\sigma_{\alpha\beta} S_{\alpha\beta}^2}{\kappa_{\alpha\beta}} T \quad (5)$$

Where ,

$$\sigma_{\alpha\beta}(T,\mu) = \frac{1}{\Omega}\int \bar{\sigma}_{\alpha\beta}(\varepsilon)\left[-\frac{\partial f_\mu(T,\mu)}{\partial \varepsilon}\right] d\varepsilon \quad (6)$$

is the electrical conductivity tensor,

$$\kappa_{\alpha\beta}(T,\mu) = \frac{1}{\Omega e^2 T}\int \bar{\sigma}_{\alpha\beta}(\varepsilon)(\varepsilon - \mu)^2\left[-\frac{\partial f_\mu(T,\mu)}{\partial \varepsilon}\right] d\varepsilon \quad (7)$$

is the thermal conductivity tensor,

$$S_{\alpha\beta}(T,\mu) = \frac{1}{\Omega e T \sigma_{\gamma\alpha}(T,\mu)}\int \bar{\sigma}_{\gamma\beta}(\varepsilon)(\varepsilon - \mu)\left[-\frac{\partial f_\mu(T,\mu)}{\partial \varepsilon}\right] d\varepsilon \quad (8)$$

is the thermoelectric Seebeck coefficients,
And,

$$\bar{\sigma}_{\alpha\beta}(\varepsilon) = \frac{e^2}{N}\sum_{i,k}\tau_{i,k}v_\alpha(i,k)v_\beta(i,k)\delta(\varepsilon - \varepsilon_{i,k}) \quad (9)$$

is the kernel of all transport coefficients, that is necessary for calculating the Figure of merit.

Where α and β are tensor indices, Ω, μ and N are the volume of the unit cell, chemical potential and number of K-points implemented respectively.

Furthermore, the dynamical mean field theory (DMFT) can be applied for realistic picture of electronic system by using the Hubbard Hamiltonian for strongly correlated system as,

$$\hat{H} = \sum_{iljm\sigma} t_{iljm}\hat{c}_{il}^{\sigma\dagger}\hat{c}_{jm}^{\sigma} + \sum_{ilmno\sigma\sigma'} U_{lmno}\hat{c}_{il}^{\sigma\dagger}\hat{c}_{im}^{\sigma'\dagger}\hat{c}_{in}^{\sigma'}\hat{c}_{io}^{\sigma} \quad (10)$$

Where, $\hat{c}_{il}^{\sigma\dagger}(\hat{c}_{il}^{\sigma})$ creates (annihilates) an electron with spin σ and orbital index l at lattice site i.

t_{iljm} is the hopping amplitude between lattice sites i and j and orbitals l and m.

U_{lmno} denotes a general local Coulomb interaction [19-21].

Mapping onto the Anderson impurity model Hamiltonian for DMFT calculation as

$$\hat{H}_{AIM} = \sum_{kl\sigma}\epsilon_l(k)\hat{a}_{kl}^{\sigma\dagger}\hat{a}_{kl}^{\sigma} + \sum_{kl\sigma}\left[V_{lm}(k)\hat{a}_{kl}^{\sigma\dagger}\hat{c}_m^{\sigma} + h.c.\right] + \sum_{ilmno\sigma\sigma'} U_{lmno}\hat{c}_{il}^{\sigma\dagger}\hat{c}_{im}^{\sigma'\dagger}\hat{c}_{in}^{\sigma'}\hat{c}_{io}^{\sigma} \quad (11)$$

Where $\hat{a}_{kl}^{\sigma\dagger}(\hat{a}_{kl}^{\sigma})$ are creation and annihilation operators for non-interacting conduction electrons at wave vector k, which have a dispersion $\epsilon_l(k)$ and hybridize with the localized interacting electrons $\hat{c}_m^{\sigma\dagger}$ via $V_{lm}(k)$.

The equation with the modeled Hamiltonian (11) can be solved by various kinds of impurity solvers, such as CT-QMC, DMRG, NCA, IPT etc.

The interacting Green function and hence the self energy, $\sum(\omega)$ can be calculated by using the Dyson equation as,

$$[\mathcal{G}^0(\omega)]^{-1} = [G(\omega)]^{-1} + \sum(\omega) \quad (12)$$

The spectral function, which is associated with the imaginary part of Green function at a given momentum is a Dirac δ- function [22-25] as,

$$A(k,\omega) = -\frac{1}{\pi}Im[G(k,\omega)] = \delta(\omega - \epsilon_k) \quad (13)$$

And, the total local spectral function coincides with the Bethe density of states (DOS).

Turning on correlations, the spectral function has a Lorentzian profile as,

$$A(k,\omega) = -\frac{1}{\pi}\left[\frac{\mathrm{Im}\sum(\omega)}{(\omega+\mu-H_0(k)-\mathrm{Re}[\sum(\omega)])^2+\mathrm{Im}[\sum(\omega)]^2}\right] \quad (14)$$

The real part of the self-energy shows a shift of the non-interacting excitations, whereas the imaginary part of self-energy indicates the broadening of the quasiparticles excitations. Since, the self-energy strongly depends on the frequency and in the case of the Mott insulator, it will lead to a notable transfer of spectral weights.

The maximum likelihood of spectral function, A(ω), is obtained by maximizing the probability using Bayesian theorem[26] as,

$$P[A(\omega)|G(\omega)] = \frac{P[G(\omega)|A(\omega)]}{P[G(\omega)]} P[G(\omega)] \sim e^{\alpha S-\frac{1}{2}\chi^2} \quad (15)$$

The Green function, G(ω) is data obtained from the DMFT calculation using CT-QMC-hybridization technique as the impurity solver. The reliable features of the spectral function, such as height and width of the central peak, and the overall weight and position of the Hubbard bands are obtained by using the maximum entropy method with the optimized value of adjustable parameter, α that will have the required information of the system concerned. The algorithm first computes the solution to min $(\chi^2 - \alpha S)$ for a large range of α. The location of the optimal value of α can be found by plotting a graph between $\log_{10}(\chi^2)$ as a function of $\log_{10}(\alpha)$, which gives the maximum likelihood of the required information lies somewhere in the portion of information fitting region of the logistic regression curve (sigmoid curve).

2.2 Computational Details and Experimental Information

The electronic structure, density of states (DOS), electronic charge density distribution and transport behaviours the cubical TMO systems are studied using the full potential-linearized augmented plane wave (FP-LAPW) with local orbitals (lo) based on DFT frameworks. The Kohn-Sham equations have been solved by the method of self-consistent total energy calculations within the generalized gradient approximation (GGA) developed by three scientists Perdew, Burke and Ernzerhof [26, 27] for approximating the electronic exchange and correlation effects.

We have employed the various schemes, such as GGA+U, GGA+U+J, GGA+SOC, GGA+mBJ etc. for improving the underestimated electronic structure based on the conventional density functional theory [28,29].

Despite the whole story of DFT calculation, we have employed the dynamical mean field theory (DMFT) with the continuous time quantum Monte Carlo (CT-QMC) -hybridization technique as the impurity solver for computing the realistic picture of electronic structure of TMOs, so as to explore the Mott-Hubbard metal-insulator transition [30,31]. The statistical inferences are implemented by applying Maximum Entropy Model for obtaining the spectral density distribution from DMFT data [32, 33].

The Mott-Hubbard band splitting of strongly correlated system have been investigated by using dynamical mean field theory (DMFT)

The theoretical study of MIT is done using the density functional theory (DFT) and the dynamical mean field theory (DMFT) [34, 35]. A band controlled transition metal oxide system, $La_{(1-x)}Sr_xTiO_3$, which are reconstructed by site substitution of extended pristine superlattice of cubic perovskite, $SrTiO_3$. The MIT phase transition are investigated for the strongly correlated parameter, U and the thermodynamic parameter, β through DFT + DMFT [36, 37].

In the present study, we have used Monk-horst pack of 7×7×7 k-mesh grid for the pristine TMOs unit cell. The k-mesh grid of 13× 13 ×2 for both of the superstructures is used for DFT calculation with the energy and charge convergence criteria for the entire systems are 10^{-5} eV and 10^{-3} e respectively. And the force convergence criterion is 0.05 eV/^{0}A used for the entire calculation.

Furthermore, the BoltzTraP codes are used for computing the thermal conductivity, electrical conductivity, Seebeck coefficients and figure of merit (ZT) etc. of the $La_{1-x}Sr_xTiO_3$ superlattices.

The transport properties of interfaces of $LaTiO_3$ and $SrTiO_3$ i.e. Mott and band insulators have shown high mobility of electron gas due to charge redistribution of substitutional dopant such as La or Sr, by charge transfer, crystal polarity etc. [38]. All the heterostructures are grown on $SrTiO_3$ (100) substrates preannealed at 900 ^{0}C and $LaTiO_3$ films were grown using pulsed laser deposition at a substrate temperature of 500 ^{0}C and an oxygen

background pressure of 10^{-6} Torr. using polycrystalline $La_2Ti_2O_7$ target. All of the heterostructures grown found to be metallic on measuring the transport and Hall measurement of the system upto 5 T of magnetic field [39].

3. RESULTS AND DISCUSSION

3.1 Structural Stability and Optimization

The optimized parameters for the given TMOs (systems) are obtained through energy minimization technique using first-principle method.

The cubic phase of $SrTiO_3$, which belongs to the space group pm-3m is known to be a band insulating material. The cubic unit cell contains one molecule with the Sr-atom sitting at the origin (0.0, 0.0, 0.0)a, the Ti-atom at the body center (0.5, 0.5, 0.5)a and the three O-atoms at the three face centers (0.5, 0.5, 0.0)a, (0.0, 0.5, 0.5)a, and (0.5, 0.0, 0.5)a; the lattice constant is a = 7.297 bohr. Similarly, the cubic phase unit cell of $LaTiO_3$ contains one molecule with the La-atom sitting at the origin (0.0, 0.0, 0.0)a, the Ti-atom at the body center (0.5, 0.5, 0.5)a and the three O-atoms at the three face centers (0.5, 0.5, 0.0)a, (0.0, 0.5, 0.5)a, and (0.5, 0.0, 0.5)a; the lattice constant is a = 7.100 bohr (1 bohr = 0.529 Å) [40,41].

In this study the convergence parameters, such as K-points, rKmax and Gmax values for $SrTiO_3$ are obtained as 500, 7.0 and 17.0 respectively along with RMT-values 2.50 for Sr-atom, 1.87 for Ti-atom and 1.69 for O-atoms respectively. Similarly, the convergence parameters, such as K-points, rKmax and Gmax values for $LaTiO_3$ are obtained as 500, 7.5 and 18.0 respectively along with RMT-values 2.50 for Sr-atom, 1.82 for Ti-atom and 1.65 for O-atoms respectively.

The crystal structure of $SrTiO_3$ and $LaTiO_3$ (inset) with their lattice parameters optimization curves is shown in Fig. 2.

The optimized unitcell of $LaTiO_3$ is promoted to 1×1×5 supercell, so as to study the effect of the site substitution of Sr-atom on $LaTiO_3$ supercell on the electronic structure and transport properties of $La_{(1-x)}Sr_xTiO_3$ superlattice system[42-44]. The superlattice, $La_{0.80}Sr_{0.20}TiO_3$ system of space group p4/mm with lattice parameters, a = b =3.592 ^{0}A and c = 18.126 ^{0}A with RMT values for La-, Sr-, Ti-, O- are found to be 2.50, 2.36, 1.65 and 1.49 respectively. For superlattice, $La_{0.20}Sr_{0.80}TiO_3$ system of space group p4/mm with lattice parameters, a = b =3.853 ^{0}A and c = 19.445 ^{0}A with RMT values for La-, Sr-, Ti-, O- are found to be 2.50, 2.50, 1.77 and 1.60 respectively.

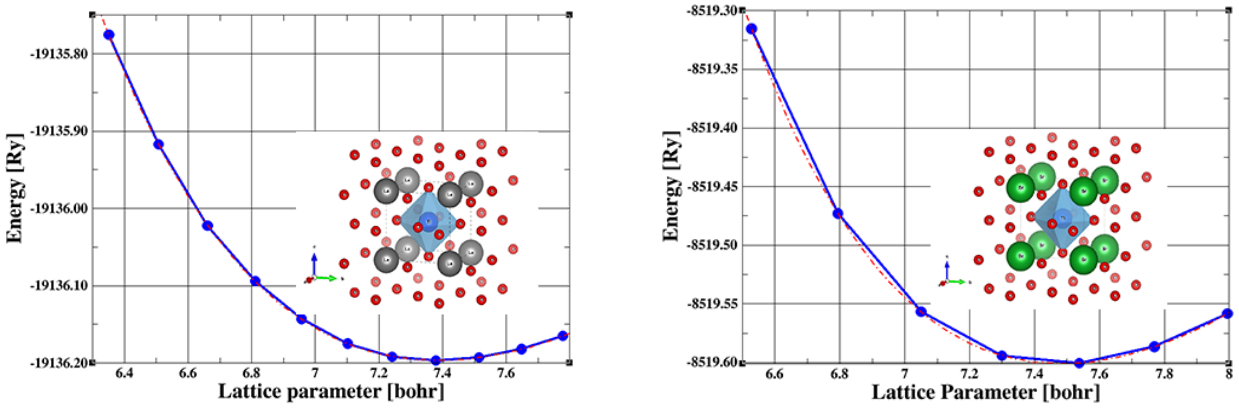

(a) (b)

Fig. 2: (color online) The lattice parameter optimization curves of the cubic phases of (a) $LaTiO_3$ and (b) $SrTiO_3$ systems (crystal structures in inset).

3.2 Electronic band structure and Density of States (DOS)

The optimized pristine $SrTiO_3$ and $LaTiO_3$ systems have been taken through self-consistent calculation for investigating their electronic structure and transport properties [45-47]. The ground state calculation was performed through the energy minimization technique for the given system. The calculated energy band structure for cubic phases $SrTiO_3$ is shown in Fig. 3(a).

In the case of $LaTiO_3$ system Fig. 3(b), it is observed that the band at around the Fermi-level is

mostly contributed by e_g and t_{2g} orbitals of transition metals (Ti). The crystal field and the electrostatic interaction between the V-cation and the non-bonding O-2p electrons that produces the splitting of d-orbitals [48].

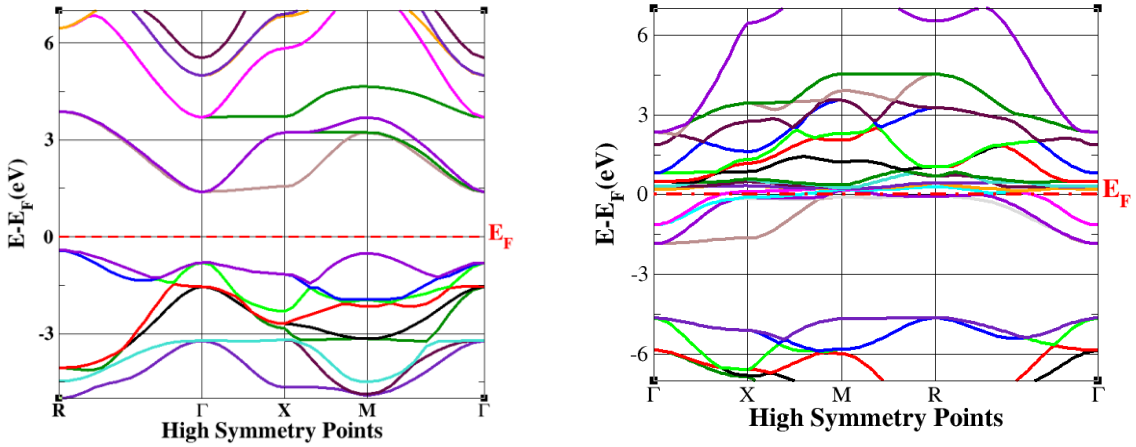

Fig. 3: (color online) The band structure plotted between the total energy versus the various symmetry points for $SrTiO_3$ (left) and $LaTiO_3$ (right) unit cell.

There are three doubly degenerate valence bands are derived mainly from the oxygen 2p orbital which are separated by a direct gap of 2.20 eV (at the Γ point) from the transition-metal d-derived (Ti) conduction band. This band gap is corrected to 3.423 eV by applying the modified Beck-Johnson interaction potential. It is somewhat lower than the experimental band gap of 3.75 eV for $SrTiO_3$ [49, 50].

The fatbandstrutures of the Ti-atom of $LaTiO_3$ system is shown in Fig. 4.

The bandstructure of $LaTiO_3$ is shifted by introducing the Coulomb interaction U and it is shifted further with higher value of U and Hund's exchange interactions, J and along with spin-orbit coupling, (SOC) as in Fig. 5 (a),(b).

It has been revealed that the introduction of modified Beck-Johnson interaction potential with GGA calculation for the strongly correlated system, $SrTiO_3$ increases the band gap [49- 51].

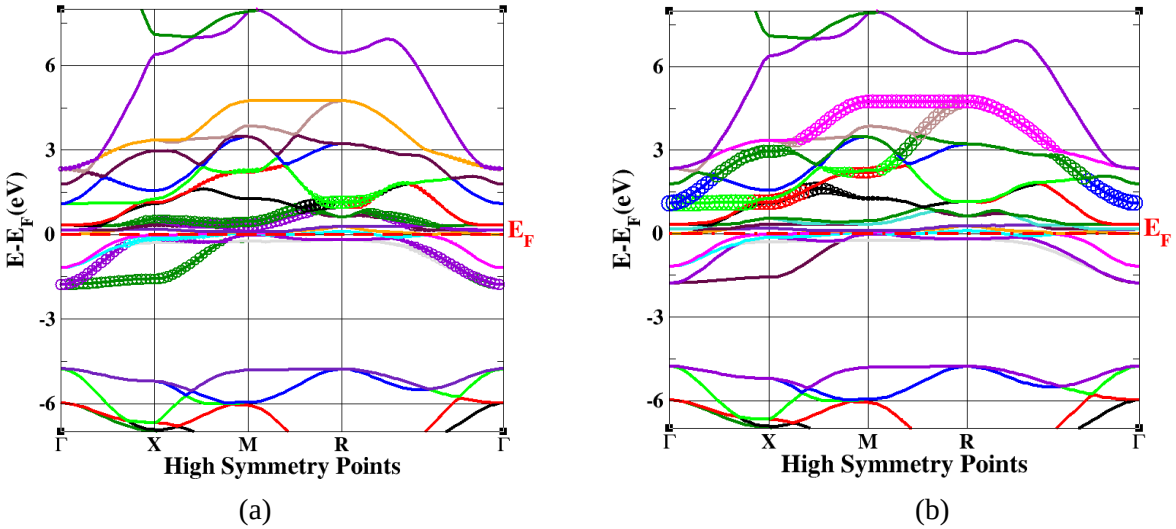

Fig. 4: (color online) Fatbandstrutures of (a) Ti-t_{2g}-orbitals on (left) and (b) Ti-e_g-orbitals on (right) of $LaTiO_3$

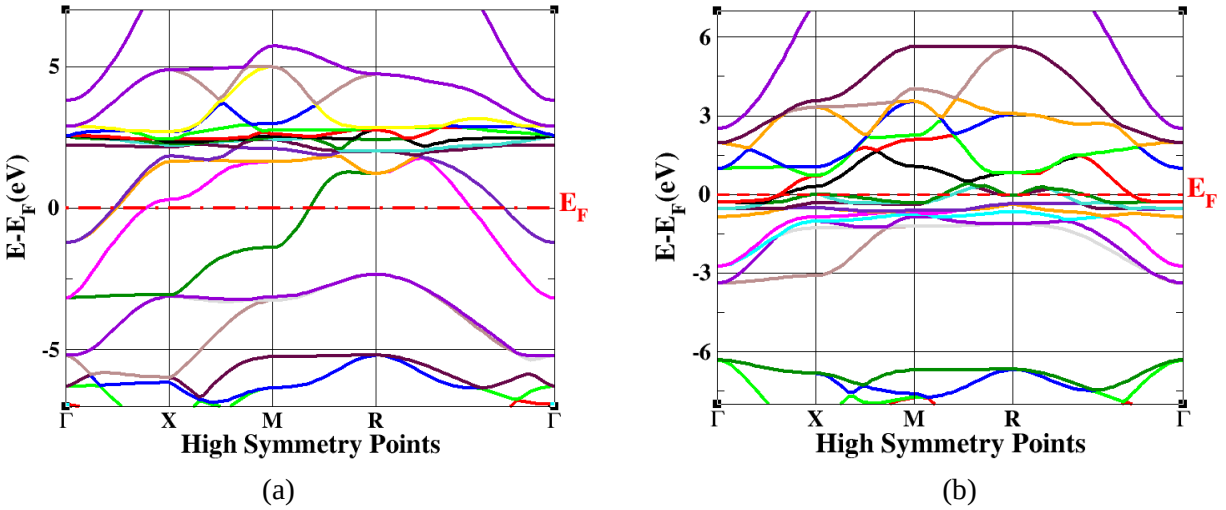

Fig. 5: (a) (color online) The shifting of band of $LaTiO_3$ with, U =2.11eV and J 0.20 =eV (b) The effect of spin-orbit coupling (SOC) in $LaTiO_3$ system.

The electronic bandstructure of superlattice, $La_{0.80}Sr_{0.20}TiO_3$ reveals that the system is metallic and the introduction of Coulombian interaction, U and exchange interaction, J along with spin-orbit coupling (SOC) seems to be the important parameters for determining the electronic structures of the materials as shown in Fig. 6.

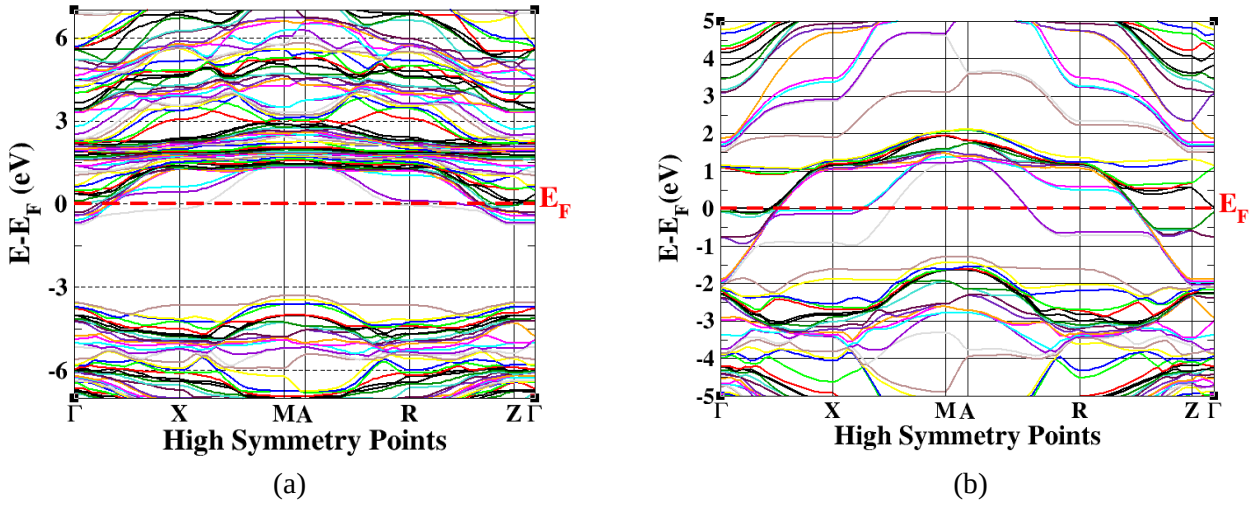

Fig. 6: (a) (color online) Bandstructure of the $La_{0.80}Sr_{0.20}TiO_3$ system without U and J (b) Bandstructure of same system with U =2.11 eV, J =0.25 eV and SOC.

The density of states (DOS) is essentially the number of different states at a particular energy level that electrons are allowed to occupy i.e the number of electronic states per unit volume per unit energy is a useful computational tools to find the electronic structures of materials in the ground states [14,15]. In order to find the constituent atomic contribution in the electronic structure and magnetic behaviors of the system, the partial density of states (PDOS) have been employed with consideration of the spin polarization, so as to calculate the contribution on electronic structure of individual atom. The DOS in the vicinity of the Fermi level within the band structure of $LaTiO_3$ were attributed mostly to these octahedral hybrid orbitals. In Fig. 7 (a) The DOS of $SrTiO_3$ with mBJ interaction is consistent with the experimental result [49-51].

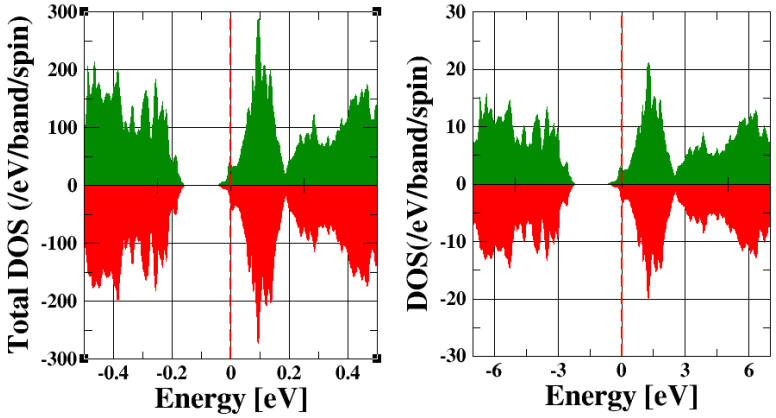

Fig. 7: (color online) The DOS of $La_{0.20}Sr_{0.80}TiO_3$ system for both up and down spin channels.

The symmetrical distribution of DOS for both channels of the superstructures indicate that these systems are non-magnetic or paramagnetic in behaviour.

3.3 Charge Density Distribution and Fermi Surface of the system

The charge density 3D plot with 2D contour plot (in inset) of $LaTiO_3$ are illustrated Fig. 8(a), and 8(b) respectively.

The strong covalent bondings between Ti- and O-atoms have been observed due to the overlap (hybridization) of O-2p and Ti-3d orbitals, which is in good agreement with the previously published papers of perovskites compounds [52,53]. The 2D-contour plot shows that the chemical bonding is mainly takes place nearest neighboring atoms.

The 3D-electron density distribution map for $LaTiO_3$ as shown in Fig. 8(a), with the planes (011) confirms that the electron density distribution is mainly localized near the ionic cores as expected, the high peaks of 3D plots shows the contribution of Ti-atoms, which is symmetric about the core of the atoms.

The study of Fermi surface of the system also supports the results obtained through band structure and DOS structure of the system. The Fermi surfaces around the various atomic lattice sites, constituted by several electron and hole orbits are demonstrated for the $LaTiO_3$ systems as shown in Fig. 8(b). The Fermi surfaces constituted by 20-40 band levels are shown (inset-1) and the actual Fermi surfaces of 30-51 band levels with the tentacles, called monster is shown (inset-2). Furthermore, the Fermi level, E_f crossing through the energy bands of 30-40 band levels of the system is demonstrated in Fig. 8(b) [54, 55].

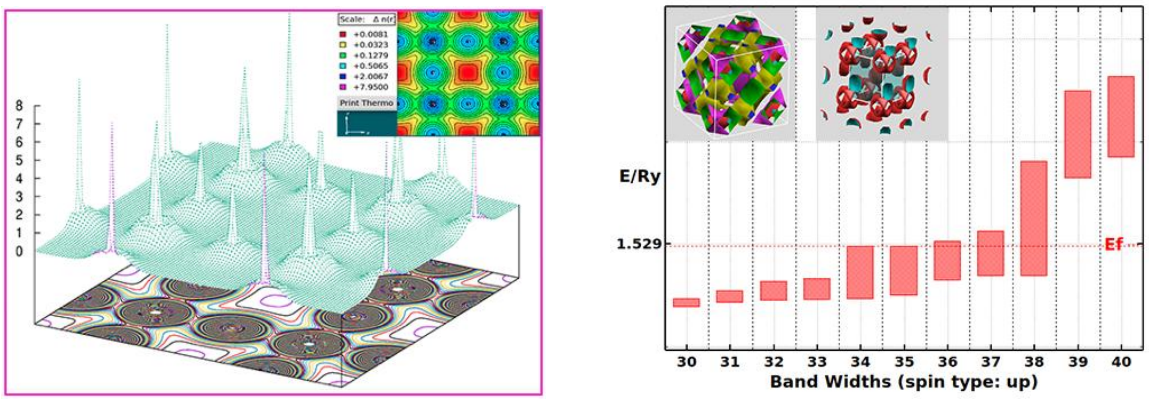

(a) (b)

Fig. 8: (color online) (a) The 3D charge density plot along with the 2D contour plot (inset) of $LaTiO_3$ in (011) plane (b) The Fermi level crossing through energy bands of 30-40 band levels of the $LaTiO_3$ system with its Fermi surface and the actual Fermi surfaces of 30-51 band levels with the tentacles (inset).

3.4 Electronic Structure by DMFT

The conventional DFT calculation is not able to predict the realistic picture of electronic structure for strongly correlated materials, so we have employed the dynamical mean field theory (DMFT) with continuous time quantum Monte Carlo (CT-QMC) hybridization technique as the impurity solver for finding the electronic structure of the transition metal oxides [56-59].

The characteristic variation of Green function of imaginary time, ($\tau = it$) with the variation of Coulombian interaction (U) for the thermodynamic parameter, $\beta=6(eV)^{-1}$ is shown in Fig. 9(a) and the corresponding Fourier transform of $G(\omega)$ for the DMFT data showing the MIT with kinks at near minimum frequency as shown in Fig.9(b).

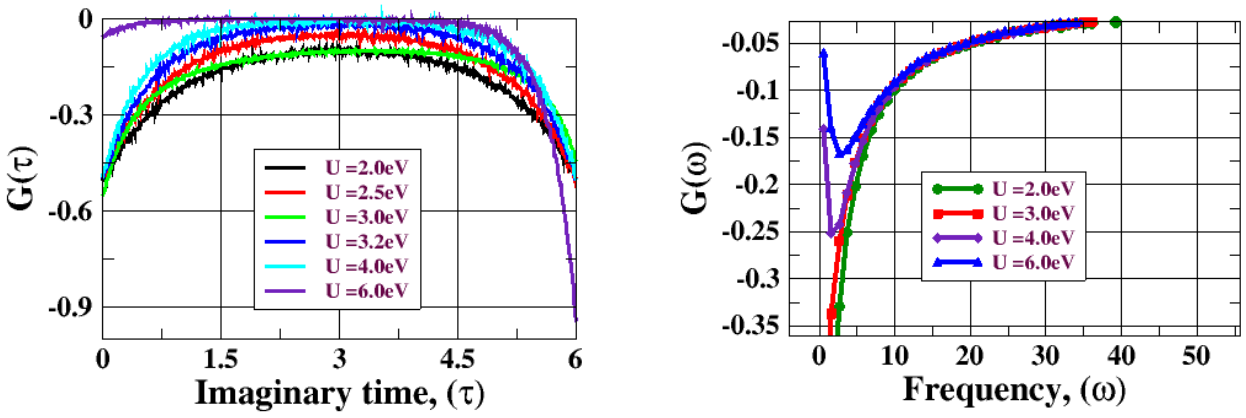

(a) (b)

Fig. 9: (color online) (a) The variation of Green function vs. imaginary time with various values of U (b) the corresponding spectral density vs. frequency showing the Mott-Hubbard splitting with U = 4.0 eV.

The complete metal-insulating phase transition is observed for U = 2.5 eV and $\beta = 6(eV)^{-1}$ for $LaTiO_3$ as shown in Fig. 10(a).

Similarly, the characteristic variation of the Green function of frequency, clearly supports the metallic and insulating phases of the materials as shown in Fig. 10(a). The oscillation of self energy, $\sum(\omega)$ oscillation with frequency is shown in Fig. 10(b) showing that there is no change in self energy, $\sum(\omega)$ with the variation of the Coulombian parameter, U.

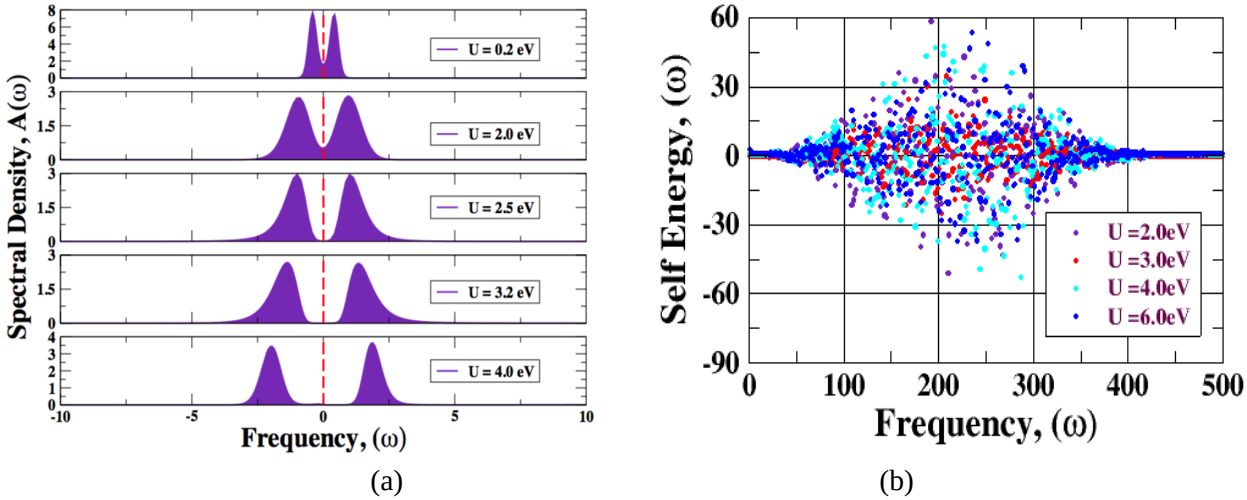

(a) (b)

Fig. 10: (color online) (a)The variation of spectral density, A(ω) vs. frequency for various U values (b) The self-energy vs. frequency.

Furthermore, the spectral density, A(ω), which is obtained from the Green function, G(τ) of superlattice, $La_{0.80}Sr_{0.20}TiO_3$ system using the Maximum Entropy model of data analysis algorithm. The metallic phase with quasi-particle peak for the superlattice, $La_{0.80}Sr_{0.20}TiO_3$ is obtained for U = 3.0eV and β = 6$(eV)^{-1}$ as shown in Fig.11(a). Furthermore, on increasing the Coulombian parameter, U for a constant β = 10 $(eV)^{-1}$, the system undergoes metal-insulator transition as shown in Fig. 11(b).

The maximum likelihood of the spectral function A(ω), having a realistic features of central peak, height, width and the overall weight, is obtained by using the optimal value of the adjustable parameter, α[60].

The cross validation error is done for obtaining a good and reliable spectral function with the maximum entropy method. The location of the optimal α can be found by choosing its value from the information fitting region of the logistic regression (sigmoid) curve as shown (inset) Fig.11 (b).

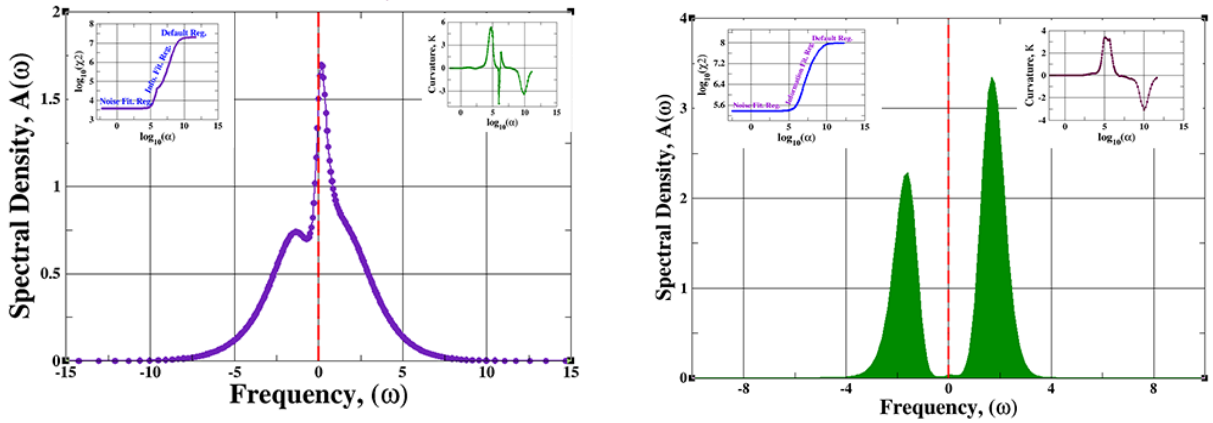

Fig. 11: (color online) (a) Green function of frequency vs. frequency showing the quasi-particle peak for $La_{0.80}Sr_{0.20}TiO_3$. The logistic regression curve or sigmoid curve (inset), which is the cross validation error analysis of calculation. (b) The metal insulator phase transition for U = 3.5 eV and β = 10 eV^{-1} for superlattice, $La_{0.20}Sr_{0.80}TiO_3$ and the logistic regression curve along with the curvature of it (inset).

3.5 Transport properties of $SrTiO_3$ and $LaTiO_3$

The various properties of materials, such as the transport properties are also associated with the electrons and lattice interactions. Here, the density functional theory (DFT) have employed for investigating electrical, thermal, and thermoelectric behaviours of TMOs based on the BoltzTrap module [11,61]. The ever-increasing computing power has made the first principles calculation more and more accurate and straightforward. As the transport properties of the materials are electronic bandstructure dependent quantities, the BoltzTrap codes, which implements the linearized Boltzmann transport equation is applicable to compute various transport coefficients including intermetallic compounds, high T_C superconductor and thermoelectric materials etc.

The study of transport properties are highly useful to predict and design a new materials for diverse fields, such as the superconductors, transparent conductors, transparent insulators, inter-metallic phases as well as the efficient thermometric materials [18, 61].

The significant variation of electrical conductivity, (σ/τ) and thermal conductivity, (κ) with temperature are observed for the different proportion of Sr-atom in the supercells for a constant chemical potential, μ = 0.821 eV. But, the change of electrical conductivity varies slowly (not significantly) with temperature whereas the thermal conductivity varies significantly with temperature along with the various proportions of Sr-atoms on the supercells.

The comparison of Figure of merit (ZT) vs. chemical potential (μ) at room temperature shows that the ZT~1.78 for a system with 40% of Sr-ions at around μ = - 0.7 eV. A remarkable thermoelectric phase transitions are observed for Seebeck Coefficient at temperature, 300 K for the systems with higher proportion of Sr-ions.

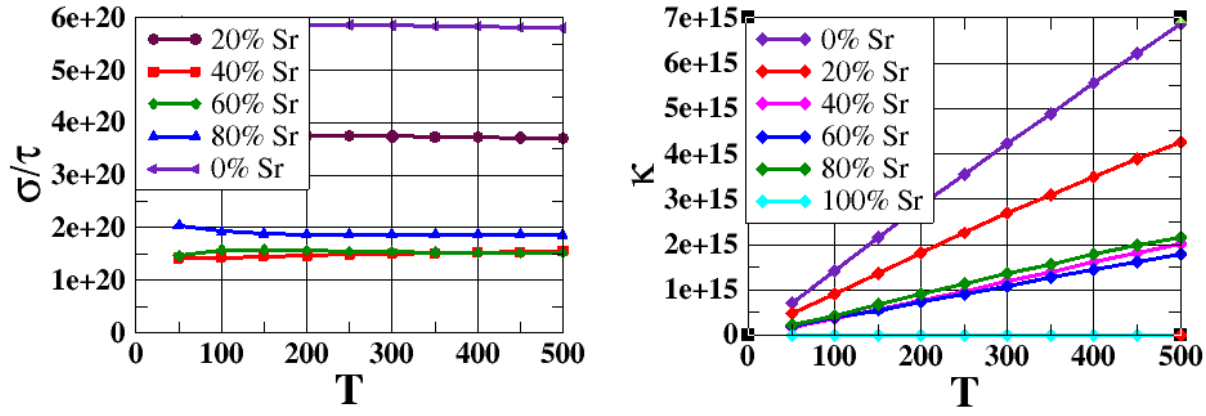

(a) (b)

Fig. 12: (color online) (a) The variation of electrical conductivity with temperature (b) The variation thermal conductivity with temperature for different proportion of Sr-ions having the same chemical potential, $\mu = 0.821$ eV.

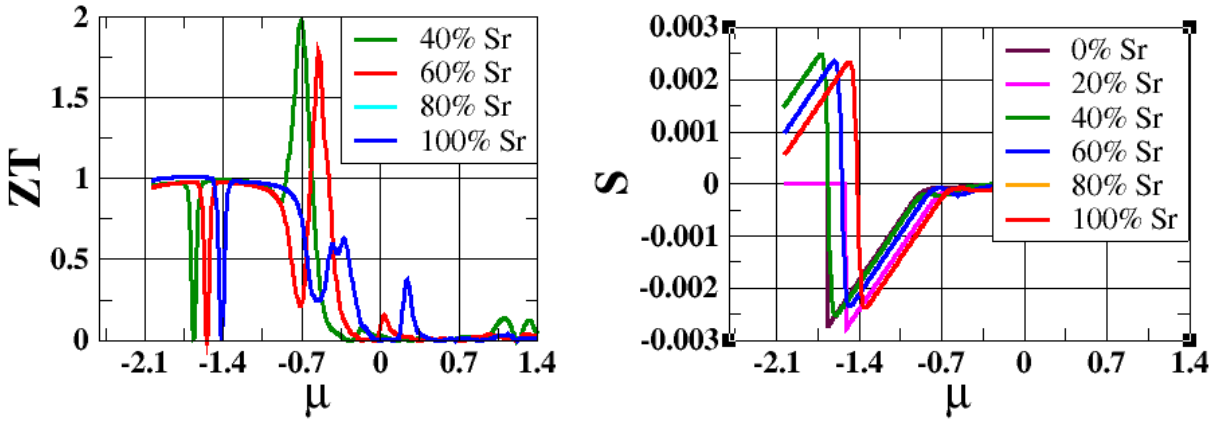

(a) (b)

Fig. 13: (color online) (a) The comparison of Figure of merit (ZT) with chemical potential (μ) at room temperature for various proportion of Sr-ions (b) The thermoelectric phase transition are observed for Seebeck Coefficient vs. chemical potential (μ) at temperature, 300 K.

The ultimate study of finding these transport properties is to investigate the possibility of promising thermoelectric materials by knowing the Figure of merit (transport coefficient) as shown in Fig.13. The higher the value of ZT confirms that the better the potential materials for thermoelectric application for recycling the wastage of heat energy [62,63].

4. CONCLUSIONS

The electronic structure and transport properties of pristine $LaTiO_3$ and $SrTiO_3$ along with their superlattice system have been studied using conventional DFT and DMFT.

The shifts in the energy bands of TMOs are clearly observed by introducing the Coulombian interaction (U), Hund's exchange (J) and spin-orbit couplings (SOC). The calculated band gap for $SrTiO_3$ is found to be 3.423 eV with mBJ interaction potential, which is clos e enough to the experimental information.

The dynamical mean field theory (DMFT) with CT-QMC-hybridization as impurity solver have employed to investigate metal-insulator (MIT) phase transition of pristine $LaTiO_3$ and the superlattice of $La_{(1-x)}Sr_xTiO_3$ system. The correlation parameters for the pristine $LaTiO_3$ for a distinct metal-insulator transition (MIT) are

obtained for U = 2.5 eV, $\beta = 6(eV)^{-1}$ and J = 0.60 eV. Whereas these parameters are found to be U = 3.2 eV, $\beta = 10\ (eV)^{-1}$ and J =0.60eV for the $La_{0.80}Sr_{0.20}TiO_3$ system and U = 3.5 eV, $\beta = 10\ (eV)^{-1}$ and J =0.60eV for the $La_{0.20}Sr_{0.80}TiO_3$ system respectively. The spike of the quasiparticles at around the Fermi level of $La_{0.80}Sr_{0.20}TiO_3$ system is observed for U =3.0eV, $\beta = 6(eV)^{-1}$, J = 0.60eV.

The thermal conductivity varies significantly with the temperature but the electrical conductivity is observed to be remains same with temperature for a system. The higher value of Figure of merit, ZT ~1.75 and 1.99 are calculated for the systems with 40% and 60% of the Sr-ions. The thermoelectric phase transition with chemical potential, μ are observed at around μ~ -1.4 eV for system with higher proportion of Sr-ions. Thus, the $La_{(1-x)}Sr_xTiO_3$ systems are the potential candidates for the thermoelectric application at higher temperature.

5. ACKNOWLEDGEMENT

The authors gratefully acknowledged UGC and NAST for their financial supports. We acknowledged the supercomputer center of KU for supporting in parts through the computational facility. The authors gratefully acknowledged the ABINIT and ALPS codes library in parts for DMFT calculations.

REFERENCES

[1] Imada, M.; Fujimori, A.; & Tokura, Y. Metal-insulator transitions. Reviews of modern physics, **70**(4): 1039 (1998).

[2] Bell, C.; Harashima, S.; Kozuka, Y., *et. al.* Dominant mobility modulation by the electric field effect at the $LaAlO_3/SrTiO_3$ interface. Phys. Rev. Lett., **103**: 226802 (2009).

[3] Larson, P.; Popović, Z. S.; & Satpathy, S. Lattice relaxation effects on the interface electron states in the perovskite oxide superlattices: $LaTiO_3$ monolayer embedded in $SrTiO_3$. Physical Review B, **77**(24): 245122 (2008).

[4] Edmondson, B. I. & Ekerdt, J. G. Effect of $SrTiO_3$ oxygen vacancies on the conductivity of $LaTiO_3/SrTiO_3$ superlattices. Journal of Applied Physics, **124**(18): 185303 (2018).

[5] Scafetta, Mark Dominic. Optical Properties and Electronic Structure of non-d^0 Perovskite Oxide Epitaxial Films and Superlattices. Drexel University (2015).

[6] Kaphle, G. C.; Adhikari, N. & Mookerjee, A. Study of Spin Glass Behavior in Disordered Pt_xMn_{1-x} Alloys: An Augmented Space Recursion Approach. *Advanced Science Letters*, **21**(9): 2681-2687 (2015).

[7] Held, K., & Vollhardt, D. Realistic investigations of correlated electron systems with LDA+ DMFT. *physica status solidi (b)*, **243**(11): 2599-2631(2006).

[8] Nekrasov, I. A., & Vollhardt, D. Calculation of photoemission spectra of the doped Mott insulator using LDA+ DMFT (QMC). *The European Physical Journal B-Condensed Matter and Complex Systems*, **18**(1): 55-61 (2000).

[9] Blümer, N. *Mott Hubbard Metal Insulator Transition and Optical Conductivity in High Dimensions*. Shaker (2003).

[10] Ramakrishnan, T. V. Strongly correlated electrons in solids. *Current Science* (00113891), **95**(9): (2008).

[11] Zhang, X., & Zhao, L. D. Thermoelectric materials: Energy conversion between heat and electricity. *Journal of Materiomics*, **1**(2): 92-105(2015).

[12] Saeed, Y. Tuning the Transport Properties of Layered Materials for Thermoelectric Applications using First-Principles Calculations (Doctoral dissertation) (2014).

[13] Takagi, H., & Hwang, H. Y. An emergent change of phase for electronics. *Science*, **327**(5973): 1601-1602 (2010).

[14] Scheiderer, P. & Claessen, R. *et. al.* Tailoring materials for mottronics: excess oxygen doping of a prototypical mott insulator. *Advanced Materials*, **30**(25): 1706708(2018).

[15] Kohn, W., & Sham, L. J. Self-consistent equations including exchange and correlation effects. Physical Review, **140**(4A): A1133 (1965).

[16] Blaha, P.; Schwarz, K.; Madsen, G. K.; Kvasnicka, D. & Luitz, J. wien2k. An augmented plane wave+ local orbitals program for calculating crystal properties (2001).

[17] Datta, S.; Kaphle, G. C.; Baral, S. & Mookerjee, A. Study of morphology effects on magnetic interactions and band gap variations for 3 d late transition metal bi-doped ZnO nanostructures by hybrid DFT calculations. *The Journal of chemical physics*, **143**(8): 084309 (2015).

[18] Shi, X.; Yang, J.; *et.al.* Multiple-filled skutterudites: high thermoelectric figure of merit through separately optimizing electrical and thermal transports. Journal of the American Chemical Society,**133**(20): 7837 (2011).

[19] Mott, N. F. Proc. Phys. Soc. A, **62**: 416 (1949).

[20] Mahmood, A., & Khan, S. U. D. First-principles study of electronic, optical and thermoelectric properties in cubic perovskite materials $AgMO_3$ (M= V, Nb, Ta). Modern Physics Letters B, **28**(10): 1450077 (2014).

[21] Hubbard, J.; Electron Correlations in Narrow Energy Bands, Proc. Roy. Soc. A **276**: 238 (1963).

[22] Held, K. Electronic structure calculations using dynamical mean field theory. Advances in physics, **56**(6): 829-926 (2007).

[23] Gull, E. Continuous-time quantum Monte Carlo algorithms for fermions (Doctoral dissertation, ETH Zurich) (2008).

[24] Paul, A., & Birol, T. Applications of dft+ dmft in materials science. Annual Review of Materials Research, **49**: 31-52 (2019).

[25] Nekrasov, I. A., Anisimov, V. I. *et.al.* Comparative study of correlation effects in $CaVO_3$ and $SrVO_3$. Physical Review B, **72**(15): 155106 (2005).

[26] Bergeron, D. and Tremblay, A.-M. S. Phys. Rev. E **94**: 023303 (2016).

[27] Perdew, J. P.; Burke, K., & Ernzerhof, M. Generalized gradient approximation made simple. Physical review letters, **77**(18): 3865 (1996).

[28] Martin, R. M. Electronic structure: basic theory and practical methods. Cambridge university press (2004).

[29] Mizutani, U. Introduction to the electron theory of metals. Cambridge University Press (2001).

[30] Kaphle, G. C.; Ganguly, S., *et.al.* "A study of magnetism in disordered Pt-Mn, Pd-Mn and Ni-Mn alloys: an augmented space recursion approach. Journal of Physics Condensed Matter, **24**(29): 295501 (2012).

[31] Georges, A.; Kotliar, G.; Krauth, W., & Rozenberg, M. J. Dynamical mean-field theory of strongly correlated fermion systems and the limit of infinite dimensions. Reviews of Modern Physics, **68**(1): 13 (1996).

[32] Okamoto, S. & Millis, A. J. Theory of Mott insulator–band insulator superlattices. Physical Review B, **70**(7): 075101 (2004).

[33] Fuchs, S. *Thermodynamic and spectral properties of quantum many-particle systems* (Doctoral dissertation, Niedersächsische Staats-und Universitätsbibliothek Göttingen) (2011).

[33] Dymkowski, K. Strain-induced insulator-to-metal transition in d^1 perovskite systems within density functional theory plus dynamical mean field theory (Doctoral dissertation, ETH Zurich) (2015).

[34] Backes, S. *Density Functional Theory and Dynamical Mean-field Theory: A Way to Model Strongly Correlated Systems* (Doctoral dissertation, Universitätsbibliothek Johann Christian Senckenberg) (2017).

[35] Assaad, F. F. 7 Continuous-time QMC Solvers for Electronic Systems in Fermionic and Bosonic Baths. *DMFT at 25: Infinite Dimensions*, **51**: (2014).

[36] Hirayama, S.; Imada, M. *et.al.* "Ab initio Low-energy model of transition-metal-oxide superlattice $LaAlO_3/SrTiO_3$." Journal of the Physical Society of Japan 81.8: 084708 (2012).

[37] Hosoda, M., ….& Hwang, H. Y. Compositional and gate tuning of the interfacial conductivity in $LaAlO_3/LaTiO_3/SrTiO_3$ superlattices. Applied Physics Letters, **102**(9): 091601 (2013).

[38] Ohtsuka, R.; Matvejeff, M.; Nishio, K.; Takahashi, R., & Lippmaa, M. Transport properties of $LaTiO_3/SrTiO_3$ heterostructures. *Applied Physics Letters*, **96**(19): 192111 (2010).

[39] Nishio, K.; Matvejeff, M.; Takahashi, R.; Lippmaa, M.; Sumiya, M.; Yoshikawa, H. & Yamashita, Y. Delta-doped epitaxial La: $SrTiO_3$ field-effect transistor. *Applied Physics Letters*, **98**(24): 242113(2011).

[40] Piskunov, S.; Heifets, E.; Eglitis, R. I., & Borstel, G. Bulk properties and electronic structure of $SrTiO_3$, $BaTiO_3$, $PbTiO_3$ perovskites: an ab initio HF/DFTstudy. *Computational Materials Science*, **29**(2): 165-178 (2004).

[41] Sclauzero, G.; Dymkowski, K., & Ederer, C. Tuning the metal-insulator transition in d^1 and d^2 perovskites by epitaxial strain: A first-principles-based study. *Physical Review B*, **94**(24): 245109 (2016).

[42] Biscaras, J.; & Lesueur, J. Two-dimensional superconducting phase in $LaTiO_3/SrTiO_3$ superlattices induced by high-mobility carrier doping. Physical review letters, **108** (24): 247004 (2012).

[43] Yoshida, C.; & Yokoyama, N. Electric field effect in $LaTiO_3/SrTiO_3$ superlattice. Japanese journal of applied physics, **35**(11R): 5691(1996).

[44] Christen, H. M.; Kim, D. H., & Rouleau, C. M. Interfaces in perovskite superlattices. Applied Physics A, **93**(3): 807-811 (2008).

[45] Ohtomo, A., & Hwang, H. Y. A high-mobility electron gas at the $LaAlO_3/SrTiO_3$ heterointerface. Nature, **427**(6973): 423(2004).

[46] Ohtsuka, R. & Lippmaa, M. Transport properties of $LaTiO_3/SrTiO_3$ superlattices. Applied Physics Letters, **96**(19): 192111 (2010).

[47] Paudyal, D.; Pecharsky, V. K., & Gschneidner Jr, K. A. Electronic structure, magnetic properties, and magnetostructural transformations in rare earth dialuminides. Journal of Applied Physics, **115**(17): 17E127 (2014).

[48] Cwik, M.; Braden, M. *et. al.* Crystal and magnetic structure of $LaTiO_3$: Evidence for nondegenerate t_{2g} orbitals. Physical Review B, **68**(6): 060401 (2003).

[49] Ramay, S. M.; Mahmood, A. *et.al.* The study of electronic, magnetic, magneto-optical and thermoelectric properties of XCr_2O_4 (X= Zn, Cd) through modified Becke and Johnson potential scheme (mBJ). Current Applied Physics, **17**(8): 1038-1045 (2017).

[50] Pandey, S.; Kaphle, G. C. & Adhikari, N. P. Electronic structure and magnetic properties of bulk elements (Fe and Pd) and ordered binary alloys (FePd and Fe_3Pd): TB-LMTO-ASA. *BIBECHANA*, **11**: 60-69(2014).

[51] Gopal, P.; De Gennaro, R.; dos Santos Gusmao, M. S.; Al Orabi, R. A. R.; Wang, H.; Curtarolo, S.; & Nardelli, M. B. Improved electronic structure and magnetic exchange interactions in transition metal oxides. *Journal of Physics: Condensed Matter*, **29**(44): 444003(2017).

[52] Dong, S.; Yu, R.; Yunoki, S.; Alvarez, G.; Liu, J. M., & Dagotto, E. Magnetism, conductivity, and orbital order in $(LaMnO_3)_2n/(SrMnO_3)n$ superlattices. Physical Review B, **78**(20): 201102 (2008).

[53] Zhong, Z. & Hansmann, P. Tuning the work function in transition metal oxides and their superlattices. Physical Review B, **93**(23): 235116 (2016).

[54] Veit, M. J.; *et al.* "Three-dimensional character of the Fermi surface in ultrathin $LaTiO_3/SrTiO_3$ superlattices." Physical Review B 99.11: 115126 (2019).

[55] Kachhava, C. M. Solid state physics. McGraw-Hill Publishing Company Ltd. (1992).

[56] Santana, J. A. & Reboredo, F. A. Electron Confinement and Magnetism of $(LaTiO_3)_1/(SrTiO_3)_5$ Superlattice: A Diffusion Quantum Monte Carlo Study. Journal of Chemical Theory and Computation, **16**(1): 643-650 (2019).

[57] Wang, L.; Li, Y.; Bera, A.; Ma, C.; Jin, F.; Yuan, K. & Prellier, W. Device performance of the mott insulator $LaVO_3$ as a photovoltaic material. Physical Review Applied, **3**(6): 064015 (2015).

[58] Haule, Kristjan. "Quantum Monte Carlo impurity solver for cluster dynamical mean field theory and electronic structure calculations with adjustable cluster base." Physical Review B 75.15: 155113 (2007).

[59] Pavarini, E.; Koch, E.; Vollhardt, D. & Lichtenstein, A. (Eds.). Dmft at 25: Infinite dimensions: Lecture notes of the autumn school on correlated electron (Vol. 4). Forschungszentrum Jülich (2014).

[60] Van Campenhout, J. & Cover, T. Maximum entropy and conditional probability. IEEE Transactions on Information Theory, **27**(4): 483-489(1981).

[61] Sevik, C. & Çağın, T. Ab initio study of thermoelectric transport properties of pure and doped quaternary compounds. Physical Review B, **82**(4): 045202 (2010).

[62] Zhang, Y.; Sugo, K.; Cho, H. J. & Ohta, H. Thermoelectric phase diagram of the $SrTiO_3$-$LaTiO_3$ solid-solution system through a metal to Mott insulator transition. *Journal of Applied Physics*, **126**(7): 075104 (2019).

[63] Walia, S. & Kalantar-zadeh, K. Transition metal oxides–Thermoelectric properties. *Progress in Materials Science*, **58**(8): 1443-1489(2013).

[64] Sulpizio, J. A. & Levy, J. Nanoscale phenomena in oxide superlattices. Annual Review of Materials Research, **44**: 117-149 (2014).

[65] Assmann, E. & Sangiovanni, G. Oxide superlattices for efficient solar cells. Physical review letters, **110**(7): 078701 (2013).

[66] Ghising, P. & Hossain, Z. Kondo effect with tunable spin–orbit interaction in $LaTiO_3/CeTiO_3/SrTiO_3$ superlattice. Journal of Physics: Condensed Matter.

[67] Chen, H. A First Principles Study on Oxide Surfaces (2012).

[68] Xue, Y. & Xu, H. Tunable magnetism in the $LaAlO_3/SrTiO_3$ superlattice: Insights from first-principles calculations. Physica E: Low-dimensional Systems and Nanostructures, **98**: 120-124 (2018).

[69] Tully, J. Crisp: The center for research on interface structures and phenomena, Yale university. Advanced Materials, **22**(26-27): 2837 (2010).

[70] Hirayama, M.; Miyake, T. & Imada, M. Ab initio Low-energy model of transition-metal oxide superlattice $LaAlO_3/SrTiO_3$. Journal of the Physical Society of Japan, **81**(8): 084708 (2012).

[71] Gandolfi, M.; Giannetti, C. *et. al.* Emergent ultrafast phenomena in correlated oxides and superlattices. Physica Scripta, **92**(3): 034004 (2017).

[72] Paudyal, D.; Pecharsky, V. K. & Gschneidner Jr, K. A. Electronic structure, magnetic properties, and magnetostructural transformations in rare earth dialuminides. Journal of Applied Physics, **115**(17): 17E127(2014).

[73] Zhong Z. and Kelly, P. J. Europhys. Lett. **84**: 27001 (2008).

[74] Fennie, C. J. Ferroelectrically induced weak ferromagnetism by design. Physical review letters, **100**(16): 167203 (2008).

[75] Bousquet, E.; Ghosez, P. *et. al.* Improper ferroelectricity in perovskite oxide out artificial superlattices. Nature, **452**(7188): 732 (2008).

[76] Brito, W. H.; Aguiar, M. C. O.; Haule, K. & Kotliar, G. Metal-insulator transition in VO_2: A DFT+ DMFT perspective. Physical review letters, **117**(5): 056402 (2016).

[77] Ishida, H. & Liebsch, A. Origin of metallicity of $LaTiO_3$/ $SrTiO_3$ superlattices. Physical Review B, **77**(11): 115350 (2008).

[78] Wang, L.; Liu, Y. H. & Harcos, G. *et. al.* Split orthogonal group: A guiding principle for sign-problem-free fermionic simulations. *Physical review letters*, **115**(25): 250601 (2015).

[79] Dine, K.; Zaoui, A. & Bouhafs, B. Fermi Surfaces of Compensated and Uncompensated Metals: GGA+U+ SO Comparative Ab Initio Study. *Journal of Superconductivity and Novel Magnetism*, **29**(8): 2195-2201(2016).

[80] Lieb, E. H. The Hubbard model: Some rigorous results and open problems. In *Condensed Matter Physics and Exactly Soluble Models* (pp. 59-77). Springer, Berlin, Heidelberg (2004).

[82] Araizi-Kanoutas, G. & Fatermans, J. *et. al.* Co valence transformation in isopolar $LaCoO_3/LaTiO_3$ perovskite heterostructures via interfacial engineering. *Physical Review Materials*, **4**(2): 026001(2020).

[83] Okamoto, S.; Millis, A. J. & Spaldin, N. A. Lattice relaxation in oxide superlattices: $LaTiO_3/SrTiO_3$ superlattices. Physical review letters, **97**(5): 056802 (2006).

[84] Nazir, S.; Bernal, C. & Yang, K. Modulated Two-Dimensional Charge-Carrier Density in $LaTiO_3$–Layer-Doped $LaAlO_3/SrTiO_3$ Superlattice. ACS applied materials & interfaces, **7**(9): 5305-5311 (2015).

Electronic and Transport Properties of Sr-site Substituted: $Ca_xSr_{(1-x)}VO_3$

R. K. Rai, R. B. Ray, G. C. Kaphle, O. P. Niraula

Journal of Nepal Physical Society

Volume 7, Issue 1, April 2021

(Special Issue: ANPA Conference, 2020)

ISSN: 2392-473X (Print), 2738-9537 (Online)

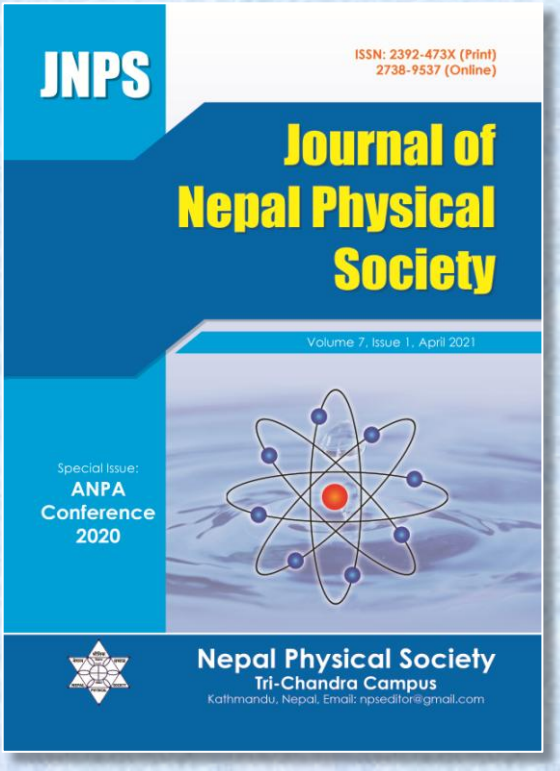

JNPS, **7** (1), 6-17 (2021)

DOI: http://doi.org/10.3126/jnphyssoc.v7i1.36968

Published by:

Nepal Physical Society

P.O. Box: 2934

Tri-Chandra Campus

Kathmandu, Nepal

Email: npseditor@gmail.com

JNPS 7 (1): 6-17 (2021)
ISSN: 2392-473X (Print), 2738-9537 (Online)
Research Article *© Nepal Physical Society*
DOI: http://doi.org/10.3126/jnphyssoc.v7i1.36968

Electronic and Transport Properties of Sr-site Substituted: $Ca_xSr_{(1-x)}VO_3$

R. K. Rai[1, 2], R. B. Ray[1, 3], G. C. Kaphle[1,*], O. P. Niraula[1]
[1]Central Department of Physics, Tribhuvan University, Kirtipur, Kathmandu, Nepal
[2]Patan Multiple Campus, Tribhuvan University, Lalitpur, Nepal
[3]Amrit Campus, Tribhuvan University, Kathmandu, Nepal
[*]Corresponding Email: gck223@gmail.com

Received: *9 August, 2020;* ***Revised:*** *10 January, 2021;* ***Accepted:*** *5 February, 2021*

ABSTRACT

The Mott-insulator phase transition behaviour of the superstructure of strongly correlated system, $Ca_xSr_{(1-x)}VO_3$ (x =0, 0.33, 0.67, 1) have studied using the conventional density functional theory and the dynamical mean field theory. The Mott-Hubbard metal-insulator phase transition of superstructures, $Ca_{0.33}Sr_{0.67}VO_3$ and $Ca_{0.67}Sr_{0.33}VO_3$ formed by the $CaVO_3$ and $SrVO_3$ correlated metals, are obtained at U=4.5 eV with β= 6 $(eV)^{-1}$ and U=4.5 eV with β= 7 $(eV)^{-1}$ respectively. The values of U and β calculated through the Maximum Entropy model using the Green's function data, are consistent with the experimental results. The value of Seebeck coefficient (S) of superstructure $Ca_{0.33}Sr_{0.67}VO_3$ and $Ca_{0.67}Sr_{0.33}VO_3$ are found to be +0.0011[V/K] and -0.0011[V/K] within the chemical potential $\mu = -1.266$ eV to $\mu = -0.938$ eV. The figures of merit (ZT) are found to be 0.97 at room temperature for these systems. The variation of electrical and thermal conductivities has also been discussed.

Keywords: Complex TMOs, DFT, DMFT, Superstructures, Strongly Correlated System.

1. INTRODUCTION

The superstructure of perovskite materials have gained a lot of interest due to their promising applications for the electronic and transport properties as well as from its fundamental aspects. The transition metal oxides (TMOs) in the perovskites (ABO_3) geometry are smart materials found abundantly on the earth crusts. These materials are used for numerous applications in the field of electrical, electronics, medical, defense technology and etc. [1, 2]. The modern technology assisted human civilizations through scientific revolution are being upgraded by exploring the smart materials. One of the categories of promising smart materials for the future is regarded as the TMOs in their nano-structures and superstructures [3]. The present study focused on the structural, electronic and transport properties of energetically stable superstructures $Ca_{0.33}Sr_{0.67}VO_3$ and $Ca_{0.67}Sr_{0.33}VO_3$.

The pristine $SrVO_3$ is found in cubic phase, belongs to the space-group Pm-3m with the Ca-atom sitting at the body center (½ , ½ , ½)a. The transition metal, V-atom is sitting at the origin (0.0 , 0.0 , 0.0)a and the three O-atoms siting at the three face centers with Wyckoff's coordinates (½ , ½ , 0.0)a, (0.0, ½ , ½)a, and (½ , 0.0, ½)a[4].

Similarly, the pristine $CaVO_3$ system in cubic phase belonging to the space-group Pm-3m with V-atom at the body center (½ , ½, ½)a. The Ca-atom is sitting at the origin (0.0, 0.0, 0.0)a and the three O-atoms sitting with Wyckoff's coordinates at (0.0 , ½ , 0.0)a, (0.0, 0.0 , ½)a, and (½ , 0.0, 0.0)a[4]. The stable crystal structures for the pristine $CaVO_3$ and the superstructure, $Ca_{0.33}Sr_{0.67}VO_3$ are shown in fig.1 (a), (b).

The study of metal-to-insulator transition (MIT) caused by a strong electron correlation along with anomalous electronic properties in the metallic phase near the Mott transition, provide the various information regarding application in Mottronics, such as the volume resistive switching action, Mott FET, quantum gates etc. [5].

Though, MIT of the compounds can be studied through the hole or electron doping to the system either by band control or filling control methods [6]. Here, we used band controlling method to explain the MIT of experimentally synthesized compounds, $Ca_{0.33}Sr_{0.67}VO_3$ by substituting Ca-ion in place of Sr-ion within the framework of 1 ×1 ×2 supercell of $CaVO_3$ as shown in Fig. 1.

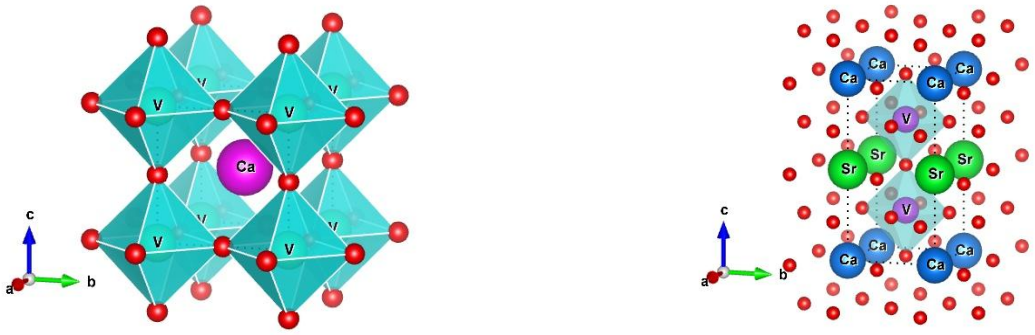

(a) (b)

Fig.1: (a) (color online) The crystal structure of the pristine $CaVO_3$ at which V-ion is octahedrally co-ordinated by oxygen ligands (left) (b) the superstructure, $Ca_{0.33}Sr_{0.67}VO_3$ (right)

The Mott transition behaviours of such systems are also studied using the density functional theory (DFT) and the dynamical mean field theory (DMFT) by various groups [7, 8]. A simple transition metal oxide system $Ca_{1-x}Sr_xVO_3$ with a $3d^1$ electronic configuration and a cubic perovskite lattice structure with the orthorhombically distorted $SrVO_3$ upon increasing the Ca-doping have been investigated using LDA+DMFT [9-11].

In the present study, the stable structures, electronic properties are studied through conventional DFT and the MIT phase transition of pristine TMOs and their superstructures are studied through DMFT. The transport properties are also investigated through BoltzTrap frameworks (explained elsewhere). The materials under study are highly applicable for electrical, electronic, memory, and energy devices. The superstructure and nanostructure are of great interest of their Mottness, high efficiency of power conversion and high ZT factors. The Mott transition phenomena is useful for designing a leaky integrate and fire (LIF) artificial neurons [12-17], for neurocomputing, artificial neural network, machine learning etc.

Though, the MIT has various applications in different purposes, there is lack of systematic theoretical study compare to the experimental study. So, we are motivated to go more insight into the newly reconstructed superstructures for exploring MIT and thermoelectric properties.

Furthermore, the transition metal oxides have narrow conduction bands due to weak orbital overlap, which leads to localized electrons with low carrier mobilities. Transition metal oxides have recently been considered as thermoelectric (TE) materials that can operate at high temperature and they have their transport properties with high Seebeck coefficients (S) and low thermal conductivity (κ) and hence the higher value of figure of merit (ZT).

We have computed the thermal conductivity κ, electrical conductivity (σ/τ), Seebeck coefficients (S), and Figure of merit (ZT) for the designed superstructure [18] using semi-classical linearized Boltzmann transport equation.

2. THEORETICAL, COMPUTATIONAL DETAILS AND EXPERIMENTAL INFORMATION

2.1 Theoretical Details:

The electronic structure and transport properties of correlated electronic system are investigated employing ab-initio approaches through the full potential linearized augmented plane wave (FP-LAPW) method with local orbitals (lo) [19, 20]. The optimized cubic phases of $CaVO_3$ and $SrVO_3$ and their superstructure framework are taken through the self-consistent calculation based on Kohn-Sham equation as given by,

$$\left[-\frac{\hbar^2}{2m}\nabla^2 + v_{eff}(r)\right]\psi_i = \varepsilon_i\psi_i \text{ --- (1)}$$

Where the effective Kohn-Sham potential is expressed as,

$$v_{eff}(r) = v(r) + \int e^2 \frac{[n_e(r')]}{|r-r'|} dr' + v_{xc}(r) \quad \text{--- (2)}$$

With, $v_{xc}(r) = \frac{\delta E[n_e(r)]}{\delta n_e(r)}$ is the exchange correlation potential with the probability density, $n_e(r) = \sum_{i=1}^{N} |\psi_i(r)|^2$.

The optimized value of the lattice parameter, a is calculated using the concept of Birch-Murnaghan equation of state as given by,

$$E_{tot}(a) = E_0 + \frac{9V_0B_0}{16}\left\{\left[\left(\frac{a_0}{a}\right)^2 - 1\right]^3 B_0' + \left[\left(\frac{a_0}{a}\right)^2 - 1\right]^2 \left[6 - 4\left(\frac{a_0}{a}\right)^2\right]\right\} \text{--- (3)}$$

Where, B_0 is the bulk modulus of elasticity at equilibrium (pressure =0), V_0 is the equilibrium volume per atom/unit cell, $B_0' = \left(\frac{\partial B}{\partial P}\right)_{P=0}$ and E_0 is the total energy at equilibrium are treated as fitting parameters [20,21]. All the calculations were performed using the optimized parameters.

The theoretical prediction of transport coefficients of the TMOs are investigated for the optimized systems by using BoltzTraP code, a patching module of WIEN2k framework, which implements the linearized Boltzmann Transport Equation (BTE) [18, 22] as given by,

$$\frac{\partial f_\mu(T,\mu)}{\partial t} = -v_\alpha(i,k).\frac{\partial f_\mu(T,\mu)}{\partial r} - \frac{e}{\hbar}\left(E - \frac{1}{c}v_\alpha(i,k) \times H\right).\frac{\partial f_\mu(T,\mu)}{\partial k_\alpha} + \left.\frac{\partial f_\mu(T,\mu)}{\partial t}\right|_{scattering} \text{--- (4)}$$

with $f_\mu(T,\mu) = \frac{1}{\exp^{[\mu - E_F]/k_B T} + 1}$ is the Fermi-Dirac distribution for electron and $v_\alpha(i,k) = \frac{1}{\hbar}\frac{\partial \varepsilon_{i,k}}{\partial k_\alpha}$ is the group velocity of the carriers.

For the figure of merit (ZT), the following equation is employed,

$$ZT = \frac{\sigma_{\alpha\beta} S_{\alpha\beta}^2}{\kappa_{\alpha\beta}} T \text{ --- (5)}$$

Where, $\sigma_{\alpha\beta}(T,\mu)$ is the electrical conductivity tensor, $\kappa_{\alpha\beta}(T,\mu)$ is the thermal conductivity tensor, $S_{\alpha\beta}(T,\mu)$ is the thermoelectric Seebeck coefficients, Where α and β are tensor indices, μ and N are the chemical potential and number of K-points implemented respectively [22].

Furthermore, the actual metal-insulator transition can be understood by using the dynamical mean field theory (DMFT), which starts from the Hubbard Hamiltonian [23-25] for single site interaction of opposite spin electrons as,

$$H = \sum_{\langle\alpha\beta\rangle} t_{\alpha\beta} c_\alpha^\dagger c_\beta + U \sum_\alpha n_{\alpha\uparrow} n_{\alpha\downarrow} \text{ --- (6)}$$

Where, $t_{\alpha\beta}$ is tight-binding hopping amplitude between the lattice sites α and β, $c_\alpha^\dagger(c_\alpha)$ are the creation (annihilation) operators of electrons on localized orbitals on site, α and $n_\alpha = c_\alpha^\dagger c_\alpha$ is the localized occupation number on site, α.

The DMFT maps the lattice problem (Hubbard Hamiltonian) of Eq. (6) onto a self-consistent auxiliary impurity problem, which is here solved numerically by the quantum Monte Carlo (QMC) technique, combined with the maximum entropy method [26], this technique allows us to calculate spectral functions.

The DMFT self-consistency cycle starts with an initial guess for the hybridization function, $\Delta(i\omega_n) = \sum_v \frac{|V_v|^2}{i\omega_n - \epsilon_v}$

or bath Green's function,

$$\mathcal{G}_0(i\omega_n) = [i\omega_n + \mu\Delta(i\omega_n)]^{-1} \text{ --- (7)}$$

which determines the initial "bath" for the modified quantum impurity model.

Where, V_v is the hybridization amplitude, ϵ_v is the bath energy level and $(i\omega_n)$ is the Matsubara frequency associated with the imaginary time, (τ). Using one of the quantum impurity solvers with the imaginary-time Green's function,

$$G(\tau) = -\langle T_\tau c(\tau) c^\dagger(0)\rangle \text{ --- (8)}$$

or its Fourier transform $G(i\omega_n)$ and the Matsubara self-energy is,

$$\Sigma(i\omega_n) = \mathcal{G}_0^{-1}(i\omega_n) - G^{-1}(i\omega_n) \text{ --- (9)}$$

are computed. This is actually the Fourier transform of Dyson equation, which computes the new bath Green's function, for the next iterative self-consistent cycle [27-29]. The Green's function is then used for calculating the spectral function $A(k,\omega)$, which is the imaginary part of the single-particle Green's function and therefore contains full information about the temporal and spatial evolution of a single electron/hole in the interacting many-electron system.

$$A(k,\omega) = -\frac{1}{\pi}\mathrm{Im}G(k,\omega) \text{ --- (10)}$$

The spectral function $A(\omega)$ is analogous to the density of states(DOS) of conventional DFT.

2.2 Computational Details

The first-principles based approach has been used to deal with the structural, electronic properties of TMOs and their superstructures, employed on FPLAPW [30, 31]. The transport properties of the superstructures are calculated by solving the Boltzmann transport equation using BoltzTrap codes.

The conventional DFT is used for bandstructure and DOS calculation, which is used for the DMFT calculations. For the DFT calculation we have employed generalized gradient approximation (GGA) with the correlation functional as proposed by Perdew, Burke and Ernzerhof (PBE) exchange energy scheme [21,32].

The optimized parameters for the pristine systems and superstructures used for the present study are listed in the table 1.

Table 1: The required values of lattice parameters, K-points, rKmax, Gmax and RMT* of the compounds with their space group used for the calculation.

S.N.	Name of system	Space group	Optimized lattice constant	K-points	rKmax	Gmax	RMT
1.	$CaVO_3$	*pm-3m* (221)	3.65 Å	800	3.97 Å	14	Ca = 2.42, V = 1.79 and O = 1.62
2.	$SrVO_3$	*pm-3m* (221)	3.86 Å	750	3.97 Å	16	Sr = 2.46, V = 1.83 and O = 1.65
3.	$Ca_{0.33}Sr_{0.67}VO_3$	*P4/mmm* (123)	a = b = 3.96 ^{0}A and c = 7.93 Å	800	3.97 Å	16	Ca = 2.50, Sr = 2.50, V = 1.95 and O = 1.77
4.	$Ca_{0.67}Sr_{0.33}VO_3$	*P4/mmm* (123)	a = b = 3.95^{0}A and c = 7.91 Å	750	3.95 Å	15	Ca = 2.50, Sr = 2.50, V = 1.95 and O = 1.77

*RMT = Muffin-Tin radius of the elements

(All the values are consistent with the experimental results)

The Monk-horst pack of 11×11×5 k-mesh grid is used for the superstructures. The DMFT calculations are performed for various sets of coulombian interaction, U and the thermodynamical parameter, β in order to identify the critical value of MIT for each of the superstructures [33-35]. The energy and charge convergence criteria for the entire system are 10^{-5} eV and 10^{-3} e with force convergence 0.05 eV/ ^{0}A.

2.3 Experimental Information

The single crystals of superstructures, $Ca_{1-x}Sr_xVO_3$ (x = 0, 0.25, 0.5, 1) have grown for studying optical conductivity using a triple spectrometer, Photometrics and the optical reflectivity measurements using a Michelson-type Fourier-transform infrared spectrometer [36]. The spectra of $SrVO_3$ and $CaVO_3$ are also studied with bulk-sensitive high-resolution PES and XAS [37]. The Mott–Hubbard insulating gap for different values of U for vanadates and titanates system were also studied from the various groups [38-40].

These experimental facts motivate us to perform the theoretical study to go more insight into the electronic and transport properties used for various applications in Mottronics.

3. RESULTS AND DISCUSSION

3.1 Structural Stability

The structural stability of the compounds $CaVO_3$, $SrVO_3$ are calculated through energy minimization process. The value of the optimized lattice parameter for pristine $CaVO_3$ and $SrVO_3$ are found to be consistent with the experimental results [41, 42]. The reconstructed superstructure, $Ca_xSr_{(1-x)}VO_3$ (x =0.33, 0.67) using the base of 1×1×2 supercell of $SrVO_3$ and the site substitution of Sr-atoms by Ca-atoms on the supercell have been studied for their various properties.

These superstructures with space-group P4/mmm, are also examined their stability through energy minimization process. The optimized lattice parameters of the superstructures, $Ca_{0.33}Sr_{0.67}VO_3$ and $Ca_{0.67}Sr_{0.33}VO_3$ are obtained and tabulated as in table-1.

The optimized structure of the sample $CaVO_3$ and $Ca_{0.67}Sr_{0.33}VO_3$ are shown in inset along with the energy vs. lattice parameter plot as shown in Fig. 2.

The lattice parameters of the superstructures are yet to be verified by experimentation.

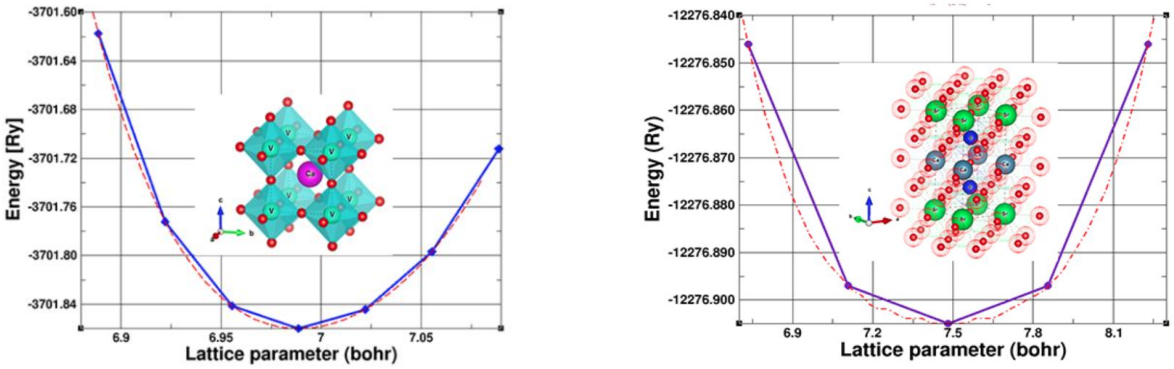

(a) (b)

Fig. 2: (color online) The crystal structures (inset) and lattice parameter optimization curves for (a) $CaVO_3$ system (b) $Ca_{0.33}Sr_{0.67}VO_3$ system.

3.2 Electronic Structure of $Ca_xSr_{(1-x)}VO_3$ System

3.2.1 The Band structure and DOS

The bandstructure and the DOS plots of $CaVO_3$ and $SrVO_3$ systems are found to be well agreed with the previously calculated theoretical and experimental results. Both of these systems are correlated metals [45].

The combined plot of bandstructure and DOS of $Ca_{0.33}Sr_{0.67}VO_3$ and $Ca_{0.67}Sr_{0.33}VO_3$ are shown in Fig. 3 (a) and (b) indicating that these superstructures are also found to be correlated metal from the conventional DFT calculation.

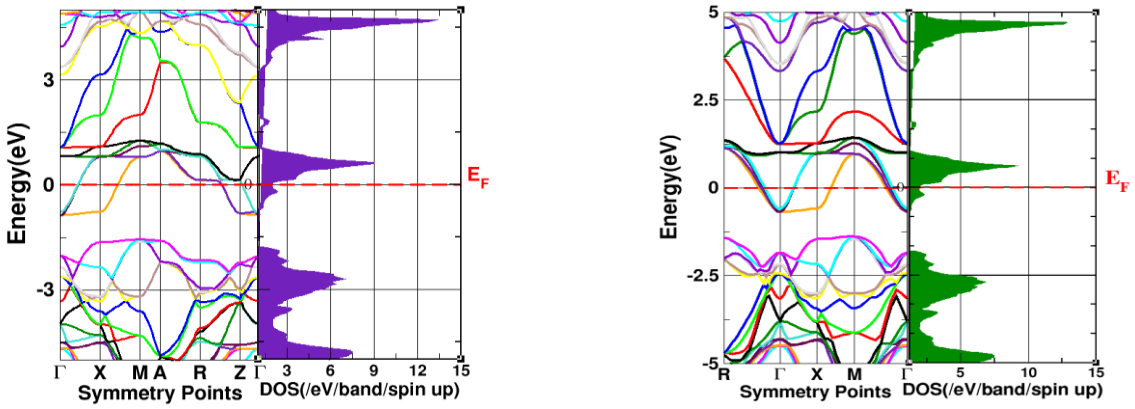

(a) (b)

Fig. 3: (color online) The comparison of bandstructure and DOS for spin up channels of (a) $Ca_{0.33}Sr_{0.67}VO_3$ system, and (b) $Ca_{0.67}Sr_{0.33}VO_3$ system.

Furthermore, the asymmetric distribution of DOS in spin up and spin down channels (Fig. 4) for the both superstructures $Ca_{0.33}Sr_{0.67}VO_3$ and $Ca_{0.67}Sr_{0.33}VO_3$ indicating that they show magnetism in ferromagnetic orderings. The magnetic moments are found to be 1.47 μ_B and 0.78 μ_B for $Ca_{0.33}Sr_{0.67}VO_3$ and $Ca_{0.67}Sr_{0.33}VO_3$ systems respectively.

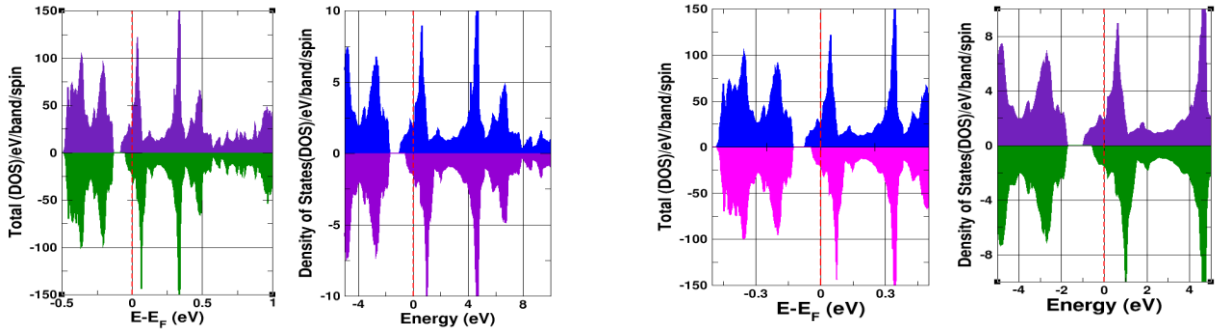

(a) (b)

Fig. 4: (color online) The DOS plots for (a) $Ca_{0.33}Sr_{0.67}VO_3$ and (b) $Ca_{0.67}Sr_{0.33}VO_3$ systems.

3.2.2 The Charge Density Map and Fermi Surface of the $Ca_xSr_{(1-x)}VO_3$:

The charge density contour plot shows that the $Ca_{0.33}Sr_{0.67}VO_3$ system have a strong covalent bonding between V and O-atoms which is mainly due to p-d hybridization of O-2p and V-3d orbitals as shown in Fig. 5(a) [46-49].

The Fermi surface plot (in inset) with band crossing by Fermi level of superstructures also supports the electronic structure calculations as shown in Fig. 5(b) [50, 51].

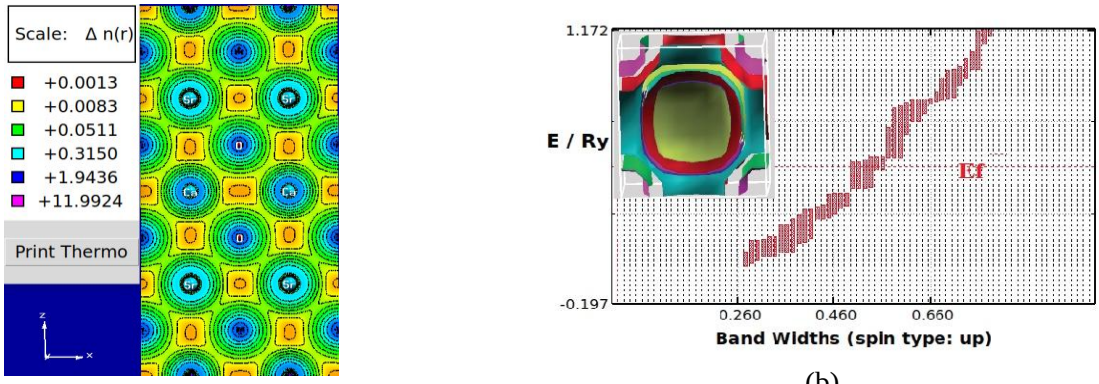

(a) (b)

Fig. 5: (color online) (a) The 2D-contour plot of charge density distributions showing the bonding between neighboring atoms (b) The Fermi-surface (in inset) showing band crossing of Fermi level with 30-65 band levels.

3.3 The Dynamical Mean Field Theory (DMFT) calculation:

The Mott-Hubbard metal-insulator transition phenomena of the strongly correlated system are investigated using the numerical simulation of the data obtained from the conventional DFT calculation.

In general, the conventional DFT (GGA) underestimates the electronic bandstructure of strongly correlated system. Thus, we have used the dynamical mean field theory (DMFT) along with the DFT for the realistic calculation of electronic structure of superstructures [52 - 54]. From the DMFT calculations, the value of U and β required for Mott-Hubbard band splitting are calculated with the help the Green's function vs. imaginary time and its Fourier transform plots as shown in Fig. 6(a), (b).

(a) (b)

Fig. 6: (color online) (a) The variation of Green's function $G_\uparrow(\tau)$ with imaginary time (b) The plot of Fourier transform of Green's function, $G_\uparrow(\omega)$ [54].

The characteristic variation of Green function of imaginary time, $G_\uparrow(\tau)$with the imaginary time (τ) for various values of U, for the superstructure of $Ca_xSr_{(1-x)}VO_3$ system is shown in Fig. 6(a) and the corresponding variation of spectral density, $A(\omega)$ with the frequency (ω) is shown in Fig. 6(b), which is obtained by using the maximum entropy method of data analysis algorithm[55,56].

Moreover, Fig. 6 shows that the Mott-Hubbard band splitting starts from U =4.5 eV for the value of β =6 $(eV)^{-1}$. The corresponding spectral density plot of $G_\uparrow(\tau)$ for the superstructure, $Ca_{0.33}Sr_{0.67}VO_3$ with β =6 $(eV)^{-1}$ and various values of U is shown in Fig.7 (a).

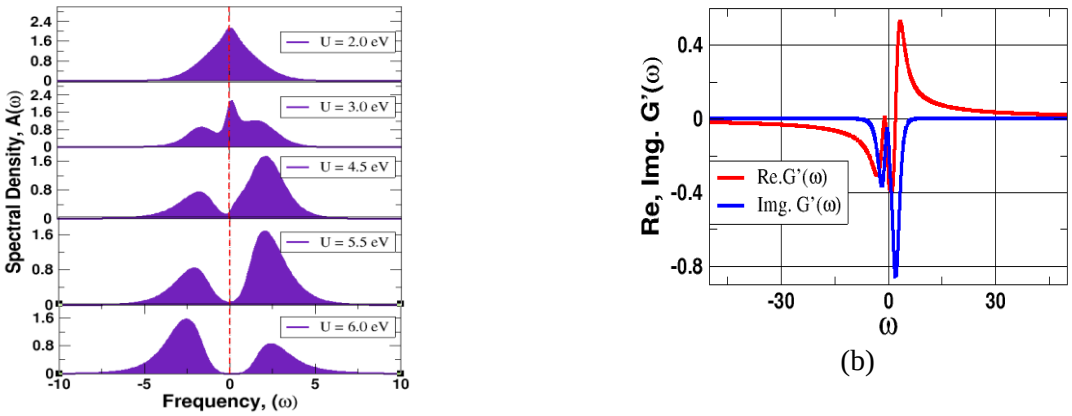

(a) (b)

Fig. 7: (color online) (a) The spectral density vs. frequency for showing metal-insulator transition (MIT) with the variation of U for β =6 $(eV)^{-1}$. (b) The plot of real and imaginary part of retarded Green's function vs. frequency with U = 4.5 eV and β =6 $(eV)^{-1}$.

The Mott-Hubbard splitting of $Ca_{0.67}Sr_{0.33}VO_3$ system is obtained at U = 4.5 eV with β = $7(eV)^{-1}$(not shown in the graph).

Similarly, the corresponding real and imaginary part of retarded Green's function of frequency is shown in Fig. 7(b). In the Fermi liquid regime, the real part of the self energy leads to the shift of the non-interacting excitations, whereas the imaginary part is responsible for the broadening of the quasiparticle excitations. As the self-energy strongly depends on the frequency and in the case of Mott insulator, it will lead to a notable transfer of spectral weights.

The validity of spectral function, $A(\omega)$ obtained from the maximum entropy model is checked through cross validation error (logistic regression analysis) as shown in fig. 8(a), (b) [56, 57].

From the sigmoid curve of logistic regression, the optimized value of α lies in the information-fitting region indicating that the data obtained by our calculation is realistic and information are close to the experimental results [58].

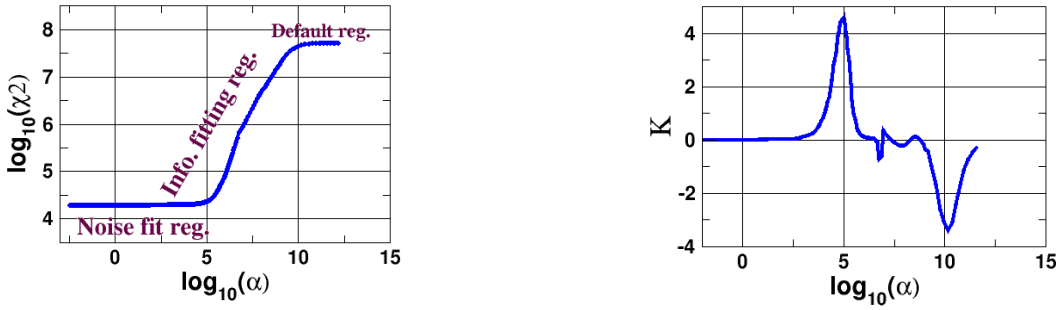

(a) (b)

Fig. 8: (color online) (a) The logistic regression curve (sigmoid curve) for the optimized value of α (b) The error of logistic regression curve obtained by the curvature of the $\log_{10}\chi^2$ (K) versus $\log_{10}(\alpha)$.

3.4 Transport properties of for $Ca_xSr_{(1-x)}VO_3$ system:

The transport properties of the superstructure are calculated using semiclassical linearized form of BTE through BoltzTrap frameworks implemented on ab-initio codes [59]. The graph showing the comparison of (a) Electrical conductivity (σ/τ) and (b) Thermal conductivity (κ) at room temperature are shown in fig. 9 (a), (b) for the superstructures, $Ca_{0.33}Sr_{0.67}VO_3$ and $Ca_{0.67}Sr_{0.33}VO_3$ with blue and red colors respectively. And the variation of Seebeck coefficient (S) with respect to the chemical potential, (μ) at room temperature for $Ca_{0.33}Sr_{0.67}VO_3$ and $Ca_{0.67}Sr_{0.33}VO_3$ systems are shown in Fig. 10 (a) with blue and red colors respectively [18, 58, 59].

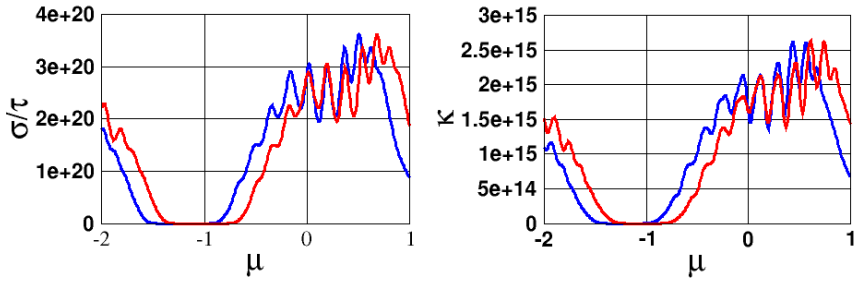

(a) (b)

Fig. 9: (color online) (a) The variation of electrical conductivity (σ/τ) vs. (μ) (b) The variation of thermal conductivity (κ) vs. (μ) for $Ca_{0.33}Sr_{0.67}VO_3$ and $Ca_{0.67}Sr_{0.33}VO_3$ with blue and red colors respectively [59, 60].

From the study of thermoelectric properties the figure of merit (ZT) factor for the superstructure $Ca_{0.33}Sr_{0.67}VO_3$ with blue color and $Ca_{0.67}Sr_{0.33}VO_3$ with red color are nearly equal to unity (≈ 1) at near from $\mu = -1.266$ eV to $\mu = -0.938$ eV Fig. 10(b).

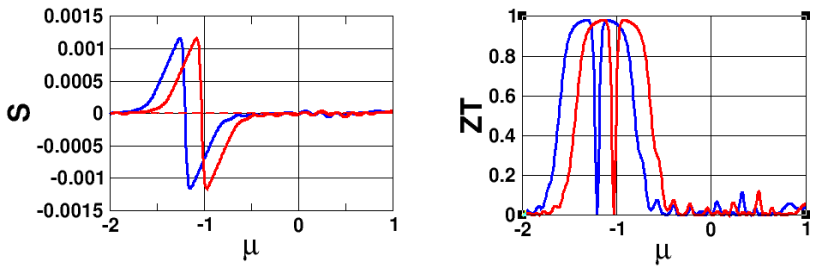

(a) (b)

Fig. 10: (color online) (a) Variation of Seebeck coefficient (S) with chemical potential (μ) (b) Figure of merit (ZT) at room temperature with chemical potential (μ) for superstructures, $Ca_{0.33}Sr_{0.67}VO_3$ and $Ca_{0.67}Sr_{0.33}VO_3$ with blue and red curves respectively [60-63].

The similar kind of thermoelectric properties are observed for both the superstructures, which can be used for the Mottronics applications.

4. CONCLUSIONS

The stability of the pristine and their superstructure are examined through energy minimization method. From the calculations, the lattice parameters for the stable superstructures, $Ca_{0.33}Sr_{0.67}VO_3$ is found to be, a=b=3.96 A^0 and c=7.93 A^0 and for $Ca_{0.67}Sr_{0.33}VO_3$ is found to be, a = b = 3.95 ^{0}A and c = 7.91 A^0. The Mott-Hubbard metal-insulator transition for their superstructure, $Ca_{0.33}Sr_{0.67}VO_3$ and $Ca_{0.67}Sr_{0.33}VO_3$ are obtained at U = 4.5eV with $\beta = 6(eV)^{-1}$ and U = 4.5eV with $\beta = 7(eV)^{-1}$ respectively, through DFT and DMFT with the continuous time quantum Monte Carlo (CT-QMC)–hybridization method. This clearly indicates that both compounds are useful for Mottronics application. Furthermore, the ZT factor of the superstructures are approximately unity (~1). The estimated values of Seebeck coefficients and transport coefficients for the superstructure framework reveal that they can be used as the promising candidates for thermoelectric materials.

5. ACKNOWLEDGEMENT

The authors are gratefully acknowledged to UGC and NAST for financial supports. We thankfully acknowledge to supercomputer center (HPC) of KU for supporting in part through computational facility. NPA of the central department of Physics (CDP), T.U. is acknowledged for computational resources**.**

Editor's Note: This manuscript was submitted to Association of Nepali Physicists in America (ANPA) Conference 2020 for publication in special issue of Journal of Nepal Physical Society.

REFERENCES

[1] Imada, M.; Fujimori, A.; & Tokura, Y. Metal-insulator transitions. *Reviews of modern physics*, **70**(4): 1039 (1998).

[2] Morosan, E.; Natelson, D.; Nevidomskyy, A. H.; & Si, Q. Strongly correlated materials. *Advanced Materials*, **24**(36): 4896-4923 (2012).

[3] Nekrasov, I. A.; Keller, G.; Kondakov, D. E.; Kozhevnikov, A. V.; Pruschke, T.; Held, K.; & Anisimov, V. I. Comparative study of correlation effects in $CaVO_3$ and $SrVO_3$. Physical Review B, **72**(15): 155106 (2005).

[4] Piskunov, S.; Heifets, E.; Eglitis, R. I.; & Borstel, G. Bulk properties and electronic structure of $SrTiO_3$, $BaTiO_3$, $PbTiO_3$ perovskites: an ab initio HF/DFTstudy. *Computational Materials Science*, **29**(2): 165-178 (2004).

[5] Son, J.; Rajan, S.; Stemmer, S.; & James Allen, S. A heterojunction modulation-doped Mott transistor. *Journal of Applied Physics*, **110**(8): 084503 (2011).

[6] Makino, H.; Inoue, I. H.; Rozenberg, M. J.; Aiura, Y.; Hase, I.; & Onari, S. Band-width control in a perovskite-type $3d^1$ correlated metal $Ca_{1-x}Sr_xVO_3$. II. Optical spectroscopy investigation. *arXiv preprint cond-mat/9801086* (1998).

[7] Inoue, I. H.; Morikawa, K.; Fukuchi, H.; Tsujii, T.; Iga, F.; & Nishihara, Y. Metal-Insulator Transition in Nearly Stoichiometric $CaVO_3$. *Japanese Journal of Applied Physics*, **32**(S3): 451 (1993).

[8] Rozenberg, M. J.; Inoue, I. H.; Makino, H.; Iga, F.; & Nishihara, Y. Low Frequency Spectroscopy of the Correlated Metallic System $Ca_x Sr_{1-x}VO_3$. *Physical review letters*, **76**(25): 4781 (1996).

[9] Maiti, K.; Sarma, D. D.; Rozenberg, M. J.; Inoue, I. H.; Makino, H.; Goto, O.; & Cimino, R. Electronic structure of $Ca_{1-x}Sr_xVO_3$: A tale of two energy scales. *EPL (Europhysics Letters)*, **55**(2): 246 (2001).

[10] Pavarini, E.; Yamasaki, A.; Nuss, J.; & Andersen, O. K. How chemistry controls electron localization in $3d^1$ perovskites: a Wannier-function study. *New Journal of Physics*, **7**(1): 188 (2005).

[11] Sondhi, S. L.; Girvin, S. M.; Carini, J. P.; & Shahar, D. Continuous quantum phase transitions. *Reviews of modern physics*, **69**(1): 315 (1997).

[12] Si, Q.; Rabello, S.; Ingersent, K.; & Smith, J. L. Locally critical quantum phase transitions in strongly correlated metals. *Nature*, **413**(6858): 804-808 (2001).

[13] Mott, N. F. Reviews of Modern Physics, **40**: 677-683 (1968).

[14] Pickett, M. D.; Medeiros-Ribeiro, G.; & Williams, R. S. A scalable neuristor built with Mott memristors. *Nature materials*, **12**(2): 114-117 (2013).

[15] Sangwan, V. K.; Jariwala, D.; Kim, I. S.; Chen, K. S.; Marks, T. J.; Lauhon, L. J.; & Hersam, M. C. Gate-tunable memristive phenomena mediated by grain boundaries in single-layer MoS_2. *Nature nanotechnology*, **10**(5): 403-406 (2015).

[16] Kravtsov, K.; Fok, M. P.; Rosenbluth, D.; & Prucnal, P. R. Ultrafast all-optical implementation of a leaky integrate-and-fire neuron. *Optics*

express, **19**(3): 2133-2147(2011).

[17] Kurenkov, A.; Dutta Gupta, S.; Zhang, C.; Fukami, S.; Horio, Y.; & Ohno, H. Artificial neuron and synapse realized in an antiferromagnet/ferromagnet heterostructure using dynamics of spin–orbit torque switching. *Advanced Materials*, **31**(23): 1900636 (2019).

[18] Saeed, Y. *Tuning the Transport Properties of Layered Materials for Thermoelectric Applications using First-Principles Calculations* (Doctoral dissertation) (2014).

[19] Kaphle, G. C.; Ganguly, S.; Banerjee, R.; Khanal, R.; & Mookerjee, A. "A study of magnetism in disordered Pt-Mn, Pd-Mn and Ni-Mn alloys: an augmented space recursion approach. Journal of Physics Condensed Matter, **24**(29): 295501, (2012).

[20] Sholl, D.; & Steckel, J. A. *Density functional theory: a practical introduction*. John Wiley & Sons (2011).

[21] Martin, R. M. *Electronic structure: basic theory and practical methods*. Cambridge university press (2004).

[22] Adewale, A. A., et al. "Thermoelectric Transparent Properties of $SrTiO_3$ Doped with Pm." Solid State Phenomena, *Trans Tech Publications*, **280** (2018).

[23] Anderson, P. W. Localized magnetic states in metals. *Physical Review*, **124**(1): 41 (1961).

[24] Hubbard, J. Electron Correlations in Narrow Energy Bands, Proc. Roy. Soc. A 276, 238 (1963).

[25] Lancaster, T.; & Blundell, S. J. *Quantum field theory for the gifted amateur*. OUP Oxford (2014).

[26] Skilling, J. (Ed.). *Maximum Entropy and Bayesian Methods: Cambridge, England, 1988*. Springer Science & Business Media, **36** (2013).

[27] White, S. R.; Scalapino, D. J.; Sugar, R. L.; & Bickers, N. E. Monte Carlo calculation of dynamical properties of the two-dimensional Hubbard model. *Physical review letters*, **63**(14): 1523(1989).

[28] Sondhi, S. L.; Girvin, S. M.; Carini, J. P.; & Shahar, D. Continuous quantum phase transitions. *Reviews of modern physics*, **69**(1): 315(1997).

[29] Pavarini, E.; Koch, E.; Vollhardt, D.; & Lichtenstein, A. (Eds.). Dmft at 25: Infinite dimensions: Lecture notes of the autumn school on correlated electron. *Forschungszentrum Jülich*, **4** (2014).

[30] Schwarz, K.; and Peter B. "Solid state calculations using WIEN2k." Computational Materials Science, **28**(2): 259 (2003).

[31] Kaphle, G. C.; Adhikari, N.; & Mookerjee, A. Study of Spin Glass Behavior in Disordered $Pt_x Mn_{1-x}$ Alloys: An Augmented Space Recursion Approach. *Advanced Science Letters*, **21**(9): (2015).

[32] Kohn, W.; & Sham, L. J. Self-consistent equations including exchange and correlation effects. *Physical review*, **140** (4A): A1133 (1965).

[33] Held, K.; Andersen, O. K.; Feldbacher, M.; Yamasaki, A.; & Yang, Y. F. Bandstructure meets many-body theory: the LDA+ DMFT method. *Journal of Physics: Condensed Matter*, **20**(6): 064202 (2008).

[34] Inoue, I. H.; Hase, I.; Aiura, Y.; Fujimori, A.; Haruyama, Y.; Maruyama, T.; & Nishihara, Y. Systematic Development of the Spectral Function in the $3d^1$ Mott-Hubbard System $Ca_{1-x} Sr_xVO_3$. *Physical review letters*, **74**(13): 2539 (1995).

[35] Pavarini, E.; Yamasaki, A.; Nuss, J.; & Andersen, O. K. How chemistry controls electron localization in 3d1 perovskites: a Wannier-function study. *New Journal of Physics*, **7**(1): 188 (2005).

[36] Makino, H.; Inoue, I. H.; Rozenberg, M. J.; Iga, F.; Aiura, Y.; & Onari, S. Optical spectra of the correlated metallic system $Ca_{1-x}Sr_xVO_3$. *Physica B: Condensed Matter*, **237**: 56-58 (1997).

[37] Makino, H.; Inoue, I. H.; Rozenberg, M. J.; Hase, I.; Aiura, Y.; & Onari, S. Bandwidth control in a perovskite-type 3 d 1-correlated metal $Ca_{1-x} Sr_xVO_3$. II. Optical spectroscopy. *Physical Review B*, **58**(8): 4384 (1998).

[38] Sekiyama, A.; Fujiwara, H.; Imada, S.; Suga, S.; Eisaki, H.; Uchida, S. I.; & Keller, G. Mutual Experimental and Theoretical Validation of Bulk Photoemission Spectra of $Sr_{1-x}Ca_xVO_3$. *Physical review letters*, **93**(15): 156402 (2004).

[39] Liebsch, A. Surface versus Bulk Coulomb Correlations in Photoemission Spectra of $SrVO_3$ and $CaVO_3$. *Physical review letters*, **90**(9): 096401 (2003).

[40] Inoue, I. H.; Bergemann, C.; Hase, I.; & Julian, S. R. Fermi Surface of $3d^1$ Perovskite $CaVO_3$ near the Mott Transition. *Physical review letters*, **88**(23): 236403 (2002).

[41] Bocquet, A. E.; Mizokawa, T.; Morikawa, K.; Fujimori, A.; Barman, S. R.; Maiti, K., & Onoda, M. Electronic structure of early 3d-transition-metal oxides by analysis of the 2p core-level photoemission spectra. *Physical Review B*, **53**(3): 1161 (1996).

[42] Eguchi, R.; Kiss, T.; Tsuda, S.; Shimojima, T.; Mizokami, T.; Yokoya, T.; & Watanabe, S. Bulk- and surface-sensitive high-resolution photoemission study of two Mott-Hubbard systems: $SrVO_3$ and $CaVO_3$. *Physical review letters*, **96**(7): 076402 (2006).

[43] Mossanek, R. J. O.; Abbate, M.; Yoshida, T.;

Fujimori, A.; Yoshida, Y.; Shirakawa, N.; & Vicentin, F. C. Evolution of the spectral weight in the Mott-Hubbard series $SrVO_3$-$CaVO_3$-$LaVO_3$-YVO_3. *Physical Review B*, **78**(7): 075103 (2008).

[44] Mete, E. *Electronic properties of transition metal oxides* (Doctoral dissertation, METU) (2003).

[45] Mizutani, U. *Introduction to the electron theory of metals*. Cambridge University Press (2001).

[46] Sekiyama, A.; Fujiwara, H.; Imada, S.; Suga, S.; Eisaki, H.; Uchida, S. I.; & Keller, G. Mutual Experimental and Theoretical Validation of Bulk Photoemission Spectra of $Sr_{1-x}Ca_xVO_3$. *Physical review letters*, **93**(15): 156402 (2004).

[47] Hussain, M. I.; Khalil, R. A.; Hussain, F.; Imran, M.; Rana, A. M.; & Kim, S. Investigations of structural, electronic and optical properties of TM-GaO3 (TM= Sc, Ti, Ag) perovskite oxides for optoelectronic applications: a first principles study. *Materials Research Express*, **7**(1): 015906 (2020).

[48] Joshy, L. D.; Rai, R. K.; & Kaphle, G. C. Study of Electronic Properties and Chemical Bonding of Perovskite $LaFeO_3$. *International Technology and Science Publication*, **3**(1): 28-35 (2019).

[49] Paudyal, D.; Pecharsky, V. K.; Gschneidner Jr., K. A.; & Harmon, B. N. Electron correlation effects on the magnetostructural transition and magnetocaloric effect in $Gd_5Si_2Ge_2$. *Physical Review B*, **73**(14): 144406 (2006).

[50] Veit, M. J., et al. "Three-dimensional character of the Fermi surface in ultrathin $LaTiO_3/SrTiO_3$ heterostructures." Physical Review B **99**(11): 115126 (2019).

[51] Kachhava, C. M. Solid state physics. McGraw-Hill Publishing Company Ltd. (1992).

[52] Held, K.; Nekrasov, I. A.; Keller, G.; Eyert, V.; Blümer, N.; McMahan, A. K.; & Vollhardt, D. Realistic investigations of correlated electron systems with LDA+ DMFT. *Physica status solidi (b)*, **243**(11): 2599 (2006).

[53] Gull, E. *Continuous-time quantum Monte Carlo algorithms for fermions* (Doctoral dissertation, ETH Zurich) (2008).

[54] Haule, Kristjan. "Quantum Monte Carlo impurity solver for cluster dynamical mean-field theory and electronic structure calculations with adjustable cluster base." Physical Review B, **75**(15):155113 (2007).

[55] Rubtsov, A. N.; Savkin, V. V.; & Lichtenstein, A. I. Continuous-time quantum Monte Carlo method for fermions. *Physical Review B*, **72**(3): 035122 (2005).

[56] Bergeron, D. and Tremblay, A. M. S. Phys. Rev. E 94, 023303 (2016).

[57] Van Campenhout, J.; & Cover, T. Maximum entropy and conditional probability. *IEEE Transactions on Information Theory*, **27**(4): 483-489 (1981).

[58] Levy, R.; LeBlanc, J. P. F.; & Gull, E. Implementation of the maximum entropy for analytic continuation. *Computer Physics Communications*, **215**: 149-155 (2017).

[59] Madsen, G. K.; Carrete, J.; & Verstraete, M. J. $BoltzTraP_2$, a program for interpolating band structures and calculating semi-classical transport coefficients. *Computer Physics Communications*, **231**: 140-145 (2018).

[60] Liu, W.; Zhang, Q.; Yin, K.; Chi, H.; Zhou, X.; Tang, X.; & Uher, C. High figure of merit and thermoelectric properties of Bi-doped $Mg_2Si_{0.4}Sn_{0.6}$ solid solutions. *Journal of Solid State Chemistry*, **203**: 333-339 (2013).

[61] Ge, Z. H.; Zhao, L. D.; Wu, D.; Liu, X.; Zhang, B. P.; Li, J. F.; & He, J. Low-cost, abundant binary sulfides as promising thermoelectric materials. *Materials Today*, **19**(4): 227-239 (2016).

[62] LaLonde, A. D.; Pei, Y.; Wang, H.; & Snyder, G. J. Lead telluride alloy thermoelectrics. *Materials today*, **14**(11): 526-532 (2011).

[63] Sclauzero, G.; Dymkowski, K.; & Ederer, C. Tuning the metal-insulator transition in d 1 and d 2 perovskites by epitaxial strain: A first-principles-based study. *Physical Review B*, **94**(24): 245109 (2016).

[64] Vaz, C. A. F.; Hoffman, J.; Segal, Y.; Reiner, J. W.; Grober, R. D.; Zhang, Z.; & Walker, F. J. Origin of the magnetoelectric coupling effect in $Pb(Zr_{0.2}Ti_{0.8})O_3/La_{0.8}Sr_{0.2}MnO_3$ multiferroic heterostructures. *Physical review letters*, **104**(12): 127202(2010).

[65] Anisimov, V. I.; Kondakov, D. E.; Kozhevnikov, A. V.; Nekrasov, I. A.; Pchelkina, Z. V.; Allen, J. W.; & Sekiyama, A. Full orbital calculation scheme for materials with strongly correlated electrons. *Physical Review B*, **71**(12): 125119 (2005).

[66] Nekrasov, I. A.; Held, K.; Blümer, N.; Poteryaev, A. I.; Anisimov, V. I.; & Vollhardt, D. Calculation of photoemission spectra of the doped Mott insulator using LDA+ DMFT (QMC). *The European Physical Journal B-Condensed Matter and Complex Systems*, **18**(1): 55-61 (2000).

[67] Fujimori, A.; Hase, I.; Nakamura, M.; Namatame, H.; Fujishima, Y.; Tokura, Y.; & Strebel, O. Doping-induced changes in the electronic structure of $La_xSr_{1-x}TiO_3$: Limitation of the one-electron rigid-band model and the Hubbard model. *Physical Review B*, **46**(15): 9841 (1992).

[68] Solovyev, I.; Hamada, N.; & Terakura, K. t_{2g} versus all 3d localization in $LaMO_3$ perovskites (M= Ti–Cu): First-principles study. *Physical Review B*, **53**(11): 7158 (1996).

[69] Huai-Hong, G.; Teng, Y.; Peng, T.; & Zhi-Dong, Z. Theoretical study of thermoelectric properties of MoS_2. *Chinese Physics B*, **23**(1): 017201 (2013).

[70] Yakoubi, A.; Baraka, O.; & Bouhafs, B. Structural and electronic properties of the Laves phase based on rare earth type BaM_2 (M= Rh, Pd,Pt). *Results in Physics*, **2**: 58-65 (2012).

[71] Antonov, V.; Harmon, B.; & Yaresko, A. *Electronic structure and magneto-optical properties of solids*. Springer Science & Business Med [69] Sachdev, S. Quantum criticality: competing ground states in low dimensions. *Science*, **288** (5465): 475-480 (2000).

[72] Jaiswal, A.; Roy, S.; Srinivasan, G.; & Roy, K. Proposal for a leaky-integrate-fire spiking neuron based on magnetoelectric switching of ferromagnets. *IEEE Transactions on Electron Devices*, **64**(4): 1818-1824 (2017).

[73] Zhong, Z.; Wallerberger, M.; Tomczak, J. M.; Taranto, C.; Parragh, N.; Toschi, A.; & Held, K. Electronics with correlated oxides: $SrVO_3/SrTiO_3$ as a Mott transistor. *Physical review letters*, **114**(24): 246401 (2015).

[74] Wang, L.; Li, Y.; Bera, A.; Ma, C.; Jin, F.; Yuan, K.; & Prellier, W. Device performance of the mott insulator $LaVO_3$ as a photovoltaic material. *Physical Review Applied*, **3**(6): 064015 (2015).

[75] Zubko, Pavlo, et al. "Interface physics in complex oxide heterostructures." *Annu. Rev. Condens. Matter Phys.* **2**(1): 141 (2011).

[76] Tokura, Y. Critical features of colossal magnetoresistive manganites. Rep. Prog. Phys., **69**(3): 797 (2006).

[77] Scafetta, Mark Dominic. *Optical Properties and Electronic Structure of non-d^0 Perovskite Oxide Epitaxial Films and Heterostructures*. Drexel University (2015).

[78] Poizot, P. L. S. G.; Laruelle, S.; Grugeon, S.; Dupont, L.; & Tarascon, J. M. Nano-sized transition-metal oxides as negative-electrode materials for lithium-ion batteries. *Nature*, **407**(6803): 496-499 (2000).

[79] Ghimire, M. P.; Kaphle, G. C.; & Thapa, R. K. Electronic and magnetic properties of double perovskites Nd_2MgIrO_6. *Journal of Nepal Physical Society*, **3**(1): 50-54 (2015).

[80] Pandey, S.; Kaphle, G. C.; & Adhikari, N. P. Electronic structure and magnetic properties of bulk elements (Fe and Pd) and ordered binary alloys (FePd and Fe_3Pd): TB-LMTO-ASA. *BIBECHANA*, **11**: 60-69 (2014).

[81] Yadav, D. K.; Bhandari, S. R.; Belbase, B. P.; Kaphle, G. C.; Rai, D. P.; & Ghimire, M. P. Effects of electron-correlation, spin-orbit coupling, and modified Becke-Johnson potential in double perovskites SrLaBB′ O6 (B= Ni, Fe; B′= Os, Ru). *Computational Materials Science*, **170**: 109168 (2019).

[82] Nepal, S.; Dhakal, R.; & Galanakis, I. Ab initio study of the half-metallic full-Heusler compounds Co_2ZAl [Z= Sc, Ti, V, Cr, Mn, Fe]; the role of electronic correlations. *Materials Today Communications*, **25**: 101498 (2020).

[83] Abu-Mostafa, Y. S.; & Psaltis, D. Optical neural computers. *Scientific American*, **256**(3): 88-95 (1987).

A Continuous Time Quantum Monte Carlo as an Impurity Solver for Strongly Correlated System

R. K. Rai, R. B. Ray, G. C. Kaphle, and O. P. Niraula

Journal of Nepal Physical Society
Volume 7, No 3, 2021
(Special Issue: ANPA Conference, 2021)
ISSN: 2392-473X (Print), 2738-9537 (Online)

JNPS, **7** (3), 14-26 (2021)
DOI: http://doi.org/10.3126/jnphyssoc.v7i3.42185

Published by: Nepal Physical Society
P.O. Box: 2934
Tri-Chandra Campus
Kathmandu, Nepal
Email: npseditor@gmail.com

ANPA Conference 2021
ISSN:2392-473X (Print), 2738-9537 (Online)

Review Article ©Nepal Physical Society
DOI:http://doi.org/10.3126/jnphyssoc.v7i3.42185

A Continuous Time Quantum Monte Carlo as an Impurity Solver for Strongly Correlated System

R. K. Rai,[1, a)] R. B. Ray,[2] G. C. Kaphle,[3, b)] and O. P. Niraula[3]

[1)]*Patan Multiple Campus, Tribhuvan University, Patandhoka, Lalipur, Nepal*
[2)]*Amrit Campus, Tribhuvan University, Lainchaur, Kathmandu, Nepal*
[3)]*Central Department of Physics, Tribhuvan University, Kirtipur, Kathmandu, Nepal*

[a)]*Corresponding Email: rairajk@gmail.com*
[b)]*Corresponding Email: gck223@gmail.com*

Abstract. We assess the continuous-time quantum Monte Carlo (CT-QMC) technique with hybridization expansion for solving the electronic structure of the strongly correlated system $La_xSr_{1-x}VO_3$. The impurity solver method implemented here shows the fair agreement with the other available Monte Carlo techniques. From the study, it is found that the CT-QMC technique clearly distinguishes metallic phase, quasiparticle phase and insulating phases of the system depending upon the strength of the correlation. In case of $La_{0.33}Sr_{0.67}VO_3$ system the metal-insulator transition is found to be at U = 4.5 eV for $\beta = 6(eV)^{-1}$. The value of U depends with the value of β, and also the value of Hund's coupling (J) and bandwidth (W). This technique allows the particle to exchange with the reservoir of the particles and the impurity sites, which is accounted numerically to treat the temporal fluctuation of the fermionic systems termed as dynamical mean field theory (DMFT). This theory is used to explain the phenomena of Mott-Hubbard metal insulator transition of the materials which are applicable for designing the Mottronics, Neuromorphic computing, Quantum computing and resistive memory devices.

Received: 14 August 2021; **Revised**: 30 October 2021; **Accepted**: 15 November 2021

Keywords: CT-QMC, DFT, DMFT, MIT, Neuromorphic Computing.

INTRODUCTION

The strongly correlated systems, having Mott-Hubbard metal-insulator transition (MIT), are of great interest because of their application in Mottronics, Neuromorphic computing, Quantum computing and volume resistive memory devices [1]. The properties of such materials are depending on tunable parameters like Coulomb interaction (U), thermodynamic parameter (β), Hund's coupling (J), and bandwidth (W) [2]. In particular the MIT phenomena is explained through dynamical mean-field theory in addition to the density functional theory (DFT), which accounts the temporal fluctuations in many-body system at which spatial fluctuation is negligible [3]. Here, we describe CT-QMC technique with hybridization expansion as the impurity solver of DMFT equation to study MIT for strongly correlated system, $La_xSr_{1-x}VO_3$. The strongly correlated systems have incoherent electronic property, which is mainly due to the electron-electron interaction on the lattice sites. MIT mainly causes due to charge and spin degree of freedom, and orbital orderings. These are the parameters, which also explain the nature of Anderson localization, Jahn-Teller distortion and the unpredictable incoherent metallic behaviours near the Mott metal-insulator phase transition. The orbital degree of freedom essentially important to understand the nature of d-orbital ordering associated to behavior of MIT [2, 3, 4]. Controlling the parameters U, J and β through filling control, bandwidth control and dimensionality control can tune these properties. For this, one can adopt the DFT plus the DMFT approach as well as experimental approach [5]. Kim, M. et al. used DMFT combining with ab initio density functional methods with the generalized gradient approximation (GGA) to account the itinerancy and localization of electrons [6]. Streltsov et al. also used the DMFT to predict the Hubbard satellite, which splits the conduction band of a metal and hence explain the Mott insulator [7]. Rubtsov et al. developed CT-QMC algorithm to study the interactions and superexchange of fermions, which is successfully implemented in multi-band model on non-local spin-flip terms

[8]. Dirks et al. implemented the CT-QMC to obtain the precise and unbiased imaginary time data and the corresponding physical observables are obtained through analytic continuation using Maximum entropy model [9]. Chatterjee et al. explain how amplitudes of Friedel oscillations and the screening charge decrease with increasing the interaction, which is finally ceases in the Mott insulator regime with finite residual screening charges using CT-QMC [10]. Similarly, this technique used to study the realistic calculation of strongly correlated materials having d- and f- electrons by using a set of SU(2)-symmetric Kanamori Hamiltonian by Parragh et al. [11]. Kowalski et al. developed CT-QMC hybridization algorithm to study the splitting of d-orbitals and local Coulomb interactions, which is extremely useful to explain the Mott insulating behavior [12]. Experimentally, the angle resolved photoemission spectroscopy (ARPES) was used to probe the presence of Hubbard bands [13]. Here, in this communication we review the theoretical background of the solution of DMFT equation implementing CT-QMC technique with hybridization expansion to explain the phenomena of Mott-Hubbard kinetics in superstructure of strongly correlated systems $La_xSr_{1-x}VO_3$ [14, 15, 16, 17, 18, 19]. The process of implementation of reconstructing data from CT-QMC through maximum entropy model, which is useful to predict Mott phase transition of TMOs, has been discussed [20, 21, 22, 23, 24, 25, 26, 27]. We believe present study helps to understand the properties of field driven MIT which is applicable for designing the Mottronics, Neuromorphic computing, Quantum computing, other resistive memory devices [28, 29, 30, 31, 32, 33, 34].

METHODOLOGY AND COMPUTATIONAL DETAILS

We discuss the theoretical background of Monte Carlo technique, the kernel of the CT-QMC through which computer generates a series of pseudo random numbers. These pseudo random numbers are then used to either simulate naturally random processes, such as electronic fluctuation in lattice sites [35, 36]. The explanations of theory related to CT-QMC for estimating Mott-Hubbard MIT phase and implementation of technique to the $La_xSr_{1-x}VO_3$ has been discussed. Further computational detail and codes used for the generation of data were also be discussed. The Mott-Hubbard MIT in a solid, in fact arise due to quasi-particles behaviours of electrons, which can be characterized by (a) the presence or absence of spontaneously broken symmetry (b) the gapped or gapless low energy neutral particle excitations (c) the presence or absence of topological phase transitions [37]. The Mott transition problem of strongly correlated electronic system is directly addressed by the DMFT framework for such materials [38]. The single site Hubbard Hamiltonian for representing an interacting system is,

$$H = -t\sum_{ij,\sigma} c^{\dagger}_{i\sigma}c_{j\sigma} + U\sum_{i} n_{i\uparrow}n_{i\downarrow}, \tag{1}$$

The non-local part of interaction is,

$$H_{non-local} = -t\sum_{ij,\sigma}\left(c^{\dagger}_{i\sigma}c_{j\sigma} + c^{\dagger}_{j\sigma}c_{i\sigma}\right) \tag{2}$$

And the local part of interaction on site i is

$$H_{local} = U\sum_{i} c^{\dagger}_{i\uparrow}c_{i\uparrow}c^{\dagger}_{i\downarrow}c_{i\downarrow} \tag{3}$$

Considering the fermionic cases on site i, we must realize that the hopping term does not conserve the particles number at the site. The single-site lattice model (Hubbard model) is then mapped onto a self-consistent quantum impurity model (Anderson impurity model) representing the interaction on real crystal lattice site i as in Fig. 1. The impurity Hamiltonian is the basis of DMFT in which the various kinds of impurity solvers including CT-QMC method are implemented [39].

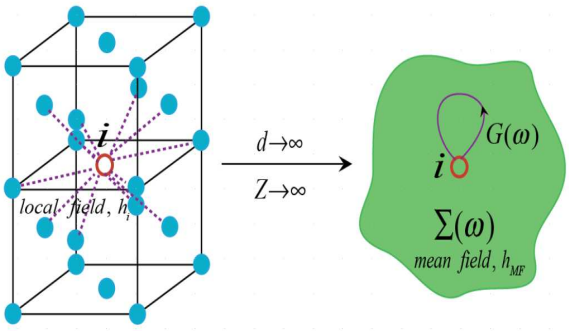

FIGURE 1. (Color online) The local field interaction for a fcc lattice. In the limit of infinite dimension $d \to \infty$ or $Z \to \infty$, the local field h_i surrounding a single atom can be described by an effective field h_{MF} with no spatial but only the fluctuations of the electronic system [40]

The Anderson impurity model:

The Anderson impurity Hamiltonian representing the many-body system is,

$$\begin{aligned}\mathscr{H} &= \sum_{\sigma=\uparrow,\downarrow}\varepsilon_0(k)\, a^{\dagger}_{\sigma}a_{\sigma} + U n_{a\uparrow}n_{a\downarrow} \\ &+ \sum_{k,\sigma}[V_{k,\sigma}(k)c^{\dagger}_{k,\sigma}c_{\sigma} + h.c.] \\ &+ \sum_{k,\sigma}\varepsilon_{k,\sigma}(k)c^{\dagger}_{k,\sigma}c_{k,\sigma}\end{aligned} \tag{4}$$

Where, $\varepsilon_0(k)$ is the energy level of the impurity, $a^{\dagger}_{\sigma}$ (corr. a_{σ}) is the creation (corr. annihilation) operator for an electron with spin σ on the impurity, $\varepsilon_{k,\sigma}(k)$ is the energy spectrum of the bath $c^{\dagger}_{\sigma}$ (corr. c_{σ}) is the creation (corr. annihilation) operator for an electron with spin σ and momentum k in the bath and $V_{k,\sigma}(k)$ is the hybridization parameter(coupling constant) [41]. The partition function associated with the impurity and its fermionic bath is,

$$Z = \mathrm{Tr}[exp - \beta \mathscr{H}] \tag{5}$$

A very successful way to analyze the system using the numerical technique with the imaginary time formalism, the partition function is the path integral over Grassman variables [42] $a^{\dagger}_{\sigma}$ and a_{σ} expressed as,

$$Z_{=} \int D\left[a^{\dagger}_{\sigma}, a_{\sigma}\right] \exp(-S_{\mathrm{eff}}) \tag{6}$$

Where, S_{eff} is the effective action associated with the lattice Hubbard model Hamiltonian, which is solved by mapping onto a single-site impurity Anderson model Hamiltonian Eq. (4).

$$\begin{aligned} S_{\mathrm{eff}} = &-\sum_{\sigma} \int_0^{\beta} d\tau d\tau' a^{\dagger}_{\sigma}(\tau) \mathscr{G}^{-1}_{0\sigma}(\tau - \tau') a_{\sigma}(\tau') \\ &+ \int_0^{\beta} d\tau U n_{a\uparrow}(\tau) n_{a\downarrow}(\tau) \end{aligned} \tag{7}$$

The non-interacting (U = 0) Green's function

$$\mathscr{G}^{-1}_{0\sigma}(i\omega_{\nu}) = i\omega_{\nu} - \varepsilon_0 - \Delta_{\sigma}(i\omega_{\nu}) \tag{8}$$

According to Matsubara, the hybridization part of interaction is,

$$\Delta_{\sigma}(i\omega_{\nu}) = \sum_{k} \frac{|V_{k\sigma(k)|^2}}{i\omega_{\nu} - \varepsilon_{k\sigma}(k)} \tag{9}$$

Which describes the transition between the bath and the various orbitals [43].

Evaluating the partition function with Monte Carlo sampling:

The varieties of quantum Monte Carlo (QMC) methods are the most useful tools for the numerical study of many-body systems with strong correlated fermionic system [44]. Here, we are focusing our discussion on the CT-QMC algorithm for fermions. This algorithm is a family of stochastic process for solving the Anderson impurity model at finite temperature. These methods consist of a Hamiltonian involving a finite number of states and hybridization process, which allows particle exchange with the fermionic bath of these particles. They are important both in their own right and as a crucial ingredient in the dynamical mean field method of approximating the properties of interacting fermions on an infinite dimensional lattice sites [45]. The principle behind all of these algorithms is the same, which is stemming from earlier work on diagrammatic Monte Carlo [46]. In all cases, we need to implement the Monte Carlo Integration, in which the integral of a function can be converted to a discrete sum of the form,

$$\int_a^b f(x)dx = \frac{b-a}{N} \sum_{i=1}^{N} f\left(a + i\frac{b-a}{N}\right) + O\left(\frac{1}{N}\right) \tag{10}$$

There are other higher order numerical integrators such as Trapezoidal rule, Simpson rule etc. The Monte Carlo technique constitutes the sampling, errors, Markov chains and Metropolis-Hastings arguments for obtaining the result [47]. In fact, the Monte Carlo is a method computes the sums for a probability distribution, p(x) for a sampling function f(x) of the given configuration space C [40].

$$\sum_{x} p(x) f(x),$$

where, $p(x) > 0$,

$$\sum_{x} p(x) = 1 \tag{11}$$

The variable, $x = (\tau, \sigma, ...)$ represents the set of variables under study.

Continuous time Partition Function Expansions in Configuration Space:

The continuous-time partition function expansions for Monte-Carlo sampling with a typical infinite series on imaginary time parameters is,

$$Z = \sum_{n=0}^{\infty} \iiint_0^{\beta} d\tau_1 .. d\tau_n p(\tau_1, \tau_2, ..., \tau_n) \tag{12}$$

This is the partition function representing the sum of the expansion orders from zero to infinity over n slices of imaginary time steps $\tau_1, ...\tau_n$, which is integrated over the probability densities, $p(\tau_1, ...\tau_n)$ from $\tau = 0$ to β, imaginary time intervals [48]. We need to sample terms with the weight, which is associated with the infinite configurations C (moves in the phase space) of this integral, contributing to the partition function. As for examples, let us start to write down some of the lowest orders of the integral explicitly. The first order calculation of the partition function of single parameter is,

$$Z_1 = \int_0^\beta d\tau_1 p(\tau_1) \tag{13}$$

The integrand is described uniquely by a set of imaginary time $\{(\tau_1)\}$, so that we can sample Eq. (12) up to first order using Monte Carlo technique [49], which generates a uniformly distributed random numbers of imaginary time, τ_1 in the interval $(0, \beta)$, we may write,

$$Z_1 = \lim_{N\to\infty} \frac{1}{N} \sum_0^\beta p(\tau_j) \tag{14}$$

Using analogy, the second order calculation is obtained by the another set of imaginary time $\{(\tau_1, \tau_2)\}$ and generating uniformly distributed value pairs (τ_1, τ_2) in the interval $(0, \beta)$, we may write,

$$Z_1 = \lim_{N\to\infty} \frac{1}{N} \sum_0^\beta p(\tau_j, \tau_2) \tag{15}$$

We need to sample the integral up to some finite order n max (say) and then truncate it. For sampling, the various terms, we employ Metropolis' algorithm [50] to accept or reject the possible transitions. The number of Monte Carlo samples may have only the Monte Carlo error, which scales as $\frac{1}{\sqrt{N}}$ with the samples [51]].

Let us define all the possible orders of configuration space C as,

C ={ {..} ,$\{\tau_1\}$,$\{\tau_1, \tau_2\}$,...,$\{\tau_1, ..., \tau_n\}$ }

Which is the set of continuous imaginary time variables τ_j. We should consider that the configurations are time-ordered, i.e.$\tau_1 < \tau_2 < ... < \tau_n$ Each configuration contributes some value to the whole partition function. To avoid the sign problems, the expansion coefficients above are taken to be positive [52] otherwise sampling will be difficult.

Markov Chain Transition (move):

We use the Markov chain Monte Carlo method for sampling the configurations C that contributes to the value of the partition function Z. Assuming, x_0 be the initial configuration (or zeroth order configuration), we need to proceed with random walk from a present configuration, x to a new one $y(x_j)$ in phase space as,

$$x_0 \to x_1 \to x_2 \to ... \to x_{n+1} .... \tag{16}$$

We have implemented the diagrammatic Monte Carlo codes by raising of the order for updating the transition, $x_n \to x_{n+1}$ i.e. the insertion of an additional vertex (τ_j) (adding link), or, lowering of the order, i.e. removal of an additional vertex (τ_1) (removal of link), or a local change on the same site with the same order $(\tau_j \to \tau'_j)$, like a spin-flip or the change of a τ [53] as in Fig. 2. For summing up all the probabilities, the Markov chain must reach a stationary distribution. We must make sure that the system be thermalized as well as the successive points in the Markov chain are clearly correlated. The autocorrelation effects must be taken into account while computing the Monte Carlo statistical errors [45]. To create a Markov chain of diagrams (moves) by assuming any two "moves", we can purpose the following moves: (i) Insertion of a link (anti-link): we choose a random imaginary time and insert a vertex with a spin randomly up or down with the imaginary time step, τ_i. (ii) Removal of a link: choosing a random vertex of imaginary time step τ_i and remove it.

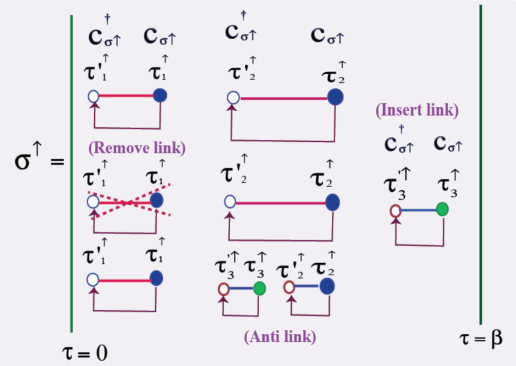

FIGURE 2. (Color online) Insertion and removal of vertices (interactions) update are illustrated in the above diagrams. The sampling process samples configurations according to their contribution to the partition function [54]

Starting from an arbitrary distribution of Markov chain process will converge exponentially to a stationary distribution p(x) if two the following two conditions are satisfied: (i) Ergodicity: any configuration x is reachable from any other configuration y in a finite number of Markov steps. That is to say,

$\forall xy \exists n : (W^n)_{xy} \neq 0$

(ii) Detailed balance: The probability W_{xy} of transitioning from configuration x with probability density p(x) to configuration y with weight p(y) satisfies the detailed balance condition,

$$\int_c W_{xy} p(x) = p(y) \tag{17}$$

This probability needs to fulfill the detailed balance condition to perform our updates using the Metropolis algorithm. Assuming that we have a configuration $x = \{(\tau_1), ..., (\tau_n)\}$ and try to insert a time vertex (τ_{n+1}) to obtain a configuration $y = \{(\tau_1), ..., (\tau_n), (\tau_{n+1})\}$, we have to guarantee the detailed balance condition. The

transition probability density $W_{x,y}$ of going from state x to state y is,

$$W_{x,y} = W_{prop}(x \to y) A_{acc}(x \to y) \tag{18}$$

Where, $W_{prop}(x \to y)$ is the proposal probability density and $A_{acc}(x \to y)$ is the acceptance probability density of moving from x to y respectively.

Similarly, the transition probability $W_{y,x}$ of going from state y to x is,

$$W_{y,x} = W_{prop}(y \to x) A_{acc}(y \to x) \tag{19}$$

Furthermore, the proposal probability density $W_{prop}(x \to y)$ of inserting a time vertex (τ_{n+1}) is given by the probability of picking the imaginary time location τ_{n+1}:

$$W_{prop}(x \to y) = \frac{d\tau}{\beta} \tag{20}$$

On the other hand, the proposal probability of removing a time vertex is just the one of selecting that particular vertex out of the n+1 available vertices:

$$W_{prop}(y \to x) = \frac{1}{n+1} \tag{21}$$

Choosing the acceptance probabilities $A_{acc}(x \to y)$ and $A_{acc}(y \to x)$ such that

$$\begin{aligned} \frac{W_{x,y}}{W_{y,x}} &= \frac{d\tau}{\beta} \frac{n+1}{1} \frac{A_{acc}(x \to y)}{A_{acc}(y \to x)} \\ &= \frac{p(y)}{p(x)} \frac{A_{acc}(x \to y)}{A_{acc}(y \to x)} = \frac{p(y)}{p(x)} \frac{1/(n+1)}{d\tau/\beta} \end{aligned} \tag{22}$$

Applying Metropolis' algorithm to fulfill detailed balance we obtain the acceptance ratio as,

$$\begin{aligned} A_{acc} &= \min\left[1, \frac{p(y) W_{prop}(y \to x)}{p(x) W_{prop}(x \to y)}\right] \\ &= \min\left[1, \frac{1}{n+1} \frac{\beta}{d\tau} \frac{p(y)}{p(x)}\right] \end{aligned} \tag{23}$$

The configuration probability densities ratio p(y)/p(x) is infinitesimally small, the transition rate from configuration x to y remains finite [55]. The partition function is computed through the CT-QMC hybridization algorithm for various configuration with weight $\omega(C)$. From which, we compute the Green's function of imaginary time or frequency.

Hybridization-expansion CT-QMC:

For this calculation, we have to focus on the simplest Anderson impurity model that can easily be generalized as the generic multi-orbital problems. To derive an expansion around the atomic limit, which could be understood as the expansion in the hybridization technique [56]. The effective action as the sum of an "atomic" term having all the local terms and a term with the hybridization to the bath as given by,

$$\begin{aligned} S_{eff} &= S_{loc} + \sum_\sigma \int_0^\beta d\tau d\tau' c_\sigma^\dagger(\tau) \Delta_\sigma(\tau - \tau') d_\sigma(\tau') \\ &= S_{loc} + \sum_\sigma S_{hyb}^\sigma \end{aligned} \tag{24}$$

From Eq.(6), we get,

$$\begin{aligned} Z &= \int D\left[a_\sigma^\dagger, a_\sigma\right] \exp(-S_{loc} + \sum_\sigma S_{hyb}^\sigma) \\ &= \int D\left[a_\sigma^\dagger, a_\sigma\right] \exp(-S_{loc}) \left[pod_\sigma \frac{(-1)^n_\sigma}{n_{\sigma!}} \left(S_{hyb}^\sigma\right)^n\right] \end{aligned} \tag{25}$$

Using the idea of path integral QMC with stochastic series expansion [58], we may write,

$$Z = \sum_{n\uparrow, n\downarrow=0}^\infty \left\langle Tr \prod_\sigma \frac{(-1)^n_\sigma}{n_{\sigma!}} \left(S_{hyb}^\sigma\right)^n \right\rangle_{loc} \tag{26}$$

$$\begin{aligned} Z = \sum_{n\uparrow, n\downarrow=0}^\infty & \int_0^\beta d\tau_1^\sigma ... d\tau_{n\uparrow}^{\prime\sigma} \int_0^\beta d\tau_1^{\sigma'} ... d\tau_{n\downarrow}^{\prime\sigma'} \\ & \prod_\sigma \frac{(-1)^n_\sigma}{n_{\sigma!}} \prod_{i=1}^{n\sigma} \Delta_\sigma\left(\tau_i^\sigma - \tau_i^{\prime\sigma}\right) \end{aligned}$$

$$\times Tr\left[e^{-\beta \mathscr{H}_{loc}} Tr \prod_{i=1}^{n\uparrow} c_\uparrow^\dagger(\tau_i^\sigma) c_\uparrow\left(\tau_i^{\prime\sigma}\right) \prod_{i=1}^{n\sigma'} c_\downarrow^\dagger\left(\tau_i^{\sigma'}\right) c_\downarrow^\dagger\left(\tau_i^{\prime\sigma'}\right)\right] \tag{27}$$

Which is the sum over many continuous variables and the product of hybridization functions times the trace involving spin up and spins down operators.

$$\therefore Z = \int_C \omega(C) \approx \Sigma_C^{MC} sign(\omega C) \tag{28}$$

Where $\omega(C)$ is the weights of configurations C in the limit $N \to \infty$ gives the probability,

$$p(C) = \frac{1}{Z} \omega(C) \tag{29}$$

$$\therefore Z = \frac{1}{Z} \int_C \omega(C) f(C) \sim \frac{1}{Z} \Sigma_C^{MC} f(C) sign(\omega(C)) \tag{30}$$

The weight of the configuration is computed as,

$$\omega(\mathrm{C}) = \mathrm{Tr} \times \mathrm{e}^{-\beta \mathscr{H}_{\mathrm{loc}}} \mathrm{Tr} \prod_{\mathrm{i}=1}^{\mathrm{n}\uparrow} \mathrm{a}_{\uparrow}^{\dagger}\left(\tau_{\mathrm{i}}^{\sigma}\right) \mathrm{a}_{\uparrow}\left(\tau_{\mathrm{i}}^{\prime \sigma}\right) \prod_{i=1}^{n\downarrow} a_{\downarrow}^{\dagger}\left(\tau_{i}^{\sigma^{\prime}}\right) a_{\downarrow}\left(\tau_{i}^{\prime \sigma^{\prime}}\right)$$

$$\times \prod_{\sigma} \frac{(-1)_{\sigma}^{\mathrm{n}}}{\mathrm{n}_{\sigma!}} \prod_{\mathrm{i}=1}^{\mathrm{n}_{\sigma}} \Delta_{\sigma}\left(\tau_{\mathrm{i}}^{\sigma}-\tau_{\mathrm{i}}^{\sigma}\right) \tag{31}$$

Unfortunately, these calculations have alternating signs problems (-ve sign problem) For evaluating the partition function, we start from a imaginary time step diagram and sum of the possible permutations of the fluctuations.

Computing Green's Function from Partition Function:

The impurity Green's function could also be regarded as 8the logarithmic derivative of Z w. r. to the hybridization, $\Delta(\tau)$ as given by,

$$\mathrm{G}_{\sigma}(\tau) = -\frac{1}{\beta} \frac{\delta \log \mathrm{Z}}{\delta \Delta_{\sigma}(-\tau)} \left[\because \mathrm{G}(\tau) = -\frac{\delta \log \mathrm{Z}}{\delta \Delta(\tau)} \right] \tag{32}$$

$$\mathrm{G}_{\uparrow}(\tau) = -\frac{1}{\mathrm{Z}\beta} \int_{\mathrm{C}} \frac{\delta \det \Delta_{\uparrow \mathrm{C}}}{\delta \Delta_{\uparrow}(-\tau)} \times (-1)^{\mathrm{n}\uparrow+\mathrm{n}\downarrow} \det \Delta_{\downarrow \mathrm{C}} \mathrm{TrC} \tag{33}$$

Each configuration give contributions for a discrete set of imaginary times:

$$\mathrm{G}_{\sigma}(\tau) \sim -\frac{1}{\mathrm{Z}\beta} \sum_{\mathrm{C}}^{\mathrm{MC}} \sum_{\mathrm{k,l}} \delta\left(\tau_{\mathrm{k}}^{\sigma}-\tau_{\mathrm{l}}^{\prime \sigma}+\tau\right) \times \left[\Delta_{\sigma \mathrm{C}}^{-1}\right]_{\mathrm{k,l}} \times \mathrm{sign}\left(\omega(\mathrm{C})\right) \tag{34}$$

In fact, these contributions can be computed by considering a very fine imaginary time slices. This creates a high frequency noise in Matsubara frequencies. To compute single particle Green's function in Legendre representation, we consider the single-particle imaginary time Green's function $\mathrm{G}(\tau)$ defined on the interval [0, β] [57, 58]. Expanding $\mathrm{G}(\tau)$ in terms of the Legendre polynomials $\mathrm{P_l(x)}$, Fig.3 (left) which are considered to be the basis for expressing the function defined over an interval [-1, 1] to calculate the imaginary-time Green's function as,

$$\mathrm{G}(\tau) = \sum_{\mathrm{l} \geq 0} \frac{\sqrt{2\mathrm{l}+1}}{\beta} \mathrm{P_l}[\mathrm{x}(\tau)] \mathrm{G_l} \tag{35}$$

Where, $\mathrm{x}(\tau) = \frac{2\tau}{\beta} - 1$ and G_l is the Legendre coefficients that decays very quickly, which may be defined as,

$$\mathrm{G_l} = \sqrt{2\mathrm{l}+1} \int_0^{\beta} \mathrm{d}\tau \mathrm{G}(\tau) \mathrm{P_l}[\mathrm{x}(\tau)] \tag{36}$$

The number of Legendre coefficients considered to be important for the accurate representation of a given observable under consideration and is difficult to infer from looking at the coefficients themselves. Recently, it has been proposed to improve this method by employing the Kernel polynomial method with model independent basis, what is termed as intermediate representation (IR) basis [59]. Truncating the Legendre coefficients that are zero within their error bars can reduce the Matsubara frequency noise. The imaginary part of Green's function of Matsubara frequency vs. Matsubara frequency is shown in Fig.3 (right), which is one of the typical outcomes of this method of calculation.

Green's Functions, Self-Energy and Spectral Function:

The dynamical equation of motion (Dyson equation):

$$\mathrm{G}_{\sigma}^{-1}(\mathrm{i}\omega_{\nu}) = \mathscr{G}_{0}^{-1}(\mathrm{i}\omega_{\nu}) - \Sigma_{\sigma}(\mathrm{i}\omega_{\nu}) = \mathrm{i}\omega_{\nu} + \mu - \varepsilon_{\mathbf{k}} - \Sigma_{\sigma}(\mathrm{i}\omega_{\nu}) \tag{37}$$

Where, $\Sigma_{\sigma}(\mathrm{i}\omega_{\nu})$ self-energy of Matsubara frequency and $\omega_{\nu} = \left[\frac{(2\nu+1)\pi}{\beta}\right]$ is the Matsubara frequency [60]. In the DMFT limit, the self-energy Σ_{σ} becomes a local quantity and the lattice Green's function retains its momentum-dependence via the non-interacting lattice dispersion ε_k.

The momentum dependent lattice Green's function in the DMFT limit is,

$$\mathrm{G}_{\sigma}(\mathrm{k}, \mathrm{i}\omega_{\nu}) = \frac{1}{\mathrm{i}\omega_{\nu} + \mu - \varepsilon_{\mathbf{k}} - \Sigma_{\sigma}(\mathrm{i}\omega_{\nu})} \tag{38}$$

Which leads to the equation for the effective Weiss field,

$$\mathscr{G}_{0}^{-1}(\mathrm{i}\omega_{\nu}) = \Sigma_{\sigma}(\mathrm{i}\omega_{\nu}) + \mathrm{G}_{\sigma}^{-1}(\mathrm{i}\omega_{\nu}) = \Sigma_{\sigma}(\mathrm{i}\omega_{\nu}) + \left[\int \frac{\mathrm{D}(\varepsilon)}{\mathrm{i}\omega_{\nu}+\mu-\varepsilon_{\mathbf{k}}-\Sigma_{\sigma}(\mathrm{i}\omega_{\nu})}\right]^{-1} \tag{39}$$

Where, $\mathrm{D}(\varepsilon)$ is the non-interacting density of states of the original lattice. And the imaginary time (thermal) Green function,

$$\mathrm{G}_{\mathrm{ij},\sigma}(\tau) = -\langle \mathrm{T} \mathrm{c}_{\mathrm{i}\sigma}(\tau) \mathrm{c}_{\mathrm{j}\sigma'}^{\dagger}(0) \rangle \rightarrow \Sigma_{\sigma}(\mathrm{i}\omega_{\nu}) \tag{40}$$

Where T is the time-ordering operator w.r.to t or τ and $\mathrm{c}_{\mathrm{i}\sigma} = \exp(\mathrm{iH}\tau)\mathrm{c}_{\mathrm{il}}\exp(-\mathrm{iH}\tau)$ in both cases [61, 62]. The Fourier transform $\mathrm{G}(\mathrm{i}\omega_{\nu})$ of $\mathrm{G}_{\mathrm{ij},\sigma}(\tau)$ and the Matsubara self-energy are computed as,

$$\Sigma_{\sigma}(\mathrm{i}\omega_{\nu}) = \mathscr{G}_{0}^{-1}(\mathrm{i}\omega_{\nu}) - \mathrm{G}_{\sigma}^{-1}(\mathrm{i}\omega_{\nu}) \tag{41}$$

This is the most expensive part of the calculation, which actually provides the new Green's function, $\mathscr{G}_0$

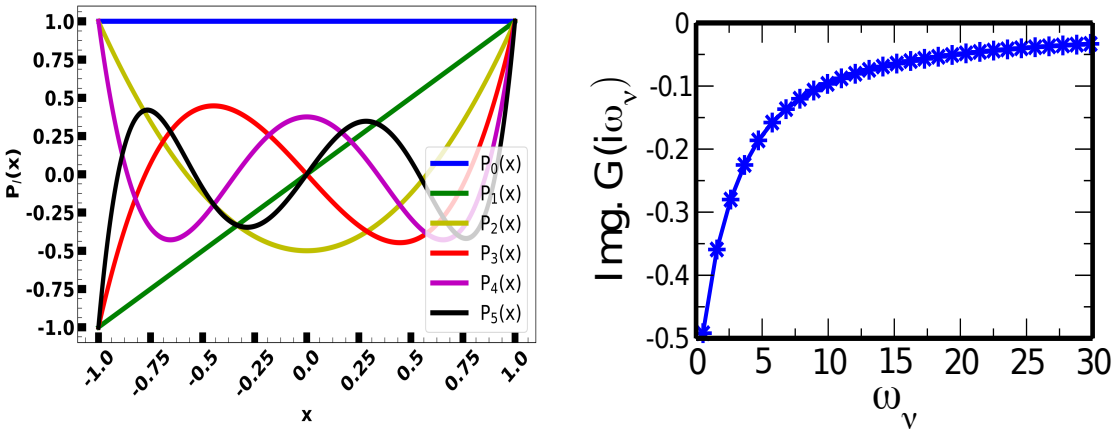

FIGURE 3. (Color online) First five orders of Legendre's polynomials of x (left). A typical outcome of calculation of Green's function of Matsubara frequency (right).

for the next iteration of self-consistency calculation [63, 64]. In the non-interacting system, the spectral function at a given momentum is a Dirac δ-function at $\omega = \varepsilon_k$,

$$A(k,\omega) = \delta(\omega - \varepsilon_k) \tag{42}$$

The possible excitation of the system is encoded in the interacting Green's function on the real axis as given by,

$$G^R(k,\omega) = \frac{1}{\omega + \mu - \varepsilon(k) + \Sigma^R(k,\omega)} \tag{43}$$

with the corresponding spectral function is,

$$A(k,\omega) = -\frac{1}{\pi}\mathrm{Im}\left[G^R(k,\omega)\right] \tag{44}$$

In the infinite coordination limit, the momentum dependence of the self-energy $\Sigma(k,\omega) \simeq \Sigma(\omega)$ .The solution of a quantum many body systems may be obtained as the solution of a quantum impurity model subject to an appropriately defined self-consistency condition. Thus, the spectral function simply be expressed as,

$$A(\omega) = -\frac{1}{\pi}\mathrm{Im}\left[G^R(\omega)\right] \tag{45}$$

The usual bandstructure (spaghetti plot) is replaced by a plot of the above spectral function, which can be compared with the experimental results of angular-resolved photoemission spectroscopy (ARPES) [13, 65]. Turning on correlations, the spectral function has a Lorentzian profile as,

$$A(k,\omega) = -\frac{1}{\pi}\frac{\mathrm{Im}\Sigma^R(k,\omega)}{\left[\omega+\mu-\varepsilon(k)+\mathrm{Re}\Sigma^R(k,\omega)\right]^2+\left[\Sigma^R(k,\omega)\right]^2} \tag{46}$$

The imaginary part of the self-energy introduces a broadening of the original Delta-function like excitation, whereas the real part is responsible for a shift of excitation energies. The program can treat data that can be expressed as the periodic imaginary time Green's function as,

$$G(i\omega_\nu) = \int_{-\infty}^{\infty} e^{i\omega_\nu} G(\tau) d\tau = \int_{-\infty}^{\infty} \frac{d\omega}{2\pi}\left(\frac{A(\omega)}{i\omega_n - \omega}\right) \tag{47}$$

Or,

$$G(\tau) = \int_{-\infty}^{\infty} \frac{d\omega}{2\pi}\left(\frac{e^{-\omega\tau}A(\omega)}{1 \pm e^{-\beta\omega}}\right), \tag{48}$$

Where ω_ν is the Matsubara frequency. The Green's function $G(\tau)$ or $G(\omega)$ as QMC data, we further apply analytic continuation method to obtain the real-frequency data, $A(\omega)$ using Maximum entropy model. The Maximum entropy model algorithm [66, 67, 68] is based on the Bayes theorem as given by,

$$P(A|G) = \frac{P(G|A)P(A)}{P(G)} \propto e^{\left(-\frac{\chi^2}{2}-\alpha S\right)}, \tag{49}$$

Where,

$$\chi^2 = \sum_i \frac{(G_i - \bar{G}_i)^2}{\sigma_i^2}. \tag{50}$$

with $\bar{G} = \mathbf{K}A$ And the differential entropy of information is,

$$S = -\int \frac{d\omega}{2\pi} A(\omega) \ln \frac{A(\omega)}{D(\omega)} \tag{51}$$

Where $D(\omega)$, is called the *default model*. For maximizing the posterior probability, we need to choose the optimal

value of α using the Bayesian inference [24, 68] as,

$$P(\alpha|G) \propto \frac{P(\alpha)}{Z_\alpha^S} \int \mathscr{D}A\, e^{\alpha S - \frac{\chi^2}{2}}, \qquad (52)$$

The value of α is then taken as the most probable one. To find the maximum, one needs a guess for the prior $P(\alpha)$.

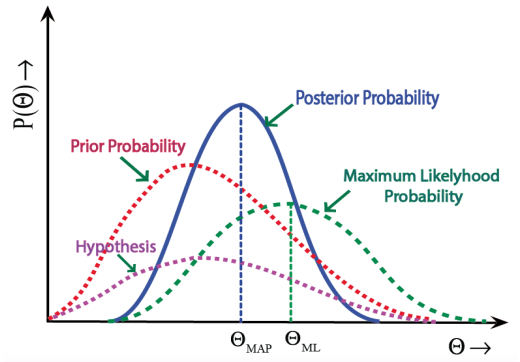

FIGURE 4. (Color online) The maximum a posteriory Θ_{MAP} is obtained through the Bayesian statistical inferences [24]

The maximum posterior probability is regarded as the realistic representation of data for the real materials. It is estimated through Bayesian theorem out of the given conditional probabilities by maximizing the entropy of information as shown in Fig.4. We have used density functional theory to calculate the density of states (DOS), which is the input data for DMFT calculation. DMFT generates the Green's function data in imaginary time or Matsubara frequency through CT-QMC algorithm with hybridization expansion, which is considered to be a rough data. The real frequency data (spectral density) are computed from the Green's function data using Maximum Entropy model, which is equivalent to the experimental observation. By analyzing spectral density, MIT is predicted with the adjustment parameters U, β and J values.

RESULTS AND DISCUSSION

The electronic structure of $La_xSr_{1-x}VO_3$ ($0 < x < 1$) system has been studied through the conventional DFT along with the DMFT. This system is the typical examples of the extended transition metal oxide system with a $3d^1$ electronic configuration. The supercell of $SrVO_3$ is reconstructed within the frameworks of $1 \times 1 \times 2$ for the ab-initio calculation. With the k-mesh grid, the Monk-horst pack of $11 \times 11 \times 5$, the convergence criteria are chosen to be 10^{-3}e, 10^{-5} eV and 0.05 eV/ ^0A respectively [69, 70, 71]. The optimized lattice parameter 4.12 ^0A and crystal structure for the sample is in Fig. 5. The conventional DFT results for DOS and Band structure of $La_xSr_{1-x}VO_3$ show the sample is metallic as in Fig.6, which is in agreement with others works [72]. The outcomes of the numerical simulation are discussed here as the followings:

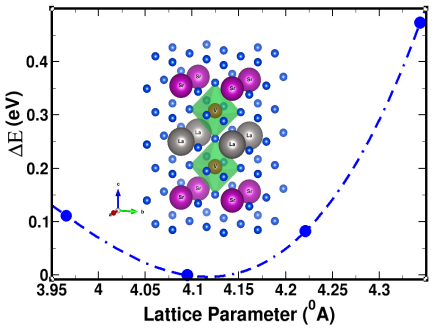

FIGURE 5. (Color online)(a) Lattice parameter optimization curve with crystal structure of $La_xSr_{1-x}VO_3$

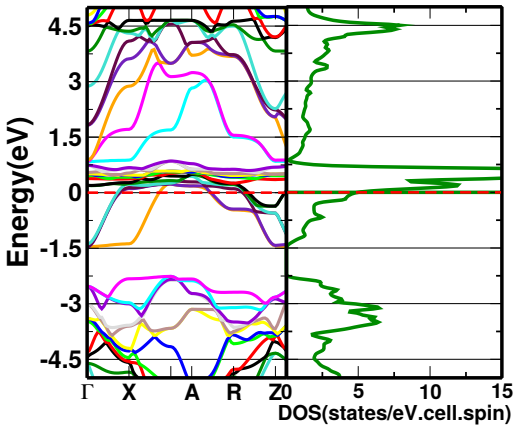

FIGURE 6. (Color online) The electronic structure (DOS and Bandstructure) of $La_xSr_{1-x}VO_3$

The characteristic QMC data, such as $G(\tau)$ or $G(\omega)$ are obtained through CT-QMC with hybridization techniques as shown in Fig. 7-10 for $La_xSr_{1-x}VO_3$ system. These data are used for analyzing Mott-Hubbard metal insulator transition at first hand. In general, the QMC data are noisy, incomplete and over-sampled one, so we need to use analytic continuation (reconstruction of data) to obtain the real frequency data for comparing the experimental results. We have used Maximum Entropy model based upon the Bayesian statistical inferences for the analytic continuation [73, 74]. In fact, it gives the spectral function $A(\omega)$ along with the error estimation of calculation.

The real frequency spectral function $A(\omega)$ is computed using the QMC data through Maximum entropy model (MEM), which works on the Bayesian statistical

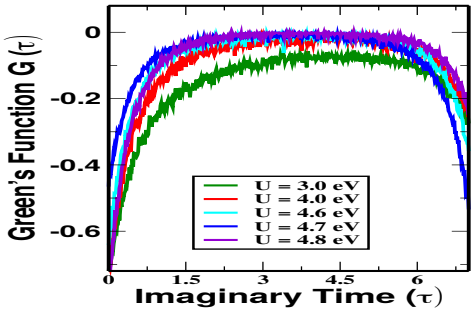

FIGURE 7. (Color online) The Green's Function vs. imaginary time (τ) of $La_{0.67}Sr_{0.33}VO_3$ with various U values

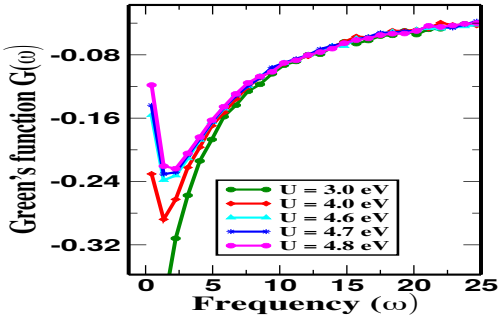

FIGURE 8. (Color online) Green's Function vs. frequency (ω) of $La_{0.67}Sr_{0.33}VO_3$ is the Fourier transform of G(τ)

inferences [75, 76]. The metal insulator transition for

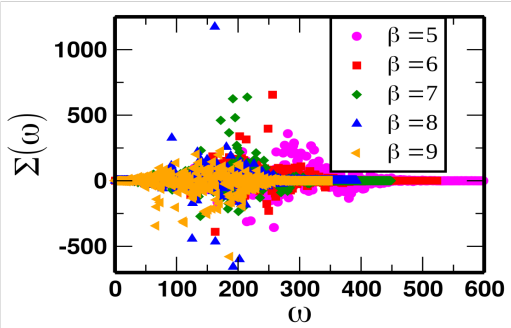

FIGURE 9. (Color online) The self-energy vs. frequency (ω) for U = 3.5 eV and various β values

$La_{0.33}Sr_{0.67}VO_3$ system is computed for U = 4.5 eV, and as in Fig. 11 which may vary with other parameters such as Hund's coupling (J) and bandwidth (W) as well.

The optimal value of hyperparameter or adjustable parameter (α) is crucial to represent the real data of the materials. For choosing the optimal value of α we use the logistic regression method for the reconstruction of data

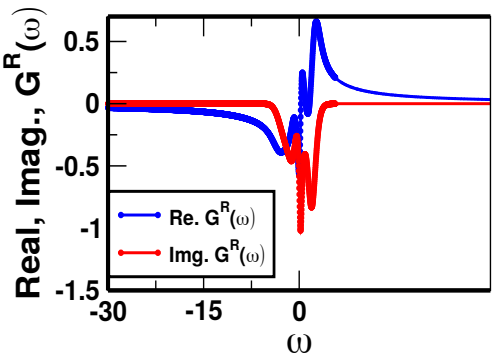

FIGURE 10. (Color online) The spectral function vs. frequency (ω) for U = 3.5 eV and various β values of $La_{0.33}Sr_{0.67}VO_3$ system.

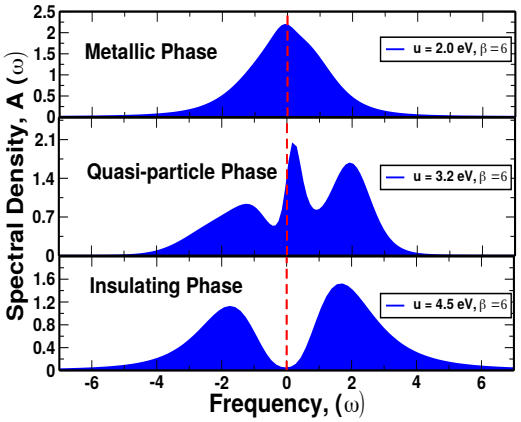

FIGURE 11. (Color online)The variation of spectral function A(ω) with U values for the optimal value of α

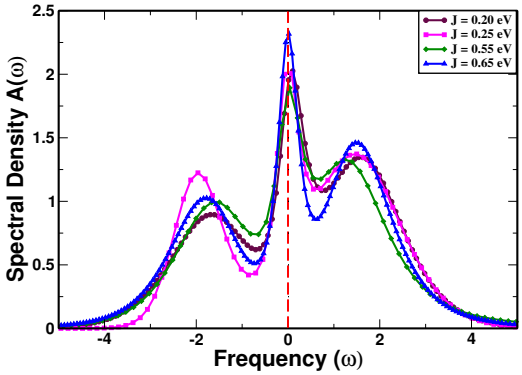

FIGURE 12. (Color online) The distribution of spectral function A(ω) with the various values of J.

A(ω) from the QMC data G(τ). The lower part of the information-fitting region as in Fig. 13 are chosen to be

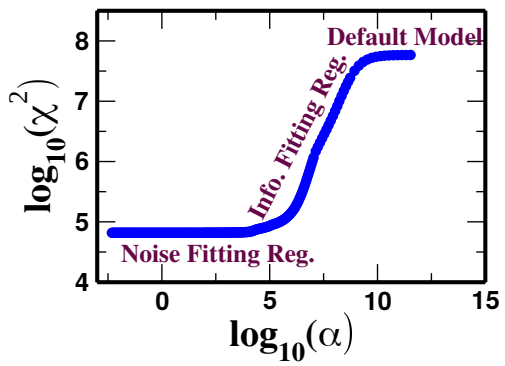

FIGURE 13. (Color online) The logistic regression curve for choosing the optimal value of for better representation of data obtained through MEM

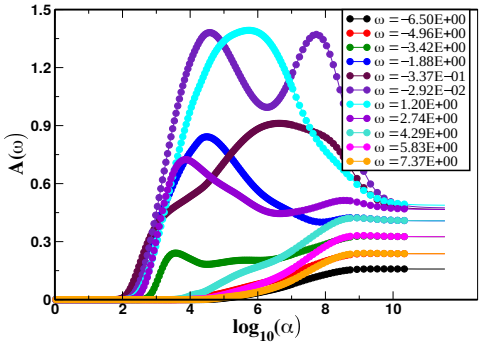

FIGURE 14. (Color online) The distribution of spectral function A(ω) with the sample frequencies for the optimal value of α .

optimal value of α, which is determined by the maximum value of the curvature of $\log_{10}\chi^2$ vs. $\gamma\log_{10}\alpha$ curve [77]. We may also use sample frequencies for predicting the optimal values of α as in Fig. 14. The statistical error

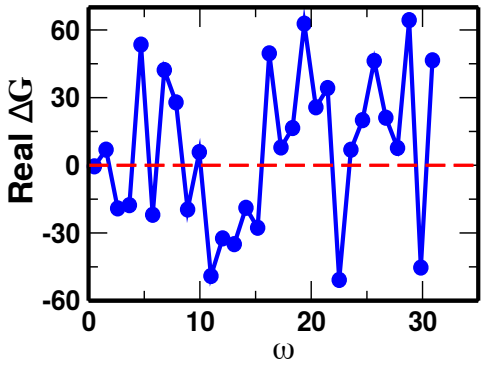

FIGURE 15. (Color online) The normalized deviation (ND) of real part of ΔG for the data computed with MEM

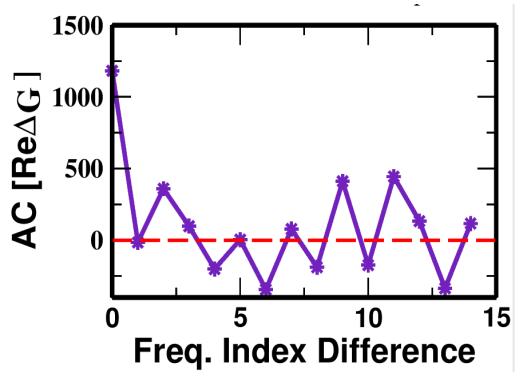

FIGURE 16. (Color online) The autocorrelation (AC) of real part of ΔG for the data computed with MEM.

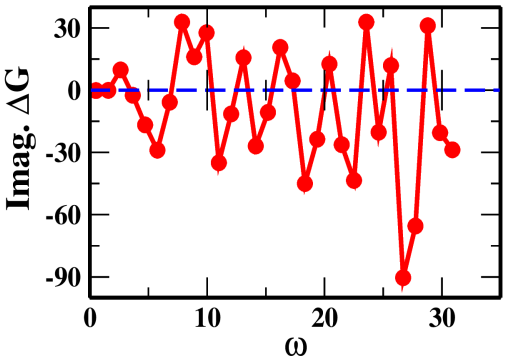

FIGURE 17. (Color online) The normalized deviation (ND) of imaginary part of ΔG for the data computed with MEM.

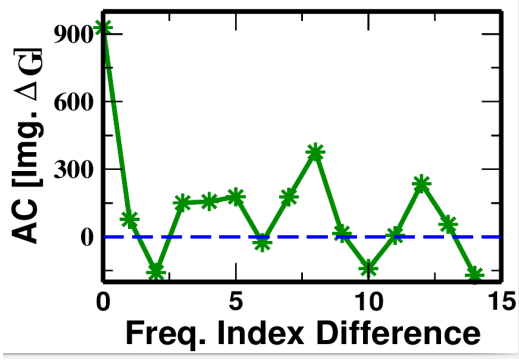

FIGURE 18. (Color online) The autocorrelation (AC) of imaginary part of ΔG for the data computed with MEM.

such as the normalized deviation of real and imaginary parts of the uncertainty of Green's function of frequency ΔG and its auto correlation are computed within the permissible standard error bar Fig. 15-18 [78, 79, 80, 81, 82, 83].

CONCLUSIONS

We review the theoretical concept of DFT +DMFT approximation to calculate the electronic properties of strongly correlated system through CT-QMC algorithm as an impurity solver. Implementation of Maximum Entropy model for the real frequency data (spectral function) to investigate the Mott-Hubbard MIT is also discussed. From the calculation, the lattice parameters of optimized $La_xSr_{1-x}VO_3$ are a = 4.12 ^{0}A, b = 4.12 ^{0}A and c = 7.93^{0}A. The electronic band structure from conventional DFT shows metallic behavior of the sample. However, after the application of DMFT with CT-QMC hybridization expansion it turns out to be a Mott insulator at U = 4.5 eV, and $\beta = 6(\text{eV})^{-1}$. The optimal value of adjustable parameter α is obtained through logistic regression. Statistical error confirms that present calculation are within the permissible error bar limit.

ACKNOWLEDGMENTS

The authors are gratefully acknowledged to UGC and NAST for their financial supports. CDP of TU and HPC of KU are also acknowledged for their computational resources. We also acknowledge the ALPS open source library for our calculation.

EDITOR'S NOTE

This manuscript was submitted to the Association of Nepali Physicists in America (ANPA) Conference 2021 for publication in the special issue of Journal of Nepal Physical Society.

REFERENCES

1. K Held. Electronic structure calculations using dynamical mean field theory. *Advances in physics*, 56(6):829–926, 2007.
2. Walter Metzner and Dieter Vollhardt. Correlated lattice fermions in $\mathbf{d} = \infty$dimensions. *Physical review letters*, 62(3):324, 1989.
3. Nevill F Mott. The basis of the electron theory of metals, with special reference to the transition metals. *Proceedings of the Physical Society. Section A*, 62(7):416, 1949.
4. Masatoshi Imada, Atsushi Fujimori, and Yoshinori Tokura. Metal-insulator transitions. *Reviews of modern physics*, 70(4):1039, 1998.
5. C Bell, S Harashima, Y Kozuka, M Kim, Bog G Kim, Y Hikita, and HY Hwang. Dominant mobility modulation by the electric field effect at the laalo 3/srtio 3 interface. *Physical review letters*, 103(22):226802, 2009.
6. Minjae Kim and BI Min. Nature of itinerant ferromagnetism of srruo 3: A dft+ dmft study. *Physical Review B*, 91(20):205116, 2015.
7. S Streltsov, II Mazin, and K Foyevtsova. Localized itinerant electrons and unique magnetic properties of srru 2 o 6. *Physical Review B*, 92(13):134408, 2015.
8. Alexey N Rubtsov, Vladimir V Savkin, and Alexander I Lichtenstein. Continuous-time quantum monte carlo method for fermions. *Physical Review B*, 72(3):035122, 2005.
9. Andreas Dirks, Philipp Werner, Mark Jarrell, and Thomas Pruschke. Continuous-time quantum monte carlo and maximum entropy approach to an imaginary-time formulation of strongly correlated steady-state transport. *Physical Review E*, 82(2):026701, 2010.
10. B Chatterjee, J Skolimowski, K Makuch, and K Byczuk. Real-space dynamical mean-field theory of friedel oscillations in strongly correlated electron systems. *Physical Review B*, 100(11):115118, 2019.
11. Nicolaus Parragh, Alessandro Toschi, Karsten Held, and Giorgio Sangiovanni. Conserved quantities of s u (2)-invariant interactions for correlated fermions and the advantages for quantum monte carlo simulations. *Physical Review B*, 86(15):155158, 2012.
12. Alexander Kowalski, Andreas Hausoel, Markus Wallerberger, Patrik Gunacker, and Giorgio Sangiovanni. State and superstate sampling in hybridization-expansion continuous-time quantum monte carlo. *Physical Review B*, 99(15):155112, 2019.
13. Akira Sekiyama and Shigemasa Suga. High-energy bulk-sensitive angle-resolved photoemission study of strongly correlated systems. *Journal of electron spectroscopy and related phenomena*, 137:681–685, 2004.
14. JH Shim, Kristjan Haule, and G Kotliar. X-ray absorption branching ratio in actinides: Lda+ dmft approach. *EPL (Europhysics Letters)*, 85(1):17007, 2009.
15. Gabriel Kotliar and Dieter Vollhardt. Strongly correlated materials: Insights from dynamical mean-field theory. *Physics today*, 57(3):53–60, 2004.
16. VI Anisimov, DE Kondakov, AV Kozhevnikov, IA Nekrasov, ZV Pchelkina, JW Allen, S-K Mo, H-D Kim, P Metcalf, S Suga, et al. Full orbital calculation scheme for materials with strongly correlated electrons. *Physical Review B*, 71(12):125119, 2005.
17. Frank Lechermann, Alexander I Lichtenstein, and Michael Potthoff. Realistic many-body approaches to materials with strong nonlocal correlations. *The European Physical Journal Special Topics*, 226(11):2591–2613, 2017.
18. B Amadon, F Lechermann, A Georges, F Jollet, TO Wehling, and AI Lichtenstein. Plane-wave based electronic structure calculations for correlated materials using dynamical mean-field theory and projected local orbitals. *Physical Review B*, 77(20):205112, 2008.
19. F Aryasetiawan, M Imada, A Georges, G Kotliar, S Biermann, and AI Lichtenstein. Frequency-dependent local interactions and low-energy effective models from electronic structure calculations. *Physical Review B*, 70(19):195104, 2004.
20. Antoine Georges, Gabriel Kotliar, Werner Krauth, and Marcelo J Rozenberg. Dynamical mean-field theory of strongly correlated fermion systems and the limit of infinite dimensions. *Reviews of Modern Physics*, 68(1):13, 1996.
21. Sandro Sorella. Generalized lanczos algorithm for variational quantum monte carlo. *Physical Review B*, 64(2):024512, 2001.
22. Daisuke Tahara and Masatoshi Imada. Variational monte carlo method combined with quantum-number projection and multivariable optimization. *Journal of the Physical Society of Japan*, 77(11):114701, 2008.
23. Jan M Tomczak and Silke Biermann. 8 scientific highlight of the month:" optical properties of correlated materials–or why intelligent windows may look dirty".
24. Dominic Bergeron and A-MS Tremblay. Algorithms for optimized maximum entropy and diagnostic tools for analytic continuation. *Physical Review E*, 94(2):023303, 2016.
25. Dominic Bergeron. ■maxent user guide. 2016.

26. Pavlo Zubko, Stefano Gariglio, Marc Gabay, Philippe Ghosez, and Jean-Marc Triscone. Interface physics in complex oxide heterostructures. *Annu. Rev. Condens. Matter Phys.*, 2(1):141–165, 2011.
27. Motoaki Hirayama, Takashi Miyake, and Masatoshi Imada. Ab initio low-energy model of transition-metal-oxide heterostructure laalo3/srtio3. *Journal of the Physical Society of Japan*, 81(8):084708, 2012.
28. AV Mahajan, DC Johnston, DR Torgeson, and F Borsa. Magnetic and electronic properties of laxsr1- xvo3. *Physica C: Superconductivity*, 185:1195–1196, 1991.
29. Igor A Nekrasov, Georg Keller, DE Kondakov, AV Kozhevnikov, Th Pruschke, Karsten Held, Dieter Vollhardt, and VI Anisimov. Comparative study of correlation effects in ca v o 3 and sr v o 3. *Physical Review B*, 72(15):155106, 2005.
30. Marcus Kollar. The foundations of dynamical mean-field theory. 2018.
31. Ciro Taranto, M Kaltak, N Parragh, G Sangiovanni, Georg Kresse, A Toschi, and K Held. Comparing quasiparticle g w+ dmft and lda+ dmft for the test bed material srvo 3. *Physical Review B*, 88(16):165119, 2013.
32. Peter Anders, Emanuel Gull, Lode Pollet, Matthias Troyer, Philipp Werner, Michael Bachmann, and Ofer Biham. Diagrammatic monte carlo method for bosonic impurity problems. *Chem. Phys*, 127:144703, 2007.
33. JE Gubernatis, Mark Jarrell, RN Silver, and DS Sivia. Quantum monte carlo simulations and maximum entropy: Dynamics from imaginary-time data. *Physical Review B*, 44(12):6011, 1991.
34. Matthew D Pickett, Gilberto Medeiros-Ribeiro, and R Stanley Williams. A scalable neuristor built with mott memristors. *Nature materials*, 12(2):114–117, 2013.
35. Karsten Held, IA Nekrasov, G Keller, Volker Eyert, Nils Blümer, AK McMahan, RT Scalettar, Th Pruschke, VI Anisimov, and Dieter Vollhardt. Realistic investigations of correlated electron systems with lda+ dmft. *physica status solidi (b)*, 243(11):2599–2631, 2006.
36. Antoine Georges, Gabriel Kotliar, Werner Krauth, and Marcelo J Rozenberg. Dynamical mean-field theory of strongly correlated fermion systems and the limit of infinite dimensions. *Reviews of Modern Physics*, 68(1):13, 1996.
37. John Hubbard. Electron correlations in narrow energy bands. *Proceedings of the Royal Society of London. Series A. Mathematical and Physical Sciences*, 276(1365):238–257, 1963.
38. Steffen Backes. Density functional theory and dynamical mean-field theory. a way to model strongly correlated systems. 2017.
39. Emilia Morosan, Douglas Natelson, Andriy H Nevidomskyy, and Qimiao Si. Strongly correlated materials. *Advanced Materials*, 24(36):4896–4923, 2012.
40. Dieter Vollhardt. Dynamical mean-field theory for correlated electrons. *Annalen der Physik*, 524(1):1–19, 2012.
41. Hung T Dang, Xinyuan Ai, Andrew J Millis, and Chris A Marianetti. Density functional plus dynamical mean-field theory of the metal-insulator transition in early transition-metal oxides. *Physical Review B*, 90(12):125114, 2014.
42. Lucas K Wagner. Transition metal oxides using quantum monte carlo. *Journal of Physics: Condensed Matter*, 19(34):343201, 2007.
43. IA Nekrasov, NS Pavlov, and MV Sadovskii. Consistent lda'+ dmft approach to the electronic structure of transition metal oxides: Charge transfer insulators and correlated metals. *Journal of Experimental and Theoretical Physics*, 116(4):620–634, 2013.
44. Shintaro Hoshino and Yoshio Kuramoto. Itinerant versus localized heavy-electron magnetism. *Physical review letters*, 111(2):026401, 2013.
45. Philipp Werner, Armin Comanac, Luca De'Medici, Matthias Troyer, and Andrew J Millis. Continuous-time solver for quantum impurity models. *Physical Review Letters*, 97(7):076405, 2006.
46. Lode Pollet, Kris Van Houcke, and Stefan MA Rombouts. Engineering local optimality in quantum monte carlo algorithms. *Journal of Computational Physics*, 225(2):2249–2266, 2007.
47. Bela Bauer, LD Carr, Hans Gerd Evertz, Adrian Feiguin, J Freire, S Fuchs, Lukas Gamper, Jan Gukelberger, E Gull, Siegfried Guertler, et al. The alps project release 2.0: open source software for strongly correlated systems. *Journal of Statistical Mechanics: Theory and Experiment*, 2011(05):P05001, 2011.
48. EY Loh Jr, JE Gubernatis, RT Scalettar, SR White, DJ Scalapino, and RL Sugar. Sign problem in the numerical simulation of many-electron systems. *Physical Review B*, 41(13):9301, 1990.
49. ML Reinle-Schmitt, C Cancellieri, Danfeng Li, Denis Fontaine, M Medarde, E Pomjakushina, CW Schneider, Stefano Gariglio, Ph Ghosez, J-M Triscone, et al. Tunable conductivity threshold at polar oxide interfaces. *Nature communications*, 3(1):1–6, 2012.
50. Emanuel Gull, Philipp Werner, Olivier Parcollet, and Matthias Troyer. Continuous-time auxiliary-field monte carlo for quantum impurity models. *EPL (Europhysics Letters)*, 82(5):57003, 2008.
51. IA Nekrasov, EE Kokorina, EZ Kuchinskii, MV Sadovskii, S Kasai, A Sekiyama, and S Suga. Arpes spectral functions and fermi surface for la 1.86 sr 0.14 cuo 4 compared with lda+ dmft+ σ k calculations. *Journal of Experimental and Theoretical Physics*, 110(6):989–994, 2010.
52. Emanuel Gull. *Continuous-time quantum Monte Carlo algorithms for fermions*. PhD thesis, ETH Zurich, 2008.
53. Kristjan Haule. Quantum monte carlo impurity solver for cluster dynamical mean-field theory and electronic structure calculations with adjustable cluster base. *Physical Review B*, 75(15):155113, 2007.
54. Gabriel Kotliar, Sergej Y Savrasov, Kristjan Haule, Viktor S Oudovenko, O Parcollet, and CA Marianetti. Electronic structure calculations with dynamical mean-field theory. *Reviews of Modern Physics*, 78(3):865, 2006.
55. Steven R White. Density matrix formulation for quantum renormalization groups. *Physical review letters*, 69(19):2863, 1992.
56. H Makino, IH Inoue, MJ Rozenberg, F Iga, Y Aiura, and S Onari. Optical spectra of the correlated metallic system ca1- xsrxvo3. *Physica B: Condensed Matter*, 237:56–58, 1997.
57. Mauro Iazzi and Matthias Troyer. Efficient continuous-time quantum monte carlo algorithm for fermionic lattice models. *Physical Review B*, 91(24):241118, 2015.
58. Lewin Boehnke, Hartmut Hafermann, Michel Ferrero, Frank Lechermann, and Olivier Parcollet. Orthogonal polynomial representation of imaginary-time green's functions. *Physical Review B*, 84(7):075145, 2011.
59. Alessandro Toschi, AA Katanin, and Karsten Held. Dynamical vertex approximation: A step beyond dynamical mean-field theory. *Physical Review B*, 75(4):045118, 2007.
60. Robert Peters and Thomas Pruschke. Half-filled hubbard model on a bethe lattice with next-nearest-neighbor hopping. *Physical Review B*, 79(4):045108, 2009.
61. Gabriel Kotliar, Sergej Y Savrasov, Gunnar Pálsson, and Giulio Biroli. Cellular dynamical mean field approach to strongly correlated systems. *Physical review letters*, 87(18):186401, 2001.
62. Satoshi Okamoto, Andrew J Millis, Hartmut Monien, and Andreas Fuhrmann. Fictive impurity models: An alternative formulation of the cluster dynamical mean-field method. *Physical Review B*, 68(19):195121, 2003.
63. Eva Pavarini, Erik Koch, Dieter Vollhardt, and Alexander Lichtenstein. *Dmft at 25: Infinite dimensions: Lecture notes of the autumn school on correlated electrons 2014*, volume 4. Forschungszentrum Jülich, 2014.
64. Michael Potthoff. Self-energy-functional approach to systems of correlated electrons. *The European Physical Journal B-Condensed Matter and Complex Systems*, 32(4):429–436, 2003.
65. Andreas Fuhrmann, Satoshi Okamoto, Hartmut Monien, and Andrew J Millis. Fictive-impurity approach to dynamical mean-

field theory: A strong-coupling investigation. *Physical Review B*, 75(20):205118, 2007.
66. Robert O Jones and Olle Gunnarsson. The density functional formalism, its applications and prospects. *Reviews of Modern Physics*, 61(3):689, 1989.
67. Richard N Silver, Devinderjit S Sivia, and James E Gubernatis. Maximum-entropy method for analytic continuation of quantum monte carlo data. *Physical Review B*, 41(4):2380, 1990.
68. Mark Jarrell, Th Maier, C Huscroft, and S Moukouri. Quantum monte carlo algorithm for nonlocal corrections to the dynamical mean-field approximation. *Physical Review B*, 64(19):195130, 2001.
69. Gopi Chandra Kaphle, Shreemoyee Ganguly, Rudra Banerjee, Radheshyam Banerjee, Rabi Khanal, Chandra Mani Adhikari, Narayan Prasad Adhikari, and Abhijit Mookerjee. A study of magnetism in disordered pt–mn, pd–mn and ni–mn alloys: an augmented space recursion approach. *Journal of Physics: Condensed Matter*, 24(29):295501, 2012.
70. P Blaha, K Schwarz, GK Madsen, D Kvasnicka, and J Luitz. Wien2k: An augmented plane wave plus local orbitals program for. *Calculating Crystal Properties, Karlheinz Schwarz, Techn. Universitat Wien*, 2001.
71. Durga Paudyal, VK Pecharsky, and KA Gschneidner Jr. Electronic structure, magnetic properties, and magnetostructural transformations in rare earth dialuminides. *Journal of Applied Physics*, 115(17):17E127, 2014.
72. Alyn DN James, Markus Aichhorn, and James Laverock. Quantum confinement induced metal-insulator transition in strongly correlated quantum wells of srvo 3 superlattices. *Physical Review Research*, 3(2):023149, 2021.
73. Anders W Sandvik. Constrained sampling method for analytic continuation. *Physical Review E*, 94(6):063308, 2016.
74. Evan Sheridan, Cédric Weber, Evgeny Plekhanov, and Christopher Rhodes. Continuous-time quantum monte carlo solver for dynamical mean field theory in the compact legendre representation. *Physical Review B*, 99(20):205156, 2019.
75. Emanuel Gull, Andrew J Millis, Alexander I Lichtenstein, Alexey N Rubtsov, Matthias Troyer, and Philipp Werner. Continuous-time monte carlo methods for quantum impurity models. *Reviews of Modern Physics*, 83(2):349, 2011.
76. O Gunnarsson, MW Haverkort, and G Sangiovanni. Analytical continuation of imaginary axis data for optical conductivity. *Physical Review B*, 82(16):165125, 2010.
77. E Müller-Hartmann. Correlated fermions on a lattice in high dimensions. *Zeitschrift für Physik B Condensed Matter*, 74(4):507–512, 1989.
78. Anders W Sandvik and Juhani Kurkijärvi. Quantum monte carlo simulation method for spin systems. *Physical Review B*, 43(7):5950, 1991.
79. Walter Kohn and Lu Jeu Sham. Self-consistent equations including exchange and correlation effects. *Physical review*, 140(4A):A1133, 1965.
80. Eva Pavarini, Dieter Vollhardt, Erik Koch, and Alexander Lichtenstein. Dmft: From infinite dimensions to real materials. Technical report, Theoretische Nanoelektronik, 2018.
81. R Martin. Electronic structure–basic theory and practical methods, cambridge univ. *Pr., West Nyack, NY*, 2004.
82. MJ Veit, MK Chan, BJ Ramshaw, Rémi Arras, R Pentcheva, and Y Suzuki. Three-dimensional character of the fermi surface in ultrathin latio 3/srtio 3 heterostructures. *Physical Review B*, 99(11):115126, 2019.
83. KSD Beach, RJ Gooding, and F Marsiglio. Reliable padé analytical continuation method based on a high-accuracy symbolic computation algorithm. *Physical Review B*, 61(8):5147, 2000.